



HAL
open science

Evaluation of GNSS and C2Link jamming margins

Guillaume Novella

► **To cite this version:**

Guillaume Novella. Evaluation of GNSS and C2Link jamming margins. Other [cs.OH]. Institut National Polytechnique de Toulouse - INPT, 2023. English. NNT : 2023INPT0037 . tel-04521688

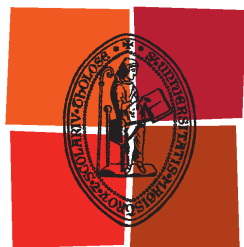
HAL Id: tel-04521688

<https://theses.hal.science/tel-04521688>

Submitted on 26 Mar 2024

HAL is a multi-disciplinary open access archive for the deposit and dissemination of scientific research documents, whether they are published or not. The documents may come from teaching and research institutions in France or abroad, or from public or private research centers.

L'archive ouverte pluridisciplinaire **HAL**, est destinée au dépôt et à la diffusion de documents scientifiques de niveau recherche, publiés ou non, émanant des établissements d'enseignement et de recherche français ou étrangers, des laboratoires publics ou privés.



Université
de Toulouse

THÈSE

En vue de l'obtention du

DOCTORAT DE L'UNIVERSITÉ DE TOULOUSE

Délivré par :

Institut National Polytechnique de Toulouse (Toulouse INP)

Discipline ou spécialité :

Informatique et Télécommunication

Présentée et soutenue par :

M. GUILLAUME NOVELLA

le vendredi 10 février 2023

Titre :

Evaluation des marges de brouillage GNSS et C2Link drones

Ecole doctorale :

Mathématiques, Informatique, Télécommunications de Toulouse (MITT)

Unité de recherche :

Laboratoire de Télécommunications (TELECOM-ENAC)

Directeur(s) de Thèse :

M. CHRISTOPHE MACABIAU

M. AXEL JAVIER GARCIA PEÑA

Rapporteurs :

T ÈDENPIS T ĚAKOS, UNIVERSITY OF COLORADO AT BOULDER

T ÈMARCO LUISE, UNIVERSITA DI PISA

Membre(s) du jury :

MME MARIE-LAURE BOUCHERET, TOULOUSE INP, Président^

M. AXEL JAVIER GARCIA PENA, ECOLE NATIONALE DE L'AVIATION CIVILE, Membre

M. CHRISTOPHE MACABIAU, ECOLE NATIONALE DE L'AVIATION CIVILE, Membre

M. CHRISTOPHER HEGARTY, MITRE Corporation, Membre

MME CATHERINE RONFLE-NADAUD, DIRECTION GENERALE DE L'AVIATION CIVILE, Membre

M. PIERRE LADOUX, DIRECTION GENERALE DE L'AVIATION CIVILE, Membre

Abstract

In 2012, the international telecommunications union (ITU) adopted a new terrestrial allocation for aeronautical mobile route service (AM(R)S) in the frequency band 5030-5091 MHz. Also, ITU WRC-12 (world radiocommunications conference) adopted resolution No.5.443D, which highlights the advantage of this frequency band for aeronautical mobile satellite route system (AMS(R)S). One aeronautical system which is a candidate for an authorization to use the 5030-5091 MHz frequency band is the drone command and control link (C2Link). C2Link in this frequency band is indeed the drone command and control communication system under consideration at an ICAO (International Civil Aviation Organization) level for future drone operations in non-segregated airspace.

Jamming is the main tool which is currently considered by military authorities for defense against rogue drone purpose. During anti-drone jamming or during state GNSS jamming exercises, some non-targeted drones or aircrafts may be hit by the jamming signal and loose the GNSS and C2Link services. However, the determination of the distance at which a GNSS and C2Link receiver performance objectives may not be met is currently widely over-estimated. An over-estimation may cause efficiency and economic problems as aircrafts may be requested to avoid the zone which is assumed to be impacted by the jamming signal, and such a request may increase the flight path.

As a consequence, a request from the French ANSP (Air Navigation Service Provider) is to improve the precision of the calculation of the impacted area during C2Link and GNSS jamming operations. To provide an answer to this problematic requires the characterization of the capacity of GNSS and C2Link receivers to meet minimum performance objectives. Also, a precise characterization of the interference environment encountered by GNSS and C2Link victim receivers must be conducted.

In last decade, the number of GNSS jamming events reported by civil aviation and caused by illegal civil jammers called portable privacy devices (PPD) has increased. These jammers often use a remarkable chirp waveform. This characteristic waveform is also the signature of modern jamming guns which are used for military jamming exercises. The impact of these chirp signals on GNSS receiver performance degradation, although widely observed in the literature, remains difficult to be predicted because of the influence of many parameters. One objective of this PhD is therefore to propose a characterization model of the impact of chirp jamming signal on several GNSS performance indicators: carrier to noise power spectral density ratio (C/N_0), code and phase measurements.

This PhD is also motivated by on-going standardization activities for a new generation of GNSS receivers, called dual frequency multi constellation (DFMC) GNSS receiver. DFMC receiver is expected to have better performances than the legacy receiver (current generation, which only processes GPS L1C/A and SBAS L1 signals), since DFMC receiver will process GPS, Galileo and SBAS signals on both the L1 and L5 frequency bands. This PhD has contributed to the following standardization activities. First, the revision of the ICAO SARPS (Standards and Recommended Practices, adopted in November 2021) defines the GNSS interference mask for DFMC receivers. Second, RTCA DO-235C (adopted in July 2021) characterizes the L1/E1 interference environment for legacy and DFMC receivers. Third, RTCA DO-292A (expected for November 2022) characterizes the L5/E5a interference environment for legacy and DFMC receivers. Fourth, Eurocae ED-259A defines test procedures for DFMC receiver certification.

Keywords

GNSS, C2Link, RPAS, civil aviation, interference, jamming, C/N_0 , chirp, PPD

Acknowledgements

I would like to express here my acknowledgements to people who have contributed to the good progress of this thesis.

I acknowledge my reviewers, Dennis Akos from Boulder University of Colorado and Marco Luise from University of Pisa for having accepted to review this thesis.

I also thank my PhD supervisors Christophe Macabiau and Axel Garcia Peña for their advice and supervision during these last three years, and for letting me participate to civil aviation standardization activities. I would like to thank Anaïs Martineau for following my research activities during my thesis as well.

This thesis subject has been chosen by the French civil aviation authorities (Direction Générale de l'Aviation Civile) so I thank the people involved in that choice for their confidence. In particular, I acknowledge Pierre Ladoux, Philippe Estival, Olivier Troubet-Lacoste, Christian Fleury and Catherine Ronfle-Nadaud from the Direction des Services de la Navigation Aérienne (the French Air Navigation Service Provider, ANSP) for having followed this PhD, and for their availability to answer my questions.

Table of contents

Chapitre 0: Résumé en français	15
0-1 Introduction.....	15
0-2 Marges de brouillage GNSS	16
0-3 Impact des interférences de type « chirp » sur les performances des récepteurs aviation civile 18	
0-4 Impact des interférences sur la performance des récepteurs C2Link.....	21
Chapter 1: Introduction.....	23
1-1 Context and motivation.....	23
1-2 Innovations brought in this Ph.D. thesis	24
1-3 Thesis organization.....	27
1-4 Main products of the PhD thesis.....	28
Chapter 2: Impact of interferences on civil aviation GNSS receivers.....	31
2-1 Introduction on GNSS.....	31
2-1.1 GNSS definition.....	31
2-1.1.1 GNSS constellations.....	31
2-1.1.1.1 Satellite navigation systems.....	32
2-1.1.1.2 Augmentation systems	32
2-1.1.2 ICAO GNSS minimum performances	33
2-1.2 GNSS principle	35
2-2 GNSS signals modulation.....	35
2-2.1 GPS L1C/A signal.....	36
2-2.1.1 GPS L1C/A mathematical signal.....	36
2-2.1.2 Spectrum properties of the GPS L1C/A PRN signal	36
2-2.2 Galileo E1 signal.....	39
2-2.2.1 Galileo E1 mathematical signal	39
2-2.2.2 Galileo E1 spectrum.....	39
2-2.3 GPS L5 signal.....	41
2-2.3.1 GPS L5 signal.....	41
2-2.3.2 GPS L5 spectrum.....	42
2-2.4 Galileo E5 signal.....	42
2-2.5 Summary on GNSS signals	43
2-3 GNSS signal processing.....	44
2-3.1 Generic GNSS receiver.....	44
2-3.2 Received GNSS signal at antenna port	46

2-3.3	GNSS signal processing	47
2-3.3.1	Correlation	48
2-3.3.1.1	Correlation of GNSS signal	48
2-3.3.1.2	Correlation of the noise	51
2-3.3.1.3	Impact of correlation on signal to noise ratio (SNR)	52
2-3.3.2	Acquisition	53
2-3.3.2.1	GPS L1C/A acquisition strategy	53
2-3.3.2.2	Alternative strategy for GNSS signals with two components	56
2-3.3.3	Tracking	56
2-3.3.3.1	Phase lock loop (PLL)	57
2-3.3.3.2	Delay lock loop	58
2-3.4	C/N_0 estimation	60
2-3.4.1	Mathematical definition of C	60
2-3.4.2	C/N_0 estimation algorithms	61
2-4	Impact of interferences on GNSS receiver	62
2-4.1	RFI model at the RF front-end output	62
2-4.2	RFI power at the correlator output	62
2-4.3	Impact of RFI on GNSS receiver performance	64
2-4.3.1	Signal to noise plus interference ratio and RFI equivalent noise	64
2-4.3.2	Impact of RFI on C/N_0	65
2-5	Interference environment	67
2-5.1	Aeronautical RFI sources	67
2-5.2	Non-aeronautical RFI sources	68
2-5.3	Classical jamming signals	69
2-5.3.1	Rectangular RFI	69
2-5.3.2	Chirp RFI	70
2-6	Review of GNSS regulation	71
2-6.1	GNSS signal RF characteristics	71
2-6.2	GNSS receiver characteristics	72
2-6.3	GNSS RFI masks	74
2-7	Conclusion	75
Chapter 3:	C2Link Signal Processing and Civil Aviation Requirements	76
3-1	From UAS to RPAS operations in non-segregated airspace	78
3-1.1	ICAO UAS definition and classification	78
3-1.2	RPAS concept	78
3-1.2.1	RPAS	78

3-1.2.2	ICAO RPAS regulation	79
3-1.2.3	French RPAS regulation	80
3-1.2.3.1	RPAS categories.....	80
3-1.2.3.2	Open category.....	81
3-1.2.3.3	Specific category	81
3-1.2.3.4	Certified category.....	82
3-1.3	Concept of C2Link.....	83
3-1.3.1	C2Link information	83
3-1.3.2	C2Link architecture.....	84
3-2	C2Link signal and civil aviation requirements	86
3-2.1	C2Link civil aviation Required Link Performance	86
3-2.2	5GHz C2Link frequency band	87
3-2.3	C2Link requirements	88
3-2.3.1	Data class definition	88
3-2.3.2	Subframe error rate threshold	89
3-2.4	C2Link signal definition.....	89
3-2.4.1	Channel division method and channel coding	89
3-2.4.2	Data rate.....	90
3-2.4.3	Modulation	90
3-2.4.4	Power.....	90
3-2.4.5	Spectral occupation.....	91
3-3	Mathematical model of DO-362 C2Link signal	92
3-4	Conclusion	94
Chapter 4:	GNSS interference mask and protection area during jamming operations	95
4-1	RFI mask: elaboration, interpretation, limitation.....	96
4-1.1	Presentation of GNSS RFI masks	96
4-1.2	Traditional methodology for jamming protection area determination	96
4-1.2.1	Traditional methodology to determine jamming protection area.....	97
4-1.2.2	Limitation of the traditional methodology.....	97
4-2	New methodology for jamming protection area determination	98
4-2.1	Step 1: C/N_0 link budget and allowable non-aeronautical equivalent noise	101
4-2.1.1	Presentation of C/N_0 link budget	101
4-2.1.2	Step 1.1: Recovered useful GNSS signal power.....	102
4-2.1.3	Step 1.2: Effective noise in presence of aeronautical RFI	105
4-2.1.3.1	L1/E1 effective noise in presence of aeronautical RFI.....	105
4-2.1.3.2	Aeronautical RFI equivalent noise.....	105

4-2.1.3.2.1	AMSS equivalent noise.....	106
4-2.1.3.2.2	Case emission equivalent noise	106
4-2.1.3.2.3	Inter intra system RFI equivalent noise	107
4-2.1.4	Step 1.3: Link budget margin and maximum tolerated non-aeronautical equivalent noise	110
4-2.2	Non-aeronautical RFI equivalent noise	110
4-2.2.1	On-board portable electronic devices.....	111
4-2.2.2	Terrestrial emitters.....	111
4-2.2.2.1	Terrestrial emitters equivalent noise.....	112
4-2.2.2.2	Input parameters for $I_{0,terr}$ calculation.....	113
4-2.2.2.2.1	Transmitted EIRP P_0 by each terrestrial source	113
4-2.2.2.2.2	GNSS receiver antenna gain.....	114
4-2.2.2.2.3	Propagation channel model.....	114
4-2.2.2.2.4	Distribution of terrestrial emitters.....	115
4-2.2.3	Jammer equivalent noise	117
4-2.3	Determination of the protection area.....	118
4-3	Derivation of the protection zone on an illustrative jamming scenario	118
4-3.1	Jamming scenario description	118
4-3.2	Protection radius with the new methodology	119
4-3.2.1	Step 1: Maximum tolerable non-aeronautical equivalent noise.....	119
4-3.2.1.1	Step 1.1	119
4-3.2.1.2	Step 1.2	121
4-3.2.1.3	Step 1.3	122
4-3.2.2	Step 2: Non-aeronautical equivalent noise faced by victim receiver.....	125
4-3.2.3	Step 3: Protection radius.....	127
4-3.3	Protection radius from RFI mask.....	128
4-4	Conclusion	128
Chapter 5:	Impact of chirp RFI on civil aviation GNSS receiver performance.....	130
5-1	Mathematical model of chirp RFI signal.....	130
5-1.1	Mathematical model for linear sweep CW signal	131
5-1.2	Impact of propagation channel on chirp RFI signal.....	132
5-1.3	Impact of RFFE block on chirp RFI	133
5-1.4	Second order wide sense stationarity analysis	135
5-2	Theoretical impact of chirp RFI on C/N_0	137
5-2.1	Power spectral density of chirp signal.....	137
5-2.2	Spectral separation coefficient of a linear sweep PPD signal	139

5-2.2.1	Theoretical calculation of chirp RFI SSC	139
5-2.2.2	Influence of chirp RFI characteristics on SSC.....	141
5-3	Impact of chirp RFI on C/N_0 : simulations.....	143
5-3.1	Simulation with Matlab software receiver.....	143
5-3.1.1	Description of simulations.....	143
5-3.1.2	Results	145
5-3.1.3	Discussion	148
5-3.2	Simulation with IFEN receiver	152
5-3.2.1	Description of experiment testbench.....	152
5-3.2.2	Description of simulations.....	153
5-3.2.2.1	Results	155
5-3.3	Conclusion on simulations.....	158
5-4	Impact of chirp RFI on GPS signal processing stage	159
5-4.1	Chirp RFI at the correlator output.....	159
5-4.1.1	Prediction of tracking error in presence of chirp RFI	166
5-4.1.1.1	Prediction of phase and Doppler estimations φ_k and $f_{D,k}$	167
5-4.1.1.2	Prediction of code delay estimation τ_k	168
5-4.1.2	Validation of tracking error prediction model.....	168
5-4.1.3	Interest and significance of time analysis	169
5-4.1.4	Investigation of C/N_0 estimators' difficulties on non-ergodicity scenarios	170
5-4.2	Conclusion	171
Chapter 6:	Impact of interference on GMSK C2Link receiver performance	173
6-1	Development of a GMSK C2Link receiver.....	173
6-1.1	C2Link digital receiver architecture.....	174
6-1.2	Laurent decomposition of GMSK signal	174
6-1.2.1	Mathematical model of the Laurent decomposition of the GMSK modulated signal	174
6-1.2.2	Signal power analysis of the Laurent decomposition of the GMSK modulated signal	175
6-1.3	Design of C2Link synchronization module	178
6-1.3.1	Synchronization by maximum likelihood criterion.....	178
6-1.3.2	Synchronization by maximum likelihood function	179
6-1.3.3	Development of the log-likelihood function	180
6-1.3.3.1	Local replica derivation	180
6-1.3.3.2	Integral calculation.....	181
6-1.3.3.3	Data removal from a NDA algorithm	182

6-1.3.3.4	Log-likelihood function	182
6-1.3.3.5	Simplification under low SNR assumption	183
6-1.3.4	Design of Phase Lock Loop	183
6-1.3.4.1	Design of PLL discriminator	183
6-1.3.4.2	Design of PLL loop filter and NCO	187
6-1.3.5	Design of Delay Lock Loop	187
6-1.3.5.1	DLL discriminator	188
6-1.3.5.2	DLL discriminator normalization	189
6-1.3.5.3	Design of DLL loop filter and NCO	191
6-1.4	Demodulation module	191
6-1.5	Performances of C2Link signal processing modules	193
6-1.5.1	Synchronization performance	193
6-1.5.2	Demodulation performance	194
6-2	Impact of continuous wideband RFI on GMSK C2Link receivers	196
6-2.1	Theoretical model of RFI impact on BER	196
6-2.2	Validation of the theoretical RFI impact model	198
6-2.2.1	BER degradation for large bandwidth RFI	198
6-2.2.2	BER degradation for narrow bandwidth RFI	199
6-3	Conclusion	200
Chapter 7:	Conclusion and future work	201
7-1	Results from PhD	201
7-2	Future work	204
Appendix A:	GNSS acquisition, tracking and demodulation C/N_0 thresholds	206
A-1	C/N_0 acquisition thresholds	206
A-1.1	DFMC GNSS acquisition thresholds	206
A-1.2	Legacy C/N_0 acquisition threshold	221
A-2	C/N_0 tracking and demodulation thresholds	221
Appendix B:	ICAO GNSS RFI mask	223
B-1	Maximum tolerated power from non-aeronautical sources	223
B-1.1	Fundamental idea of GNSS RFI mask	223
B-1.2	Detail of the calculation of the maximum tolerable non-aeronautical RFI power	224
B-1.3	Step 1: C/N_0 link budget analysis in presence of aeronautical RFI	224
B-1.4	Step 2: Maximum tolerable non-aeronautical RFI power	227
B-2	Legacy RFI mask	229
B-2.1	Legacy C/N_0 link budgets	229
B-2.2	Legacy in-band RFI mask	230

B-2.3	Legacy out-of-band RFI mask	231
B-3	DFMC RFI masks	233
B-3.1	DFMC C/N_0 link budgets.....	233
B-3.2	DFMC in-band RFI mask.....	237
B-3.3	DFMC out-of-band RFI mask	238
B-4	Conclusion	240
Appendix C:	Autocorrelation of chirp signal	241
Appendix D:	Power spectral density of chirp signal.....	244
Appendix E:	Asymptotic behavior of C/N_0 estimators in presence of RFI.....	248
Appendix F:	Fourier transform of chirp signal.....	253
Appendix G:	Laurent decomposition of GMSK signal	255
Appendix H:	GMSK local replica derivation	258
Appendix I:	Derivative of GMSK log-likelihood function with respect to θ	259
Appendix J:	GMSK receiver phase discriminator	261
J-1	Development of noise free non-normalized discriminator.....	261
J-2	Normalization of the phase discriminator.....	263
Appendix K:	GMSK delay discriminator	264
K-1	Noise free delay discriminator	264
K-2	Normalization of the delay discriminator	267

List of figures

Figure 2-1: Autocorrelation of PRN 1 sequence	37
Figure 2-2: Power spectral density of PRN1 signal.....	38
Figure 2-3: Power spectral density of Galileo E1 PRN 1 signal at baseband	41
Figure 2-4: Galileo E5a sub-carriers.....	43
Figure 2-5: Generic GNSS receiver block diagram.....	45
Figure 2-6: Equivalent model of RF front-end block	46
Figure 2-7: Representation of the correlation process	48
Figure 2-8: Correlation function for GPS L1C/A (left) and Galileo E1 (right) signals	51
Figure 2-9: Acquisition strategy based on one channel processing	54
Figure 2-10: Impact of the number of non-coherent summations on the acquisition detector	55
Figure 2-11: Acquisition principle for data + pilot components signals... ..	56
Figure 2-12: Block diagram of the equivalent linear model of a PLL.....	57
Figure 2-13: DLL discriminator principle	59
Figure 2-14: Current Systems in the L5/E5 frequency band	68
Figure 2-15: Power spectral density of a rectangular spectrum signal.....	69
Figure 2-16: Instantaneous frequency pattern of a triangular and linear chirp signal	71
Figure 2-17: 1 dB compression point of the legacy and DFMC antennas	73
Figure 2-18: Legacy and DFMC receiver antenna patterns	73
Figure 2-19: Minimum legacy and DFMC antennas frequency rejection.....	74
Figure 2-20: Out-of-band and in-band RFI masks	75
Figure 3-1: Extract of SUP AIP 037/22 on creation of unmanned aircraft segregated airspace	77
Figure 3-2 Extract of SUP AIP 177/22 on creation of unmanned aircraft segregated airspace	77
Figure 3-3: Illustration of RPAS operations for the different RPAS categories of the European legislation	83
Figure 3-4: Terrestrial C2Link architecture.....	85
Figure 3-5: C2Link satellite architecture.....	85
Figure 3-6: TDD channel division method (DO-362)	90
Figure 3-7: C2Link power spectral density mask.....	91
Figure 3-8: GMSK modulating waveform	92
Figure 3-9: Illustration of $\varphi(t)$	93
Figure 4-1: Out of band and in band L1/E1 RFI masks	96
Figure 4-2: Illustration of the new methodology of jamming protection area determination.....	100
Figure 4-3: Correlation functions between the filtered GNSS signals and their respective local replica	104
Figure 4-4: Normalized received GNSS power as a function of SV elevation.....	109
Figure 4-5: Average antenna gain for I_{gnss} analysis.....	109
Figure 4-6: Position of the terrestrial emitter with respect to the aircraft.....	114
Figure 4-7: Population density accross Western Europe	116
Figure 4-8: Density of mobile phone users as a function of population density for eight Spanish cities	116
Figure 4-9: Terrestrial emitters density.....	117
Figure 4-10: Evolution of the elevation of GPS, Galileo and EGNOS SV during period of jamming....	120
Figure 4-11: Evolution of the minimum legacy and DFMC antenna gain for GPS, Galileo and EGNOS SVs during jamming period.....	121
Figure 4-12: Evolution of $I_{0,GNSS}$ during jamming period.....	122

Figure 4-13: Link budget margin for the different pairs of signal and receiver operation	123
Figure 4-14: Maximum tolerable non aeronautical RFI equivalent noise for the different pairs of signal and receiver operation	124
Figure 4-15: Terrestrial emitters equivalent noise (2000 ft AGL, not including 6 dB safety margin) .	126
Figure 4-16: Jammer and aggregate non-aeronautical RFI equivalent noise.....	127
Figure 4-17: Protection radius for the different pairs of signal and receiver operation, for legacy and DFMC GNSS receivers.....	127
Figure 5-1: Plot of $f_{J,RFout}$ and influence of the random time offset δ on the chirp signal, and illustration of T_{sweep} and B	134
Figure 5-2: Influence of φ_0 on the chirp signal.....	135
Figure 5-3: Impact of B on the baseband power spectral density at the RFFE output of the chirp signal	139
Figure 5-4: Impact of T_{sweep} on the baseband power spectral density at the RFFE output of the chirp signal.....	139
Figure 5-5 : Power spectral density of the GNSS local replica at the integrate and dump filter output	140
Figure 5-6 Impact of stationary received chirp jammer signal settings on the spectral separation coefficient to GPS L1C/A.....	141
Figure 5-7: Received chirp jammer signal SSC to GPS L1 C/A as a function of received jammer to local GPS frequency offset Δf_J for different values of T_{sweep} and T_i	142
Figure 5-8: Evolution of the C/N0 estimators for the different simulations.....	146
Figure 5-9: Distribution of the chirp contribution on the correlator outputs for simulations 6 and 8	149
Figure 5-10: Time distribution of δ_{kTi} and φ_{kTi} for simulations 7 and 8.....	151
Figure 5-11: Testbench of simulations of injection of chirp RFI in IFEN GNSS receiver	152
Figure 5-12: Evolution of C/N0 estimations as a function of time for IFEN simulations 1 (left) and 2 (right).....	155
Figure 5-13: Evolution of C/N0 estimations as a function of time for IFEN simulations 3 (left) and 4 (right).....	155
Figure 5-14: Evolution of C/N0 estimations as a function of time for IFEN simulations 5 (left) and 6 (right).....	156
Figure 5-15: Mean C/N_0 degradation for different T_{sweep} (IFEN simulation 7).....	157
Figure 5-16: Evolution of C/N_0 estimations as a function of time of IFEN simulation 8.....	158
Figure 5-17: Spectrum of GPS L1C/A PRN1 modulated signal	163
Figure 5-18: Prediction and observed correlator output from a software receiver, when a PPD signal is correlated with PRN1 local replica	166
Figure 5-19: Validation of tracking errors prediction model in presence of chirp RFI.....	169
Figure 5-20: Time evolution of chirp and GNSS signal to correlator output.....	170
Figure 6-1: Simplified block diagram of digital receiver.....	174
Figure 6-2: Amplitude modulated pulses of C2Link signal Laurent decomposition.....	175
Figure 6-3: Correlation functions of Laurent pulses.....	185
Figure 6-4: Phase discriminator S curve	186
Figure 6-5: C2Link PLL block diagram	187
Figure 6-6: Derivative of correlation functions	189
Figure 6-7: Delay discriminator output	191
Figure 6-8: 4 states C2Link demodulation Viterbi algorithm	192
Figure 6-9: Code and delay tracking errors	193
Figure 6-10: Code and delay tracking errors in absence of loop filter	194
Figure 6-11: Performance of GMSK C2Link demodulation module	195

Figure 6-12: Comparison between observed and theoretical BER performance of GMSK C2Link receiver	196
Figure 6-13: GMSK C2Link matched filters transfer functions	197
Figure 6-14: BER performance degradation in presence of a 1 MHz RFI, targeting a 3 dB E_b/N_0 degradation	199
Figure 6-15: BER performance degradation in presence of a narrow RFI, targeting a 3 dB E_b/N_0 degradation	199
Figure A-1: GPS acquisition strategy compliant with DMS:199	214
Figure A-2: Galileo acquisition strategy compliant with DMS:210.....	215
Figure A-3: Probability of detection for GPS L1C/A SVs	219
Figure A-4: Probability of detection for Galileo E1 SVs	219
Figure A-5: Probability of detection for GPS L5 and Galileo E5a SVs	220
Figure A-6: Acquisition thresholds as a function of the number of correlators.....	220
Figure B-1: Power spectral density of the victim GPS L1C/A PRN 1 local replica after filtering by the integrate and dump filter	228
Figure B-2: Maximum in-band non-aeronautical RFI tolerable power $C_{max}^{in\ band}$ for legacy receiver and in-band legacy RFI mask	231
Figure B-3: Minimum and monotonous RFFE rejection for GPS L1C/A legacy receivers	232
Figure B-4: Maximum out-of-band non-aeronautical RFI tolerable power $C_{max}^{out\ of\ band}(\Delta f)$ for legacy receiver and out-of-band RFI mask	233
Figure B-5: $I_{0,GNSS}^{mask}(sig)$ for DFMC GNSS receivers	234
Figure B-6: Minimum elevation and minimum DFMC antenna gain of highest GPS SVs (24 SVs constellation) as a function of latitude	235
Figure B-7: Minimum elevation and minimum DFMC antenna gain of highest Galileo SVs (24 SVs constellation) as a function of latitude	235
Figure B-8: $I_{0,non\ aero}^{max}(sig, op)$ for GPS L1C/A and Galileo E1 signals, for acquisition and tracking receiver operations	236
Figure B-9: Maximum tolerable power and in-band RFI mask for DFMC receivers.....	238
Figure B-10: Maximum tolerable power and out-of-band RFI mask for DFMC receivers.....	239
Figure G-1: Illustration of function Ψ	255

List of tables

Table 2-1: ICAO minimum performance objectives for civil aviation operations	34
Table 2-2: Summary of GNSS characteristics	44
Table 2-3: Acquisition of GPS L1C/A PRN 16, settings.....	54
Table 2-4: Transfer function of the PLL filter	58
Table 2-5: Minimum GNSS signal power as specified in ICAO Annex 10	72
Table 3-1: Definition of RPAS classes C0 to C4.....	80
Table 3-2: Definition of Open operation sub-categories.....	81
Table 3-3: Specific category standard scenarios	82
Table 3-4: Information transiting through C2Link for the different service classes	88
Table 3-5: Data class definition	89
Table 3-6: Number of bits within one subframe for the different data classes.....	89
Table 3-7: Data rate of the different data classes	90
Table 3-8: Maximum transmitted power for low power and high power modes	91
Table 3-9: Channel bandwidths for the different data classes	91
Table 4-1: Investigated pairs of signals and GNSS receiver signal processing operations.....	101
Table 4-2: C/N_0 link budget analysis table.....	101
Table 4-3: Acquisition, tracking and demodulation C/N_0 thresholds in dB-Hz for legacy and DFMC receivers	102
Table 4-4: Implementation losses computation	105
Table 4-5: Characteristics of GNSS signals	108
Table 4-6: Jammer settings for illustrative situation.....	118
Table 4-7: Parameters to compute minimum recovered signal power C_{min}	119
Table 4-8: Main inputs to compute effective noise in presence of aeronautical RFI	122
Table 4-9: Main inputs to derive link budget margins	123
Table 4-10: Main inputs to derive $I_{0,non\ aero}^{max}(sig, op, t)$	123
Table 4-11: Maximum tolerable equivalent noise from non-aeronautical sources for the different GNSS signals and receiver operations.....	124
Table 4-12: Comparison of limiting link budget with RFI mask link budget.....	125
Table 4-13: Protection radius for DFMC and legacy receivers computed with the new methodology	128
Table 4-14: Transmitter and receiver antenna gains for protection radius calculation with traditional method based on RFI masks.....	128
Table 4-15: Protection radius derived from RFI masks	128
Table 5-1: Chirp jammer settings	144
Table 5-2: Analysis of the mean value of the chirp RFI at the correlator output.....	148
Table 5-3: Prediction of the convergence value of C/N_0 estimators for simulation 6	149
Table 5-4 Variance of correlator outputs for simulations 6 and 8	150
Table 5-5 Comparison of predicted and observed RFI power at the correlator output	152
Table 5-6: Chirp RFI settings for simulations with the IFEN GNSS receiver	154
Table 5-7: Settings used for validation of PPD correlator output mathematical model.....	165
Table 5-8: GPS signal and chirp RFI settings for validation of tracking errors prediction model.....	168
Table 6-1: Contribution of Laurent pulses to GMSK signal power	178
Table 6-2: Tracking errors standard deviation with and without tracking loop filters.	194
Table A-1: Cross correlation RFI for acquisition	208

Table A-2: Proposed allocated time to perform a first fix for each pair of constellation and frequency band.....	212
Table A-3: Sharing of the allocated time between the different first fix computation steps	213
Table A-4: Doppler uncertainty for the different GNSS signals.....	216
Table A-5: Code delay uncertainty for the different GNSS signals to acquire	216
Table A-6: Size of the acquisition matrix for the different GNSS signals to acquire	217
Table A-7: Probabilities of false detection for the different signals to acquire	218
Table A-8: Acquisition thresholds identified by standardization for DFMC equipment	221
Table A-9: Tracking and demodulation performance indicators, and associated targeted performance	222
Table A-10: Thresholds for the different tracking performance indicators, and selected tracking/demodulation C/N_0 thresholds (dB-Hz)	222
Table B-1: C/N_0 link budget table for GNSS RFI mask elaboration	224
Table B-2: Aeronautical RFI equivalent noise components for legacy link budgets	229
Table B-3: C/N_0 link budgets at critical locations for legacy RFI mask elaboration	230
Table B-4: DFMC link budgets at worst worldwide locations	237

Chapitre 0: Résumé en français

0-1 Introduction

Les applications des drones, également connus sous l'acronyme UAS (Unmanned Aircraft System), sont en plein essor. Le nombre de drones volant dans l'espace aérien est en constante augmentation. Un rapport SESAR [1] estime que les opérations effectuées par les drones représenteront un marché annuel de 10 milliards d'euros en 2035 et 15 milliards d'euros en 2050, avec une flotte de drones commerciaux et gouvernementaux composée de 400 000 appareils en 2050. Les secteurs économiques favorables à l'utilisation de drones sont :

- L'agriculture : les opérations effectuées par les drones gagneront en précision et en efficacité, ce qui contribuera à une meilleure productivité.
- L'énergie : les opérations de maintenance et d'inspection sur les infrastructures seront facilitées par l'utilisation des drones.
- Livraison : la rapidité de livraison sera fortement augmentée par l'utilisation de drones.
- Sécurité publique : une forte demande sur l'utilisation de drones provient de ce secteur. En effet, l'utilisation de drones permettrait d'améliorer la rapidité et la sécurité des secours lors de catastrophes. Les opérations de police (surveillance) sont également facilitées.

Afin d'apporter une solution à cette forte demande en termes de capacité d'espace aérien, un fort besoin d'intégration des drones dans l'espace aérien non-ségrégué se fait ressentir. L'espace aérien non-ségrégué se définit comme l'espace aérien partagé avec l'aviation civile. Au contraire, l'espace aérien ségrégué est une espace aérien dédié à certaines opérations et dans lequel des restrictions d'accès existent. Le concept de ciel unique européen, qui est un projet ambitieux de modernisation du système de gestion du trafic aérien, prend en compte ce besoin à travers plusieurs projets analysant la sécurité, la sûreté et l'efficacité des opérations de drones en espace aérien non-ségrégué [2].

Comme l'acquisition de drone par le grand public est très facile, un système de défense doit être mis en place afin de lutter contre les usages de drones malveillants, et ainsi les empêcher d'accéder aux espaces aériens qui leur sont prohibés. La lutte anti-drone est en effet un sujet important et sensible, car il a des enjeux de sûreté et de protection des personnes. En effet, [3] relève un nombre croissant d'incidents impliquant des drones entre 2014 et 2019, atteignant 2000 incidents en 2019.

Le moyen de lutte anti-drone majoritairement utilisé est le brouillage des fréquences radioélectriques. En effet, cette méthode permet d'interrompre le lien de commande et de contrôle du drone entre le pilote au sol et l'UAS, ainsi que la réception du signal GNSS (Global Navigation Satellite System).

Ainsi, lors d'une opération ponctuelle de lutte anti-drone, ou lors d'un exercice de brouillage étatique, les prestataires de service de navigation aérienne (PSNA) est en charge de déterminer la zone dans laquelle les systèmes C2Link et GNSS sont susceptibles de ne pas satisfaire les exigences minimums de performance. A l'intérieur de ces zones, appelées zones de protection, les pilotes sont notifiés d'une potentielle perte du service GNSS et C2Link à travers un NOTAM (NOTice To AirMen). Cette zone de protection doit donc être déterminée de façon précise. D'un côté, une zone de protection trop faible pourrait induire des problèmes de sécurité. Inversement, une zone de protection trop large dégraderait l'efficacité opérationnelle du transport aérien, avec des distances à parcourir plus importantes pour contourner la zone de protection par les aéronefs dans certaines situations.

Il y a donc un besoin pour les PSNA de déterminer de façon précise les zones de protection. Le premier objectif de cette thèse est l'élaboration d'une méthodologie permettant de déterminer les zones de protection lors d'une opération de brouillage GNSS et C2Link.

Le deuxième objectif de cette thèse est l'analyse de l'impact de plusieurs types d'interférences sur les récepteurs GNSS standardisés pour des applications aviation civile. Une attention particulière sera portée sur les interférences de type « chirp ». En effet, ce type d'interférence dont la forme d'onde est particulière, est la signature de la plupart des brouilleurs illégaux plus connus sous le nom de PPD (Portable Privacy Device). Les dispositifs anti-drones modernes peuvent également utiliser cette forme de signal.

Cette thèse se divise en 5 chapitres principaux :

- Le chapitre 2 est un état de l'art sur le GNSS. Il présente les différents signaux GNSS utilisés pour l'aviation civile, un modèle d'impact des interférences sur un récepteur GNSS ainsi que les performances minimales attendues d'un récepteur GNSS utilisé pour l'aviation civile.
- Le chapitre 3 est un état de l'art sur le C2Link. Il présente une classification des différents drones et leur prise en compte dans la réglementation. Comme plusieurs technologies sont actuellement à l'étude pour supporter le C2Link, la description d'une en particulier, pressentie pour être implémentée dans un réseau terrestre, est approfondie.
- Le chapitre 4 propose une méthodologie de détermination de la zone de protection à appliquer lors de brouillages GNSS. Cette méthode se base sur une estimation fine du niveau d'interférences aéronautiques rencontrées par un récepteur victime de façon à déduire le niveau d'interférence non aéronautique qu'il pourrait tolérer tout en gardant ses objectifs de performance remplis.
- Le chapitre 5 caractérise l'impact des interférences de type chirp sur un récepteur GNSS aéronautique. Plusieurs études y sont menées et différents indicateurs étudiés, notamment la dégradation induite par l'interférence sur le C/N_0 ainsi que la dégradation des mesures de pseudo-distance.
- Le chapitre 6 étudie l'impact des interférences sur les performances de démodulation des récepteurs C2Link.

0-2 Marges de brouillage GNSS

Le premier objectif de cette thèse est la définition d'une méthodologie permettant de déterminer la zone de protection lors d'un brouillage GNSS. La zone de protection représente un volume à l'intérieur duquel un récepteur victime pourrait ne pas satisfaire les exigences de performance minimum. Ce travail est motivé par une demande du principal PSNA français. En effet, la détermination de cette zone de protection repose aujourd'hui sur le masque d'interférence de l'organisation de l'aviation civile internationale (OACI). Cependant, cette zone de protection semble être trop large par rapport aux reports d'évènements d'interférence remontés par les pilotes impactés et suite à des mesures en vol réalisées au moyen de différents récepteurs certifiés.

Les raisons pour lesquelles le masque d'interférence ne permet pas de déterminer de façon précise la zone de protection sont :

- Le but initial du masque d'interférence GNSS est de définir les conditions de test des récepteurs GNSS aviation civile dans le cadre de leur certification. Ainsi, le masque d'interférence reflète la pire situation d'interférence à travers le monde. Par conséquent, le niveau d'interférence aéronautique dans cette situation est élevé. Pour la bande L1 (1563-1587 MHz) en particulier, le masque d'interférence donne le niveau maximal d'interférence

non-aéronautique que peut tolérer un récepteur aéronautique lors d'une approche de précision à Honolulu. Par conséquent, l'environnement d'interférence aéronautique à proximité du lieu d'un brouillage peut être très différent de la situation d'interférence associée au masque d'interférence.

- La notion de masque d'interférence GNSS est apparue en 1996 avec la définition des conditions de test de certification des récepteurs GNSS aéronautiques dans le standard DO-229. Depuis, ce masque a subi quelques modifications dans la partie hors bande, mais le niveau acceptable d'interférence non-aéronautique dans la bande GNSS est resté inchangé. Cependant, le niveau d'interférence aéronautique a lui augmenté depuis 1996, avec le lancement de constellations GNSS supplémentaires ainsi que l'apparition de nouveaux signaux dans la bande de fréquence L1/E1. Par conséquent, l'environnement d'interférence considéré lors de l'élaboration du masque d'interférence GNSS n'est pas à jour et peut ne pas être adapté pour caractériser des environnements d'interférence aujourd'hui.
- Les masques d'interférence GNSS ne sont pas adaptés à toutes les formes d'interférences. En effet, ces masques sont adaptés à des interférences continues dont la densité spectrale de puissance est rectangulaire. Ils ne garantissent donc pas le respect des objectifs de performance minimum dans le cas d'une interférence avec une densité spectrale de puissance différente.
- Le masque d'interférence GNSS indique la puissance totale de la part d'une interférence non-aéronautique que peut tolérer un récepteur aéronautique. Cette puissance totale doit être partagés entre plusieurs sources d'interférences non-aéronautiques. La puissance maximale autorisée par le masque ne peut donc pas être allouée en totalité au signal de brouillage.

Afin de remédier aux limites du masque d'interférence, une nouvelle méthodologie permettant la détermination de la zone de protection lors d'un exercice de brouillage est proposée. Cette nouvelle méthodologie repose sur une caractérisation précise de l'environnement d'interférence rencontré par un récepteur aéronautique victime. La limite de la zone de brouillage est déterminée de sorte que le niveau agrégé d'interférence (aéronautique + non-aéronautique) soit égal au niveau maximal d'interférence que peut tolérer le récepteur tout en gardant les objectifs de performance remplis. Cette nouvelle méthodologie se décompose en trois étapes.

- 1- Un bilan de liaison précis en termes de C/N_0 , dépendant de la situation géographique et de la date du brouillage et tenant compte des interférences aéronautiques, permet de déterminer le niveau d'interférence non-aéronautique que peut tolérer un récepteur aéronautique.
- 2- Le niveau d'interférence non-aéronautique rencontré par un récepteur est calculé en tout point autour de la position du brouilleur.
- 3- La zone de protection est déterminée en identifiant toutes les positions potentielles d'un récepteur aéronautique victime pour lesquelles le niveau d'interférence non-aéronautique dépasse le niveau maximum acceptable pour remplir les exigences de performance.

Le gain de cette nouvelle méthode par rapport à l'utilisation du masque d'interférence GNSS est illustré au Chapitre 4 à travers l'étude d'un exercice de brouillage fictif. Les caractéristiques de cet exercice de brouillage sont données dans la Table 0-1.

Position brouilleur	Date	Durée	Puissance (W)	Gain antenne (dBi)	Largeur de bande (MHz)	Fréquence centrale
46.1°N, 0.18°E	29/12/2020	24h	12	5 (antenne supposée omni-directionnelle)	50	L1

				dans l'hémisphère supérieur)		
--	--	--	--	------------------------------	--	--

Table 0-1 : Description d'un exercice de brouillage fictif

Sur l'exercice de brouillage décrit ci-dessus, la zone de protection est fortement réduite avec la nouvelle méthode, en comparaison de la zone de protection calculée avec le masque d'interférence GNSS :

- Réduction de 116 km à 60 km pour les récepteurs ancienne génération ;
- Réduction de 103 km à 38 km pour les récepteurs nouvelle génération (DFMC).

Le gain apporté par la nouvelle méthode repose notamment sur une relaxation des hypothèses sur le nombre de satellites nécessaires pour respecter les exigences de performance GNSS minimales. Alors que le masque d'interférence suppose que tous les signaux provenant de satellites au-dessus de 5° d'élévation doivent être traités, la nouvelle méthode considère que les exigences de performance GNSS seront respectées dès lors que 6 satellites sont disponibles. De plus, les récepteurs DFMC tirent profit de meilleures performances en termes de gain d'antenne récepteur, de perte d'implémentation, et de seuils de poursuite.

Cette méthode doit être adoptée dans le cas de brouillage forte puissance, afin de prendre en compte la réflexion troposphérique qui n'est pas considérée ici. De plus, et pour des raisons de sécurité, la nouvelle méthode de détermination des zones de protection doit être validée lors d'un exercice de brouillage réel, en comparant la zone réellement impactée et identifiée par les retours d'expérience de la part des pilotes avec la zone déterminée à partir de la nouvelle méthodologie.

0-3 Impact des interférences de type « chirp » sur les performances des récepteurs aviation civile

Le chapitre 5 analyse l'impact d'un type d'interférence particulier sur les récepteurs certifiés pour l'aviation civile. Une interférence de type « chirp » correspond à une interférence dont la fréquence instantanée décrit un motif périodique dans le temps. Ce type d'interférence est en effet une préoccupation croissante pour l'aviation civile, car de plus en plus de brouilleurs illégaux, aussi appelés PPD, utilisent cette forme d'onde. Certains brouilleurs GNSS étatiques modernes émettent également des signaux de type chirp. Bien que largement observé dans la littérature, l'impact de ce type de brouilleur sur des récepteurs GNSS reste difficilement prévisible, à cause de la multitude de paramètres à prendre en considération.

Les objectifs de cette partie sont les suivants :

- Proposer un modèle théorique de l'impact des interférences chirp sur les performances d'un récepteur GPS L1C/A en termes de C/N_0 et d'erreurs de poursuite,
- D'analyser les conditions de validité de ce modèle théorique,
- De valider ce modèle à travers des simulations jouées sur un récepteur logiciel (Matlab) et sur un récepteur de laboratoire (IFEN SX3).

Une interférence chirp est principalement caractérisée par trois paramètres :

- La bande de fréquences impactée B ,
- Le motif périodique de la fréquence instantanée f_i ,
- La période de répétition T_{sweep} du motif décrit par la fréquence instantanée.

Dans cette thèse, une étude approfondie est menée sur l'impact des interférences chirp dont la fréquence instantanée effectue des balayages linéaires de la bande de fréquence visée.

Tout d'abord, un modèle mathématique d'une interférence chirp au niveau du port de l'antenne d'un récepteur GNSS est proposé. L'interférence chirp peut en effet être modélisée comme un signal aléatoire exprimé par (Eq 0-1).

$$s_{PPD}(t) = \sqrt{2C_J} \cos \left(2\pi(f_0 + \Delta f)t + 2\pi \int_0^t f_i(u + \delta) du + \varphi_0 \right) \quad (\text{Eq 0-1})$$

$$f_i(u) = -\frac{B}{2} + \frac{B}{T_{sweep}} \left(u - \left\lfloor \frac{u}{T_{sweep}} \right\rfloor T_{sweep} \right)$$

- C_J est la puissance du signal chirp au port de l'antenne.
- δ est une variable aléatoire temporelle, uniformément distribuée sur l'intervalle $[0, T_{sweep}]$. Elle caractérise le retard de propagation, supposé inconnu.
- φ_0 est une variable aléatoire représentant la phase initiale, uniformément distribuée sur l'intervalle $[0; 2\pi]$.
- Δf est l'écart fréquentiel entre le signal chirp et la fréquence centrale du signal GPS L1C/A étudié.

Grâce à la modélisation de l'interférence comme un signal aléatoire, il peut être démontré que ce signal est stationnaire au sens large au deuxième ordre. Par conséquent, la notion de densité spectrale de puissance peut être introduite.

Pour comprendre l'impact d'une interférence chirp sur le C/N_0 d'un signal GPS L1C/A, plusieurs définitions du C/N_0 en présence d'interférence sont introduites ci-dessous.

- C/N_0 réel :

Le C/N_0 réel est défini par (Eq 0-2).

$$\left(\frac{C}{N_0} \right)_{real} = \frac{1}{4T_i} \frac{C}{P_{n,real} + P_{J,real}} \quad (\text{Eq 0-2})$$

$$P_{n,real} = \mathbb{E}[I_{noise,n}^2 + Q_{noise,n}^2]$$

$$P_{J,real} = \frac{1}{N} \sum_N (I_{PPD,n}^2 + Q_{PPD,n}^2)$$

$I_{X,k}$ et $Q_{X,k}$ représentent respectivement les $k^{\text{ème}}$ sorties de corrélateur sur les voies I et Q du signal X. C représente la puissance du signal utile et T_i la période d'intégration. Le C/N_0 réel est le C/N_0 effectif rencontré en pratique par le récepteur.

- C/N_0 statistique :

Le C/N_0 statistique est défini par (Eq 0-3).

$$\left(\frac{C}{N_0} \right)_{stat} = \frac{1}{4T_i} \frac{C}{P_{n,stat} + P_{J,stat}} \quad (\text{Eq 0-3})$$

$$P_{n,stat} = \frac{N_0}{4T_i} \int_{-\infty}^{+\infty} |H_{RF,BB}(f)|^2 S_{c_{mL}}(f) df$$

$$P_{J,stat} = \frac{C_J}{4T_i} \int_{-\infty}^{+\infty} |H_{RF,BB}(f - f_D)|^2 S_{j,BB}(f - f_D) (S_{c_m}(f) * |\bar{H}_{ID}(f)|^2) df$$

$H_{RF,BB}$ est la fonction de transfert du filtre RF/IF, $S_{c_{m_L}}$ est la densité spectrale de puissance de la réplique locale du signal GPS L1C/A, $S_{j,BB}$ est la densité spectrale de puissance normalisée de l'interférence en bande de base, et \bar{H}_{ID} est la fonction de transfert du filtre équivalent de l'étage de corrélation. Le C/N_0 statistique est défini à partir d'une approche théorique et ne peut pas être renvoyé par le récepteur.

Le C/N_0 réel est équivalent au C/N_0 statistique si la distribution de l'interférence en sortie de corrélateur est ergodique. En effet, lorsque la condition d'ergodicité est vérifiée, le calcul de la puissance de l'interférence en sortie de corrélateur avec une approche statistique est équivalent au calcul de la puissance de l'interférence à partir d'un nombre suffisamment grand de sorties de corrélateur successives.

- C/N_0 estimé :

Du fait que le C/N_0 réel et le C/N_0 statistique ne peuvent être calculés par un récepteur GNSS, le C/N_0 est habituellement estimé par le récepteur à partir des sorties de corrélateur à l'aide d'un algorithme tel que décrit dans la section 2-3.4.2. La validité du C/N_0 estimé est conditionnée à plusieurs hypothèses. Tout d'abord, l'interférence en sortie de corrélateur doit être centrée et indépendante du signal utile. Ensuite, comme les algorithmes utilisés pour l'estimation du C/N_0 font certaines hypothèses sur la distribution de l'interférence en sortie de corrélateur, celles-ci doivent être vérifiées. Par exemple, l'estimateur des moments suppose que les sorties de corrélateurs ont une distribution gaussienne. Si ce n'est pas le cas, alors le C/N_0 estimé sera différent du C/N_0 réel.

Le calcul du C/N_0 statistique en présence d'une interférence chirp est déterminé en exploitant la stationnarité au sens large de l'interférence en sortie de filtre RF. L'effet de plusieurs paramètres de l'interférence est souligné : le décalage fréquentiel entre l'interférence et le signal utile, la période de balayage de l'interférence ainsi que la période d'intégration. En particulier, lorsque T_i est faible (1 ms par exemple), la puissance de l'interférence en sortie de corrélateur varie peu en fonction du décalage fréquentiel. Au contraire, lorsque T_i est grand (20 ms par exemple), la puissance de l'interférence en sortie de corrélateur dépendra fortement du décalage fréquentiel étant donné que la densité spectrale de puissance de la réplique locale du signal GPS, tout comme celle de l'interférence, tendrait vers un spectre de raies. Cette dépendance est accentuée si T_{sweep} est un diviseur de la période du code PRN (égal à 1 ms pour GPS L1 C/A), car dans ce cas, toutes les raies de la densité spectrale de puissance de l'interférence chirp seraient alignées avec les raies de S_{c_m} .

Ces calculs théoriques sont validés par des observations en sortie de récepteur. Deux récepteurs sont utilisés :

- Un récepteur logiciel Matlab,
- Un récepteur IFEN SX3.

L'analyse des observations du C/N_0 en sortie de récepteur valide la nécessité de la condition d'ergodicité afin que le modèle théorique (C/N_0 statistique) soit conforme au C/N_0 réel. L'ergodicité des sorties de corrélateur ne sera pas vérifiée si :

- T_{sweep} est un diviseur du temps d'intégration T_i ou
- L'écart fréquentiel entre l'interférence et le signal utile est un multiple de la période du code PRN.

Un modèle alternatif est proposé pour caractériser les interférences chirp hors condition d'ergodicité en analysant l'impact d'une interférence chirp sur les erreurs de poursuite. Tout d'abord, l'impact

d'une interférence chirp sur la déformation des sorties de corrélateurs est calculé mathématiquement en fonction des paramètres de l'interférence et des estimations de code, de phase et de fréquence Doppler renvoyées par les boucles de poursuite. Ce modèle mathématique est validé par comparaison avec les sorties de corrélateur en présence d'une interférence chirp. A partir de ce modèle théorique de sortie de corrélateur, les sorties des boucles de poursuite peuvent alors être calculées de façon itérative, permettant d'obtenir les estimations de code, de phase et de fréquence Doppler sous la forme de suites numériques. Cette analyse temporelle est importante pour la définition des tests de certification de récepteur GNSS aéronautique, dans la mesure où elle permet d'identifier les caractéristiques de l'interférence amenant au plus fort impact sur le traitement du signal GNSS.

0-4 Impact des interférences sur la performance des récepteurs C2Link

Le C2Link se définit comme le lien de commande et contrôle d'un drone. En tant que système identifié comme contribuant à la sécurité de la vie par l'Union Internationale des Télécommunications, le C2Link doit être protégé des brouillages préjudiciables.

Plusieurs architectures C2Link sont aujourd'hui considérées comme de potentiels candidats. Le système le plus avancé en termes de standardisation est un système terrestre dont les exigences sont données dans le standard aéronautique DO-362 du RTCA. Ce système utilise notamment une modulation GMSK (Gaussian Modulation Shift Keying). Cette thèse utilisera ces définitions comme support d'étude.

Le Chapitre 5 caractérise l'impact d'une interférence continue sur les performances d'un récepteur C2Link GMSK. Cette étude se divise en trois parties :

- Tout d'abord, un prototype de récepteur logiciel C2Link GMSK est développé. Plus précisément, cette thèse analyse les performances de l'étage de traitement du signal, qui peut se décomposer comme un module de synchronisation et un module de démodulation fonctionnant en parallèle.
- Ensuite, l'impact d'une interférence est modélisé comme une augmentation du bruit effectif perçu par le récepteur.
- Enfin, ce modèle est validé en comparant les performances de démodulation du récepteur logiciel en présence d'une interférence avec les performances anticipées.

Les modules de synchronisation et de démodulation sont dans un premier temps élaborés théoriquement et implémentés sous la forme d'un récepteur logiciel Matlab. Les boucles de poursuite de phase et du décalage temporel sont élaborées par maximisation de la fonction du maximum de vraisemblance. Le module de démodulation est quant à lui élaboré à l'aide de l'algorithme de Viterbi permettant d'annuler l'interférence inter-symboles due à la modulation GMSK. Le comportement des modules de synchronisation et de démodulation implémentés dans le récepteur logiciel est analysé. L'analyse des performances du taux d'erreur binaire (BER) du récepteur logiciel démontre que la présence de l'étage de synchronisation ne dégrade pas la démodulation : même en présence d'un signal dont le rapport E_b/N_0 est faible, la synchronisation ne contraindra pas la performance de BER. Par conséquent, le BER est un indicateur pertinent pour caractériser la capacité d'un récepteur C2Link GMSK à respecter les exigences de performance minimale.

Dans un deuxième temps, un modèle théorique caractérisant l'impact d'une interférence continue sur le BER d'un récepteur GMSK est développé. Pour cette partie, le récepteur est supposé fonctionner dans sa zone de linéarité sans saturation du récepteur. Dans le modèle proposé, l'impact de

l'interférence est modélisée comme équivalente à une augmentation du bruit effectif perçu par le récepteur. Ainsi, l'interférence peut être caractérisée comme un bruit blanc équivalent de densité I_0 . Ce bruit équivalent est défini par (Eq 0-4).

$$I_0 = \frac{C_J}{T_s} \int_{-\infty}^{+\infty} (|C_0^{mf}(f)|^2 + |C_1^{mf}(f)|^2) \bar{S}_{in}(f) df \quad (\text{Eq 0-4})$$

C_J correspond à la puissance de l'interférence, T_s à la période d'un symbole, C_X^{mf} à la fonction de transfert du filtre adapté au pulse X de la décomposition de Laurent du signal GMSK, et \bar{S}_{in} à la densité spectrale de puissance normalisée de l'interférence en sortie de filtre RF.

La dégradation de la performance de démodulation est ainsi caractérisée par une diminution du rapport E_b/N_0 effectif induite par l'interférence. Ce modèle théorique est validé par l'injection d'une interférence continue dans un récepteur GMSK. La puissance de l'interférence C_J est calculée de façon à viser une dégradation de 3 dB sur le rapport E_b/N_0 effectif. Le BER obtenu en présence de l'interférence est représenté par la Figure 0-1 en fonction du rapport E_b/N_0 , pour deux largeurs de bande différentes (1 MHz et 30 kHz).

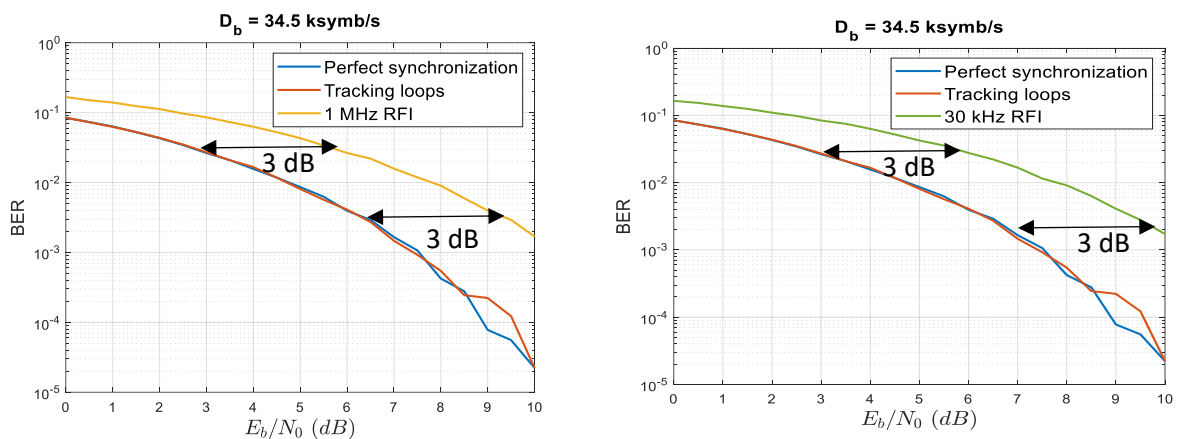


Figure 0-1: Dégradation du BER causée par une interférence continue

Comme attendu, l'introduction d'une interférence induit un décalage de la courbe de BER de 3 dB par rapport aux performances nominales. La validité du modèle est également indépendante de la largeur de bande d'interférence utilisée.

La thèse ne va pas plus loin dans la détermination de la zone de protection lors de brouillage C2Link pour les raisons suivantes :

- Comme la sélectivité en fréquence des antennes C2Link et des filtres RF des récepteurs C2Link ne sont pas standardisés à ce jour, l'énergie par bit E_b reçu par un récepteur est difficile à calculer précisément.
- Même si des prévisions du trafic de drones pour les années à venir existent, elles ne sont pas consolidées à cause d'une grande incertitude sur les systèmes qui seront utilisés. Par conséquent, les interférences intra système sont difficiles à estimer de façon précise.

Ces deux points mériteraient d'être étudiés plus en détail dans le cadre de la lutte anti-drone, afin de proposer une méthodologie pour déterminer une zone de protection lors d'un brouillage du lien C2Link.

Chapter 1: Introduction

1-1 Context and motivation

Drone (or equivalently unmanned aircraft system: UAS) applications are currently flourishing. The number of UAS flying in a given airspace is actually increasing. A 2016 SESAR report [1] estimates that the UAS market would generate 10 billion euros annually in 2035 and 15 billion euros annually in 2050, with a commercial and government fleet of 400,000 UAS in 2050. Sectors among the most demanding when it comes to UAS technology include:

- Agriculture: UAS would improve the agriculture precision, helping in optimizing the productivity.
- Energy: UAS would make some maintenance operations and inspection on infrastructures easier.
- Delivery: UAS would be very helpful for fast and safe delivery of medical supplies.
- Public safety and security: A strong demand on UAS technology exists in this sector, as UAS would allow safe and efficient rescue to people after natural disaster. Police surveillance operation would be also simplified.

To bring a solution to this strong demand in terms of airspace capacity, there is a real need to integrate unmanned aircraft (UA) within non-segregated airspace; the non-segregated airspace is defined as the airspace that UAs will share with the conventional aviation, contrary to the segregated airspace which is reserved to UAs only. The concept of European Single Sky, which is an ambitious project of modernization of Air Traffic Management (ATM) European system, considers this need through several projects testing the security, safety, and efficiency of UAS operation in non-segregated airspace [2].

As the access to UAS by the general public is very easy, a defensive system must be put in place to counter rogue UAS and prevent them from entering prohibited airspaces. The counter UAS fight is indeed a very significant and sensitive topic as it has public safety stakes in the protection of people. As a matter of fact, [3] reports a growing number of incidents implying UAS between 2014 and 2019, reaching almost 2,000 incidents in 2019.

Several counter-UAS solutions have been considered. Some armies have initially considered the use of raptors as an intervention tool against UAS [4]. However, since UAS are becoming more rapid and agile, this technique will not probably be very effective. In addition, rotors may be harmful for raptors. Another technology that is used to capture small UA is an interceptor UAS equipped with net gun. However, this technology only targets small UAS and is therefore insufficient to cope with the whole public safety stakes. Another counter-UAS technology under development is laser [5]. The technology consists in generating a very high-power beam capable to damage its target. The advantage of such a technology is the directivity of the beam. The main inconvenient is that the power, which is more than 50 kW, is sufficient to cause collateral victims even at a very long range if a non-targeted aircraft or UA is hit by the laser.

The main counter UAS solution which is currently in use is jamming. Indeed, this technology allows the police to disrupt the command-and-control signal between the remote pilot on the ground and the UAS, as well as the GNSS reception by the UAS. Even though jamming may hit untargeted aircraft, and thus creating collateral victims, it does not fully prevent the piloting of manned aircrafts. To summarize, when used as part of counter-UAS struggle, jamming systems often target two services:

- Command-and-control link: This link allows the pilot to communicate with its remote aircraft. When the command-and-control link is jammed, the remote aircraft cannot receive instruction

from the pilot anymore. Most of civil UAS contains a safety procedure in case the command-and-control link is lost, which consists in interrupting the flight and performing an immediate automatic landing, or a steady flight, or a return to the departure point. More evolved and malicious UAS may pursue their missions autonomously; however, these UAS are out of the scope of this thesis. As a matter of fact, jamming is not expected to be an effective tool to prevent these malicious operations. Finally, the command-and-control link can be transmitted by several services, such as Wifi, cellular channel (3G, 5G), or dedicated frequency bands for civil aviation certified command-and-control link. This PhD thesis focuses on this last category of links.

- Positioning service: This service is provided by global navigation satellite service (GNSS). Indeed, a loss of the GNSS link would likely prevent a rogue UAS from pursuing its mission, since the UA will be unable to know its position, except if the UA is equipped with an alternative navigation mean (lidar, video navigation for example). However, most of the UAS are nowadays equipped with GNSS navigation tool, so the jamming of the GNSS service should be an effective part of the counter-UAS struggle. In this PhD, C2Link and positioning systems are considered independently, assuming they are uncoupled.

When such a public safety counter-UAS jamming operation occurs, or during coordinated state jamming military exercises, Air Navigation Service Provider (ANSP) is in charge of determining the area within which the jamming may prevent civil aviation GNSS and C2Link receivers from meeting minimum requirements. In these areas, referred as protection areas or protection zones, pilots are notified of a potential loss of GNSS or C2Link links through a NOTAM (Notice to Airmen). The reliability in the determination of this zone has a major significance. On the one hand, a too small protection zone will induce safety problems, since the receiver may not be able to meet minimum requirements. On the other hand, too large a protection zone will decrease the flights resources consumption efficiency as explained next. Indeed, pilots would be asked to avoid the protection zone in order to make sure the navigation system meets the performance objectives, resulting in traffic limitations, a larger flight time, larger covered distance and higher fuel consumption. Eurocontrol is currently gathering reasonable guidelines for this type of situations, to be published in a few months.

Therefore, there is a need for ANSPs to be able to precisely determine protection areas from the knowledge of jamming signal and jamming transmitter (antenna, power, etc) characteristics. The first part of the objective of this thesis is thus to provide a methodology allowing the determination of protection areas for civil aviation GNSS and C2Link receivers during jamming operations.

The second part of the objective is to analyze the impact of common interferences on civil aviation GNSS receivers. A focus is made on one particular type of interference, referred as chirp interference. Indeed, chirp interference is a particular waveform which is the signature of many illegal civil jammers called Portable Privacy Devices (PPD) and of current military counter-UAS jamming guns. This analysis is needed to refine the protection area determination during state jamming exercises which use this type of interference. For GNSS standardization purposes, there is also a need to characterize the degradation of civil aviation GNSS receiver performance caused by chirp interference in order to define relevant test procedures for civil aviation GNSS receiver certification.

This PhD is funded by the French ANSP (Direction des services de la Navigation Aérienne, DSNA).

1-2 Innovations brought in this Ph.D. thesis

To fulfill this objective, three analyses must be performed for each of the considered service (GNSS and C2Link).

1. Capacity of receiver to meet requirements:

The capacity of the receiver to meet minimum ICAO requirements is often characterized by a minimum received power relatively to the noise plus radio frequency interference (RFI) equivalent power or power density. For GNSS receiver, the receiver RFI environment is characterized in standardization documents DO-235C [6] and DO-292A [7] by a minimum carrier power C to effective noise power spectral density ($N_{0,eff}$) ratio where RFI impact is included within the effective noise power spectral density. For C2Link receivers, the capacity of the receiver to meet requirements in standardization documents DO-362A [8] and DO-377A [9] is defined by a minimum useful signal to RFI signal power ratio. In this PhD, the approach of minimum $C/N_{0,eff}$ is kept for GNSS receivers. Regarding C2Link receivers, an alternative approach than the desired to undesired signal power ratio is proposed, characterizing undesired signal as an equivalent noise. The capacity of C2Link receivers to meet requirements can therefore be defined by a minimum C2Link signal energy E_b to effective noise power spectral density ratio.

What is already done

DO-235B [10] translates GPS L1C/A receiver requirements of DO-229 [11] into assumed minimum acquisition, tracking and demodulation thresholds, $C/N_{0,th}$. DO-292 [12] also proposes acquisition, tracking and demodulation thresholds, $C/N_{0,th}$, for GPS L5. $C/N_{0,th}$ are compared to link budgets $C/N_{0,eff}$ to determine if the minimum ICAO requirements are fulfilled. DO-362 [8] determined the minimum $E_b/N_{0,eff}$ ratio needed to meet C2Link requirements.

Innovation brought by this PhD: New Galileo E1 acquisition thresholds

GNSS receiver requirements for dual constellation multi frequencies (DFMC) SBAS receiver are currently being developed in ED-259 [13] standard. This newer generation of GNSS receivers will be capable to process GNSS signals from GPS and Galileo constellations, on both the L1/E1 (1559-1591 MHz) and L5/E5a (1164-1189 MHz) frequency bands. As part of revision of DO-235B [10] and DO-292 [12] standards to cover DFMC receivers, this PhD thesis computes C/N_0 thresholds, $C/N_{0,th}$, above which it is assumed that ED-259 requirements are met, in particular for Galileo E1 signals. Galileo E1 initial acquisition requirements of ED-259 are explored in great depth to derive new civil aviation Galileo E1 acquisition thresholds. A simple DFMC acquisition strategy compliant with new ED-259 DFMC initial acquisition requirements is proposed. From this initial acquisition strategy, acquisition thresholds for DFMC receivers can be computed.

2. Interference environment:

The interference environment must be investigated and characterized in order to estimate its impact on GNSS and C2Link receivers' capability to meet minimum requirements. In this PhD thesis, RFI impact on the receiver is usually characterized as an increase of an equivalent noise power spectral density, resulting in the decrease of the effective C/N_0 or E_b/N_0 indicators, $C/N_{0,eff}$ or $E_b/N_{0,eff}$, (for GNSS and C2Link receivers respectively). The objective of this analysis is to identify an exhaustive list of RFI sources inherently impacting the receiver, and to characterize their impact in terms of increase of equivalent noise power spectral density.

What is already done

DO-235B [10] and DO-292 [12] analyzes the RFI sources impacting GPS receivers on the L1 and L5/E5a frequency bands respectively. In these documents, the impact of RFI sources on receiver capability to

meet minimum requirements is characterized as an increase of the equivalent noise power spectral density. This approach is kept in this PhD.

Innovation brought by this PhD: review of all aeronautical RFI sources, terrestrial emitters and chirp

The main innovation of this PhD on RFI environment analysis consists in contributing to the revision of DO-235B [10] and DO-292 [12] into DO-235C [6] and DO-292A [7] to cover the new generation DFMC GNSS receivers. As part of this revision, the impact of RFI on DFMC receivers is updated. In particular, this PhD has made the analysis of inherent RFI sources impact on Galileo E1 receivers in terms of equivalent noise. Moreover, the impact in terms of equivalent noise of some RFI sources on Galileo E5a receivers has been characterized as part of DO-292 revision. Some interference sources are fully investigated and characterized in terms of equivalent noise in this thesis. Indeed, the equivalent noise caused by inter and intra system interference are fully re-computed for DFMC receivers. Moreover, another interference source referred to as terrestrial emitters is widely investigated. Indeed, as detailed in Chapter 4, the equivalent noise estimation caused by this interference source is deeply refined in this thesis. The aim of this interference environment characterization is to verify the capacity of DFMC receiver to fulfill minimum requirements. This verification is performed computing effective C/N_0 link budgets, $C/N_{0,eff}$, which is compared to C/N_0 thresholds, $C/N_{0,th}$. All this analysis about interference characterization and the demonstration of DFMC requirements fulfillment has been included in DO-235C and is re-used in Chapter 4.

Finally, the impact of chirp jamming transmitted by PPDs or jamming gun on the degradation of GNSS receiver acquisition, tracking and demodulation performances, although widely observed, is highly difficult to predict. Therefore, this PhD proposes a characterization of these devices under the form of an equivalent noise when conditions are met. Indeed, a model of C/N_0 degradation caused by PPD-like signals (also called chirp signals) is proposed, addressing the situation where this chirp signal is random stationary, and the situation where this signal is not stationary because not ergodic in the observation window. This theoretical model is compared to simulation observations and its validity conditions are widely discussed. Additionally, their impact on tracking accuracy is investigated. A theoretical prediction model of correlator outputs, phase and code tracking estimations in presence of chirp RFI is indeed proposed. This model is validated with simulations and is thus a first step on the mathematical prediction of chirp signals impact on demodulation, tracking and acquisition performance.

This analysis of the RFI environment does not address C2Link, since the C2Link RFI environment remains difficult to be predicted because of the high uncertainty in the UAS traffic increase in the upcoming years.

3. Impact of jamming RFI on the capacity of the receiver to meet minimum requirements:

The two analyses presented in the above points 1 and 2 allow the knowledge of the capacity of the receiver to meet requirements under normal RFI environment. However, the presence of abnormal RFI source such as jamming may strongly degrade the capacity of the receiver to meet requirements. The objective of this analysis in point 3 is therefore to characterize the impact of the jamming signal on the capacity of the receiver to meet its requirements.

What is already done

Concerning GNSS, a general model characterizes the interference as an equivalent random noise from its spectrum footprint. However, concerning C2Link, an equivalent model does not exist as far as we are aware. Indeed, since C2Link system definition and standardization is still on-going, the

characterization of interference impact on C2Link receiver is not completely agreed. This PhD focuses on the frequency band 5030-5091 MHz identified for C2Link. Indeed, this frequency band has an AMS(R)S (Aeronautical Mobile Satellite (Route) Service) allocation, meaning that it is dedicated for aeronautical applications. Other frequency band, such as ISM for example, not identified for aeronautical applications, may also hold C2Link for non-safe operations. However, the RFI characterization and prediction within that bands would be very difficult, as these bands are shared by many applications. As a result, to address the characterization of RFI within these non-aeronautical bands by this PhD is not suitable.

Innovation of this PhD: new C2link performance degradation model

An equivalent model for C2 link signal is developed from the existing equivalent noise model for GNSS RFI in this PhD. This model characterizes the degradation of effective C2Link signal energy per bit to noise power spectral density ratio (E_b/N_0) caused by interference, called $E_b/N_{0,eff}$. E_b/N_0 is indeed the indicator identified in DO-362 to characterize C2Link capacity to meet required link performance (RLP). This E_b/N_0 degradation prediction model is then validated with simulations done with a C2Link receiver developed during this PhD. This RFI equivalent model can then be applied in order to determine a protection area during jamming activities.

1-3 Thesis organization

This PhD is divided in five main chapters in addition to Chapter 1 (Introduction) and Chapter 7 (Conclusion). They are presented below:

- **Chapter 2** is the review of the state of the art for characterization of RFI impact on GNSS receiver. After a short presentation of GNSS from a civil aviation point of view, signal processing modules are introduced. The impact of RFI on several signal processing indicators such as carrier to noise power spectral density C/N_0 is presented. GNSS RFI environment is introduced and current GNSS regulations are presented.
- **Chapter 3** is the review of the state of the art of C2Link definition and regulation. It introduces UAS operations, and the necessity to define a standardization. Afterwards, it fully describes the standardized command and control link, called C2Link, and presents two architecture candidates. Civil aviation C2Link requirements are listed. Eventually, the mathematical model of Gaussian Maximum Shift Keying (GMSK) C2Link signal is detailed.
- **Chapter 4** proposes a new methodology to derive protection areas for civil aviation GNSS usage during jamming operations. The three steps presented in section 1.2 are investigated. First, the capacity of the GNSS receiver to meet requirements is analyzed based on DO-235C [6] analysis, and is fully detailed for Galileo E1 receiver. Second, the impact of nominal RFI environment on GNSS receiver is characterized as an equivalent noise. RFI sources composing the nominal RFI environment are listed in DO-235C [6]. Some of them, which have been reviewed during this PhD as part of the elaboration of DO-235C [6], are detailed in this chapter. Third, the impact of the jammer signal on the capacity to respect requirements is computed. This methodology is illustrated with an example.
- **Chapter 5** focuses on a particular RFI type, which appears to be common in current GNSS jammers. This RFI source is referred to as chirp signal. This chapter starts with a mathematical definition of this chirp jammer waveform and analyzes its stationarity at the receiver radio frequency front-end module output. Afterwards, chirp RFI impact on C/N_0 degradation

indicator is mathematically modeled, and the theoretical prediction is compared to results obtained with a GNSS Matlab software receiver, as well as with a real IFEN SX3 receiver. As the theoretical prediction of the C/N_0 degradation induced by chirp matches the observation only at some conditions detailed in this chapter, an additional analysis is performed to predict code and phase tracking estimates in presence of chirp RFI. The prediction of code and phase tracking estimates is eventually compared to observations obtained using our Matlab GNSS software receiver.

- **Chapter 6** is dedicated to the analysis of resiliency of C2Link receivers facing RFI. It first designs synchronization and demodulation modules. The impact of RFI on the C2Link receiver capability to meet requirements is predicted in a second time, analyzing the BER degradation induced by the RFI.

1-4 Main products of the PhD thesis

The work performed during this PhD thesis has strongly contributed to the elaboration of civil aviation GNSS receiver standards. It required understanding of existing state of the art approaches and mathematical models, the definition of original approaches and models, the proposition and consideration of rich feedback in multiple ICAO NSP, RTCA SC159 WG6, EUROCAE WG62, RTCA SC159 WG 2 meeting sessions all along the 3 years of the thesis.

In particular, the following contributions to standardization were provided:

- **DO-235C - Assessment of RFI relevant to the L1/E1 frequency band:** This document is the revision of DO-235B document. This revision aims at updating the L1/E1 RFI environment and at developing ED-259 DFMC SBAS receiver MOPS. The following analyses of this PhD are included in DO-235C:
 - o Calculation of C/N_0 acquisition thresholds for DFMC receiver: A new acquisition strategy is developed in accordance with new ED-259A initial acquisition requirements and endorsed by RTCA SC-159 WG-6. From this strategy, acquisition thresholds are computed. Acquisition thresholds refer to the minimum C/N_0 of GNSS signals to fulfill initial acquisition requirements. Moreover, a full review of Galileo E1 tracking and demodulation thresholds is performed.
 - o Characterization of the impact of the RFI environment on Galileo E1 receiver in terms of C/N_0 degradation: The difference RFI sources identified in DO-235 are characterized in terms of equivalent noise for Galileo E1 receivers.
 - o C/N_0 link budget analysis: The demonstration of the capacity of Galileo E1 receivers to meet requirements is done through the calculation of effective C/N_0 link budgets in various relevant situations (world-wide Asian interference hot spot, high latitude low GNSS antenna gain, landing situations, etc.).

All this work is included in DO-235C.

- **DO-292A - Assessment of RFI relevant to the L5/E5a frequency band:** This document is the revision of DO-292 document. This revision aims at updating the L5/E5a RFI environment in order to develop DFMC SBAS ED-259 MOPS. The main contributions of this PhD to DO-292A are:
 - o Characterization of terrestrial emitters RFI: The characterization of the impact of one RFI source, referred to as terrestrial emitters, in terms of equivalent noise.

- C/N_0 link budget analysis: The demonstration of the capacity of GPS L5 and Galileo E5a receivers to meet requirements is done through the calculation of effective C/N_0 link budgets in various relevant situations in Europe.
- **ED-259A - Minimum operational performances standard for DFMC based augmentation system airborne equipment**: This standard defines minimum requirements and testing procedures for DFMC GNSS receivers. The work performed in this PhD allows the definition of the RFI environment to be considered during these testing procedures. Indeed, testing procedures aim at verifying that the receiver under test is compliant with the requirement in nominal interference environment. As interferences are injected under the form of wideband noise, the nominal interference environment must be characterized as an equivalent wideband noise. More precisely, the elements of this PhD included in ED-259 are:
 - RFI environment identification: Identification of the most relevant interference environment to define each test procedure.
 - RFI characterization: Characterization of these interference environments in terms of equivalent noise.

The characterization of the RFI environment has been included in ED-259A Appendix C.

Moreover, three scientific articles were published in ION GNSS+ conference proceedings during this Ph.D thesis. These articles are:

- **From ICAO GNSS interference mask to jamming protection area for safe civil aviation operation**. This article is included in ION GNSS+ 2021 proceedings. It describes a methodology refining the protection area during state jamming operations.
- **Impact of terrestrial emitters on civil aviation GNSS receivers**. This article is included in ION GNSS+ 2022 proceedings. It characterizes the impact of one particular RFI source, referred as terrestrial emitters, on the GNSS receiver equivalent noise.
- **GNSS acquisition thresholds for DFMC civil aviation GNSS receivers**. This article is included in ION GNSS+ 2022 proceedings. It computes GNSS acquisition thresholds, which are the assumed minimum C/N_0 values of GNSS signals that are needed to meet initial acquisition requirements.

In addition to these articles, it is planned to submit at least three journal papers.

- **GNSS L1/E1 ICAO interference mask derivation**. This article provides the mathematical background behind the ICAO interference mask which provides the maximum allowable power from non-aeronautical sources. It also checks that this ICAO mask, which has initially been elaborated to protect GPS L1C/A civil aviation legacy receiver, is still usable with DFMC receivers.
- **GPS L1C/A receiver C/N_0 degradation model in presence of chirp interference**. This article characterizes the impact of chirp RFI on C/N_0 degradation for GPS L1C/A receivers. It proposes a theoretical model predicting the C/N_0 degradation, and compares the prediction to C/N_0 degradation observed at a GNSS matlab software receiver output.
- **Impact of RFI on UAS C2Link receivers**. This article presents a design for synchronization and tracking loops modules of a GMSK C2Link receiver compliant with UAS requirements from civil

aviation standards. It also proposes a theoretical model to characterize the impact of the RFI on the BER performance.

Finally, the original method for prediction of protection areas during jamming developed during this thesis is under consideration by the French civil aviation services and by Eurocontrol for inclusion in their procedures and guidelines.

Chapter 2: Impact of interferences on civil aviation GNSS receivers

Global Navigation Satellite System (GNSS) signals are transmitted from global coverage satellites from Medium Earth Orbit (MEO) constellations which are around 20,000 km from the Earth surface. The received power on the Earth is thus very low. Most of GNSS signals have a CDMA (Code Division Multiple Access) structure, which allows to process low power signals dominated by the wideband noise environment. However, because of the low power of GNSS signals, GNSS is very sensitive to interference. Interference is defined by International Telecommunications Union (ITU) as “the effect of unwanted energy due to one or a combination of emissions, radiations, or inductions upon reception in a radiocommunication system, manifested by any performance degradation, misinterpretation, or loss of information which could be extracted in the absence of such unwanted energy” [14].

To assess the impact of interference on GNSS receiver performance, it is first important to describe GNSS signals modulation and the processing of GNSS signals. GNSS signals which have been considered during this PhD thesis are GPS L1C/A, Galileo E1, SBAS L1, GPS L5, Galileo E5a and SBAS L5. This chapter is divided in six sections. First, an introduction on GNSS is done, describing the current satellite constellations, and presenting the general principle. Second, GNSS signals modulation is described, focusing on GPS L1C/A, Galileo E1, GPS L5 and Galileo E5a signals. Third, signal processing performed in a GNSS receiver is detailed, analyzing the different operations (acquisition, tracking, demodulation) done by the receiver. Fourth, the impact of interference on GNSS receiver performance degradation is computed. Fifth, the interference environment faced by civil aviation GNSS receivers is described from the existing literature. Sixth, current regulation and certification characteristics about GPS and Galileo signal and civil aviation receiver are presented.

2-1 Introduction on GNSS

This section presents and defines the concept of GNSS. It is decomposed into two subsections. First, the GNSS definition, from an International Civil Aviation Organization (ICAO) point of view, is given, and the main existing GNSS constellations are described. Second, it presents the general principle of GNSS.

2-1.1 GNSS definition

[15] defines the GNSS as “a worldwide position and time determination system that includes one or more satellite constellations, aircraft receivers and system integrity monitoring, augmented as necessary to support the required navigation performance for the intended operation”. GNSS is thus defined by an architecture and a positioning and timing service. This subsection first presents the different constellations, and second presents the minimum navigation performances defined by the ICAO.

2-1.1.1 GNSS constellations

This paragraph first describes the core and regional satellite navigation systems. Second, since core satellite navigation systems are not sufficient to fulfill ICAO minimum required performance, augmentation systems are presented.

2-1.1.1.1 *Satellite navigation systems*

Current core and regional satellite navigation systems, which are an element of the GNSS architecture, follow the same principle which will be described in the next subsection. Nowadays, it exists four global constellations (also called core constellations) and three regional constellations.

Global constellations:

- GPS (Global Positioning System) is the American system. Its concept started around 1960. It was first a military only system. Civil aviation started to use GPS positioning service in 1994. Nowadays, approximately 30 satellites are operational. GPS satellites transmit several signals: GPS L1C/A, GPS L1P and for some satellites also GPS L1 M-code and GPS L1C in the 1559-1591 MHz frequency band, GPS L2 (L2P and for some satellites also L2c) in the 1215-1239.6 MHz frequency band, and GPS L5 in the 1164-1189 MHz frequency band. Civil aviation only uses GPS L1C/A and will use GPS L5 since these signals are in an aeronautical radio navigation system (ARNS) frequency band. GPS L1P is a military signal. GPS L1C is under consideration for future civil aviation usage.
- GLONASS is the Russian system.
- Beidou-2 and Beidou-3 are Chinese systems.
- Galileo is the European system. Currently, it holds approximately 22 active satellites.

Regional constellations:

- QZSS is the Japanese system.
- IRNSS (also called NavIC) is the Indian regional system.
- Beidou-1 is the Chinese regional system.

All of these satellite navigation systems can be divided into three segments:

- A space segment, which is composed of the satellites.
- A control segment, which is composed of ground stations monitoring and transmitting data to the satellites.
- A user segment, which is composed of all receivers using signals coming from the navigation satellite constellation.

2-1.1.1.2 *Augmentation systems*

Performance of satellite navigation systems is not sufficient to fulfill ICAO GNSS minimum performance. Therefore, augmentation systems must be added in the GNSS architecture. Three types of augmentation systems are used in civil aviation: the satellite-based augmentation system (SBAS), the ground-based augmentation system (GBAS) and the aircraft based augmentation system (ABAS).

Satellite based augmentation system

SBAS is composed of a ground station network, and of several satellites which cover a regional area. ICAO defines SBAS as an augmentation system in which the augmentation information is transmitted from a satellite. The SBAS satellites transmit information on ephemeris errors and satellite clocks errors, relatively to the information transmitted by the satellite navigation system in the navigation message. Single frequency SBAS also relay information on ionospheric errors. SBAS has the advantage of covering a wide (continental scale) area. SBAS is based on the inversed GNSS principle: a network of ground stations whose position is known collects and processes signals from the satellite navigation system. From these measurements, a central station computes orbital and satellite clock corrections with respect to the navigation message of the satellite navigation system. Then, these corrections are

sent to the geostationary satellites which relays the corrections to all the users. Single frequency SBAS also use dual frequency receivers on the ground to estimate ionospheric errors relayed to the users.

Currently, SBAS systems include [16]:

- WAAS (Wide Area Augmentation System) for North America continent.
- EGNOS (European Geostationary Navigation Overlay Service) for Europe.
- MSAS (MTSAT Satellite Augmentation System) for Japan.
- GAGAN (GPS-aided GEO Augmentation Navigation) for India.

And also under development:

- KASS (Korean Augmentation Satellite System) for South-Korea.
- SDCM (System for Differential Correction and Monitoring) for Russia.
- SouthPAN (Southern Positioning Augmentation Network) for Australia and New-Zealand.
- ASECNA (Association pour la SECurité de la Navigation Aérienne en Afrique et à Madagascar) for Africa.

Ground based augmentation system

GBAS is composed by one station which is generally installed in the vicinity of an airport. It is defined by the ICAO as an augmentation system in which the augmentation information is transmitted by a ground station. Since the positions of the GBAS station antennas are precisely known, the station can deduce some errors (ionospheric and tropospheric error, satellite clock error and ephemeris error), which are then transmitted by the ground station to the user. Because of the cost of maintenance of GBAS station for the airport operator, and considering that the coverage area is limited to one airport, only a few GBAS stations are installed worldwide [17].

Aircraft based augmentation system

ABAS monitors the integrity of the estimated position using the redundancy of GNSS information. It exists two types of ABAS:

- The Receiver Autonomous Integrity Monitoring (RAIM), for which only the GNSS information is used.
- The Aircraft Autonomous Integrity Monitoring (AAIM), for which the GNSS information is compared to information coming from other sensors (Inertial Navigation System, baro-altimeter, clock).

The RAIM is an algorithm to detect and potentially exclude faulty satellite measurements. It only uses GNSS measurements. One potential implementation of RAIM Fault Detection algorithm is to compare the pseudo-range measurement predicted from the computed position to the real measurements. If the normalized squared norm of this difference exceeds a given threshold, then an integrity failure can be detected. RAIM has a false alarm and missed detection guaranteed if the pseudorange measurements errors distribution is bounded by the assumed distribution. In addition, an important hypothesis for current RAIM is that at the more one faulty measurement can occur. The advantage of RAIM is that this augmentation system does not necessitate additional equipment.

2-1.1.2 ICAO GNSS minimum performances

ICAO defines the Signal In Space (SiS) as the aggregate guiding signal reaching the antenna of a fault free receiver. ICAO performance for SiS is defined through for performance objective terms [18].

1. Accuracy at 95%: The accuracy at 95% is the positioning error threshold such that the probability that the positioning error is lower than this threshold is equal to 95%.
2. Availability: The availability of a system is its capacity to provide a service with the required performances at the beginning of the operation. When it comes to GNSS, the availability is the probability that the SiS respects the accuracy at 95% performance objective.
3. Continuity: The continuity of a system is its ability to provide a service without unexpected discontinuities.
4. Integrity: The integrity is a measure of a confidence on the information returned by the system. The integrity includes the capacity of a system to raise alarm when the system does not meet the performance objectives. The integrity performance objective is defined through three parameters:
 - The alert limit is the maximum positioning error allowed for a given operation.
 - The integrity risk is the probability to not raise an alert within a given period even though the positioning error exceeds the alert limit.
 - The time to alert (TTA) is the maximum time so raise an alarm if the positioning error exceeds the alert limit.

Table 2-1 provides the performances objectives for the different civil aviation operations given in [15].

Operation	Accuracy		Integrity				Continuity	Availability
	Horizontal	Vertical	TTA	Integrity risk	Horizontal alert limit	Vertical alert limit		
En-route (oceanic)	3.7 km	N/A	5 min	$1 \cdot 10^{-7} h^{-1}$	7.4 km	N/A	$1 \cdot 10^{-4}$ to $1 \cdot 10^{-8} h^{-1}$	0.99 to 0.99999
En-route (continental)	3.7 km	N/A	5 min	$1 \cdot 10^{-7} h^{-1}$	3.7 km	N/A	$1 \cdot 10^{-4}$ to $1 \cdot 10^{-8} h^{-1}$	0.99 to 0.99999
En-route (terminal)	0.74 km	N/A	15 s	$1 \cdot 10^{-7} h^{-1}$	1.85 km	N/A	$1 \cdot 10^{-4}$ to $1 \cdot 10^{-8} h^{-1}$	0.99 to 0.99999
Approach, NPA, Departure	220 m	N/A	10 s	$1 \cdot 10^{-7} h^{-1}$	556 m	N/A	$1 \cdot 10^{-4}$ to $1 \cdot 10^{-8} h^{-1}$	0.99 to 0.99999
APV1	16 m	20 m	6 s	$1 \cdot 2 \cdot 10^{-7}$ per app	40 m	50 m	$1 \cdot 8 \cdot 10^{-6}$ per 15 s	0.99 to 0.99999
APV2	16 m	8 m	6 s	$1 \cdot 2 \cdot 10^{-7}$ per app	40 m	20 m	$1 \cdot 8 \cdot 10^{-6}$ per 15 s	0.99 to 0.99999
Cat1	16 m	6m to 4m	6 s	$1 \cdot 2 \cdot 10^{-7}$ per app	40 m	35 m to 10 m	$1 \cdot 8 \cdot 10^{-6}$ per 15 s	0.99 to 0.99999

Table 2-1: ICAO minimum performance objectives for civil aviation operations

APV1 and APV2 refers to two levels of GNSS approach and landing operations with vertical guidance.

For each operation, Table 2-1 provides the availability in a range. Indeed, the availability depends on other factors, such as weather, presence of alternative conventional navigation aids, traffic density. An availability of 0.99 means that GNSS is practicable, but it may be safe to also use conventional navigation aids. With an availability of 0.99999, GNSS can be used as the unique navigation aid [19].

Similarly, a range of values is given for continuity for en-route and NPA operations, since this requirement depends on other factors such as traffic density and the presence of alternative navigation aids.

2-1.2 GNSS principle

This section presents the principle of the GNSS positioning. The principle is inspired from the trilateration principle, in which the receiver measures the propagation delay between the satellite transmitter and the receiver antenna. In GNSS, the propagation delay is accessed by comparing the transmission instant, driven by the transmitter and expressed in the transmitter clock frame, to the received instant in the receiver time frame. Since the receiver time frame is different from the satellite transmitter time frame, the receiver must also compute the time offset between the transmitter and the receiver time frame in order to compute the position.

To summarize, the receiver measures the propagation delay between the satellite and its receiver antenna which is biased by the receiver and transmitter time frame offset. This biased propagation delay between the receiver antenna and satellite i , multiplied by the propagation velocity c , is called the pseudo-range P_i and can be expressed by (Eq 2-1).

$$P_i = c\Delta\tau_i + c\Delta t_{u,i} + w_i \quad (\text{Eq 2-1})$$

$\Delta\tau_i$ is the true propagation delay between the satellite and the receiver antenna. $\Delta t_{u,i}$ is the time offset between the receiver and satellite i clocks. w_i is measurement error.

The clock offset between the receiver and transmitter clocks can be decomposed under a reference time frame, called the GPS time as expressed in (Eq 2-2).

$$\Delta t_{u,i} = \Delta t_u - \Delta t_i \quad (\text{Eq 2-2})$$

Δt_u is the receiver clock offset with respect to the GPS time, and Δt_i is the receiver clock offset with respect to the GPS time.

The satellite clock offset term Δt_i is corrected thanks to information transmitted by the signal issued from the satellite, and thanks to correction information transmitted by SBAS or GBAS station by an estimation $\Delta\hat{t}_i$ of the satellite clock error with respect to the GPS time. The corrected pseudo-range is then given in (Eq 2-3).

$$\begin{aligned} P_i^c &= P_i + \Delta\hat{t}_i = c\Delta\tau_i + c\Delta t_u + w_i \\ &= c\sqrt{(x - x_i)^2 + (y - y_i)^2 + (z - z_i)^2} + c\Delta t_u + w_i \end{aligned} \quad (\text{Eq 2-3})$$

(x, y, z) is the receiver position in the Earth centered earth fixed (ECEF) at reception time and (x_i, y_i, z_i) is the satellite i position in the ECEF frame at emission time. The position of the satellite is estimated by the receiver thanks to orbital data transmitted in the signal.

Therefore, four terms remain unknown in (Eq 2-3): the satellite position x, y and z , and the receiver clock offset with respect to the GPS time. A minimum of four corrected pseudo-ranges is thus needed to compute the position and the time.

As developed previously, the receiver needs to know the satellite position and the satellite clock error with respect to the GPS time in order to deduce the corrected pseudo-range. These pieces of information can be deduced from data transmitted by the signal, under the form of a navigation message which modulates the GNSS signal. Therefore, in order to compute a position, the receiver must be able to measure pseudo-range as well as to demodulate information transmitted by the satellite.

2-2 GNSS signals modulation

The objective of this section is to describe the GNSS signals modulation. The mathematical signal model of four GNSS signals of interest for this PhD thesis (GPS L1C/A, Galileo E1, GPS L5 and Galileo E5a) is detailed.

2-2.1 GPS L1C/A signal

This section first describes the mathematical expression for GPS L1C/A signal component. Second, it analyzes some spectrum and statistical properties about correlation and cross-correlation between two GPS L1C/A signals.

2-2.1.1 GPS L1C/A mathematical signal

GPS L1C/A signal is a BSPK modulated signal component. The emitted GPS L1C/A signal can be mathematically expressed by (Eq 2-4).

$$s_{GPS L1}(t) = \sqrt{2P_{L1}^T} c_m(t) d(t) \cos(2\pi f_0 t + \varphi_0) \quad (\text{Eq 2-4})$$

P_{L1}^T is the power of the emitted GPS L1C/A signal. $c_m(t)$ is the modulation pseudo random noise (PRN) signal and $d(t)$ is the navigation message signal. The bits of the navigation message are sent with a 50 Hz rate. f_0 is the carrier frequency and φ_0 is the initial phase of the GPS L1C/A signal.

The primary PRN sequence $c_m(t)$ has particular statistical properties that are key to the functioning of CDMA systems. In particular, the power spectral density and autocorrelation of the PRN sequence are very similar to the ones of a white noise. Primary PRN sequence are characterized by their length L_{PRN} and their chip duration T_c . For GPS L1C/A, the PRN sequence is composed by $L_{PRN} = 1023$ chips and the chip rate is 1.023 Mchip/s. The generation of the primary PRN sequence is described in the Interface Specification documents (IS, [20]) and is out of the scope of this thesis so not developed here. (Eq 2-5) gives the mathematical expression of the modulated PRN signal.

$$c_m(t) = \left(\sum_{k=0}^{L_{PRN}-1} c_k \delta(t - kT_c) \right) * \left(\sum_{j=-\infty}^{+\infty} \delta(t - jT_R) \right) * m(t) \quad (\text{Eq 2-5})$$

Where the star operator $*$ is the convolution operator. The convolution of the two sum terms corresponds to the repetition over time of the finite PRN code. $(c_k)_{k \in [0; L_{PRN}-1]} \in \{-1; +1\}^{L_{PRN}}$ are the L_{PRN} bits of the PRN sequence. T_R is the period of repetition of the PRN sequence. T_R is linked to the number of bits in the sequence L_{PRN} and the chip period T_c : $T_R = L_{PRN} T_c$. For GPS L1C/A, the PRN code repeats every 1 ms. Finally, m is the shaping waveform. GPS L1C/A PRN code is modulated with a rectangular signal, whose duration is equal to the bit period T_c . Therefore, the shaping waveform $m(t)$ is given by (Eq 2-6).

$$m(t) = \text{rect}_{T_c}(t) \quad (\text{Eq 2-6})$$

2-2.1.2 Spectrum properties of the GPS L1C/A PRN signal

Section 2-2.1.1 established a mathematical model for GPS L1C/A signal. The objective of this section is to derive the power spectral density of the GPS L1C/A PRN signal. As it will be detailed in section 2-4 of this chapter, the knowledge of the power spectral density of GNSS signal is important to determine the impact of interference on the GPS L1C/A receiver performance.

The calculation of the power spectral density of the GPS L1C/A PRN signal is done in two steps. First, the autocorrelation function of the PRN sequence is computed. Second, the power spectral density is deduced taking the Fourier transform of the autocorrelation. In this section, the influence of the navigation bits is neglected, because the navigation bit rate (50 Hz) is much lower than the chip rate (1.023 Mchip/s). In other words, the power spectral density of $s_{L1CA}(t) = \sqrt{2P_{L1}^T} c_m(t) \cos(2\pi f_0 t + \varphi_0)$ is computed.

Calling K_X the autocorrelation function of a given signal X , it can be shown that the deterministic periodic autocorrelation of the PRN signal c_m given in (Eq 2-5) is expressed in (Eq 2-7).

$$K_{c_m}(\tau) = K_c * \left(\sum_{j=-\infty}^{+\infty} \delta(t - jT_R) \right) * K_m(\tau) \quad (\text{Eq 2-7})$$

With

$$c(t) = \left(\sum_{k=0}^{L_{PRN}-1} c_k \delta(t - kT_c) \right)$$

$c(t)$ is the time limited PRN sequence.

First, the deterministic autocorrelation of the rectangular shaping waveform m is given in (Eq 2-8).

$$K_m(\tau) = T_c \text{tri}_{T_c}(\tau) \quad (\text{Eq 2-8})$$

Second, since c is time limited within $[0; T_R]$ and deterministic, its autocorrelation function is given by (Eq 2-9).

$$K_c(\tau) = \int_{-\infty}^{+\infty} c(t)c(t-\tau)dt = \int_0^{T_R} c(t)c(t-\tau)dt \quad (\text{Eq 2-9})$$

Injecting the expression of $c(t)$ in (Eq 2-9) and developing the calculation, it comes that $K_c(\tau)$ can be expressed by (Eq 2-10). Denoting $K(m) = \frac{1}{L_{PRN}} \sum_{k=0}^{L_{PRN}-1} c_k c_{k-m}$ the autocorrelation of the PRN sequence,

$$K_c(\tau) = \begin{cases} 0 & \text{if } \tau/T_c \notin \llbracket 0; L_{PRN} - 1 \rrbracket \\ \frac{1}{T_R} \sum_{k=0}^{L_{PRN}-1} c_k c_{k-\tau} & \text{if } \tau/T_c \in \llbracket 0; L_{PRN} \rrbracket \end{cases} = \frac{1}{T_c} \sum_{m=0}^{L_{PRN}-1} K(m) \delta(\tau - mT_c) \quad (\text{Eq 2-10})$$

For GPS L1C/A, PRN sequences are Gold codes. In particular and as shown in Figure 2-1, the autocorrelation of the PRN sequence is similar to the autocorrelation of a white noise, which is a pure line.

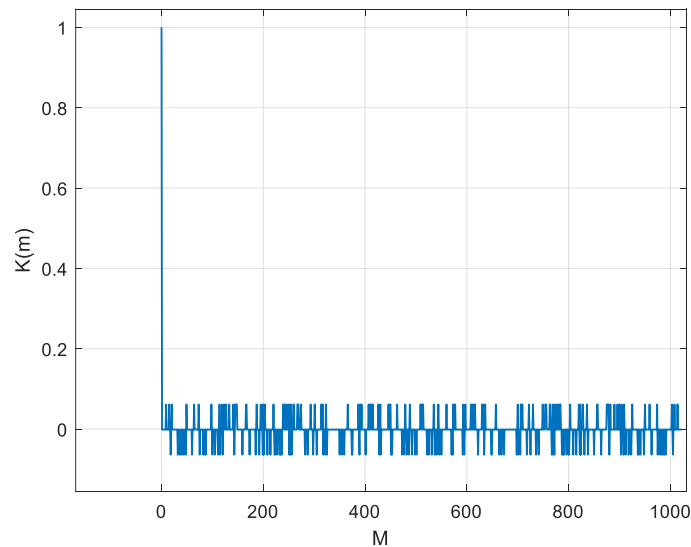


Figure 2-1: Autocorrelation of PRN 1 sequence

In addition, the cross-correlation function between two PRN sequences is below -11.95 dB (in amplitude), so below -23.9 dB in power. This isolation between two GPS L1C/A signals allows the processing of a given GPS L1C/A signal embedded with other GNSS signals.

Injecting (Eq 2-10) and (Eq 2-8) in (Eq 2-7), the autocorrelation of the deterministic periodic PRN signal is given by (Eq 2-11).

$$K_{c_m}(\tau) = \left(\sum_{m=0}^{L_{PRN}-1} K(m) \text{tri}_{T_c}(t - mT_c) \right) * \left(\sum_{j=-\infty}^{+\infty} \delta(t - jT_R) \right) \quad (\text{Eq 2-11})$$

Then, the PRN signal power spectral density S_{c_m} is computed taking the Fourier transform of K_{c_m} . The expression for S_{c_m} is given by (Eq 2-12).

$$\begin{aligned} S_{c_m}(f) &= T_c \left(\sum_{m=0}^{L_{PRN}-1} K(m) \text{sinc}^2(\pi f T_c) e^{-i2\pi f m T_c} \right) \frac{1}{T_R} \sum_{j=-\infty}^{+\infty} \delta\left(f - \frac{j}{T_R}\right) \\ &= \frac{1}{L} \sum_{j=-\infty}^{+\infty} \left(\sum_{m=0}^{L_{PRN}-1} K(m) e^{-i2\pi \frac{mj}{L}} \right) \text{sinc}^2\left(\frac{\pi j}{L}\right) \delta\left(f - \frac{j}{T_R}\right) \end{aligned} \quad (\text{Eq 2-12})$$

Denoting $C_{\text{sinc}}(j) = \left(\sum_{m=0}^{L_{PRN}-1} K(m) e^{-i2\pi \frac{mj}{L_{PRN}}} \right) \text{sinc}^2\left(\frac{\pi j}{L_{PRN}}\right)$, (Eq 2-12) can be reduced to the expression of (Eq 2-13).

$$S_{c_m}(f) = \frac{1}{L_{PRN}} \sum_{j=-\infty}^{+\infty} C_{\text{sinc}}(j) \delta\left(f - \frac{j}{T_R}\right) \quad (\text{Eq 2-13})$$

As it can be noticed in (Eq 2-13), the PRN signal has a line spectrum, with lines regularly spaced every inverse PRN period. This observation can be justified by the T_R -periodicity of the PRN signal.

Figure 2-2 shows the power spectral density S_{c_m} of the deterministic periodic PRN 1 signal.

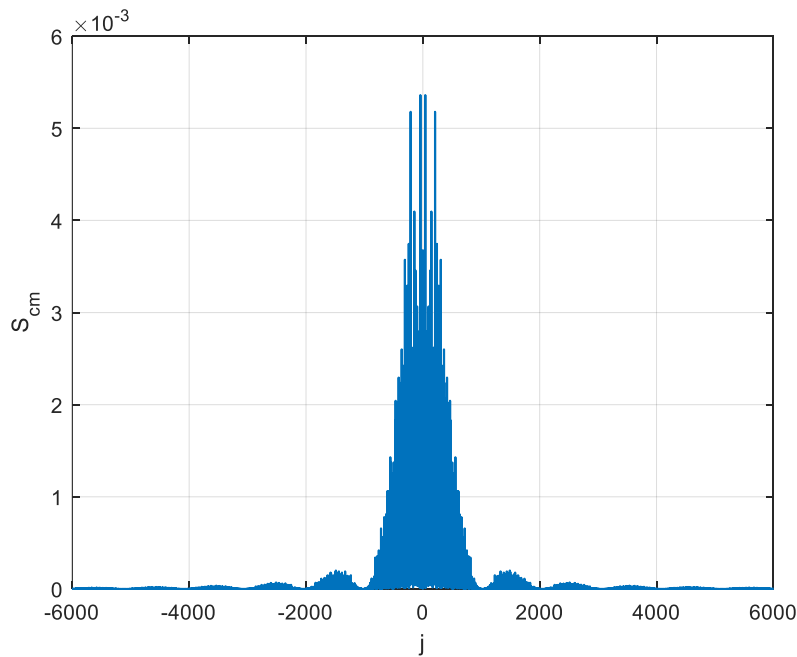


Figure 2-2: Power spectral density of PRN1 signal

As predicted by (Eq 2-13), Figure 2-2 shows a line spectrum with line regularly spaced every 1 kHz. In addition, the spectrum has a sinc² shape due to the rectangular waveform. The main spectrum lobe single sided width is equal to the chip rate (1.023 Mchips/s). Among all PRN allocated to GPS L1C/A, PRN 24 has the highest spectrum line, which is 123 kHz from the L1 frequency.

Finally, the power spectral density of a GPS L1C/A signal is given by (Eq 2-14).

$$S_{L1CA}(f) = \frac{P_{L1}^T}{2} S_{c_m}(f) * (\delta(f - f_0) + \delta(f + f_0)) \quad (\text{Eq 2-14})$$

2-2.2 Galileo E1 signal

First satellites of Galileo constellation have been launched in 2014. As of 2022 there are 22 operational satellites, the final constellation is expected to be composed of 30 satellites. Therefore, it is expected that civil aviation uses Galileo signals in the coming years. This section first describes the Galileo E1 mathematical signal. Second, it analyzes the spectral properties of this signal.

2-2.2.1 Galileo E1 mathematical signal

Galileo E1 uses a CBOC modulation. The signal holds two in-phase components, called data and pilot components. Note that Galileo satellites also transmit another signal in phase quadrature in the L1/E1 band, called PRS. The PRS signal is not used for civil aviation application, so it is not developed here. The mathematical expression for Galileo E1 signal is given in (Eq 2-15).

$$S_{Gal E1}(t) = \sqrt{2P_{D,E1}^T} c_D(t) d(t) m_D(t) \cos(2\pi f_0 t + \varphi) - \sqrt{2P_{P,E1}^T} c_P(t) h_P(t) m_P(t) \cos(2\pi f_0 t + \varphi) \quad (\text{Eq 2-15})$$

- $P_{D,E1}^T$ and $P_{P,E1}^T$ are respectively the power of the data and pilot components. Each component holds half of the total Galileo E1 power, so $P_{P,E1}^T$ and $P_{D,E1}^T$ are equal to $P_{E1}^T/2$.
- c_D and c_P are respectively the PRN codes of the data and pilot components. They are defined in [21]. One PRN sequence is associated to a space vehicle (SV). The PRN sequence is 4092 bits long, with a data rate of $D_c = 1.023 \text{ Mchip/s}$. Thus, it is repeated every $T_R = 4 \text{ ms}$.
- h_P is the secondary code. The secondary code is a fixed sequence containing 25 bits with a repetition period of 100 ms. It is defined in [21] and is common for all SV.
- d is the navigation message. The data rate is 250 bit/s.
- m_D and m_P are respectively the modulation waveforms of the data and pilot components. The data component has a CBOC(6,1,1/11,+) modulation whereas the pilot component has a CBOC(6,1,1/11,-) modulation. The mathematical expressions of m_D and m_P are given in (Eq 2-16).

$$m_D(t) = \sqrt{\frac{10}{11}} \text{sign}(\sin(2\pi t D_c)) + \sqrt{\frac{1}{11}} \text{sign}(\sin(2\pi 6t D_c))$$

$$m_P(t) = \sqrt{\frac{10}{11}} \text{sign}(\sin(2\pi t D_c)) - \sqrt{\frac{1}{11}} \text{sign}(\sin(2\pi 6t D_c)) \quad (\text{Eq 2-16})$$

- f_0 is the carrier frequency, and φ is the initial phase.

2-2.2.2 Galileo E1 spectrum

Section 2-2.2.1 presented the Galileo E1 mathematical signal. The objective of section 2-2.2.2 is to analyze the spectrum of Galileo E1 signals. As in section 2-2.1.2, the influence of the navigation

message is not considered in this section. In addition, since the secondary code is at a lower rate than the PRN signals, it is also not considered in this section. The derivation of the power spectrum density of Galileo E1 signal follows the same steps than section 2-2.1.2. First, the autocorrelation is computed. Second, the power spectral density is derived.

Data and pilot PRN sequences are chosen such that the cross-correlation between the two sequences is low. As a consequence, each component can be considered individually, and the Galileo E1 power spectral density can be approximated by the sum of the power spectral densities of each component.

Similarly to section 2-2.1.2, the autocorrelation of the component X of the Galileo E1 signal at baseband can be expressed by (Eq 2-17), where X denotes either the Data ($X = D$) or pilot ($X = P$) component.

$$K_{c_m^X}(\tau) = K_{c_X} * \left(\sum_{j=-\infty}^{+\infty} \delta(t - jT_R) \right) * K_m(\tau) \quad (\text{Eq 2-17})$$

K_{c_X} expression is given in (Eq 2-10). Since K_{c_X} is a sum of regularly spaced diracs, (Eq 2-17) can be reduced to (Eq 2-18).

$$K_{c_m^X}(\tau) = \left(\sum_{m=0}^{L_{PRN}-1} K_X(m) K_m(t - mT_c) \right) * \left(\sum_{j=-\infty}^{+\infty} \delta(t - jT_R) \right) (\tau) \quad (\text{Eq 2-18})$$

Taking the Fourier transform of (Eq 2-18), the power spectral density of the X component of Galileo E1 signal at baseband is given in (Eq 2-19).

$$\begin{aligned} S_X(f) &= \left(\sum_{m=0}^{L_{PRN}-1} K_X(m) S_{m_X}(f) e^{-i2\pi f m T_c} \right) \frac{1}{T_R} \sum_{j=-\infty}^{+\infty} \delta\left(f - \frac{j}{T_R}\right) \\ &= \frac{1}{T_R} \sum_{j=-\infty}^{+\infty} C_m(j) S_{m_X}\left(\frac{j}{T_R}\right) \delta\left(f - \frac{j}{T_R}\right) \end{aligned} \quad (\text{Eq 2-19})$$

With $C_m(j) = \sum_{m=0}^{L_{PRN}-1} K_X(m) e^{\frac{i2\pi m j}{L_{PRN}}}$ and S_m is the power spectral density of the waveform of pilot ($X = P$) or data ($X = D$) component.

It can be shown [22] that the power spectral density of the modulation waveforms of pilot and data components can be expressed as in (Eq 2-20).

$$\begin{aligned} S_{m_D}(f) &= \frac{10}{11} S_{BOC(1,1)}(f) + \frac{1}{11} S_{BOC(6,1)}(f) \\ S_{m_P}(f) &= \frac{10}{11} S_{BOC(1,1)}(f) - \frac{1}{11} S_{BOC(6,1)}(f) \end{aligned} \quad (\text{Eq 2-20})$$

$S_{BOC(1,1)}$ and $S_{BOC(6,1)}$ are respectively the power spectral density of a BOC(1,1) and BOC(6,1) modulations. Their respective analytical expressions are given in (Eq 2-21).

$$\begin{aligned} S_{BOC(1,1)}(f) &= T_c (\text{sinc}(\pi f T_c) \tan(\pi f T_c))^2 \\ S_{BOC(6,1)}(f) &= T_c \left(\text{sinc}(\pi f T_c) \tan\left(\frac{\pi f T_c}{6}\right) \right)^2 \end{aligned} \quad (\text{Eq 2-21})$$

Finally, the power spectral density of the Galileo E1 signal is given in (Eq 2-22).

$$S_{E1}(f) = \left(P_{D,E1}^T S_D(f) + P_{P,E1}^T S_P(f) \right) * \frac{\delta(f - f_0) + \delta(f + f_0)}{2} \quad (\text{Eq 2-22})$$

Galileo E1 signal has a line spectrum, with lines regularly spaced every $\frac{1}{T_R} = 250 \text{ Hz}$. Figure 2-3 shows the normalized power spectral density of the Galileo E1 signal at baseband.

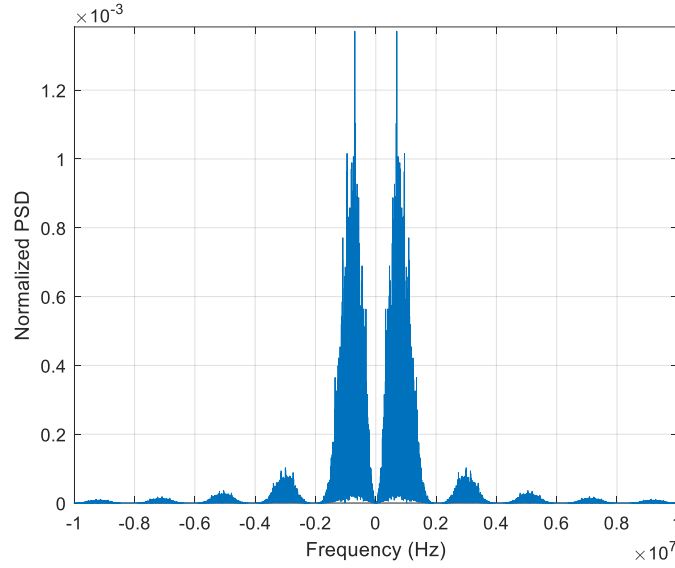


Figure 2-3: Power spectral density of Galileo E1 PRN 1 signal at baseband

As predicted in (Eq 2-19), Figure 2-3 is composed of lines at each multiple of the inverse of the PRN sequence repetition rate (250 Hz). In addition, Figure 2-3 presents two main lobes that are characteristic of the Galileo E1 CBOC modulation.

2-2.3 GPS L5 signal

Some GNSS signals such as GPS L5 signals are also transmitted on the L5/E5a frequency band (1164 – 1189 MHz). The objective of this section is to mathematically express GPS L5 signals, and to derive the spectrum of these signals.

2-2.3.1 GPS L5 signal

GPS L5 and Galileo E5a signals holds two components in phase quadrature, called data and pilot components. Each of these components is BPSK modulated. The mathematical expression of GPS L5 and Galileo E5a signals is given in (Eq 2-23).

$$s_{L5}(t) = \sqrt{2P_{D,L5}^T} d(t)c_D(t)h_D(t) \cos(2\pi f_0 t + \varphi) + \sqrt{2P_{P,L5}^T} c_P(t)h_P(t) \sin(2\pi f_0 t + \varphi) \quad (\text{Eq 2-23})$$

- $P_{D,L5}^T$ and $P_{P,L5}^T$ are respectively the power of the data and pilot components. Each component holds half of the total GPS L5 power, so $P_{P,L5}^T$ and $P_{D,L5}^T$ are equal $P_{L5}^T/2$.
- c_D and c_P are respectively the PRN codes of the data and pilot components. They are defined in [23]. One PRN sequence is associated to a space vehicle (SV). The PRN sequence is 10230 bits long, with a data rate of $D_c = 10.23 \text{ Mchip/s}$. Thus, it is repeated every $T_R = 1 \text{ ms}$.
- h_D and h_P are respectively the materialization of the secondary code (Neuman-Hoffman for GPS) used on the data and pilot components. The data secondary code is a fixed sequence containing 10 bits with a repetition period of 10 ms. The pilot secondary code is a fixed sequence containing 20 bits with a repetition period of 20 ms. The data rate is thus 1 ms for both secondary codes. They are defined in [23] and are common for all SV.

- d is the navigation message. The data rate is 50 bit/s. Since the navigation message is rate 1/2 convolution encoded with a Forward Error Correction (FEC) code, the resulting sample rate is 100 samp/s.
- f_0 is the carrier frequency, and φ is the initial phase.

2-2.3.2 GPS L5 spectrum

Section 2-2.3.1 presented the GPS L5 and Galileo E5a mathematical signals. The objective of section 2-2.3.2 is to derive the spectrum of GPS L5 and Galileo E5a signals.

The derivation of the power spectral density of GPS L5 signal is not completely detailed here since it is very similar to the calculation done in sections 2-2.2.2 and 2-2.1.2. It can be shown that the power spectral density of GPS L5 and Galileo E5a signal can be expressed by (Eq 2-24).

$$S_{L5}(f) = \left(P_{D,L5}^T S_D(f) + P_{P,L5}^T S_P(f) \right) * \frac{\delta(f - f_0) + \delta(f + f_0)}{2} \quad (\text{Eq 2-24})$$

Since the data and pilot components are both BPSK modulated, $S_X(f)$ can be expressed as in (Eq 2-13), where X denotes either the data ($X = D$) or the pilot ($X = P$) component.

2-2.4 Galileo E5 signal

This section presents the Galileo E5 mathematical model and highlights the similarity with GPS L5. Galileo E5 signal is AltBoc modulated and holds two components, called E5a and E5b. According to [21] and [24], Galileo E5 normalized signal mathematical model at baseband is given by (Eq 2-25).

$$\begin{aligned}
s_{E5, BB}(t) = & \frac{1}{2\sqrt{2}} (e_{E5a-D}(t) + i e_{E5a-P}(t)) \left(s_{CE5-S}(t) - i s_{CE5-S} \left(t - \frac{T_s}{4} \right) \right) + \\
& \frac{1}{2\sqrt{2}} (\bar{e}_{E5a-D}(t) + i \bar{e}_{E5a-P}(t)) \left(s_{CE5-P}(t) + i s_{CE5-P} \left(t - \frac{T_s}{4} \right) \right) + \\
& \frac{1}{2\sqrt{2}} (e_{E5b-D}(t) + i e_{E5b-P}(t)) \left(s_{CE5-S}(t) - i s_{CE5-S} \left(t - \frac{T_s}{4} \right) \right) + \\
& \frac{1}{2\sqrt{2}} (\bar{e}_{E5b-D}(t) + i \bar{e}_{E5b-P}(t)) \left(s_{CE5-P}(t) + i s_{CE5-P} \left(t - \frac{T_s}{4} \right) \right) \\
e_{E5a-D}(t) = & \sum_{i=-\infty}^{+\infty} c_{E5a}^D(t) d_a(t) \text{rect}_{T_c}(t - iT_c) \\
e_{E5a-P}(t) = & \sum_{i=-\infty}^{+\infty} c_{E5a}^P(t) \text{rect}_{T_c}(t - iT_c) \\
e_{E5b-D}(t) = & \sum_{i=-\infty}^{+\infty} c_{E5b}^D(t) d_b(t) \text{rect}_{T_c}(t - iT_c) \\
e_{E5b-P}(t) = & \sum_{i=-\infty}^{+\infty} c_{E5b}^P(t) \text{rect}_{T_c}(t - iT_c) \\
\bar{e}_{E5a-D} = e_{E5a-P} e_{E5b-D} e_{E5b-P} & \quad \bar{e}_{E5b-D} = e_{E5b-P} e_{E5a-D} e_{E5a-P} \\
\bar{e}_{E5a-P} = e_{E5a-D} e_{E5b-D} e_{E5b-P} & \quad \bar{e}_{E5b-P} = e_{E5b-D} e_{E5a-D} e_{E5a-P}
\end{aligned} \quad (\text{Eq 2-25})$$

In (Eq 2-25), c_{E5x}^Y is the PRN code of component Y (Y=D or P, for Data or Pilot) of signal E5x (x is either a or b). d_x is the navigation message of signal E5x. T_s is the inverse of the AltBoc subcarrier rate ($T_s = \frac{1}{15.345 \cdot 10^6}$ s). Sub-carriers s_{CE5-S} and s_{CE5-P} are illustrated in Figure 2-4.

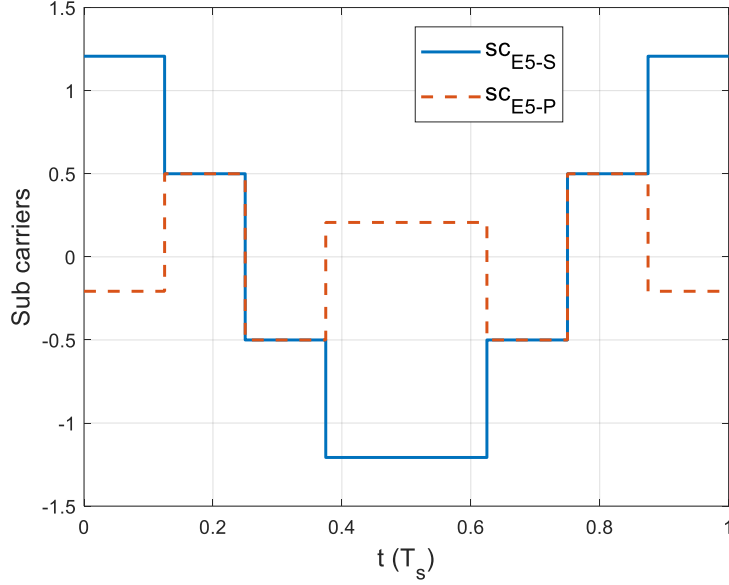


Figure 2-4: Galileo E5a sub-carriers

Eventually, Galileo E5 real signal is expressed in (Eq 2-26).

$$s_{E5}(t) = \sqrt{P_{E5}^T} \text{Re}\{s_{E5,BB}(t)\} \cos(2\pi f_{E5} t) - \sqrt{P_{E5}^T} \text{Im}\{s_{E5,BB}(t)\} \sin(2\pi f_{E5} t) \quad (\text{Eq 2-26})$$

P_{E5}^T is the total transmitted Galileo E5 signal power. f_{E5} is the Galileo E5 carrier frequency (1191.795 MHz).

According to [21], Galileo E5 signal can be approximated as the sum of two QPSK modulated signals: E5a around frequency L5 (1176.45 MHz), and E5b around 1207.14 MHz. Only Galileo E5a is used in the civil aviation domain, so E5b is no more considered in this thesis. Galileo E5a is then approximated by (Eq 2-27).

$$s_{E5a}(t) = \sqrt{2P_{D,E5a}^T} c_{E5a}^D(t) d_a(t) \cos(2\pi f_{E5a} t) - \sqrt{2P_{P,E5a}^T} c_{E5a}^P(t) \sin(2\pi f_{E5a} t) \quad (\text{Eq 2-27})$$

- $P_{X,E5a}^T$ is the power of component X ($X = D$ or $X = P$) of Galileo E5a. Since the power is equally shared between the data and pilot component, $P_{D,E5a}^T = P_{P,E5a}^T = P_{E5a}^T/2$.
- $f_{E5a} = 1176.45 \text{ MHz}$ is the Galileo E5 carrier frequency.

It can be noticed that Galileo E5a signal has a very similar structure than GPS L5, with two components data and pilot in phase quadrature which are BPSK modulated. The main difference between Galileo E5a signal and GPS L5 signal of (Eq 2-23) is the absence of secondary code. Therefore, in this thesis, a common model of Galileo E5a and GPS L5 is assumed, and the common mathematical expression that will be used is given by (Eq 2-23). Likewise, Galileo E5a spectrum can also be deduced by (Eq 2-24), replacing $P_{D,L5}^T$ and $P_{P,L5}^T$ by $P_{D,E5a}^T$ and $P_{P,E5a}^T$ respectively.

2-2.5 Summary on GNSS signals

Sections 2-2.1, 2-2.2, 2-2.3 and 2-2.4 presented the mathematical GNSS signals used for civil aviation navigation and derived the spectrum of these signals. Spectrum of GNSS signals has a key role when it comes to estimate the impact of interference on the receiver performance. Table 2-2 summarizes the characteristics of the four signals analyzed in this section.

	GNSS signal					
	GPS L1C/A		Galileo E1		GPS L5/Galileo E5a	
Number of components	1		2 (in phase)		2 (in phase quadrature)	
Carrier frequency (MHz)	1575.42		1575.42		1176.45	
Component			Data	Pilot	Data	Pilot
Modulation	BPSK		CBOC(6,1,1/11,+)	CBOC(6,1,1/11,-)	BPSK(10)	BPSK(10)
PRN code chip rate (MHz)	1.023		1.023	1.023	10.23	10.23
PRN code length (bits)	1023		4092	4092	10230	10230
Secondary code	No		No	Yes	Yes	Yes
Secondary code bit rate (Hz)	-		-	250	1000	1000
Secondary code length (bits)	-		-	25	10	20
Data rate (symb/s)	50		250	No data	100	No data

Table 2-2: Summary of GNSS characteristics

2-3 GNSS signal processing

Section 2-2 presented the mathematical GNSS signals expression. Section 2-3 focuses on the GNSS signal processing performed by the receiver. The objective of this section is to describe the signal processing operations performed by the receiver to extract useful information from the incoming GNSS signal (pseudoranges for example). This section is divided in three parts. First, the classical architecture of a GNSS receiver is presented. Second, the received GNSS signal at the antenna port is described. Third, the signal processing stages of the receiver are detailed. Mathematical developments in this section are performed for GPS L1C/A signal, but the signal processing principle remains the same for other signals described in section 2-2.

2-3.1 Generic GNSS receiver

[25] describes a generic GNSS receiver with 8 functions, as shown in Figure 2-5.

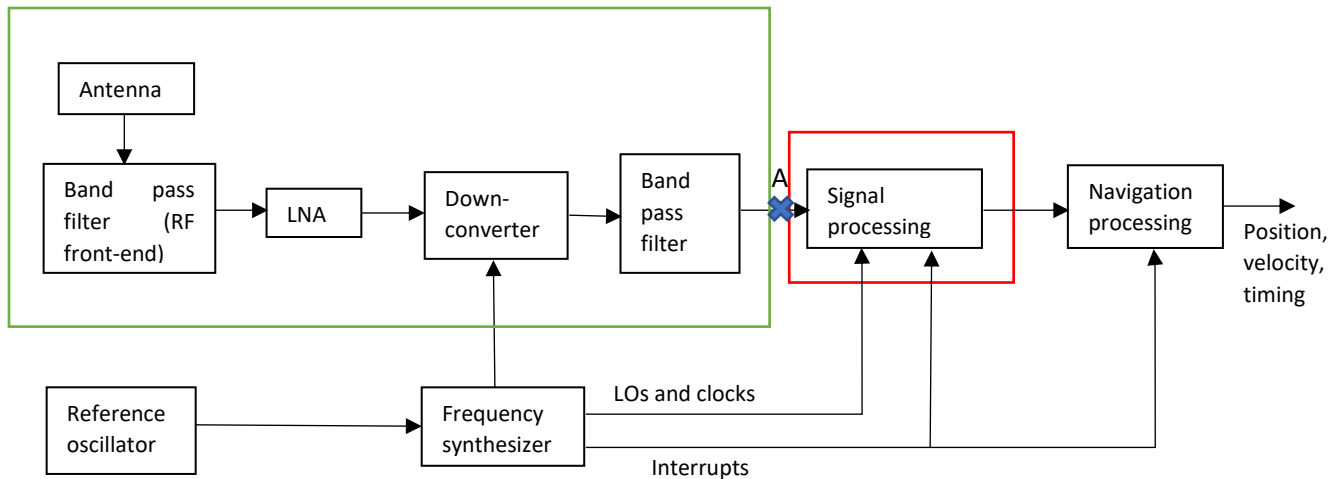


Figure 2-5: Generic GNSS receiver block diagram

After being received by the antenna, the GNSS signal passes through a preamplifier whose goal is to set the receiver noise figure. The preamplifier is composed of a band pass filter (RF front-end filter) and a low noise amplifier (LNA). The RF front-end filter helps in rejecting out-of-band interference, and to limit the sampling frequency. Then, the GNSS signal center frequency is shifted to a lower frequency, called intermediate frequency (IF). The down-conversion consists in multiplying the signal at the LNA output with a sine wave whose frequency offset from the carrier frequency is the targeted intermediate frequency f_{IF} . After a very selective band pass filtering, the signal at point A in Figure 2-5 is the GNSS signal offset around f_{IF} , and it is converted into a digital signal. The discrete GNSS signal around the intermediate frequency can then be processed to extract code and phase measurements, as well as navigation bits. Next, a navigation solution is output from the navigation processing block, in which a PVT (Position, Velocity and Timing) algorithm compute the navigation solution from the pseudorange measurements inputs. The reference oscillator, which drives the frequency synthesizer, has a key role. Indeed, common time needs to be distributed to all receiver elements.

This thesis mainly focuses on the blocks boxed in green and red in Figure 2-5: the GNSS front-end (boxed in green), and the signal processing stage (boxed in red). The mathematical operations done in these three blocks are detailed in this section.

First, the GNSS signal received by the antenna passes through the RF front-end module. Three operations are done in the RF front-end module.

- Amplification: The antenna and LNA bring some gain to the incoming GNSS signal.
- Frequency down-conversion: The role of down-conversion is to shift the signal spectrum central frequency down to lower central frequency in particular to ease out of band frequency rejection around final IF.
- Filtering: The RF front-end module has two band pass filters. The combination of the RF front-end and IF filters limit the spectrum bandwidth so that the receiver can use a reasonable sampling frequency limiting aliasing. The combination of these two filters will be referred as RF/IF filter.

As long as the received signal does not saturate the LNA and linearity is conserved, the RF front-end block can be seen as an equivalent amplification stage, a down conversion stage and a filtering stage, as depicted on Figure 2-6. In order to guarantee that the receiver is not saturated and operates in a linear way, the received power must be below the 1 dB compression point. This notion of 1 dB compression point is introduced later.

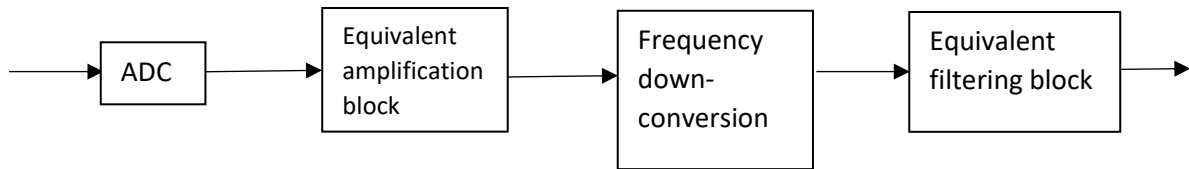


Figure 2-6: Equivalent model of RF front-end block

The equivalent front-end chain starts with the digitalization of the received signal through the analog to digital converter (ADC). The equivalent amplification block includes the amplification brought by the antenna and the LNA. The frequency down-conversion is identical to the one presented in Figure 2-6. The equivalent filter includes frequency rejection brought by the antenna, RF filter and IF filter. This block also generates noise, which is modeled as equivalent input noise at the antenna port, as will be presented later.

Second, the signal processing stage performs three operations.

- Acquisition: The goal of the acquisition operation is to detect a given GNSS signal and to provide a first estimation of the code delay and doppler frequency, in order to start synchronizing the local replica with the incoming GNSS signal.
- Tracking: The goal of the tracking operation is to keep the code delay, phase and Doppler estimations synchronized with the incoming GNSS signal, in order to determine pseudoranges and to perform data demodulation.
- Demodulation: The goal of the demodulation operation is to recover the navigation message. Indeed, the navigation message holds some information which are essential to compute a navigation solution and possibly to perform integrity monitoring. For example, the navigation message contains information on the satellite orbit, allowing the receiver to compute the satellite position.

In the following sub-sections, the mathematical GNSS signal at point A in Figure 2-5 (commonly called antenna port) is first derived. Then, the mathematical operations performed in the signal processing block are detailed.

2-3.2 Received GNSS signal at antenna port

This sub-section mathematically models the GNSS signal at the antenna port (point A in Figure 2-5). The generic mathematical formulas given in this sub-section are illustrated for GPS L1C/A signal.

The generic received useful signal component at the output of the antenna transducer, or at antenna input can be modeled by (Eq 2-28).

$$r_{ant}(t) = [s_{GNSS}^T(t) * g(t)] \quad (\text{Eq 2-28})$$

s_{GNSS}^T is the transmitted GNSS signal assumed with central frequency f_0 , g is the aggregate impulse response of the propagation medium including the transmitting and receiving antennas transducers.

In this thesis, the propagation medium behaves only as a pure delay (representative of the propagation time) which can vary in time and a propagation loss term L . It entails that the equivalent propagation filter impulse response can be expressed by $\frac{1}{\sqrt{L}}\delta(t - \tau(t))$, where $\tau(t)$ is the propagation delay between the transmitter and the receiver.

In addition, it is supposed that the magnitude gain of the antenna and preamplifier is constant over the bandwidth of the GNSS signal. As a consequence, the combination of the antenna and preamplifier is characterized by a gain denoted G_R .

Then, the down-conversion operation consists in multiplying the incoming signal by a sinusoidal signal with frequency $f_0 - f_{IF}$. The resulting signal contains one band-limited component around $2f_0 + f_{IF}$ and one band-limited component around f_{IF} . The high frequency term is filtered by the image rejection filter.

Then, filtering operations in the RF front-end module are characterized by the RF/IF equivalent filter. The RF/IF filter is characterized by its equivalent center frequency (which is either L1 or L5, depending on the GNSS signal to be processed) and its transfer function at baseband $H_{RF,BB}(f)$. One objective of the RF/IF filter is to limit the frequency bandwidth of the received signal, so that out-of-band components can be severely rejected and Shannon sampling criteria is respected when processing the GNSS signal.

The RF/IF filter transfer function model is given by (Eq 2-29).

$$H_{RF}(f) = H_{RF,BB}(f) * (\delta(f - f_{IF}) + \delta(f + f_{IF})) \quad (\text{Eq 2-29})$$

The GNSS signal at the output of the RF front-end filter is given by (Eq 2-30).

$$\begin{aligned} r_{RF}(t) &= \sqrt{G_R} r_{ant}(t) * h_{RF}(t) \\ &= \sqrt{G_R/L} [S_{GNSS}^T(t - \tau(t)) \cos(2\pi(f_0 - f_{IF})t)] * h_{RF}(t) \end{aligned} \quad (\text{Eq 2-30})$$

r_{ant} is expressed in (Eq 2-28) and h_{RF} is the impulse response of the RF front-end filter.

The useful signal only consists in one wide band term: the PRN signal. Indeed, the other terms of the useful GNSS signal are narrowband: the navigation bit rate and the secondary code rate are also much lower than the PRN chip rate. As a consequence, the RF front-end filter only affects this component of the useful signal. For example, the GPS L1C/A signal at the antenna port is given by (Eq 2-31).

$$r_{RF}^{L1}(t) = A_{L1} \tilde{c}_m(t - \tau(t)) d(t - \tau(t)) \cos(2\pi f_{IF}t - 2\pi f_0 \tau(t) + \varphi_0) \quad (\text{Eq 2-31})$$

$\tilde{c}_m = h_{RF} * c_m$ is the PRN signal filtered by the RF front-end filter. $A_{L1} = \sqrt{2G_R P_{L1}/L}$ is the signal amplitude at the RF front-end filter input.

Denoting $\varphi(t) = -2\pi f_0 \tau(t) + \varphi_0$, (Eq 2-32) expresses the received GPS L1C/A signal at the antenna port under its well-known form.

$$r_{RF}^{L1}(t) = A_{L1} \tilde{c}_m(t - \tau(t)) d(t - \tau(t)) \cos(2\pi f_{IF}t + \varphi(t)) \quad (\text{Eq 2-32})$$

The phase $\varphi(t)$ can be approximated on a short time interval introducing the GNSS Doppler frequency f_D by (Eq 2-33).

$$\varphi(t) = 2\pi f_D t + \varphi_0 \quad (\text{Eq 2-33})$$

In addition, the RF chain is assumed to be affected by additive noise originating from antenna black-body reception and receiver chain. This noise noted n is assumed to be centered white gaussian noise, and is characterized by its constant power spectral density equal to $N_0/2$ W/Hz. After filtering, the power spectral density of the noise at the RF/IF filter output is given by (Eq 2-34).

$$S_{n_{RF}}(f) = \frac{N_0}{2} |H_{RF}(f)|^2 \quad (\text{Eq 2-34})$$

2-3.3 GNSS signal processing

Subsection 2-3.2 described the mathematical GNSS signal and noise model at the antenna port. The objective of subsection 2-3.3 is to present the mathematical GNSS signal processing performed by the receiver to extract useful information, such as pseudorange measurements, carrier to noise density ratio, ... This subsection is divided in four parts. First, it describes the correlation operation, which has

a key role in CDMA signal processing. Second, it describes the acquisition process, which consists in synchronizing the receiver with the received GNSS signal. Third, it describes the tracking stage whose role is to keep the GNSS receiver synchronized with the received GNSS signal. Fourth, carrier to noise power spectral density (C/N_0) estimation is investigated.

2-3.3.1 Correlation

In order to recover the navigation message present in the transmitted signal, the receiver must perform several steps such as:

- Synchronization with the incoming carrier phase.
- Synchronization with the incoming PRN signal component.
- Symbol demodulation

These steps are all based on a specific operation referred to as the correlation operation. This subsection describes the mathematical model of GNSS signal and noise at the correlator output.

2-3.3.1.1 Correlation of GNSS signal

The correlation operation consists in computing the correlation between the incoming signal and a local replica of the GNSS signal. The local replica $s_L(t)$ is composed of:

- A local carrier,
- A local PRN signal, denoted c_{m_L} . Note that the local PRN signal is defined as the PRN code after waveform shaping.
- Alternatively, in some signals like BOC signals, a sub-carrier is also used, but not described here.

The correlation operation is performed in two steps. First, the signal at the RF module output is multiplied by the local replica. Second, the output of the multiplier is integrated over the coherent integration period T_i . Correlations are thus output at a rate $1/T_i$.

Figure 2-7 represents the correlation operation.

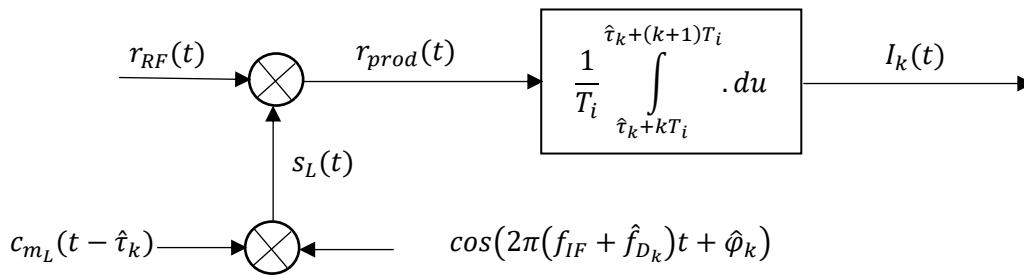


Figure 2-7: Representation of the correlation process

The local replica can be expressed as in (Eq 2-35).

$$s_L(t) = c_{m_L}(t - \hat{t}_k) \cos(2\pi f_{IF}t + 2\pi \hat{f}_{D,k}(t - kT_i) + \hat{\phi}_k) \quad (\text{Eq 2-35})$$

\hat{t}_k , $\hat{\phi}_k$ and $\hat{f}_{D,k}$ are respectively the estimations of code delay, phase and Doppler frequency at iteration k .

The first step of the correlation consists in multiplying the incoming signal with the local replica, resulting in a signal $r_{prod}(t)$ expressed in (Eq 2-36).

$$r_{prod}(t) = r_{RF}(t)s_L(t) = r_{RF}(t)c_{m_L}(t - \hat{t}_k) \cos(2\pi f_{IF}t + 2\pi \hat{f}_{D,k}(t - kT_i) + \hat{\phi}_k) \quad (\text{Eq 2-36})$$

For GPS L1C/A, r_{RF} is given by (Eq 2-32) and (Eq 2-36) can be expressed as in (Eq 2-37).

$$\begin{aligned} r_{prod}^{L1}(t) &= \frac{A_{L1}}{2} \tilde{c}_m(t - \tau(t)) c_{m_L}(t - \hat{\tau}_k) d(t) \\ &- \tau(t) \left(\begin{aligned} &\cos(2\pi(2f_{IF})t + 2\pi(f_D + \hat{f}_{D,k})(t - kT_i) + 2\pi f_D kT_i + \varphi_0 + \hat{\varphi}_k) \\ &+ \cos(2\pi(f_D - \hat{f}_{D,k})(t - kT_i) + 2\pi f_D kT_i + \varphi_0 - \hat{\varphi}_k) \end{aligned} \right) \end{aligned} \quad (\text{Eq 2-37})$$

r_{prod}^{L1} is the sum of two cosines. The first term has a high frequency in comparison to the second term, since f_{IF} has a magnitude of several MHz whereas the magnitude order of the Doppler frequency is only some kHz.

Next, the multiplier output passes through the correlator. The correlator acts as a low pass filter, called integrate and dump (ID) filter, whose impulse response h_{ID} and transfer function H_{ID} is given in (Eq 2-38).

$$\begin{aligned} h_{ID}(t) &= \frac{1}{T_i} \text{rect}_{T_i} \left(t - \frac{T_i}{2} \right) \\ H_{ID}(f) &= \text{sinc}(\pi f T_i) e^{-i\pi f T_i} \end{aligned} \quad (\text{Eq 2-38})$$

The output of the integrate and dump filter is given by (Eq 2-39).

$$I_{L_1}^D(k) = \frac{1}{T_i} \int_{\hat{\tau}_k + kT_i}^{\hat{\tau}_k + (k+1)T_i} r_{prod}(u) du \quad (\text{Eq 2-39})$$

For GPS L1C/A, since the integrator acts as a low-pass filter, the high frequency term in (Eq 2-37) is eliminated. Also, the code delay $\tau(t)$, phase $\varphi(t)$ and Doppler f_D are assumed constant during the integration period. In addition, it is supposed that the navigation bit $d(t)$ is constant over the integration period, and equal to $d(k) \in \{-1; +1\}$. [26] approximates the useful signal component at correlator output by (Eq 2-40) and [27] analyzed the validity of this approximation.

$$I_{L_1}^D(k) = \sqrt{\frac{P_{L1}}{2}} d(k) \tilde{R}_{c_m, c_{m_L}}^{L1}(\varepsilon_\tau) \text{sinc}(\pi \varepsilon_f T_i) \cos(\pi \varepsilon_f T_i + \varepsilon_\varphi) \quad (\text{Eq 2-40})$$

$\tilde{R}_{X,Y}$ is the cross-correlation function between filtered signal \tilde{X} and Y . $\varepsilon_\tau = \tau(kT_i) - \hat{\tau}_k$, $\varepsilon_f = f_D - \hat{f}_{D,k}$ and $\varepsilon_\varphi = 2\pi f_D kT_i + \varphi_0 - \hat{\varphi}_k$ are respectively the code, Doppler and phase tracking errors. Another correlation operation is performed at the correlation stage, correlating the received signal with a local replica in quadrature compared to (Eq 2-35). The useful signal component at quadrature phase correlator output expression is given by (Eq 2-41).

$$Q_{L_1}^D(k) = \sqrt{\frac{P_{L1}}{2}} d(k) \tilde{R}_{c_m, c_{m_L}}^{L1}(\varepsilon_\tau) \text{sinc}(\pi \varepsilon_f T_i) \sin(\pi \varepsilon_f T_i + \varepsilon_\varphi) \quad (\text{Eq 2-41})$$

GPS L5 and Galileo E5a signals are different from GPS L1C/A signal since they have two components, called data and pilot. Each component is in quadrature-phase from each other. GPS L5 and Galileo E5a are both BPSK chip modulated with the same chip rate and, although the PRN code data rate is 10 times higher for GPS L5 and Galileo E5a than for GPS L1C/A, they still have a similar mathematical expression in terms of mathematical model. [28] models the correlator output of the pilot and data components of Galileo E5a and GPS L5 signals as in (Eq 2-42).

$$\begin{aligned}
I_{L5\ E5a}^D(k) &= \sqrt{\frac{P_{L5}}{4}} \left(d(k)h_{10}(k)\tilde{R}_{c_D,c_D}^{L5\ E5a}(\varepsilon_\tau) + h_{20}(k)\tilde{R}_{c_P,c_D}^{L5\ E5a}(\varepsilon_\tau) \right) \text{sinc}(\pi\varepsilon_f T_i) \cos(\pi\varepsilon_f T_i + \varepsilon_\varphi) \\
Q_{L5\ E5a}^D(k) &= \sqrt{\frac{P_{L5}}{4}} \left(d(k)h_{10}(k)\tilde{R}_{c_D,c_D}^{L5\ E5a}(\varepsilon_\tau) + h_{20}(k)\tilde{R}_{c_P,c_D}^{L5\ E5a}(\varepsilon_\tau) \right) \text{sinc}(\pi\varepsilon_f T_i) \sin(\pi\varepsilon_f T_i + \varepsilon_\varphi) \\
I_{L5\ E5a}^P(k) &= \sqrt{\frac{P_{L5}}{4}} \left(d(k)h_{10}(k)\tilde{R}_{c_D,c_P}^{L5\ E5a}(\varepsilon_\tau) + h_{20}(k)\tilde{R}_{c_P,c_P}^{L5\ E5a}(\varepsilon_\tau) \right) \text{sinc}(\pi\varepsilon_f T_i) \cos(\pi\varepsilon_f T_i + \varepsilon_\varphi) \\
Q_{L5\ E5a}^P(k) &= \sqrt{\frac{P_{L5}}{4}} \left(d(k)h_{10}(k)\tilde{R}_{c_D,c_P}^{L5\ E5a}(\varepsilon_\tau) + h_{20}(k)\tilde{R}_{c_P,c_P}^{L5\ E5a}(\varepsilon_\tau) \right) \text{sinc}(\pi\varepsilon_f T_i) \sin(\pi\varepsilon_f T_i + \varepsilon_\varphi)
\end{aligned} \tag{Eq 2-42}$$

- P_{L5} is the total GNSS power (data plus pilot components power) at the antenna port.
- h_{10} is the bit of the data component secondary code (equal to 1 for Galileo E5a, since Galileo E5a signal does not have secondary code).
- h_{20} is the bit of the pilot component secondary code (equal to 1 for Galileo E5a, since Galileo E5a signal does not have secondary code).
- $\tilde{R}_{X,Y}^{L5\ E5a}$ is the cross-correlation function between the received filtered PRN signal X and the local replica Y . Since data and pilot use the same modulation, BPSK(10), then $\tilde{R}_{c_D,c_D}^{L5\ E5a} = \tilde{R}_{c_P,c_P}^{L5\ E5a}$. Note that in reality Galileo E5A does not implement a BPSK(10) modulation for the data and pilot components since the signal really implements the AltBOC modulation; nevertheless, the approximation is very tight for the purposes of the this work.

Galileo E1 signal also have one pilot and one data component. The main differences with GPS L5 and Galileo E5a signal are a different chip modulation, the absence of the secondary code on the data component and a shorter PRN code (but longer than for GPS L1 C/A). [29] models the data and pilot correlator outputs as in (Eq 2-43).

$$\begin{aligned}
I_{E1}^D(k) &= \sqrt{\frac{P_{E1}}{4}} \left(d(k)\tilde{R}_{c_D,c_D}^{E1}(\varepsilon_\tau) - s_c(k)\tilde{R}_{c_P,c_D}^{E1}(\varepsilon_\tau) \right) \text{sinc}(\pi\varepsilon_f T_i) \cos(\pi\varepsilon_f T_i + \varepsilon_\varphi) \\
Q_{E1}^D(k) &= \sqrt{\frac{P_{E1}}{4}} \left(d(k)\tilde{R}_{c_D,c_D}^{E1}(\varepsilon_\tau) - s_c(k)\tilde{R}_{c_P,c_D}^{E1}(\varepsilon_\tau) \right) \text{sinc}(\pi\varepsilon_f T_i) \sin(\pi\varepsilon_f T_i + \varepsilon_\varphi) \\
I_{E1}^P(k) &= \sqrt{\frac{P_{E1}}{4}} \left(-d(k)\tilde{R}_{c_D,c_P}^{E1}(\varepsilon_\tau) + s_c(k)\tilde{R}_{c_P,c_P}^{E1}(\varepsilon_\tau) \right) \text{sinc}(\pi\varepsilon_f T_i) \cos(\pi\varepsilon_f T_i + \varepsilon_\varphi) \\
Q_{E1}^P(k) &= \sqrt{\frac{P_{E1}}{4}} \left(-d(k)\tilde{R}_{c_D,c_P}^{E1}(\varepsilon_\tau) + s_c(k)\tilde{R}_{c_P,c_P}^{E1}(\varepsilon_\tau) \right) \text{sinc}(\pi\varepsilon_f T_i) \sin(\pi\varepsilon_f T_i + \varepsilon_\varphi)
\end{aligned} \tag{Eq 2-43}$$

- P_{E1} is the total Galileo E1 power (data plus pilot components power) at the antenna port.
- s_c is the Galileo E1 secondary code of the pilot component.
- $\tilde{R}_{X,Y}^{E1}$ is the cross-correlation function between the received filtered Galileo E1 PRN signal X and the local replica Y . In this paper, the local replica is $BOC(1,1)$ modulated whereas the received data and pilot components have respectively a $CBOC(6,1,1/11,+)$ and $CBOC(6,1,1/11,-)$ modulations. This mismatch between the received signal, which is in addition distorted by RFFE filter, and local replica induces some additional losses dependent on the receiver bandwidth.

\tilde{R}_{c_D, c_D}^X is represented in Figure 2-8, for different values of the double-sided bandwidth of the RF/IF filter ($X \in \{E1, L1\}$).

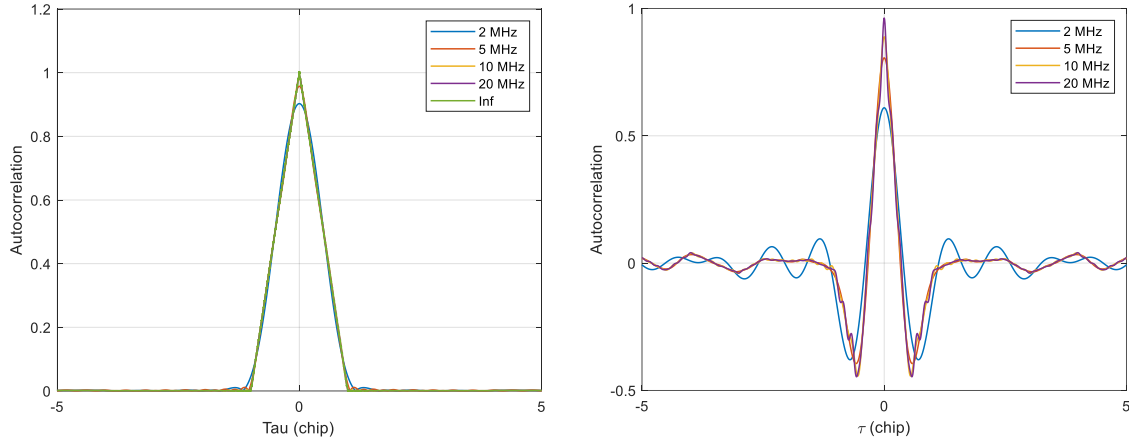


Figure 2-8: Correlation function for GPS L1C/A (left) and Galileo E1 (right) signals

The imperfect matching between the filtered PRN code and the local replica PRN code induces a loss of the recovered GNSS power at the correlator output by reducing the magnitude of the correlation peak.

It can be seen from (Eq 2-40) and Figure 2-8 that the useful part of the correlator output will have a significant value only if:

- The local PRN signal uses the same PRN code as the one used by the incoming signal. Indeed, this is one of the key points of CDMA signal processing, since PRN sequences must be known by emitter and receiver, and are chosen to be as uncorrelated as possible as a function of delay offset and across all sequences of the same family so that other communications in the channel influence the output in a negligible manner.
- The code delay estimation error ε_τ is below 1 chip, so that \tilde{R}_{c_D, c_D}^X is near its maximum value.
- The carrier phase estimation error ε_φ is small enough such that $\cos(\varepsilon_\varphi) \approx 1$.

2-3.3.1.2 Correlation of the noise

This subsection describes the mathematical model of the noise at the correlator output. The power spectral density of the noise at the front-end output $n_{RF}(t)$ is given in (Eq 2-34). As described in 2-3.3.1.1, the correlation stage performs two successive operations: the multiplication with the local replica and the integrate and dump filtering. This subsection derives first the power spectral density of the noise at the correlator output. Second, it derives the noise power at the correlator output.

It can be shown that the power spectral density of the noise component after the multiplication by the local replica is given by (Eq 2-44).

$$S_{n,prod}(f) = \frac{1}{4} (\delta(f - f_{IF}) + \delta(f + f_{IF})) * S_{n_{RF}}(f) * S_{c_{m_L}}(f) \quad (\text{Eq 2-44})$$

$S_{c_{m_L}}$ is the power spectral density of the PRN code of the local replica. Combining (Eq 2-29), (Eq 2-34) and (Eq 2-44), $S_{n,prod}$ can be rewritten by (Eq 2-45).

$$S_{n,prod}(f) = \frac{N_0}{8} |H_{RF,BB}(f)|^2 * (\delta(f - 2f_{IF}) + 2\delta(f) + \delta(f + 2f_{IF})) * S_{c_{m_L}}(f) \quad (\text{Eq 2-45})$$

Finally, since the integrator acts as a low-pass filter whose transfer function H_{ID} is given by (Eq 2-38), the noise power spectral density at the correlator output expressed in (Eq 2-46) is deduced from Wiener-Lee equation.

$$S_{n_l}(f) = |H_{ID}(f)|^2 S_{n,prod}(f) \quad (\text{Eq 2-46})$$

(Eq 2-46) can be developed and simplified. Indeed, the double-sided width of the main lobe of H_{ID} is $2/T_i$. In addition, the bandwidth of $S_{n,prod}$ is higher than the bandwidth of $S_{c_{m_L}}$ according to (Eq 2-44). Therefore, $S_{n,prod}$ is significantly wider than H_{ID} . It is thus possible to assume that $S_{n,prod}$ is constant over the bandwidth of the integrate and dump filter. (Eq 2-46) can then be reduced to the expression given in (Eq 2-47).

$$S_{n_l}(f) \approx |H_{ID}(f)|^2 S_{n,prod}(0) \quad (\text{Eq 2-47})$$

Using the expression of (Eq 2-45), and considering that $H_{RF,BB}$ is low-pass, (Eq 2-47) can be reduced to (Eq 2-48).

$$S_{n_l}(f) = \frac{\beta N_0}{4} |H_{ID}(f)|^2 \quad (\text{Eq 2-48})$$

β is defined in (Eq 2-49). It characterizes the impact of the front-end filtering and of the correlation on the noise.

$$\beta = \int_{-\infty}^{+\infty} |H_{RF,BB}(f)|^2 S_{c_{m_L}}(f) df \quad (\text{Eq 2-49})$$

Finally, the noise power at the correlator output P_{n_l} is deduced from (Eq 2-48). Using Parseval formula, P_{n_l} is given by (Eq 2-50).

$$P_{n_l} = \int_{-\infty}^{+\infty} S_{n_l}(f) df = \frac{\beta N_0}{4} \int_{-\infty}^{+\infty} |H_{ID}(f)|^2 df = \frac{\beta N_0}{4} \int_{-\infty}^{+\infty} |h_{ID}(t)|^2 dt = \frac{\beta N_0}{4T_i} \quad (\text{Eq 2-50})$$

(Eq 2-50) highlights that the noise power at the correlator output mainly depends on the noise density level at the front-end module output (N_0) and on the correlation duration T_i : the longer T_i , the lower the noise power at the correlator output.

2-3.3.1.3 Impact of correlation on signal to noise ratio (SNR)

Sections 2-3.3.1.1 and 2-3.3.1.2 computed the analytical expressions of the GNSS signal and the noise at the correlator output. From the results of sections 2-3.3.1.2 and 2-3.3.1.3, this subsection highlights the benefit of the correlation on the signal to noise ratio (SNR). First, the SNR at the front-end module output is computed from results of section 2-3.2. Second the SNR at the correlator output is derived from results of 2-3.3.1. Third, the correlation gain is derived. The correlation gain is defined by the ratio between the SNR at the correlator output and the SNR at the correlator input.

The noise power at the RF front-end module output is deduced by integrating (Eq 2-34). Considering RF/IF filter transfer function as rectangular with double-sided bandwidth B_{RF} , then the noise power at the correlator input is given by $P_{n,RF} = N_0 B_{RF}$.

Despite that the calculation is not fully detailed here, it can be shown that the power of the useful signal at the front-end output is $P_{GNSS,RF} = \frac{A_{GNSS}^2}{2} R_{\tilde{c}_m}(0)$, where A_{GNSS} is the amplitude of the GNSS signal at the RF front-end input, and $R_{\tilde{c}_m}$ is the autocorrelation of the filtered PRN code.

The noise power at the correlator output has been computed in (Eq 2-50). Supposing weak tracking errors, the GNSS signal power at the correlator output can be deduced from (Eq 2-40) and (Eq 2-41)

and is equal to $P_{GNSS,corr} = \frac{P_{GNSS}}{2} \tilde{R}_{\tilde{c}_m, c_{mL}}^X(0)^2$, where P_{GNSS} is the power of the considered component (data or pilot) of GNSS signal X (L1, E1, L5 or E5a).

Therefore, the processing gain is given by (Eq 2-51).

$$G_{corr} = \frac{P_{GNSS}/P_{n_I}}{P_{GNSS,RF}/P_{n,RF}} = 2T_i B_{RF} \frac{\tilde{R}_{\tilde{c}_m, c_{mL}}^X(0)^2}{\beta R_{\tilde{c}_m}(0)} \quad (\text{Eq 2-51})$$

For example, considering a GPS L1C/A signal, a BPSK modulated local replica, a 20 MHz double sided rectangular RF/IF filter and a 1 ms integration time, the correlation gain is equal to 46 dB. Therefore, the correlation significantly increases the SNR. The correlation gain grows with the integration duration and the RF/IF filter bandwidth. Such a large correlation gain authorizes to have an incoming signal with a very small SNR at the RF front-end output. In fact, GNSS signals generally have a SNR at the RF output that is strongly negative: GNSS signal power is below the thermal noise floor. However, this is generally not a problem at the correlator output for the users knowing the PRN sequence used thanks to the correlation operation.

Therefore, section 2-3.3.1 highlights the importance of the correlation in CDMA signal processing. Following subsections show how to extract useful information from the correlator outputs, and to keep the local replica synchronized with the received GNSS signal.

2-3.3.2 Acquisition

The objective of the acquisition is to perform algebraic operations on correlator outputs in order to:

- Detect the presence of the useful signal.
- Give a rough estimation of the code delay and Doppler frequency ($\hat{\tau}$ and \hat{f}_D), which are needed to initialize the tracking loop.
- Find the beginning and the end of a PRN sequence (synchronization).

The usual way to detect the presence of a signal is to compute a detection criterion to be compared against a threshold. This section first describes one acquisition strategy using only one component of the GNSS signal. Second, it proposes an alternative strategy for the acquisition of Galileo E5a, GPS L5 and Galileo E1 signals, which hold two components (data and pilot).

2-3.3.2.1 GPS L1C/A acquisition strategy

The noisy in phase and quadrature phase correlator output models have been established in 2-3.3.1.1 and 2-3.3.1.2, and are reminded in (Eq 2-52).

$$\begin{aligned} I_{L1}^D(k) &= \sqrt{\frac{P_{L1}}{2}} d_k \tilde{R}_{\tilde{c}_m, c_{mL}}^{L1}(\varepsilon_\tau) \text{sinc}(\pi \varepsilon_f T_i) \cos(\pi \varepsilon_f T_i + \varepsilon_\varphi) + n_{I,L1}(k) \\ Q_{L1}^D(k) &= \sqrt{\frac{P_{L1}}{2}} d_k \tilde{R}_{\tilde{c}_m, c_{mL}}^{L1}(\varepsilon_\tau) \text{sinc}(\pi \varepsilon_f T_i) \sin(\pi \varepsilon_f T_i + \varepsilon_\varphi) + n_{Q,L1}(k) \end{aligned} \quad (\text{Eq 2-52})$$

$n_{I,L1}(k)$ and $n_{Q,L1}(k)$ are independent random samples and follow a centered Gaussian distributions with variance equal to P_{n_I} . Using algebraic operations on successive correlator outputs, it is possible to build a detection test, as described on Figure 2-9.

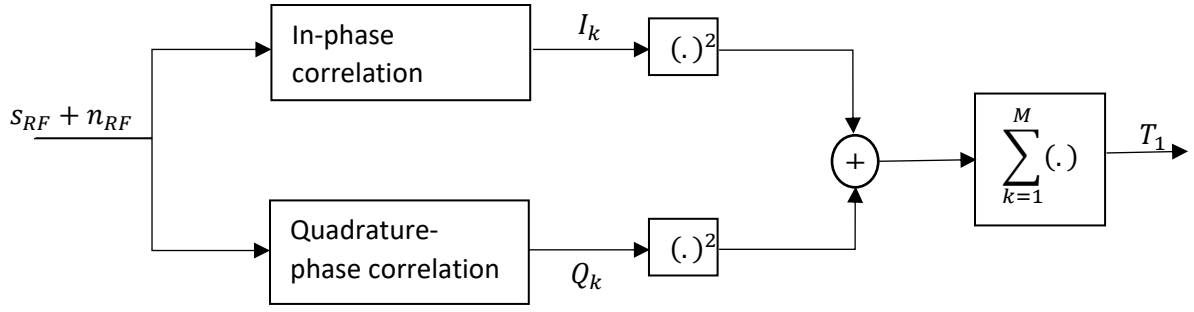


Figure 2-9: Acquisition strategy based on one channel processing

The detection test T_1 , expressed in (Eq 2-53), is built summing the squared magnitude of M successive correlator outputs.

$$T_1 = \sum_{k=1}^M I_{L_1}^D(k)^2 + Q_{L_1}^D(k)^2 \quad (\text{Eq 2-53})$$

Assuming that ε_τ and ε_f do not vary during the M non-coherent summations, and under low noise assumption, (Eq 2-53) can be reduced to (Eq 2-54).

$$T_1 \rightarrow \frac{P_{L1}}{2} M \tilde{R}_{c_m, c_{m_L}}^{L1}(\varepsilon_\tau)^2 \text{sinc}^2(\pi \varepsilon_f T_i) \quad (\text{Eq 2-54})$$

This detector accumulates the GNSS signal energy during the total non-coherent integration time MT_i (also called dwell time). Taking into account the noise components, (Eq 2-53) can be rewritten as in (Eq 2-55).

$$T_1 = \frac{P_{L1}}{2} M \tilde{R}_{c_m, c_{m_L}}^{L1}(\varepsilon_\tau) \text{sinc}^2(\pi \varepsilon_f T_i) + \sum_{k=1}^M (n_{I, L1}(k)^2 + n_{Q, L1}(k)^2) + \sum_{k=1}^M \sqrt{2P_{L1}} \tilde{R}_{c_m, c_{m_L}}^{L1}(\varepsilon_\tau) \text{sinc}(\pi \varepsilon_f T_i) \begin{bmatrix} n_{I, L1}(k) d(k) \cos(\varepsilon_\phi) \\ + n_{Q, L1}(k) \sin(\varepsilon_\phi) \end{bmatrix} \quad (\text{Eq 2-55})$$

When the GNSS signal power at the correlator output is much higher than the noise power at correlator output, GNSS signal term is predominant on the noise terms in (Eq 2-55) when ε_τ and ε_f are close to zero and the PRN code of the local replica is the same than the PRN code of the incoming signal. Figure 2-10 shows the detection test T_1 computed for several values of ε_τ and ε_f when running a simulation that simulates noisy PRN code and correlation outputs. Settings presented in Table 2-3 have been used to obtain this figure.

	Figure a)	Figure b)	Figure c)
Received GNSS signal	GPS L1C/A PRN 16	GPS L1C/A PRN 16	GPS L1C/A PRN 16
Local replica	PRN 16	PRN 16	PRN 2
C/N0 (dB-Hz)	45	45	45
M	50	1	50
T_i	1 ms	1 ms	1 ms

Table 2-3: Acquisition of GPS L1C/A PRN 16, settings

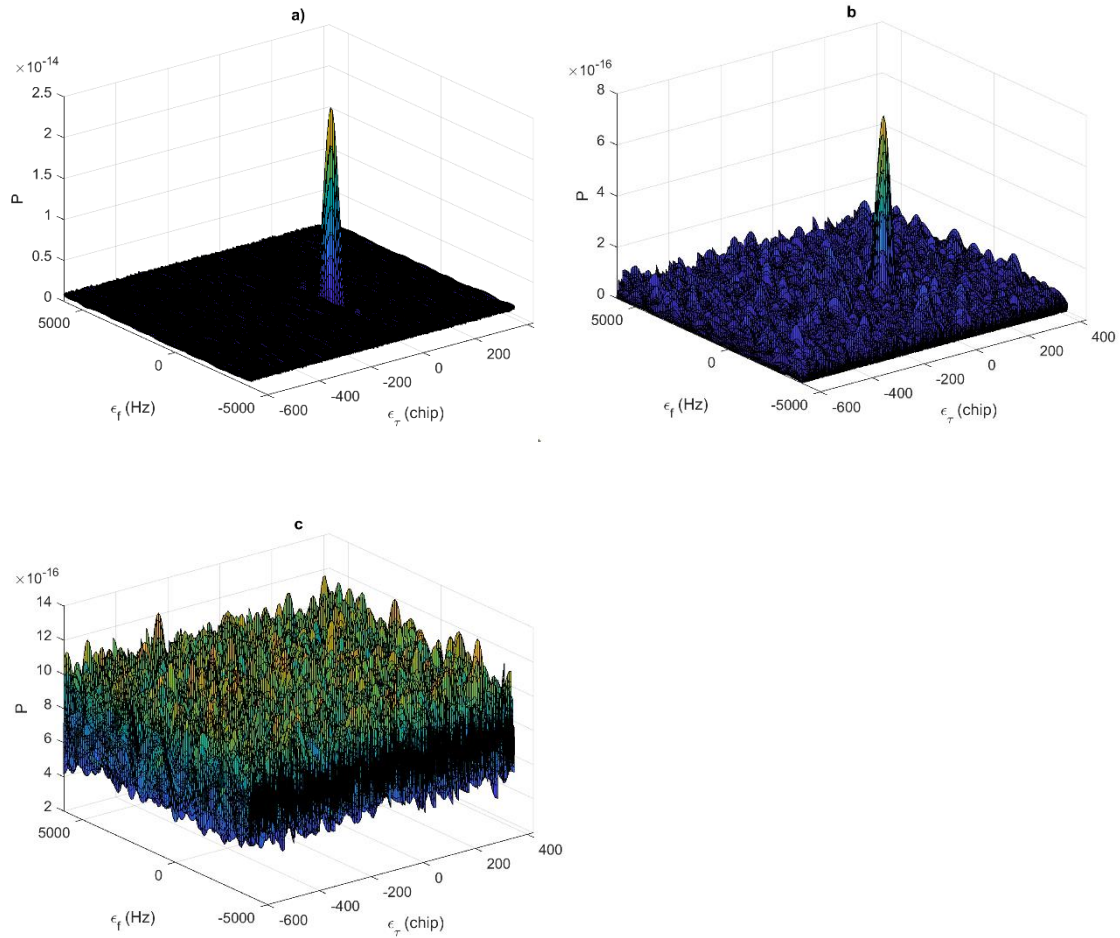


Figure 2-10: Impact of the number of non-coherent summations on the acquisition detector

Figure 2-10-a highlights that when ϵ_τ and ϵ_f are small and the PRN code of the local replica is the same than the PRN code of the incoming signal, the accumulated GNSS power at the correlator output is well above the noise power. The comparison between Figure 2-10-a and Figure 2-10-b shows the importance to accumulate the signal power during several non-coherent integrations. Indeed, the detection peak amplitude with respect to the noise component amplitude is lower when M is small. Eventually, Figure 2-10-c illustrates the acquisition when the PRN code of the local replica is different from the PRN code of the received GNSS signal. In this case, and as discussed in section 2-3.3.1.1 the cross-correlation function is not significant enough to be visible and the detector peak is buried into the noise.

Acquisition principle is based on either the research of all peaks exceeding a threshold or the research of a maximum of T_1 that exceeds a threshold. The goal is to maximize T_1 browsing an acquisition matrix. This matrix has rows and columns which are an ensemble of couples composed by a code delay t and a frequency value f that will define the generation of the local replica. A GNSS signal will be detected if T_1 is higher than a threshold. In this case, code delay and Doppler estimations will be:

$$(\hat{t}, \hat{f}_D) = \max_{t \in T, f \in F} T_1(t, f) \quad (\text{Eq 2-56})$$

The size of the research step is defined from the maximum allowed error of estimation of P . Indeed, the width of the detection peak in the frequency domain decreases when the integration time grows. Also, the correlation function is limited over 1 chip. Therefore, the step in the code delay and frequency research domains must be calibrated to be able to detect the signal for the code delay and frequency

resolutions chosen. For example, a research step in the time domain of 0.5 chip induces a maximum 2.5dB degradation of the detection criterion for GPS L1C/A. The research step in the frequency domain depends on T_i . Typical values for the step are $\frac{2}{3T_i}$ or $\frac{1}{2T_i}$. These sizes induce respectively a maximum degradation of 0.4 dB and 0.9 dB on a GPS L1C/A detector.

2-3.3.2.2 Alternative strategy for GNSS signals with two components

Galileo E1, Galileo E5a and GPS L5 hold one data and one pilot components. It can be taken advantage of these two components when performing acquisition.

The acquisition method proposed here uses both pilot and data components correlator outputs observations. The scheme of the corresponding acquisition is described in Figure 2-11.

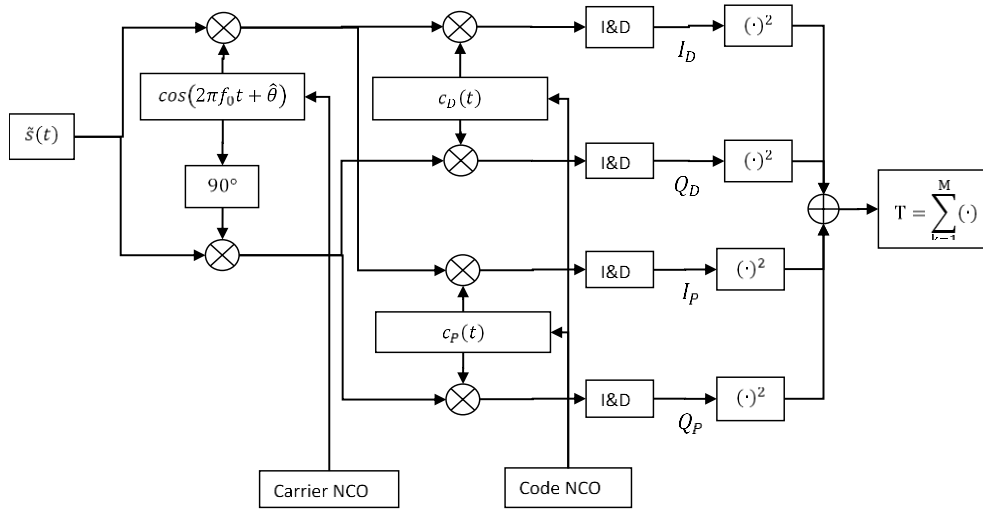


Figure 2-11: Acquisition principle for data + pilot components signals. For GALILEO E1, cp and cd include sub-carrier component.

The detection test for signals with data and pilot components is given in (Eq 2-57).

$$T_2 = \sum_{k=1}^M \left((I_X^D(k))^2 + (Q_X^D(k))^2 + (I_X^P(k))^2 + (Q_X^P(k))^2 \right) \quad (\text{Eq 2-57})$$

X is the GNSS signal with a data and a pilot component, either Galileo E1, GPS L5 or Galileo E5a.

The advantage of this acquisition detector is to accumulate the energy of both the pilot and data components. The drawback of this strategy is that more correlators are needed to compute the acquisition. The comparison of the acquisition performance using strategies presented in 2-3.3.2.1 and 2-3.3.2.2 is done in Appendix A.

2-3.3.3 Tracking

Acquisition module provides a rough estimation of the code delay and Doppler frequency of the received GNSS signal. The objective of the tracking stage is to maintain the synchronization between the local replica and the received GNSS signal so that demodulation can be performed and useful information such as pseudorange can be extracted. To generate the local replica, a phase (or equivalently a Doppler) and a code delay estimation must be returned by the tracking loop. We here present two tracking loops that operate in parallel: one phase lock loop (PLL) and one delay lock loop (DLL). This section describes the operations performed in the tracking loops.

2-3.3.3.1 Phase lock loop (PLL)

The objective of the PLL is to feed the local replica generator with the successive estimations of the carrier phase $\hat{\varphi}_k$ and Doppler frequency $\hat{f}_{D,k}$.

Figure 2-12 presents the equivalent linear model of a PLL. This equivalent model is an equivalent low pass filter characterized by its closed loop bandwidth.

This model is composed of three successive blocks.

- Discriminator: The discriminator performs algebraic operations on the correlator outputs to estimate the phase tracking error ε_φ . In the equivalent linear model, it is simply a difference operator between φ and $\hat{\varphi}$.
- PLL filter: The PLL filter is a low pass filter. Its role is to limit the effect of the noise on the discriminator outputs.
- Numerically controlled oscillator (NCO): The role of the NCO is to generate the local replica from the input instantaneous frequency as a control signal. It is here represented in the equivalent linear model of the PLL as an integrator.

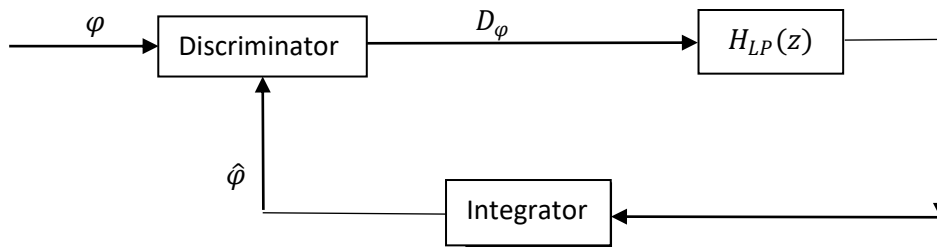


Figure 2-12: Block diagram of the equivalent linear model of a PLL

The phase discriminator is a mathematical operator which estimates the carrier phase difference ε_φ between the incoming and local carrier, which is also referred as phase tracking error. In the real implementation, the phase discriminator inputs are the in-phase and quadrature phase correlator outputs. The most common phase discriminator is the atan discriminator which is defined in (Eq 2-58).

$$D_\varphi^{atan} \left(I_D^X(k), Q_D^X(k) \right) = -\operatorname{atan} \left(\frac{Q_D^X(k)}{|I_D^X(k)|} \right) \quad (\text{Eq 2-58})$$

Another classical phase discriminator is the dot-product, which is defined in (Eq 2-59).

$$D_\varphi^{DP} \left(I_D^X(k), Q_D^X(k) \right) = \frac{I_D^X(k)Q_D^X(k)}{I_D^X(k)^2 + Q_D^X(k)^2} \xrightarrow{\text{no noise}} \frac{1}{2} \sin(2\varepsilon_\varphi) \xrightarrow{\varepsilon_\varphi \rightarrow 0} \varepsilon_\varphi \quad (\text{Eq 2-59})$$

The advantage of the dot-product discriminator compared to the atan discriminator is its complexity (it only needs multiplications) whereas its drawbacks are:

- The dot-product discriminator needs to be normalized by the correlator output power to remove the influence of the GNSS signal amplitude and cross-correlation term to recover ε_φ .
- The dot-product discriminator is proportional to ε_φ only in the linearity region of the sine function.

The discriminator output, denoted $V_d(k)$, then feeds a low pass filter whose discrete transfer function is denoted $H_{LP}(z)$. The discrete version of the PLL filter is fully characterized by its order, the integration time and the targeted loop bandwidth. The link between the order of the PLL filter, the loop bandwidth and the integration time is recapped in Table 2-4.

	Transfer function of loop filter $H_{LP}(z)$	Coefficients		
		K_1	K_2	K_3
1 st order	$\frac{K_1}{2\pi T_i}$	$4B_\phi T_i$	-	-
2 nd order	$\frac{1}{2\pi T_i} \frac{(K_1 + K_2) + K_1 z^{-1}}{1 - z^{-1}}$	$\frac{8}{3} B_\phi T_i$	$\frac{K_1^2}{2}$	-
3 rd order	$\frac{1}{2\pi T_i} \frac{K_1 + K_2 + K_3 - (2K_1 + K_2)z^{-1} + K_1 z^{-2}}{1 - 2z^{-1} + z^{-2}}$	$\frac{60}{23} B_\phi T_i$	$\frac{4}{9} K_1^2$	$\frac{2}{27} K_1^3$

Table 2-4: Transfer function of the PLL filter

The z transform of the PLL filter output is then given by (Eq 2-60).

$$V_c(z) = H_{LP}(z)V_d(z) \quad (\text{Eq 2-60})$$

The PLL filter output feeds a numerically controlled oscillator (NCO). A NCO is an electronic device which is able, from a digital input signal V_c , to generate a carrier with an instantaneous frequency given by (Eq 2-61).

$$f_{NCO}(k+1) = f_{NCO}(k) + V_c(k) \quad (\text{Eq 2-61})$$

Therefore, the NCO is equivalent to an integrator from the carrier phase point of view, so that the transfer function between $V_c(z)$ and $\hat{\phi}(z)$ is given by (Eq 2-62).

$$F_{NCO}(z) = 2\pi T_i \frac{z^{-1}}{1 - z^{-1}} \quad (\text{Eq 2-62})$$

Eventually, (Eq 2-63) represents the transfer function of the equivalent filter of the whole closed loop using a z-transform.

$$\hat{\phi}(z) = F_{NCO}(z)H_{LP}(z)V_d(z) = \hat{\phi}(z) = F_{NCO}(z)H_{LP}(z) \left(\varepsilon_\phi(z) + n_\phi(z) \right) \quad (\text{Eq 2-63})$$

$\varepsilon_\phi(z)$ is the z-transform of the phase tracking error and $n_\phi(z)$ is the z-transform of the noise component at the phase discriminator output.

2-3.3.3.2 Delay lock loop

The PLL allows to maintain the phase and Doppler synchronization between the received GNSS signal and the local replica. The third term which must be estimated to generate the local replica is the code delay. The code delay estimation is an important parameter since it is the source of the pseudorange measurement. The goal of the delay lock loop (DLL) is to estimate the code delay in order to keep the local PRN code replica synchronized with the received signal.

The fundamental principles of a DLL are the same as those of a PLL. The only difference is that a different discriminator must be chosen. The DLL needs additional correlators to estimate the code delay tracking error. Traditionally, three complex correlators will be used:

- The prompt correlator is obtained generating the local replica as in (Eq 2-35). The corresponding correlator outputs, for GNSS signal X (X is either L1, E1, E5a or L5) and component Y (data or pilot) are denoted $I_{X,P}^Y(k)$ and $Q_{X,P}^Y(k)$.
- The late correlator is obtained delaying the local replica by $C_s/2$, where C_s is the chip spacing (time difference between the early and late correlator). The corresponding correlator outputs are denoted $I_{X,L}^Y(k)$ and $Q_{X,L}^Y(k)$.
- The early correlator is obtained advancing the local replica by $C_s/2$. The corresponding correlator outputs are denoted $I_{X,E}^Y(k)$ and $Q_{X,E}^Y(k)$.

The mathematical simplified model for the additional early and late correlators is given in (Eq 2-64).

$$\begin{aligned}
I_{X,L}^Y(k) &= \sqrt{\frac{P_X^Y}{2}} d(k) \tilde{R}_{C_Y, C_Y}^X \left(\varepsilon_\tau + \frac{C_s}{2} \right) \text{sinc}(\pi \varepsilon_f T_i) \cos(\varepsilon_\phi) + n_{E,I}(k) \\
Q_{X,E}^Y(k) &= \sqrt{\frac{P_X^Y}{2}} d(k) \tilde{R}_{C_Y, C_Y}^X \left(\varepsilon_\tau + \frac{C_s}{2} \right) \text{sinc}(\pi \varepsilon_f T_i) \sin(\varepsilon_\phi) + n_{E,Q}(k) \\
I_{X,L}^Y(k) &= \sqrt{\frac{P_X^Y}{2}} d(k) \tilde{R}_{C_Y, C_Y}^X \left(\varepsilon_\tau - \frac{C_s}{2} \right) \text{sinc}(\pi \varepsilon_f T_i) \cos(\varepsilon_\phi) + n_{L,I}(k) \\
Q_{X,L}^Y(k) &= \sqrt{\frac{P_X^Y}{2}} d(k) \tilde{R}_{C_Y, C_Y}^X \left(\varepsilon_\tau - \frac{C_s}{2} \right) \text{sinc}(\pi \varepsilon_f T_i) \sin(\varepsilon_\phi) + n_{L,Q}(k)
\end{aligned} \tag{Eq 2-64}$$

Noise components $n_{E,I}$, $n_{E,Q}$, $n_{L,I}$ and $n_{L,Q}$ are all assumed to be gaussian following assumptions on the input noise given previously, with equal power $\frac{\beta N_0}{4T_i}$, and all independent from each other.

To estimate the code delay error, the discriminator takes advantage of the correlation function. This is illustrated on Figure 2-13.

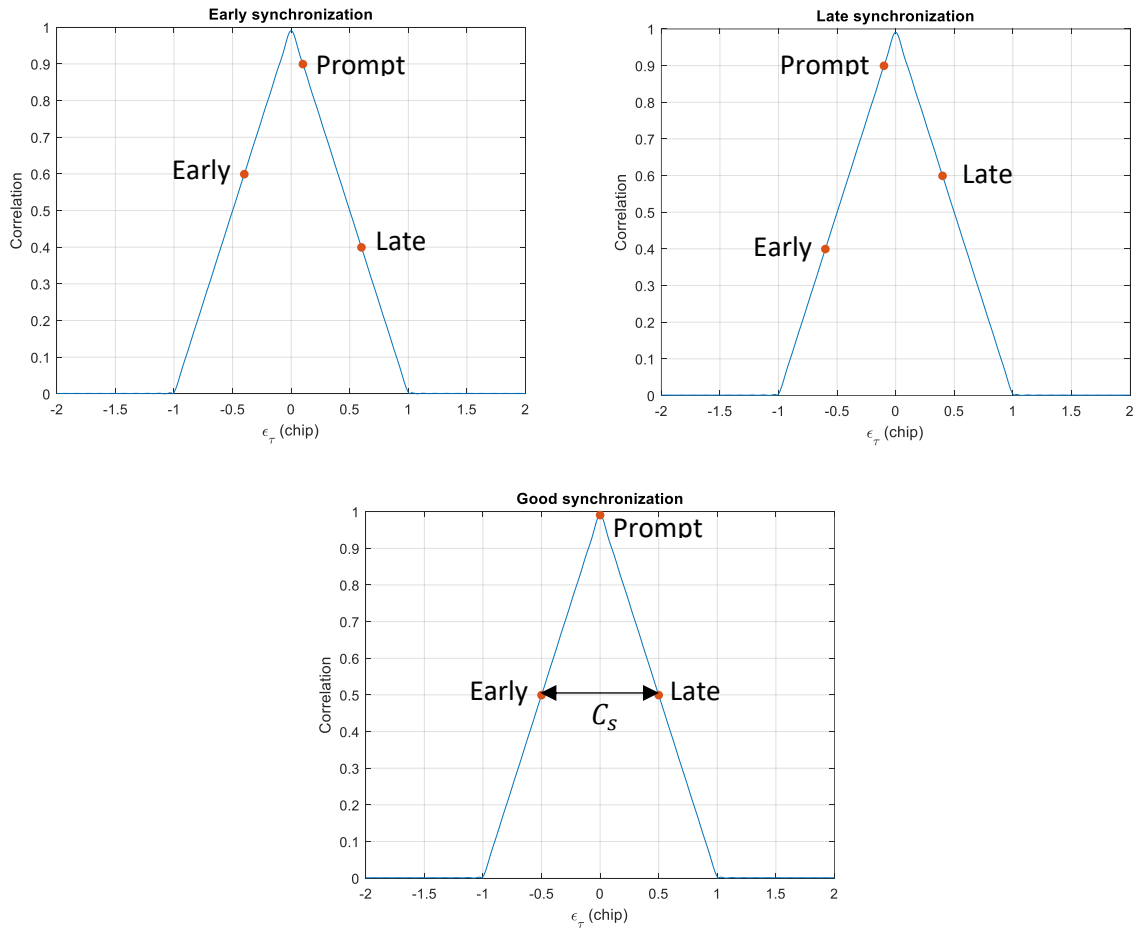


Figure 2-13: DLL discriminator principle

The Early-Minus-Late Power (EMLP) estimator, defined in (Eq 2-65), estimates the code delay tracking error comparing the power of the early correlator output with the power of the late correlator output.

$$D_\tau(k) = \frac{I_{X,E}^Y(k)^2 + Q_{X,E}^Y(k)^2 - I_{X,L}^Y(k)^2 - Q_{X,L}^Y(k)^2}{2(2 - C_s)(I_{X,P}^Y(k)^2 + Q_{X,P}^Y(k)^2)} \tag{Eq 2-65}$$

Then, the code delay discriminator output passes through the DLL low pass filter and the NCO. The DLL low pass filter and the NCO operate similarly as the ones of the PLL, except that instead of feeding the carrier generator, they feed the E, L, P code generators. The code delay estimation $\hat{\tau}_k$ is recovered at the output of the NCO, and that code delay estimation is further multiplied by the velocity of light in vacuum to build the pseudorange measurements.

Note that in order to reduce the impact of noise on the pseudorange measurements, it is often implemented a very narrow bandwidth DLL. However, in order to keep good resistance to at least order 2-time variations of the delay, the DLL discriminator is added to the PLL discriminator divided by the ratio between the carrier frequency and the code rate. In that case, it is also not necessary to implement a 3rd order DLL, a 1st order DLL is sufficient. However, in this thesis, the two blocks are kept independent in order to control the fidelity to theoretical prediction.

As a conclusion, the PLL and the DLL allow to keep the local replica synchronized with the received GNSS signal. The tracking stage is important to guarantee the capacity to demodulate the information message, and to guarantee continuity of the positioning service. The phase and code delay measurements are then used to compute the pseudoranges and next to deduce a navigation solution.

2-3.4 C/N_0 estimation

Signal to noise power spectrum density ratio, C/N_0 , is a significant indicator characterizing the capability of any receiver to process the GNSS signal. ICAO and RTCA/EUROCAE GNSS receiver requirements on message demodulation, pseudorange accuracy and acquisition performances can be translated in terms of equivalent assumed minimum C/N_0 [10]. In other words, airborne receiver GNSS signal C/N_0 is supposed to exceed a particular C/N_0 threshold in order to guarantee that each basic operation of the receiver (acquisition, tracking, demodulation) meets its required performance. Since interference degrades the efficient signal to noise density ratio, it is important to quantify the degradation as a function of the jammer parameters. C/N_0 degradation in presence on an interference is studied in particular in [30] or [31]. [32] indicated that C/N_0 monitoring is among the main methods to detect jamming situation.

2-3.4.1 Mathematical definition of C

The GNSS signal power C estimated by the GNSS receiver in the signal processing stages is the recovered signal power of the GNSS signal. This term includes:

- The received GNSS signal power P_{GNSS} at antenna port can be related to the specified minimum received power by considering the amplification by the antenna transducer gain and the LNA. This power at signal processing stage input is linked to the GNSS signal amplitude A_{GNSS} used to express the correlator outputs. Note that this term does not include power losses due to RF/IF filtering.

$$P_{GNSS} = \frac{A_{GNSS}^2}{2} \quad (\text{Eq 2-66})$$

- Implementation losses: Implementation losses are defined in [33] as “signal to noise ratio due to bandlimiting, quantization and sampling”. However, this definition does not take into account miscellaneous losses due to actual implementation nor losses caused by payload imperfection (also called correlation losses in GPS and Galileo ICD [20], [34]) that are part of implementation losses. Three parameters must be investigated to estimate an upper bound of implementation losses when ignoring miscellaneous losses (assumed equal to 0 dB in this thesis). First, quantization and sampling cause a loss of GNSS signal power. Losses due to quantization depends partly on the number of bits that are available in the Analog to Digital

Converter (ADC), and on the AGC amplification level. GNSS signal loss due to quantization under optimum AGC setting has been computed in [33]. Second, according to Interface Specification documents [20], [34], satellite payload may output an imperfect GNSS signal, inducing some signal recovered power losses due to a mismatch between the GNSS signal and the local replica. Third, the RF front-end filter also distorts the incoming GNSS signal in particular by limiting the recovered signal bandwidth. As a consequence, the received GNSS signal does not perfectly match with the local replica. For example, for GPS L1C/A, losses caused by RFFE filtering can be expressed by (Eq 2-67).

$$L_{filt} = \frac{K_{\tilde{c}_m, c_{mL}}(0)}{\beta} \quad (\text{Eq 2-67})$$

Implementation losses calculation will be detailed in Chapter 4 section 4-2.1.2.

2-3.4.2 C/N_0 estimation algorithms

Several signal to noise power spectrum density ratio estimators can be found in the literature [35]. There is no standard on the C/N_0 estimator for civil aviation receiver, therefore civil aviation receiver manufacturers can choose the method to estimate the carrier to noise density ratio. This thesis focuses on three C/N_0 estimators: the Beaulieu estimator, the moment method estimator and the SNV (Signal to noise variance) estimator. All of these estimators are based on assumptions on the noise distribution at the correlator output. Compared to some other estimators, the Beaulieu estimator and the moment method estimator have the advantage of presenting a reduced bias at high C/N_0 values in presence of phase tracking error [36] [37]. This point is important since the presence of an interference increases the phase tracking error variance. The main drawback of Beaulieu estimator and the moment method estimator is their complexity (high number of elementary operations). Denoting N_s the number of samples used for each C/N_0 estimation, the C/N_0 Beaulieu estimation is given by [38] and expressed in (Eq 2-68) for component Y (data or pilot) of GNSS signal X (L1C/A, E1, L5 or E5a).

$$C/\widehat{N}_{0,eff} = \frac{1}{T_i} \cdot \left(\frac{1}{N_s} \cdot \sum_{k=1}^{N_s} \frac{(|I_{X,P}^Y(k)| - |I_{X,P}^Y(k-1)|)^2}{\frac{1}{2}(I_{X,P}^Y(k)^2 + I_{X,P}^Y(k-1)^2)} \right)^{-1} \quad (\text{Eq 2-68})$$

The moment method estimator uses second and fourth order moments of correlator outputs in order to estimate the signal to noise density ratio [39]. The C/N_0 moment method estimator is given by (Eq 2-69).

$$\begin{aligned} \widehat{M}_2 &= \frac{1}{N_s} \cdot \sum_{k=1}^{N_s} I_{X,P}^Y(k)^2 + Q_{X,P}^Y(k)^2 & \widehat{M}_4 &= \frac{1}{N_s} \sum_{k=1}^{N_s} (I_{X,P}^Y(k)^2 + Q_{X,P}^Y(k)^2)^2 \\ C/\widehat{N}_{0,eff} &= \frac{1}{T_i} \frac{\sqrt{2\widehat{M}_2^2 - \widehat{M}_4}}{\widehat{M}_2 - \sqrt{2\widehat{M}_2^2 - \widehat{M}_4}} \end{aligned} \quad (\text{Eq 2-69})$$

The SNV estimator has the advantage to be less complex than Beaulieu and moment estimators. It compares the power on the in-phase channel (useful signal) to the variance of the quadrature phase channel (noise power). The C/N_0 estimation is given by (Eq 2-70).

$$C/\widehat{N}_{0,eff} = \frac{1}{2T_i} \frac{\left(\frac{1}{N_s} \sum_{k=1}^{N_s} I_{X,P}^Y(k) \right)^2}{\frac{1}{N_s} \sum_{k=1}^{N_s} Q_{X,P}^Y(k)^2 - \left(\frac{1}{N_s} \sum_{k=1}^{N_s} Q_{X,P}^Y(k) \right)^2} \quad (\text{Eq 2-70})$$

2-4 Impact of interferences on GNSS receiver

Signal to noise power spectrum density ratio compares the received GNSS signal power C with the effective noise power spectral density level $N_{0,eff}$ at antenna transducer output. Usually, the main impact of an interference on a GNSS receiver is to increase the noise level at the correlator output. Thus, an interference j is characterized by its equivalent additive noise density $I_{0,j}$, which is defined by the power spectral density level that a noise-like interference must have in order to create the same power at the correlator output than the interference j does. Then, the effective noise $N_{0,eff}$ contains the aggregation of all interference equivalent noises in addition to the thermal noise power spectral density, as expressed in (Eq 2-71).

$$N_{0,eff} = N_0 + \sum_j I_{0,j} \quad (\text{Eq 2-71})$$

Note that this approach on the impact of interference is only valid as long as the interference is not powerful enough to saturate the LNA of the receiver. In addition, the model presented in this section only applies for continuous RFI. Pulsed RFI impact on GNSS receiver has been analyzed in [12] and [40]. But since pulsed RFI has not been analyzed during this thesis, they are not addressed in this section.

This section provides the traditional method, based on the spectral separation coefficient, to compute the equivalent noise of a given interference. This section is divided in three parts. First, it provides a spectral model of the interference at the RF front-end module output. Second, it computes the power of the RFI at the correlator output. The equivalent noise $I_{0,j}$ of the RFI is then deduced from the RFI power at the correlator output. Third, it analyzes the impact of RFI on a particular GNSS receiver performance indicator, which is C/N_0 .

2-4.1 RFI model at the RF front-end output

The objective of section 2-4 is to compute the power of the interference at the correlator output. Assuming the interference signal can be considered to be a random stationary signal, the RFI is here characterized by its power spectrum density. The type of RFI considered here is a continuous RFI such that its power spectral density after down-conversion can be expressed as in (Eq 2-72).

$$S_{j,in}(f) = \frac{P_j}{2} S_{j,BB}(f) * (\delta(f - f_{IF}) + \delta(f + f_{IF})) \quad (\text{Eq 2-72})$$

P_j is the RFI power after down conversion. It includes the antenna gain as well as the gain brought by the LNA. $S_{j,BB}$ is the unit power spectral density of the equivalent baseband RFI. Next, the interference passes through the equivalent RF/IF filter. According to Wiener-Lee equation, the power spectral density of the RFI at the front-end output is given by (Eq 2-73).

$$\begin{aligned} S_{j,RFout}(f) &= |H_{RF}(f)|^2 S_{j,in}(f) \\ &= \frac{P_j}{2} \left(S_{j,BB}(f) * (\delta(f - f_{IF}) + \delta(f + f_{IF})) \right) \left(|H_{RF,BB}(f)|^2 \right) \\ &\quad * (\delta(f - f_{IF}) + \delta(f + f_{IF})) \\ &= \frac{P_j}{2} \left(S_{j,BB}(f) |H_{RF,BB}(f)|^2 \right) * (\delta(f - f_{IF}) + \delta(f + f_{IF})) \end{aligned} \quad (\text{Eq 2-73})$$

2-4.2 RFI power at the correlator output

The RFI has been spectrally characterized in (Eq 2-73) under the assumption that RFI is a stationary random signal. Now, the objective is to derive the RFI power spectral density at the correlator output in order to deduce its power. Eventually, the equivalent noise level of the interference will be deduced.

The steps followed to derive the power of the RFI at the correlator output are similar to the ones of section 2-3.3.1.2.

- First the power spectral density after the multiplication of the RFI with the local replica is deduced by analogy with the results obtained for the noise in section 2-3.3.1.2.
- Second, considering the integration as an equivalent low-pass filter, the power spectral density of the interference at the correlator output is deduced using Wiener-Lee equation.
- Third, the power is computed integrating the RFI power spectral density at the correlator output.

First, the interference is multiplied by the local carrier and PRN signal. The resulting signal is denoted $r_{prod,j}$. The multiplication with the PRN signal creates the spreading of the interference over the bandwidth of the PRN signal. By analogy with the case of an incoming white noise, the power spectral density of $r_{prod,j}$ can be expressed as in (Eq 2-74).

$$S_{prod,j}(f) = \frac{P_j}{8} \left(S_{j,BB}(f) |H_{RF,BB}(f)|^2 \right) * (\delta(f - 2f_{IF}) + 2\delta(f) + \delta(f + 2f_{IF})) * S_{cm_L}(f) \quad (\text{Eq 2-74})$$

$S_{prod,j}(f)$ can be developed as the sum of three components: one bandpass component around $-2f_{IF}$, one low pass component and one bandpass component around $2f_{IF}$.

Second, $r_{prod,j}$ passes through the integrate and dump low pass filter. According to Wiener Lee equation, the power spectral density of the interference is given by (Eq 2-75).

$$S_{j,corr out}(f) = |H_{ID}(f)|^2 S_{prod,j}(f) \quad (\text{Eq 2-75})$$

Since the integrate and dump filter acts as a low pass filter, high frequency terms are strongly attenuated by the correlation and are neglected in the rest of the calculation of the RFI power at the correlator output. The RFI power at the correlator output is obtained integrating (Eq 2-75).

$$P_{j,corr out} = \int_{-\infty}^{+\infty} S_{j,corr out}(f) df \quad (\text{Eq 2-76})$$

Injecting (Eq 2-74) and (Eq 2-75) in (Eq 2-76) and neglecting the high frequency terms as discussed previously, (Eq 2-76) can be developed as detailed in (Eq 2-77).

$$\begin{aligned} P_{j,corr out} &= \frac{P_j}{4} \int_{-\infty}^{+\infty} \left[(S_{j,BB}(f) |H_{RF,BB}(f)|^2) * S_{cm_L}(f) \right] |H_{ID}(f)|^2 df \\ &= \frac{P_j}{4} \int_{-\infty}^{+\infty} |H_{ID}(f)|^2 \int_{-\infty}^{+\infty} (S_{j,BB}(u) |H_{RF,BB}(u)|^2) S_{cm_L}(f - u) du df \\ &= \frac{P_j}{4} \int_{-\infty}^{+\infty} (S_{j,BB}(u) |H_{RF,BB}(u)|^2) \int_{-\infty}^{+\infty} |H_{ID}(f)|^2 S_{cm_L}(f - u) df du \\ &= \frac{P_j}{4} \int_{-\infty}^{+\infty} |H_{RF,BB}(u)|^2 S_{j,BB}(u) \left(|H_{ID}(u)|^2 * S_{cm_L}(u) \right) du \end{aligned} \quad (\text{Eq 2-77})$$

(Eq 2-77) can be generalized for non-null GNSS Doppler frequency. (Eq 2-78) provides the generalized result on RFI power at the correlator output.

$$P_{j,corr out} = \frac{P_j}{4} \int_{-\infty}^{+\infty} |H_{RF,BB}(u - f_D)|^2 S_{j,BB}(u - f_D) \left(|H_{ID}(u)|^2 * S_{cm_L}(u) \right) du \quad (\text{Eq 2-78})$$

Let us introduce the spectral separation coefficient (SSC) defined by (Eq 2-79).

$$SSC_j = \int_{-\infty}^{+\infty} |H_{RF,BB}(f - f_D)|^2 S_{j,BB}(f - f_D) (S_{c_m}(f) * |\bar{H}_{ID}(f)|^2) df \quad (\text{Eq 2-79})$$

\bar{H}_{ID} is the normalized transfer function of the integrate and dump filter; it represents the integration process with duration T_i .

$$\bar{H}_{ID}(f) = \sqrt{T_i} H_{ID}(f) = \sqrt{T_i} \text{sinc}(\pi f T_i) \quad (\text{Eq 2-80})$$

The last convolution term in (Eq 2-79) corresponds to the power spectral density of the locally generated replica filtered by the integrate and dump filter.

RFI power at the correlator output of (Eq 2-78) can eventually be re-expressed by (Eq 2-81).

$$P_{J,corr out} = \frac{P_J}{4T_i} SSC_j \quad (\text{Eq 2-81})$$

2-4.3 Impact of RFI on GNSS receiver performance

This section analyzes the impact of RFI on C/N_0 degradation. It first defines the signal to noise plus interference power ratio (SNIR) and introduces the concept of RFI equivalent noise. Second, C/N_0 degradation is computed and the conditions of validity of this model are investigated.

2-4.3.1 Signal to noise plus interference ratio and RFI equivalent noise

The calculation of the RFI power at the correlator output allows to define the signal to noise plus interference power ratio (SNIR) at the correlator output. The SNIR is defined by (Eq 2-82).

$$SNIR = \frac{C}{P_n + P_{J,out}} \quad (\text{Eq 2-82})$$

C is the GNSS signal power and P_n is the noise power at the correlator output, given in (Eq 2-50).

Another common definition of the SNIR is given in [31]:

$$SNIR = 2 \frac{\mathbb{E}(I_{X,P}^Y)^2}{\mathbb{V}(I_{X,P}^Y)} = 2 \frac{\mathbb{E}(I_{X,P}^Y)^2}{\mathbb{V}(Q_{X,P}^Y)} \quad (\text{Eq 2-83})$$

Where $I_{X,P}^Y$ is the in-phase prompt correlator outputs of component Y (data or pilot) of GNSS signal X (L1C/A, E1, E5a or L5) seen as a random variable. SNIR definition of (Eq 2-83) is equivalent to the general definition of (Eq 2-82) under the following assumption. The RFI contribution to the correlator output should be stationary and centered around 0. In this case, and since the noise at the correlator output is also assumed to be a centered gaussian random process, only the GNSS signal influences $\mathbb{E}(I_{X,P}^Y)$. In addition, it is assumed that tracking errors do not induce GNSS signal power loss. In this case, the GNSS signal is considered deterministic. Under these assumptions, $\mathbb{E}(I_{X,P}^Y)^2 = C/2$.

If the conditions of validity of (Eq 2-83) are fulfilled, and since the RFI at the correlator output is assumed to be uncorrelated with the useful signal and with the noise, then the noise plus interference power at the correlator output is given by (Eq 2-84).

$$\mathbb{V}(I_{X,P}^Y) = P_{J,corr out} + P_n = \beta \frac{N_0 + C_j SSC_j / \beta}{4T_i} \quad (\text{Eq 2-84})$$

In this case, by analogy with the first term in this sum, the equivalent noise power spectral density of the RFI can be defined as in (Eq 2-85).

$$I_{0,j} = \frac{C_j}{\beta} SSC_j \quad (\text{Eq 2-85})$$

2-4.3.2 Impact of RFI on C/N_0

The C/N_0 degradation compares the signal to noise density ratio in absence of interference (nominal C/N_0 or $C/N_{0,nom}$) to the C/N_0 when the useful signal as well as the interference are present at the antenna port (effective C/N_0 or $C/N_{0,eff}$). The C/N_0 degradation is expressed as

$$D_{C/N_0} = \frac{C/N_{0,nom}}{C/N_{0,eff}} = \frac{N_0 + I_0}{N_0} = 1 + \frac{C_j}{N_0} SSC_j \quad (\text{Eq 2-86})$$

A more accurate and complex model of C/N_0 can be found in RTCA DO-235B [10] and RTCA DO-292 [12]. Effects of pulse blanker or analog to digital converter saturation are indeed not considered in (Eq 2-86).

The main remaining question to tackle about C/N_0 estimators' behavior in presence of RFI is whether they can provide an estimated C/N_0 value close to theoretical true effective $C/N_{0,eff}$ relying on SSC coefficient in the presence of random stationary RFI signal knowing that C/N_0 estimators were designed to work in the presence of AWGN only. To answer this question, it is necessary to identify the assumptions on the prompt correlator outputs made by: (1) the C/N_0 estimators design and (2) the theoretical $C/N_{0,eff}$ model. On one hand, C/N_0 estimators assume a specific behavior and distribution of the prompt correlators outputs to correctly estimate the received signal C/N_0 . Indeed, C/N_0 estimators assume that the correlators outputs are the addition of the useful signal term, modelled as a constant deterministic term, and a centered stationary randomly distributed noise term. Depending on the C/N_0 estimator, assumptions on the correlator output distribution are made (or more specifically on the noise term distribution), for example a Gaussian distribution, as well as assumptions on the presence of the useful term in the I correlator output only or in the I and Q correlators outputs (and thus considering carrier phase estimation errors). On the other hand, the theoretical $C/N_{0,eff}$ model using the SSC coefficient assumed specific random distributions on some of the correlator outputs parameters.

Analyzing the previous discussion, the conditions to be respected by the correlator outputs are the following.

1. Condition 1: Validity of SNIR definition of (Eq 2-83) (centered RFI, uncorrelated with GNSS)
The C/N_0 estimators are based on the SNIR definition of (Eq 2-83). Therefore, the assumption of validity described in section 2-4.3.1 of this definition should be verified. In particular, GPS signal is deterministic, so it is assumed that there is no loss of signal power because of tracking. Only the noise and the RFI are considered as random. Therefore, the contribution of the RFI to the correlator output should be uncorrelated with the contribution of the GPS signal to the correlator output. As an important remark, RFI contribution to correlator outputs is assumed random and centered.
2. Condition 2: C/N_0 estimator assumptions
 C/N_0 estimators may make some assumptions on the distribution of the RFI on the in-phase and quadrature phase correlator outputs. For example, Beaulieu estimator, using only the in-phase correlator output, assumes an identical distribution on the in-phase and quadrature phase RFI contribution on correlator outputs. In addition, moment estimator assumes relationships between second and fourth order moments of a gaussian distribution. If the RFI distribution at the correlator output is different from a gaussian distribution, then moment method might not reflect the correct noise plus interference variance. Behavior of C/N_0 estimators in presence of RFI will be analyzed further in detail in this thesis. The hypothesis on the correlator outputs' distribution considered by the different C/N_0 estimators are identified in Appendix E.

3. Condition 3: Ergodicity of correlator outputs

C/N_0 estimator estimates the statistical variance of the correlator output from time samples. As a reminder, $C/N_{0,eff}$ model predicting the $C/N_{0,eff}$ degradation using the SSC coefficient in presence of the chirp signal assumes the chirp is modeled as a random signal with two random parameters δ and φ_0 . In addition, SNIR definition of (Eq 2-83) is based on a probabilistic approach. Therefore, to be consistent with the predicted C/N_0 degradation, the C/N_0 estimators should be able to reflect the statistical properties of the correlator outputs from the knowledge of one sufficiently long observation period. In other words, the correlator outputs must be ergodic. If this condition is not fulfilled, then C/N_0 estimators may not be able to correctly estimate the true SNIR of (Eq 2-83). Also, the predicted effective C/N_0 may not be consistent with the true $C/N_{0,eff}$.

In order to illustrate the impact of RFI on C/N_0 , several definitions of C/N_0 are introduced below.

1. Statistical C/N_0

The statistical C/N_0 is computed from a theoretical approach, assuming that the interference is a random signal. The statistical C/N_0 is defined by (Eq 2-87).

$$\left(\frac{C}{N_0}\right)_{stat} = \frac{1}{4T_i} \frac{C}{P_{n,stat} + P_{j,stat}} \quad (\text{Eq 2-87})$$

Where $P_{n,stat}$ and $P_{j,stat}$ are respectively the noise and interference power at correlator output, computed with (Eq 2-50) and (Eq 2-81) respectively. Note that statistical C/N_0 is defined from a theoretical approach and it cannot be computed by the receiver, as this definition does not rely on observables.

2. Real C/N_0

Real C/N_0 is defined by (Eq 2-88). This C/N_0 notion is based on SNIR definition of (Eq 2-82).

$$\begin{aligned} \left(\frac{C}{N_0}\right)_{real} &= \frac{1}{4T_i} \frac{C}{P_{n,real} + P_{j,real}} \\ P_{n,real} &= P_{n,stat} = \mathbb{E}[I_{noise,n}^2 + Q_{noise,n}^2] \\ P_{j,real} &= \frac{1}{N} \sum_N (I_{PPD,n}^2 + Q_{PPD,n}^2) \end{aligned} \quad (\text{Eq 2-88})$$

$P_{n,real}$ and $P_{j,real}$ are respectively the noise and interference power at correlator output, computed from correlator output samples. Real C/N_0 is the effective C/N_0 faced in reality by the receiver. Real C/N_0 is equivalent to statistical C/N_0 if interference distribution at correlator output is ergodic. As a matter of fact, if the ergodicity condition is fulfilled, then the estimation of the interference power at correlator output with the statistical approach is equivalent to the power computed from a set of RFI correlator output samples computed over a sufficiently long time interval. However, because the noise and interference contribution to correlator output cannot be separated in reality, real C/N_0 cannot be output by a receiver.

3. Estimated C/N_0

Because both statistical C/N_0 and real C/N_0 are not observable at the receiver output, C/N_0 is usually estimated from correlator outputs using one of the algorithms of section 2-3.4.2 for example. These C/N_0 algorithms are based on SNIR definition of (Eq 2-83). As a consequence, the estimated C/N_0 will adequately reflect the effective C/N_0 faced in reality by the receiver (real C/N_0) only if conditions of validity of (Eq 2-83) are fulfilled. In addition, since these estimators also make some assumptions on

the distribution of the RFI at the correlator output, these assumptions must be fulfilled so that estimated C/N_0 fit with real C/N_0 .

2-5 Interference environment

This section describes the interference environment faced by civil aviation GNSS receivers. This description of the RFI environment is based on the observation reported in the literature.

RFI can be split in two categories: aeronautical RFI and non-aeronautical RFI. Aeronautical RFI refers to RFI coming from a coordinated aeronautical system (system which is part of ARNS: Aeronautical Radio Navigation service), but which transmits in the GNSS band because of imperfect filtering, or because of a coordinated sharing of the frequency band. Non-aeronautical RFI refers to RFI coming from non-aeronautical equipment which transmits some energy in the GNSS frequency band without coordination with civil aviation services, either voluntarily or involuntarily. This section exhaustively describes the different RFI sources faced by GNSS receivers.

2-5.1 Aeronautical RFI sources

[10] and [12] identifies three aeronautical RFI sources that are common to both the GNSS L1/E1 band (1559-1610 MHz) and the GNSS L5/E5 band (1164-1189 MHz):

- 1) Case Emission: Cockpit devices screens radiate unwanted energy in the GNSS L1 band. This aeronautical RFI source, comprised of 10 installed devices and 2 portable tablets since DO235C, is referred as case emission. Current cockpit installed equipment are tested and certified according to [41] Cat M requirements. In particular, undesired radiation in the GNSS frequency band from each cockpit equipment device is limited to 53.3 dB μ V/m for this category of equipment. Newer cockpit devices will be certified according to Cat P and Cat Q requirements and will be allowed to transmit no more than 40 dB μ V/m.
- 2) Inter and intra system RFI: Inter and intra system RFI refers to GNSS signals coming from other GNSS constellations or from the same constellation but different from the signal of interest. For example, Galileo E1 signals and GPS L1C/A PRN 6 signal act as an RFI on the receiver channel processing GPS L1C/A PRN 2 signal. Since there are more and more GNSS constellations, inter system RFI should be regularly revised. In particular, the set of civil aviation interference thresholds given in standardization document RTCA DO-292 Appendix F, also called RFI mask, is based on an inter/intra system RFI analysis performed in 2004, which do not consider Beidou signals. Thus, aeronautical RFI computation is not up to date in the DO-292 RFI mask.

In addition, the GPS L1 and Galileo E1 receiver processing channels face aeronautical RFI induced by the Aeronautical Mobile Satellite System (AMSS). Some aircrafts hold an aeronautical mobile satellite system (AMSS) equipment. This on-board equipment allows communication between the aircraft and the ground through satellite communications. AMSS has a frequency allocation in the [1626-1660] MHz band and thus, AMSS transmission does not directly hit the GNSS L1 band. However, 5th and 7th order intermodulation products fall into the L1 GNSS band and may degrade GNSS signal processing.

Furthermore, as described in Figure 2-14, GNSS L5/E5a receivers share their frequency band with other aeronautical systems.

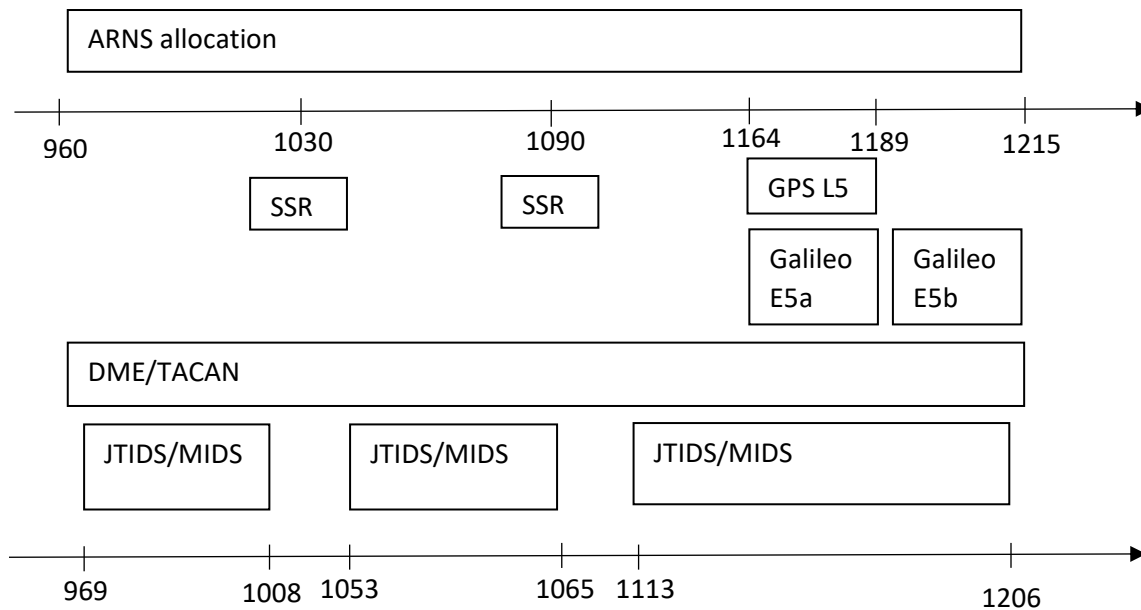


Figure 2-14: Current Systems in the L5/E5 frequency band

Aeronautical systems transmitting in the ANRS allocated [960; 1215] MHz frequency band include:

- Secondary surveillance radar (SSR) interrogations: ground to air signal transmitted using a 1030 MHz carrier frequency.
- Secondary surveillance radar (SSR) response: air to ground and air to air signal transmitted by the transponder using a 1090 MHz carrier frequency.
Thanks to the frequency isolation between the SSR carrier frequencies and the GNSS band, [12] showed that the impact of SSR signals on the GNSS band is negligible.
- Distance Measurement Equipment (DME): DME is an aeronautical system allowing an aircraft to estimate its distance from a ground beacon. The military version of this system is called TACAN (Tactical Air Navigation). DME and TACAN signals are high power (typically 1 kW for an en-route DME) pulsed signals that affect the GNSS signal processing, since some DME/TACAN channels share the same frequency band than GNSS L5/E5 signals. Impact of DME/TACAN on GNSS C/N_0 degradation has been analyzed in [40].
- Joint Tactical Information Distribution System (JTIDS) and Multifunctional Information Distribution System (MIDS) are military systems, using the allocation of the NATO (North Atlantic Treaty Organization) link 16 in the [960;1215] MHz frequency band. JTIDS/MIDS signals are pulsed signal. Impact of JTIDS/MIDS on GNSS C/N_0 degradation has been analyzed in [42].

2-5.2 Non-aeronautical RFI sources

At least two non-aeronautical sources have been identified in [10], [12] and involuntarily and permanently radiate in the GNSS bands.

1. On-board PEDs: Passengers are allowed to use their electronic devices during some phases of the flight. These electronic devices carried by passengers are referred to as on-board Portable Electronic Devices (PEDs). NASA performed measurements on several kinds of PEDs (laptop, mobile phones, etc) [43] [44], in order to estimate their transmitted power in the GNSS bands as well as propagation losses between the airplane windows and the aircraft fuselage GNSS antenna.

2. **Terrestrial emitters:** Terrestrial emitters refer to a wide variety of devices unvoluntary radiating in the GNSS band with low power: PEDs, wifi sources, etc. The terrestrial emitter RFI level received by a victim GNSS antenna depends on the environment. Indeed, the density of emitters is much higher above urban areas than above desertic areas. Moreover, the altitude of the aircraft also influences the impact of terrestrial emitters on the receiver. On the one hand, the number of emitters visible from the on-board antenna grows with the altitude of the aircraft. On the other hand, attenuation due to propagation losses also grows with the aircraft altitude. Impact of terrestrial emitters has first been estimated in [10, p. 235] and revised in [45]. In Chapter 4 section 4-2.2.2, an alternative estimation of the equivalent noise caused by terrestrial emitters is done, considering an alternative propagation losses model developed in [46].

Other non-aeronautical RFI sources, such as jammers, may impact the GNSS receiver signal processing. Some of the most common jamming signals are described in section 2-5.3.

2-5.3 Classical jamming signals

This section describes jamming signals often encountered in the literature.

2-5.3.1 Rectangular RFI

Rectangular RFI refers to random stationary jamming signals whose power spectral density (PSD) is rectangular. Therefore, this interference is fully characterized by its double-sided bandwidth B , its central frequency f_j and its power C_j . Note that this is the type of RFI which has been considered to define the set of interference thresholds also called the RFI mask in the International Civil Aviation Organization (ICAO) SARPs (Standard and Recommended Practices) [15], which provide the maximum RFI power tolerated by a receiver to maintain minimum performance requirements fulfilled. The power spectral density of such an interference is illustrated on Figure 2-15.

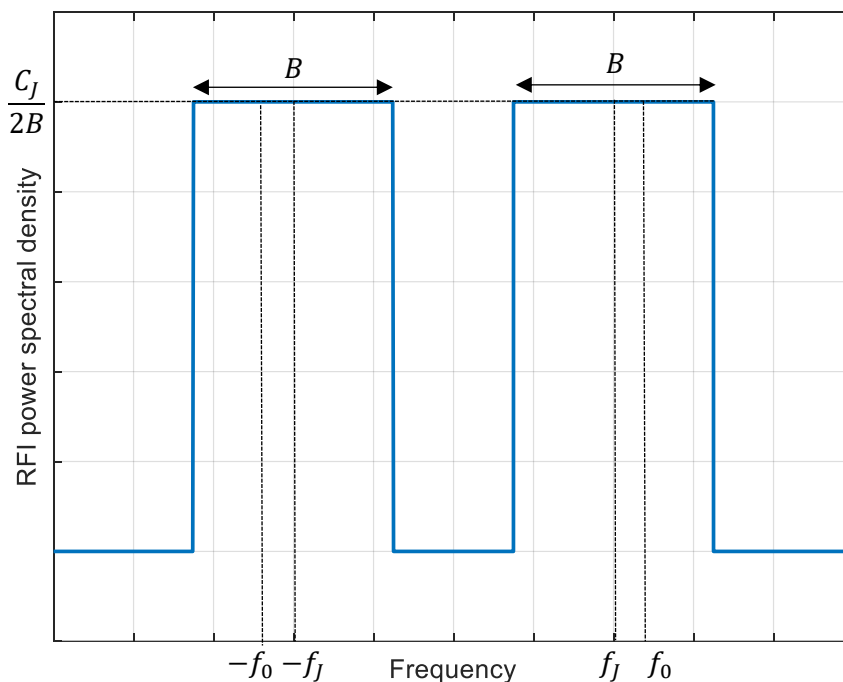


Figure 2-15: Power spectral density of a rectangular spectrum signal

In Figure 2-15, f_0 refers to the GNSS carrier frequency (either L1=1575.42 MHz or L5=1176.45 MHz) and f_j is the rectangular RFI central frequency.

2-5.3.2 Chirp RFI

As part of GNSS strike 3 project, [47] monitored RFI encountered in several environments, including airports, installing some monitoring stations in the vicinity of major roads. The aim of this project was to analyze the interference environment mainly caused by in-car jammers. These jammers are called portable privacy devices (PPD). These illegal jammers indeed represent a major threat for civil aviation. Indeed, jamming situations involving PPDs are increasingly observed. [47] reported more than 600 monthly RFI events in an airport environment that can very likely be accounted as intentional jamming events, over the period February 2018 to June 2018, with a consequent threat on the aircrafts' flight safety. [48] analyzed several jamming situations impacting civil aviation. In particular at Newark airport (New Jersey) from March 2009 to April 2011, the Ground Based Augmentation System (GBAS) station was frequently jammed by a PPD installed on a truck traveling near the airport [49]. Another example of the impact of PPD on civil aviation took place in Nantes (France) in April 2017. A PPD in a parked car was transmitting a strong enough jamming signal to impact GNSS receiver onboard aircrafts parked at the closest gates, forcing the airport to tow some aircrafts to remote locations for startup. Due to the increasing number of jamming events caused by chirp RFI, EUROCAE WG62 and RTCA SC159 plan to include some tests of the robustness of the receiver facing chirp RFI in the civil aviation receiver certification process.

The PPD signals analyzed by [47] appear to have particular frequency characteristics. Indeed, the spectrogram of PPD signals depicts a periodic pattern. Thus, PPD signal can be seen as a carrier wave whose instantaneous frequency varies along time. The instantaneous frequency depicts a periodic pattern over time: linear sweep within the targeted bandwidth with a triangular time pattern for example. This thesis will address the case where the spectrogram of the PPD signal is a saw tooth function, and the PPD signal will be referred as a chirp signal.

[50] mathematically model the chirp signal by (Eq 2-89).

$$s(t) = A_{PPD} \sin\left(2\pi \int_0^t f_i(u) du\right) \quad (\text{Eq 2-89})$$

A_{PPD} is the chirp signal amplitude, assumed constant. $f_i(t)$ is the pattern depicted by the instantaneous frequency.

Figure 2-16 represents the instantaneous frequency pattern for two particular chirp signal: the triangular PPD signal and the saw-tooth PPD signal. The PPD signal is therefore characterized by the instantaneous frequency pattern, its central frequency $f_j = f_0 + \Delta f_j$, the impacted bandwidth B and the sweep period T_{sweep} .

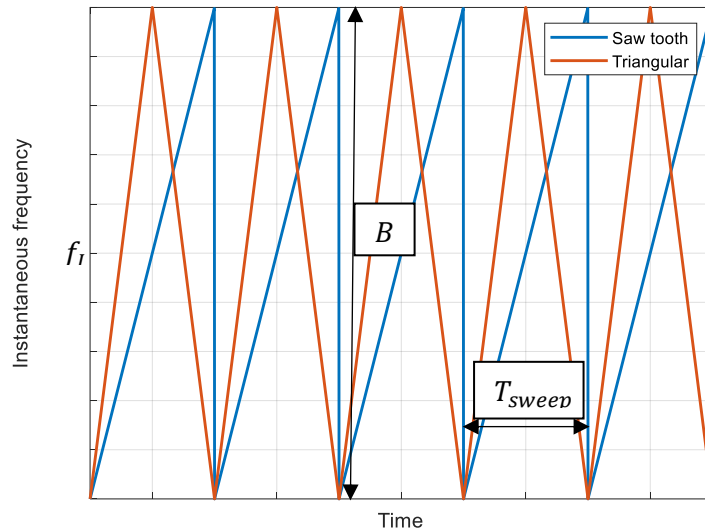


Figure 2-16: Instantaneous frequency pattern of a triangular and linear chirp signal

2-6 Review of GNSS regulation

This section describes minimum requirements that must be fulfilled by GNSS receivers and minimum RF characteristics of GNSS signals, according to the current regulation.

Two types of receivers have been considered in this thesis.

- Legacy receiver: Legacy receiver is currently the category of GNSS receiver the most installed on-board aircrafts. This type of receivers allows to process only GPS L1C/A signals. Legacy receiver must be coupled with an antenna fulfilling requirements from DO-301 [51].
- Dual Frequency Multi Constellation (DFMC) receiver: DFMC receiver is the new-coming generation of GNSS receiver. This category of receivers must be able to process signals from the L1/E1 frequency band and signals on the L5/E5 frequency band. In addition, a DFMC receiver shall be able to process signals transmitted by two constellations: GPS and Galileo. In the future, Beidou signals may also be included in the signals to be processed. Characteristics and test conditions of DFMC receiver are developed in ED-259A [52], which is based on input given in DO-292 [12] for L5/E5a signals and on DO-235C [6] for the L1/E1 signals. DFMC receiver must also be coupled with an antenna fulfilling requirements from [53].

This section is divided in three parts. First, minimum GNSS signals RF characteristics set in ICAO SARPs [15] are recalled. Second, GNSS receiver antenna pattern is discussed depending on the category of the receiver. Third, the notion of RFI mask is introduced to discuss the minimum resistance of GNSS receiver facing RFI.

2-6.1 GNSS signal RF characteristics

GNSS signals RF characteristics are presented on [21] and [20]. The ICAO, in the Annex 10 of the Convention of Chicago [15], recalled these characteristics. This section presents the minimum and maximum GNSS signal power at the Earth surface given in ICAO Annex 10, and the bandwidth of the GNSS signals.

[15] provides the minimum GNSS signal power at the port of a 3 dBi linearly polarized antenna, provided that the GNSS signal comes from a satellite which is at a higher elevation than 5° . 5° is indeed

the elevation mask. Note that the 3 dBi reference antenna gain is compensated by polarization losses, since GNSS signals are circularly polarized. The minimum received GNSS signal power at all unobstructed locations near the ground from which the satellite is observed at an elevation angle of 5 degrees or higher is summarized in Table 2-5.

In addition, there is also a constraint on the maximum received power. Indeed, a GNSS signal power must be over bounded to avoid causing too strong inter-system RFI on a different GNSS system. The signal powers given in Table 2-5 are associated to a reference bandwidth which is also indicated in Table 2-5.

	GPS L1C/A	GPS L5	Galileo E1	Galileo E5	SBAS L1	SBAS L5
Minimum GNSS signal power (dBW)	-158.5	-154.9	-157.9	-155.9	-158.5	-153.5
Maximum GNSS signal power (dBW)	-153	-147	-151.45	-149.45	-152.5	-150.5
Reference bandwidth (MHz)	24	24	24.552	20.46	2.2-24 (95% power)	20-24 (95% power)

Table 2-5: Minimum GNSS signal power as specified in ICAO Annex 10

For SBAS signals, it is specified that:

- The SBAS L1 signal bandwidth should be at least 2.2 MHz and that at least 95% of the power should be in a 24 MHz double sided bandwidth.
- At least 95 per cent of the L5 broadcast power shall be contained within a bandwidth centered on the L5 frequency and between 20 MHz to 24 MHz.

2-6.2 GNSS receiver characteristics

The legacy receiver is associated to the antenna standardized in DO-301 [51], whereas the DFMC receiver will use a new-generation antenna capable of receiving signals on both the L1/E1 and L5/E5 frequency bands standardized in DO373A. In this thesis, three characteristics of the antenna influence the characterization of RFI impact on a GNSS receiver:

- Antenna 1 dB compression point.
- Antenna gain pattern, described as the maximum and minimum antenna gain as a function of the satellite elevation.
- Antenna frequency rejection.

These three elements are presented in this section.

Antenna 1 dB compression point

First, the LNA 1 dB compression point is the minimum power at the input of the LNA such that the ratio between the LNA power output and the LNA power input differs from the LNA gain by more than 1 dB. The antenna 1 dB compression point characterizes the capacity of the receiver to operate in a linear way. If the signal power at the antenna input is above the 1 dB compression point, then there is a risk of power saturation and the receiver observables, such as pseudo-ranges, may be affected. Figure 2-17 shows the minimum requirements in term of 1 dB compression point for the DFMC and the legacy antennas. This curves are given by DO-373 and DO-301 respectively.

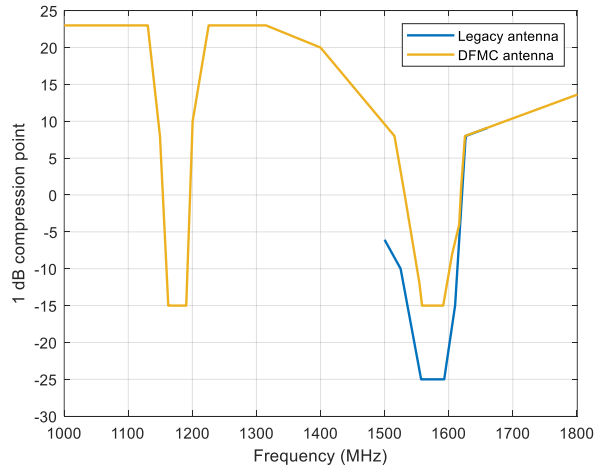


Figure 2-17: 1 dB compression point of the legacy and DFMC antennas

The 1 dB compression point is higher for the DFMC antenna by 10 dB in the L1/E1 band compared to the legacy antenna.

Antenna gain pattern

Second, the antenna gain pattern plays a key role in the determination of the RFI impact on the GNSS receiver. Indeed, the antenna gain is directly linked to recovered power at the antenna port. Therefore, antennas are standardized so that their antenna gain remains between a minimum value and a maximum value. The minimum and maximum antenna gains as a function of the satellite elevation (for positive elevation) are shown in Figure 2-18a. Figure 2-18b shows the maximum antenna gain for signals arriving from below the aircraft (negative elevation angle).

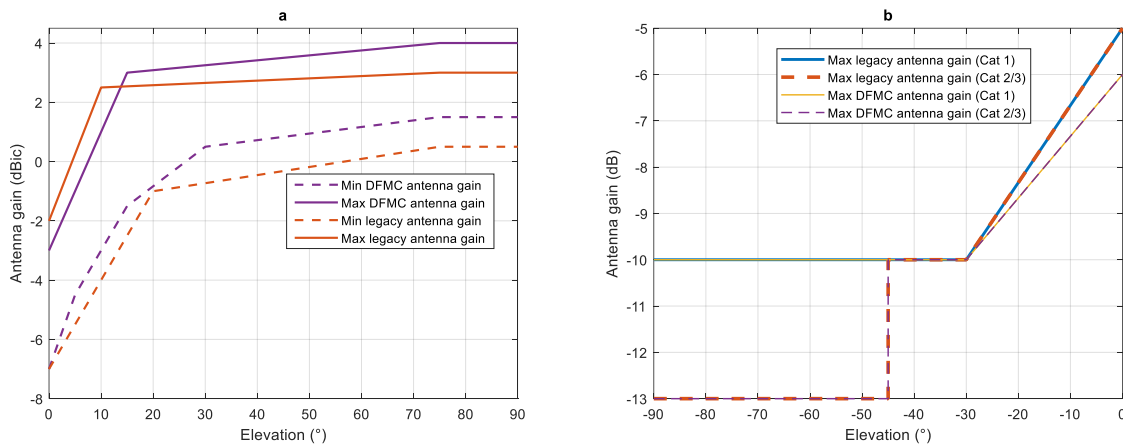


Figure 2-18: Legacy and DFMC receiver antenna patterns

The lower hemisphere antenna pattern, represented in Figure 2-18b, is not issued from a certification requirement but it is derived from measurements performed on an antenna prototype. This lower hemisphere antenna pattern is necessary to estimate the received power from signals coming from the ground.

Since the GNSS antenna is installed on the top of the aircraft, the aircraft fuselage may shadow the signal. On the other hand, the fuselage may also act as a waveguide for the terrestrial emitter RFI signal. In any case, the impact of the fuselage for signals arriving with a negative elevation angle is already taken into account in the antenna gain plots of Figure 2-18b, since the maximum antenna gain

at lower hemisphere has been defined from measurements performed on manufactured antennas installed on an aircraft model (see Appendix G of DO-235B, [10]). A linear polarization is assumed.

In addition, the maximum antenna gain for lower hemisphere depends on the category of approach for which the receiver is certified. Indeed, as GNSS guidance should be performed at a lower altitude for Cat 2/3 compared to Cat 1 approach, the maximum antenna gain for areas below the airplane (for elevation angles below -45°) must be lower, to attenuates the impact of ground RFI sources.

Antenna frequency rejection

Third, the antenna frequency rejection also plays a key role in the attenuation of out-of-band RFI. The minimum legacy and DFMC antennas frequency rejection is plotted in Figure 2-19. These curves are issued from DO-373 and DO-301 respectively.

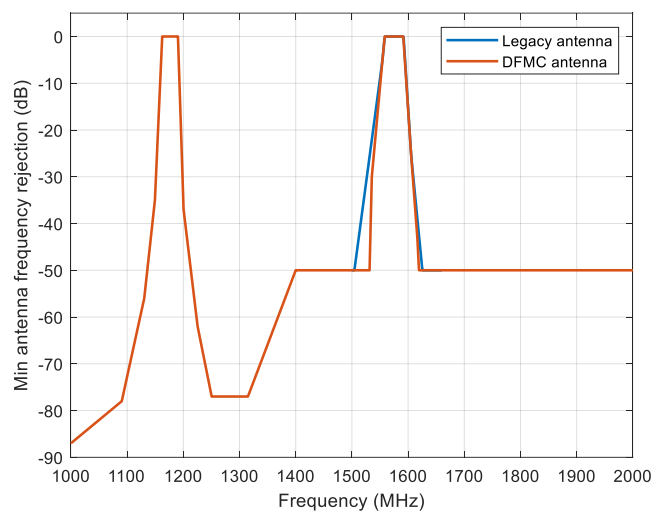


Figure 2-19: Minimum legacy and DFMC antennas frequency rejection

Figure 2-19 shows that the newer-generation DFMC antenna is more rejective in the near L1 band.

As a conclusion, the antenna 1 dB compression point is a key element to determine the maximum RFI power tolerable by the receiver, as a RFI power exceeding the 1 dB compression point would induce non-linearities matters and misbehavior of the receiver. The antenna gain pattern and antenna frequency rejection play a key role in the determination of the RFI received power and thus on the impact of RFI on a GNSS receiver.

2-6.3 GNSS RFI masks

The notion of interference thresholds, or RFI mask is introduced in [11] for L1 and in [12] for L5. The RFI mask provides the maximum power from a non aeronautical interference source that can be tolerated by an aeronautical receiver at the antenna port to guarantee the fulfillment of $1.\sigma$ performance objective defined by ICAO SARPs [15]. The in-band RFI mask provides the maximum tolerable power of a non-aeronautical RFI hitting the GNSS band ($L1 \pm 10$ MHz for L1/E1 band or $L5 \pm 10$ MHz for L5/E5 band) as a function of its bandwidth (double sided). The out-of-band RFI mask gives the maximum tolerable power of a 700Hz CW non aeronautical RFI as a function of its central frequency.

Two RFI out-of-band masks can be encountered in regulations documents. The first RFI mask has been developed from analysis presented in [54] to protect GPS L1C/A legacy receiver. This mask is still used for receiver testing. The second RFI out-of-band mask, which is published in ICAO SARPs has the

objective to protect DFMC receivers. These two RFI out-of-band masks are represented in Figure 2-20-a. For compatibility purpose, the more restrictive between these two masks shall be applied. Note also that a third version of this out-of-band mask has been published in DO235C Appendix F, proposed by receiver manufacturers.

Likewise, two in-band masks can be encountered in regulation documents: one for the L5/E5 band and one for the L1/E1 band. In band masks are represented in Figure 2-20-b.

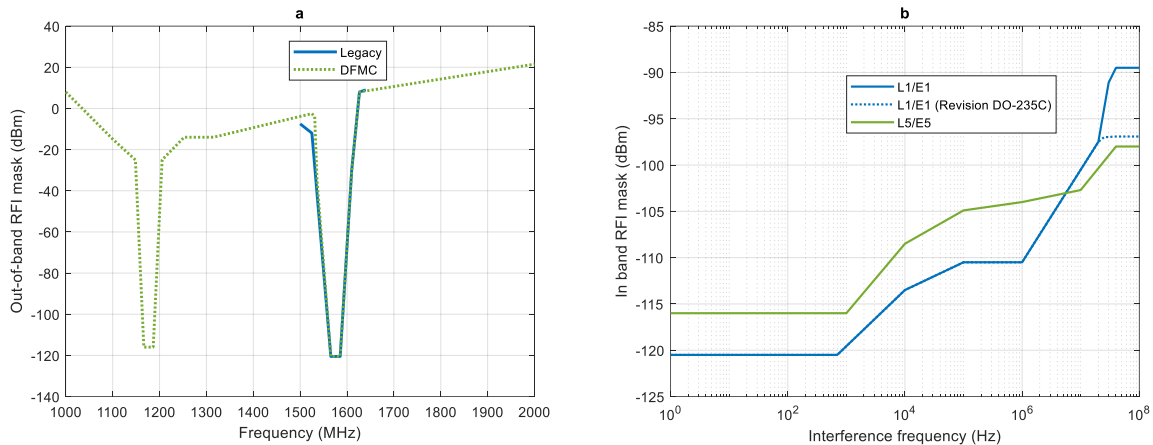


Figure 2-20: Out-of-band and in-band RFI masks

As it can be noted in Figure 2-20-b, the L1/E1 in-band RFI mask has been revised in DO-235C [6] for RFI bandwidth above 20 MHz.

The RFI mask is well known in the civil aviation community. However, assumptions used to elaborate this mask are not clearly given by ICAO and ITU. As a consequence, misinterpretation of the RFI mask may occur. In addition, the legacy interference mask is empirically derived. Appendix B proposes a theoretical methodology to derive RFI masks.

2-7 Conclusion

This chapter browses the GNSS state of the art, and is oriented to present elements regarding civil aviation and RFI threats. After having presented GNSS systems, high level ICAO requirements for civil aviation, and mathematical GNSS signal models used for civil aviation purpose, this chapter presents the architecture of GNSS receivers, and describes in particular the signal processing stage. Next, this chapter models the impact of RFI as equivalent to an additive white noise and describes the associated model. The RFI environment is then presented. Eventually, some elements necessary to analyze the impact of interference on GNSS receiver, extracted from regulation and certification documents, are presented. These elements include GNSS signals power and bandwidth, GNSS antenna characteristics and RFI masks.

The main goal of this chapter was to present fundamental points to analyze the RFI impact on GNSS receivers. These elements will be re-used in Chapter 4 and Chapter 5.

Chapter 3: C2Link Signal Processing and Civil Aviation Requirements

Unmanned Aircraft System (UAS) is defined by International Civil Aviation Organization as an aircraft and its associated elements which are operated with no pilot on board [55].

With the improvement of UAS technologies, UASs' usage is diversifying. Among the main UAS usages, one can cite:

- Recreative activities, which refer to operations where the UAS is flown for fun and personal enjoyment.
- Public safety activities, which refer to operations whose objective is law enforcement. In the future, safe and rescue operations in dangerous areas are also expected to be part of public safety activities.
- Military activities, which refer to flights operated in a military framework.
- Industrial or professional activities, which refer to operations performed for financial purpose, or in an associative or professional framework. For example, infrastructure surveillance or UAS used for photography are part of this category.

Due to the wide diversity of usage, UAS traffic is raising. International Telecommunications Union (ITU) proposes two methodologies estimating the density of UAS (not considering recreative UASs) in 2030 [56]. Both methodologies return similar results with a density of around 10 UASs per 10 km² operating simultaneously.

Currently, unmanned aircraft are only allowed to fly in segregated airspace. Segregated airspace refers to areas allocated to unmanned aircraft operations and on which the penetration of manned aircraft is regulated. Figure 3-1 shows an extract of SUP AIP 037/22 (Aeronautical Information Publications Supplements) which constraints the penetration of manned aircrafts into zones dedicated to unmanned aircraft transit.

 <p>Service de l'Information Aéronautique</p> <p>DSNA</p>	 <p>Liberté • Égalité • Fraternité RÉPUBLIQUE FRANÇAISE</p> <p>E-mail : sia.qualite@aviation-civile.gouv.fr Internet : www.sia.aviation-civile.gouv.fr</p>	<p>AIP SUP 037/22 Publication date : 10 MAR</p>
--	---	--

Subject : Creation of 92 temporary areas (ZRTs/ZDTs) for transits and operations of State unmanned aircraft in the south of France

In force : From 24 March 2022 to 19 April 2023

Location: FIRs: Bordeaux LFBB, Marseilles LFMM, Brest LFRR

<p style="text-align: center;">GENERAL</p> <p>Transits and operations of State unmanned remote-controlled aircraft.</p>
<p style="text-align: center;">DATES AND TIMES OF ACTIVITY</p> <p>Can be activated according to protocol. Activation announced by NOTAM with 6-hour prior notice when the ZRTs are activated for security reasons and on D-1 working day before 1200 local time for an exercise or training.</p>
<p style="text-align: center;">MANAGING AUTHORITY</p> <p>Mont de Marsan, Lyon and Cinq-Mars-la-Pile Control and Detection Center (CDC) or replacement CDC. For each area, a managing authority in charge is indicated in the user information table.</p>
<p style="text-align: center;">ENTRY CONDITIONS</p> <p>ZRT parts: GAT/Military Air Traffic: entry after coordination. ZDT parts: air users' attention is drawn to the particularly dangerous nature of the activities performed in these zones. Therefore, during the activity time slots, it is strongly recommended to avoid entering these areas.</p>

Figure 3-1: Extract of SUP AIP 037/22 on creation of unmanned aircraft segregated airspace

SUP AIP 037/22 allows manned aircraft to enter the segregated airspace after radio coordination. The penetration of other segregated airspace may also be prohibited to manned aircraft depending on the operation performed by the UAS and the density of UASs flying within the segregated airspace, as it is the case in SUP AIP 177/2022 shown in Figure 3-2.

<p style="text-align: center;">AIP SUP No 177/22</p>
<p style="text-align: center;">ACTIVITY</p> <p>Unmanned aircraft flight.</p>
<p style="text-align: center;">DATES AND TIMES OF ACTIVITY</p> <p>ZRT CIFED 1 : - Can be activated from MON to FRI : 0500-2359 (SUM : - 1 HR), - other time slots announced by NOTAM.</p> <p>ZRT CIFED 2 : - Can be activated from MON to FRI : 0500-2359 (SUM : - 1 HR), - other time slots announced by NOTAM.</p> <p>ZRT CIFED 3 : - Can be activated from MON to FRI : 0600-2300 (SUM : - 1 HR), - other time slots announced by NOTAM.</p>
<p style="text-align: center;">USER INFORMATION</p> <p>Actual time slots provided by : SALON APP : 135.150 MHz MARSEILLE INFO : 120.550 MHz</p>
<p style="text-align: center;">MANAGING AUTHORITY</p> <p>SALON APP</p>
<p style="text-align: center;">STATUS</p> <p>Temporary Restricted Areas (ZRT) replacing the portions of airspaces with which they overlap.</p>
<p style="text-align: center;">ENTRY CONDITIONS</p> <p>GAT / OAT : compulsory avoidance during the activation time slots except for aircraft conducting assistance, rescue or public safety missions when their route is not compatible with the ZRTs' avoidance; entry is possible after authorisation from SALON APP.</p>

Figure 3-2 Extract of SUP AIP 177/22 on creation of unmanned aircraft segregated airspace

However, due to the raising demand for UAS operation, there is a real need to insert unmanned aircrafts into the non-segregated airspace. In order to avoid catastrophic events such as collisions, UAS technologies must be certified to fulfill ICAO performance objectives. In particular, the C2Link is the

command and control signal allowing the remote pilot to communicate with the UAS. C2link is equivalently referred to CNPC link (or Control and Non-Payload Communication) This chapter focuses on the C2Link communications. It is divided in 3 sections. First, it provides an introduction to UAS operations, and it gives some important definitions. Second, it presents in detail the C2Link signal implementation of MOPS DO-362 standard [8], detailing the functionality and the signal design . Third, it presents the mathematical C2Link signal that will be considered in this thesis.

3-1 From UAS to RPAS operations in non-segregated airspace

This section presents and define the concept of UAS and remotely piloted aircraft system (RPAS). It is decomposed in three subsections. First, it provides a classification of different UAS. Second, as this PhD thesis focuses on a particular category of UAS, RPAS, the concept of RPAS is detailed. Third, C2Link, which refers to command and control link, is introduced.

3-1.1 ICAO UAS definition and classification

This section presents in detail the concept of UAS. Definitions provided in this section are taken from ICAO Cir 328 [55]. UAS is defined as an “aircraft and its associated elements which are operated with no pilot on board”. ICAO defines an aircraft as “any machine that can derive support in the atmosphere from the reactions of the air other than the reactions of the air against the earth’s surface”. The definition of an UAS is therefore very large and UAS refers to a wide diversity of systems. ICAO provides a good illustration of the different categories of UAS in its 2020/1 Unmanned Aviation Bulletin [57]. According to this bulletin, the following systems are part of UAS:

- Unmanned free balloon, which are “non-power driven, unmanned, lighter than air aircraft in free flight”. Most of unmanned free balloon are weather balloons whose usage is dedicated to meteorology prediction of scientific purpose (analysis of the atmosphere, etc.). Another usage example of unmanned free balloons is the Loon project, which consists in using an unmanned free balloons network to provide telecommunication facilities and Internet access to some regions of the world [58].
- Model aircraft are “small size unmanned aircraft, generally representing a scaled down version of full-size aircraft and used for recreational purposes in the sport and pastime of aeromodelling”.
- Remotely Piloted Aircraft Systems (RPAS) is “a set of configurable elements consisting of a remotely piloted aircraft, its associated remote pilot station(s), the required command and control link and any other elements as may be required, at any point during flight operation”.

This PhD will focus on RPAS category, which is detailed in section 3-1.2.

3-1.2 RPAS concept

RPAS is defined in section 3-1.1. Because of the potential high economic and societal benefit brought by RPAS, demand for RPAS operations is growing and civil aviation authorities must adapt their rules to include RPAS operations. This section introduces RPAS concept, analyzing RPAS operation categories defined in the legislation. It is divided in three sub-sections. First, the different elements composing RPAS are detailed. Second, RPAS regulation proposed to member states by ICAO is analyzed, highlighting different types of operations performed by RPAS. Third, the translation of ICAO proposed regulation to the French legislation is described.

3-1.2.1 RPAS

From RPAS definition of section 3-1.1, ICAO Concept of Operations (CONOPS) [59] details the different elements composing an RPAS. RPAS is composed by:

- A remotely piloted aircraft (RPA), which is an aircraft where the flying pilot is not on-board. Note that the notion of RPA excludes autonomous aircraft, as autonomous aircraft does not tolerate action of a human pilot during its flight.
- Remote pilot station(s) which are the stations at which the remote pilot manage the flight of the RPA. These remote pilot stations are usually on the ground.
- Command and control link, which is the link between the remote pilot station and the RPA whose purpose is the management of the flight. Note that data exchange between the RPA and the remote pilot stations concerning the payload (for example, transmission of photos or videos which do not concern pilot operations such as take-off and landing) is not included within command and control link.
- Other components related to the RPAS flight and dependent on the RPAS type. In particular, operational safety systems on-board RPAS depends on the operation performed by the RPAS. For example, weather radar is needed for RPAS flying under Instrument Flight Rules (IFR), whereas it may not be required for VFR (Visual Flight Rules) missions.

RPAS elements are thus strongly linked to the type of operations performed by the RPAS. For example, RPAS used for search and rescue would be equipped with advanced equipment (such as weather radar) whereas recreative RPAS would probably have limited equipment. The different categories of operations are detailed in sub-sections 3-1.2.2 and 3-1.2.3.

3-1.2.2 ICAO RPAS regulation

ICAO proposes a three levels RPAS regulation to its member states, depending on the size and operation type of the RPAS. Note that this regulation proposition is not prescriptive, mandatory, or construed and it is the role of Civil Aviation Authorities of each state to elaborate their own regulation. This ICAO regulation is defined in ICAO Model UAS Regulations [60] and [61]. Main points of the three level regulations are described below.

- Part 101: Part 101 applies to all RPAS whose weight is under 25 kg and whose operation conditions respect standard unmanned aircraft operating conditions defined in [60] (definition 101.7) and recapped hereinafter.
 - o The RPAS is operated within the visual line-of-sight (VLOS) of the person operating the UA,
 - o The RPAS is operated at or below 120 m above ground level (AGL) by day,
 - o The RPAS is not operated within 30 m, measured horizontally of a person who is not directly associated to the operation of the UA.

In addition, small RPAS are forbidden to:

- o Operate in a prohibited, restricted or over a populated area,
- o Operate within 4 km of the movement area of a controlled aerodrome. In addition, small UA are not allowed to operate within 4 km of the movement area of an uncontrolled aerodrome, unless the operation is undertaken in accordance with an agreement with the aerodrome operator.

In any case, a NOTAM (Notice to Airmen) must be issued to operate Part 101 RPAS. Even though no RPAS pilot license is required to operate under Part 101, the RPAS shall be registered and an inspection compliant to definition 101.21 or 102.301 of [60] must be conducted for remote pilot aircraft (RPA) above 15 kg.

- Part 102: Part 102 addresses RPAs operations whose RPA weight exceeds 25 kg and RPAS operation not fitting to Part 101 requirements and whose RPA weight is below 25 kg. Part 102 RPAS operator must pass unmanned remote aircraft pilot certification.

- **Part 149:** Part 149 describes privileges of an Approved Aviation Organization. In particular, the holder of an approved aviation organization certificate, which is issued by the civil aviation authorities, can authorize some RPAS operations according to the privilege of its certification. The objective of Part 149 RPAS operations is to designate approved aviation organizations which will serve as a substitute of civil aviation authorities to provide authorization on particular RPAS operations. The application for a RPAS operation is indeed expected to be faster processed by dedicated organizations.

ICAO RPAS regulation are high level regulations, and it is asked to civil aviation authorities to adapt this regulation to their legislation.

3-1.2.3 French RPAS regulation

This section describes the French legislation for RPAS. The French legislation for RPAS is the transposition of European regulations 2019/945 and 2019/947 of the European commission [62] [63]. European regulations 2019/945 and 2019/947 identified three RPAS operation categories, and the associated rules and procedures depend on the nature and risks of the RPAS operation. The three RPAS operations categories identified by European regulation 2019/945 and their associated rules are first recapped. The three identified RPAS operation categories are then detailed.

3-1.2.3.1 RPAS categories

French regulation divides RPAS in seven categories. Categories C0 to C4 depends on the RPAS maximum take-off weight and the presence of an identification system which transmits information on the RPAS by Wi-Fi while it is flying. RPAS categories C0 to C4 are summarized in Table 3-1.

Class	C0	C1	C2	C3	C4
MTOW	250 g	900 g	4 kg	25 kg	25 kg
Identification system	No	Yes	Yes	Yes	No

Table 3-1: Definition of RPAS classes C0 to C4

Main requirements of RPAS classes C5 and C6 are given hereinafter:

- **Class C5:** The RPAS must be equipped with a geo-awareness function. The geo-awareness function provides alert to the remote pilot when a potential violation of the airspace is detected, or when the navigation and positioning system cannot provide the geo-awareness service. The RPAS must also provide to the remote pilot during the flight information on the altitude and on the quality of the command and control link. A slow flight mode must also be included, allowing the RPA to fly slower than 5 m/s. Eventually, the remote pilot shall be able to terminate the flight at any instant, with a system independent from the guidance system, forcing the descent without horizontal displacement.
- **Class C6:** Similarly to class C5 RPAS, C6 RPAS must be equipped with a geo-awareness function, must provide information on altitude and command and control link and must be able to interrupt the flight at any instant. In addition, class C6 RPAS speed is limited to 50 m/s and the RPAS must return to remote pilot the precise position of the RPA. The trajectory shall be programmable, and some means must be provided to prevent the RPA from breaching horizontal and vertical limits of a programmable operational volume.

3-1.2.3.2 Open category

General characteristics

The RPAS open category operations are detailed in [64]. It concerns low risk RPAS operations. The RPAS MTOW shall not exceed 25 kg, consistently to ICAO part 101 operations. In addition, the RPAS shall remain below 120 m AGL, and operations are limited to VLOS by day. The maximum height fly is lowered to 100 m between 1 km and 7 km around aerodrome, and to 50 m when the distance between an aerodrome and the RPAS is below 1 km.

Open operation sub-categories

Three Open operation sub-categories A1, A2, A3 are then identified depending on the risk of undesirable event. These sub-categories are defined as a function of the distance between the RPA and people, and the number of people overflown by the RPA. Open operation sub-categories are defined in Table 3-2. For each sub-category, classes of RPAS allowed to perform operations of this sub-category is also specified.

Sub-category	A1	A2	A3
Definition	No fly over people group Close to people	30 m from people	150 m from residential, commercial, industrial and recreative areas
RPAS classes	C0 (tolerated overfly of isolated people) C1	C2 (this distance can be lowered to 5 m if C2 RPAS are able to fly slower than 5 m/s)	C2 C3 C4

Table 3-2: Definition of Open operation sub-categories

As an RPA loss of control may have catastrophic consequences for people on the ground (injuries, etc.), fly over people is only tolerated for light RPAS of class C0, and forbidden for other Open category classes. Moreover, since the risk of catastrophic consequences increase with the weight of the RPAS, French legislation makes the minimum distance to people on the ground increase with the RPA maximum MTOW.

Note that RPAS built by amateur builders do not have any class. These private RPAS are allowed to perform A1 operation if their MTOW is below 250 g, and A3 operations if their MTOW is between 250 g and 25 kg. An electronic identification is necessary for private RPAS above 800 g.

Pilot requirements

Even regulated, the Open category is tolerative. In particular, there is no requirement on the certification of the remote pilot. Because of the limitation of the maximum height AGL to 120 m, RPA conducted open operations are separated from civil and general aviation. Indeed, civil and general aviation are not allowed to fly below 150 m (500 ft) above ground level, except for take-off and landing purpose and simulated engine failure exercises. These exceptions are the reason why the maximum RPA height fly is reduced in the vicinity of aerodromes.

3-1.2.3.3 Specific category

General characteristics

Specific category is described in [65]. Specific category gathers moderately risky operations. Most of specific category operations concerns professional activities. Specific categories operations can either take place after declaration of operation under a European standard scenario (the definition is given below) by the RPAS operator to the civil aviation authority (in France, the concerned civil aviation

authority is the Direction de la Surveillance de l'Aviation Civile, DSAC); or with a special operation authorization delivered by DSAC. This special authorization is based upon risk analysis of the targeted operation.

Specific category operation shall be conducted with RPAS of class C5 or C6.

Specific category standard scenarios

Standard scenarios describe operations which do not necessitate specific authorization from DSAC. Standard scenarios are described below:

- STS-01: STS-01 scenario refers to VLOS operations with a class C5 RPAS. The maximum height of the RPA is 120 m and the RPA can fly in an environment with people on the ground. The RPA shall only fly above controlled area, meaning that the operator must be able to control the access to this zone.
- STS-02: STS-02 scenario refers to operations that may be beyond visual line of sight (BVLOS), operated with class C6 RPAS. The distance between the remote pilot and the RPA must be below 1 km. This distance can be increased to 2 km in presence of airspace observers. RPAS operations take place at a maximum height of 120 m over controlled area, in which density of people is low.

Specific category standard scenarios are summarized in Table 3-3.

	STS-01	STS-02
Definition	<ul style="list-style-type: none"> • 120 m maximum height • Airspace area under controlled access • VLOS • Above surface with people 	<ul style="list-style-type: none"> • 120m maximum height • Airspace area under controlled access. • BVLOS (max 1 km distance, or 2 km in presence of airspace observers). • Above surface with low density of people
RPAS class	C5	C6

Table 3-3: Specific category standard scenarios

These scenarios allow professional activities, such as taking photos during events. These scenarios are defined in the European legislation and will become effective in January 2024.

Pilot requirements

As STS-01 and STS-02 allows flight above people, a loss of control of the RPA may have catastrophic consequences such as people injuries. This is the reason why class C5 and class C6 RPAS, allowed to perform Specific category operations, have stronger operational constraints compared to RPAS classes C0 to C4. In addition, remote pilot performing Specific category operations must have obtained a theoretical certificate delivered by the DGAC (Direction Générale de l'Aviation Civile), and must have followed a practical formation to RPAS flying.

3-1.2.3.4 Certified category

General characteristics

RPAS operations are part of the certified category when:

- At least one of the three conditions below is verified:

- RPAS is flying over people groups.
- RPAS is transporting people.
- RPAS is transporting dangerous products that may, in case of accident, present high risks for impacted people.
- The RPAS operation risk cannot be sufficiently attenuated.

Under certified operations category, RPAS may enter the controlled airspace. Therefore, requirements in term of flight safety are expected to be very similar to the ones applied for civil aviation. All these requirements have not yet been issued.

Pilot requirements

Pilots who want to operate in the certified category must pass professional RPAS pilot formation which is under development by the European Union.

Figure 3-3 illustrates the operations for each RPAS categories.

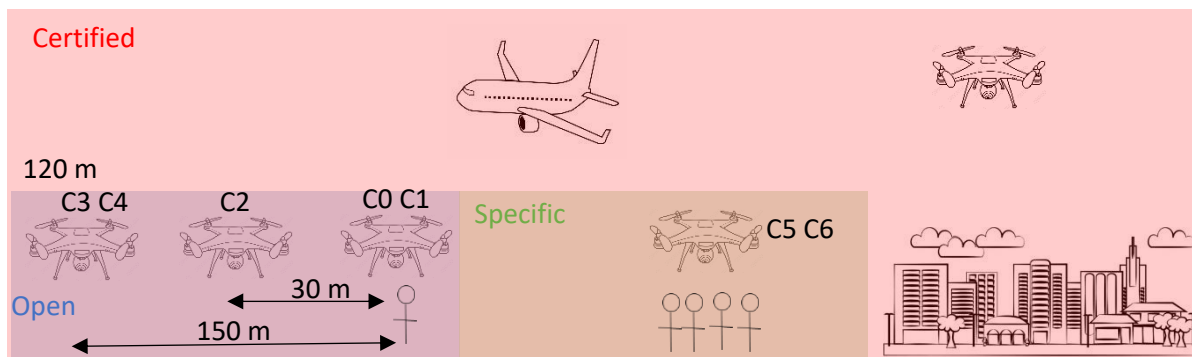


Figure 3-3: Illustration of RPAS operations for the different RPAS categories of the European legislation

3-1.3 Concept of C2Link

This section describes the concept of C2Link. C2Link refers to command and control link between the remote pilot on the ground and the RPA. Some organizations such as ITU and RTCA (Radio Technical Commission for Aeronautics) calls this link Control Non-Payload Communication (CNPC) instead of C2Link. C2Link is a key component of RPAS as it ensures the safe monitoring of the RPAS. From now on, this chapter focuses on RPAS allowed to perform certified operations which are conducted in the non-segregated aero-space and where the RPAS is subjected to civil aviation safety rules. This section is divided in two sub-sections. First, the content of the information exchanged between the remote pilot and the RPA through the C2link is described. Second, different architectures allowing to perform RLOS and BRLOS communications are described.

3-1.3.1 C2Link information

Information content transmitted through C2Link is described in ITU-R M.2171 [56]. C2Link communication can be divided in two parts. First, the uplink refers to the communication issued from the remote pilot toward the RPA. Information contained into the uplink includes:

- Telecommand: The telecommand allows the remote pilot to safely control the RPA in normal and non-normal operating conditions. The remote pilot gives instructions about the safe managing of flight: altitude, heading, next waypoint to reach, engine commands. Other functionalities concerning the aircraft are also included, such as lights switch on and switch off, command of the landing gear and brake for example.

- Remote pilot to Air Traffic Control (ATC) communications: As civil aviation safety rules must be respected by RPAS, and in particular the separation requirements which are at the expense of ATC, the remote pilot must be in contact with the ATC. Therefore, remote pilot transmits through C2Link its communications with ATC to the RPA, which relays this communication re-broadcasting it in the aeronautical VHF (Very high frequency) channel.
- Navigation aids: Remote pilot commands to set navigation aids such as VOR radial settings are transmitted through C2Link.

Second, the downlink refers to communications issued from the RPA toward the remote pilot. C2Link information exchanged through the downlink is:

- Telemetry: Telemetry provides information about the flight and the aircraft state: speed, pitch, roll, lights (switched on or off), weather conditions, landing gear, remaining fuel, position for example.
- ATC to remote pilot communications: The RPA receives vocal communications from ATC through aeronautical VHF channel and relays these communications to the remote pilot using C2Link.
- Detect and Avoid system (DAA): Depending on the operation performed by the RPA, some information about the RPA environment can be transmitted through C2Link. First, in order to avoid collision with other aircrafts, and to fulfill safety requirements of civil aviation, a detection and avoidance system must be present onboard of RPA. This system substitutes the eyes of the pilot. DAA functionality detects landform and surrounding aircrafts and send an avoidance instruction to the RPA. ADS-B, TCAS, radar and lidar could be candidates as DAA system. Second, RPAS that are likely to fly in IFR conditions must hold a weather radar allowing to detect areas where flying is dangerous. Weather information are transmitted to remote pilot through C2Link. Third, some RPAS must be equipped with camera. This camera, when used for RPAS control purpose, may transmit information with the remote pilot through C2Link during critical flight phases such as take-off, landing or in case of emergency.
- Navigation aids information: Information returned by navigation aids are transmitted from the RPA to the remote pilot.

3-1.3.2 C2Link architecture

Two architectures are currently under consolidation at an ICAO level for RPAS operation: the terrestrial and the satellite architecture. Both architectures are expected to coexist in the future. The choice to use whether one or the other should depend on the RPA environment. These two architectures are described below.

Terrestrial architecture

The terrestrial architecture is described in [8]. This architecture is suited for RPAS RLOS operations, as the communication link between the RPA and the remote pilot station is direct. Figure 3-4 illustrates the C2Link architecture.

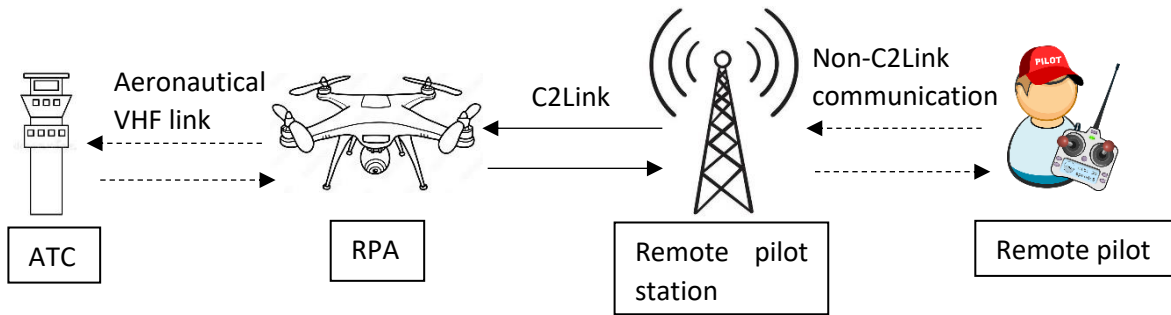


Figure 3-4: Terrestrial C2Link architecture

Only the communications between the remote pilot station and the RPA are part of the C2Link. Note that usually, the remote pilot uses a telecommand to pilot the RPA, in this case, remote pilot and remote pilot station are mingled. The main drawback of terrestrial architecture is that it cannot support operations for which the RPA is BRLOS from the remote pilot station. Future improvements may include the development of RPS networks in order to maximize the time the RPA is in RLOS over a given territory.

Satellite architecture

The C2Link satellite architecture is an alternative to the terrestrial architecture. A satellite serves as a relay for C2Link communications between the remote pilot station and the RPA. Figure 3-5 illustrates the C2Link satellite architecture.

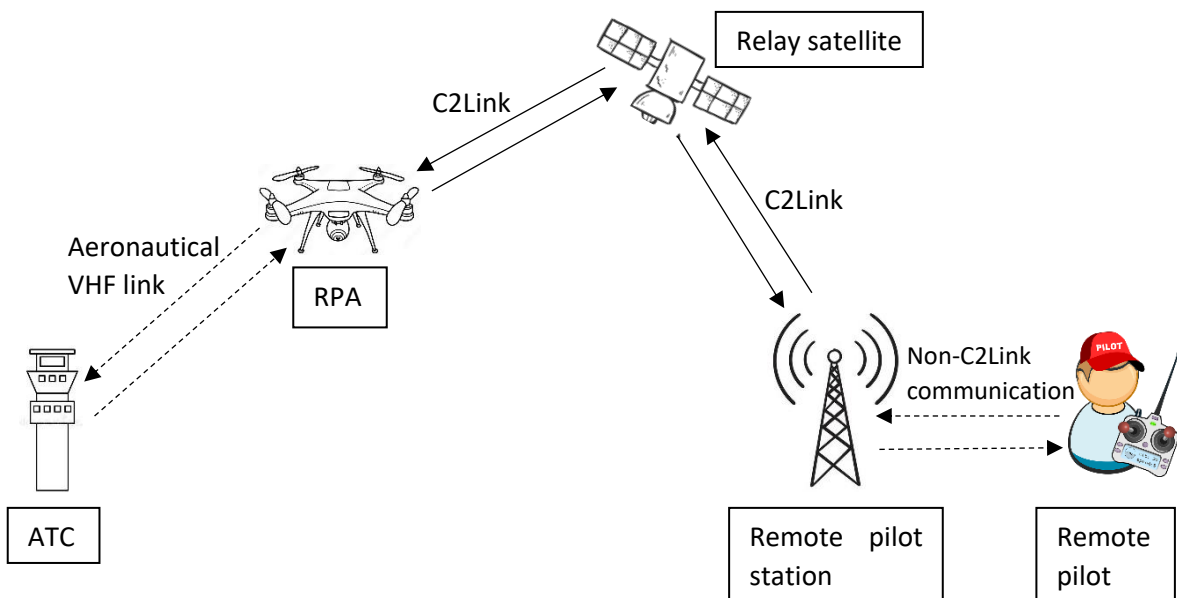


Figure 3-5: C2Link satellite architecture

In the C2Link satellite architecture, C2Link includes the uplink and downlink between the satellite and remote pilot station, as well as the uplink and downlink between RPA and satellite. As for the terrestrial architecture, the link between the remote pilot and the remote pilot station as well as communications between RPA and ATC are not part of the C2Link.

The advantage of the satellite architecture compared to the terrestrial architecture is that the radius of operation is increased, since the RPA is no longer limited to RLOS operations. Indeed, the remote pilot and the RPA can be maintained as long as the relay satellite is visible from both the remote pilot

station and the RPA. The main drawback is the cost of this architecture and the latency (mainly the ATC latency). Moreover, terrestrial C2Link system should probably present a higher user capacity or a higher usage of the resources (time/spectrum) than the satellite C2Link system.

3-2 C2Link signal and civil aviation requirements

Several C2Link technologies have been considered to support RPAS command and control, including Wi-Fi. Wi-Fi has indeed the advantage of being quite simple and do not require expensive development since network infrastructures (relay antenna for cellular telecommunications for example) already exist. Therefore, this C2Link technology seems relevant for open operations category. However, the risk of loss of continuity is high with Wi-Fi. As a consequence, and since the risk of catastrophic consequence is higher for Specific and Certified operation categories in case of a loss of the command and control link, Wi-Fi cannot be used for RPAS performing certified or specific operations since it will not miss the Required Link Performance (RLP) associated to this type of operations.

Potential candidates to support RPAS certified and specific operations C2Link are:

- 5 GHz C2Link as described in MOPS DO-362 [8] .
- C2Link in L band, as initially considered in MOPS DO-362 [8].
- Cellular networks, especially 4G and 5G, which has been identified in Eurocae working group (WG) 105 terms of references [66] as a potential candidate to support C2Link for certified and specific operations. This solution is not under consideration at an ICAO level currently.
- Fixed satellite system (FSS)
- Mobile satellite system (MSS): MSS service providers such as Iridium and Inmarsat could be interested in providing C2Link services.

Standardization documents approved up to the PhD publication date are only the 5 GHz C2Link standard documents for terrestrial architecture. Therefore, the C2Link signal considered in this PhD thesis is the one described in DO-362 in the 5 GHz frequency band.

The objective of this section is to describe minimum C2Link civil aviation requirements, and the C2Link signal as defined in DO-362. This section is divided in four parts. First, C2Link performance requirements indicators are presented. Second, the frequency band 5030-5091 MHz, which is a candidate to support C2Link, is investigated. Third, the classification of C2Link signals into different data classes depending on the amount of information which must be transmitted is presented. This classification is proposed in DO-362. Fourth, DO-362 C2Link signal definitions are detailed.

3-2.1 C2Link civil aviation Required Link Performance

Joint Authorities for Rulemaking of Unmanned Systems (JARUS) defines RPAS Required C2 Link Performance (RLP) in [67]. These RLP should be used for the certification process of RPAS performing specific and certified operations. Four RLP indicators have been identified.

- Availability: The availability is the probability that an operational communication transaction can be initiated when needed.
- Continuity: Continuity is the minimum proportion of operational communication transactions to be completed within the specified transaction time, given that the service was available at the start of the transaction.
- Transaction Time: Transaction time is the maximum time for completion of a proportion of operational communication transactions after which the initiator should revert to an alternative procedure. Two values are specified:

- The maximum nominal time within which 95% of operational communication transactions is required to be completed.
- The transaction expiration time is the maximum time for completion of the operational communication transaction after which the initiator is required to revert to an alternative procedure.
- Integrity: Integrity is the probability that an operational communication transaction is completed with no undetected error.

These RLP objectives are defined in DO-377 section 3 for the different flight phases. Nevertheless, these RLP were mainly customized for the terrestrial system. Moreover, ICAO SARPS states that these RLP are defined by the State responsible for the safety of the airspace in which the RPA is operating and are related to those airspace safety requirements.

3-2.2 5GHz C2Link frequency band

The frequency band 5030-5091 MHz is an aeronautical band and was allocated to AMRS and AM(S)RS services during WRC 2012, where the frequency band was specially reserved for C2Link systems. Additionally, this frequency band was already allocated to another aeronautical system, Microwave Landing Systems (MLS). Therefore, this band is shared by three aeronautical services:

- The Aeronautical Radio Navigation Service (ARNS): One system that is part of the ARNS uses the frequency band 5030-5091 MHz nowadays, the Microwave Landing Systems (MLS), which was designed as the evolution of the ILS (Instrument Landing System). This system is implemented around some airports. Its goal is to help aircrafts to land in bad weather conditions. The MLS monitors the alignment of the aircraft that intends to land and the axis of the runway; as well as the glidepath. But the number of installed MLS decreases, since many airports prefer installing a GBAS station instead of a MLS.
- The Aeronautical Mobile (Route) Service (AM(R)S): The AM(R)S is defined, according to the article 1.33 of the ITU Radio Regulation (RR) [68] as *“An aeronautical mobile service reserved for communications relating to safety and regularity of flight, primarily along national or international civil air routes”*. An aeronautical mobile service is defined by the article 1.32 as *“A mobile service between aeronautical stations and aircraft stations, or between aircraft stations, in which survival craft stations may participate; emergency position-indicating radio-beacon stations may also participate in this service on designated distress and emergency frequencies”*.
- The Aeronautical Mobile Satellite (Route) Service (AMS(R)S): The AMS(R)S is defined, according to the article 1.36 of the International Telecommunication Union (ITU) Radio Regulation (RR) [68] as *“An aeronautical mobile-satellite service reserved for communications relating to safety and regularity of flights, primarily along national or international civil air routes”*. The definition of the aeronautical mobile-satellite service is given by the article 1.35: *“A mobile-satellite service in which mobile earth stations are located on board aircraft; survival craft stations and emergency position-indicating radio-beacon stations may also participate in this service”*.

This frequency band is particularly well suited to support C2Link for two reasons. First, only MLS transmits in this frequency band. Because of the low number of installed MLS, RFI between C2Link and other systems is limited. Second, terrestrial C2Link is part of AM(R)S, with the remote pilot station (RPS) acting as the aeronautical station and the RPA acting as the aircraft station. Similarly, satellite C2Link is part of AMS(R)S and a satellite system is expected to be standardized in the 5030-5091 MHz frequency band by EUROCAE. Indeed, a joint working group between RTCA and EUROCAE has been created in order to make the system compatible by design. Final compatibility studies between the

two systems should be presented at the ICAO RPAS Panel WG2 and potentially included in the SARPs (or a manual of the SARPs).

3-2.3 C2Link requirements

This section describes C2Link requirements extracted from DO-362 [8]. First, it presents the of RPAS classification proposed in DO-362 depending on the amount of information that must be transmitted by C2Link. Some C2Link signals characteristics, which will be detailed in 3-2.4, indeed depends on this classification. Second, it provides the minimum targeted subframe error rate, which is chosen as the main indicator to characterize C2Link signal quality and the capacity of the receiver to meet required link performances described in section 3-2.1.

3-2.3.1 Data class definition

DO-362 identifies four service classes depending on the volume of information transiting through C2Link. These service classes, which would be applicable to RPAS specific and certified operation categories, are defined in Table 3-4.

	Service class 1	Service class 2	Service class 3	Service class 4
Uplink	<ul style="list-style-type: none"> Telemetry 	<ul style="list-style-type: none"> Telemetry Pilot/ATC communication 	<ul style="list-style-type: none"> Telemetry Pilot/ATC communication Navaid settings 	<ul style="list-style-type: none"> Telemetry Pilot/ATC communication Navaid settings
Downlink	<ul style="list-style-type: none"> Telecommand 	<ul style="list-style-type: none"> Telecommand ATC/Pilot communication 	<ul style="list-style-type: none"> Telecommand Pilot/ATC communication Navaid information Detect and Avoid 	<ul style="list-style-type: none"> Telecommand Pilot/ATC communication Navaid information Detect and Avoid Weather radar

Table 3-4: Information transiting through C2Link for the different service classes

Two C2Link modes are considered in DO-362. Manual (M) mode means that the pilot is directly controlling the RPAS flight commands and other operational functions. Automatic (A) mode means that the commands sent by the remote pilot passes through a processor installed on-board the RPAS, and it is the processor which activates flight commands and other operational functions. It appears that manual mode is more demanding in terms of data rate than automatic mode. From the quantity of information to be transmitted for the different service classes and the C2Link mode, DO-362 Appendix J defines four data classes that will have different signal requirements from each other. The different service class uplink and downlink signals are associated to their respective data class in Table 3-5.

Data class	Signals
Data class 1	Service class 1 uplink (A) Service class 1 downlink (A)
Data class 2	Service class 1 uplink (M) Service class 1 downlink (M) Service class 2 uplink (A) Service class 2 downlink (A) Service class 3 uplink (A) Service class 4 uplink (A)
Data class 3	Service class 2 uplink (M) Service class 2 downlink (M)

	Service class 3 uplink (M) Service class 4 uplink (M)
Data class 4	Service class 3 downlink (A & M) Service class 4 downlink (A & M)

Table 3-5: Data class definition

3-2.3.2 Subframe error rate threshold

Subframe error rate is the indicator identified by DO-362 to analyze the capacity of C2Link receiver to meet RLP. Subframe error rate is the probability of incorrectly demodulating a subframe. The number of bits to be transmitted within one subframe depends on the data class. Indeed, since high rank data classes have more functionalities and therefore more information to be transmitted within one frame than lower rank data class, the subframe contains a longer bit sequence. The number of bits within a subframe for the different data classes is given in Table 3-6.

	Data class 1	Data class 2	Data class 3	Data class 4
Number of bits within one subframe	790.5	1584	2376.5	3174

Table 3-6: Number of bits within one subframe for the different data classes

The number of bits within one subframe given in Table 3-6 include bits allocated to acquisition, preamble, and control parity bits in addition to the information data sequence.

Next, coding is also added on the transmitted data sequence to lower the number of errors. The selected coder is a rate 1/3 turbo encoder with a puncturing matrix depending on the targeted data class. The description of this encoder is fully described in DO-362 section 2.2.2.3.7.1. However, channel coding has not been analyzed during this PhD. For conciseness purpose, it is thus not fully described here.

DO-362 proposes to translate C2Link civil aviation performance requirements into a subframe error rate objective. DO-362 sets the subframe error rate probability to 10^{-3} to meet C2Link civil aviation performance requirements and to achieve “safe and efficient” RPAS operations. In other world, C2Link receivers are assumed to respect minimum requirements and to meet RLP as long as subframe error rate is below 10^{-3} . Considering a rate 1/3 turbo encoder, such a subframe error rate is achieved for a wide variety of binary and quaternary modulations for $E_b/N_0 = 3.5 \text{ dB}$, where E_b is the energy within one bit duration and N_0 is the thermal noise power spectral density according to DO-362 Appendix L. Considering a TCC error code correction type with rate 5/8, the minimum E_b/N_0 ratio to reach a subframe error rate of 10^{-3} is reduced to 2.5 dB according to DO-362A Appendix R.

3-2.4 C2Link signal definition

This section describes some C2Link signal definitions of interest which are described in DO-362. These elements include:

- Channel division method and channel coding.
- Data rate.
- Modulation.
- Signal power.
- Spectral occupancy.

3-2.4.1 Channel division method and channel coding

As presented previously, a channel dedicated to a given C2Link communication between the remote pilot and the RPA must be shared between the uplink and the downlink. This sharing of the channel is

done adopting a time division duplex (TDD) structure. Therefore, uplink and downlink are transmitted on different time slots sharing the same carrier frequency. DO-362 proposes a 50 ms frame shared between uplink, downlink and guard bands as presented in Figure 3-6.

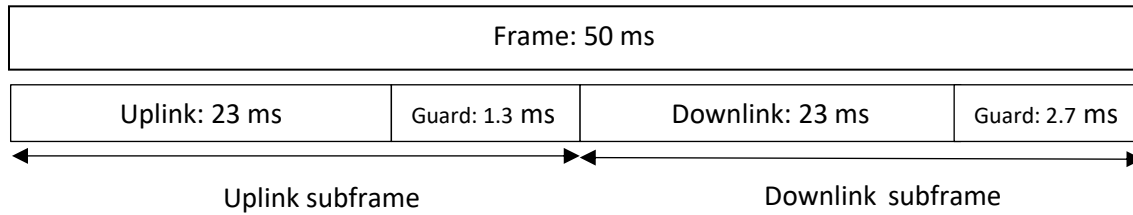


Figure 3-6: TDD channel division method (DO-362)

The 50 ms of a frame are equally shared between the uplink (23 ms) and the downlink (23 ms). Between the uplink and the downlink, a guard time interval is inserted. This guard time interval accounts for time propagation delay and timing error.

Note that this access method only applies for the terrestrial C2Link architecture. Indeed, larger propagation delays must be covered by the guard band for a satellite system using a TDD scheme. Therefore, the frame duration requirement is expected to be modified in future revision of MOPS DO-362 (MOPS-DO362B) to allow compatibility with satellite architectures targeting global coverage.

3-2.4.2 Data rate

The duration of a C2Link subframe (either the uplink or downlink part of the frame illustrated in Figure 3-6) is fixed to 23 ms as described in section 3-2.4.1. From the knowledge of the C2Link frame duration and the number of bits contained within one frame for the different date classes reported in Table 3-6, the data rate can be computed. The data rate for the different data classes are reported in Table 3-7.

	Data class 1	Data class 2	Data class 3	Data class 4
Data rate (ksymb/s)	34.5	69	103.5	138

Table 3-7: Data rate of the different data classes

3-2.4.3 Modulation

In DO-362A, for both the uplink and downlink, the C2Link signal is requested to use either a Gaussian Minimum Shift Keying (GMSK) or a quadrature phase shift keying waveform. This thesis focuses on the GMSK option. GMSK waveform is a binary modulation equivalent to a MSK (Minimum Shift Keying) waveform filtered by a gaussian filter. The product between the gaussian filter 3dB bandwidth and transmitted symbol period is called BT product. BT product is an important parameter defining GMSK modulated signal. A low BT product results in a GMSK signal with a good spectral footprint but induces high inter symbol interferences. As the frequency band is limited and because a lot of allocations are expected to be requested, DO-362 sets the BT product to 0.2.

3-2.4.4 Power

DO-362 identifies two power modes depending on the position of the aircraft. The high-power mode allows to have higher communication ranges but induces higher intra system RFI to other C2Link surrounding systems. On the contrary, the low power mode constraints the communication range but is adapted for airspaces with a high RPAS traffic. The maximum mean powers over 1 s for low-power and high-power modes are respectively 100 mW and 10 W per link. The low-power mode is used when:

- The RPA is less than 10 NM (nautical mile) from any take-off or landing, and under 500 ft AGL.
- The RPA is more than 10 NM from any take-off or landing and below 3000 ft AGL.

The high-power mode is used when:

- The RPA is less than 10 NM (nautical mile) from any take-off or landing, and above 500 ft AGL.
- The RPA is more than 10 NM from any take-off or landing and above 3000 ft AGL.

The maximum transmitted powers for the two modes are summarized in Table 3-8.

	Low power mode	High power mode
Maximum transmitted power	100 mW	10 W

Table 3-8: Maximum transmitted power for low power and high power modes

3-2.4.5 Spectral occupation

In addition to the maximum power, the spectral occupancy is also constrained in DO-362 in order to limit inter channel interference and to optimize the occupancy of the frequency band. Table 3-9 provides the channel bandwidth for the different data classes.

	Data class 1	Data class 2	Data class 3	Data class 4
Channel bandwidth (kHz)	30	60	90	120

Table 3-9: Channel bandwidths for the different data classes

As it can be seen on Table 3-9, the channel bandwidth increases with the data rate.

The spectral occupancy is also constrained at the transmitter level by power spectral density mask. C2Link power spectral density mask provides the maximum power spectral density of a transmitted C2Link signal. Its objective is to limit the level of interference that one C2Link signal can cause to another RPAS communication chain. C2Link power spectral density mask is provided by DO-362A and illustrated in Figure 3-7.

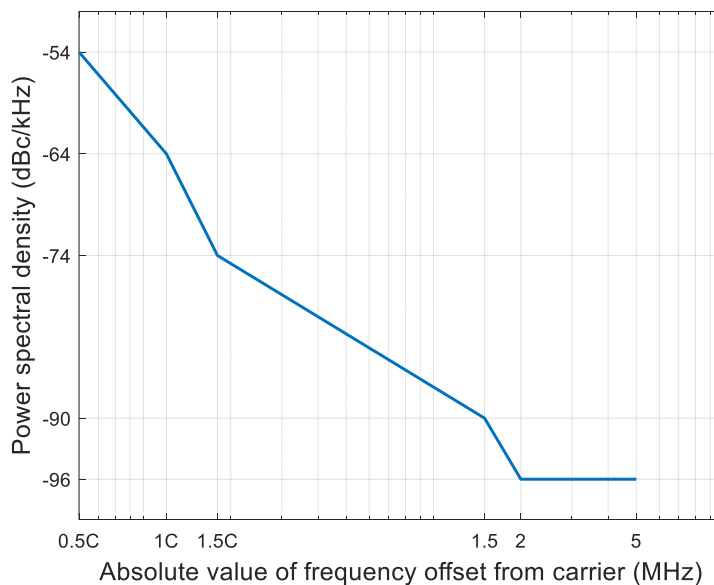


Figure 3-7: C2Link power spectral density mask

In Figure 3-7, the C2Link transmission mask breakpoints depend on the channel bandwidth C (expressed in MHz). The floor of the C2Link transmission mask is set to -96 dBc/kHz and it is reached at 2 MHz from the carrier frequency.

3-3 Mathematical model of DO-362 C2Link signal

This section provides a mathematical model of DO-362 C2Link signal. This model is established from DO-362 C2Link signal definitions presented in section 3-2.3.

GMSK modulation is a particular form of binary continuous phase frequency shift keying (CPFSK). Mathematical binary CPFSK signal model is described in [69]. First, information bits allow to define a pulse amplitude modulation (PAM) as in (Eq 3-1).

$$g(t) = \sum_{n=-\infty}^{+\infty} a_n q(t - nT_s) \quad (\text{Eq 3-1})$$

$(a_n)_{n \in \mathbb{N}}$ is the mapping of binary digits from the information sequence into amplitude levels ± 1 . q is the modulating waveform. For GMSK modulation, the modulating waveform is given by (Eq 3-2).

$$q(t) = \frac{1}{2T_s} \text{rect}_{T_s} * h(t) \quad (\text{Eq 3-2})$$

T_s is the symbol period and is equal to the inverse of the modulation symbol rate provided in Table 3-7. h is a gaussian low pass filter impulse response whose 3 dB bandwidth B is deduced from the BT product (BT is equal to 0.2 for C2Link) and the symbol period T_s . $*$ denotes for the convolution. The impulse response of the gaussian filter h is given in (Eq 3-3).

$$h(t) = \sqrt{\frac{2\pi}{\ln(2)}} B e^{-\frac{2\pi^2 B^2}{\ln(2)} t^2} \quad (\text{Eq 3-3})$$

Figure 3-8 represents the modulating waveform $q(t)$.

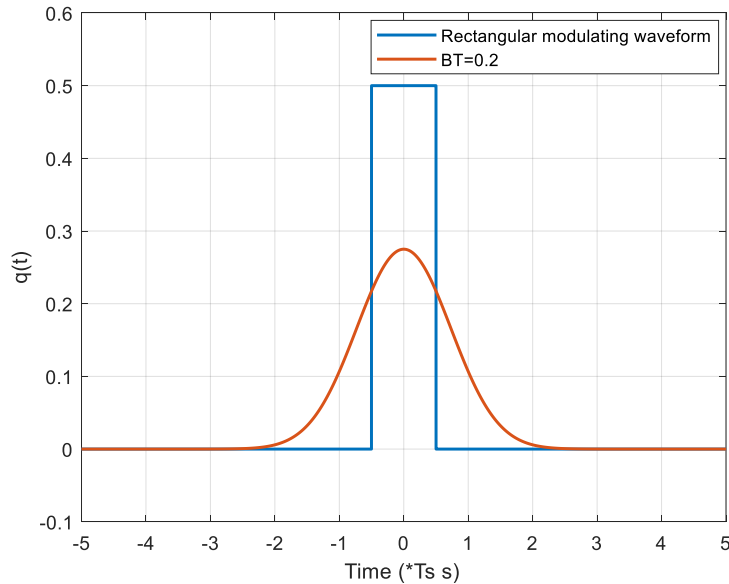


Figure 3-8: GMSK modulating waveform

Figure 3-8 shows $q(t)$ (in orange) and compares it to the MSK rectangular modulating waveform (in blue). The gaussian filter spreads the transmitted bit over a given time interval inducing inter-symbol interference; nevertheless, an adapted demodulator can be implemented to mitigate its effect.

The instantaneous phase $p_o(t)$ is obtained integrating $g(t)$ over $] -\infty; t]$. $p_o(t)$ is given by (Eq 3-4).

$$p_o(t) = 2\pi m_f \int_{-\infty}^t g(u) du = 2\pi m_f \sum_{n=-\infty}^{+\infty} a_n \int_{-\infty}^t q(u - nT_s) du \quad (\text{Eq 3-4})$$

$m_f = 1/2$ is the GMSK modulation index. Denoting $\varphi_o(t) = \int_{-\infty}^t q(u) du$, $p_o(t)$ can be reduced to (Eq 3-5).

$$p_o(t) = 2\pi m_f \sum_{n=-\infty}^{+\infty} a_n \varphi_o(t - nT_s) \quad (\text{Eq 3-5})$$

$\varphi_o(t)$ is represented in Figure 3-9 for a $BT=0.2$.

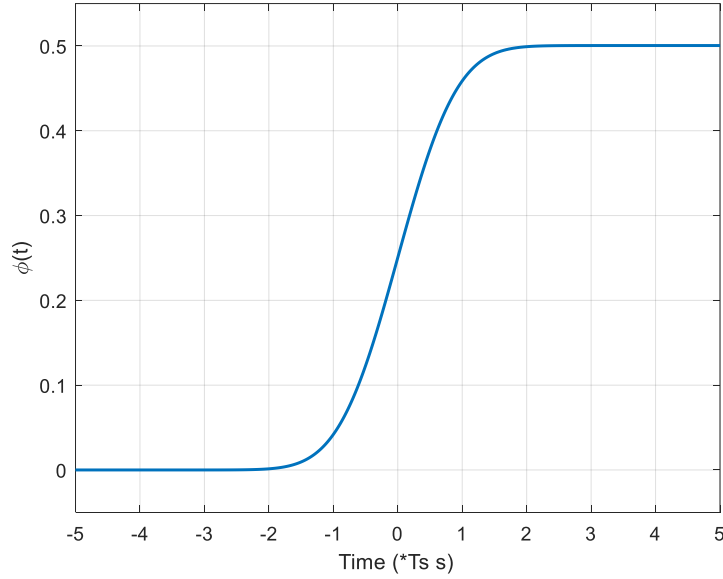


Figure 3-9: Illustration of $\varphi(t)$

As an important remark, $\varphi_o(t)$ tends toward 0 when t is lower than approximately $-2.5T_s$, and $\varphi_o(t)$ tends toward $1/2$ when t is higher than approximately $2.5T_s$. Let us introduce offset versions of φ_o and p_o defined in (Eq 3-6).

$$\begin{aligned} \varphi(t) &= \varphi_o(t - 2.5T_s) \\ p(t) &= p_o(t - 2.5T_s) = 2\pi m_f \sum_{n=-\infty}^{+\infty} a_n \varphi(t - nT_s) \end{aligned} \quad (\text{Eq 3-6})$$

It can be considered that $\varphi(t) = 0$ for $t \leq 0$ and $\varphi(t) = 1/2$ for $t \geq L_{BT}T_s$, with $L_{BT} = 5$. Therefore, the influence of bit a_n on the instantaneous phase starts at instant $t = nT_s$.

Considering this assumption, the instantaneous phase $p(t)$ can be approximated as in (Eq 3-7), supposing that $t \in [NT_s; (N + 1)T_s]$.

$$p(t) = \pi m_f \sum_{n=-\infty}^{N-5} a_n + 2\pi m_f \sum_{n=N-4}^N a_n \varphi(t - nT_s) \quad (\text{Eq 3-7})$$

The instantaneous phase $p(t)$ is therefore the sum of one accumulated term, and one time-varying term which depends on the last five transmitted bits, highlighting inter-symbol interferences of GMSK modulation.

Eventually, the transmitted GMSK signal is given by (Eq 3-8).

$$s_{GMSK}(t) = \sqrt{2P} \cos(2\pi f_0 t + p(t) + \varphi_0) \quad (\text{Eq 3-8})$$

P is the transmitted mean EIRP. P is limited by requirements on the maximum C2Link power presented in section 3-2.3. φ_0 is a random initial phase uniformly distributed on $[0; 2\pi]$.

3-4 Conclusion

The objective of this chapter is to provide an overview of the C2Link signal, which is the command and control link for RPAS operations. This chapter first starts by presenting the UAS and RPAS definitions. UAS refers to system for which the aircraft is flying without any pilot on-board. RPAS is a sub-category of UAS and refers to system where aircraft is remotely piloted. European and French legislation on RPAS operations is detailed and provides a categorization of RPAS operations in three categories: open, specific and certified.

Next, the concept of C2Link is introduced. Information contained within C2Link depends on the operation category performed by the RPAS, and include telecommand and telemetry, communications between the remote pilot and ATC, navigation aids settings and potentially video or weather radar information.

Two C2Link architecture candidates are detailed. Terrestrial architecture allows RLOS communications whereas satellite architecture, for which communications are relayed through a satellite, allows BRLOS communications. This PhD focuses on the terrestrial architecture for which standardization is already developed.

Second, C2Link required link performance (RLP) indicators are detailed and C2Link signal definitions for the terrestrial architecture are presented. Last evolutions of C2Link system standardization may be not taken into account because of the timing of the thesis. C2Link RLP indicators include availability, continuity, transaction time and integrity. Performance objectives are still under discussion. Performance objectives values would be determined by each ICAO state members based on ICAO recommendations that are expected to be published in the next years. In this thesis and in current standardization document, subframe error rate is the selected indicator to characterize C2Link receivers' capacity to meet RLP. A subframe error rate of 10^{-3} is chosen as a targeted minimum performance.

Then, the investigated terrestrial C2Link system is planned to use the ARNS allocated frequency band 5030-5091 MHz. This frequency band is indeed only used by MLS. Therefore, the risk of inter-system interference is limited.

Next, a waveform which is among the most relevant ones to support terrestrial C2Link is the GMSK. Even though one drawback of GMSK is inter-symbol interference, this modulation has the advantage to present an excellent spectrum efficiency, and therefore, a good optimization between the number of allocated C2Link channels and the limited frequency band. Other signal requirements, extracted from DO-362, are also detailed. In particular, one requirement of interest to propose a mathematical model of the C2Link signal is the data rate. Data rate depends on the data class, which characterizes the amount of data to be transmitted to perform the considered RPAS operation.

Third and last, a mathematical model is proposed for GMSK C2Link signal from requirements of interest. This mathematical C2Link signal model will be re-used in Chapter 6 when analyzing the robustness of C2Link signals to RFI.

Chapter 4: GNSS interference mask and protection area during jamming operations

One of the most important types of Radio Frequency Interference (RFI) affecting civil aviation is intentional (targeted victims) or unintentional jamming (collateral victims), especially state jammers which usage is continuously increasing in order to cope with new emerging safety threats. Indeed, state jamming is expected to become a significant topic of interest due to the main two following reasons. First, state jamming is used as the main defense tool to counter rogue UAs which is a rising safety-threatening event. Second, testing exercises for jammer development continues to grow. To avoid insufficient GNSS performance during state jamming, the ANSP (Air Navigation Service Provider) is in charge of determining the zone where GNSS receivers may not achieve ICAO minimum requirements. In these zones, referred as protection areas (or protection zones), pilots are notified of a potential loss of the GNSS link through NOTAM (Notice to Airmen). The reliability in the determination of this zone has a major significance. On the one hand, a too small protection zone will induce safety problems, since the GNSS receiver may not be able to meet minimum ICAO performance requirements. On the other hand, a too large protection zone will decrease the flights resources consumption efficiency as explained next. Indeed, pilots would be asked to avoid the protection zone in order to make sure the navigation system meets the minimum ICAO performance requirements, resulting in traffic limitations, a larger flight time, larger covered distance and higher fuel consumption.

The methodology currently applied by ANSPs to determine the zone impacted by state jamming relies mainly on the use of the ITU standardized RFI mask. The RFI mask provides the maximum power of non-aeronautical RFI that can be tolerated by a receiver to still meet the minimum ICAO performance requirements. However, the ITU standardized RFI mask is derived from a global worst-case or limiting scenario. Indeed, the mask is computed in order to guarantee that GNSS receivers meet minimum ICAO performance requirements at the world's location where the margin between the required C/N_0 by the different signal processing operations and the link budget C/N_0 obtained in presence of aeronautical RFI sources yields the smallest tolerable power for all potential non aeronautical RFI sources. As a consequence, the protection area against non-aeronautical RFI which is derived from the RFI mask is an upper bound of any position on Earth which should be too high when only considering the state jammer position and local RFI constraints.

The aim of this chapter is thus to provide a methodology allowing to refine the protection area where GNSS receivers are potentially impacted by the state jamming.

To achieve this objective, this chapter is divided in three parts. First, this section defines and introduces the RFI mask, detailing how it has been elaborated and its limits when it comes to determine a protection area for state jamming. Second, the new methodology to derive the protection area during jamming operation is introduced. This new methodology relies on a precise analysis of the RFI environment characterized as an equivalent additive white noise, or equivalently as a degradation of the C/N_0 . The characterization of the RFI environment faced by the GNSS receiver is proposed in this section, at the time of the jamming operation and for victim GNSS receiver positions in the vicinity of the jammer. At the end of the second section, all inputs needed to apply the new methodology will be covered. Third, this new methodology is applied on a jamming scenario example. The reduction of the

size of the protection area using the new proposed methodology instead of the one based on RFI masks will be analyzed.

4-1 RFI mask: elaboration, interpretation, limitation

This section first introduces the notion of RFI mask, and second details its application when it comes to derive protection area during GNSS jamming exercises. Protection area gather all locations for which the fulfillment of minimum ICAO performance objectives is not guaranteed.

4-1.1 Presentation of GNSS RFI masks

The notion of RFI mask is introduced in [11] for L1 and in [70] for L5. The RFI mask provides the maximum power that can be tolerated by an aeronautical receiver at the antenna port to guarantee the fulfillment of pseudorange accuracy performance objective defined by ICAO SARPs [15]. In this chapter, a focus on the L1 band in proposed. The in-band RFI mask provides the maximum power of a RFI hitting the L1/E1 band (the RFI central frequency is within the frequency range [1559; 1591] MHz) as a function of its bandwidth (double sided). The out-of-band RFI mask gives the maximum power of a 700 Hz CW RFI as a function of its central frequency. L1/E1 RFI masks, under their latest version of DO-235C [6] for legacy and DFMC GNSS receivers, are plotted in Figure 4-1.

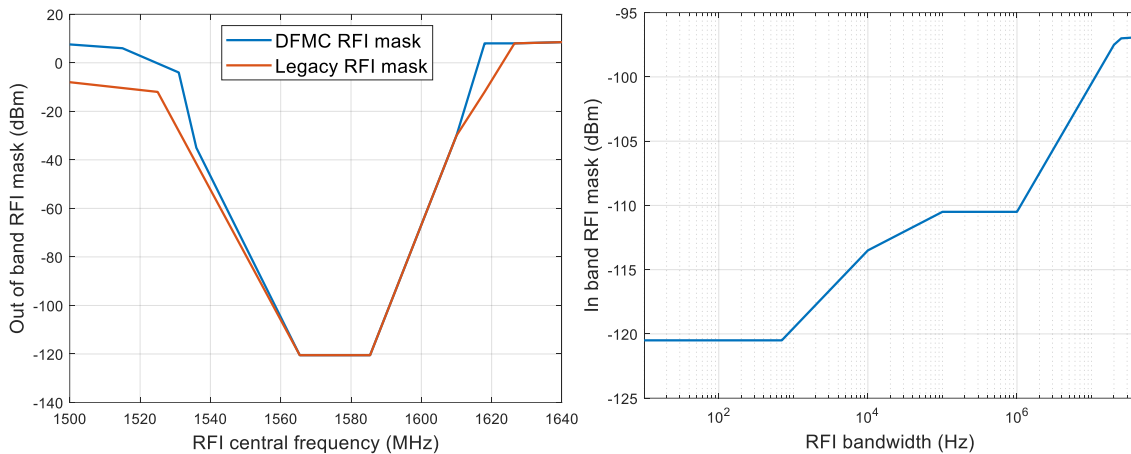


Figure 4-1: Out of band and in band L1/E1 RFI masks

Historically, the first elaborated mask was the legacy RFI mask, published in DO-229 in 1996. In 2020, as part of the work of standardization of DFMC GNSS receivers, the DFMC RFI mask was elaborated and published in the ICAO SARPs. Note that out-of-band legacy and DFMC RFI masks are different, because of differences on specifications on the frequency rejection brought by the antenna and the RFFE filter. Conversely, the in-band RFI mask is identical for the two generations of GNSS receivers.

Empirical assumptions which were initially considered to elaborate the legacy RFI mask remain unknown. Therefore, one task of this PhD consisted in providing a mathematical approach allowing to justify the choice of such a power limitation for non-aeronautical RFI power level. This theoretical analysis of RFI mask is not indispensable to understand the GNSS jamming protection area calculation methodology, so it is not further detailed in this section. However, more elements of interpretation of RFI masks are presented in Appendix B.

4-1.2 Traditional methodology for jamming protection area determination

Air Navigation Service Providers (ANSP) often use RFI mask when it comes to determine the protection area during a jamming operation. This section details the methodology followed by ANSP and highlights the limitation of such a methodology.

4-1.2.1 Traditional methodology to determine jamming protection area.

RFI mask is the input information usually used to derive protection areas during state jamming exercises. For notation simplifications, the traditional methodology based on the RFI mask as input information will be called the RFI mask method. The ANSP traditional method, which is compliant with guidelines provided by Eurocontrol in [71], consists in allocating to the jammer signal all the non-aeronautical power at the antenna port allowed by the RFI mask. Therefore, the protection zone computed from the RFI mask method when only considering free space losses is a half sphere whose radius is given by (Eq 4-1).

$$r(G_J, G_{Rx}) = \frac{\lambda}{4\pi} \sqrt{\frac{P_J G_J G_{Rx}}{C_{max}}} \quad (\text{Eq 4-1})$$

G_J is the jammer antenna gain and P_J is the jammer transmitted power. λ is the jammer carrier wavelength. C_{max} is the maximum non-aeronautical RFI power at the GNSS antenna port authorized by the RFI mask for the considered RFI bandwidth and central frequency. G_{Rx} is the receiver antenna gain.

Usually, it is assumed that the jammer transmission direction is unknown. Therefore, to compute the protection zone radius, the maximum values of the transmitter and receiver antenna gain patterns are used in (Eq 4-1), and the radius of the jamming protection area is given by (Eq 4-2).

$$r_{max} = r(G_{J,max}, G_{Rx,max}) \quad (\text{Eq 4-2})$$

$G_{J,max}$ and $G_{Rx,max}$ are respectively the maximum antenna gains of the jammer and the victim GNSS receiver. Usually, the jammer is located of the ground, and therefore the jamming signal reached the aircraft with a negative elevation angle. Consequently, $G_{Rx,max}$ is usually read in the civil aviation lower hemisphere antenna pattern presented in Figure 2-18 for 0° elevation angle. Thus, $G_{Rx,max} = -5 \text{ dB}$ for legacy receiver (DO-301 antenna [51]) and $G_{Rx,max} = -6 \text{ dB}$ for DFMC receiver (DO-373 antenna [53]).

4-1.2.2 Limitation of the traditional methodology

The use of the RFI mask as the basic input parameter is not always adapted to the elaboration of protection areas for the following reasons identified in Appendix B.

1. RFI masks aim to assess the worst situation of GNSS receivers in presence of aeronautical RFI in any point on Earth. Therefore, RFI masks reflect a situation where aeronautical RFI are strong (equal or close to its highest power value). For the L1 band in particular, the RFI mask reflects the maximum tolerable power that can be tolerated in Honolulu during precision approach. Honolulu was indeed the location, among those analyzed in DO-235B, where the link budget margin is the lowest. As a consequence, the aeronautical RFI environment in the vicinity of the jammer may not correspond to the situation from which the RFI mask is derived (Honolulu).
2. RFI masks has initially been issued in DO-229 in 1996. Even though they have been slightly modified in the out-of-band frequency range, the in-band part has not been modified. L1/E1 RFI masks thus rely on RFI environment of 1996. However, this RFI environment has evolved since 1996, with the launching of additional GNSS satellites and the apparition of other GNSS signals in the L1/E1 frequency band. Therefore, the RFI environment considered when deriving the RFI mask is not relevant to address current RFI situations during jamming operations.
3. RFI masks are not adapted to all types of RFI. Indeed, RFI masks represented in Figure 4-1 are derived for RFI whose power spectral density has a rectangular shape. As a result, RFI masks do not guarantee the fulfillment of minimum GNSS requirements if the RFI has a different

power spectral density shape, since the processing gain (Spectral Separation Coefficient) should also be different.

4. RFI masks presents the total non-aeronautical RFI power. This non-aeronautical power must be shared between several non-aeronautical sources which are already present on the surroundings of the state jammer. Therefore, all the non-aeronautical level presented in the RFI mask cannot be solely allocated to the jamming signal.

4-2 New methodology for jamming protection area determination

The new proposed methodology to elaborate protection zones during jamming exercises is expected to remove disadvantages of the traditional method based on the RFI mask as input information. In most locations in the world, the aeronautical RFI has a weaker impact in comparison to the aeronautical RFI environment impact associated to the RFI mask derivation. Therefore, in these locations, the GNSS receiver should be able to tolerate more non-aeronautical RFI power than the power indicated by the RFI mask. Indeed, the GNSS RFI mask is derived such that the aggregate RFI equivalent additive white noise level (aeronautical RFI plus non-aeronautical RFI) is equal to the RFI equivalent additive white noise level that can be tolerated by the receiver while keeping fulfilled minimum ICAO performance requirements. As a consequence, if aeronautical RFI power is lower than the aeronautical RFI power considered when elaborating the RFI mask, then the receiver should be able to operate even though the non-aeronautical RFI level is above the level presented in the RFI mask under the following condition: the total RFI equivalent additive white noise level (aeronautical plus non-aeronautical) remains lower than the maximum aggregate RFI equivalent additive white noise level tolerated by the receiver to meet minimum ICAO performance requirements.

The fundamental idea of this new method consists thus in allocating the extra margin, (in power or equivalently in equivalent additive white noise level) left by a favorable aeronautical situation in comparison to the RFI situation associated with the RFI mask, to non-aeronautical RFI. In addition, the RFI mask has been elaborated to protect legacy GNSS receivers from non-aeronautical RFI. Dual Frequency Multi Constellation (DFMC) receivers are more robust facing RFI than legacy receiver, thanks to lower implementation losses and a better antenna gain (DO-373, [53]). Therefore, the jamming protection area computed for DFMC receivers should be lower than jamming protection area computed for legacy receivers, as DFMC equipment inherently brings some capability to tolerate more non-aeronautical RFI. Moreover, note that ITU standardized RFI mask will not tolerate more RFI power with the introduction of DFMC receivers since the RFI mask has still to protect legacy receivers.

In conclusion, since the GNSS receiver can tolerate more non-aeronautical RFI power than the power indicated by the RFI mask, due to a potential decrease of aeronautical RFI power and due to the use of DFMC receivers, then minimum ICAO performance requirements can be met even though the victim receiver is inside the protection zone determined by the traditional methodology.

One important remark to consider about the new proposed methodology is the following one. During their certification phase, the GNSS receiver resiliency to RFI is tested by injecting non-aeronautical RFI, which power is determined by the RFI mask, and by injecting aeronautical RFI, which power is chosen as a function of the receiver's test location. This means that if this new method for the determination of the protection area is used, the receiver should be able to tolerate a higher level of non-aeronautical RFI than the one used for receiver testing. However, the total RFI level (aeronautical and non-aeronautical) to which the receiver is tested remains unchanged.

This section is divided in 3 parts, corresponding to the three successive steps of this new methodology.

- 1) The maximum equivalent noise from non-aeronautical RFI sources tolerated by the GNSS receiver to keep minimum requirements fulfilled is computed. This first step is achieved by performing a C/N_0 link budget calculation, where the minimum effective C/N_0 in presence of aeronautical RFI during the jamming period and under the local aeronautical RFI situation in the vicinity of the jammer is compared to the C/N_0 thresholds for the different signal processing operations (acquisition, tracking, demodulation) guaranteeing the fulfilment of the minimum ICAO performance requirements. C/N_0 thresholds, which characterize the capacity of the GNSS receiver to meet requirements, are derived in Appendix A.
- 2) The equivalent noise of all non-aeronautical sources for victim receiver positions for which the jammer is visible is computed. The contribution of the jammer is included in non-aeronautical equivalent noise.
- 3) The protection area can be designed, identifying all victim receiver positions for which the received non-aeronautical equivalent noise exceeds the non-aeronautical level that can be tolerated by the GNSS receivers.

This methodology is illustrated in Figure 4-2.

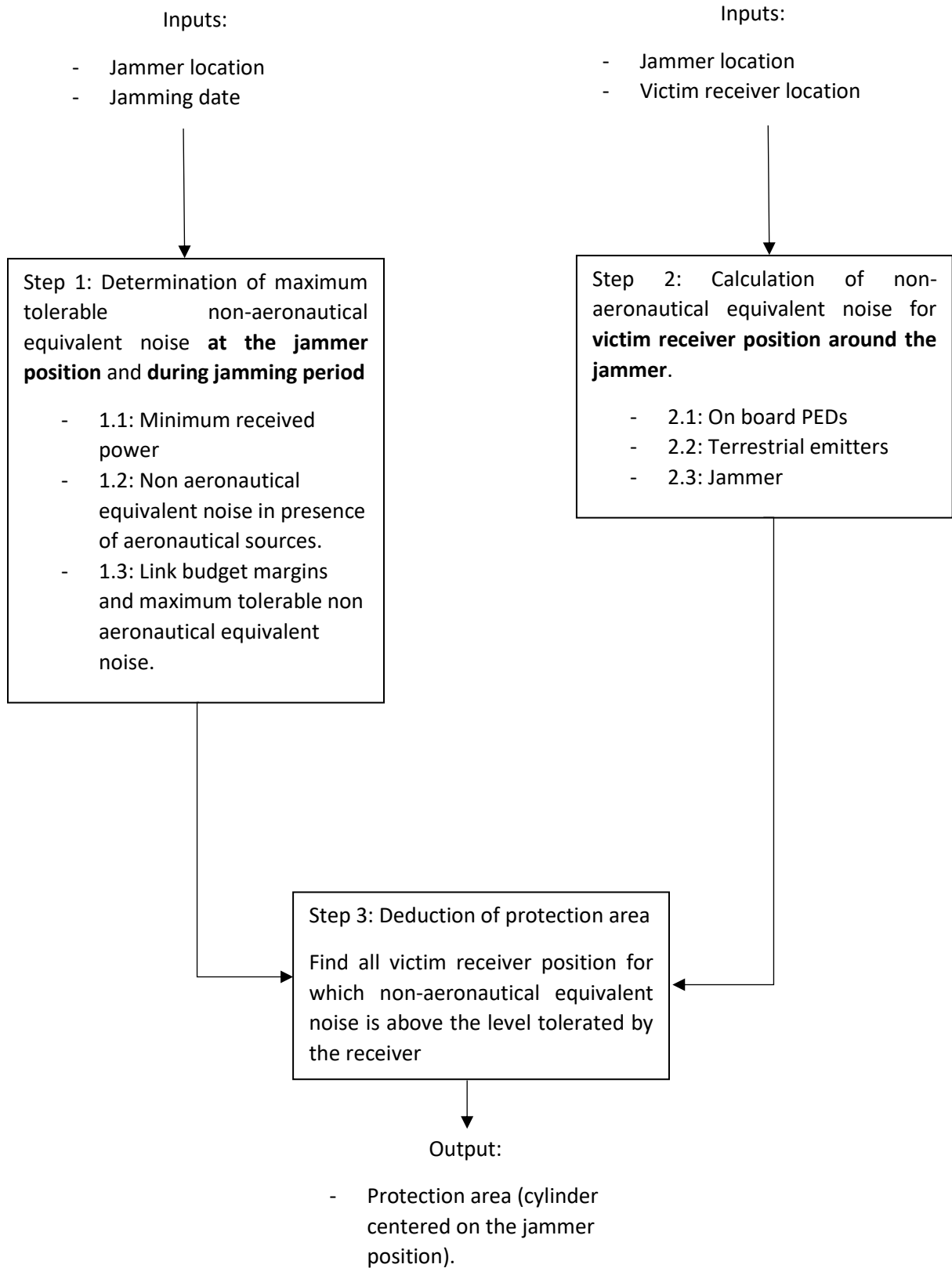


Figure 4-2: Illustration of the new methodology of jamming protection area determination

4-2.1 Step 1: C/N_0 link budget and allowable non-aeronautical equivalent noise

The first step of the new proposed methodology consists in establishing a C/N_0 link budget for each pair of signal, sig , and receiver operation, op , for which minimum ICAO operation requirements must be fulfilled. The aim is to determine the maximum non-aeronautical equivalent noise which can be tolerated by the GNSS receiver to keep minimum ICAO performance requirements fulfilled. Pairs of signal and operation that must be investigated are recapped in Table 4-1.

	GPS L1C/A	Galileo E1	SBAS L1
Acquisition	✓	✓	
Tracking/demodulation	✓	✓	✓

Table 4-1: Investigated pairs of signals and GNSS receiver signal processing operations

SBAS L1 acquisition is not investigated. Indeed, SBAS L1 acquisition requirements also required that the receiver can demodulate the SBAS message. Therefore, SBAS L1 acquisition is covered by SBAS L1 demodulation analysis.

The C/N_0 link budget is computed in three steps detailed below:

- Step 1.1: Computation of the recovered useful GNSS signal power at the antenna port (inputs: receiver position and jamming period).
- Step 1.2: Computation of the effective noise in presence of aeronautical RFI.
- Step 1.3: Deduction of the link budget margin and calculation of the maximum tolerated equivalent noise from non-aeronautical RFI sources.

This section is split in four parts. First, the details the C/N_0 link budget are presented. Then, details on each of the step 1.1 to 1.3 are provided.

4-2.1.1 Presentation of C/N_0 link budget

The C/N_0 link budget is performed completing Table 4-2.

Line	Parameter	Value
1	Minimum received power of the total signal from the SV	
2	Minimum antenna gain $G_{min}(t)$	
3	Implementation losses	
4	Recovered satellite power C	(1)+(2)-(3)
5	Thermal noise PSD N_0	
6	Total wideband equivalent continuous aeronautical RFI PSD $I_{0,aero,WB}(t)$	
7	Effect of the receiver saturation: N_{Lim}, PDC_{Lim}	
8	Efficient noise PSD $N_{0,eff,aero}$	
9	Receive carrier to noise density ratio $C/N_{0,eff,aero}$	(4)-(8)
10	C/N_0 operation threshold of the total signal	
11	Margin	(9)-(10)
	Remaining I0tolerable	

Table 4-2: C/N_0 link budget analysis table

The main inputs needed to complete the link budget analysis are in bold in Table 4-2 and are introduced below:

- The minimum received power of the GNSS signal refers to the GNSS power level on the Earth surface, or equivalently the GNSS signal power received at the output of a 0 dBi right hand circularly polarized (RHCP) antenna.
- The antenna gain refers to the GNSS receiver antenna gain. GNSS receiver antenna gain patterns are given in Figure 2-18.
- Implementation losses refers to various losses which are due to finite quantization, GNSS signal distortion, finite bandwidth RFFE filtering and other losses due to imperfections of the GNSS receiver. Implementation losses are mathematically defined later in this section.
- N_0 is the receiver thermal noise power spectral density.
- The link budget is computed in presence of aeronautical RFI. The impact of aeronautical RFI in the L1/E1 frequency band is characterized as an equivalent noise $I_{0,aero,WB}$.
- The link budget also covers the impact of receiver saturation on the C/N_0 even though such an event is expected to be rare, and time limited in the L1/E1 band. Receiver saturation is characterized through parameters N_{Lim} and PDC_{Lim} , respectively defined as the ratio of analog to digital saturation level to 1σ noise voltage established by AGC (N_{Lim}) and as the pulse duty cycle which corresponds to the amount of time that the LNA is saturated and does not operate in a linear way (PDC_{Lim}).
- The C/N_0 threshold for a given pair of signal and operation is the assumed minimum C/N_0 of the considered GNSS signal such that minimum requirements corresponding to the considered operation are fulfilled. They are computed in Appendix A and reminded in Table 4-3 for legacy and DFMC receivers.

	GPS L1C/A			SBAS L1	Galileo E1		
	1 st SV acquisition	Subsequent SV acquisition	Tracking	Demodulation	1 st SV acquisition	Subsequent SVs acquisition	Tracking
Legacy	32.4	31.7	29.93	30	-	-	-
DFMC	32.4	31.7	29	30	34.1	30.6	29

Table 4-3: Acquisition, tracking and demodulation C/N_0 thresholds in dB-Hz for legacy and DFMC receivers

4-2.1.2 Step 1.1: Recovered useful GNSS signal power

This section describes point 1.1 of Figure 4-2. Recovered signal power designates the power of the useful signal at the antenna port as if all subsequent elements (RFFE, AGC/ADC, correlator) are ideal and do not bring any power losses. Equivalently, the recovered signal power is also the GNSS signal power at the correlator input.

C depends on the signal sig (GPS L1C/A, Galileo E1OS, SBAS L1) as well as the GNSS receiver signal processing operation (acquisition, tracking, demodulation) op through the influence of the receiver antenna gain (different lowest elevation angles are considered for each operation). More specifically, C can be computed from the received signal power at the antenna input, the antenna gain and the received implementation losses. C is also time dependent and $C(sig, op, t)$ is mathematically expressed by (Eq 4-3).

$$C(sig, op, t) = C_{min}(sig)G_{min}(sig, op, t)L_{imp}(sig) \quad (\text{Eq 4-3})$$

The minimum receiver power C_{min} corresponds to the minimum received useful GNSS signal total power (data and pilot components are considered for Galileo E1 signals) on Earth. C_{min} can be recovered from the signal SARPs [15].

The minimum antenna gain as a function of the elevation angle G_{min} is published in DO-373 [53] for DFMC receivers and DO-301 [51] for legacy receivers. The minimum antenna gain as a function of the elevation angle is also presented in Figure 2-18. The minimum antenna gain value to be used on the calculation depends on the signal operation which determines the elevation angle to be considered.

On one hand, acquisition requirement imposes to obtain a position, navigation and timing (PNT) solution considering that almanacs are known. Therefore, only the four highest available satellites are needed to achieve the requirement. Consequently, the minimum antenna gain for acquisition scenario depends on the satellite elevation angles during the jamming period and thus on the configuration of the GNSS constellations configuration. In the zone impacted by the jammer (up to some hundreds of kilometers), the satellite elevation does not vary a lot. Therefore, a position independent value G_{min} is used when completing Table 4-2 for acquisition scenario for all positions of the victim receiver.

On the other hand, for core constellation systems (GPS and Galileo) tracking and demodulation cases, the tracking of all visible satellites is not mandatory to meet position accuracy performance objective. In this Chapter, it will be supposed that the availability of six satellites of each core constellation is sufficient to obtain a navigation position accuracy compliant with the requirements with integrity monitoring. Therefore, G_{min} depends on the elevation of the four highest SV for acquisition operation, and on the elevation of the sixth highest SV for GPS and Galileo tracking operation. The elevation of the six highest elevation angle satellites varies during the jamming period, depending on the sky plot at the position of the victim receiver. Therefore, $G_{min}(t)$ is computed running GNSS constellations from available almanacs at the jamming period. Since SBAS SV are geostationary, the minimum antenna gain $G_{min}(t)$ does not vary during the jamming period. Similarly to the acquisition case, a position independent value G_{min} is used when completing Table 4-2 for tracking and demodulation scenarios for all positions of the victim receiver.

Implementation losses are defined in [72] as “signal to noise ratio due to bandlimiting, quantization and sampling”; additionally, loss of power due to payload distortions as well as additional power loss due to receiver imperfections must also be accounted for. Three parameters must be investigated to estimate an upper bound of implementation losses knowing that power loss due to receiver imperfections (miscellaneous losses) is a margin allocated to receiver manufacturers to account for the imperfections on their proprietary design (and cannot be mathematically modelled). First, quantization causes a loss of GNSS signal power. Losses due to quantization and sampling depends on the number of bits that are available in the Analog to Digital Converter (ADC). Quantization losses has been analyzed in [72]. For a 1-bit ADC (legacy receiver, as specified in section 2.5.2.1), minimum signal loss due to quantization is 1.961 dB. For a 1.5-bit ADC (DFMC receiver, as specified in section 2.5.2.1, L1/E1 channels), minimum signal loss due to quantization is reduced to 0.916 dB. Second, according to GNSS interface control documents ([20] and [21], and ICAO SARPs [15]), satellite payload may distort the GNSS signal, inducing some signal recovered power losses due to a mismatch between the GNSS signal and the local replica. Galileo E1, GPS L1 C/A and SBAS L1 signal power losses due to payload distortion can be as up as 0.6 dB according to [21]. Third, the RF front-end filter also distorts the incoming GNSS signal. As a consequence, the received GNSS signal does not perfectly match with the local replica. For GPS L1C/A signal, losses due to RF filtering are computed by (Eq 4-4).

$$L_{mis} = \frac{\tilde{R}_{BPSK}^2(0)}{\beta} \quad (\text{Eq 4-4})$$

\tilde{R}_{BPSK} is the cross-correlation function between a BPSK modulated signal and the BPSK modulated filtered signal. β traduces the effect of the filtering on the noise and is mathematically expressed in (Eq 2-49).

ED-259A [13] states that pilot (CBOC(6,1,1/11,+)) modulation) component is tracked with a BOC (1,1) local replica. The expression of the signal to noise ratio losses due to RF filtering is then given by (Eq 4-5) for acquisition operation, for which both pilot and data channel are used.

$$L_{mis} = \frac{\tilde{R}_{CBOC+,BOC(1,1)}^2(0) + \tilde{R}_{CBOC-,BOC(1,1)}^2(0)}{2\beta} \quad (\text{Eq 4-5})$$

$\tilde{R}_{CBOC+,BOC(1,1)}$ is the correlation function between the filtered data signal and the BOC(1,1) local replica; and $\tilde{R}_{CBOC-,BOC(1,1)}$ is the correlation function between the filtered pilot signal and the BOC(1,1) local replica. β is given by equation (Eq 2-49) considering a BOC(1,1) signal power spectral density. For tracking operation, only pilot channel is used, so L_{mis} is expressed by (Eq 4-6).

$$L_{mis} = \frac{\tilde{R}_{CBOC-,BOC(1,1)}^2(0)}{\beta} \quad (\text{Eq 4-6})$$

L_{mis} values computed with (Eq 4-5) and (Eq 4-6) are very close. For simplicity, a common value will be assumed.

Figure 4-3 illustrates cross-correlation functions \tilde{R}_{BPSK} , $\tilde{R}_{CBOC+,BOC(1,1)}$ and $\tilde{R}_{CBOC-,BOC(1,1)}$ for several receiver bandwidths.

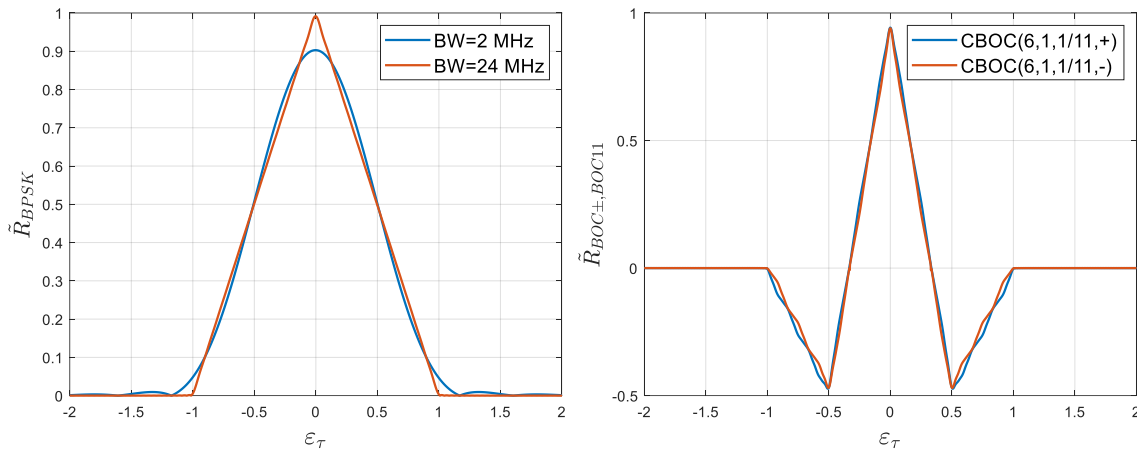


Figure 4-3: Correlation functions between the filtered GNSS signals and their respective local replica

[20] indicates a maximum correlation loss (aggregate of payload distortion and RF filtering losses) of 0.6 dB, considering a 20.46 MHz double sided receiver. Finally, the computation of the total implementation losses is performed in Table 4-4.

	Quantization losses (dB)	RF filtering losses (dB)	Losses due to payload distortion (dB)	Miscellaneous losses (dB)	Total (dB)
GPS L1C/A legacy receiver (20.46 MHz)	1.9	0.02	0.6	0	2.52
GPS L1C/A DFMC receiver (20.46 MHz)	0.9	0.02	0.6	0	1.52

Galileo receiver (12 MHz)	E1	0.9	0.36	0.6	0	1.86
---------------------------	----	-----	------	-----	---	------

Table 4-4: Implementation losses computation

Eventually, implementation losses that are used in this chapter are:

- 2.5 dB for GPS L1C/A legacy receiver.
- 1.5 dB for GPS L1C/A DFMC receiver.
- 1.9 dB for Galileo E1 DFMC receiver.

4-2.1.3 Step 1.2: Effective noise in presence of aeronautical RFI

This section describes point 1.2 of Figure 4-2. It explains how to derive the effective noise in presence of aeronautical RFI. First, the general formula of the effective noise power spectral density in presence of aeronautical RFI, $N_{0,eff,aero}$ is introduced, and second, the impact of each aeronautical source in the L1/E1 frequency band on $N_{0,eff,aero}$ is detailed.

4-2.1.3.1 L1/E1 effective noise in presence of aeronautical RFI

Effective noise power spectral density in presence of aeronautical RFI, $N_{0,eff,aero}$, is derived from (Eq 4-7) in the L1/E1 band.

$$N_{0,eff,aero}(t) = \frac{N_0/\beta}{1 - PDC_{Lim}} \left(1 + \frac{I_{0,aero}(t)}{N_0} + N_{lim}^2 \frac{PDC_{Lim}}{1 - PDC_{Lim}} \right) \quad (\text{Eq 4-7})$$

N_0 is the thermal noise power spectral density level. The maximum value for L1 receiver is -201.5 dBW/Hz, according to [6]. PDC_{Lim} is the pulse duty cycle and corresponds to the amount of time that the LNA is saturated and does not operate in a linear way. Even though the L1/E1 band is in theory not impacted by high power pulsed RFI, a 1% value is proposed for PDC_{Lim} [6]. $I_{0,aero}$ is the aggregate of all continuous aeronautical RFI equivalent noise power density level and is fully detailed later in section 4-2.1.3.2. N_{lim} is the ratio of analog to digital saturation level to 1σ noise voltage established by AGC (equal to 1.5 for a 1.5 bit ADC of DFMC receiver, and equal to 1 for 1 bit ADC of legacy receiver). Note that (Eq 4-7) assumes that the L1/E1 frequency band is not impacted by pulsed RFI. This assumption is verified in nominal RFI environment.

Note that $N_{0,eff,aero}$ depends on the time. Indeed, as detailed in section 4-2.1.3.2, one aeronautical RFI source (inter and intra system RFI) depends on the satellites in view configuration which is time dependent. However, $N_{0,eff,aero}$ is supposed to be independent on the victim receiver location in the vicinity of the jammer.

4-2.1.3.2 Aeronautical RFI equivalent noise

[6] identifies three aeronautical RFI sources transmitting in or in the vicinity of the GNSS L1 band (1559-1610 MHz):

- 1) AMSS: Some aircrafts have an aeronautical mobile satellite system (AMSS) equipment. This on-board equipment allows communication between the crew and the ground through satellite communications. AMSS has a frequency allocation in the [1626-1660] MHz band and thus, AMSS transmission does not directly hit the GNSS L1 band. However, the 5th and 7th order intermodulations fall into the L1 GNSS band and may degrade GNSS signal processing.
- 2) Case Emission: Cockpit devices screens also radiate unwanted energy in the GNSS L1 band. This aeronautical RFI source is referred as “case emission”. Current cockpit installed

equipment are tested and certified according to DO-160G [41] Cat M requirements. In particular, undesired radiation is the GNSS frequency band from each cockpit equipment device is limited to 53.3 dB μ V/m for this category of equipment. Newer cockpit devices will be certified according to Cat P and Cat Q requirements and will be allowed to transmit no more than 40 dB μ V/m.

- 3) Inter and intra system RFI: Inter and intra system RFI refers to GNSS signals coming from other GNSS constellations or from the same constellation but different from the signal of interest. For example, Galileo E1 signals and GPS L1C/A PRN 6 signal act as an RFI on the receiver channel processing GPS L1C/A PRN 2 signal. Since there are more and more GNSS constellations, inter system RFI should be regularly reviewed. In particular, the current in force RFI mask is based on a inter/intra system RFI analysis performed in 1996, which do not consider Beidou signals. Therefore, aeronautical RFI computation is not up to date compared to the intra/inter system RFI used for the RFI mask elaboration. Moreover, inter and intra system RFI at a given instant depends on the skyplot, so the inter intra system equivalent noise is time dependent.

The aggregate aeronautical equivalent noise in the L1/E1 frequency band is given by (Eq 4-8).

$$I_{0,aero}(t) = I_{0,AMSS} + I_{0,case\ em} + I_{0,GNSS}(t) \quad (\text{Eq 4-8})$$

$I_{0,x}$ is the equivalent noise induced by RFI source X .

The equivalent noise of each of these aeronautical RFI sources has been reviewed as part of DO-235C elaboration process and is presented in the following subsections. One contribution of this PhD is the calculation of inter and intra system equivalent noise faced by Galileo E1 receivers.

4-2.1.3.2.1 AMSS equivalent noise

AMSS services transmit in the sub-bands [1545-1559] MHz and [1646.5-1660.5] MHz. Even though a selection on transmitting AMSS channels is done in order to avoid that high order inter modulation products fall close to L1, the L1/E1 band may be affected by the AMSS signal fifth and seventh order inter modulation product with a total power up to -159 dBW (measured in a 1 MHz bandwidth) according to DO-235C. Assuming that the bandwidth of the AMSS inter-modulation is large enough to be considered as AWGN, each AMSS terminal creates an equivalent noise equal to -159 dBW/MHz. It is considered in DO-235C [6] that two AMSS terminal in idle mode (each creating an equivalent noise equal to -162 dBW/MHz) and one AMSS terminal operating creates RFI on the GNSS L1 band. As a consequence, the total equivalent noise induced by AMSS is given by:

$$I_{0,AMSS} = -155.98\ \text{dBW/MHz} \quad (\text{Eq 4-9})$$

4-2.1.3.2.2 Case emission equivalent noise

The calculation of case emission equivalent noise performed in DO-235C is here detailed. First, even though Cat M cockpit equipment are allowed to radiate up to 53.3 dB μ V/m in the L1/E1 band, measurements performed by [6] show that the cockpit devices transmit at a lower level in this L1/E1 frequency band. Therefore, it is proposed to bound the electric field transmitted in the L1 band by one cockpit equipment by 40 dB μ V/m, measured on a 1 MHz bandwidth [6]. Moreover, newer generation Cat P and Cat Q equipment are not allowed to radiate more than 40 dB μ V/m in the L1/E1 band. Second, the path loss (PL) between the cockpit window and the GNSS antenna is measured by [43] at PL=65 dB. Third and last, 10 devices are assumed to be installed in the cockpit. In addition, 2 additional devices are considered, corresponding to electronic flight bags (EFB) often carried by pilots. Although

EFB are not restricted by DO-160 standard, measurement shows that their radiation in the L1 band is lower than $E=40$ dB μ V/m. Case emission RFI is also modelled as an equivalent AWGN. Therefore, the equivalent noise caused by case emission RFI source is given by (Eq 4-10).

$$I_{0,case\ em} = \frac{E^2}{30} N PL = -148.98\ dBW/MHz \quad (\text{Eq 4-10})$$

$N = 12$ is the number of cockpit devices interfering with the GNSS signal.

4-2.1.3.2.3 Inter intra system RFI equivalent noise

Inter and intra system RFI depends on the constellations configuration at the time of the state jamming operation. The inter and intra system RFI equivalent noise at a position (lat, lon) can be computed using (Eq 4-11).

$$I_{0,GNSS}(lat, lon, t) = L_{imp,gnss} \sum_{system} I_{0,system}(lat, lon, t)$$

$$= \sum_{SV\ visible} G_{norm}(lat, lon, SV, t) G_{Rx}(lat, lon, SV, t) \sum_{sig} P(sig) SSC(sig, vict) \quad (\text{Eq 4-11})$$

$$SSC(sig, vict) = \int_{-\infty}^{+\infty} |H_{RF,BB}(f)|^2 S_{sig}(f) S_{vict}(f) df$$

system refers to GNSS constellation (SBAS and core and regional constellations), and *sig* refers to GNSS signal transmitted in the L1/E1 band. *vict* refers to the victim receiver local replica modulation.

$L_{imp,gnss}$ is the correlation and quantization losses of a generic GNSS signal. G_{norm} is the normalized (with respect to the maximum value) received power. It depends on the satellite elevation at instant t and takes into account the GNSS transmitter antenna gain as well as propagation channel attenuation as a function of the elevation. G_{Rx} is the GNSS receiver antenna gain and it also depends on the satellite elevation at instant t . $P(sig)$ is the maximum power received at the output of a 0 dBi RHCP antenna for the considered GNSS signal *sig* and is provided by ICAO SARPs. Eventually, $SSC(sig, vict)$ is the spectral separation coefficient between interfering signal *sig* and the victim receiver local replica modulation. It depends on the RFFE filter transfer function at baseband $H_{RF,BB}$, the normalized interfering signal power spectral density S_{sig} , and the normalized power spectral density S_{vict} of the victim receiver local replica. It can be computed using (Eq 2-79).

Table 4-5 summarizes some characteristics of the different GNSS systems and signals in the L1/E1 frequency band.

System	Signal	Modulation	Central Frequency (MHz)	Orbit	Min Power (dBW)	Max Power (dBW)
BEIDOU	B1-C data	BOC(1,1)	1575,42	MEO+ IGSO+ GEO	-163.77 (MEO) -165.77 (IGSO)	-157.27 (MEO) -158.27 (IGSO)
	B1-C pilot	QMBOC(6,1,4/33)	1575,42		-160.76 (MEO) -162.76 (IGSO)	-154.26 (MEO) -155.26 (IGSO)
	SBAS	BPSK(1)	1575.42		-158,5	-152,5

	E2I	BPSK(2)	1561.098		-163	-160
	E2Q	BPSK(2)	1561.098		-157	-150
Galileo	E1-F data	CBOC(6,1,1/11,'+')	1575,42	MEO	-160,9	-154,45
	E1-F pilot	CBOC(6,1,1/11,'-')	1575,42		-160,9	-154,45
	E1-P	BOC(15,2,5)	1575,42		-157	-150
GPS	L1 C/A	BPSK(1)	1575,42	MEO	-158,5	-153
	L1C - data	BOC(1,1)	1575,42		-163	-156
	L1C - pilot	TMBOC(6,1,4/33)	1575,42		-158,25	-151,25
	P(Y)	BPSK(10)	1575,42		-161,5	-150
	M-Code	BOC(10,5)	1575,42		-157	-150
QZSS	L1 C/A	BPSK(1)	1575,42	HEO+ GEO	-158,5	-153
	L1C data	BOC(1,1)	1575,42		-163	-160
	L1C pilot	TMBOC(6,1,4/33)	1575,42		-158,25	-155,25
	SBAS	BPSK(1)			-158,5	-152,5
	L1 SAIF	BPSK(1)	1575,42		-161	-153
EGNOS	SBAS	BPSK(1)	1575,42	GEO	-161	-152,5
WAAS	SBAS	BPSK(1)	1575,42	GEO	-158,5	-152,5
GAGAN	SBAS	BPSK(1)	1575,42	GEO	-158,5	-152,5
SDCM	SBAS	BPSK(1)	1575,42	GEO	-158,5	-152,5
KASS	SBAS	BPSK(1)	1575,42	GEO	-158,5	-152,5
African SBAS	SBAS	BPSK(1)	1575,42	GEO	-158,5	-152,5

Table 4-5: Characteristics of GNSS signals

The emitter antenna gain, and the different propagation attenuation depending on the signal travelled distance are taken into account through G_{norm} according to Figure 4-4 as a function of the elevation, for the different core constellation (GPS, Galileo, Beidou) and satellite-based augmentation systems transmitting in the L1/E1 band. The patterns shown in Figure 4-4 is consistent with the ones used for the inter and intra system RFI analysis performed in [6].

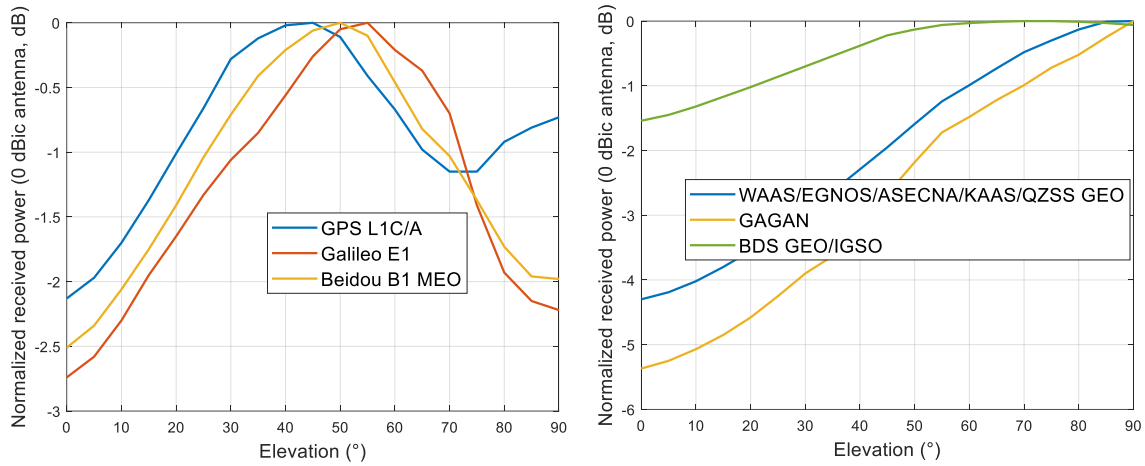


Figure 4-4: Normalized received GNSS power as a function of SV elevation

To consider the maximum antenna gain of Figure 2-18 when evaluating inter and intra system RFI equivalent noise seems to be very pessimistic. Instead, [6] proposes to consider an average antenna pattern determined by taking the mean antenna gain measured on several antenna prototypes. This average antenna gain, which is used for this inter/intra system RFI analysis, is represented in Figure 4-5.

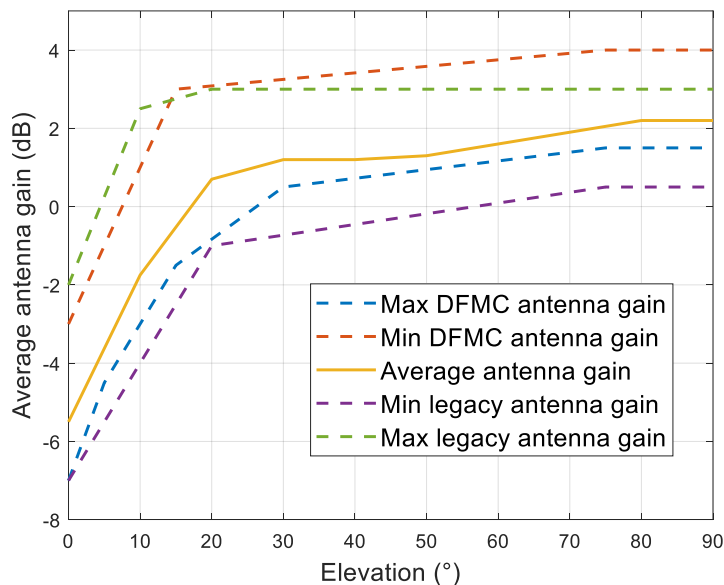


Figure 4-5: Average antenna gain for I_{gnss} analysis

Finally, the power loss, $L_{imp,gnss}$, of the interfering signals due to the quantization and correlation (payload distortion) is very difficult to assess since it depends upon a large number of factors that can be difficult to quantify and that are usually just to calculate the loss with respect to the synchronized signal, such as the local replica, the sampling rate, the types of interference (including the non-GNSS ones) and their power [72]. Note that the loss of power due to the bandlimiting effect is not considered since the RF filter impact is already modelled inside the SSC formula of (Eq 4-11). Therefore, although $L_{imp,gnss}$ of the interfering signals (GNSS signals in this case) due to the quantization and payload distortion can theoretically be positive or negative (leading to an increase of the $I_{0,GNSS}$ in the later case), early work on the specific case of Galileo E1C showed that $L_{imp,gnss}$ would be slightly negative

in the worst case. In order to be conservative, it is then decided to assume that the apparent loss of the interfering signals due to the receiver quantization and payload distortion is 0 dB.

Even though $I_{0,GNSS}(lat, lon, t)$ depends on the victim receiver location (lat, lon) , the variation of $I_{0,GNSS}(lat, lon, t)$ in the vicinity of the jammer is small. Therefore, $I_{0,GNSS}(t)$ is computed at the position of the jammer and is assumed valid at all victim receiver positions from which the jammer is visible.

4-2.1.4 Step 1.3: Link budget margin and maximum tolerated non-aeronautical equivalent noise

Step 1.1 and step 1.2 allows the calculation of the minimum carrier to effective noise power spectral density ratio in presence of aeronautical RFI ($C/N_{0,eff,aero}$). The next step 1.3 of Figure 4-2 consists thus in comparing $C/N_{0,eff,aero}$ to the C/N_0 threshold, $C/N_{0,th}$, for the considered pair of signal and operation to deduce the margin. For a given pair of signal and operation, the C/N_0 link budget margin is defined by (Eq 4-12).

$$Margin(sig, op, t) = \frac{C(sig, op, t)/N_{0,eff}(t)}{C/N_{0,Th}(sig, op)} \quad (Eq 4-12)$$

Next, the maximum equivalent noise from non-aeronautical sources that a receiver can tolerate so that the $C/N_{0,eff}$ in presence of aeronautical and non-aeronautical RFI remains above the C/N_0 threshold for the considered operation is computed in (Eq 4-13).

$$I_{0,non\ aero,max}(sig, op, t) = \beta N_{0,eff,aero}(t) \cdot (Margin(sig, op, t) - 1)(1 - PDC_{Lim}) \quad (Eq 4-13)$$

Eventually, the maximum non-aeronautical equivalent noise that can be tolerated by the receiver is the minimum $I_{0,non\ aero,max}(sig, op, t)$ value among all considered signals and operations. It is given in (Eq 4-14).

$$I_{0,non\ aero,max}(sig, op) = \min_t I_{0,non\ aero,max}(sig, op, t) \quad (Eq 4-14)$$

4-2.2 Non-aeronautical RFI equivalent noise

This section computes the non-aeronautical equivalent noise faced by a victim GNSS receiver around the jammer. The maximum tolerable non-aeronautical equivalent noise $I_{0,non\ aero,max}$ must be shared between the different non-aeronautical RFI sources that impact the L1 band. Three non-aeronautical RFI sources impacting the L1 band are identified. First, portable electronic devices (PEDs) carried by passengers on-board of the airplane radiate unwanted energy in the L1 band. Second, the GNSS antenna receive undesired energy from ground emitters of various type (PEDs, cellular antenna, Wifi) [13]. Finally, the jammer is also part of the non-aeronautical RFI sources in this step of the methodology.

The total non-aeronautical equivalent noise at a victim receiver position (lat, lon) is then given by (Eq 4-15).

$$I_{0,non\ aero}(lat, lon) = M \cdot I_{0,terr}(lat, lon) + M \cdot I_{0,PED} + I_{0,jammer}(lat, lon) \quad (Eq 4-15)$$

- $I_{0,terr}$ is the equivalent noise caused by terrestrial emitters.
- $I_{0,PED}$ is the equivalent noise caused by on-board PEDs.

- $I_{0,jammer}$ is the equivalent noise caused by the jamming signal.

M is a safety margin which is often added on on-board PEDs and terrestrial emitters components to cover uncertainty in the estimation of their contribution to $I_{0,non\ aero}$. However, the power of the jamming signal which is used during GNSS jamming exercises is often controlled and monitored, so the addition of a safety margin is not essential. The equivalent additive white noise induced by each non-aeronautical RFI source is detailed in this section.

4-2.2.1 On-board portable electronic devices

This section describes point 2.1 of Figure 4-2. The calculation of on-board PEDs equivalent noise performed in DO-235C is here presented. Passengers are allowed to use their electronic devices during some phases of the flight. These electronic devices carried by passengers are referred to as on-board portable electronic devices (on-board PEDs). NASA performed measurements on several kinds of PEDs (laptop, mobile phones, etc) [43] [44]. The equivalent noise caused by on-board PEDs is calculated in (Eq 4-16).

$$I_{0,PED} = \sum_{seat} EIRP \cdot PL(seat) \quad (Eq\ 4-16)$$

$I_{0,PED}$ is the aggregate of equivalent noise components caused by each active on-board PEDs. The mean EIRP transmitted by a single device is estimated at -75.2 dBm in [10]. Taking into account the correction due to the antenna used by NASA during their measurement, and supposing that the PEDs transmission is broadband, the equivalent noise transmitted by a single on-board PED is estimated to -96.2 dBW/Hz. [43] also performed measurement on the path loss (PL) between all seats inside a Boeing 737-200 aircraft and the GNSS antenna. Path losses varies between 64.2 dB and 90.1 dB for seats located close to a window. Note that this path loss includes the shielding from the aircraft frame. Considering that all passengers are simultaneously using an electronic device, the on-board PEDs equivalent noise becomes -208.9 dBW/Hz. However, the hypothesis considering that all passengers are simultaneously using an electronic device seems quite conservative. Instead, [10] considers that half of the front half seats and 25% of rear half seats near windows are using a PED. Considering this hypothesis, the equivalent noise transmitted by PEDs carried by passengers reduces to $I_{0,PED} = -212.5$ dBW/Hz. This calculation holds some uncertainties: power transmitted by each individual PED, number of passengers carrying PED, path losses between the cabin and the GNSS antenna for example. Therefore, a $M=6$ dB safety margin is added on the equivalent additive white noise caused by on-board PEDs to cover all potential power fluctuation from the mean power as well as the listed uncertainties.

4-2.2.2 Terrestrial emitters

This section describes point 2.2 of Figure 4-2. Terrestrial emitters refer to ground electronic devices involuntarily transmitting spurious emissions in the GNSS band. Therefore, these electronic devices behave as a RFI source from a GNSS receiver perspective. Code of Federal Regulations CFR Part 15 [73] classifies electronic devices which may involuntarily radiate in other bands within two categories. Class A gathers digital devices marketed for professional usage in a commercial, industrial and business environment. Class B gathers digital devices marketed for a usage in a residential environment. Because of the high number of electronic devices involuntarily transmitting in the GNSS band, the impact analysis of these electronic devices on the GNSS receiver capability to meet minimum signal processing requirement is of the utmost importance.

This section proposes a mathematical model to derive terrestrial emitters equivalent additive white noise. The proposed mathematical formula to derive $I_{0,terr}$ is adapted from the calculation model of

[45]. This section is split in two parts. First, the mathematical approach to estimate $I_{0,terr}$ is provided. Second, the main inputs to compute $I_{0,terr}$ are described.

4-2.2.2.1 Terrestrial emitters equivalent noise

The power P_{terr} from terrestrial emitters received at the GNSS receiver antenna port (inside a 1MHz bandwidth) is modeled as a random variable. Let us define N the number of active terrestrial emitters visible by the aircraft GNSS antenna. In [45], N follows a Poisson distribution with mean value \bar{N} given by (Eq 4-17).

$$\bar{N} = \mathbb{E}[N] = \int_0^{R_{LOS}} \int_0^{2\pi} d(r, \varphi) dr d\varphi \quad (\text{Eq 4-17})$$

$d(r, \varphi)$ is the *density* of terrestrial emitters at the position (r, φ) and R_{LOS} is the radio line of sight horizon. (r, φ) are the polar coordinates on a horizontal frame centered on the aircraft.

Let us define $(X_k)_{k \in \llbracket 1, N \rrbracket}$ the contribution of each individual terrestrial emitter to P_{terr} . The position of each terrestrial emitter, defined in polar coordinates (r_k, φ_k) , is also assumed to be random. The family of random variables $(r_k, \varphi_k)_{k \in \llbracket 1, N \rrbracket}$ is independent and identically distributed. The *probability density function* of the position of a given terrestrial emitter, f (the probability of finding a terrestrial emitter at a given position), depends on the *density* of terrestrial sources at the corresponding position, $d(r, \varphi)$. The *probability density function* of the position of a given terrestrial emitter is given by (Eq 4-18).

$$f(r, \varphi) = \frac{d(r, \varphi)}{\int_0^{R_{LOS}} \int_0^{2\pi} d(r, \varphi) dr d\varphi} = \frac{d(r, \varphi)}{\bar{N}} \quad (\text{Eq 4-18})$$

Let us define $X_k(r_k, \varphi_k)$ as the received power in a 1 MHz bandwidth at the receiver antenna port from one terrestrial emitter source located at position (r_k, φ_k) . The contribution $X_k(r_k, \varphi_k)$ of each terrestrial emitter to P_{terr} depends on three parameters:

- 1) The equivalent isotropic radiated power P_0 in a 1 MHz bandwidth by the RFI source. As discussed in the next section, this term is assumed to be a representative value for all terrestrial emitters.
- 2) The receiver antenna gain $G_{RX}(r_k, \varphi_k)$.
- 3) Propagation losses $L_{prop}(r_k, \varphi_k)$.

The expression of $X_k(r_k, \varphi_k)$ as a function of P_0 , G_{RX} and L_{prop} is given in (Eq 4-19).

$$X_k(r_k, \varphi_k) = P_0 G_{RX}(r_k, \varphi_k) L_{prop}(r_k, \varphi_k) \quad (\text{Eq 4-19})$$

The received power in a 1 MHz bandwidth at the antenna port from terrestrial emitters is then given by (Eq 4-20).

$$P_{terr} = \sum_{k=1}^N X_k(r_k, \varphi_k) \quad (\text{Eq 4-20})$$

The equivalent noise induced by terrestrial emitters on GNSS receiver is then defined by the mean value of P_{terr} . The calculation of $I_{0,terr}$ is performed in (Eq 4-21).

$$\begin{aligned}
I_{0,terr} &= \mathbb{E}(P_{terr}) = \mathbb{E}\left(P_0 \sum_{k=1}^N G_{RX}(r_k, \varphi_k) L_{prop}(r_k, \varphi_k)\right) \\
&= P_0 \mathbb{E}_N \left(\mathbb{E}_{r_k, \varphi_k} \left(\sum_{k=1}^N G_{RX}(r_k, \varphi_k) L_{prop}(r_k, \varphi_k) \mid N\right)\right) \\
&= \mathbb{E}_N \left(N P_0 \mathbb{E}_{r_k, \varphi_k} \left(G_{RX}(r_k, \varphi_k) L_{prop}(r_k, \varphi_k)\right)\right) \\
&= P_0 \mathbb{E}_N(N) \mathbb{E}_{r_k, \varphi_k} \left(G_{RX}(r_k, \varphi_k) L_{prop}(r_k, \varphi_k)\right) \tag{Eq 4-21} \\
&= P_0 \bar{N} \int_0^{R_{LOS}} \int_0^{2\pi} G_{RX}(r, \varphi) L_{prop}(r, \varphi) f(r, \varphi) d\varphi dr \\
&= P_0 \int_0^{R_{LOS}} \int_0^{2\pi} G_{RX}(r, \varphi) L_{prop}(r, \varphi) d(r, \varphi) d\varphi dr
\end{aligned}$$

Note that considering the average received power to define $I_{0,terr}$ may sound unsafe, since the received power would regularly exceed the mean value. In order to avoid an underestimation of the impact of terrestrial emitters on equivalent noise, a M=6 dB safety margin, is usually added on the estimated non-aeronautical RFI equivalent noise. The goal of this safety margin is to cover for uncertainties in the calculation of non-aeronautical RFI equivalent noise, and to cope with the potential exceedance of the non-aeronautical RFI received power compared to the average received power. [45] showed that the probability that the terrestrial emitter received power P_{terr} exceeds $I_{0,terr}$ plus the 6 dB safety margin is very low (around $3 \cdot 10^{-4}$).

Finally, from (Eq 4-21) it can be seen that in order to precisely estimate $I_{0,terr}$, an accurate knowledge of P_0 , L_{prop} and d is needed. The modeling of these parameters is discussed hereinafter. This modeling is a key point to obtain a realistic estimation of $I_{0,terr}$.

4-2.2.2.2 Input parameters for $I_{0,terr}$ calculation

Each of the main input parameters allowing to derive $I_{0,terr}$ are now discussed from a civil aviation point of view in a dedicated section. As highlighted in (Eq 4-21), main contributors to $I_{0,terr}$ include the radiated EIRP by one ground source P_0 , the receiver antenna gain G_{RX} , propagation losses L_{prop} (determined by the propagation channel model) and the distribution of terrestrial emitters d . This section discusses these parameters from a civil aviation point of view.

4-2.2.2.2.1 Transmitted EIRP P_0 by each terrestrial source

For simplicity purposes, it is proposed to select a representative value for P_0 which would be applied to any individual terrestrial emitter. Transmitted emissions of electronic devices in the GNSS band are constrained by 47 CFR Part 15 [73]. In particular, the field strength of unintentional radiators such as terrestrial emitters, measured at a distance of 3 m from the radiator, shall not exceed 500 $\mu\text{V/m}$ at frequencies higher than 960 MHz. The transmitted EIRP P_0 is linked to the field strength through the commonly used relation between the field strength and the power on a sphere centered on the radiating source given by (Eq 4-22).

$$\frac{P_0}{4\pi d_r^2} = \frac{E^2}{120\pi} \tag{Eq 4-22}$$

E is the electric field measured at a distance d_r from the radiating source. From 47 CFR Part 15 constraint on the radiated electric field, the maximum EIRP in 1 MHz bandwidth value transmitted by a given terrestrial emitter is thus equal to $P_0 = -71.25 \text{ dBW/MHz}$.

NASA (National Aeronautics and Space Administration) performed measurement on the involuntarily transmitted power by a wide diversity of electronic devices: laptops, WLAN (wireless local area network) devices, Bluetooth devices, FRS (family radio service) and GMRS (general mobile radio service) radios, etc. The results of this measurement campaign are presented in [74]. From these measurements, it appears that the transmitted power in the GNSS band is much lower than what is allowed by 47 CFR Part 15. Therefore, [45] decided to use the value $P_0 = -81.1 \text{ dBW/MHz}$ as a representative value of EIRP radiated by terrestrial emitters. For consistency with the previous analysis, this value is adopted in this chapter.

4-2.2.2.2.2 GNSS receiver antenna gain

RFI from terrestrial emitters usually arrive with a negative elevation angle. Therefore, the antenna gain pattern used in this analysis is the lower hemisphere diagram of Figure 2-18. Diagram antenna is presented as a function of the signal elevation angle of arrival, E ; therefore, the determination of this angle is a key parameter to determine the antenna gain of each terrestrial emitter position.

Figure 4-6 represents the position of the ground RFI source with respect to the aircraft. The position of the emitter with respect to the victim receiver is characterized by the horizontal distance r (slant range projection on the ground) and the elevation angle φ . Let us define H_a as the height of the aircraft GNSS antenna above ground level (AGL), and h_B the AGL height of the terrestrial source.

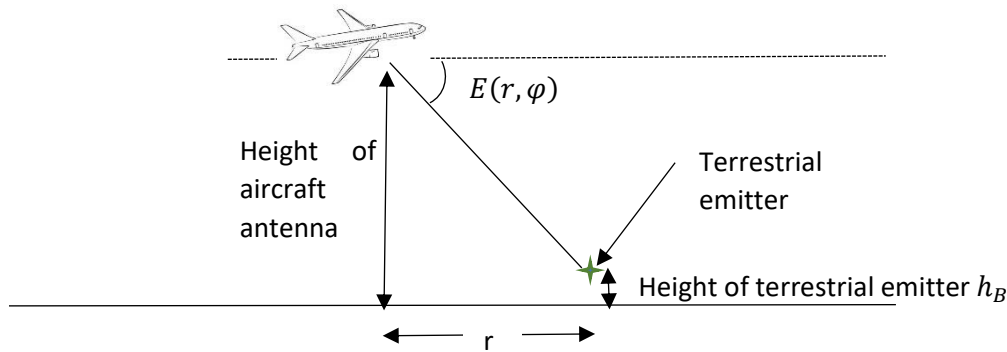


Figure 4-6: Position of the terrestrial emitter with respect to the aircraft

Under flat Earth assumption, the elevation angle of the terrestrial emitter signal inputting the GNSS antenna can be expressed as in (Eq 4-23).

$$E(r, \varphi) = -\text{atan}\left(\frac{H_a - h_B}{r}\right) \quad (\text{Eq 4-23})$$

4-2.2.2.2.3 Propagation channel model

In this specific case, the targeted propagation channel models are narrowband propagation channels which are thus completely defined, from a RFI impact point of view, by the propagation losses term. Moreover, since the worst case is searched for, only the statistical propagation losses are inspected without considering the time-evolution.

Initial estimation of $I_{0,terr}$ in L1/E1 band performed in DO-235B [10] was based on the free space loss model. A refinement of the propagation channel model was later adopted in DO-235C [6]. This new propagation channel model is in fact composed by several empirical models depending on the horizontal distance, r , between the RFI source and the aircraft. Eventually, ITU developed its own model for UHF propagation channel which is called ITU P-528. This model is particularly adapted for computing propagation losses between a ground source and the aircraft. These three propagation models have been analyzed and compared in [75]. The recommendation was the use of the ITU P-528 model, so this propagation model is the one which is considered in this chapter.

ITU P-528 model is the propagation channel model recommended by the International Telecommunications Union to evaluate propagation losses for aeronautical systems transmitting in the 100 MHz – 30 GHz frequency range. ITU P-528 can be applied for transmitter and receiver antennas heights between 1.5 m and 20,000 m. The objective of ITU P528 model is to be more accurate than free space loss model. Indeed, ITU P528 model includes additional propagation considerations with respect to free space loss model. First, attenuation due to atmospheric absorption is added to free space losses. Second, two-rays model is implemented to account for reflection on the ground of the interfering signal. Third, smooth Earth diffraction losses are also considered. Fourth, ITU P-528 model also includes transhorizon propagation, considering reflection on the troposphere. Note that this troposcatter component can be neglected for low power interference sources such as terrestrial emitters but may be not negligible when it comes to high power interference such as DME/TACAN or jammer. Fifth, ITU P-528 ray tracing uses ITU R P676-12 model [76] instead of the traditional “4/3 Earth” method. The main difference is the consideration of the variation of the atmosphere refractive index with altitude. However, ITU R P676-12 model is expected to be very close to the “4/3 Earth” method when the aircraft receiver is at low altitude.

The method to compute propagation losses is widely detailed in [46], and thus it is not developed in this chapter. In this chapter, the p parameter of the P-528 model, which refers to the time probability that propagation losses exceed the returned value, is set to 50%. Indeed, $I_{0,terr}$ is defined by an average value of the different random parameters in (Eq 4-21). However, since a safety margin is added to $I_{0,terr}$, the probability that the effective terrestrial emitters equivalent noise exceeds $M \cdot I_{0,terr}$ is negligible. In addition, a C software providing propagation losses under P-528 model is given by ITU. This software has been used to obtain P-528 propagation loss results in this chapter.

4-2.2.2.2.4 Distribution of terrestrial emitters

Several assumptions were considered in the past to estimate the distribution of terrestrial emitters, d . However, these assumptions seemed quite conservative leading to an over estimation of $I_{0,terr}$. In this section, a new distribution of emitters model is proposed, based on population density data. Note that in this section the mathematical function defining the distribution of terrestrial emitters as a function of (r, φ) is referred to as distribution of terrestrial emitters, whereas specific numerical values associated to a given position $d(r, \varphi)$ are referred to as density of terrestrial emitters (unit: emitter per square meter).

In order to make the distribution of terrestrial emitters more accurate compared to past assumptions (DO-235B, and [45]), it is proposed to link the density of active terrestrial emitters (numerical value) to the population density. The European density of population which is used in this chapter is taken from [77]. Figure 4-7 represents the population density in inhabitants per square kilometer across western Europe, with a resolution of 1 km*1 km (translated into latitude and longitude coordinates). Number of inhabitants per square kilometer is clipped to 1000 in Figure 4-7 for illustration purpose, even though the maximum population density from the population density dataset is 40,000 inh/km².

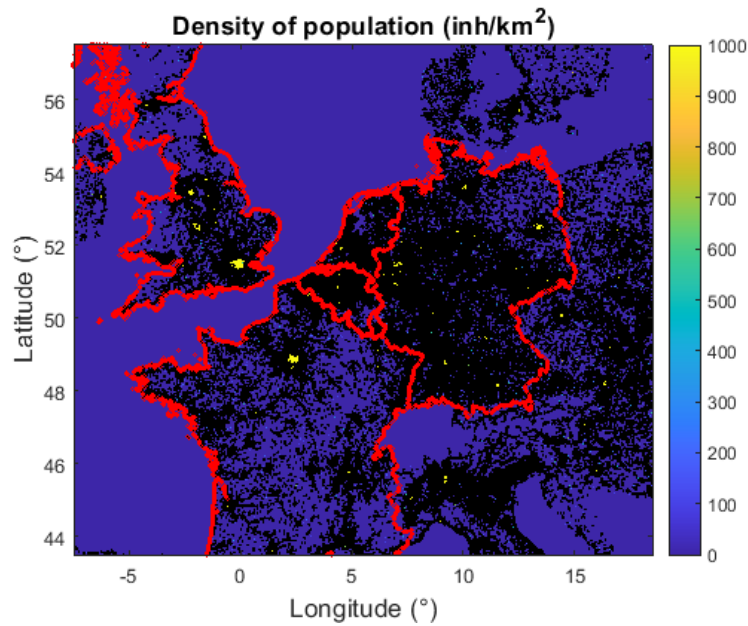


Figure 4-7: Population density across Western Europe

Moreover, [78] analyzes the number of mobile phone users per hour in several Spanish cities (Madrid, Barcelona, Malaga, Murcia, Zaragoza, Valencia, Sevilla, Bilbao). From these data, the peak of simultaneous mobile phone users has been extracted. The mobile phone users per hour peak is plotted on Figure 4-8 for each city, as a function of the population density of the city.

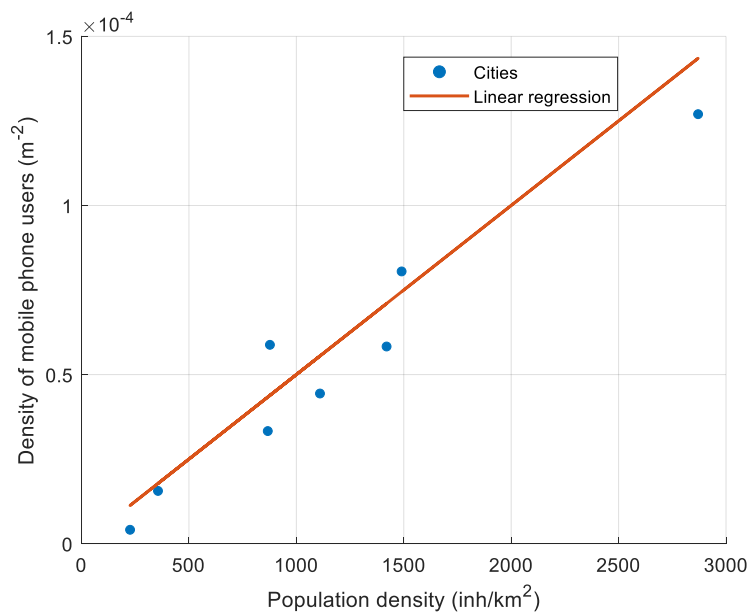


Figure 4-8: Density of mobile phone users as a function of population density for eight Spanish cities

Figure 4-8 shows that the number of simultaneously active terrestrial emitters (or distribution of terrestrial emitters), d , can be linearly linked to the population density, d_{pop} . In addition, [74] shows that electronic devices such as mobile phone are part of the most powerful terrestrial emitters category. Moreover, density of mobile phone is expected to be higher than the density of other terrestrial emitters. Consequently, it is proposed to define the distribution of terrestrial emitter as shown in (Eq 4-24).

$$d(r, \varphi) = \alpha_{terr} d_{pop}(r, \varphi) \quad (\text{Eq 4-24})$$

$\alpha_{terr} = 5 \cdot 10^{-2}$ is the linear regression slope issued from Figure 4-8 data. Unit of $d(r, \varphi)$ is emitter per square meter if $d_{pop}(r, \varphi)$ is in inhabitant per square meter.

Eventually, Figure 4-9 represents the density of terrestrial emitters, d , in Western Europe, computed following Equation (Eq 4-24).

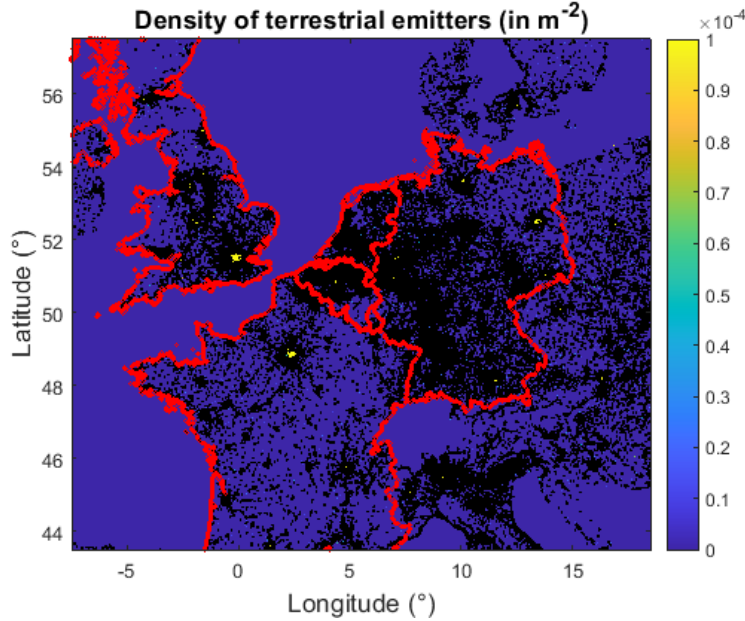


Figure 4-9: Terrestrial emitters density

Finally, note that the advantage of this method with respect to previous DO-235B method is its capacity to precisely reflect the terrestrial RFI environment, with a good resolution (data set allow a resolution up to 100m * 100m). For example, it takes advantage of the real density of population in rural non-inhabited areas to compute $I_{0,terr}$ whereas DO-235B clipped the density of emitter to a non-null value. Therefore, the distribution of emitters function described in this paragraph is expected to give a lower and more precise $I_{0,terr}$ value in comparison to terrestrial emitters distribution of DO-235B.

4-2.2.3 Jammer equivalent noise

This section describes point 2.3 of Figure 4-2. The effect of the jammer signal on the receiver is characterized by the increase of the effective noise at the antenna port. This increase can be modelled using the SSC formula of (Eq 2-79) if the jammer power spectral density is known. The equivalent additive white noise output induced by the jammer is given by (Eq 4-25).

$$I_{0,jammer}(lat, lon) = C_J(lat, lon) \cdot SSC_J \quad (\text{Eq 4-25})$$

C_J is the power of the jamming signal at the antenna port. SSC_J is the spectral separation coefficient between the jamming signal and the locally generated GNSS signal. In order to be conservative, and since the impact of ADC on jamming RFI power is not precisely known, no implementation loss is added on the jamming RFI power. A free space loss propagation model is adopted in this chapter. As a result, the power of the jamming signal at the antenna port is given by (Eq 4-26).

$$C_J(lat, lon) = P_J G_J G_{Rx}(E_{jam}(lat, lon)) \left(\frac{\lambda}{4\pi r_{jam}} \right)^2 \quad (\text{Eq 4-26})$$

P_j is the power of the jammer transmitter, G_j is the antenna gain of the transmitter antenna in the direction of the aircraft. G_{Rx} is the receiver antenna gain, which depends on the elevation angle $E_{jam}(lat, lon)$ of the jammer with respect to the aircraft at position (lat, lon) . λ is the jamming signal wavelength and r_{jam} is the distance between the jammer and the victim antenna.

4-2.3 Determination of the protection area

This section describes point 3 of Figure 4-2. The third and last step of the new proposed method consists in deriving the protection zone. The protection zone is derived as follows.

First, for each pair of signal sig and GNSS receiver fundamental operation op and at a given altitude h , an intermediate protection circle is derived. This intermediate protection circle associated to signal sig and receiver operation op , gathers all aircraft positions (lat, lon) for which the minimum requirement on signal sig and fundamental operation op may not be fulfilled at altitude h . The radius of this protection circle is given by (Eq 4-27).

$$r_{sig,op}(h) = \max_{lat,lon} \{D_j(lat, lon) \mid I_{0,non\ aero}(lat, lon, h) \geq I_{0,non\ aero,max}(sig, op)\} \quad (\text{Eq 4-27})$$

$D_j(lat, lon)$ is the horizontal distance between the jammer and position (lat, lon) .

Second, the protection zone that is derived with the new methodology has a cylinder shape whose height is the maximum aircraft altitude (FL550) and radius $r_{protection\ area}$ is the worst protection radius $r_{sig,op}(h)$ among all signals, receiver operations and altitudes. $r_{protection\ area}$ is given by (Eq 4-28).

$$r_{protection\ area} = \max_{sig,op,h} r_{sig,op}(h) \quad (\text{Eq 4-28})$$

4-3 Derivation of the protection zone on an illustrative jamming scenario

The traditional and proposed methodologies to derive protection areas during jamming exercises have been presented in sections 4-1 and 4-2 respectively. In this section, an example of their application is conducted on an illustrative jamming scenario allowing to make a numerical comparison of the two. This section is divided in two parts. First, the characteristics of the jamming scenario are introduced. Second, the methodologies are computed step by step and the protection radius derived with the two methodologies are compared.

4-3.1 Jamming scenario description

The analyzed fictive jamming exercise is assumed to take place in France, at the position 46.1°N,0.18°E. The date of jamming is 2020, December 29th and is assumed to last 24h. The state jammer is located on the ground (antenna is at 0 m AGL) and transmits a signal with rectangular shape power spectral density. The jamming signal characteristics are presented in Table 4-6. As an important hypothesis, the jamming signal is assumed linearly polarized.

Power (W)	Antenna gain (dB)	Bandwidth (MHz)	Central frequency
12	5 (antenna supposed to be approximately omnidirectional on the upper hemisphere)	50	L1

Table 4-6: Jammer settings for illustrative situation

4-3.2 Protection radius with the new methodology

This section computes the protection radius with the new methodology. It is divided in three parts, corresponding to the three steps of the method.

4-3.2.1 Step 1: Maximum tolerable non-aeronautical equivalent noise

This section applies point 1 of Figure 4-2. The maximum tolerable non-aeronautical equivalent noise $I_{0,non\ aero,max}(sig, op, t)$ for the considered signal sig and operation op to fulfil minimum requirement is computed. As a reminder of section 4-2.1.1, pairs of signal and operation that must be investigated are presented in Table 4-1.

As highlighted in section 4-2.1, the link budget is time dependent as two parameters depends on the GNSS constellations which vary along the time: the minimum receiver antenna gain and inter and intra system RFI equivalent noise.

4-3.2.1.1 Step 1.1

Step 1.1 of the new methodology consists in computing the minimum recovered power $C_{min}(sig, op)$ from (Eq 4-3). $C_{min}(sig, op)$ depends on:

- The maximum power at earth surface of signal sig ,
- The minimum antenna gain for signal sig and receiver operation which is further discussed later,
- Implementation losses.

These three elements are recapped in Table 4-7.

Signal	Minimum power at Earth surface	Minimum Antenna Gain	Imp losses
GPS L1 C/A	-158.5	See Figure 4-11	2.5 (legacy) or 1.5 (DFMC)
Galileo E1	-157.9	See Figure 4-11	1.9
SBAS L1	-158.5	See Figure 4-11	2.5 (legacy) or 1.5 (DFMC)

Table 4-7: Parameters to compute minimum recovered signal power C_{min}

Receiver antenna gain

Let us first focus on the receiver antenna gain evolution along the specified 24h period . The receiver antenna gain is needed to compute $C_{min}(sig, op)$ from (Eq 4-3). The elevation of the 1st highest and 4th highest elevation angle GPS and Galileo SV (SV of interest to perform acquisition), as well as the elevation of the 6th highest elevation angle GPS and Galileo SV (section 4-2.1.2 indeed states that 6 GPS and Galileo SVs are sufficient to output a navigation solution compliant with positioning accuracy requirements) and the elevation of highest elevation angle SBAS SV, are plotted in Figure 4-10.

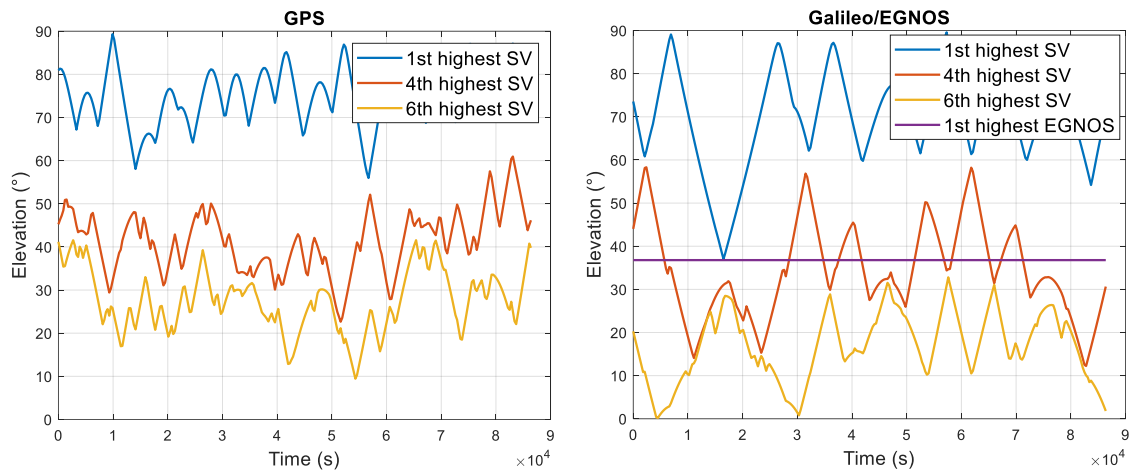


Figure 4-10: Evolution of the elevation of GPS, Galileo and EGNOS SV during period of jamming

Figure 4-10 shows that the elevation of satellites of interest evolves within the period of jamming. This evolution is observed from a variation of the minimum receiver antenna gain. In addition, Figure 4-10 indicates that at some instants, the 6th highest Galileo is below the 5° ICAO angle mask. That is due to the fact that considered Galileo almanacs, taken from GSA (European GNSS Agency) website [79], only indicates 22 available Galileo satellites. However, the complete Galileo constellation will have additional SVs, so that the elevation of the 6th highest SV is above the curve presented in Figure 4-10. In this analysis, the receiver is asked to be able to track either the 6th highest elevation angle SV, or a SV at 5° elevation, which either is the maximum.

Figure 4-11 represent the corresponding minimum receiver antenna gain, for legacy antenna of DO-301 and DFMC antenna of DO-373. In these figures, the minimum receiver antenna gain for Galileo SVs signals is clipped to the antenna gain at 5° as discussed before, -5.5dB for DO-301 legacy antenna and DO-373 DFMC antenna.

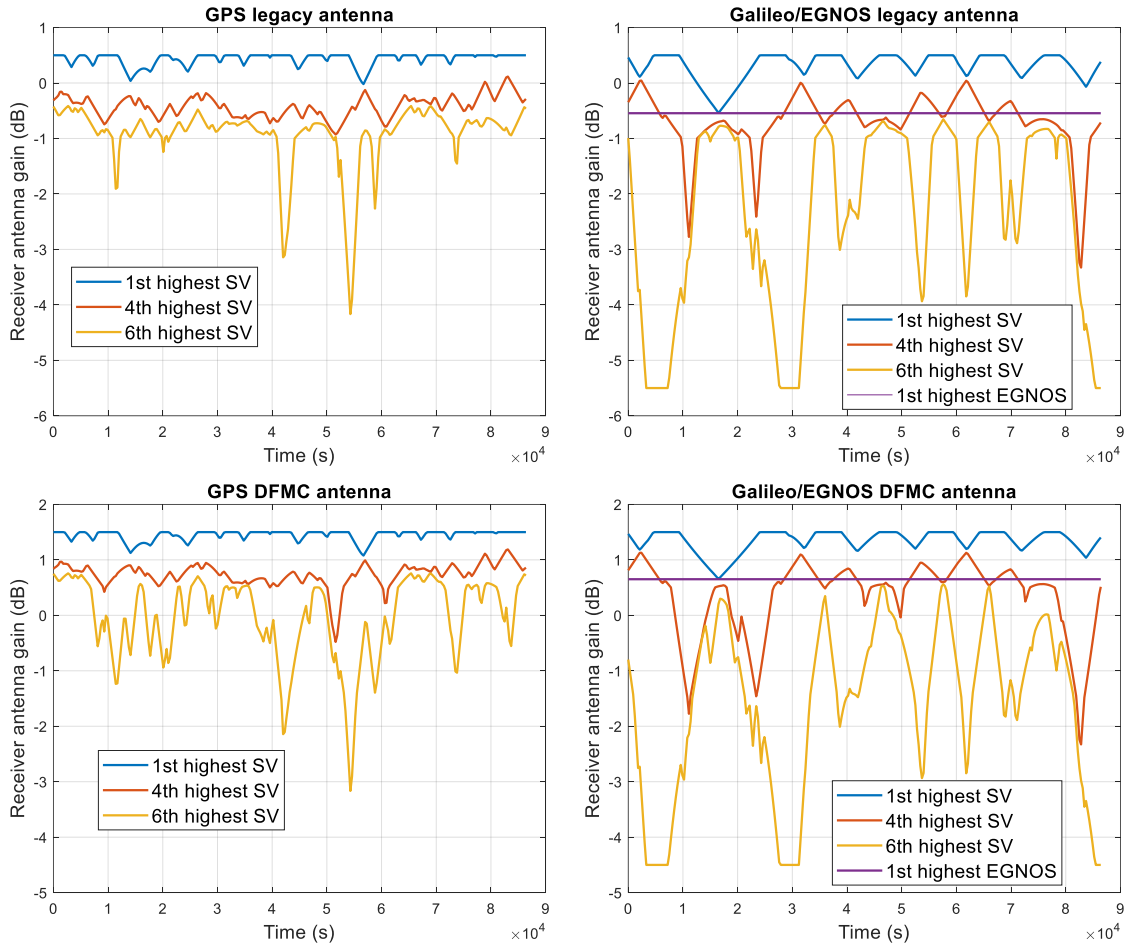


Figure 4-11: Evolution of the minimum legacy and DFMC antenna gain for GPS, Galileo and EGNOS SVs during jamming period

From Figure 4-11, it appears that receiver antenna gain for GPS SVs signals is more frequently higher than receiver antenna gain for Galileo SVs signals. This phenomenon can be explained by the fact that GPS constellation holds 31 SVs whereas Galileo constellation only has 22 SVs for the used almanac files.

4-3.2.1.2 Step 1.2

Step 1.2 consists in computing the effective noise in presence of aeronautical RFI from (Eq 4-7) and (Eq 4-8). The different inputs needed to compute (Eq 4-7) are recapped in Table 4-8.

	GPS L1C/A	Galileo E1	SBAS L1
AMSS equivalent noise (dBW/Hz)	-215.98	-215.98	-215.98
Case emission equivalent noise (dBW/Hz)	-208.98	-208.98	-208.98
Inter/intra system equivalent noise	Figure 4-12	Figure 4-12	Figure 4-12
Aeronautical equivalent noise	Computed with (Eq 4-8)	Computed with (Eq 4-8)	Computed with (Eq 4-8)
N_0 (dBW/Hz)	-201.5	-201.5	-201.5
N_{lim}	1 (legacy) or 1.5 (DFMC)	1 (legacy) or 1.5 (DFMC)	1 (legacy) or 1.5 (DFMC)

PDC_{lim}	0.01	0.01	0.01
$N_{0,eff,aero}$	Computed with (Eq 4-7)	Computed with (Eq 4-7)	Computed with (Eq 4-7)

Table 4-8: Main inputs to compute effective noise in presence of aeronautical RFI

Inter/intra system RFI equivalent noise

$I_{0,GNSS}$ is also time dependent according to (Eq 4-16). The evolution of $I_{0,GNSS}$ is computed by running GPS, Galileo, Beidou and SBAS constellations along the specified 24h period, and by calculating at each instant the inter and intra system equivalent noise with (Eq 4-11). The evolution of $I_{0,GNSS}$ during the jamming period is illustrated in Figure 4-12, for a BOC(1,1) Galileo E1 GNSS receiver and a BPSK(1) GPS L1C/A/SBAS L1 receiver. The double-sided bandwidth of the receiver is 12 MHz.

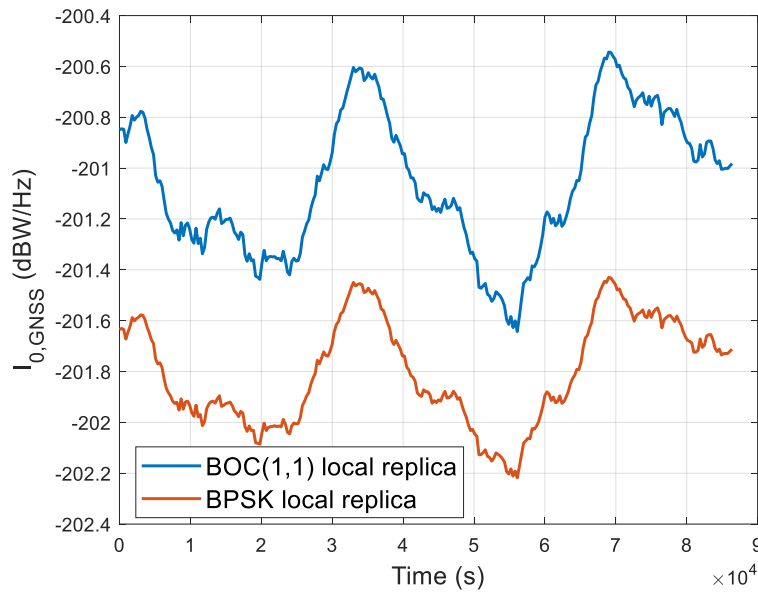


Figure 4-12: Evolution of $I_{0,GNSS}$ during jamming period

Figure 4-12 shows the $I_{0,GNSS}$ with a time variation of approximately 1dB during the observation period. Moreover, $I_{0,GNSS}$ is higher for Galileo E1 receiver, which local replica is BOC(1,1) modulated, than for GPS and SBAS receivers which local replica is BPSK(1) modulated. Note that inter and intra system RFI equivalent noise do not depend on the receiver generation (legacy or DFMC), as the same average antenna of Figure 4-5 is considered in both cases.

4-3.2.1.3 Step 1.3

The objective of step 1.3 is to compute the maximum tolerable equivalent noise from non-aeronautical sources for each pair of signal and receiver operations. For each pair of signal and receiver operation, the link budget margin is first derived from (Eq 4-12). Second, the maximum tolerable equivalent noise from non-aeronautical RFI sources is deduced from (Eq 4-13) and (Eq 4-14).

Link budget margin

The link budget margin, for each pair of signal and receiver operation, can be computed as a function of time from (Eq 4-12). The main inputs to derive link budget margins are recapped in Table 4-9.

$C_{min}(sig, op, t)$	Computed with inputs of Table 4-7 with
$N_{0,eff,aero}(t)$	Computed with inputs of Table 4-8 with
$C/N_{0Th}(sig, op)$	See Table 4-3

$Margin(sig, op, t)$	Computed with (Eq 4-12) and represented in Figure 4-13
----------------------	--

Table 4-9: Main inputs to derive link budget margins

Link budget margin results are plotted in Figure 4-13, considering the two receiver types (legacy and DFMC), for each pair of signal and operation.

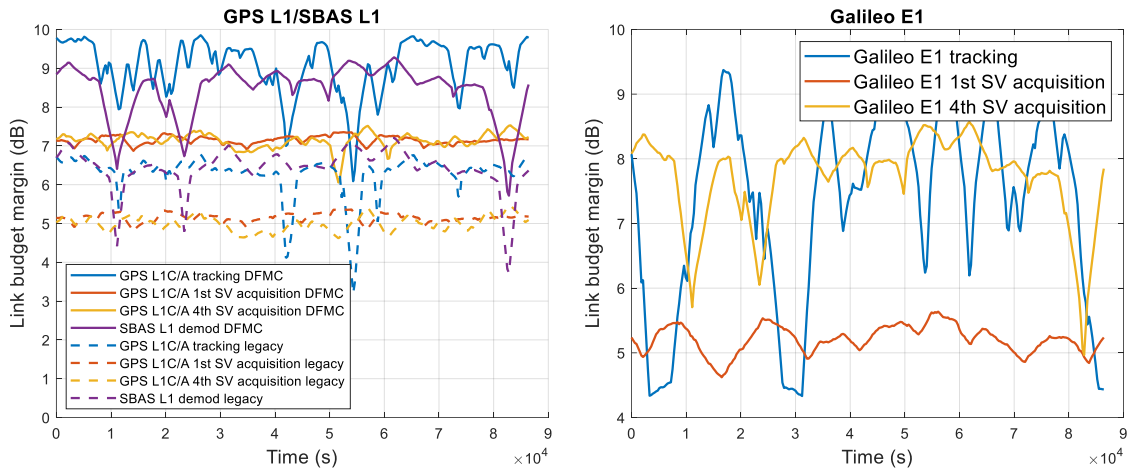


Figure 4-13: Link budget margin for the different pairs of signal and receiver operation

Link budget margins present strong time variations because of time dependence of $I_{0,GNSS}(t)$ and mainly of $G_{min}(t)$. In addition, Figure 4-13 highlights the significance of the receiver type, as the DFMC receiver capacity improves the link budget margin by at least 2 dB in comparison to the legacy receiver due to the receiver antenna gain and the implementation losses.

Maximum tolerable non-aeronautical equivalent noise

$I_{0,non\ aero,max}(sig, op, t)$ is deduced from the link budget margin using (Eq 4-13). The main inputs to derive $I_{0,non\ aero,max}(sig, op, t)$ are recapped in Table 4-10.

$N_{0,eff,aero}(t)$	Computed from inputs of Table 4-8 using (Eq 4-7)
$Margin(sig, op, t)$	Computed in Figure 4-13.
PDC_{lim}	0.01

Table 4-10: Main inputs to derive $I_{0,non\ aero,max}(sig, op, t)$

Figure 4-14 represents the maximum non-aeronautical RFI equivalent noise $I_{0,non\ aero,max}(sig, op, t)$ for the considered signal and receiver operation.

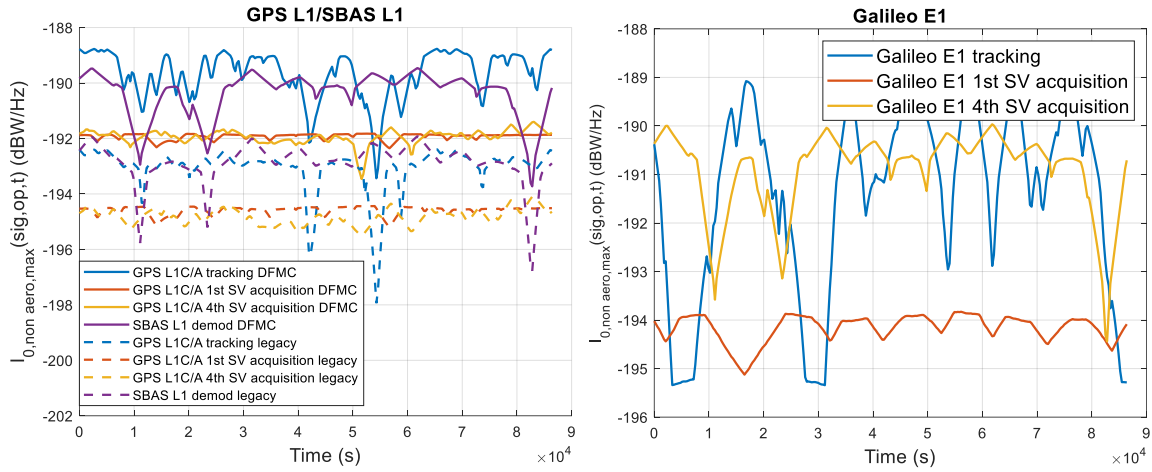


Figure 4-14: Maximum tolerable non aeronautical RFI equivalent noise for the different pairs of signal and receiver operation

Similar conclusions than the ones for link budget margins can be deduced from Figure 4-14:

- $I_{0,non\ aero,max}(sig, op, t)$ varies during the jamming period by several dB due to mainly the receiver antenna gain.
- DFMC receiver can tolerate a higher level of non-aeronautical RFI, mainly thanks to improved performance in terms of receiver antenna gain and tracking threshold.

For each signal and receiver operation, the minimum value of $I_{0,non\ aero,max}(sig, op, t)$ during the jamming period and derived according to (Eq 4-14) is reported in Table 4-11. Note that the minimum $I_{0,non\ aero,max}$ value for a given pair of signal x_1 and operation y_1 can be obtained, and is usually the case, at a different time epoch than the minimum value obtained for a given pair of signal x_2 and operation y_2 .

Receiver operation	GPS L1C/A			SBAS L1	Galileo E1		
	1st SV acquisition	4th SV acquisition	Tracking	Demodulation	1st SV acquisition	4th SV acquisition	Tracking
Legacy	-195.19	-195.51	-197.94	-192.69	-	-	-
DFMC	-192.35	-193.46	-193.44	-190.04	-195.12	-194.44	-195.34

Table 4-11: Maximum tolerable equivalent noise from non-aeronautical sources for the different GNSS signals and receiver operations

In comparison, the maximum non-aeronautical equivalent noise which serves as an input to derive RFI L1 masks is -200.5 dBW/Hz. The maximum tolerable equivalent noise values from RFI sources reported in Table 4-11 are higher than -200.5 dBW/Hz. This comparison illustrates one of the fundamental ideas of this new methodology: to compute the local and time dependent parameters, such as the antenna gain as well as the aeronautical equivalent additive white noise, $I_{0,aero,WB}$, to allow the accurate computation of the location and time-dependent $I_{0,non-aero}$ which should be higher than its worst global and no-time dependent value.

Table 4-12 details the link budget tables at instant $t(sig, op)$ associated to the values reported in Table 4-7 ($t(sig, op) = \underset{t}{\operatorname{argmin}} I_{0,non\ aero,max}(sig, op, t)$) and compares these link budgets to the link budgets from which the RFI mask is derived. The objective of such an analysis is to highlight parameters allowing to increase $I_{0,non\ aero,max}(sig, op)$. Investigated pairs of signal and receiver operation reported in Table 4-12 are:

- GPS L1C/A legacy receiver tracking,

- SBAS L1 legacy receiver tracking,
- GPS L1C/A DFMC receiver tracking,
- Galileo E1 DFMC receiver tracking.

These pairs of signal and receiver operation are indeed the most constraining cases for the different signals and types of receiver (legacy or DFMC).

Parameter (Units)	GPS L1C/A legacy tracking	GPS L1C/A DFMC tracking	Galileo E1 tracking	SBAS L1 demodulation	RFI mask
Min. SV Earth Surface Power (dBW)	-158,50	-158,50	-157,90	-158,50	-158,50
Receive Antenna Gain (dBic)	-4,17	-3,17	-4,50	-0,55	-5,50
Implementation Loss (dB)	2,50	1,50	1,90	2,50	2,50
RFI-free Post-Corr Carrier Pwr (dBW)	-165,17	-163,17	-164,30	-161,55	-166,50
I _{0aero} (dBW/Hz)	-201,19	-201,19	-200,05	-200,79	-201,89
N _{lim}	1,00	1,00	1,00	1,00	1,00
PDC	0,01	0,01	0,01	0,01	0,01
N _{0,EFF} dBW/Hz	-198,27	-198,27	-197,64	-198,05	-198,61
Effective C/N _{0eff} (dB-Hz)	33,10	35,10	33,34	36,51	32,11
C/N ₀ threshold (dB-Hz)	29,93	29,00	29,00	30,00	29,93
Link Margin (dB)	3,17	6,10	4,34	6,51	2,18
Remaining I ₀ tolerable (dBW/Hz)	-198,00	-193,43	-195,34	-192,69	-200,51

Table 4-12: Comparison of limiting link budget with RFI mask link budget

Table 4-12 shows the parameters allowing to improve the link budget margins. The key parameter is the receiver the antenna gain. While the RFI mask link budget is derived with an antenna gain corresponding to a 5° elevation SV, GPS L1C/A legacy tracking link budget antenna gain is increased by 1.33 dB considering a SV at a higher elevation. In addition, DFMC link budgets take advantage of lower C/N₀ thresholds and implementation losses.

The extra $I_{0,non-aero}$ margin can then be used to reduce the protection area since the receiver can locally and time-specific tolerate a higher value of $I_{0,non-aero}$.

4-3.2.2 Step 2: Non-aeronautical equivalent noise faced by victim receiver

This section applies point 2 of Figure 4-2. This section computes the non-aeronautical equivalent noise faced by the victim receiver. As detailed in section 4-2.2, three non-aeronautical RFI sources are faced by the victim receiver: on-board PEDs, terrestrial emitters and jamming signal.

On-board PEDs

As discussed in section 4-2.2.1, on board PEDs equivalent noise is estimated at -212.5 dBW/Hz. A M=6 dB safety margin is added, leading to $MI_{0,PED} = -206.5 \text{ dBW/Hz}$. Note that DO-235B [10] and DO-235C [6] consider that on-board PEDs may be operational only for aircraft operations above 2500 ft AMSL. This assumption is also applied in this analysis: for victim GNSS receiver altitude below 2500 ft AMSL, on-board PEDs are supposed to be switched off, and therefore, $MI_{0,PED} = 0 \text{ dBW/Hz}$.

Terrestrial emitters

Terrestrial emitters equivalent noise is estimated with the method presented in section 4-2.2.2. Figure 4-15 illustrates the terrestrial emitters equivalent noise for victim GNSS receiver located at 2000 ft and

around the jammer. The DFMC antenna maximum gain pattern at lower hemisphere has been considered to draw Figure 4-15.

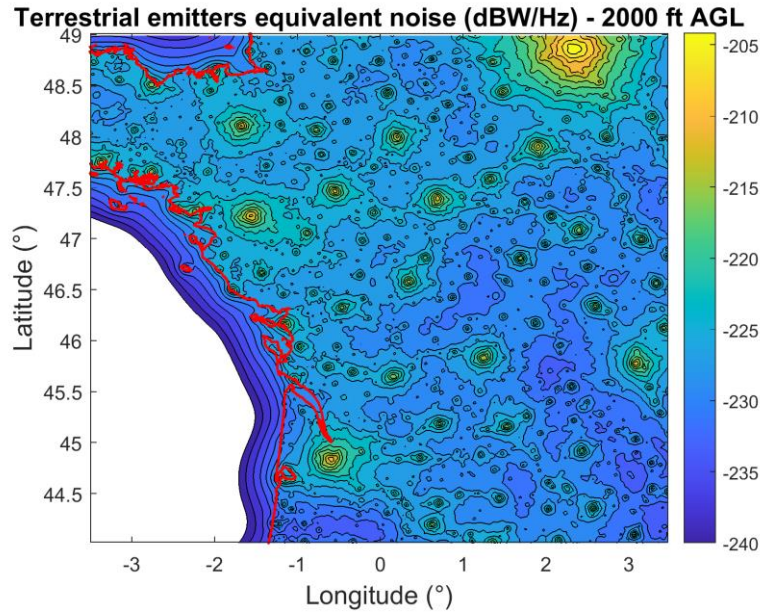


Figure 4-15: Terrestrial emitters equivalent noise (2000 ft AGL, not including 6 dB safety margin)

Figure 4-15 shows that terrestrial emitter equivalent noise is higher when the aircraft is above urban area, because the density of terrestrial emitters is higher even though the receiver antenna gain is evaluated near the nadir. Moreover, it can be noticed that the terrestrial emitter equivalent noise is null above the ocean since no terrestrial emitter would be visible from the victim receiver.

Despite not being illustrated here, the terrestrial emitter equivalent noise decreases when the aircraft altitude grows, even though the number of terrestrial sources in view increases with the aircraft altitude. The main reason for this decrease of $I_{0,terr}$ is the higher propagation losses when the aircraft altitude increases.

Jammer

Equivalent noise induced by jamming signal at a given position is computed from (Eq 4-25) and (Eq 4-26). Opposite to terrestrial emitters and on-board PEDs, the jamming EIRP is usually perfectly known. As a result, the addition of a safety margin is not required. The equivalent noise caused by the jamming signal is illustrated in Figure 4-16, supposing that the victim GNSS receiver altitude is 2000 ft. A DFMC antenna has been used to plot Figure 4-16. Moreover, the right part of Figure 4-16 also represents the aggregate non-aeronautical RFI equivalent noise, $I_{0,non-aero}$, at 2000 ft calculated from (Eq 4-15). Note that at this altitude, on-board PEDs are supposed to be switched off; therefore, the right part of Figure 4-16 is computed with only the addition of the jammer and the terrestrial emitters impact.

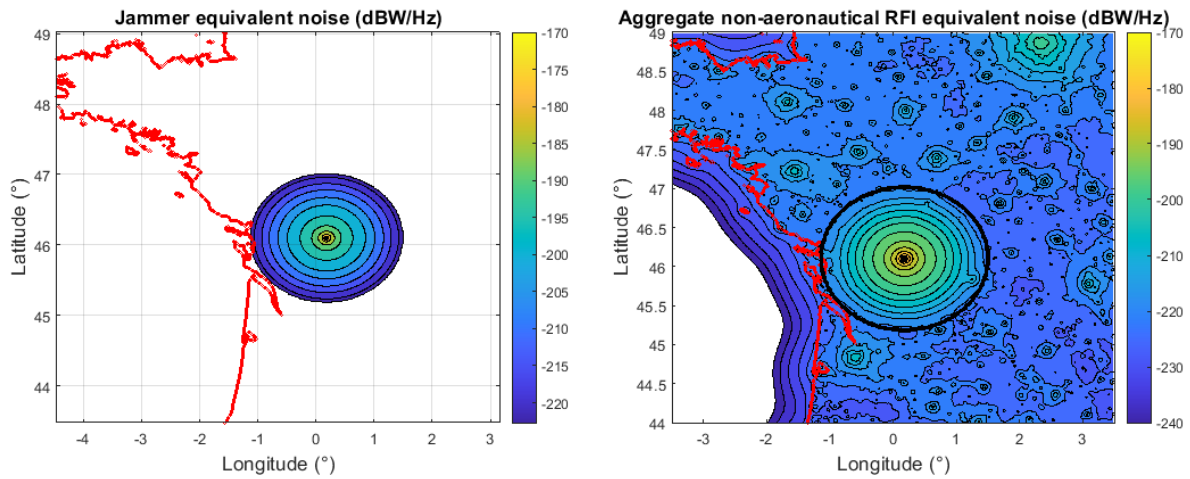


Figure 4-16: Jammer and aggregate non-aeronautical RFI equivalent noise

The large black circle in Figure 4-16 represents the state jammer radio line of sight radius R_{LOS} . It can be noticed from Figure 4-16 that when the GNSS receiver is close to the jammer (and at 2000 ft), the contribution of the jamming signal to $I_{0,non\ aero}$ is much higher than the contribution of terrestrial emitters. However, when the victim GNSS receiver is close to the radio horizon, the contribution of terrestrial emitters cannot be neglected.

4-3.2.3 Step 3: Protection radius

Finally, this section applies point 3 of Figure 4-2. The protection radius $r_{sig,op}(h)$, for each pair of signal and receiver operation, is computed for different altitudes h using (Eq 4-27). The evolution of $r_{sig,op}$ as a function of the aircraft altitude h is represented in Figure 4-17 for legacy and DFMC receivers.

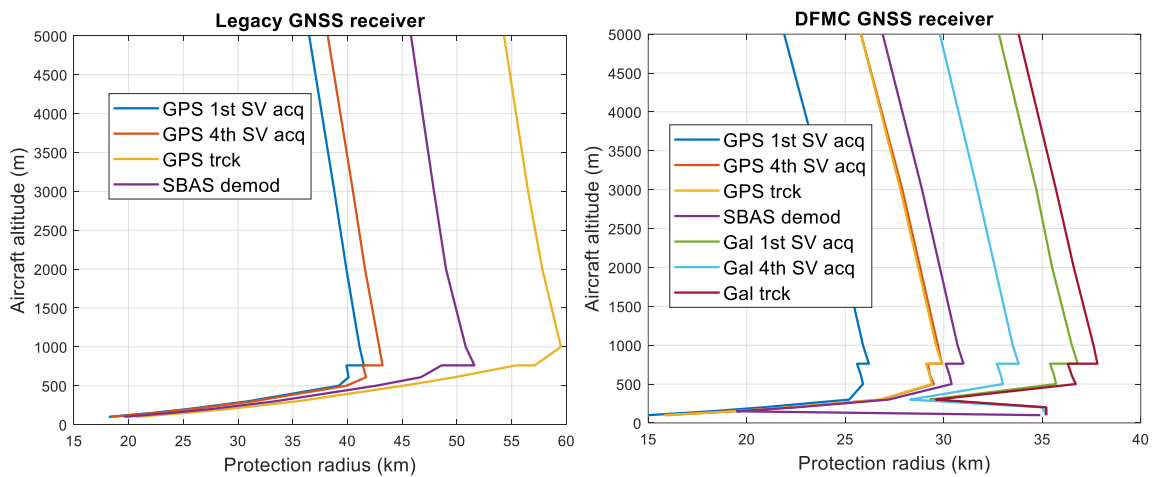


Figure 4-17: Protection radius for the different pairs of signal and receiver operation, for legacy and DFMC GNSS receivers

From Figure 4-17, it appears that the limiting pairs of signals and GNSS receiver operations are GPS L1C/A tracking and Galileo E1 tracking for legacy and DFMC GNSS receiver respectively. This observation may have been anticipated as these are the receiver operations with the lowest associated $I_{0,non\ aero,max}(sig,op)$. Remember that Galileo E1 link budgets are strongly penalized by the fact that the considered Galileo constellation only holds 22 SVs at the date of the jamming according to the almanacs issued by [79], whereas GPS constellation almanacs at the date of the jamming holds 31 SVs. Therefore, Figure 4-17 should not be interpreted as a lack of robustness of Galileo E1 receivers in comparison to GPS L1C/A receivers.

Table 4-13 recaps the protection radius for legacy and DFMC receivers which are obtained with the new methodology.

	Legacy receiver	DFMC receiver
Protection radius (km)	60	38

Table 4-13: Protection radius for DFMC and legacy receivers computed with the new methodology

4-3.3 Protection radius from RFI mask

For comparison purpose, the protection radius derived from RFI mask methodology with (Eq 4-2) is derived in this section. Two values are computed in this section:

- One protection radius for legacy GNSS receiver, derived with the legacy antenna pattern of Chapter 2 Figure 17.
- One protection radius for DFMC GNSS receiver, derived with the DFMC antenna pattern of Chapter 2 Figure 17.

Maximum receiver and jammer antenna gain needed as inputs of (Eq 4-2) are recapped in Table 4-14. Remember that the jammer antenna height is assumed to be 0 m, and therefore the jamming signal comes from below the aircraft. Thus, the lower hemisphere antenna pattern of Figure 2-18 is used, and the maximum antenna gain is obtained for an elevation angle of 0°. Moreover, as described in section 4-3.1, the transmitter antenna is supposed to be isotropic.

	Legacy receiver	DFMC receiver
Maximum receiver antenna gain (dB) $G_{Rx,max}$	-5	-6
Maximum transmitter antenna gain (dB) $G_{J,max}$	5	5

Table 4-14: Transmitter and receiver antenna gains for protection radius calculation with traditional method based on RFI masks

In addition, for a 50 MHz jamming signal considered in this analysis, the maximum power from non-aeronautical sources allowed by RFI mask is $C_{max} = -96.92 \text{ dBm}$. Using (Eq 4-1) with inputs of Table 4-14, the protection radius for legacy and DFMC GNSS receivers derived from RFI mask are recapped in Table 4-15.

	Legacy receiver	DFMC receiver
Protection radius (km)	116	103

Table 4-15: Protection radius derived from RFI masks

Comparing results of Table 4-13 and Table 4-15, it can be seen that the new method allows to strongly reduce the size of the protection area. Legacy receiver protection radius is indeed decreased from 116 km to 60 km, and DFMC receiver protection radius passes from 103 km to 38 km. Therefore, the new methodology allows to reduce by a factor 1.9 the protection radius for legacy receiver, and by a factor 2.7 the protection radius for DFMC receivers.

4-4 Conclusion

This chapter provides a methodology to derive a protection radius during state jamming operations. This work is motivated by a request of the French ANSP (Air Navigation Service Provider), since the observed impact radius of the jammer during state jamming operation was much lower than the radius predicted from the RFI mask.

A protection area is an airspace determined by the regulator and communicated to pilots on which GNSS minimum ICAO performance requirements may not be met. The fundamental idea of the method

proposed in this chapter to derive the protection area consists in a precise characterization of the RFI situation faced by the victim receiver. The protection area limit will be such that the aggregate RFI level is equal to the maximum RFI level tolerated by the receiver at the limits of this area. The three main steps of the method are recalled hereinafter:

- 1) A fine location and time-dependent C/N_0 link budget allows to determine how much non-aeronautical RFI can be tolerated by the receiver.
- 2) The aggregate location-dependent non-aeronautical RFI faced by the victim receiver is computed. Non-aeronautical RFI sources include portable electronic devices carried on-board by passengers, diverse ground sources and the jamming signal.
- 3) Protection area is derived. The protection area includes all positions for which the non-aeronautical RFI equivalent noise received by the victim aircraft exceed the non-aeronautical equivalent additive white noise level which can be tolerated to meet minimum ICAO performance requirements.

In the illustrative example presented above, the protection area is reduced by almost a factor 2 in comparison to the protected zone derived from the RFI mask method from legacy and DFMC receivers: from 116 km to 60 km for legacy receiver, and from 103 km to 38 km for DFMC receiver. Thanks to a higher elevation of the 6 SVs which are assumed to be sufficient to provide a valid GNSS service than the 5° elevation mask, the new methodology allows to reduce the protection area in comparison to the protection area derived with RFI mask. Also, DFMC equipment has more favorable antenna gain, implementation losses and tracking threshold than legacy equipment. This helps in reducing the protection area for DFMC GNSS receiver. As a way forward, this new methodology must be adapted in case of high jamming power, taking into account tropospheric reflection which is not considered here. For safety reasons and prior to be adopted, this method should be validated during a real jamming scenario, comparing the zone impacted in reality with the protection area derived with the new methodology.

Chapter 5: Impact of chirp RFI on civil aviation GNSS receiver performance

A new RFI source appeared several years ago, representing a threat for civil aviation GNSS service. This new RFI source is represented by time dependent frequency signatures, generically considered here as chirp signals, such as emitted for example by Portable Privacy Devices (PPD). PPD are low cost GNSS jammers. They are typically used by drivers to avoid having the position of the driven vehicle tracked with a GNSS logger. The objective of such an action can be for example to obfuscate geolocation evidence related to unauthorized activity, to avoid paying toll charges, or to protect the driver's private life. In most countries, buying and using a PPD is illegal. However, buying PPD online is very cheap and easy. Moreover, PPD just requires a cigarette lighter socket to be powered and, as a consequence, can be used in all types of vehicles.

Because of the GNSS's vulnerability to RFI and of the low price of PPD jammers, jamming situations involving PPDs are increasingly observed. [47] lists RFI encountered between February 2016 and October 2018, in a wide diversity of observation places. In particular, more than 600 monthly RFI events in an airport environment were reported where such events could very likely be accounted as intentional jamming events, with a consequent threat on the aircrafts' flight safety. In [48], several jamming situations impacting civil aviation were analyzed. In particular at Newark airport (New Jersey) from March 2009 to April 2011, the Ground Based Augmentation System (GBAS) station was frequently jammed by a PPD installed on a truck traveling near the airport [49]. Another example of the impact of PPD on civil aviation took place in Nantes (France) in April 2017. A PPD in a parked car was transmitting a strong enough jamming signal to impact GNSS receiver onboard aircrafts parked at the closest gates, forcing the airport to tow some aircrafts to remote locations for startup.

The objective of this chapter is to theoretically predict the impact of chirp RFI on civil aviation GNSS receiver performances. The first performance indicator considered in this chapter is the C/N_0 . This approach assumes that the impact of chirp RFI is equivalent to the impact of an additive white noise. However, it will be highlighted that C/N_0 indicator performance may not be relevant in some particular situations of stationarity of the chirp RFI compared to the GNSS signal. To address these situations, code and phase tracking accuracy in presence of chirp RFI are theoretically derived to analyze the impact of chirp RFI on pseudo-range measurements.

This chapter is divided in three parts. First, a mathematical model of chirp RFI is detailed in great depth based on observation reported in literature. Second, impact of chirp RFI on C/N_0 indicators is mathematically predicted, and this prediction is compared to observations issued from simulations run using a Matlab software receiver and an IFEN receiver. Identifying situations for which C/N_0 is not a relevant indicator to characterize the impact of chirp RFI on GNSS receiver performances, a mathematical model of code and carrier tracking errors in presence of chirp RFI is third developed for these situations.

5-1 Mathematical model of chirp RFI signal

The objective of this section is to provide a mathematical model of the linear sweep PPD-like RFI at the output of the radio frequency front-end (RFFE) block of a victim GNSS receiver. For simplification purposes, the effect of the AGC/ADC is not considered, assuming the aggregate received signal power remains in the linear operating region of the receiver, and the C/N_0 degradation due to AGC/ADC in

presence of this RFI (quantization noise power) can be modeled as a constant because AGC/ADC is operating around its optimum setting. First, an analytical expression of a PPD-like signal model is proposed. Second, impact of propagation channel on chirp RFI signal is investigated. Third, the combined RF/IF filter impact and frequency down-conversion are analyzed in the particular case where the receiver bandwidth is larger than the RFI bandwidth. Fourth, the 2nd order wide sense stationarity of the chirp filter at the RFFE output is analyzed.

5-1.1 Mathematical model for linear sweep CW signal

As detailed in Chapter 2 section 2-5.3.2, chirp signals are characterized by their periodic instantaneous frequency. This chapter will focus on a chirp signal whose instantaneous frequency depicts a saw-tooth pattern. This type of chirp RFI signature is indeed one of the most commonly detected in RFI surveillance project such as [47]. The transmitted chirp PPD-like signal at input of jamming emitter antenna can be mathematically modeled as shown in (Eq 5-1).

$$s_{PPD}(t) = A_J \cos \left(2\pi \int_{t_0}^t f_i(u) du + \varphi_{J0} \right) \quad (\text{Eq 5-1})$$

- A_J is the jamming signal amplitude at emitter antenna input.
- f_i is the instantaneous cosine frequency, varying with time, usually periodic and following a predetermined pattern over time.
- φ_{J0} is the initial phase of the emitted jamming signal, assumed as random in this work, t_0 is the reference time of the integration, supposed random and uniformly distributed within one period of the frequency pattern. The integral between t_0 and t is equivalent to the integral between 0 and t , plus an additional random phase. Therefore, an equivalent signal is given by (Eq 5-2).

$$s_{PPD}(t) = A_J \cos \left(2\pi \int_0^t f_i(u) du + \varphi_0 \right) \quad (\text{Eq 5-2})$$

φ_0 is a random phase which is uniform on the interval $[0; 2\pi]$.

As a difference with (Eq 2-89), the received signal of (Eq 5-2) contains a random phase φ_0 . From (Eq 5-2), it can be seen that $s_{PPD}(t)$ is a periodic signal made of a periodic sine wave pattern with periodic instantaneous frequency, but with random initial carrier phase offset incorporating the effect of a random initial integration start.

Note that in addition to the pre-determined frequency pattern described above, the emitted chirp signal will also be affected by some frequency offset reflecting the overall jammer oscillator quality that will be modeled. Also, phase noise will be present, but this effect is not modeled in this paper.

For simplicity in the coming calculation, let us define the chirp frequency signature depicting a saw-tooth pattern by (Eq 5-3).

$$f_{i_0}(u) = -\frac{B_{ini}}{2} + \frac{B_{ini}}{T_{ini}} \left(u - \left\lfloor \frac{u}{T_{ini}} \right\rfloor T_{ini} \right) \quad (\text{Eq 5-3})$$

$\lfloor . \rfloor$ is the flooring integer part operator. B_{ini} is the swept double-sided bandwidth and T_{ini} is the sweep duration. T_{ini} is therefore fundamentally defined as the repetition period of the periodic pattern of the instantaneous frequency at the output of the transmitter, but as a consequence it is also the duration of the chirp sine wave periodic pattern of $s_{PPD}(t)$ defined in (Eq 5-2).

Note that f_{i_0} , which is the periodic frequency function of time of the PPD, is deterministic, and is equal to $-\frac{B_{ini}}{2}$ at time $u = 0$.

For a linear chirp signal, the instantaneous frequency at the output of the transmitter is mathematically expressed by (Eq 5-4).

$$f_i(t) = f_0 + \Delta f_j^c + f_{i_0}(t) \quad (\text{Eq 5-4})$$

$f_0 = 1575.42 \text{ MHz}$ is the L1 carrier frequency. Δf_j^c denotes the intrinsic jammer frequency offset to L1, since the PPD signal may not be centered at L1 by design or by implementation. This offset Δf_j^c is considered as constant in this work.

The emitted signal model is therefore given by (Eq 5-5).

$$s_{PPD}(t) = A_j \cos \left(2\pi(f_0 + \Delta f_j^c)t + 2\pi \int_0^t f_{i_0}(u)du + \varphi_0 \right) \quad (\text{Eq 5-5})$$

Note that at this stage, this emitted signal model does not include carrier doppler offset, modulation doppler offset, nor any time offset for the frequency pattern. All these effects are assumed to arise after propagation to the victim receiver and will be introduced in the next section.

5-1.2 Impact of propagation channel on chirp RFI signal

At the output of the victim GPS L1C/A receiver passive radiating antenna element, using a simplified propagation channel model with constant group delay across jammer bandwidth and no additional initial carrier phase offset, the received PPD signal can be mathematically expressed as an attenuated and delayed version of $s_{PPD}(t)$ and is expressed in (Eq 5-6):

$$s_{PPD,in}(t) = a \cdot s_{PPD}(t - \tau(t)) \quad (\text{Eq 5-6})$$

a is the attenuation term due to propagation losses as well as emitter antenna gain products (depending on viewing angles). $\tau(t)$ is the propagation delay. The time variation of $\tau(t)$ induces the Doppler frequency offset. By definition, the Doppler frequency offset of the jammer signal is related to the propagation delay according to (Eq 5-7).

$$f_{J,dopp} = -f_0 \frac{d\tau(t)}{dt} \quad (\text{Eq 5-7})$$

In this chapter, the Doppler frequency offset $f_{J,dopp}$ of the jammer signal is assumed to be constant. This is a reasonable assumption for civil aviation operations as long as the analysis period is below a few tens of seconds. Therefore, the propagation delay can be expressed as a function of the chirp signal Doppler frequency offset and carrier frequency as in (Eq 5-8) using a first order approximation and denoting δ_{ini} as the initial time delay offset.

$$\tau(t) = -\frac{f_{J,dopp}}{f_0}t + \delta_{ini} \quad (\text{Eq 5-8})$$

δ_{ini} is the propagation delay at instant $t=0$. δ_{ini} is also the time offset of the periodic transmitted signal pattern $s_{PPD}(t)$. δ_{ini} is here modeled as a random variable, uniformly distributed over $[0; T_{ini}]$ and independent from φ_0 . As a consequence, the instantaneous frequency pattern, even though its shape is deterministic, is modeled as a random function of time.

Let us introduce $C_{J,in} = \frac{(aA_j)^2}{2}$, the average jammer power at the victim GNSS receiver passive antenna input. Denoting $\alpha = -\frac{f_{J,dopp}}{f_0}$, $s_{PPD,in}$ can thus be re-expressed by (Eq 5-9).

$$s_{PPD,in}(t) = \sqrt{2C_{J,in}} \cos \left(\begin{aligned} &2\pi(f_0 + \Delta f_j^c)(1 - \alpha)t + 2\pi \int_0^{t(1-\alpha) - \delta_{ini}} f_{i_0}(u) du \\ &+ \varphi_0 - 2\pi(f_0 + \Delta f_j^c)\delta_{ini} \end{aligned} \right) \quad (\text{Eq 5-9})$$

We can see that in this model the propagation channel induces an initial time offset δ_{ini} on the frequency pattern, and the time variation of the group delay introduces the doppler offset or equivalently a scaling factor $1 - \alpha$ on the time scale that will significantly impact the coherence between the chirp and the locally generated GNSS signal.

First, assuming the inherent jammer frequency offset to L1 is negligible in front of L1, $\Delta f_j^c \ll f_0$, $(f_0 + \Delta f_j^c)(1 - \alpha)$ can be approximated by $f_0 + \Delta f_j^c + f_{J,dopp}$.

Let us denote $\varphi_\delta = 2\pi(f_0 + \Delta f_j^c)\delta_{ini}$.

Second, performing a variable change $u' = \frac{u}{1-\alpha}$ in the integral term, (Eq 5-9) can be re-expressed as in (Eq 5-10).

$$s_{PPD,in}(t) = \sqrt{2C_{J,in}} \cos \left(\begin{aligned} &2\pi(f_0 + \Delta f_j^c + f_{J,dopp})t + \\ &t \frac{\delta_{ini}}{1-\alpha} \\ &2\pi(1 - \alpha) \int_0^{t \frac{\delta_{ini}}{1-\alpha}} f_{i_0}((1 - \alpha)u) du + \varphi_0 - \varphi_\delta \end{aligned} \right) \quad (\text{Eq 5-10})$$

The chirp signature pattern at the victim receiver antenna input is therefore in the inner part of the integral and is given by (Eq 5-11).

$$\begin{aligned} f_{i_0,in}(u) &= (1 - \alpha)f_{i_0}((1 - \alpha)u) \\ &= -\frac{B_{ini}(1 - \alpha)}{2} + \frac{B_{ini}(1 - \alpha)}{T_{ini}} \left((1 - \alpha)u - \left\lfloor \frac{(1 - \alpha)u}{T_{ini}} \right\rfloor T_{ini} \right) \\ &= -\frac{B_{ini}(1 - \alpha)}{2} + \frac{B_{ini}(1 - \alpha)}{T_{ini}/(1 - \alpha)} \left(u - \left\lfloor \frac{u}{T_{ini}/(1 - \alpha)} \right\rfloor \frac{T_{ini}}{1 - \alpha} \right) \end{aligned} \quad (\text{Eq 5-11})$$

As a consequence, the impact of the time variation of the group delay, that could for example be due to the relative motion of the transmitter with respect to the receiver, is a modification of the sweep period of the chirp spectrogram pattern and a modification of the swept bandwidth.

Let us now denote $T_{sweep} = \frac{T_{ini}}{1-\alpha}$ the period of the chirp instantaneous frequency of the chirp pattern at the victim GNSS receiver antenna output, $B = B_{ini}(1 - \alpha)$ the chirp bandwidth at the victim receiver antenna output and $\delta = \frac{\delta_{ini}}{1-\alpha}$. δ follows a uniform distribution over $[0, T_{sweep}]$. Then, the instantaneous frequency of the chirp signal at the antenna input is expressed in (Eq 5-12).

$$\begin{aligned} f_{j,in}(t) &= f_0 + \Delta f_j^c + f_{J,dopp} + f_{i_0,in}(t - \delta) \\ &= f_0 + \Delta f_j^c + f_{J,dopp} - \frac{B}{2} + \frac{B}{T_{sweep}} \left(t - \delta - \left\lfloor \frac{t - \delta}{T_{sweep}} \right\rfloor T_{sweep} \right) \end{aligned} \quad (\text{Eq 5-12})$$

5-1.3 Impact of RFFE block on chirp RFI

As presented in Chapter 2 section 2-3.1, the RFFE block can be equivalently modeled as a cascading of four operations on the received signal: analog to digital conversion, amplification, down-conversion and filtering. The amplification is characterized by a gain G_r which takes into account amplification brought by antenna and LNA. Let us denote $C_J = G_r C_{J,in}$ the chirp RFI signal power at the RFFE block output. The down-conversion module translates the signal around an intermediate frequency f_{IF} . In

this chapter, it is assumed that the targeted bandwidth of the jammer B_{ini} (and by extension B) is expected to be narrower than GPS L1C/A receiver bandwidth, and thus, RF/IF filter does not impact the spectrum of the chirp signal.

As a consequence, the instantaneous frequency of the chirp signal at the RFFE block output can be expressed as in (Eq 5-13).

$$f_{J,RFout}(t) = f_{IF} + \Delta f_J^c + f_{J,dopp} + f_{i_0,in}(u - \delta) \quad (\text{Eq 5-13})$$

Assuming that $t - \delta \in [MT_{sweep}, (M + 1)T_{sweep}]$, it is possible to simplify the expression of $S_{PPD,RFout}$ computing the integral term in (Eq 5-10). The simplified result is given in (Eq 5-14).

$$S_{PPD,RFout}(t) = \sqrt{2C_J} \cos \left(\begin{array}{l} 2\pi(f_{IF} + \Delta f_J^c + f_{J,dopp})t \\ +\pi \frac{B}{T_{sweep}} (t - \delta - MT_{sweep})^2 \\ -\pi B(t - \delta - MT_{sweep}) + \varphi_0 - \varphi_\delta \end{array} \right) \quad (\text{Eq 5-14})$$

To summarize, the chirp transmitted signal at the RFFE block output is modeled as a random signal, due to the presence of two independent random parameters: the phase φ_0 and the time offset of the frequency pattern δ . Figure 5-1 shows a plot of $f_{J,RFout}(t)$ and illustrates the influence of δ . In Figure 5-1-a, $\delta = 0$ and the instantaneous frequency pattern starts at $t = 0$. In Figure 5-1-b, $\delta \neq 0$, and the sweep starts at $t = \delta$.

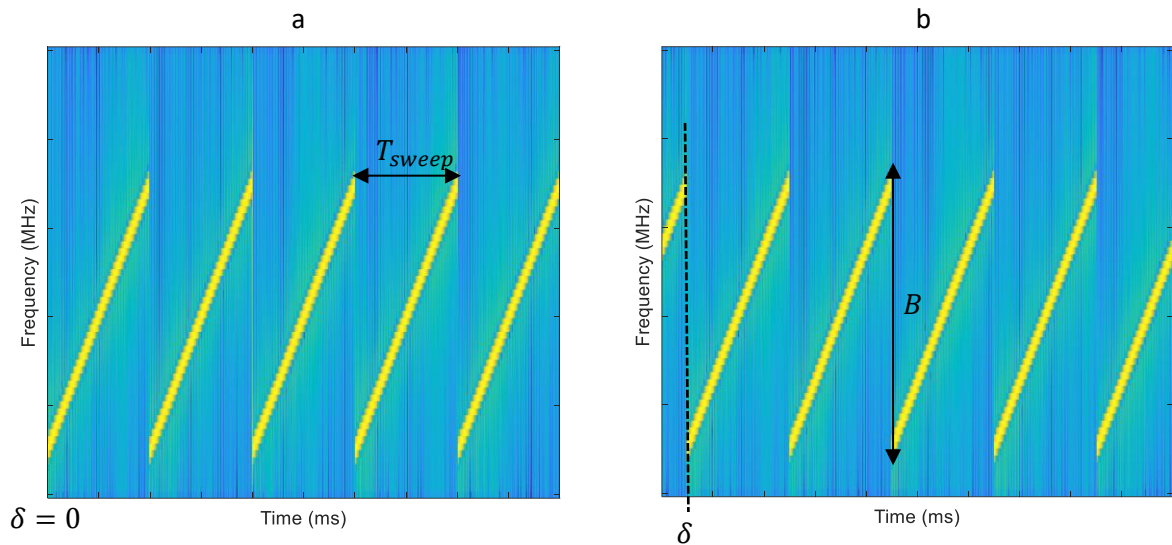


Figure 5-1: Plot of $f_{J,RFout}(t)$ and influence of the random time offset δ on the chirp signal, and illustration of T_{sweep} and B .

Figure 5-2 illustrates the influence of the random initial phase φ_0 . Notice that the signal phase is always continuous, even between the end and the beginning of the pattern, even though the phase and the signal are not derivable at this point.

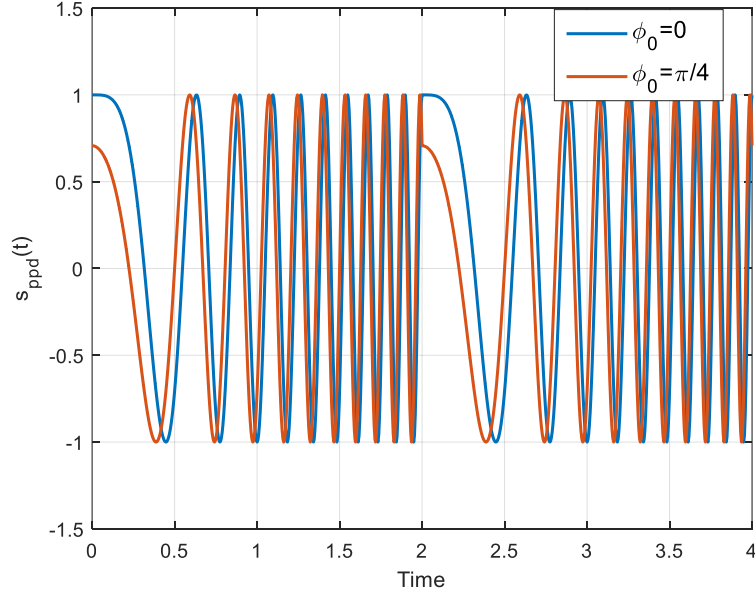


Figure 5-2: Influence of ϕ_0 on the chirp signal

5-1.4 Second order wide sense stationarity analysis

The possible wide sense stationarity of the random chirp signal at the RFFE output is now investigated. The wide sense stationarity of the chirp signal is here demonstrated, considering the assumptions on the random chirp signal detailed above. By definition, a random signal is 2nd order wide sense stationary if

1. Condition 1: Its mean power is finite.
2. Condition 2: Its mean value $\mathbb{E}[s_{PPD,RF_{out}}(t)]$ does not depend on t .
3. Condition 3: Its autocorrelation $R_s(t, \tau) = \mathbb{E}[s_{PPD,RF_{out}}(t)s_{PPD,RF_{out}}(t - \tau)]$ does not depend on t .

The demonstration that the chirp signal satisfies the three conditions is developed hereinafter.

Condition 1:

Performing a calculation similar to the calculation of the mean power of a pure sine wave with 2π -uniform random phase, it is possible to prove that the mean power of the random chirp signal $s_{PPD,RF_{out}}(t)$ is $A_f^2/2$. The calculation is not detailed here for simplicity matters. Since the mean power of the random chirp jamming signal is finite, condition 1 is fulfilled.

Condition 2:

Let us define in (Eq 5-15) the instantaneous phase of the random chirp signal $s_{PPD,RF_{out}}(t)$ defined in (Eq 5-10).

$$\theta_\delta(t) = 2\pi(f_{IF} + \Delta f_j^c + f_{J,dopp})t + 2\pi \int_0^{t-\delta} f_{i_0,in}(u)du \quad (\text{Eq 5-15})$$

As an important remark, the instantaneous phase $\theta_\delta(t)$ is continuous over time. The mean value of the chirp signal is derived in (Eq 5-16).

$$\begin{aligned}\mathbb{E}[S_{PPD,RF_{out}}(t)] &= \mathbb{E}[\mathbb{E}(S_{PPD,RF_{out}}(t)|\delta)] \\ &= \sqrt{2C_J} \mathbb{E} \left[\frac{1}{2\pi} \int_0^{2\pi} \cos(\theta_\delta(t) + \varphi_0 - \varphi_\delta) d\varphi_0 \right] = 0\end{aligned}\quad (\text{Eq 5-16})$$

$\mathbb{E}[S_{PPD,RF_{out}}(t)]$ is constant and equal to 0 for all instant, so Condition 2 is verified.

Condition 3:

The chirp signal can be re-written under its Rice representation, isolating the carrier terms (central frequency $f_0 + \Delta f_j^c$ and initial phase φ_0) from the chirp frequency signature $f_{i_0,in}$, defined by (Eq 5-11).

The chirp signal can thus be re-expressed by (Eq 5-17).

$$\begin{aligned}S_{PPD,RF_{out}}(t) &= \sqrt{2C_J} \cos \left(2\pi(f_{IF} + \Delta f_j^c + f_{J,dopp})t + 2\pi \int_0^{t-\delta} f_{i_0,in}(u) du + \varphi_0 - \varphi_\delta \right) \\ &= \sqrt{2C_J} \cos \left(2\pi \int_0^{t-\delta} f_{i_0,in}(u) du \right) \cos(2\pi(f_{IF} + \Delta f_j^c + f_{J,dopp})t + \varphi_0 - \varphi_\delta) \\ &\quad - \sqrt{2C_J} \sin \left(2\pi \int_0^{t-\delta} f_{i_0,in}(u) du \right) \sin(2\pi(f_{IF} + \Delta f_j^c + f_{J,dopp})t + \varphi_0 - \varphi_\delta)\end{aligned}\quad (\text{Eq 5-17})$$

Due to the fact that $f_{i_{RF}}$ is periodic and centered around 0, the functions $t \rightarrow \cos \left(2\pi \int_0^t f_{i_0,in}(u) du \right)$ and $t \rightarrow \sin \left(2\pi \int_0^t f_{i_0,in}(u) du \right)$ are periodic with period T_{sweep} . Therefore, they can be expressed as in (Eq 5-18).

$$\begin{aligned}\cos \left(2\pi \int_0^t f_{i_0,in}(u) du \right) &= \sum_{k=-\infty}^{+\infty} c_w(t - kT_{sweep}) \\ \sin \left(2\pi \int_0^t f_{i_0,in}(u) du \right) &= \sum_{k=-\infty}^{+\infty} s_w(t - kT_{sweep})\end{aligned}\quad (\text{Eq 5-18})$$

With

$$c_w(t) = \begin{cases} \cos \left(2\pi \int_0^t f_{i_0,in}(u) du \right) & \text{if } t \in [0; T_{sweep}] \\ 0 & \text{else} \end{cases}$$

And

$$s_w(t) = \begin{cases} \sin \left(2\pi \int_0^t f_{i_0,in}(u) du \right) & \text{if } t \in [0; T_{sweep}] \\ 0 & \text{else} \end{cases}$$

Therefore, (Eq 5-17) can be re-written by (Eq 5-19).

$$\begin{aligned}
s_{PPD,RF_{out}}(t) = & \sqrt{2C_j} \cos(2\pi(f_{IF} + \Delta f_j^c + f_{J,dopp})t + \varphi_0 - \varphi_\delta) \sum_{k=-\infty}^{+\infty} c_w(t - \delta - kT_{sweep}) \\
& - \sqrt{2C_j} \sin(2\pi(f_{IF} + \Delta f_j^c + f_{J,dopp})t + \varphi_0 - \varphi_\delta) \sum_{k=-\infty}^{+\infty} s_w(t - \delta - kT_{sweep})
\end{aligned} \tag{Eq 5-19}$$

The calculation of the autocorrelation is performed in Appendix C. It is expressed in (Eq 5-20).

$$R_{s_{PPD,RF_{out}}}(\tau) = C_j \cos(2\pi(f_{IF} + \Delta f_j^c + f_{J,dopp})\tau) \left[\begin{aligned} & \frac{1}{T_{sweep}} \sum_{m'=-\infty}^{+\infty} R_{c_w}(\tau + m'T_{sweep}) \\ & + \frac{1}{T_{sweep}} \sum_{m'=-\infty}^{+\infty} R_{s_w}(\tau + m'T_{sweep}) \end{aligned} \right] \tag{Eq 5-20}$$

As a consequence, the autocorrelation of the chirp signal does not depend on time, t . Therefore, Condition 3 is satisfied. The chirp signal at the RFE output is thus 2nd order wide sense stationary.

5-2 Theoretical impact of chirp RFI on C/N_0

Signal to noise power spectrum density ratio, C/N_0 , is a significant indicator characterizing the capability of any receiver to process the nominal GNSS signal. Indeed, for spectrum compatibility analysis, ICAO and RTCA GNSS receiver requirements on message demodulation, pseudorange accuracy and acquisition performances are assumed to be met when the GNSS signals received within a defined RFI environment are above certain C/N_0 thresholds, $C/N_{0,th}$ [10]. In other words, it is assumed that, in the presence of well-defined RFI, when the airborne effective received GNSS signal C/N_0 exceeds a particular C/N_0 threshold, it is guaranteed that each basic operation of the receiver (acquisition, tracking, demodulation) meets its required performance.

C/N_0 degradation in presence of an interference is studied in particular in [30] or [31], and [32] indicates that C/N_0 monitoring is among the main methods to detect jamming situation, in particular in the civil aviation domain. It is thus important to model the RFI induced C/N_0 degradation compared to the situation of thermal noise only, and to quantify this degradation as a function of the jammer parameters. Consequently, C/N_0 is a relevant indicator to characterize the GNSS receiver performance in presence of chirp RFI.

This section is divided in two parts. First, the power spectral density of a chirp signal, which must be known to compute the equivalent input noise defined in Chapter 2 section 4.3.1, is theoretically derived. Second, the equivalent input noise induced by a chirp RFI is computed as a function of its characteristics: T_{sweep} , B and Δf_j^c .

5-2.1 Power spectral density of chirp signal

This section focuses on the computation of the power spectral density of the linear chirp PPD interference in order to compute the SSC between the chirp signal and the GNSS signal receiver local replica as shown in (Eq 2-79). Let us first suppose that the RFI power spectral density at baseband term $S_{j,BB}$ in (Eq 2-79) is centered, ie $\Delta f_j^c + f_{J,dopp} = 0$.

As demonstrated in section 5-1.4, the chirp signal at the RFE output is 2nd order wide sense stationary and its autocorrelation has been expressed in (Eq 5-20). According to Wiener-Kinchin theorem, the power spectral density of the chirp signal will be deduced by computing the Fourier transform of the autocorrelation and can be expressed by (Eq 5-21).

$$S_{SPPD,RFout}(f) = C_J \left(\frac{1}{T_{sweep}} (|C_w(f)|^2 + |S_w(f)|^2) \sum_{m=-\infty}^{+\infty} e^{i2\pi f m T_{sweep}} \right) * \frac{\delta(f - f_{IF}) + \delta(f + f_{IF})}{2} \quad (\text{Eq 5-21})$$

The sum term corresponds to the power spectral density of a dirac comb. Therefore, (Eq 5-21) can be re-written by (Eq 5-22).

$$S_{SPPD,RFout}(f) = C_J \left[\sum_{m=-\infty}^{+\infty} c_m \delta\left(f - \frac{m}{T_{sweep}}\right) \right] * \frac{\delta(f - f_{IF}) + \delta(f + f_{IF})}{2} \quad (\text{Eq 5-22})$$

$$\text{With } c_m = \frac{1}{T_{sweep}^2} \left(\left| C_w\left(\frac{m}{T_{sweep}}\right) \right|^2 + \left| S_w\left(\frac{m}{T_{sweep}}\right) \right|^2 \right).$$

C_w and S_w are respectively the Fourier transform of the windowed truncated cosine and sine basic chirp functions c_w and s_w which are defined in section 5-1.4 (Eq 5-18).

Expressions for C_w and S_w can be derived, as shown in Appendix D. The power spectral density of the chirp jammer can be simplified as in (Eq 5-23).

$$S_{SPPD,RFout}(f) = C_J \left[\sum_{m=-\infty}^{+\infty} c_m \delta\left(f - \frac{m}{T_{sweep}}\right) \right] * \frac{\delta(f - f_{IF}) + \delta(f + f_{IF})}{2} \quad (\text{Eq 5-23})$$

As expected, since the chirp signal $s_{PPD}(t)$ at the receiver antenna output is periodic, its power spectral density is a line spectrum. Each line is regularly spaced with its neighbors by $1/T_{sweep}$.

The power spectral density of the interference at baseband is given in (Eq 5-24) for a linear chirp signal.

$$S_{SPPD,BB}(f) = 2C_J \left[\sum_{m=-\infty}^{+\infty} c_m \delta\left(f - \frac{m}{T_{sweep}}\right) \right] \quad (\text{Eq 5-24})$$

Intuitively, the impact of the chirp interference will be attenuated if the RF front-end filter bandwidth is narrower than the chirp interference bandwidth, as the chirp signal will be rejected during the time period where its instantaneous frequency is outside the RF/IF filter band. In this case, the PPD interference acts as a pulsed interference when assuming a perfect square RF/IF filter, and the equivalent noise power spectral density expression, I_0 , would be different than what is presented in (Eq 2-85) (see [12]). In order to bound the PPD interference impact on the GNSS receiver, the RF/IF front-end filter is supposed to be much wider than the interference bandwidth in this chapter.

The impact of B on the baseband power spectral density is illustrated in Figure 5-3 supposing $\Delta f_j = 0$. Figure 5-3 represents the estimated periodogram of the chirp jammer at the RFFE output calculated on generated samples, as well as the power spectral density computed from theoretical (Eq 5-24). Both spectrums fit well with each other. In addition, most of the chirp power is inside the frequency band $\left[-\frac{B}{2}; \frac{B}{2}\right]$: 97.9% when $B = 5 \text{ MHz}$ and 97.3% when $B = 2 \text{ MHz}$.

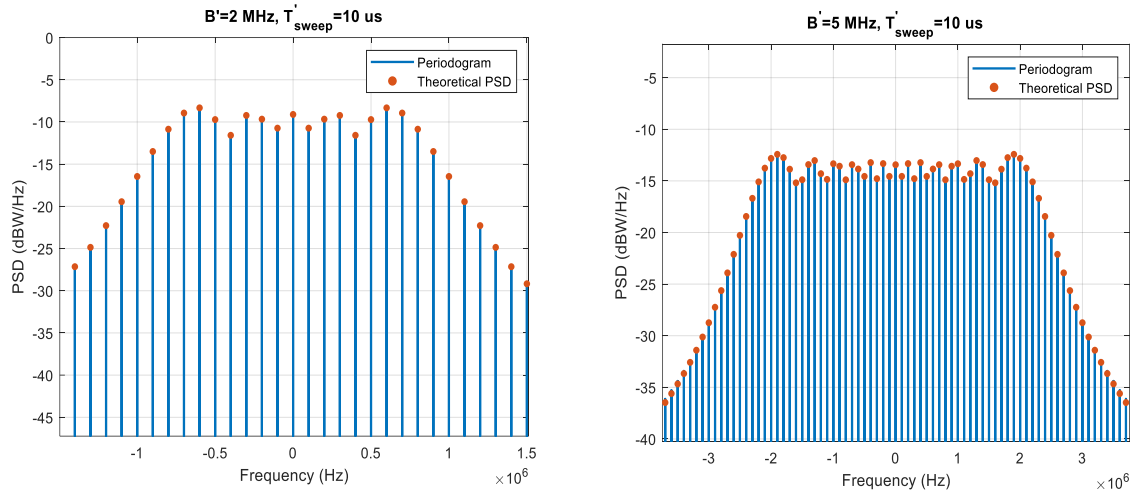


Figure 5-3: Impact of B on the baseband power spectral density at the RFFE output of the chirp signal

Figure 5-4 illustrates the impact of T_{sweep} on the power spectral density of the chirp signal at the RFFE output, assuming $\Delta f_j = 0$. As predicted by equation (Eq 5-24), the spectrum of the chirp signal is composed of lines regularly spaced every $1/T_{sweep}$. A high value for T_{sweep} leads to a high number of lines in the frequency band $\left[-\frac{B}{2}; \frac{B}{2}\right]$. However, the power level for each line decreases when T_{sweep} grows.

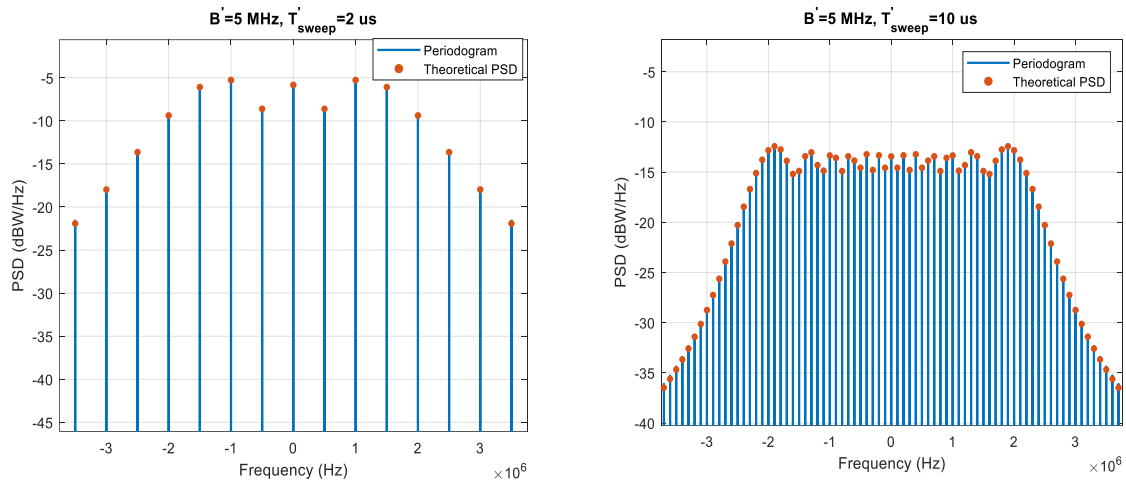


Figure 5-4: Impact of T_{sweep} on the baseband power spectral density at the RFFE output of the chirp signal

5-2.2 Spectral separation coefficient of a linear sweep PPD signal

This section has two objectives. First, it provides an analytic expression of the chirp RFI SSC based on inputs derived in section 5-2.1. Second, it highlights the influence of chirp parameters on the SSC, and thus on the predicted impact of chirp RFI on C/N_0 .

5-2.2.1 Theoretical calculation of chirp RFI SSC

The spectral separation coefficient is given in (Eq 2-79). From this expression, it can be seen that the SSC is obtained multiplying the line spectrum of the chirp interference with $S_{GNSS,corr out}(f)$; where $S_{GNSS,corr out}(f)$ is calculated by convoluting the unrestricted PSD local replica, $S_{cm}(f)$ with the squared magnitude of the integrate and dump filter transfer function. The transfer function of the integrate and dump filter is a cardinal sine where the width of the main lobe of the cardinal sine is

equal to $2/T_i$, and its amplitude grows with T_i . The PSD of the unrestricted local replica is the GPS L1 C/A PRN signal line spectrum. As a result, the convolution term is equal to an imperfect line spectrum, where the lines of S_{c_m} are transformed into a squared cardinal sine. Two examples are given in Figure 5-5 for two values of integration time T_i , 1 ms and 20 ms.

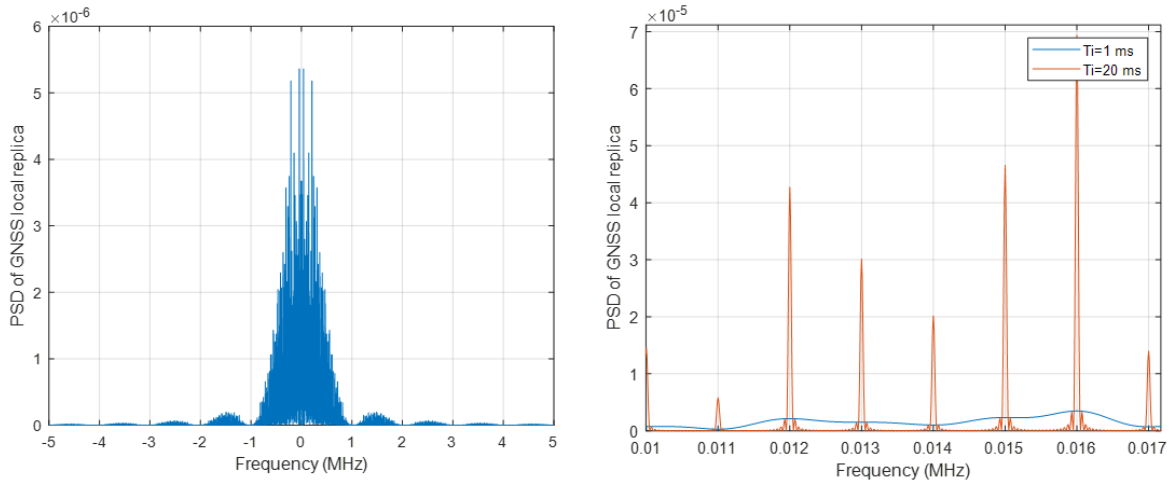


Figure 5-5 : Power spectral density of the GNSS local replica at the integrate and dump filter output

The convolutional term $S_{GNSS,corr out} = S_{c_m} * |H_{ID}|^2$ has a major influence on the SSC.

When the integration time is short (for example, 1 ms), the line spectrum of the local replica is spread by the correlation, and $S_{GNSS,corr out}$ can therefore be considered continuous. The influence of the frequency offset between the GNSS local replica and the chirp on the SSC should normally be weak because the local code spectrum is continuous and there is no sudden variation of the SSC due to frequency alignment of the spectra.

Conversely, when the integration time is long, $S_{GNSS,corr out}$ is still similar to a line spectrum, except that the lines are now represented by a narrow squared cardinal sine. The peak magnitude of the spectrum lines is higher than the peak magnitude when the integration time is short (see magnitude of blue line vs magnitude of orange line of Figure 5-5). In that case, the SSC will be significant if the lines of $S_{PPD,BB}$ are aligned with the main lobes of the square cardinal sine constituting $S_{GNSS,corr out}$, and the SSC for $T_i = 20 ms$ will be higher than the SSC computed for $T_i = 1 ms$.

The maximum worst case potential impact of the interference is thus stronger when the integration time is long. Assuming a long coherent integration time, T_i , such detrimental cases would occur only if the two following conditions are thus met at the same time: first, the interference carrier frequency is aligned with the local code or has a frequency offset between the interference and useful signal equal to a multiple of the useful signal PRN code period including code Doppler, and second, the period of the received chirp including modulation doppler offset T_{sweep} is an exact divider of the PRN code period so that the same time sequences always find correlated with each other which is a breach of chirp signal stationarity and extreme but not average correlation outputs can be observed. The worst situation, which is even more unlikely to occur, is found when the received T_{sweep} is equal to the PRN code period and when the frequency offset is equal to a multiple of 1kHz.

Another important intermediate situation is found when the received chirp has a time offset to the local code that periodically follows a similar sequence over a few tens of seconds, which then also induces a breach of the stationarity condition assumed above, and extreme but not average correlation output time series can be observed. That situation is described in further sections below.

The spectral separation coefficient can be finally expressed by (Eq 5-25).

$$SSC = \sum_{m=-\infty}^{+\infty} c_m \cdot S_{GNSS,corr\ out} \left(\frac{m}{T_{sweep}} + \Delta f_j \right) \quad (\text{Eq 5-25})$$

Where $\Delta f_j = \Delta f_j^c + f_{j,dopp} - f_D$ is defined as the overall frequency offset between the PPD signal power spectral density (PSD) central frequency and the GNSS local replica (PSD) central frequency..

As a conclusion, the combination of the C/N_0 degradation model caused by RFI presented in (Eq 2-86), and (Eq 5-25) allows to predict C/N_0 degradation caused by chirp RFI from the knowledge the chirp RFI characteristics.

5-2.2.2 Influence of chirp RFI characteristics on SSC

Received jammer signal characteristics which have an impact on the correlator output include the composite intrinsic plus doppler received jammer frequency offset to local GNSS Δf_j , the impacted double-sided bandwidth B and the period of repetition of the instantaneous frequency pattern T_{sweep} . This section looks at the influence of these parameters on the SSC.

Figure 5-6 represents the behavior of the spectral separation coefficient computed from (Eq 5-25) as a function of B, T_{sweep} considering a 20ms coherent integration time T_i . The correlation is done with GPS L1C/A PRN 1 code. The difference between interference and GNSS local replica offset frequencies, Δf_j , is supposed to be null, $\Delta f_j = 0$. Note that the behavior of the SSC as a function of the jammer characteristics has been verified to be similar if the correlation is done with another GPS L1C/A PRN code.

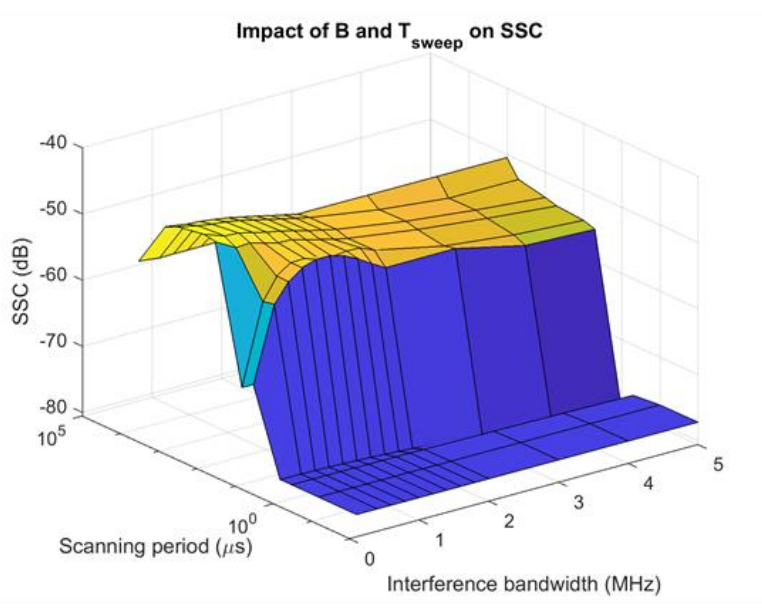


Figure 5-6 Impact of stationary received chirp jammer signal settings on the spectral separation coefficient to GPS L1C/A

Figure 5-6 brings some information on the impact of a stationary random PPD interference at the correlator output. The impact of the RFI seems to be the most significant when the scanning period, T_{sweep} , is high (around 1 ms) and when the targeted bandwidth is low (lower than 1 MHz). Indeed, when the targeted bandwidth is low, all the interference power hits the main lobe of the locally generated signal. As a result, the correlation will be more impacted for low values of the targeted bandwidth B .

However, for values of B much lower than the GNSS receiver bandwidth, it will be possible to mitigate the chirp RFI by rejecting the out-of-band frequency components of the interference [80]. Furthermore, some mitigation techniques presented in [81] or [82] allow to track and mitigate the chirp interference. However, techniques presented in [81] and [82] are not efficient if the scanning period, T_{sweep} , is lower than the sampling period of the GNSS receiver. The minimum front-end bandwidth for aeronautical GNSS receiver is 2 MHz double sided (legacy equipment), as a consequence, the minimum sampling rate should be 2 MHz. The corresponding sampling period is 0.5 μ s. Thus, a compromise between the impact of the RFI and the risk to be detected and mitigated may be found by jammer manufacturer. In most of PPD jammers presented in the literature [83], the sweep range is between 10 and 85 MHz large, and the sweep period is between 5 and 42 μ s.

Figure 5-7 provides the SSC as a function of the received jammer to local GPS frequency offset Δf_j , for several values of T_i and T_{sweep} . B is set to 2 MHz.

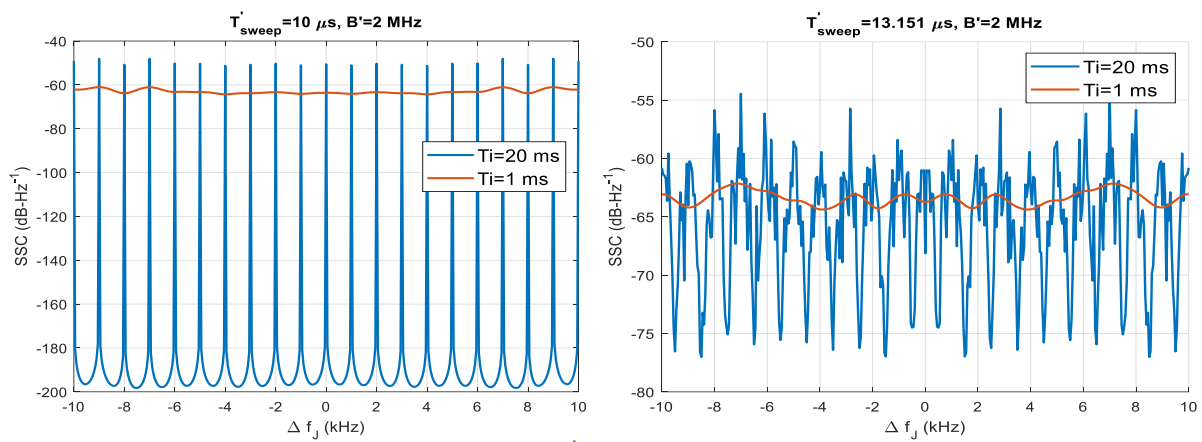


Figure 5-7: Received chirp jammer signal SSC to GPS L1 C/A as a function of received jammer to local GPS frequency offset Δf_j for different values of T_{sweep} and T_i

When $T_{sweep} = 10 \mu s$, T_{sweep} is an exact divisor of PRN code period of 1 ms. As predicted in section 5-2.2, the impact of Δf_j on the SSC is very different depending on the integration time. For a 20 ms integration time, it appears that the impact of the interference signal at the correlator output is significant only for values of Δf_j equal to multiples of 1 kHz. Peak values of the SSC can be observed every kHz. That can be explained by the line spectrum of the PRN code spectrum $S_{GNSS,corr out}$, with lines regularly spaced every kHz as previously discussed in section 5-2.2. In other words, the composite received jammer signal frequency offset to GNSS Δf_j must be a multiple of 1 kHz so that the interference at the correlator output is significant. On the contrary, when $T_i = 1 ms$, Δf_j has a lower influence of the SSC and the SSC is not negligible for all values of Δf_j .

When $T_{sweep} = 13.151 \mu s$, T_{sweep} is not a divisor of the PRN code period meaning that some of the lines of the chirp RFI spectrum, but not all, may be aligned with the PRN code spectrum lines when $T_i = 20 ms$. Therefore, on the one hand, the maximum SSC value among Δf_j is lower for $T_i = 20 ms$ when $T_{sweep} = 13.151 \mu s$ compared to the case where $T_{sweep} = 10 \mu s$. On the other hand, there are always some lines of the chirp RFI spectrum hitting $S_{GNSS,corr out}$, so the SSC is non negligible for all values of Δf_j analyzed here.

In practice, frequency synchronization offset between the received PPD signal and the received GNSS signal, Δf_j , depends on the design PPD frequency offset with respect to GNSS L1 frequency, Δf_j^c , on the Doppler frequency of the GNSS signal (satellite to GNSS receiver motion), f_{dopp} , and on the

interference doppler frequency, $f_{j,dopp}$ (PPD to GNSS receiver motion). As a consequence, it is difficult for a PPD manufacturer to monitor Δf_j^c in order to maximize the PPD signal power at the correlator output. Thus, Δf_j^c is often set to 0 Hz. In other words, the PPD transmitted signal is most of the time centered on L1.

However, having the received jammer to local GPS frequency offset Δf_j equal to a multiple of 1 kHz is not the only situation where the jammer has a worst-case impact. Indeed, when the received jammer has a repetitive time slot correspondence pattern breaking the stationarity situation, we can have repetitive worst-case alignment of spectrum lines, as shown later.

5-3 Impact of chirp RFI on C/N_0 : simulations

Two types of GNSS receiver have been used to analyze the impact of chirp RFI on C/N_0 :

- A Matlab software GNSS receiver, which has the advantage of being fully configurable.
- A IFEN GNSS receiver. This GNSS receiver has the advantage of having some parameters configurable through SX3 software. In addition, it returns correlator outputs which are used to run C/N_0 estimation algorithms described in Chapter 2 section 2-3.4.2.

5-3.1 Simulation with Matlab software receiver

This section presents the simulations performed with Matlab software receiver to analyze the impact of chirp RFI on C/N_0 . It is divided in three parts. First, settings of the simulations which are conducted are described and justified. Second, the results, showing the evolution on C/N_0 as a function of time for the different simulations, are presented. Third, these results are discussed.

5-3.1.1 Description of simulations

In order to analyze the behavior of C/N_0 estimators in presence of a chirp interference, a signal composed by one PRN GPS L1C/A (PRN 1) is processed by a Matlab software GNSS receiver during 10s. An interference is switched on after 3s of simulation.

The simulations are defined hereinafter:

- Simulation 1: A first simulation is performed injecting a RFI whose power spectral density is rectangular. The aim of this first simulation is to validate the theoretical C/N_0 degradation prediction using SSC.
- Simulation 2: An “artificial” chirp RFI signal is injected into the receiver. The objective of this simulation is to validate the theoretical SSC calculation by recreating the random distributions of the correlator outputs parameters used during theoretical SSC calculation. The chirp RFI signal is built as follows. At each starting instant of the correlation, a random phase φ_0 and a random delay δ , respectively uniformly distributed over $[0; 2\pi]$ and $[0; T_{sweep}]$, are generated. The chirp signal over the integration period is then generated using (Eq 5-14). The goal of simulation 2 is to force the ergodicity of the correlator outputs. Indeed, the prediction of the C/N_0 degradation with the SSC is based on a statistical approach. C/N_0 estimators, which are computed from one estimation of the received signal, are expected to return a consistent value with the theoretical prediction if and only if the statistical properties can be deduced from a single but sufficiently long observation (Chapter 2 section 2-4.3.2 condition 1). In other words, the ergodicity of the chirp contribution on the correlator outputs is a key point on the validity of the returned C/N_0 estimations. The ergodicity is forced in this simulation, generating independent random values of the identified random parameters following the determined distribution at each starting instant of the correlation.

- **Simulation 3:** A chirp RFI with $T_{sweep} = 10 \mu s$ and $B = 2 MHz$ is inserted. A correlation time of 1ms is set. A 2.5 kHz doppler frequency is considered on the GPS signal, f_D , so that from one correlation to the next one, the chirp pattern does not stay aligned with the PRN code (variation of δ). However, the received jammer to frequency offset Δf_j is set to 0 in this scenario.
- **Simulation 4:** chirp RFI settings are the same as in simulation 3. The integration time is set to 20 ms. The objective is to analyze the impact of the integration time on the chirp jammer impact by comparing the results with simulation 3 results.
- **Simulation 5:** Δf_j is set to 1.5 kHz and the integration time is set to 20 ms. GNSS doppler frequency, f_{dopp} , is still set to 2.5 kHz. The objective is to validate the influence of Δf_j on the C/N_0 degradation predicted in Figure 5-7.
- **Simulation 6:** T_{sweep} is set to an arbitrary value of 13.151 μs . Indeed, $T_{sweep} = 10 \mu s$ is a particular value since it is a divisor of the integration time T_i . Therefore, there is an integer number of sweep period during the integration time. $T_{sweep} = 13.151 \mu s$ is therefore a more realistic value. GNSS doppler frequency, f_{dopp} , is now switch to 0 kHz for this simulation and the remaining ones. The objective is to vary the δ parameter value at each starting instant of the correlation. Indeed, by imposing the new T_{sweep} value, the variation from correlation starting instant to the next one is higher than when δ value was only modified through f_{dopp} .
- **Simulation 7:** $T_{sweep} = 10 \mu s$ and $\Delta f_j = 234.54 Hz$. Δf_j is here set to a more realistic value than 0, since it is very improbable that that the chirp and GPS signal Doppler frequency are set to the same value. The objective is to vary the initial phase parameter φ_0 value at each starting instant of the correlation.
- **Simulation 8:** T_{sweep} and received jammer to GNSS frequency offset Δf_j are set to the selected realistic value, respectively 13.151 μs and 234.54 Hz. The objective here is to vary the two parameters δ and φ_0 values at each starting instant of the correlation.

Settings for the different simulations are recapped Table 5-1.

Simulations	1	2	3	4	5	6	7	8
B (MHz)	2 (noise like)	2 (artificial)	2	2	2	2	2	2
T_{sweep} (μs)	NA	10	10	10	10	13.151	10	13.151
N_0 (dBW/Hz)	-201.5	-201.5	-201.5	-201.5	-201.5	-201.5	-201.5	-201.5
GPS signal power (dBW)	-156.5	-156.5	-156.5	-156.5	-156.5	-156.5	-156.5	-156.5
C/N_0 in absence of RFI (dB-Hz)	45	45	45	45	45	45	45	45
GPS signal Doppler frequency f_D	0	0	2500	2500	2500	0	0	0
$\Delta f_j^c + f_{J,dopp}$ (MHz)	0	0	2500	2500	4000	0	234.54	234.54
Chirp RFI power C_j (dBW)	-133	-133	-133	-133	-133	-133	-133	-133
T_i (ms)	1	1	1	20	20	1	1	1
Theoretical SSC (dB-Hz⁻¹)	-63.45	-63.6	-63.6	-50.59	-196.91	-63.73	-63.63	-63.58
Predicted C/N_0 degradation (dB)	6.23	6.12	6.12	17.98	0	6.02	6.09	6.13

Table 5-1: Chirp jammer settings

5-3.1.2 Results

Figure 5-8 shows the evolution of the C/N_0 returned by the Beaulieu, moment and SNV estimators, as a function of the time.



Figure 5-8: Evolution of the C/N0 estimators for the different simulations

First, simulation 1 and simulation 2 plots show a convergence of the C/N_0 estimators toward the predicted value obtained from SSC model assuming jammer signal stationarity, when the interference is switched on. C/N_0 estimators are stable and accurate in presence of the noise-like interference or with the artificially ergodic chirp signal used in simulation 2. Second, plots for simulations 3 and 4 shows that the integration time plays a role on the returned C/N_0 estimations, since C/N_0 estimations for scenario 4 are lower than the ones for scenario 3. Moreover, it appears that C/N_0 estimations in simulation 3 are most of the time higher than the predicted carrier to effective noise density ratio. This difference will be further investigated in the Discussion section. Such a situation could cause some integrity and continuity problems if used to compute pseudorange sigmas and to compare to C/N_0 thresholds. Nevertheless, as predicted with the calculation of the SSC for $\Delta f_j = 0 \text{ Hz}$, the chirp jammer has a stronger impact on the C/N_0 when the integration time is large (simulation 4) than in simulation 3 when T_i is small. Third, simulation 5 highlights the influence of the received jammer to local GNSS frequency offset Δf_j parameter: as predicted with the very low value of the SSC, the impact of the chirp interference is not visible when the integration time is set to 20 ms and the GPS and chirp spectrum are not frequency aligned.

Fourth, simulation 6 is associated to a case where the sweep period is not a divisor of the PRN code period. For this simulation, SNV and Beaulieu estimators provide a mean C/N_0 degradation which is less than 0.5 dB below the predicted value. However, the MM estimator underestimates the C/N_0 . The difference in the behavior of the estimators will be explained in the Discussion section. Fifth, simulation 7 analyzes the case where the integration time is a multiple of T_{sweep} and the frequency offset between the chirp signal and the GPS signal is randomly chosen. In that situation, C/N_0 estimators have not the same behavior and are well below of the predicted value. That behavior will be discussed in the Discussion section. Sixth and last, simulation 8 focuses on the case where both T_{sweep} and Δf_j are chosen randomly. In that case, the three C/N_0 estimators are close from each other, and quite close to the predicted value (less than 1 dB below).

Finally, some conclusions can be deduced from Figure 5-8:

- 1) As predicted in section 5-2.2.2, when received jammer to local GNSS frequency offset $\Delta f_j = 0 \text{ Hz}$ (or a multiple of the inverse of the PRN code period), the chirp interference has a stronger impact on correlator outputs when the integration time is high than when the integration time is small.
- 2) Δf_j is a driving parameter of the impact, in particular when the integration time is high. Indeed, when the integration time is high enough, the chirp interference will have a significant impact only when the chirp interference and GPS signal spectrums are aligned.
- 3) T_{sweep} is an even more important driver of the impact than Δf_j , as shown by simulations 7 and 8: even if Δf_j is not a multiple of the inverse of the PRN code period, if T_{sweep} is a divider of the PRN code period then ergodicity conditions are not met.
- 4) It had already been observed in the past, but we also see here that C/N_0 estimators sometimes do not all behave in the same manner when subject to RFI.

Generally, speaking, C/N_0 estimators do not output the predicted value in the situations where some assumptions on RFI ergodicity and correlator output distribution are not met. These conditions are driven by Δf_j , but more importantly by T_{sweep} . Indeed, when T_{sweep} is a divider of the PRN code period, ergodicity is not met. It may appear that this situation of exact divider is a singular situation, but in reality because T_{sweep} is a value of a few microseconds, there is a very large set of very similar values which are exact dividers of 1ms (ex: $1\text{ms}/100=10$ microseconds, $1\text{ms}/99$, $1\text{ms}/101$, ...).

Therefore, observing very singular behaviors of a receiver in presence of a chirp may not be a rare event.

5-3.1.3 Discussion

The objective of this section is to discuss the observations made in section 5-3.1.2. Three conditions have been identified in Chapter 2 section 2-4.3.2 so that C/N_0 estimations in presence of chirp RFI fits with the predicted value. The fulfillment of these conditions, for the different scenarios where the estimated C/N_0 value does not match the predicted C/N_0 are here analyzed.

Condition 1: Valid SNIR definition in Eq-1: centered RFI, RFI uncorrelated to GPS

As C/N_0 estimators are based on SNIR definition of (Eq 2-83), the key condition of validity of this definition imposes that the mean value of the RFI at the correlator output should be equal to 0. This condition also requests the uncorrelation between the chirp RFI correlator output and the GNSS signal correlator output. This point will be analyzed in section 5-4.1.2. The assumption on the mean RFI value at the correlator output is here verified, computing the mean time value of I_{PPD} and Q_{PPD} , where I_{PPD} and Q_{PPD} are the contribution of the chirp signal to the correlator output (respectively in-phase and quadrature phase). It is indeed possible to obtain a posteriori the successive samples of I_{PPD} and Q_{PPD} . The ratio between the mean time value \bar{I}_{PPD} and \bar{Q}_{PPD} and their respective standard deviation $\sigma_{I_{PPD}}$ and $\sigma_{Q_{PPD}}$ are recapped in Table 5-2 for the different simulations.

	$\bar{I}_{PPD}/\sigma_{I_{PPD}}$	$\bar{Q}_{PPD}/\sigma_{Q_{PPD}}$
Simulation 1	10^{-2}	$-1.21 \cdot 10^{-2}$
Simulation 2	$0.83 \cdot 10^{-2}$	$0.16 \cdot 10^{-2}$
Simulation 3	0.52	$-2.68 \cdot 10^{-2}$
Simulation 4	0.52	$-4.18 \cdot 10^{-2}$
Simulation 5	$3 \cdot 10^{-2}$	$3.85 \cdot 10^{-2}$
Simulation 6	$0.1 \cdot 10^{-2}$	$-1.95 \cdot 10^{-2}$
Simulation 7	$-0.8 \cdot 10^{-2}$	$0.004 \cdot 10^{-2}$
Simulation 8	10^{-2}	$0.76 \cdot 10^{-2}$

Table 5-2: Analysis of the mean value of the chirp RFI at the correlator output

According to Table 5-2, the mean value of the RFI at the correlator output is much lower than the RFI standard deviation at the correlator output, except for scenario 3 and 4. For scenario 3 and 4, since the chirp RFI at the correlator output is not centered, then the SNIR definition of (Eq 2-83) is inappropriate. As a consequence, C/N_0 estimators are not suited to estimate effective noise, leading to inconsistency between the predicted values and the values returned by C/N_0 estimators. For all other scenarios, Condition 1 is fulfilled.

Condition 2: Assumptions of C/N_0 estimators on correlator outputs

Condition 2 deals with the conditions of validity of C/N_0 estimators. This section starts by analyzing the behavior of C/N_0 estimators in presence of centered RFI. This analysis is applied to simulation 6 to explain the difference of behavior between the three C/N_0 estimators. Then, the distribution of the RFI at the correlator output are analyzed for simulation 6 and 8.

It can be shown (see Appendix E) that, assuming:

- The GPS signal power is much higher than the RFI and noise power at the correlator outputs,
- The mean value of the RFI at the correlator output is null,
- The RFI at the correlator output is independent from the GPS signal,

C/N_0 estimators tend toward the following limits when the number of correlator outputs samples N_s used for computing these estimates is large:

$$\lim_{K \rightarrow +\infty} \widehat{C/N_0}_B = \frac{C}{N_0 + 4P_I T_i - 4T_i P_{I_k I_{k-1}}}$$

$$\lim_{K \rightarrow +\infty} \widehat{C/N_0}_M = \frac{C}{N_0 + 4P_I T_i - \frac{4P_I P_Q}{C} T_i - \frac{4(P_I^2 + P_Q^2)}{C} T_i + 2 \frac{M_I^4 + M_Q^4}{C} T_i} \quad (\text{Eq 5-26})$$

$$\lim_{K \rightarrow +\infty} \widehat{C/N_0}_{SNV} = \frac{C}{N_0 + 2(P_I + P_Q) T_i}$$

P_I and P_Q are respectively the mean time value of I_{PPD}^2 and Q_{PPD}^2 . M_I^4 and M_Q^4 are respectively the fourth order moment of I_{PPD} and Q_{PPD} , and $P_{I_k I_{k-1}} = \mathbb{E}(I_{PPD}(k)I_{PPD}(k-1))$.

Table 5-3 shows the limit of the three estimators for simulation 6 when N_s is large.

	Beaulieu	Moment	SNV
$\lim_{K \rightarrow +\infty} \widehat{C/N_0}$	38.7	37.4	38.5

Table 5-3: Prediction of the convergence value of C/N_0 estimators for simulation 6

Values obtained from (Eq 5-26) and reported in Table 5-3 indicate that the MM estimator should be below the SNV and Beaulieu estimators. This is consistent with the observation for simulation 6 on Figure 5-8. This analysis highlights the necessity to have the same distribution on the correlator outputs so that C/N_0 estimators return consistent values between each other.

Eventually, Figure 5-9 shows the distribution of the chirp contribution to the correlator outputs when the chirp RFI is switched on for simulation 6 and simulation 8. Table 5-4 recaps the variance of the in-phase and quadrature phase correlator outputs for simulations 6 and 8. Note that because the chirp correlator output is centered, the variance is equivalent to the power.

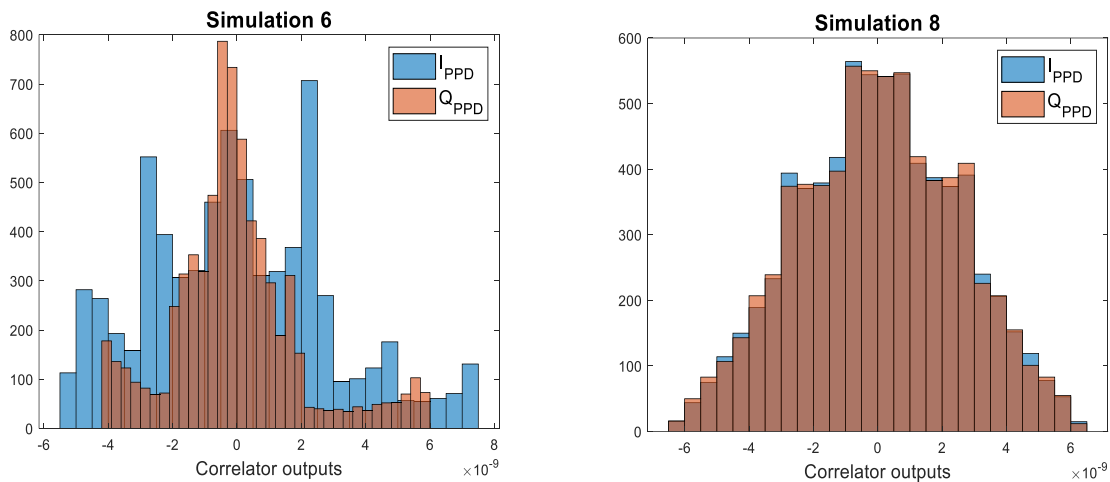


Figure 5-9: Distribution of the chirp contribution on the correlator outputs for simulations 6 and 8

Even though the chirp correlator output is centered for simulation 6, the distribution on the in-phase and quadrature phase channels is different. In addition, the distribution is not gaussian. Conversely, chirp correlator outputs for simulation 8 is centered, identical on the in-phase and quadrature phase channels and gaussian-like.

	In phase correlator output variance	Quadrature correlator output variance
Simulation 6	-170.78	-173.98
Simulation 8	-172.04	-172.04

Table 5-4 Variance of correlator outputs for simulations 6 and 8

An important assumption for Beaulieu and moment estimators is that the distribution of the noise plus interference on both the in-phase and quadrature phase are identical. Indeed, the algebraic operations performed on the correlator outputs to estimate the noise power by the estimators are different. For examples, Beaulieu estimator only use the in-phase correlator output to estimate the noise power spectral density, whereas the moment method and SNV estimators use both the in-phase and quadrature phase estimator. In addition, moment estimator uses relations between fourth and second order moments of gaussian distribution to estimate the noise plus RFI power at the correlator output. This power estimation is expected to be imperfectly estimated when the RFI distribution at the correlator output is not gaussian. Table 5-4 shows that the variance of the in-phase and quadrature phase correlator outputs for simulation 6 are different by 3.2 dB because of the chirp RFI, and Figure 5-9 shows that the distribution of the in-phase and quadrature phase correlator outputs in presence of the chirp RFI for simulation 6 are different. Conversely, the variance of the in-phase and quadrature phase correlation due to the chirp RFI for scenario 8 are identical, as well as the distribution of the correlator output.

This difference on the I/Q distribution of the RFI correlator outputs is removed when the chirp signal is not perfectly centered on L1. Indeed, when a non-null Δf_j value is considered (simulation 7), then the C/N_0 estimators return similar values that are close to the predicted C/N_0 value, according to Figure 5-8.

Condition 3: Ergodicity of the RFI correlator output

The spectral separation coefficient characterizes the interference power at the correlator output and is the result of a statistical approach. On the contrary, $P_{PPD,corr}$ and C/N_0 estimators estimate the time mean and variance of the correlator outputs. The time mean and variance of one observation is equivalent to the mean and variance of a random 2^{nd} order wide sense stationary signal only if the random signal is ergodic. Indeed, a random signal is ergodic if its statistical properties (and therefore, mean and variance) can be deduced from one sufficiently long observation of the process. For example, the noise at the correlator output is an ergodic signal since it can be modeled as a Gaussian independent and identically distributed random variable series. However, it appears that the chirp contribution to the correlator output may not be always ergodic and may depend on the value of the random variables δ and φ_0 .

In order to visualize in which cases the correlator outputs due to chirp signal can be supposed ergodic, the statistics of the time shift δ_{kT_i} of the chirp signal instantaneous frequency at each multiple of the integration period, is represented in Figure 5-10. Figure 5-10 also shows the statistics of the initial phase φ_{kT_i} at each multiple of the integration period. This time offset δ_{kT_i} is equivalent to the δ uniform random variable that was considered in section 5-1.3, and φ_{kT_i} is equivalent to the initial phase φ_0 . δ_{kT_i} is linked to the GNSS signal Doppler frequency, f_D and the sweep period T_{sweep} , whereas φ_{kT_i} is only linked to the chirp signal central frequency Δf_j .

$$\delta_{kT_i} = \text{mod} \left(\left\lceil \frac{kT_i}{T_{\text{sweep}}} \right\rceil T_{\text{sweep}} - kT_i, T_{\text{sweep}} \right), T_i = \frac{1023}{f_c(1 + f_D/f_0)} \quad (\text{Eq 5-27})$$

$$\phi_{kT_i} = \text{mod}(2\pi\Delta f_j kT_i, 2\pi)$$

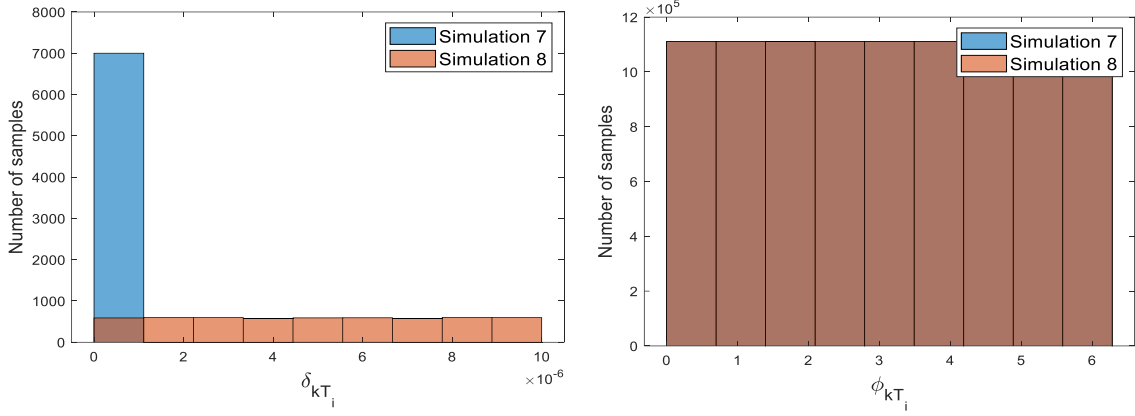


Figure 5-10: Time distribution of δ_{kT_i} and ϕ_{kT_i} for simulations 7 and 8

As it can be noted in Figure 5-10, the initial phase ϕ_{kT_i} , which is identical for simulations 7 and 8 because of the same Δf_j setting, can be identified as uniformly distributed over time and thus, verifying the assumptions considered in Chapter 2 section 2-3.4.2. However, the time offset δ_{kT_i} , which is constant and null for simulation 7, does not follow the same distribution as the distribution assumed for δ , whereas it can be considered uniform for simulation 8. Remember that the assumption on δ was necessary to prove the 2nd order wide sense stationarity of the signal and thus, to compute the chirp signal PSD. Therefore, since the time distribution of δ_{kT_i} is different from the distribution of δ for simulation 7, it is impossible to recover the mean power of the correlator outputs seen as a random variable from a time series. Indeed, the ergodicity of the correlator outputs is a necessary condition to correctly estimate the correlator output power from a time series. Even not plotted here, the ergodicity of the correlator outputs on δ_{kT_i} can be assumed for the other simulations.

Provided that the ergodicity condition is fulfilled, the mean power of the RFI at the correlator output $P_{PPD,corr}$ can be computed and compared to the predicted RFI power at the correlator outputs P_{SSC} . $P_{PPD,corr}$ and P_{SSC} are defined by (Eq 5-28).

$$P_{PPD,corr} = \frac{1}{N} \sum_N \frac{I_{PPD}^2 + Q_{PPD}^2}{2} \quad P_{SSC} = \frac{C_J SSC}{4T_i} \quad (\text{Eq 5-28})$$

N is the number of correlator output samples for which the chirp RFI is switched on. Under the hypothesis of the centrality of I_{PPD} and Q_{PPD} , $P_{PPD,corr}$ is an estimation of the variance of the chirp signal at the correlator output. However, this assumption is not verified for simulations 3 and 4; for these simulations $P_{PPD,corr} \neq (\text{var}[I_{PPD}] + \text{var}[Q_{PPD}])/2$.

Table 5-5 then compares the predicted value P_{SSC} of the RFI power at the correlator output with the observed value $P_{PPD,corr}$.

	$P_{PPD,corr}$ (dBW)	P_{SSC} (dBW)
Simulation 1	-172.48	-172.47
Simulation 2	-172.56	-172.62
Simulation 3	-172.80	-172.62
Simulation 4	-172.66	-172.62

Simulation 5	-224.30	-318.93
Simulation 6	-172.09	-172.75
Simulation 7	-166.87	-172.65
Simulation 8	-172.04	-172.6

Table 5-5 Comparison of predicted and observed RFI power at the correlator output

Table 5-5 shows that the predicted RFI power at the correlator output is consistent with the observed one, except for simulation 5 and 7. The difference between $P_{PPD,corr}$ and P_{SSC} is significant for Simulation 5, but both the predicted and observed values are very low compared to the noise power, and therefore the C/N_0 degradation is negligible. An explanation for this difference of power value in simulation 5, even though the predicted behavior is correct, is the aliasing which is not considered in the theoretical formula. Moreover, a difference of 5.78 dB between $P_{PPD,corr}$ and P_{SSC} can be noted for simulation 7. The reason for such a difference is the ergodicity condition which is not fulfilled for this simulation.

Summary

As a conclusion, this section provides some explanations on the observations done on the evolution of the C/N_0 estimations. First, a condition which must be fulfilled so that the prediction of C/N_0 estimation is accurate is the ergodicity of the correlator outputs: this assumption is correct when the sweep period T_{sweep} is not a divider of the integration time, and when Δf_j is not a multiple of 1 kHz. Second, the frequency term Δf_j is important so that the distribution of the RFI contribution to the in-phase and quadrature phase correlator outputs is the same, which is an assumption used by C/N_0 estimators (see [38]). Usually, since PPD are low-cost jammers, it is very unlikely that T_{sweep} is a divisor of the integration time and Δf_j is null. Therefore, the most realistic scenario among the ones described in scenario 8. In that case, the prediction of the C/N_0 degradation induced by chirp RFI is then expected to fit with the C/N_0 values returned by the estimators.

5-3.2 Simulation with IFEN receiver

In addition to simulations conducted with the Matlab GNSS receiver, some tests are conducted with an IFEN receiver. The objective of these tests is to validate the observations obtained through Matlab receiver simulations.

5-3.2.1 Description of experiment testbench

The testbench used to conduct experiments is described in Figure 5-11.

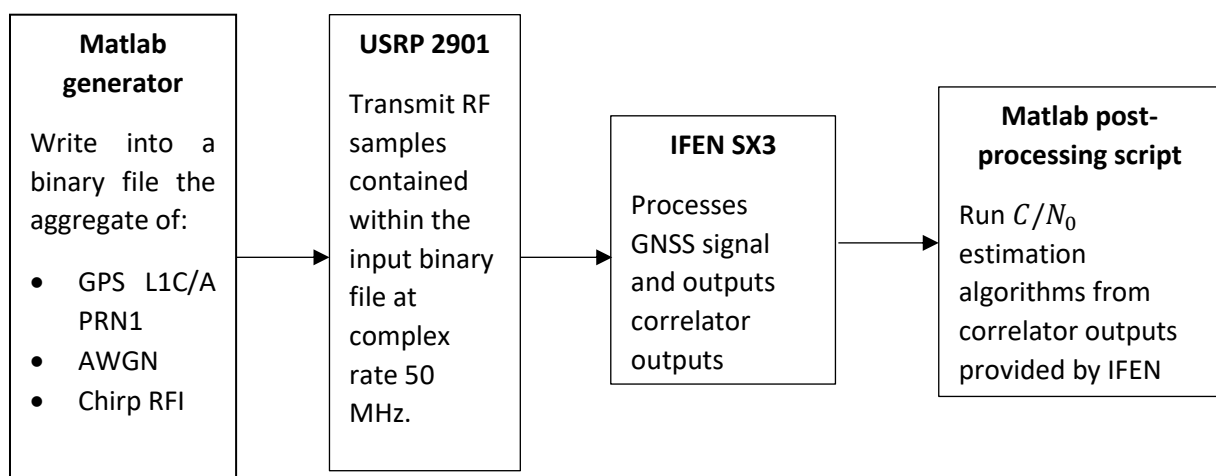


Figure 5-11: Testbench of simulations of injection of chirp RFI in IFEN GNSS receiver

The testbench used for these simulations contains four blocks.

- 1) Matlab generator file: A Matlab generator writes into a binary file the signal to be transmitted by the USRP. The file contains the sum of one GPS L1C/A signal (PRN1), AWGN and the chirp signal. There are several advantages in generating all signal components with a unique device. First, as the impact of the chirp RFI depends on the synchronization between the GPS L1C/A signal and the chirp RFI (Δf and δ), these terms are fully controlled in this setup. Second, the C/N_0 degradation caused by the chirp RFI signal depends on the overall thermal noise N_0 , which in turn depends on the specific receiver thermal noise level which is unknown. To resolve this problem, it is here proposed to generate with the USRP a white noise well above the receiver thermal noise floor. In that case, the contribution of the receiver thermal noise is negligible in comparison with the added noise. To maintain a relevant C/N_0 ratio, the GPS signal power is also higher than GPS signal level in real reception conditions. In addition to the GPS L1C/A signal and the AWGN, a chirp RFI signal is generated after 30 s of simulation. The power of the chirp RFI is set so that the ratio C_j/N_0 leads to a C/N_0 degradation of 7 dB (Eq 2-86). However, the total transmitted power is also set to not exceed the receiver LNA saturation threshold (which is monitored from the AGC level provided by the IFEN).
- 2) USRP 2091: The USRP 2901 reads the binary file which contains the GPS L1C/A signal, the AWGN and the chirp RFI, and transmits through cable RF samples with a complex data rate of 50 MHz.
- 3) IFEN receiver: The IFEN receiver processes the received signal and provides correlator outputs. The IFEN is configurable from SX3 software monitoring. In particular, it is possible to set the coherent integration time to the desired value. In these simulations, the coherent integration time is set to 1 ms.
- 4) Matlab post-processing script: Post-processing of IFEN correlator outputs can be performed. In particular, as the IFEN built-in C/N_0 estimation algorithm is not known, it is instead proposed to run C/N_0 estimation algorithms described and analyzed in Chapter 2 section 2-3.4.2 in a Matlab script. Note that these C/N_0 estimates are not further smoothed as may be done in actual receivers, so their output is generally noisy.

5-3.2.2 Description of simulations

Several simulations are conducted, sending chirp RFI signal to the IFEN receiver. These simulations are described below.

- Simulation 1: This simulation serves as a reference. The injected RFI is has a rectangular power spectral density. The double-sided RFI bandwidth is 10 MHz and the RFI power to N_0 ratio is set in order to target a 7 dB C/N_0 degradation.
- Simulation 2: The injected RFI in simulation 2 also has a rectangular power spectral density, but this time with double-sided bandwidth equal to 1 MHz. The RFI power to N_0 ratio is set in order to target a 7 dB C/N_0 degradation. The objective of this simulation is to show that the C/N_0 degradation prediction is valid for different RFI bandwidths values.
- Simulation 3: The injected RFI is a chirp RFI with bandwidth $B = 2 \text{ MHz}$ and $T_{sweep} = 10 \mu\text{s}$. In this simulation, $f_D = 0 \text{ Hz}$. Note that these settings are the ones that are expected to be adopted in ED-259 as part of tests of DFMC GNSS receiver robustness to jamming. Δf_j is set to 0 Hz. As discussed in section 0, these Δf_j and T_{sweep} jammer settings lead to a non-ergodicity case and therefore, the C/N_0 degradation is expected to be linked to the initial phase φ_0 and chirp RFI instantaneous frequency pattern time offset to GPS L1C/A PRN code δ . In this simulation, δ is set to 0 s and φ_0 is also set to 0 rad.

- **Simulation 4:** The objective of this simulation is to highlight the dependency of the C/N_0 degradation to δ under non-ergodicity conditions. Therefore, same chirp RFI settings than simulation 3 are adopted, $f_D = 0$ Hz, and the chirp RFI instantaneous frequency pattern time offset to GPS L1C/A PRN code δ is set to $T_{sweep}/4$. It is expected to observe a different C/N_0 degradation than the one observed in simulation 3. As this simulation is still conducted under non-ergodic conditions, the observed C/N_0 degradation may not fit with the targeted one (7 dB).
- **Simulation 5:** The objective of simulation 5 is to highlight the importance of Δf in the C/N_0 degradation prediction model. The chirp RFI double-sided bandwidth is set to 10 MHz and the sweep period is set to $T_{sweep} = 10.05 \mu s$, f_D is set to 0 Hz so that ergodicity condition on the chirp RFI instantaneous frequency pattern time delay to GPS L1C/A PRN code is fulfilled. Δf_j is set to 0 Hz in simulation 5 and φ_0 is set to 0 rad, such that ergodicity conditions on the phase are not fulfilled.
- **Simulation 6:** In order to demonstrate the influence of Δf_j on the C/N_0 degradation, same chirp RFI settings than simulation 5 are adopted, and Δf_j is arbitrarily set to 234.54 Hz. In this case, ergodicity conditions are fulfilled and observed C/N_0 degradation should fit with the targeted degradation (7 dB).
- **Simulation 7:** The goal of simulation 7 is to determine the ergodicity region for T_{sweep} , for which the observed C/N_0 degradation fits with the prediction. To achieve this objective, the chirp RFI bandwidth is kept at 10 MHz and Δf_j is set to 234.54 Hz (not a multiple of 1 kHz). The T_{sweep} is moved from $10 \mu s (T_i/100)$ to $10.10101 (T_i/99)$ with a step of $0.01 \mu s$, and the values of T_{sweep} for which the observed C/N_0 degradation does not fit with the prediction are identified.
- **Simulation 8:** In simulation 8, the chirp RFI bandwidth is set to 10 MHz and Δf_j to 234.54 MHz. In addition, T_{sweep} is set to $10.101 \mu s$, which is almost but not exactly a divisor of the integration time. In this case, δ_{kT_i} varies slowly and therefore, C/N_0 degradation is also expected to present variations within the time.

Table 5-6 summarizes the chirp RFI settings of the simulations performed with the IFEN receiver.

Simulations	1	2	3	4	5	6	7	8
B (MHz)	10 (noise like)	1 (noise like)	10	10	10	10	10	10
T_{sweep} (μs)	NA	NA	10 ($\delta = 0$)	10 ($\delta = T_{sweep}/4$)	10.05	10.05	Varying	10.101
Δf_j (Hz)	0	0	0	0	0	234.54	234.54	234.54
C/N_0 in absence of RFI (dB-Hz)	50	50	50	50	50	50	50	50
T_i (ms)	1	1	1	1	1	1	1	1
Theoretical SSC (dB-Hz ⁻¹)	-70.09	-61.16	-70.43	-70.43	-71.80	-71.58	NA	-69.31
C_j/N_0 (dB.Hz)	76.12	67.19	76.46	76.46	77.83	77.61	NA	75.34
Targeted C/N_0 degradation (dB)	7	7	7	7	7	7	7	7

Table 5-6: Chirp RFI settings for simulations with the IFEN GNSS receiver

5-3.2.2.1 Results

This section presents observation of C/N_0 degradation computed with the two C/N_0 estimation algorithms presented in Chapter 2 section 2-3.4.2 (Beaulieu, Moment). In addition, the NWPR (narrow band wide band power ratio) C/N_0 estimator which is expected to be used for standardization purpose in ED-259A, is also used. This estimator is introduced in [25].

Time evolution of C/N_0 estimations for simulations 3 and 4 is represented in Figure 5-12.

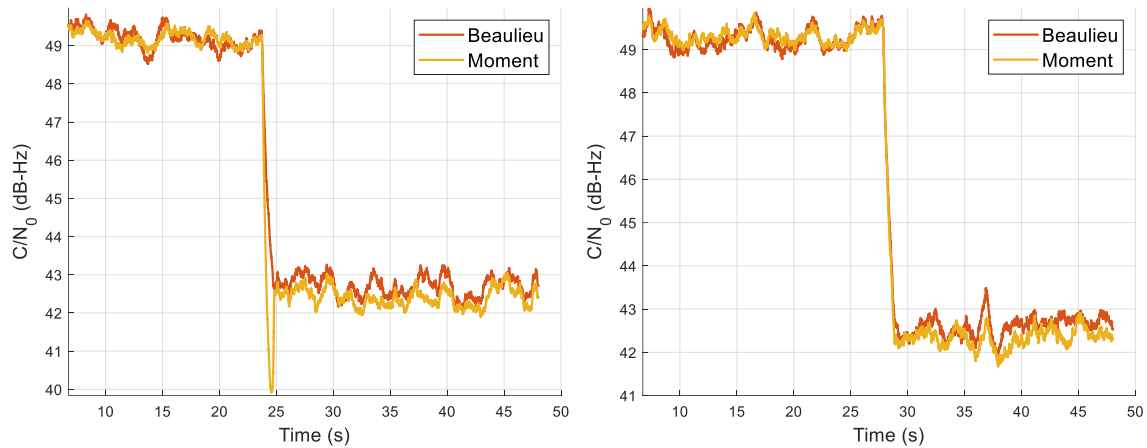


Figure 5-12: Evolution of C/N_0 estimations as a function of time for IFEN simulations 1 (left) and 2 (right)

Figure 5-12 has been obtained injecting RFI whose power spectral density is rectangular with bandwidth 10 MHz (simulation 1) and 1 MHz (simulation 2). The 7 dB targeted degradation can graphically be read on Figure 5-12. That validates the fact that C/N_0 estimators behave as predicted in presence of rectangular RFI.

Time evolution of C/N_0 estimations for simulations 3 and 4 is represented in Figure 5-13.

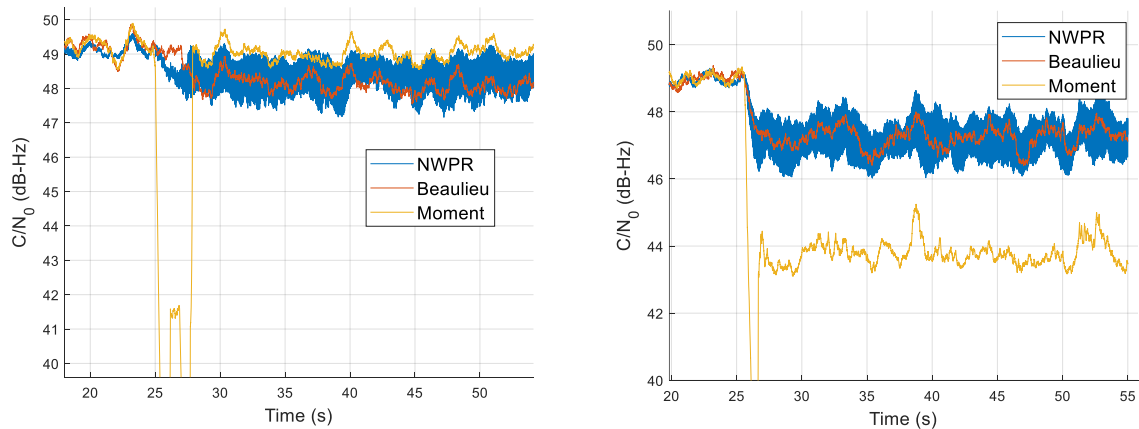


Figure 5-13: Evolution of C/N_0 estimations as a function of time for IFEN simulations 3 (left) and 4 (right)

Two observations can be done from Figure 5-13:

- 1) The three C/N_0 estimators do not behave similarly in presence of the injected chirp RFI. This is very visible for simulation 2, where the moment estimator is around 2.5 dB below the NWPR and Beaulieu estimators. For simulation 1, the moment estimator is around 0.5 dB above the Beaulieu estimator.

- 2) Even though chirp signal settings B and T_{sweep} are identical between simulations 1 and 2, the behavior of C/N_0 estimators varies between simulation and therefore depends on the time offset between the chirp RFI instantaneous frequency pattern and the GPS L1C/A PRN code. In particular, the estimated C/N_0 degradation is higher when $\delta = T_{sweep}/4$ than when $\delta = 0$.

These observations are consistent with the discussion of section 0. Ergodicity conditions are not fulfilled and therefore, C/N_0 estimations depend on δ . Such a situation may lead to potential under-estimation or over-estimation of the impact of the chirp RFI on GNSS receiver performances.

Time evolution of estimated C/N_0 for simulation 4 and 5 are shown in Figure 5-14.

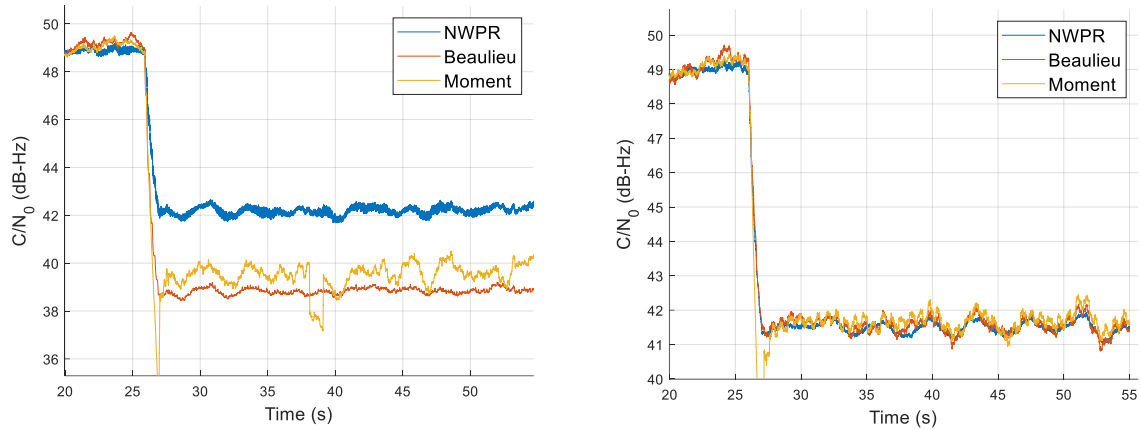


Figure 5-14: Evolution of C/N_0 estimations as a function of time for IFEN simulations 5 (left) and 6 (right)

Comparison of simulations 5 and simulations 6 on Figure 5-14 highlights the influence of Δf_j . On one hand, when $\Delta f_j = 0 \text{ Hz}$ is simulation 5, then ergodicity conditions on the phase are not satisfied. In this case, Beaulieu and Moment estimators does not match with the targeted C/N_0 degradation. In addition, the three C/N_0 estimators behave differently. On the other hand, for simulation 6 for which $\Delta f_j = 234.54 \text{ Hz}$, ergodicity conditions on both the phase and time offset are satisfied. In that case, the observed C/N_0 degradation, for the three C/N_0 estimators, is very close to the targeted value, validating the prediction model under ergodicity conditions.

The two main parameters playing a role on the ergodicity is T_{sweep} and Δf_j . Δf_j depends on the relative motion of the victim receiver, satellite, and chirp RFI transmitter, as well as clock oscillator drift of the receiver and interferer transmitter. Therefore, Δf_j is difficult to control in practice. On the contrary, T_{sweep} can be controlled by chirp RFI transmitter manufacturer by implementation. Moreover, even if Δf_j is not a multiple of 1 kHz, if T_{sweep} is an exact divider of T_i , then non ergodicity conditions appear. Therefore, it is important to determine the width of T_{sweep} intervals leading to non-ergodicity conditions and therefore on the impossibility to predict the C/N_0 degradation because of a strong variability between experiments. The objective of simulation 7 is to determine the width of T_{sweep} values for which the C/N_0 degradation prediction model is not applicable because T_{sweep} is too close from a divider of the integration time T_i . To achieve this goal, several simulations are run, using different values of T_{sweep} in the interval $\left[\frac{T_i}{100}; \frac{T_i}{99}\right]$. For each value of T_{sweep} , the C/N_0 degradation using NWPR algorithm is raised. The mean C/N_0 degradation as a function of T_{sweep} is then plotted in Figure 5-15.

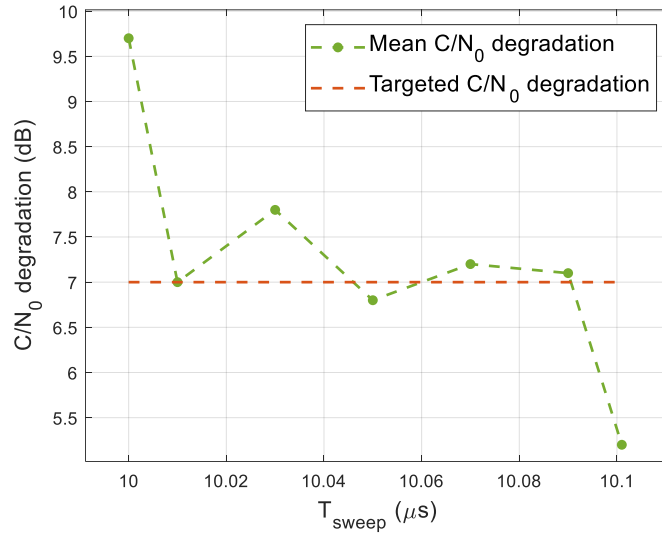


Figure 5-15: Mean C/N_0 degradation for different T_{sweep} (IFEN simulation 7)

The C/N_0 degradation is considered to fit with the prediction model if the difference between the mean observed C/N_0 degradation and the predicted C/N_0 degradation does not exceed 1 dB. Considering this criterion, the observed C/N_0 degradation for all T_{sweep} values tested as part of IFEN simulation 7 fits with the prediction model, except when T_{sweep} is an exact divider of the integration time (1 ms). Indeed, when $T_{sweep} = \frac{T_i}{100} = 10 \mu s$, then the observed C/N_0 degradation is 9.7 dB, exceeding the targeted C/N_0 degradation by 2.7 dB. When $T_{sweep} = \frac{T_i}{99}$, the observed C/N_0 degradation is 5.2 dB, which is 1.8 dB below the targeted C/N_0 degradation. Observations on Figure 5-15 concerning Simulation 7 allows to conclude that the non-ergodicity region (T_{sweep} interval for which the difference between the targeted C/N_0 degradation and the observed C/N_0 degradation is higher than 1 dB) is lower than 1 μs .

Finally, Simulation 8 analyzes a particular case where T_{sweep} is very close to a divider of the integration time T_i . Indeed, in simulation 8, $T_{sweep} = 10.101 \mu s = \frac{T_i}{99}(1 - 10^{-6})$. As a consequence, the time offset δ_{kT_i} between the chirp RFI instantaneous frequency and the GPS L1C/A PRN code, which can be derived from (Eq 5-27), slowly varies from one correlation output to the next one. More precisely, the chirp RFI instantaneous frequency pattern is time shifted compared to the GPS L1C/A PRN code by $10^{-6}/99$ s every integration period. Since δ_{kT_i} varies slowly, and because the C/N_0 degradation under non-ergodicity conditions depends on δ_{kT_i} , therefore it can be predicted that the C/N_0 degradation varies within the time. Figure 5-16 represents the C/N_0 evolution within the time for simulation 8.

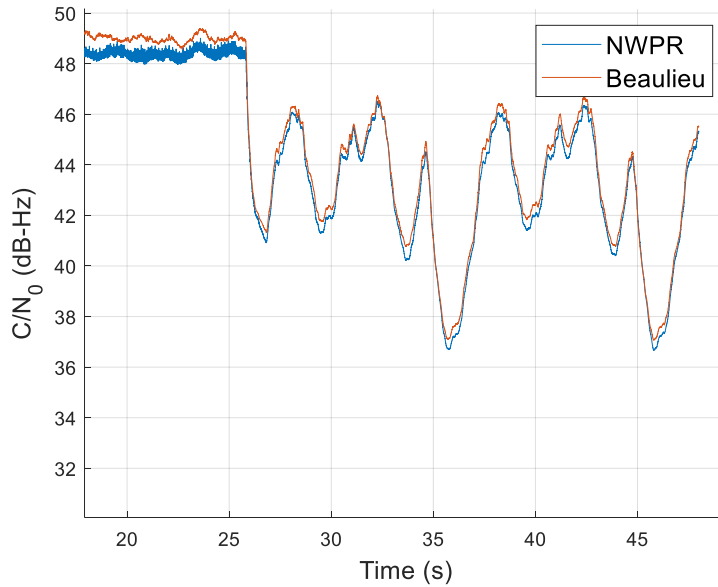


Figure 5-16: Evolution of C/N_0 estimations as a function of time of IFEN simulation 8

As predicted, the evolution of C/N_0 estimations as a function of time presents some time variations. In addition, these time variations of the estimated C/N_0 follow a periodic pattern. The corresponding period is around 10 s. This result can be theoretically recovered. Indeed, in 10 s, the chirp RFI instantaneous frequency pattern is time shifted from the GPS L1C/A PRN code by $\frac{10}{T_i} \times \frac{10^{-9}}{99} = T_{sweep}$: the periodicity of the C/N_0 pattern is driven by the periodicity of δ_{kT_i} .

These strong C/N_0 variations may be problematic when assessing the GNSS receiver robustness in presence of chirp RFI. Indeed, even though the mean C/N_0 degradation is lower than the targeted C/N_0 degradation by around 1.5 dB, the estimated C/N_0 degradation exceeds at some instant the targeted C/N_0 degradation by 4 dB. This situation may cause some continuity problems. Indeed, assuming that pseudorange accuracy flag is raised when C/N_0 goes below a threshold, pseudoranges provision may be lost if the C/N_0 depression due to chirp RFI is below the GNSS receiver tracking threshold, leading to a loss of the GNSS positioning service and a necessity to launch a re-acquisition process.

5-3.3 Conclusion on simulations

This section extracts the main conclusions of the comparison between the predicted C/N_0 degradation when injecting a chirp RFI and the observed C/N_0 degradation, where the C/N_0 is estimated with Beaulieu, Moment and NWPR algorithms. Several simulations were conducted to conduct this comparison using two different GNSS receivers: a Matlab software receiver and IFEN receiver plus a Matlab script exploiting the IFEN correlator outputs.

Matlab simulations allows to validate the three conditions of validity of the C/N_0 degradation prediction model developed in section 5-2.2, which have been identified in Chapter 2 section 2-4.3.2:

- 1) Validity of SNIR definition of (Eq 2-83): The RFI at correlator output must be such that the SNIR definition in Eq-1 is valid: centered RFI, RFI uncorrelated to GPS
- 2) C/N_0 estimators assumptions: The chirp RFI at the correlator output must have specific distribution, which depend on the C/N_0 estimation algorithm (condition of validity of C/N_0 estimator). For example, Moment estimator assumes a Gaussian distribution of the correlator output as well as the same standard deviation on the in-phase and quadrature phase channel

correlator outputs. Likewise, Beaulieu estimator assumes that successive chirp RFI correlation outputs are independent and identically distributed. If the chirp RFI does not have the correct distribution, the different C/N_0 algorithm may have different behavior.

- 3) Ergodicity of correlator outputs: The contribution of the chirp RFI at the correlator output must be ergodic (condition of validity of the prediction model). The ergodicity conditions are driven by two chirp RFI parameters: the period of repetition of the chirp RFI instantaneous frequency pattern T_{sweep} and the frequency offset between the chirp RFI and the GNSS signal Δf_j . Ergodicity conditions are: T_{sweep} should not be a divider of the integration period and Δf_j should not be a multiple of 1 kHz. If Δf_j is not a multiple of 1 kHz, if T_{sweep} is a divider of the integration period, then non ergodicity conditions happen.

Simulations with the IFEN receiver also verifies these three conditions of validity of the C/N_0 prediction model in presence of chirp RFI which is estimated by a GNSS receiver through a C/N_0 estimator. Ergodicity conditions are also further analyzed. T_{sweep} interval on which the prediction model does not fit with observation is quite narrow (less than $1 \mu s$) around T_i divisors. However, in the vicinity of these non-ergodicity points, chirp RFI causes strong C/N_0 variations which may cause GNSS loss of service.

5-4 Impact of chirp RFI on GPS signal processing stage

As C/N_0 is not a relevant indicator to characterize the impact of chirp RFI on GNSS receiver under non-ergodicity conditions, this section analyzes the impact of chirp RFI on code and phase measurements. The objective of this section is thus to derive code and phase measurement in presence of chirp RFI under the form of a time numerical series. This section is divided in three parts. First, contribution of chirp RFI to the correlator outputs is computed as a function of code, phase and doppler estimations returned by the receiver. Second, tracking loops models described in Chapter 2 section 2-3.3.3 are used to predict the code and phase tracking measurement errors in presence of chirp RFI under the form of a time series. Third, the prediction of the impact of chirp RFI on the code and phase tracking measurements are validated using the Matlab GPS L1C/A software receiver.

5-4.1 Chirp RFI at the correlator output

In this section, the mathematical expression of chirp RFI signal at the correlator output is derived. The chirp RFI signal at the correlator input is expressed in (Eq 5-14). As described in Chapter 2 section 2-3.3.1, two successive operations are performed on the signal at the correlator input: the chirp signal is first multiplied by the GPS local replica, and second, the results is integrated over one integration period T_i . The output of the integrator provides the correlator output.

The GPS L1/CA local replica can be expressed as in (Eq 2-35). The multiplication of the chirp RFI with the local replica can therefore be expressed by (Eq 5-29) for $t \in [MT_{sweep}; (M + 1)T_{sweep}]$ when assuming a constant T_i for notation simplification purposes.

$$\begin{aligned}
r_{mult}(t) &= S_{PPD,RFout}(t) \cdot s_L(t) \\
&= \sqrt{2C_J} \cdot c_L(t - \hat{t}_k) \cos\left(2\pi f_{IF}t + 2\pi \hat{f}_{D,k}(t - kT_i) + \hat{\varphi}_k\right) \cos\left(\begin{aligned} &2\pi(f_{IF} + \Delta f_j^c + f_{J,dopp})t \\ &+ \pi \frac{B}{T_{sweep}}(t - \delta - MT_{sweep})^2 \\ &- \pi B(t - \delta - MT_{sweep}) + \varphi_0 - \varphi_\delta \end{aligned}\right) \\
&= \sqrt{\frac{C_J}{2}} \cdot c_L(t - \hat{t}_k) \left(\begin{aligned} &\cos\left(\begin{aligned} &2\pi(2f_{IF} + \Delta f_j^c + f_{J,dopp})t \\ &+ \pi \frac{B}{T_{sweep}}(t - \delta - MT_{sweep})^2 \\ &- \pi B(t - \delta - MT_{sweep}) + \varphi_0 - \varphi_\delta + 2\pi \hat{f}_{D,k}(t - kT_i) + \hat{\varphi}_k \end{aligned}\right) + \\ &\cos\left(\begin{aligned} &2\pi(\Delta f_j^c + f_{J,dopp} - \hat{f}_{D,k})t + 2\pi \hat{f}_{D,k}kT_i - \hat{\varphi}_k \\ &+ \pi \frac{B}{T_{sweep}}(t - \delta - MT_{sweep})^2 - \pi B(t - \delta - MT_{sweep}) \\ &+ \varphi_0 - \varphi_\delta \end{aligned}\right) \end{aligned} \right) \quad (\text{Eq 5-29})
\end{aligned}$$

The multiplication result is the sum of two cosines. The first term has a high frequency in comparison to the first term, since f_{IF} has a magnitude of several MHz.

Then, the multiplication result is integrated over a period of duration T_i . This integration is equivalent to the application a low pass filter (called integrate and dump filter) which cut off frequency is $1/T_i$. For GPS L1C/A, the integration time is 20 ms during the tracking phase. Therefore, the integrate and dump filter attenuates all frequencies higher than 50 Hz. As a consequence, the high frequency term in (Eq 5-29) is negligible at the output of the correlator. The contribution of chirp RFI to in-phase correlator output is given by (Eq 5-30).

$$\begin{aligned}
I_{PPD}(k, \hat{t}_k, \hat{\varphi}_k, \hat{f}_{D,k}) &= \frac{1}{T_i} \int_{\hat{t}_k + kT_i}^{\hat{t}_k + (k+1)T_i} r_{mult}(t) dt = \sqrt{\frac{C_J}{2}} \frac{1}{T_i} r_I(k, \hat{t}_k, \hat{\varphi}_k, \hat{f}_{D,k}) \\
r_I(k, \hat{t}_k, \hat{\varphi}_k, \hat{f}_{D,k}) &= \sqrt{\frac{2}{C_J}} \int_{\hat{t}_k + kT_i}^{\hat{t}_k + (k+1)T_i} r_{mult}(t) dt \quad (\text{Eq 5-30})
\end{aligned}$$

Let us denote N the number of complete linear scanning of the impacted frequency band by the chirp time-frequency pattern during the integration. The integral term of (Eq 5-30) is split into a sum of integrations over successive time intervals of complete frequency scannings. Denoting $M_{\hat{t}_k} = \left\lfloor \frac{\hat{t}_k + kT_i - \delta}{T_{sweep}} \right\rfloor$ (when assuming constant T_i for notation simplification purposes), r_I can be re-written as in (Eq 5-31).

$$\begin{aligned}
& r_I(k, \hat{t}_k, \hat{\varphi}_k, \hat{f}_{D,k}) \\
&= \int_{\hat{t}_k + kT_i}^{\delta + M_{\hat{t}_k} T_{sweep}} c_L(t - \hat{t}_k) \cos \left(\begin{array}{l} \alpha(t - \delta - (M_{\hat{t}_k} - 1)T_{sweep})^2 \\ + \beta(t - \delta - (M_{\hat{t}_k} - 1)T_{sweep}) + \gamma_{-1} \end{array} \right) dt \\
&+ \sum_{n=0}^{N-1} \int_{\delta + (M_{\hat{t}_k} + n)T_{sweep}}^{\delta + (M_{\hat{t}_k} + n + 1)T_{sweep}} c_L(t - \hat{t}_k) \cos \left(\begin{array}{l} \alpha(t - \delta - (M_{\hat{t}_k} + n)T_{sweep})^2 \\ + \beta(t - \delta - (M_{\hat{t}_k} + n)T_{sweep}) \\ + \gamma_n \end{array} \right) dt \\
&+ \int_{\delta + (M_{\hat{t}_k} + N)T_{sweep}}^{\delta + (M_{\hat{t}_k} + N + 1)T_{sweep}} c_L(t - \hat{t}_k) \cos \left(\begin{array}{l} \alpha(t - \delta - (M_{\hat{t}_k} + N)T_{sweep})^2 \\ + \beta(t - \delta - (M_{\hat{t}_k} + N)T_{sweep}) \\ + \gamma_N \end{array} \right) dt
\end{aligned} \tag{Eq 5-31}$$

Coefficients α , β_n and γ_n are given by (Eq 5-32).

$$\begin{aligned}
\alpha &= \frac{\pi B}{T_{sweep}} \\
\beta &= 2\pi(\Delta f_j^c + f_{j,dopp} - \hat{f}_{D,k}) - \pi B = 2\pi(\Delta f_j + \varepsilon_f) - \pi B \\
\gamma_n &= 2\pi(\Delta f_j^c + f_{j,dopp} - \hat{f}_{D,k})(\delta + (M_{\hat{t}_k} + n)T_{sweep}) + 2\pi\hat{f}_{D,k}kT_i - \hat{\varphi}_k + \varphi_0 - \varphi_\delta
\end{aligned} \tag{Eq 5-32}$$

As discussed previously, the scanning period is up to some tens of μs in order to avoid that a notch filter is able to track and eliminate the chirp interference. Therefore, T_{sweep} is at least 100 times lower than the integration time during tracking phase. As a consequence, and considering that the jammer power is constant over the integration period, the first and last terms of equation (Eq 5-32) are considered negligible and only the sum term in is developed in the rest of this analysis. The sum term of (Eq 5-31) can be re-written as in (Eq 5-33) using the following change of variable, $u = t - \delta - (M_{\hat{t}_k} + n)T_{sweep}$.

$$\begin{aligned}
r_I &\approx \sum_{n=0}^{N-1} \int_{\delta + (M_{\hat{t}_k} + n)T_{sweep}}^{\delta + (M_{\hat{t}_k} + n + 1)T_{sweep}} c_L(t - \hat{t}_k) \cos \left(\begin{array}{l} \alpha(t - \delta - (M_{\hat{t}_k} + n)T_{sweep})^2 \\ + \beta_n(t - \delta - (M_{\hat{t}_k} + n)T_{sweep}) \\ + \gamma_n \end{array} \right) dt \\
&= \sum_{n=0}^{N-1} \int_0^{T_{sweep}} c_L(t + \delta + (M_{\hat{t}_k} + n)T_{sweep} - \hat{t}_k) \cos(\alpha t^2 + \beta t + \gamma_n) dt \\
&= \sum_{n=0}^{N-1} \int_{-\infty}^{+\infty} c_L \left((M_{\hat{t}_k} + n)T_{sweep} - \hat{t}_k + t + \delta \right) \cos \left(\begin{array}{l} \alpha t^2 + \\ \beta t + \gamma_n \end{array} \right) \text{rect}_{T_{sweep}} \left(t - \frac{T_{sweep}}{2} \right) dt \\
&= \sum_{n=0}^{N-1} I_n
\end{aligned} \tag{Eq 5-33}$$

With

$$I_n = \int_{-\infty}^{+\infty} c_L \left((M_{\hat{t}_k} + n)T_{sweep} - \hat{t}_k + t + \delta \right) \cos \left(\begin{array}{l} \alpha t^2 + \\ \beta t + \gamma_n \end{array} \right) \text{rect}_{T_{sweep}} \left(t - \frac{T_{sweep}}{2} \right) dt$$

I_n can be expressed as a convolution product between two functions g_n and f_n , where g_n and f_n are expressed in (Eq 5-34).

$$I_n = f_n(t) * g(t) \Big|_{\tau = \hat{t}_k - \delta - (M_{\hat{t}_k} + n)T_{sweep}} \tag{Eq 5-34}$$

$$g(t) = c_L(-t)$$

$$f_n(t) = \cos(\alpha t^2 + \beta t + \gamma_n) \text{rect}_{T_{\text{sweep}}}\left(t - \frac{T_{\text{sweep}}}{2}\right)$$

The computation is continued in the frequency domain where the convolution is transformed into a multiplication. Thus, the Fourier transforms of functions g and f_n are computed hereinafter. Fourier transform of g is given in (Eq 5-35).

$$G(f) = C_L^*(f) \quad (\text{Eq 5-35})$$

C_L is the Fourier transform of the PRN code c_L , expressed in (Eq 2-5) for GPS L1C/A. For the BPSK modulated PRN code of GPS L1C/A, (Eq 5-35) can be reduced to (Eq 5-36).

$$G(f) = \left(\sum_{k=0}^{L_{\text{PRN}}-1} c(k) e^{i2\pi f(k+\frac{1}{2})T_c} \right) \left(\frac{1}{T_r} \sum_{j=-\infty}^{+\infty} \delta\left(f - \frac{j}{T_r}\right) \right) T_c \text{sinc}(\pi f T_c) \quad (\text{Eq 5-36})$$

Let us denote $C_0(f) = \sum_{k=0}^{L-1} c(k) e^{i2\pi f(k+\frac{1}{2})T_c}$ the Fourier transform of the PRN code (when PRN code is assumed to start at time $t = 0$), and $C_{\text{sinc}}(j) = \frac{T_c}{T_r} \text{sinc}\left(\pi \cdot j \cdot \frac{T_c}{T_r}\right) C_0\left(\frac{j}{T_r}\right)$. Under its polar notation, C_{sinc} is expressed in (Eq 5-37).

$$C_{\text{sinc}}(f) = |C_{\text{sinc}}(f)| e^{i\varphi_{\text{sinc}}(f)} \quad (\text{Eq 5-37})$$

Note C_0 has the Hermitian symmetry since $c_L(t)$ is real, so φ_{sinc} is an odd function of f .

Eventually, (Eq 5-36) can be reduced to the expression given in (Eq 5-38).

$$G(f) = \sum_{j=-\infty}^{+\infty} C_{\text{sinc}}\left(\frac{j}{T_r}\right) \delta\left(f - \frac{j}{T_r}\right) \quad (\text{Eq 5-38})$$

$G(f)$ is a line spectrum, with lines regularly spaced every 1 kHz. Moreover, since the PRN signal is BPSK modulated, $G(f)$ has also a cardinal sinus shape, with zeros appearing every multiple of the chip rate (1.023 MHz).

Figure 5-17 represents $|G(f)|$ at each multiple of $1/T_r$ for PRN1. It can be noticed that a large part of the PRN signal energy is held in the first lobes.

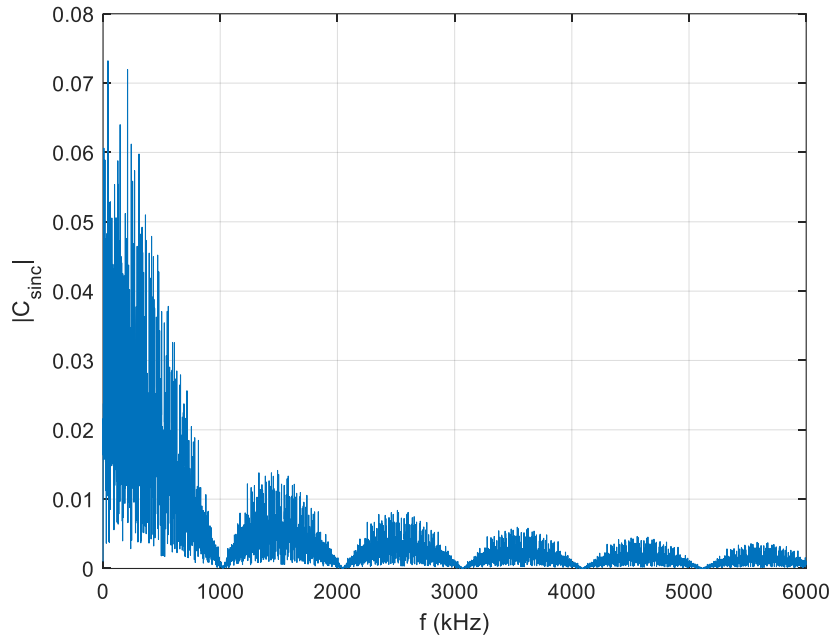


Figure 5-17: Spectrum of GPS L1C/A PRN1 modulated signal

The Fourier transform of $f_n(t)$ must be computed. $f_n(t)$ is a chirp function with finite support in the time domain. The derivation of the chirp Fourier transform is performed in Appendix F following steps described in [84]. The chirp Fourier transform is finally given by (Eq 5-39).

$$F_n(f) = \frac{Int_1(f) + Int_2(f)}{2}$$

$$Int_1 = \sqrt{\frac{T_{sweep}}{2B}} e^{-i\frac{\pi T_{sweep}}{4B}(2(f-\Delta f_j - \varepsilon_f) + B)^2 + i\gamma_n} \begin{bmatrix} C \left(\sqrt{\frac{BT_{sweep}}{2}} + \sqrt{\frac{2T_{sweep}}{B}}(f - \Delta f_j - \varepsilon_f) \right) \\ + C \left(\sqrt{\frac{BT_{sweep}}{2}} - \sqrt{\frac{2T_{sweep}}{B}}(f - \Delta f_j - \varepsilon_f) \right) \\ + iS \left(\sqrt{\frac{BT_{sweep}}{2}} + \sqrt{\frac{2T_{sweep}}{B}}(f - \Delta f_j - \varepsilon_f) \right) \\ + iS \left(\sqrt{\frac{BT_{sweep}}{2}} - \sqrt{\frac{2T_{sweep}}{B}}(f - \Delta f_j - \varepsilon_f) \right) \end{bmatrix} \quad (\text{Eq 5-39})$$

$$Int_2 = \sqrt{\frac{T_{sweep}}{2B}} e^{i\frac{\pi T_{sweep}}{4B}(2(f+\Delta f_j + \varepsilon_f) - B)^2 - i\gamma_n} \begin{bmatrix} C \left(\sqrt{\frac{BT_{sweep}}{2}} + \sqrt{\frac{2T_{sweep}}{B}}(f + \Delta f_j + \varepsilon_f) \right) \\ + C \left(\sqrt{\frac{BT_{sweep}}{2}} - \sqrt{\frac{2T_{sweep}}{B}}(f + \Delta f_j + \varepsilon_f) \right) \\ - iS \left(\sqrt{\frac{BT_{sweep}}{2}} + \sqrt{\frac{2T_{sweep}}{B}}(f + \Delta f_j + \varepsilon_f) \right) \\ - iS \left(\sqrt{\frac{BT_{sweep}}{2}} - \sqrt{\frac{2T_{sweep}}{B}}(f + \Delta f_j + \varepsilon_f) \right) \end{bmatrix}$$

F_n can be written under its exponential form in (Eq 5-40).

$$F_n(f) = |F_n(f)| e^{i\varphi_n(f)} \quad (\text{Eq 5-40})$$

Knowing the analytical expression of the Fourier transform of f_n and g , (Eq 5-34) can be developed in the frequency domain in (Eq 5-41), multiplying G (Eq 5-38) and F_n (Eq 5-40).

$$\begin{aligned} FT\{I_n\} &= G(f)F_n(f) \\ &= \sum_{j=-\infty}^{+\infty} \left| F_n\left(\frac{j}{T_r}\right) \right| \left| C_{sinc}\left(\frac{j}{T_r}\right) \right| e^{i\left(\varphi_{sinc}\left(\frac{j}{T_r}\right) + \varphi_n\left(\frac{j}{T_r}\right)\right)} \delta\left(f - \frac{j}{T_r}\right) \end{aligned} \quad (\text{Eq 5-41})$$

Finally, the computation of I_n can be completed in (Eq 5-42), taking the inverse Fourier transform of (Eq 5-41) and by evaluating the time variable at $\hat{t}_k - \delta - (M_{\hat{t}_k} + n)T_{sweep}$.

$$I_n = \sum_{j=-\infty}^{+\infty} \left| F_n\left(\frac{j}{T_r}\right) \right| \left| C_{sinc}\left(\frac{j}{T_r}\right) \right| e^{i\left(2\pi\frac{j}{T_r}(\hat{t}_k - \delta - (M_{\hat{t}_k} + n)T_{sweep})\varphi_{sinc}\left(\frac{j}{T_r}\right) + \varphi_n\left(\frac{j}{T_r}\right)\right)} \quad (\text{Eq 5-42})$$

As noted in Figure 5-17, the energy of the PRN local replica is contained in the first main lobes. As a consequence, the sum term in (Eq 5-42) can be truncated for values of j above a particular threshold.

In this chapter, only the 6000 first terms are considered ($j \leq 6000$), containing 98.3% of the local replica power and leading to a good prediction of correlator outputs.

Finally, the in-phase correlator output in presence of a PPD signal is given by (Eq 5-43).

$$I_{PPD}(k, \hat{\tau}_k, \hat{\phi}_k, \hat{f}_{D,k}) = \sqrt{\frac{C_J}{2}} \frac{1}{T_i} \sum_{n=0}^{N-1} I_n \quad (\text{Eq 5-43})$$

The calculation of the quadrature phase correlator output follows the same method. The quadrature phase local replica is rotated by $\pi/2$ compared to the in-phase local replica given by (Eq 2-35). As a consequence, value of γ_n is increased by $\pi/2$. Other expressions are not modified.

In order to validate (Eq 5-43), a linear sweep PPD interference is generated and is correlated with a GPS local replica in a Matlab script. In this section, jammer settings are fixed according to Table 5-7.

Interference bandwidth B	Sweep period T_{sweep}	Jammer power	Jammer frequency setting $\Delta f_J + f_{J,dopp}$	Integration time, T_i
2 MHz	10 μ s	-137 dBW	4 kHz	1 ms

Table 5-7: Settings used for validation of PPD correlator output mathematical model

Prediction of in phase correlator outputs due to the linear sweep PPD interference are derived from (Eq 5-43). Figure 5-18 shows the comparison between the linear sweep PPD interference in phase correlator output prediction from (Eq 5-43) and the value returned from the Matlab implemented correlation. In order to highlight the dependency of (Eq 5-43) on tracking estimations $\hat{\tau}_k, \hat{\phi}_k, \hat{f}_{D,k}$, three plots are provided. For each plot, two tracking estimations are fixed, and the remaining tracking estimations is used as the input parameter.

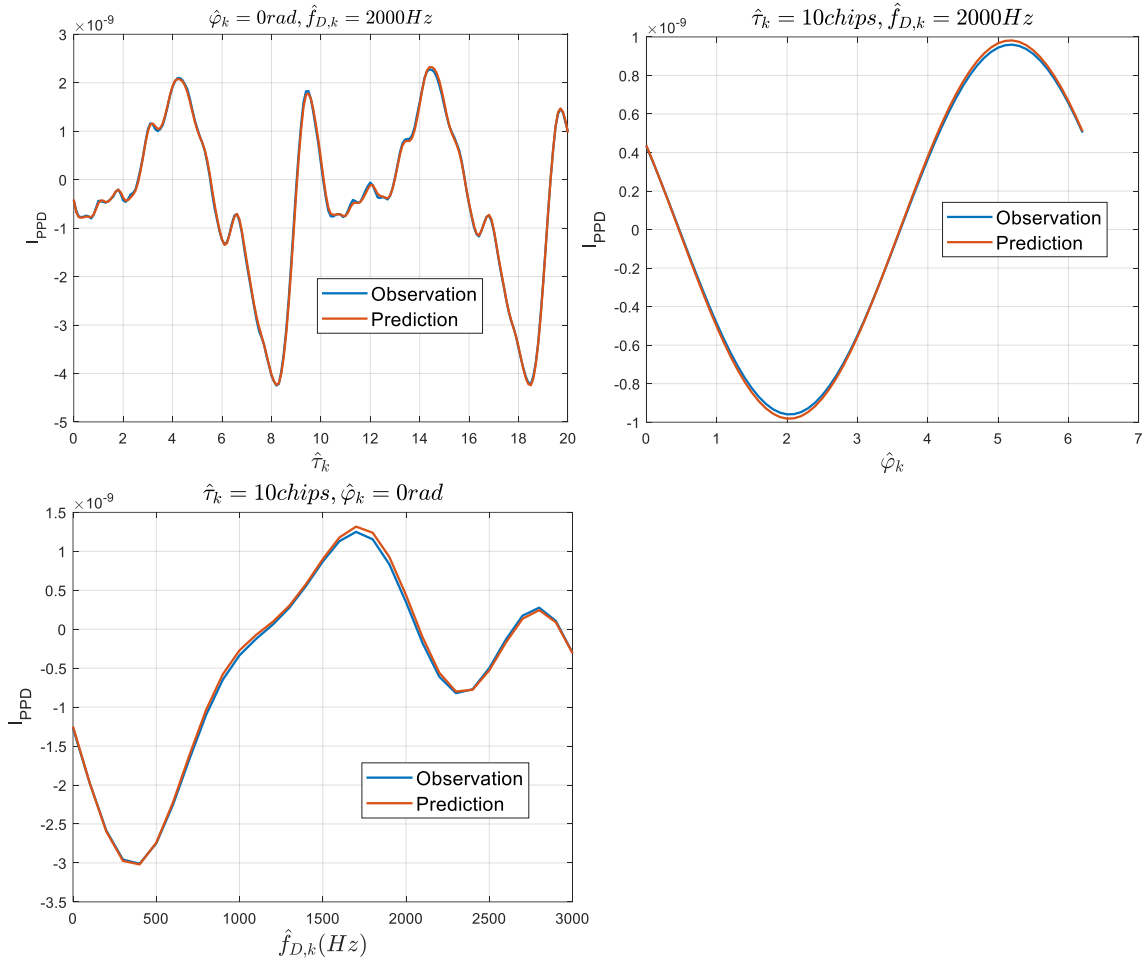


Figure 5-18: Prediction and observed correlator output from a software receiver, when a PPD signal is correlated with PRN1 local replica

Comparing the different plots on Figure 5-18, it can be observed that predictions fit tightly the correlator outputs returned by the Matlab script. (Eq 5-43) is thus validated. The small difference between the observation and the prediction can be explained by the approximation of (Eq 5-33).

5-4.1.1 Prediction of tracking error in presence of chirp RFI

The goal of this section is to predict the evolution of tracking estimation $\hat{t}_k, \hat{\varphi}_k, \hat{f}_{D,k}$ as a function of time, when a GPS L1C/A receiver processes a GPS signal impacted by a linear sweep PPD interference. The GNSS tracking stage is described in Chapter 2 section 2-3.3.3. The main inputs of tracking loops are the correlator outputs. In presence of chirp RFI, prompt (I_P, Q_P) early (I_E, Q_E) and late (I_L, Q_L) correlator outputs can be expressed as in (Eq 5-44).

$$\begin{aligned}
 I_P &= I_{GNSS}(k, \hat{t}_k, \hat{\varphi}_k, \hat{f}_{D,k}) + I_{PPD}(k, \hat{t}_k, \hat{\varphi}_k, \hat{f}_{D,k}) \\
 Q_P &= Q_{GNSS}(k, \hat{t}_k, \hat{\varphi}_k, \hat{f}_{D,k}) + Q_{PPD}(k, \hat{t}_k, \hat{\varphi}_k, \hat{f}_{D,k}) \\
 I_E &= I_{GNSS}\left(k, \hat{t}_k - \frac{C_S}{2}, \hat{\varphi}_k, \hat{f}_{D,k}\right) + I_{PPD}\left(k, \hat{t}_k - \frac{C_S}{2}, \hat{\varphi}_k, \hat{f}_{D,k}\right) \\
 Q_E &= Q_{GNSS}\left(k, \hat{t}_k - \frac{C_S}{2}, \hat{\varphi}_k, \hat{f}_{D,k}\right) + Q_{PPD}\left(k, \hat{t}_k - \frac{C_S}{2}, \hat{\varphi}_k, \hat{f}_{D,k}\right) \\
 I_L &= I_{GNSS}\left(k, \hat{t}_k + \frac{C_S}{2}, \hat{\varphi}_k, \hat{f}_{D,k}\right) + I_{PPD}\left(k, \hat{t}_k + \frac{C_S}{2}, \hat{\varphi}_k, \hat{f}_{D,k}\right)
 \end{aligned} \tag{Eq 5-44}$$

I_{GNSS} and Q_{GNSS} are the correlator output of the GNSS useful signal and have been derived in (Eq 2-40) and (Eq 2-41). I_{PPD} and Q_{PPD} are the chirp contribution to correlator output and have been derived in section 5-4.1.

5-4.1.1.1 Prediction of phase and Doppler estimations $\hat{\varphi}_k$ and $\hat{f}_{D,k}$

This section computes phase and Doppler estimations output by the PLL described in Chapter 2 section 3.3.3.1. As a reminder, the PLL is composed by three elements:

- A discriminator estimates the difference between the phase of the incoming signal and the phase of the GNSS local replica. In this section, the atan discriminator defined in (Eq 2-58) is considered. The atan discriminator output at iteration k is given by (Eq 5-45).

$$D_{\varphi,k}^{atan} = -\operatorname{atan}\left(\frac{Q_{GNSS}(k, \hat{t}_k, \hat{\varphi}_k, \hat{f}_{D,k}) + Q_{PPD}(k, \hat{t}_k, \hat{\varphi}_k, \hat{f}_{D,k})}{|I_{GNSS}(k, \hat{t}_k, \hat{\varphi}_k, \hat{f}_{D,k}) + I_{PPD}(k, \hat{t}_k, \hat{\varphi}_k, \hat{f}_{D,k})|}\right) \quad (\text{Eq 5-45})$$

- A low pass filter filters the discriminator output in order to attenuate the influence of the noise. In this section, a third order low-pass filter is considered. Its transfer function H_{LP} is given by (Eq 5-46).

$$H_{LP}(z) = \frac{1}{2\pi T_i} \frac{K_1 + K_2 + K_3 - (2K_1 + K_2)z^{-1} + K_1z^{-2}}{1 - 2z^{-1} + z^{-2}} \quad (\text{Eq 5-46})$$

Coefficients K_1, K_2 and K_3 are given in Chapter 2 Table 4 as a function of the loop bandwidth B_φ . In this section, $B_\varphi = 10 \text{ Hz}$.

- An NCO then integrates the loop filter output to provide the phase estimation $\hat{\varphi}_k$ used to generate the local replica. Its transfer function F_{NCO} is given by (Eq 2-62).

The open loop transfer function is thus obtained in (Eq 5-47).

$$\begin{aligned} H_\varphi(z) &= \frac{\hat{\varphi}(z)}{D_\varphi^{atan}(z)} = H_{LP}(z)F_{NCO}(z) \\ &= \frac{K_1 + K_2 + K_3 - (2K_1 + K_2)z^{-1} + K_1z^{-2}}{1 - 2z^{-1} + z^{-2}} \frac{z^{-1}}{1 - z^{-1}} \\ &= \frac{(K_1 + K_2 + K_3)z^{-1} - (2K_1 + K_2)z^{-2} + K_1z^{-3}}{1 - 3z^{-1} + 3z^{-2} - z^{-3}} \end{aligned} \quad (\text{Eq 5-47})$$

$\hat{\varphi}(z)$ and $D_\varphi^{atan}(z)$ are respectively the z-transform of the local replica phase estimation and the z-transform of the discriminator output.

The open loop transfer function of the PLL allows to determine the phase tracking estimation from the past phase tracking estimations and discriminator outputs. In particular, the phase tracking estimation at the iteration k is deduced from the inverse z-transform of (Eq 5-47) is given by (Eq 5-48).

$$\hat{\varphi}_k = 3\hat{\varphi}_{k-1} - 3\hat{\varphi}_{k-2} + \hat{\varphi}_{k-3} + (K_1 + K_2 + K_3)D_{\varphi,k-1}^{atan} - (2K_1 + K_2)D_{\varphi,k-2}^{atan} + K_1D_{\varphi,k-3}^{atan} \quad (\text{Eq 5-48})$$

$D_{\varphi,i}^{atan}$ is the phase discriminator output at iteration i. Similarly, the Doppler estimation at iteration k is also deduced from the loop filter transfer function. It is given by (Eq 5-49).

$$\hat{f}_{D,k} = 2\hat{f}_{D,k-1} - \hat{f}_{D,k-2} + \frac{K_1 + K_2 + K_3}{2\pi T_i} D_{\varphi,k-1}^{atan} - \frac{2K_1 + K_2}{2\pi T_i} D_{\varphi,k-2}^{atan} + \frac{K_1}{2\pi T_i} D_{\varphi,k-3}^{atan} \quad (\text{Eq 5-49})$$

5-4.1.1.2 Prediction of code delay estimation $\hat{\tau}_k$

As for the PLL, the DLL is composed by three elements as described in Chapter 2 section 2-3.3.3.2:

- The discriminator provides an estimation of the code delay tracking error. In this chapter, the Early Minus Late Power (EMLP) discriminator defined in (Eq 2-65) is considered.
- Then, the discriminator output passes through low pass filter. In this chapter, an order 1 DLL low pass filter is selected, and its transfer function is constant and equal to K_1^{DLL}/T_i . K_1^{DLL} is the code loop coefficient, and $K_1^{DLL} = 4B_L^{DLL}T_i$. B_L^{DLL} is the loop bandwidth. In our software receiver, B_L^{DLL} is set to 1 Hz.
- Next, the output of the DLL filter is integrated by the NCO, whose transfer function is given in (Eq 5-50).

$$F_{NCO}^{DLL}(z) = -T_i \frac{1}{1 - z^{-1}} \quad (\text{Eq 5-50})$$

From the DLL open loop transfer function, the code delay estimation at the following iteration $k+1$ can be computed as a function of the discriminator output. $\hat{\tau}_{k+1}$ is provided in (Eq 5-51).

$$\hat{\tau}_{k+1} = \hat{\tau}_k - K_1^{DLL} \cdot D_{\tau,k} \quad (\text{Eq 5-51})$$

As a conclusion, from the code delay, phase and Doppler of the incoming signal, it is possible to predict the code delay, phase and Doppler estimation used to generate the GNSS local replica. Tracking errors ε_τ , ε_ϕ and ε_f can therefore be deduced under the form of numerical series from the knowledge of chirp and GNSS signal characteristics.

5-4.1.2 Validation of tracking error prediction model

The objective of this section is to validate the prediction of code delay, carrier phase and Doppler frequencies estimations made in section 5-4.1.1. In order to achieve this objective, a comparison between the prediction proposed in section 5-4.1.1 and a Matlab GNSS receiver output observables is done. Settings of the GPS L1C/A signal, PPD signal and receiver are summarized in Table 5-8. The interference is switched on after 3 s of simulation.

GNSS signal	PRN	1
	Doppler frequency	2500 Hz
	Power	-156.5 dBW
Chirp RFI	Bandwidth B	2 MHz
	Scanning period T_{sweep}	10 μ s
	Power	-130 dBW
	Jammer frequency setting $\Delta f_J + f_{J,dopp}$	3500 Hz
Receiver	Thermal noise N_0	No noise added
	Intermediate frequency	40 MHz
	Integration time	1 ms

Table 5-8: GPS signal and chirp RFI settings for validation of tracking errors prediction model

It can be remarked from Table 5-8 that the chirp settings used here correspond to non-ergodicity conditions.

The power of the RFI would corresponds to the received power at the GNSS receiver antenna port, where a 10 mW EIRP jammer located at 2 km from the victim receiver (assuming a GNSS receiver antenna gain of -7.5 dB and 3 dB polarization losses).

Figure 5-19 shows the result of the comparison between the prediction of the receiver outputs on several observables:

- In-phase correlator output.
- Code delay tracking errors.
- Phase tracking error.
- Doppler tracking error.

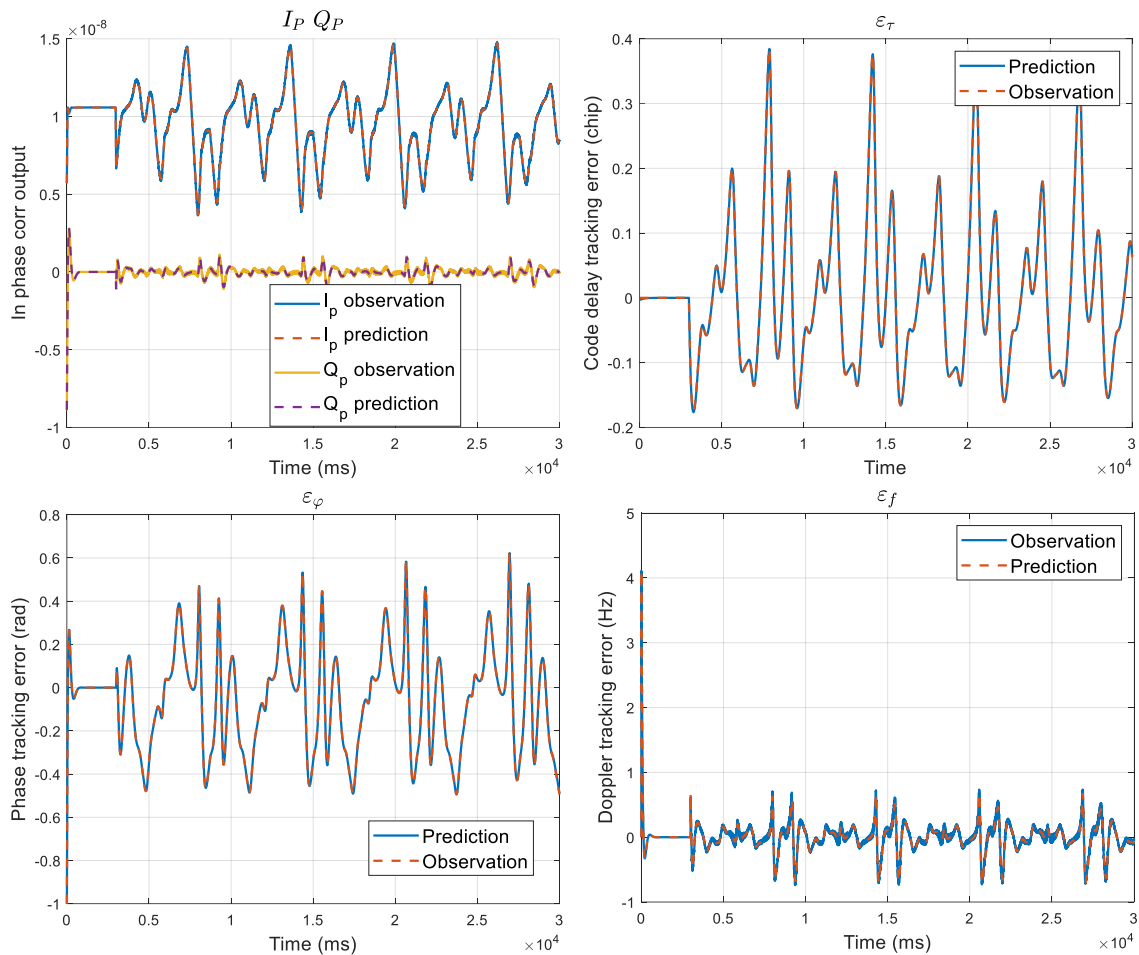


Figure 5-19: Validation of tracking errors prediction model in presence of chirp RFI

The prediction of correlator output, code tracking error, carrier phase tracking error and Doppler frequency tracking error fits very well the values calculated on the Matlab GNSS receiver. The very small difference between prediction and observation is due to the approximation made in (Eq 5-33), but this difference is negligible.

Therefore, the impact of the linear sweep PPD jammer on a receiver can be predicted from the knowledge of its main characteristics. This prediction model is then validated and available for any further use to predict correlator outputs, range errors, position errors for a chirp signal with any setting parameters.

5-4.1.3 Interest and significance of time analysis

The interest and significance of this analysis and this model of correlator outputs, and phase and code tracking estimation, are presented in this section.

First, the model can be used to predict full correlator outputs, range errors and position errors in the situation where the RFI chirp signal fulfills stationarity and thus ergodicity conditions for a given coherent integration time.

Second, section 5-3 shows that in case of ergodic chirp signal characteristics, the variance of the pseudorange error due to noise plus chirp interference can be derived from the typical relationship between the effective C/N_0 and the close-loop variance in nominal AWGN conditions. However, this relationship is no more applicable in under non-ergodicity conditions. Therefore, the prediction model developed in this section allows to predict the pseudorange error variance in non-ergodic conditions.

Third, in case of non-ergodic chirp signal characteristics, the correlator output and tracking error prediction model may help in the definition of test procedures developed for civil aviation GNSS receiver certification purpose. As a matter of fact, the most significant test parameters may be deduced from the prediction model. This capacity to identify the most relevant chirp parameters could have a major impact on the civil aviation jammer robustness test procedures definition

5-4.1.4 Investigation of C/N_0 estimators' difficulties on non-ergodicity scenarios

As already observed in Figure 5-16 for C/N_0 time evolution in presence of chirp RFI under non-ergodicity conditions, correlator outputs and tracking errors also present slow and periodic variations. The periodicity is driven by the GNSS doppler frequency as well as the chirp RFI sweep period T_{sweep} .

As the chirp RFI contribution to correlator output is now mathematically modeled and validated, the validity of C/N_0 estimators under non-ergodicity conditions can be further investigated. Figure 5-20 shows the time evolution of the contribution of the GPS signal and chirp RFI to the correlator outputs.

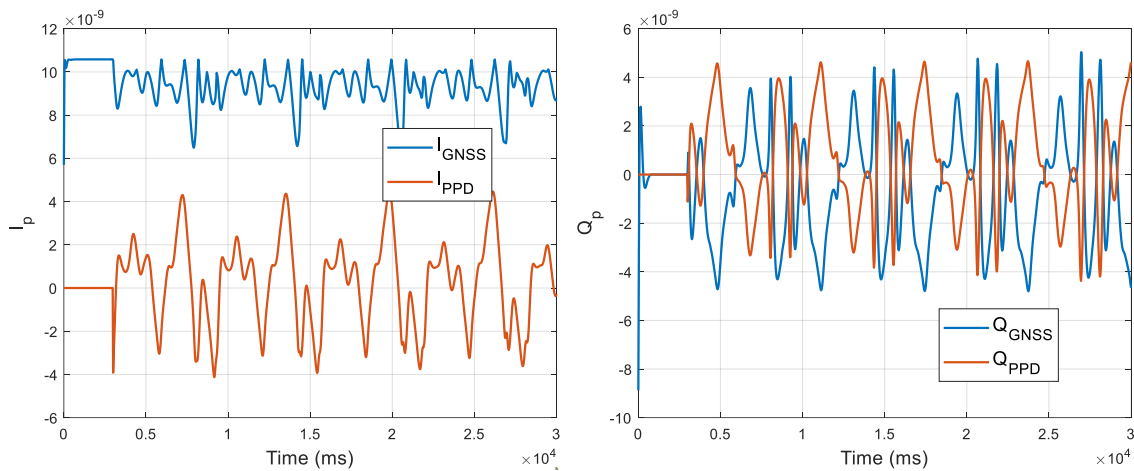


Figure 5-20: Time evolution of chirp and GNSS signal to correlator output

Several conclusions can be deduced from observations made on Figure 5-20.

- First, the presence of the chirp RFI causes a decrease of the amplitude of I_{GNSS} , and therefore a decrease of the recovered GNSS power at the correlator output.
- Second, the amplitude of GNSS contribution to correlator output has some slow time variation. This phenomenon leads to a time evolution of the recovered GNSS signal power at the correlator output, and therefore a time evolution of the C/N_0 .
- Third and more important, contributions of GNSS signal and chirp RFI to correlator outputs are not independent. This phenomenon causes the invalidity of the SNIR definition of (Eq 2-83). Indeed, the effective noise power at the correlator output is given by (Eq 5-52).

$$\mathbb{V}(Q_P) = \mathbb{V}(n_Q + Q_{GNSS} + Q_{PPD}) = \frac{\beta N_0}{4T_i} + \mathbb{V}(Q_{GNSS} + Q_{PPD}) \quad (\text{Eq 5-52})$$

Since Q_{GNSS} and Q_{PPD} are not independent, $\mathbb{V}(Q_{GNSS} + Q_{PPD}) \neq \mathbb{V}(Q_{GNSS}) + \mathbb{V}(Q_{PPD})$. In addition, Figure 5-20 shows that Q_{GNSS} and Q_{PPD} evolve in phase opposition. As a consequence, $\mathbb{V}(Q_{GNSS} + Q_{PPD})$ is very low in comparison to $\mathbb{V}(Q_{PPD})$. Indeed, in the simulation of Figure 5-20, $\frac{\mathbb{V}(Q_{GNSS}+Q_{PPD})}{\mathbb{V}(Q_{PPD})} = 0.03$. Under non-ergodicity conditions, SNIR definition of (Eq 2-83) does not correctly reflect the RFI power at the correlator output. As a result, C/N_0 estimators, which are based on that SNIR definition, are irrelevant to characterize the impact of chirp RFI on GNSS receiver under non-ergodicity conditions.

5-4.2 Conclusion

This chapter analyzes the impact of linear sweep jammers, also known as linear chirp, on GNSS receivers as a generic case of time-frequency jamming signature RFI.

First, a mathematical model of the linear chirp signal was proposed, and the 2nd order wide sense stationarity of the chirp signal at the RFFE output was proven.

Second, the computation of the carrier to effective noise density ratio in presence of linear chirp signal was conducted using the SSC term and exploiting the stationarity of the chirp signal. The effect of some of the RFI parameters on the C/N_0 were characterized. A strong dependency on the SSC (between the GNSS signal and the chirp signal) of the chirp parameters, which are (1) received jammer to local GNSS frequency offset Δf_j , (2) T_{sweep} and (3) the integration time T_i , was identified. When T_i is low, the SSC does not vary significantly as a function of Δf_j . When T_i is high, the SSC strongly depends on Δf_j since the local replica PSD is discrete-like (with narrow squared sine functions instead of actual lines). This dependency is amplified if T_{sweep} is a divider of the PRN code period, equal to 1 ms for GPS L1 C/A as all the lines of the PRN code signal spectrum and chirp signal spectrum would overlap. In addition, the analysis of three C/N_0 estimators in presence of the linear chirp RFI was performed. The main conclusions extracted from this analysis are:

- The RFI at the correlator output must be centered and independent from GPS signal so that SNIR definition of (Eq 2-83), from which C/N_0 estimators are built, is valid (condition of validity of SNIR definition).
- C/N_0 estimators make some assumptions of the distribution of correlator outputs. These assumptions must be met so that C/N_0 estimations fit to the true C/N_0 . For example, some estimators assume the same distribution on the in-phase and quadrature phase correlator outputs. Moment estimator also assumes that the correlator output distribution is gaussian.
- The ergodicity of the linear chirp signal, which is driven by the terms T_{sweep} and Δf_j , is a necessary condition so that the C/N_0 degradation prediction model assumption (linear chirp signal is 2nd order wide sense stationary) is consistent with the observation (condition of validity of the prediction model). If Δf_j is not a multiple of 1 kHz as will be very frequent in reality, if T_{sweep} is a divider of T_i , then non ergodicity situations will arise. And exact dividers of T_i are very close to each other in the region of a few microseconds.

Third, the impact of chirp RFI on GPS receiver tracking loops observables is mathematically developed and validated through simulations; this analysis is fundamental for chirp signal parameters creating scenarios where ergodicity conditions are not fulfilled and thus the use of C/N_0 estimation as key RFI presence indicator is unsuitable. A mathematical model of chirp RFI at the correlator output is derived, as a function of the chirp RFI characteristics and GNSS local replica estimations (code delay, carrier phase and Doppler frequency). From the correlator output in presence of chirp RFI, the impact of the

chirp RFI on the tracking loop is analyzed and code delay, phase and Doppler tracking errors are mathematically derived under the form of numerical series. This time analysis is significant for the definition of test procedure for certification of civil aviation GNSS receivers as it allows to identify the most relevant settings.

Finally, the reason why the C/N_0 estimation is no valid under non-ergodicity conditions is further discussed from the knowledge of chirp RFI mathematical model at the correlator output. From the chirp contribution to the mathematical model, it can be observed the dependency between the chirp RFI and GNSS signal contributions at the correlator output. Therefore, the SNIR definition on which the C/N_0 estimators are based does not correctly reflect the RFI noise power (as was theoretically modelled), leading to incorrect SNIR estimations.

Chapter 6: Impact of interference on GMSK C2Link receiver performance

The C2Link system and signals concept have been presented in Chapter 3. The objective of this chapter is to investigate the resiliency of C2Link signal receiver to radio frequency interferences (RFI). This chapter focuses on the C2Link signal used for the terrestrial architecture and which Gaussian Minimum Shift Keying (GMSK) modulated. The mathematical model of the C2Link signal has been presented in Chapter 3 section 3-3.

One objective initially identified was the determination of protection areas for C2Link receivers during jamming operations. Chapter 4 highlights the significance of the precise assessment of the RFI environment to in the calculation of the protection area. One key RFI source is the inter system RFI composed by C2Link signals different from the C2Link signal of interest. Because the future RPAS traffic remains difficult to precisely characterize, the determination of C2Link protection area would be very unprecise based on current RPAS traffic previsions assumptions. Therefore, the full calculation of C2Link protection area is not performed in this chapter.

Instead, the overall objective of this chapter is to propose a prediction model of the impact of RFI on C2Link receivers analyzing several performance indicators. Once the RPAS traffic would be precisely assessed, it will be possible to apply this impact prediction model to determine the C2Link protection area.

To achieve this objective, this chapter is divided in two sections.

- First, generic signal processing modules of a GMSK receiver compliant with DO-362 [8] definitions summarized in Chapter 3 section 3-2.4 are designed. The objective of this first part is to develop a prototype that will be used to validate the impact prediction model. Remember that channel coding is not implemented within this receiver. Designed receiver performance is analyzed from one performance indicator, the bit error rate (BER). Indeed, the word error rate (WER) is the indicator selected in DO-362 to calculate link budgets as part of C2Link receiver performance assessment in nominal RFI environment.
- Second, a mathematical model of the impact of RFI on WER is derived. This mathematical model is validated using the developed C2Link GMSK receiver.

6-1 Development of a GMSK C2Link receiver

The objective of this section is to present the main signal processing functions of a receiver developed in accordance with DO-362 requirements. This section is divided in five parts. First, the architecture of classical GMSK receiver is presented. Signal processing modules of interest to characterize the impact of RFI on C2Link receiver are identified. They include the synchronization module and the demodulation module. Indeed, the demodulation module is necessary to analyze the C2Link BER and WER performance, which is the selected C2Link performance indicator in standards. Synchronization module is also implemented to verify that synchronization errors induced by noise and RFI do not cause BER degradation. Second, GMSK modulated signal, which has been mathematically defined in Chapter 3 section 3-3, is re-written under the form of sum of amplitude modulated signals using Laurent decomposition of CPM signals. Third, the synchronization module of the software receiver is

presented. Fourth, the demodulation module of the C2Link software receiver is introduced. Fifth, the performances of the designed C2Link signal processing modules are analyzed.

6-1.1 C2Link digital receiver architecture

The architecture of a GMSK modulated signal digital receiver is presented in Figure 6-1.

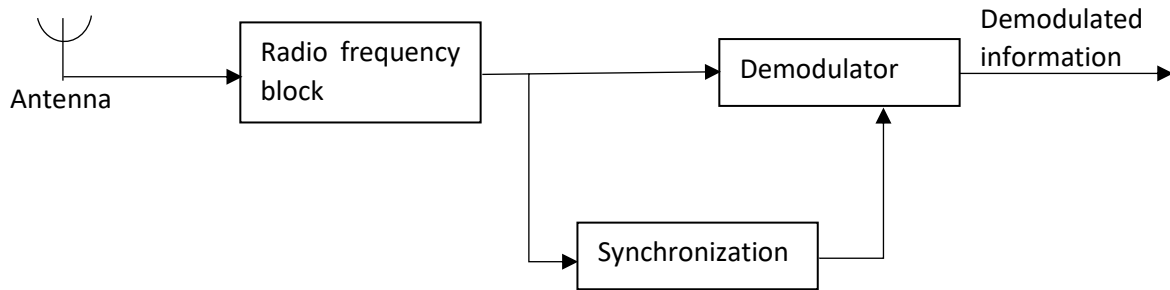


Figure 6-1: Simplified block diagram of digital receiver

The radio-frequency block of Figure 6-1 is similar to RF front-end module of GNSS receiver detailed in Chapter 2 section 2-3.1. In this chapter, it is supposed that the RF/IF equivalent filter contained within the radio frequency block does not impact the useful part of the received signal. The objective of the synchronization block is to estimate time delay and phase of the received signal at the RFFE output. This operation is necessary to sample the receiver matched filter output at the optimal instant of time and to correct the incoming signal carrier phase in order to minimize the BER. Eventually, the goal of the demodulator is to estimate the transmitted information while minimizing the BER. In this chapter, the synchronization and the demodulator blocks are investigated in detail.

6-1.2 Laurent decomposition of GMSK signal

Synchronization and demodulator modules will be constructed based on the received signal mathematical model. The complexity of these two modules will depend on the complexity of the received signal mathematical model and thus, a simplified model is desirable. The main complication of a GMSK modulated signal is the inter-symbol interference (ISI) of the modulation or, seen from another perspective, the memory of the modulation, since the transmission of symbol at epoch k impacts the signal waveform for consecutive epochs ($k + 1, k + 2$, etc.).

In this section, the Laurent decomposition of CPM signals is applied to the GMSK modulated signal of interest in order to obtain a final simplified mathematical model. Indeed, in this section, the Laurent decomposition will be used to obtain an equivalent linear amplitude modulation expression instead of the CPM expression. Moreover, from the linear modulation expression, the identified terms will be analyzed and finally omitted if their contribution to the received signal is considered to be negligible. The result of this process will be a more simplified process where the inherent ISI or modulation memory can just be greatly simplified. Therefore, the final goal of this section is to apply the Laurent decomposition to approximate the received GSMK signal as an almost memoryless modulation to simplify the design of the demodulator and the synchronization modules.

6-1.2.1 Mathematical model of the Laurent decomposition of the GMSK modulated signal

This section presents the Laurent decomposition of CPM signals. After the frequency down-conversion process, the received baseband GMSK modulated signal at the RFFE output can be expressed as in (Eq 6-1).

$$s_{Rx}(t) = \sqrt{2C_{Rx}} e^{i2\pi m_f \sum_{n=-\infty}^{+\infty} a_n \varphi(t-nT) + i\varphi_0} \quad (\text{Eq 6-1})$$

C_{Rx} is the recovered power of the real C2Link signal at the RFFE output. Note that the power of s_{Rx} as expressed in (Eq 6-1) is $2C_{Rx}$, because baseband signal power is twice the real signal power by definition.

According to Laurent decomposition [85], (Eq 6-1) can be approximated by a sum of amplitude modulation signals. This alternative method to model the GMSK signal is provided in (Eq 6-2).

$$s_{Rx}(t) \approx \sqrt{2C_{Rx}} e^{i\varphi_0} \sum_{n=-\infty}^{+\infty} \alpha_{0,n} C_0(t - nT) + \alpha_{1,n} C_1(t - nT) + \alpha_{2,n} C_2(t - nT) + \alpha_{3,n} C_3(t - nT) \quad (\text{Eq 6-2})$$

Coefficients $(\alpha_{i,n})_{i \in \llbracket 1,4 \rrbracket, n \in \mathbb{Z}}$ are linked to the transmitted bits $(a_n)_{n \in \mathbb{Z}} \in \{-1; +1\}^{\mathbb{Z}}$ and are given in (Eq 6-3), supposing that $j^{\sum_{i=-\infty}^n a_i} = 1$.

$$\begin{aligned} \alpha_{0,n} &= j^{\sum_{i=-\infty}^n a_i} = j^{a_n} \alpha_{0,n-1} = j a_n \alpha_{0,n-1} = j^{n+1} \prod_{i=-\infty}^n a_i \\ \alpha_{1,n} &= j^{\sum_{i=-\infty}^n a_i - a_{n-1}} = j^{\sum_{i=-\infty}^{n-2} a_i + a_n} = j a_n \cdot \alpha_{0,n-2} = j^n a_n \prod_{i=-\infty}^{n-2} a_i \\ \alpha_{2,n} &= j^{\sum_{i=-\infty}^n a_i - a_{n-1} - a_{n-2}} = j^{\sum_{i=-\infty}^{n-3} a_i + a_n + a_{n-1}} = j^2 a_{n-1} a_n \alpha_{0,n-3} = j^n a_n a_{n-1} \prod_{i=-\infty}^{n-3} a_i \\ \alpha_{3,n} &= j^{\sum_{i=-\infty}^n a_i - a_{n-1} - a_{n-2} - a_{n-3}} = j^{\sum_{i=-\infty}^{n-4} a_i + a_n + a_{n-1} + a_{n-2}} = j a_n \alpha_{0,n-3} = j^{n-1} a_n \prod_{i=-\infty}^{n-3} a_i \end{aligned} \quad (\text{Eq 6-3})$$

Expressions of pulses $(C_i)_{i \in \llbracket 1,4 \rrbracket}$ are provided in Appendix G. They are also plotted on Figure 6-2. The demonstration of (Eq 6-2) is done in Appendix G.

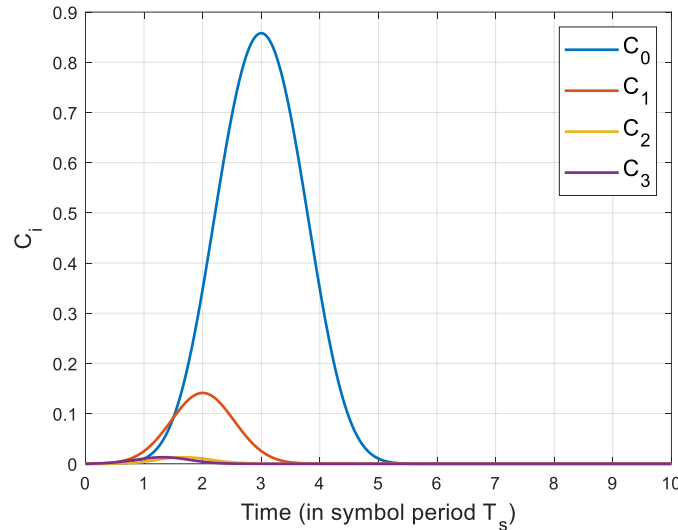


Figure 6-2: Amplitude modulated pulses of C2Link signal Laurent decomposition

As illustrated in Figure 6-2, the amplitude of pulses C_2 and C_3 is very low compared to the amplitude of C_0 . The maximum amplitude of C_0 is indeed 36 dB above the maximum amplitude of C_2 and C_3 .

6-1.2.2 Signal power analysis of the Laurent decomposition of the GMSK modulated signal

The calculation of the signal power is conducted by computing the contribution of each pulse on the total signal power. This calculation is done in two steps:

- 1) The cyclo-stationarity of the C2Link GMSK signal is demonstrated.

2) The mean power of s_{Rx} is computed and the contribution of each pulse C_i is identified.

Cyclo-stationarity property: Let us demonstrate the cyclo-stationarity of s_{Rx} with period T_s (T_s is the symbol period). The two conditions that must be fulfilled by s_{Rx} to be cyclo-stationary with period T_s are:

- Condition 1 : $\mathbb{E}(s_{Rx}(t)) = \mathbb{E}(s_{Rx}(t + T_s))$.
- Condition 2 : $\mathbb{E}(s_{Rx}(t + \tau)s_{Rx}^*(t)) = \mathbb{E}(s_{Rx}(t + \tau + T_s)s_{Rx}^*(t + T_s))$

Condition 1 :

$\mathbb{E}(s_{Rx}(t))$ is computed in (Eq 6-4). The random parameters of s_{Rx} are the transmitted bits a_n which are assumed uncorrelated and equiprobable. In addition, $a_n \in \{-1; 1\}$.

$$\begin{aligned}\mathbb{E}(s_{Rx}(t)) &= \mathbb{E}(\sqrt{2C_{Rx}}e^{j\sum_{n=-\infty}^{+\infty} a_n\varphi(t-nT_s)}) = \sqrt{2C_{Rx}} \prod_{n=-\infty}^{+\infty} \mathbb{E}(e^{ja_n\varphi(t-nT_s)}) \\ &= \sqrt{2C_{Rx}} \prod_{n=-\infty}^{+\infty} \frac{1}{2}(e^{j\varphi(t-nT_s)} + e^{-j\varphi(t-nT_s)})\end{aligned}\quad (\text{Eq 6-4})$$

$\mathbb{E}(s_{Rx}(t + T_s))$ is computed in (Eq 6-5).

$$\begin{aligned}\mathbb{E}(s_{Rx}(t + T_s)) &= \mathbb{E}(\sqrt{2C_{Rx}}e^{j\sum_{n=-\infty}^{+\infty} a_n\varphi(t-(n-1)T_s)}) \\ &= \sqrt{2C_{Rx}} \prod_{n=-\infty}^{+\infty} \mathbb{E}(e^{ja_n\varphi(t-(n-1)T_s)}) \\ &= \sqrt{2C_{Rx}} \prod_{n=-\infty}^{+\infty} \frac{1}{2}(e^{j\varphi(t-(n-1)T_s)} + e^{-j\varphi(t-(n-1)T_s)}) \\ &= \sqrt{2C_{Rx}} \prod_{n=-\infty}^{+\infty} e^{j\varphi(t-nT_s)} - e^{-j\varphi(t-nT_s)} = \mathbb{E}(s_{Rx}(t))\end{aligned}\quad (\text{Eq 6-5})$$

The change of index explaining the transition between the third line in (Eq 6-5) and the fourth line is justified by the consideration of a time infinite signal, therefore the product operator has infinite bounds.

Condition 2 :

$R_{s_{Rx}}(t, \tau) = \mathbb{E}(s_{Rx}(t)s_{Rx}^*(t - \tau))$ is computed in (Eq 6-6).

$$\begin{aligned}R_{s_{Rx}}(t, \tau) &= \mathbb{E}(2C_{Rx}e^{j\sum_{n=-\infty}^{+\infty} a_n\varphi(t+\tau-nT_s)}e^{j\sum_{n=-\infty}^{+\infty} -a_n\varphi(t-nT_s)}) \\ &= \mathbb{E}(2C_{Rx}e^{j\sum_{n=-\infty}^{+\infty} a_n[\varphi(t+\tau-nT_s)-\varphi(t-nT_s)]}) \\ &= 2C_{Rx} \prod_{n=-\infty}^{+\infty} e^{j[\varphi(t+\tau-nT_s)-\varphi(t-nT_s)]} - e^{-j[\varphi(t+\tau-nT_s)-\varphi(t-nT_s)]}\end{aligned}\quad (\text{Eq 6-6})$$

$R_{s_{Rx}}(t + T_s, \tau)$ is computed in (Eq 6-7).

$$\begin{aligned}R_{s_{Rx}}(t + T_s, \tau) &= \mathbb{E}(2C_{Rx}e^{j\sum_{n=-\infty}^{+\infty} a_n\varphi(t+T_s+\tau-nT_s)}e^{j\sum_{n=-\infty}^{+\infty} -a_n\varphi(t+T_s-nT_s)}) \\ &= \mathbb{E}(2C_{Rx}e^{j\sum_{n=-\infty}^{+\infty} a_n[\varphi(t+\tau-(n-1)T_s)-\varphi(t-(n-1)T_s)]}) \\ &= 2C_{Rx} \prod_{n=-\infty}^{+\infty} e^{j[\varphi(t+\tau-(n-1)T_s)-\varphi(t-(n-1)T_s)]} - e^{-j[\varphi(t+\tau-(n-1)T_s)-\varphi(t-(n-1)T_s)]} \\ &= 2C_{Rx} \prod_{n=-\infty}^{+\infty} e^{j[\varphi(t+\tau-nT_s)-\varphi(t-nT_s)]} - e^{-j[\varphi(t+\tau-nT_s)-\varphi(t-nT_s)]} = R(t, \tau)\end{aligned}\quad (\text{Eq 6-7})$$

As a conclusion, the C2Link GMSK modulated signal is cyclo-stationary with period T_s .

Power calculation: Let us compute the average power for the cyclo-stationary signal defined in (Eq 6-2). By definition, the mean power of a cyclo-stationary signal with period T_s is given in (Eq 6-8).

$$P_{GMSK} = \frac{1}{T_s} \int_0^{T_s} R_{s_{Rx}}(t, 0) dt \quad (\text{Eq 6-8})$$

$R_{s_{Rx}}(t, 0)$ is developed in (Eq 6-9) from the definition of (Eq 6-2).

$$R_{s_{Rx}}(t, 0) = 2C_{Rx} \mathbb{E} \left[\begin{aligned} & \sum_{n=-\infty}^{+\infty} \left[|\alpha_{0,n}|^2 C_0^2(t - nT_s) + |\alpha_{1,n}|^2 C_1^2(t - nT_s) + \right. \\ & \left. |\alpha_{2,n}|^2 C_2^2(t - nT_s) + |\alpha_{3,n}|^2 C_3^2(t - nT_s) \right] \\ & + \sum_{n=-\infty}^{+\infty} \sum_{l=-\infty}^{+\infty} \left[(\alpha_{0,n} \alpha_{1,l}^* + \alpha_{0,n}^* \alpha_{1,l}) C_0(t - nT_s) C_1(t - lT_s) + \right. \\ & (\alpha_{0,n} \alpha_{2,l}^* + \alpha_{0,n}^* \alpha_{2,l}) C_0(t - nT_s) C_2(t - lT_s) + \\ & (\alpha_{0,n} \alpha_{3,l}^* + \alpha_{0,n}^* \alpha_{3,l}) C_0(t - nT_s) C_3(t - lT_s) \left. \right] \\ & + \sum_{n=-\infty}^{+\infty} \sum_{l=-\infty}^{+\infty} \left[(\alpha_{1,n} \alpha_{2,l}^* + \alpha_{1,n}^* \alpha_{2,l}) C_1(t - nT_s) C_2(t - lT_s) + \right. \\ & (\alpha_{1,n} \alpha_{3,l}^* + \alpha_{1,n}^* \alpha_{3,l}) C_1(t - nT_s) C_3(t - lT_s) \left. \right] \\ & + \sum_{n=-\infty}^{+\infty} \sum_{l=-\infty}^{+\infty} (\alpha_{2,n} \alpha_{3,l}^* + \alpha_{2,n}^* \alpha_{3,l}) C_2(t - nT_s) C_3(t - lT_s) \end{aligned} \right] \quad (\text{Eq 6-9})$$

First, since $\alpha_{i,n} \in \{-1; +1; -i; +i\}$ for $n \in \mathbb{Z}$ and $i \in \llbracket 1; 4 \rrbracket$, $|\alpha_{i,n}|^2 = 1$.

Second, $\mathbb{E}(\alpha_{0,n} \alpha_{1,l}^*)$ is computed in (Eq 6-10) for $n > l$ from $\alpha_{i,n}$ definitions in (Eq 6-3).

$$\begin{aligned} \mathbb{E}(\alpha_{0,n} \alpha_{1,l}^*) &= \mathbb{E} \left(j^{n+1} \left(\prod_{i=-\infty}^n a_i \right) (-j)^l a_l \left(\prod_{i=-\infty}^{l-2} a_i \right) \right) \\ &= (-1)^l j^{n+1+l} \mathbb{E} \left(a_{l-1} \prod_{i=l+1}^n a_i \right) \\ &= (-1)^l j^{n+1+l} \mathbb{E}(a_{l-1}) \prod_{i=l+1}^n \mathbb{E}(a_i) = 0 \end{aligned} \quad (\text{Eq 6-10})$$

Likewise, the mathematical expectation of all the double sums terms in (Eq 6-9) is equal to 0 since the expectation of at least one independent a_l term is found on the calculation. Therefore, (Eq 6-9) is simplified in (Eq 6-11).

$$R_{s_{Rx}}(t, 0) = 2C_{Rx} \sum_{n=-\infty}^{+\infty} \left[C_0^2(t - nT_s) + C_1^2(t - nT_s) \right. \\ \left. + C_2^2(t - nT_s) + C_3^2(t - nT_s) \right] \quad (\text{Eq 6-11})$$

Eventually, the mean power of s_{Rx} is computed in (Eq 6-12) from the definition of (Eq 6-8).

$$\begin{aligned}
P_{GMSK} &= \frac{1}{T_s} \int_0^T R_{s_{Rx}}(t, 0) dt \\
&= 2C_{Rx} \sum_{n=-\infty}^{+\infty} \frac{1}{T_s} \int_0^{T_s} \left[C_0^2(t - nT_s) + C_1^2(t - nT_s) \right. \\
&\quad \left. + C_2^2(t - nT_s) + C_3^2(t - nT_s) \right] dt \\
&= 2C_{Rx} \sum_{n=-\infty}^{+\infty} \frac{1}{T_s} \int_{(-n+1)T_s}^{nT_s} [C_0^2(u) + C_1^2(u) + C_2^2(u) + C_3^2(u)] du \\
&= 2C_{Rx} \frac{1}{T_s} \left[\int_{-\infty}^{+\infty} C_0^2(t) dt + \int_{-\infty}^{+\infty} C_1^2(t) dt + \int_{-\infty}^{+\infty} C_2^2(t) dt + \int_{-\infty}^{+\infty} C_3^2(t) dt \right]
\end{aligned} \tag{Eq 6-12}$$

Knowing from (Eq 6-1) that the power of a complex envelope GMSK modulated signal is directly the squared amplitude, $2C_{Rx}$, it is possible to obtain the contribution of each pulse of the Laurent decomposition from (Eq 6-12). A numerical computation provides in Table 6-1 the contribution of each pulse on the average power of the GMSK signal.

$\frac{1}{T_s} \int_{-\infty}^{+\infty} C_0^2(t) dt$	$\frac{1}{T_s} \int_{-\infty}^{+\infty} C_1^2(t) dt$	$\frac{1}{T_s} \int_{-\infty}^{+\infty} C_2^2(t) dt$	$\frac{1}{T_s} \int_{-\infty}^{+\infty} C_3^2(t) dt$
0.9807	0.0190	$1.39 \cdot 10^{-4}$	$1.38 \cdot 10^{-4}$

Table 6-1: Contribution of Laurent pulses to GMSK signal power

As highlighted by Table 6-1, pulse C_0 contains more than 98% of the C2Link signal power. On the contrary, pulses C_2 and C_3 only contains around 0.01% of the power. As a consequence, most of C2Link receivers only use pulses C_0 and pulse C_1 in the generation of the local replica in the synchronization and demodulation modules. Remember that the advantage of only using pulses C_0 and C_1 is a reduction of the receiver's complexity as explained before.

In the following, the GMSK signal at the RFFE output is simplified by (Eq 6-13), not considering pulses C_2 and C_3 .

$$s_{Rx}(t) \approx \sqrt{2C_j} \sum_{n=-\infty}^{+\infty} \alpha_{0,n} C_0(t - nT) + \alpha_{1,n} C_1(t - nT) \tag{Eq 6-13}$$

6-1.3 Design of C2Link synchronization module

The objective of synchronization module is to estimate the delay τ and phase θ of the received signal s_{Rx} in order to keep the correct the time delay and the carrier phase of the received signal. Indeed, if the estimation process is correctly done, the correction allows the demodulation module to obtain matched filter outputs not affected by tracking errors; to obtain matched filter output interpolated at the optimal instant of time and to avoid the cross-talk between the in-phase and quadrature-phase matched filter outputs.

This section is divided in five parts: first, it presents the synchronization fundamentals based on the maximum likelihood criterion. Second, the maximum likelihood function is defined. Third, the log-likelihood function is developed. Fourth, the PLL is designed, defining a relevant phase discriminator and loop filter. Fifth, the DLL is designed, also identifying a relevant delay discriminator and loop filter.

6-1.3.1 Synchronization by maximum likelihood criterion

The received noisy equivalent baseband signal, considering delay τ and phase θ introduced by the propagation channel, is given in (Eq 6-14).

$$y(t, \tau, \theta, \mathbf{a}) = e^{i\theta} s_{Rx}(t - \tau) + n(t) \quad (\text{Eq 6-14})$$

$n(t)$ is a baseband AWGN with power spectral density N_0 . The C2Link signal energy per symbol, E_s , is defined as $E_s = E_b = C_{Rx} T_s$, where E_b is the bit energy (equal to E_s since the modulation is binary).

The objective of the receiver is to decode the useful information bits \mathbf{a} from the received noisy equivalent baseband signal $y(t, \tau, \theta, \mathbf{a})$. To achieve this objective, the maximum a posteriori (MAP) criterion is applied. Moreover, the MAP criterion is equivalent to the Maximum Likelihood (ML) criterion if the symbols are equiprobable, which is the assumption by default. The maximum likelihood criterion is presented in (Eq 6-15).

$$(\hat{\tau}, \hat{\theta}, \hat{\mathbf{a}}) = \underset{\tau, \theta, \mathbf{a}}{\text{argmax}} (\mathbb{P}(y(t)|(\tau, \theta, \mathbf{a}))) \quad (\text{Eq 6-15})$$

Although an optimal receiver would jointly estimate all the parameters $\hat{\tau}, \hat{\theta}$ and $\hat{\mathbf{a}}$, this optimal operation is difficult and very cumbersome to perform. In practice, classical digital receivers estimate each parameter separately. In this section, the focus is given to the estimation of the time delay and carrier phase and thus, the data should be removed from the ML criterion to derive optimal synchronization modules. There are two methods allowing to remove the influence of the useful message \mathbf{a} on the maximum likelihood criterion:

- 1) DA/DD methods: The decision aided (DA), or decision directed (DD), methods consider that \mathbf{a} is known thanks to the use of a preamble (for DA), or that \mathbf{a} can be estimated without errors (DD).
- 2) NDA methods: The non-data aided (NDA) synchronization method assumes that \mathbf{a} exact numerical value is unknown. The dependence of \mathbf{a} on the maximum likelihood criterion is removed by averaging the ML criterion by the distribution of the data which is assumed to be known. Therefore, the objective of a non-data aided synchronization module is to resolve (Eq 6-16).

$$(\hat{\tau}, \hat{\theta}) = \underset{\tau, \theta}{\text{argmax}} \left(\mathbb{E}_{\mathbf{a}} \left(\mathbb{P}(y(t)|(\tau, \theta, \mathbf{a})) \right) \right) \quad (\text{Eq 6-16})$$

In this chapter, a non-data aided synchronization algorithm is designed.

6-1.3.2 Synchronization by maximum likelihood function

Under AWGN channel, the maximization of the ML criterion $\mathbb{P}(y(t)|(\tau, \theta, \mathbf{a}))$ is equivalent to maximize the maximum likelihood function of (Eq 6-17).

$$\Lambda(\hat{\tau}, \hat{\theta}, \hat{\mathbf{a}}) = \exp \left(-\frac{1}{N_0} \int_{k_0 T_s}^{(k_0 + K_b) T_s} |y(t) - s_L(t, \hat{\tau}, \hat{\theta}, \hat{\mathbf{a}})|^2 dt \right) \quad (\text{Eq 6-17})$$

K_b is the length of the integration interval. $[k_0 T_s, (k_0 + K_b) T_s]$ is the time interval of the observation of the received signal. s_L is the local replica generated from delay and phase estimations ($\hat{\tau}$ and $\hat{\theta}$) and is expressed in (Eq 6-18).

$$s_L(\hat{\tau}, \hat{\theta}, \hat{\mathbf{a}}) = e^{i\hat{\theta}} \sum_{n=k_0}^{k_0 + K_b} \hat{\alpha}_{0,n} C_0(t - \hat{\tau} - nT_s) + \hat{\alpha}_{1,n} C_1(t - \hat{\tau} - nT_s) \quad (\text{Eq 6-18})$$

Developing (Eq 6-17), the maximum likelihood function can be re-expressed by (Eq 6-19).

$$\Lambda(\hat{\tau}, \hat{\theta}, \hat{\mathbf{a}}) = \exp \left(\begin{aligned} & -\frac{1}{N_0} \int_{k_0 T_s}^{(k_0+K_b)T_s} |y(t)|^2 dt - \frac{1}{N_0} \int_{k_0 T_s}^{(k_0+K_b)T_s} |s_L(t, \hat{\tau}, \hat{\theta}, \hat{\mathbf{a}})|^2 dt \\ & + \frac{2}{N_0} \operatorname{Re} \left\{ \int_{k_0 T_s}^{(k_0+K_b)T_s} y(t) s_L^*(t, \hat{\tau}, \hat{\theta}, \hat{\mathbf{a}}) dt \right\} \end{aligned} \right) \quad (\text{Eq 6-19})$$

The first integral in (Eq 6-19) does not depend on $\hat{\tau}$, on $\hat{\theta}$ nor on $\hat{\mathbf{a}}$ and therefore does not play a role in the maximization of $\Lambda(\hat{\tau}, \hat{\theta}, \hat{\mathbf{a}})$. In addition, the second integral in (Eq 6-19) is the energy of the local replica over the time interval $[k_0 T_s; (k_0 + K_b) T_s]$. Since GMSK is a constant envelope modulation, this energy is constant within the observation period and does not depend on $\hat{\tau}$, on $\hat{\theta}$ nor on $\hat{\mathbf{a}}$. As a consequence, the second integral in (Eq 6-19) does also not play a role in the maximization of $\Lambda(\hat{\tau}, \hat{\theta}, \hat{\mathbf{a}})$. The likelihood function of (Eq 6-19) can therefore be re-expressed as in (Eq 6-20).

$$\Lambda(\hat{\tau}, \hat{\theta}, \hat{\mathbf{a}}) = C \exp \left(\frac{2}{N_0} \operatorname{Re} \left\{ \int_{k_0 T_s}^{(k_0+K_b)T_s} y(t) s_L^*(t, \hat{\tau}, \hat{\theta}, \hat{\mathbf{a}}) dt \right\} \right) \quad (\text{Eq 6-20})$$

C is a constant that does not depend on $(\hat{\tau}, \hat{\theta}, \hat{\mathbf{a}})$ and is therefore omitted in the following.

Finally, in order to remove the influence of the data from the ML function, the NDA method can still be applied and be equivalent to the principle presented in (Eq 6-16) due to the linearity of the expectation as well as the integral function. The final expression leading to the theoretical development of the synchronization modules when using a NDA method to remove the data's influence is:

$$(\hat{\tau}, \hat{\theta}) = \operatorname{argmax}_{\tau, \theta} \left(\mathbb{E}_{\hat{\mathbf{a}}} \left(\exp \left(\frac{2}{N_0} \operatorname{Re} \left\{ \int_{k_0 T_s}^{(k_0+K_b)T_s} y(t) s_L^*(t, \hat{\tau}, \hat{\theta}, \hat{\mathbf{a}}) dt \right\} \right) \right) \right) \quad (\text{Eq 6-21})$$

6-1.3.3 Development of the log-likelihood function

Section 6-1.3.1 introduces the role of the synchronization and section 6-1.3.2 provides the maximum likelihood (ML) function to be maximized. In this section, the ML function is developed from the knowledge of the expression of the local replica s_L provided in (Eq 6-18) and the final expression of the log-likelihood function, the application of the natural logarithm to the ML function, is presented.

The ML function is developed in four steps:

- 1) The local replica is written under its algebraic form.
- 2) The integral term in (Eq 6-20) is computed.
- 3) The data is removed using the NDA method
- 4) The log-likelihood function is expressed as a function of matched filters outputs.
- 5) The expression of the log-likelihood function is simplified under low SNR assumption.

6-1.3.3.1 Local replica derivation

The objective is to identify the real and imaginary parts of the local replica. The local replica mathematical expression is given in (Eq 6-18). As detailed in Appendix H, the local replica can be re-expressed as in (Eq 6-22).

$$\begin{aligned}
& s_L(t, \hat{t}, \hat{\theta}, \hat{\mathbf{a}}) \\
&= e^{i\hat{\theta}} \sum_{k_0 \leq 2k < 2k+1 \leq k_0 + K_b} \left[\hat{\alpha}_{0,2k+1} C_0(t - \hat{t} - (2k+1)T_s) + \hat{\alpha}_{0,2k} \hat{\alpha}_{0,2k-1} \hat{\alpha}_{0,2k-2} C_1(t - \hat{t} - 2kT_s) \right] \\
& \quad \left[+ \hat{\alpha}_{0,2k} C_0(t - \hat{t} - 2kT_s) - \hat{\alpha}_{0,2k+1} \hat{\alpha}_{0,2k} \hat{\alpha}_{0,2k-1} C_1(t - \hat{t} - (2k+1)T_s) \right] \quad (\text{Eq 6-22})
\end{aligned}$$

In addition, from the mathematical expression of $(\hat{\alpha}_{0,n})_{n \in \mathbb{Z}}$ in (Eq 6-3), it comes that:

- If n is even, $\hat{\alpha}_{0,n} \in \{-j; +j\}$.
- If n is odd, $\hat{\alpha}_{0,n} \in \{-1; +1\}$.

Let us introduce coefficients $(\tilde{\alpha}_{0,n})_{n \in \mathbb{Z}} \in \{-1; +1\}^{\mathbb{Z}}$ defined by (Eq 6-23).

$$\tilde{\alpha}_{0,n} = \begin{cases} \text{Im}\{\hat{\alpha}_{0,n}\} & \text{if } n \text{ is even} \\ \hat{\alpha}_{0,n} & \text{if } n \text{ is odd} \end{cases} \quad (\text{Eq 6-23})$$

6-1.3.3.2 Integral calculation

The objective is now to develop $\Lambda(\hat{t}, \hat{\theta})$ as a function of \hat{t} and $\hat{\theta}$. Let us introduce first the matched filters outputs defined in (Eq 6-24).

$$R_{0,x}(\hat{t}, \hat{\theta}) = \int_{k_0 T_s}^{(k_0 + K_b) T_s} y(t) e^{-i\hat{\theta}} C_0(t - \hat{t} - xT_s) dt \quad (\text{Eq 6-24})$$

$$R_{1,x}(\hat{t}, \hat{\theta}) = \int_{k_0 T_s}^{(k_0 + K_b) T_s} y(t) e^{-i\hat{\theta}} C_1(t - \hat{t} - xT_s) dt$$

Once the matched filter outputs have been defined, the integral term of (Eq 6-21) can be calculated using their expressions. Replacing s_L by its expression of (Eq 6-22), the integral of the product between the received signal $y(t)$ and the complex conjugate of the local replica s_L of (Eq 6-18), denoted as $\Upsilon(\hat{t}, \hat{\theta}, \hat{\mathbf{a}})$, can be expressed as in (Eq 6-25).

$$\begin{aligned}
\Upsilon(\hat{t}, \hat{\theta}, \hat{\mathbf{a}}) &= \int_{k_0 T_s}^{(k_0 + K_b) T_s} y(t) s_L^*(t, \hat{t}, \hat{\theta}, \hat{\mathbf{a}}) dt \quad (\text{Eq 6-25}) \\
&= \sum_{k_0 \leq 2k < 2k+1 \leq k_0 + K_b} \left[\hat{\alpha}_{0,2k+1} R_{0,2k+1}(\hat{t}, \hat{\theta}) + \hat{\alpha}_{0,2k} \hat{\alpha}_{0,2k-1} \hat{\alpha}_{0,2k-2} R_{1,2k}(\hat{t}, \hat{\theta}) \right] \\
& \quad \left[+ \hat{\alpha}_{0,2k}^* R_{0,2k}(\hat{t}, \hat{\theta}) - \hat{\alpha}_{0,2k+1} \hat{\alpha}_{0,2k}^* \hat{\alpha}_{0,2k-1} R_{1,2k+1}(\hat{t}, \hat{\theta}) \right]
\end{aligned}$$

Eventually, considering the properties of (Eq 6-26), the real part of $\Upsilon(\hat{t}, \hat{\theta}, \hat{\mathbf{a}})$ is expressed in (Eq 6-27).

$$\begin{aligned}
\hat{\alpha}_{0,2k+1} &= \tilde{\alpha}_{0,2k+1} \in \mathbb{R} & \hat{\alpha}_{0,2k} \hat{\alpha}_{0,2k-1} \hat{\alpha}_{0,2k-2} &= -\tilde{\alpha}_{0,2k} \tilde{\alpha}_{0,2k-1} \tilde{\alpha}_{0,2k-2} \in \mathbb{R} \\
\hat{\alpha}_{0,2k}^* &= -i \tilde{\alpha}_{0,2k} \in i\mathbb{R} & \hat{\alpha}_{0,2k+1} \hat{\alpha}_{0,2k}^* \hat{\alpha}_{0,2k-1} &= -i \tilde{\alpha}_{0,2k+1} \tilde{\alpha}_{0,2k} \tilde{\alpha}_{0,2k-1} \in i\mathbb{R}
\end{aligned} \quad (\text{Eq 6-26})$$

$$\text{Re}[\Upsilon(\hat{t}, \hat{\theta}, \hat{\mathbf{a}})] = \sum_{k_0 \leq 2k < 2k+1 \leq k_0 + K_b} \begin{bmatrix} \tilde{\alpha}_{0,2k+1} \text{Re}\{R_{0,2k+1}(\hat{t}, \hat{\theta})\} \\ -\tilde{\alpha}_{0,2k} \tilde{\alpha}_{0,2k-1} \tilde{\alpha}_{0,2k-2} \text{Re}\{R_{1,2k}(\hat{t}, \hat{\theta})\} \\ \tilde{\alpha}_{0,2k} \text{Im}\{R_{0,2k}(\hat{t}, \hat{\theta})\} \\ -\tilde{\alpha}_{0,2k+1} \tilde{\alpha}_{0,2k} \tilde{\alpha}_{0,2k-1} \text{Im}\{R_{1,2k+1}(\hat{t}, \hat{\theta})\} \end{bmatrix} \quad (\text{Eq 6-27})$$

6-1.3.3.3 Data removal from a NDA algorithm

The ML function can be expressed from (Eq 6-27) by (Eq 6-28).

$$\Lambda(\hat{\tau}, \hat{\theta}, \hat{\mathbf{a}}) = \exp\left(\frac{2}{N_0} \text{Re}[Y(\hat{\tau}, \hat{\theta}, \hat{\mathbf{a}})]\right) \quad (\text{Eq 6-28})$$

The removal of the data is obtained from the application of the NDA methodology. The NDA methodology was already presented in (Eq 6-21) and can be rewritten using $Y(\hat{\tau}, \hat{\theta}, \hat{\mathbf{a}})$ as in (Eq 6-29).

$$\Lambda(\hat{\tau}, \hat{\theta}) = E_{\hat{\mathbf{a}}} \left[\exp\left(\frac{2}{N_0} \text{Re}[Y(\hat{\tau}, \hat{\theta}, \hat{\mathbf{a}})]\right) \right] \quad (\text{Eq 6-29})$$

In order to apply the NDA methodology, the following information and assumptions are used:

- 1) The symbols are binary, $a_k = \{-1, 1\}$, are equiprobable and are independent to each other
- 2) [86], [87] and [88] consider that coefficients $\alpha_{0,n}$ and $\alpha_{1,n}$ are mutually uncorrelated provided that transmitted bits are equiprobable and zero-mean. Note that although this assumption does not reflect the true situation, where there is indeed a correlation between $\alpha_{0,n}$ and $\alpha_{1,n}$ coefficients, its adoption is widely accepted, allows the simplification of the calculation and the obtained model is very close to the true one.
- 3) Coefficients $\alpha_{0,n}$ and $\alpha_{0,n+k} \forall k, k \neq 0$ are uncorrelated from their definition and from the independence of a_k

From the previous assumption, $\Lambda(\hat{\tau}, \hat{\theta})$ can be written as in (Eq 6-30).

$$\begin{aligned} & \Lambda(\hat{\tau}, \hat{\theta}) \\ &= \prod_{k_0 \leq 2k < 2k+1 \leq k_0 + K_b} \left[\begin{aligned} & \mathbb{E}_{\alpha} \left(\exp\left(\frac{2}{N_0} \tilde{\alpha}_{0,2k+1} \text{Re}\{R_{0,2k+1}(\hat{\tau}, \hat{\theta})\}\right) \right) \\ & \times \mathbb{E}_{\alpha} \left(\exp\left(-\frac{2}{N_0} \tilde{\alpha}_{0,2k} \tilde{\alpha}_{0,2k-1} \tilde{\alpha}_{0,2k-2} \text{Re}\{R_{1,2k}(\hat{\tau}, \hat{\theta})\}\right) \right) \\ & \times \mathbb{E}_{\alpha} \left(\exp\left(\frac{2}{N_0} \tilde{\alpha}_{0,2k} \text{Im}\{R_{0,2k}(\hat{\tau}, \hat{\theta})\}\right) \right) \\ & \times \mathbb{E}_{\alpha} \left(\exp\left(-\frac{2}{N_0} \tilde{\alpha}_{0,2k+1} \tilde{\alpha}_{0,2k} \tilde{\alpha}_{0,2k-1} \text{Im}\{R_{1,2k+1}(\hat{\tau}, \hat{\theta})\}\right) \right) \end{aligned} \right] \quad (\text{Eq 6-30}) \end{aligned}$$

Supposing that transmitted bits are equiprobable (as per 1)), it can be easily shown by recurrence that coefficients $\tilde{\alpha}_{0,n}$ and $g_n = \tilde{\alpha}_{0,n} \tilde{\alpha}_{0,n-1} \tilde{\alpha}_{0,n-2}$ are also equiprobable with values $[-1, +1]$. As a consequence, the mathematical expectation terms of (Eq 6-30) can be further simplified in (Eq 6-31).

$$\begin{aligned} & \mathbb{E} \left(\exp\left(\frac{2}{N_0} \tilde{\alpha}_{0,2k+1} \text{Re}\{R_{0,2k+1}(\hat{\tau}, \hat{\theta})\}\right) \right) \\ &= \frac{1}{2} \exp\left(\frac{2}{N_0} \text{Re}\{R_{0,2k+1}(\hat{\tau}, \hat{\theta})\}\right) + \frac{1}{2} \exp\left(-\frac{2}{N_0} \tilde{\alpha}_{0,2k+1} \text{Re}\{R_{0,2k+1}(\hat{\tau}, \hat{\theta})\}\right) \\ &= \cosh\left(\frac{2}{N_0} \text{Re}\{R_{0,2k+1}(\hat{\tau}, \hat{\theta})\}\right) \end{aligned} \quad (\text{Eq 6-31})$$

Other terms are computed on a similar way.

6-1.3.3.4 Log-likelihood function

The log-likelihood function is defined in (Eq 6-32).

$$\Lambda_L(\hat{\tau}, \hat{\theta}) = \ln\left(\Lambda(\hat{\tau}, \hat{\theta})\right) \quad (\text{Eq 6-32})$$

From (Eq 6-30) and (Eq 6-31), the log-likelihood function is given in (Eq 6-33).

$$\Lambda_L(\hat{\tau}, \hat{\theta}) = \sum_{k_0 \leq 2k < 2k+1 \leq k_0 + K_b} \left[\begin{array}{l} \ln \left(\cosh \left(\frac{2}{N_0} \operatorname{Re}\{R_{0,2k+1}(\hat{\tau}, \hat{\theta})\} \right) \right) \\ + \ln \left(\cosh \left(\frac{2}{N_0} \operatorname{Re}\{R_{1,2k}(\hat{\tau}, \hat{\theta})\} \right) \right) \\ + \ln \left(\cosh \left(\frac{2}{N_0} \operatorname{Im}\{R_{0,2k}(\hat{\tau}, \hat{\theta})\} \right) \right) \\ + \ln \left(\cosh \left(\frac{2}{N_0} \operatorname{Im}\{R_{1,2k+1}(\hat{\tau}, \hat{\theta})\} \right) \right) \end{array} \right] \quad (\text{Eq 6-33})$$

6-1.3.3.5 Simplification under low SNR assumption

Under low SNR assumption, (Eq 6-33) can be simplified using Taylor development reminded in (Eq 6-34).

$$\text{for } x \ll 1, \ln(\cosh(x)) \approx \frac{x^2}{2} + o(x^2) \quad (\text{Eq 6-34})$$

Applying the simplification of (Eq 6-34) in (Eq 6-33), a new expression of the log-likelihood function $\Lambda_L(\hat{\tau}, \hat{\theta})$ is obtained in (Eq 6-35).

$$\Lambda_L(\hat{\tau}, \hat{\theta}) = \frac{2}{N_0^2} \sum_{k_0 \leq 2k < 2k+1 \leq k_0 + K_b} \left[\begin{array}{l} \operatorname{Re}\{R_{0,2k+1}(\hat{\tau}, \hat{\theta})\}^2 + \operatorname{Re}\{R_{1,2k}(\hat{\tau}, \hat{\theta})\}^2 \\ + \operatorname{Im}\{R_{0,2k}(\hat{\tau}, \hat{\theta})\}^2 + \operatorname{Im}\{R_{1,2k+1}(\hat{\tau}, \hat{\theta})\}^2 \end{array} \right] \quad (\text{Eq 6-35})$$

As a conclusion, in order to remove the influence of the unknown delay τ and phase θ in the received signal, the synchronization module must find estimations $\hat{\tau}$ and $\hat{\theta}$ which maximize (Eq 6-35). To achieve this objective, PLL and DLL implement discriminators equal to the derivative of $\Lambda_L(\hat{\tau}, \hat{\theta})$. Design of PLL and DLL is detailed in the following sections.

6-1.3.4 Design of Phase Lock Loop

The objective of a PLL is to generate a local replica which carrier phase is equal to the carrier phase of the incoming signal. If the discriminator of the PLL is equal to the derivate of the log-likelihood function, the PLL generates an estimation of the phase $\hat{\theta}$ which maximize $\Lambda_L(\hat{\tau}, \hat{\theta})$ and thus an optimal estimation process is established. The PLL of a GMSK modulated signal receiver has the same architecture than the PLL of a GNSS signal receiver, which is described in Chapter 2 section 2-3.3.3.1. The PLL is made of three elements:

- A discriminator, which objective is to estimate the difference between the phase of the received signal θ and the phase generated by the PLL, $\hat{\theta}$.
- A low pass loop filter which objective is to attenuate the influence of the noise at the matched filter output, to remove high frequency terms and to control the PLL response time.
- A DVCO which objective is to update the phase estimation $\hat{\theta}$.

This section is derived in two parts. First, the discriminator is derived. The discriminator is a linear combination of matched filter outputs, and it is proportional to $\varepsilon_\theta = \theta - \hat{\theta}$. Second, the loop filter and the DVCO are designed.

6-1.3.4.1 Design of PLL discriminator

In this section, a non-normalized discriminator is first identified deriving Λ_L according to $\hat{\theta}$. Second, this non-normalized discriminator is normalized to output an estimation of ε_θ . Third, the S-curve is derived to inspect its behaviour.

Non-normalized discriminator

The discriminator is a set of algebraic operation on matched filters outputs whose objective is to estimate the difference between $\hat{\theta}$ and θ .

Appendix I shows that the derivation of the log-likelihood function according to $\hat{\theta}$ is given by (Eq 6-36).

$$\begin{aligned} \frac{d\Lambda_L}{d\hat{\theta}}(\hat{t}, \hat{\theta}) &= \frac{4}{N_0^2} \sum_{k_0 \leq 2k < 2k+1 \leq k_0 + K_b} \begin{bmatrix} Re\{R_{0,2k+1}(\hat{t}, \hat{\theta})\}Im\{R_{0,2k+1}(\hat{t}, \hat{\theta})\} \\ + Re\{R_{1,2k}(\hat{t}, \hat{\theta})\}Im\{R_{1,2k}(\hat{t}, \hat{\theta})\} \\ - Re\{R_{0,2k}(\hat{t}, \hat{\theta})\}Im\{R_{0,2k}(\hat{t}, \hat{\theta})\} \\ - Re\{R_{1,2k+1}(\hat{t}, \hat{\theta})\}Im\{R_{1,2k+1}(\hat{t}, \hat{\theta})\} \end{bmatrix} \\ &= \frac{4}{N_0^2} \sum_{k=k_0}^{k_0+K_b} (-1)^{k+1} \begin{bmatrix} Re\{R_{0,k}(\hat{t}, \hat{\theta})\}Im\{R_{0,k}(\hat{t}, \hat{\theta})\} \\ - Re\{R_{1,k}(\hat{t}, \hat{\theta})\}Im\{R_{1,k}(\hat{t}, \hat{\theta})\} \end{bmatrix} \end{aligned} \quad (\text{Eq 6-36})$$

Since $Re\{z\}Im\{z\} = \frac{1}{2}Im\{z^2\}$, (Eq 6-36) can be reduced to (Eq 6-37).

$$\frac{d\Lambda_L}{d\hat{\theta}}(\hat{t}, \hat{\theta}) = \frac{2}{N_0^2} \sum_{k=k_0}^{k_0+K_b} (-1)^{k+1} [Im\{R_{0,k}^2(\hat{t}, \hat{\theta})\} - Im\{R_{1,k}^2(\hat{t}, \hat{\theta})\}] \quad (\text{Eq 6-37})$$

A potential non-normalized phase discriminator is finally given in (Eq 6-38).

$$D_{\theta}(\hat{\theta}) = \sum_{k=k_0}^{k_0+K_b} (-1)^{k+1} [Im\{R_{0,k}^2(\hat{t}, \hat{\theta})\} - Im\{R_{1,k}^2(\hat{t}, \hat{\theta})\}] \quad (\text{Eq 6-38})$$

To be implemented in the PLL and return a direct estimation of the carrier phase tracking error (in absence of noise), this non-normalized discriminator must be normalized. The calculation of the normalization factor is performed below.

Phase discriminator normalization

The noiseless C_0 matched filter output defined in (Eq 6-24) is developed in (Eq 6-39) replacing s_{RX} by its expression of (Eq 6-13).

$$R_{0,k}(\hat{\theta}) = \sqrt{\frac{2E_b}{T_s}} e^{i\varepsilon_{\theta}} \sum_{n=-\infty}^{+\infty} \begin{bmatrix} \alpha_{0,n} \int_{k_0 T_s}^{(k_0+K_b)T_s} C_0(t-\tau-nT_s)C_0(t-\hat{t}-kT_s)dt \\ \alpha_{1,n} \int_{k_0 T_s}^{(k_0+K_b)T_s} C_1(t-\tau-nT_s)C_0(t-\hat{t}-kT_s)dt \end{bmatrix} \quad (\text{Eq 6-39})$$

Let us now introduce correlation functions K_{C_0} , K_{C_1} and $K_{C_1C_0}$ defined by (Eq 6-40).

$$\begin{aligned} K_{C_0}(xT_s) &= \int_{-\infty}^{+\infty} C_0(t)C_0(t-xT_s)dt \\ K_{C_1}(xT_s) &= \int_{-\infty}^{+\infty} C_1(t)C_1(t-xT_s)dt \\ K_{C_1C_0}(xT_s) &= \int_{-\infty}^{+\infty} C_1(t)C_0(t-xT_s)dt \end{aligned} \quad (\text{Eq 6-40})$$

Correlation functions K_{C_0} , K_{C_1} and $K_{C_1C_0}$ are plotted in Figure 6-3.

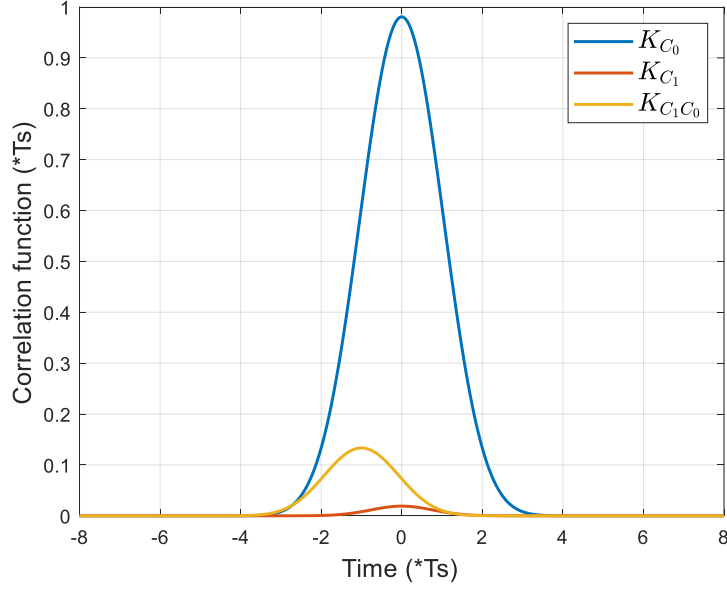


Figure 6-3: Correlation functions of Laurent pulses

Supposing K_b high enough to neglect the side effect near the integration interval bounds, (Eq 6-39) is re-expressed in (Eq 6-41) as a function of the correlation functions K_{C_0} , K_{C_1} and $K_{C_1C_0}$.

$$R_{0,k}(\hat{\theta}) = \sqrt{\frac{2E_b}{T_s}} e^{i\varepsilon\theta} \sum_{n=-\infty}^{+\infty} \alpha_{0,n} K_{C_0}((k-n)T_s - \varepsilon_\tau) + \alpha_{1,n} K_{C_1C_0}((k-n)T_s - \varepsilon_\tau) \quad (\text{Eq 6-41})$$

$\varepsilon_\tau = \tau - \hat{\tau}$ is the delay tracking error.

According to Appendix G, C_0 and C_1 have a finite support, respectively on the interval $[0; 6T_s]$ and $[0; 4T_s]$. As a consequence, $K_{C_0}((k-n)T_s)$ is not null only if $-5 \leq k-n \leq 5$ and $K_{C_1C_0}((k-n)T_s)$ is not null only if $-5 \leq k-n \leq 3$. From this consideration, the infinite sum of (Eq 6-41) can be reduced to a finite sum as in (Eq 6-42). Note that (Eq 6-42) assumes that ε_τ is small. Also for simplification purpose, $K_{C_1C_0}$ terms for $-5 \leq k-n \leq 5$ are included even though only terms for $-5 \leq k-n \leq 3$ are necessary.

$$R_{0,k}(\hat{\theta}) = \sqrt{\frac{2E_b}{T_s}} e^{i\varepsilon\theta} \sum_{n=k-5}^{k+5} \alpha_{0,n} K_{C_0}((k-n)T_s - \varepsilon_\tau) + \alpha_{1,n} K_{C_1C_0}((k-n)T_s - \varepsilon_\tau) \quad (\text{Eq 6-42})$$

A similar calculation is performed to develop $R_{1,k}(\hat{\theta})$. The result is given in (Eq 6-43). As explained above, unnecessary terms are included in (Eq 6-43) for simplicity of the equations in the development of Appendix J.

$$R_{1,k}(\hat{\theta}) = \sqrt{\frac{2E_b}{T_s}} e^{i\varepsilon\theta} \sum_{n=k-5}^{k+5} \alpha_{0,n} K_{C_1C_0}((n-k)T_s + \varepsilon_\tau) + \alpha_{1,n} K_{C_1}((k-n)T_s - \varepsilon_\tau) \quad (\text{Eq 6-43})$$

For simplicity of the following calculation, it is supposed that the C2Link signal delay is correctly estimated by the DLL and therefore, $\varepsilon_\tau = 0$. The rest of the development of the non-normalized phase discriminator of (Eq 6-37) is presented in Appendix J. According to the result of Appendix I, the noise free response of the non-normalized discriminator is given by (Eq 6-44).

$$D_{\theta}(\hat{\theta}) = \frac{2E_b}{T_s}(K_b + 1)C_{\theta} \sin(2\varepsilon_{\theta})$$

$$C_{\theta} = \sum_{z=-5}^5 (-1)^z K_{C_0}^2(zT_s) + 2(-1)^{z+1} K_{C_1}^2(zT_s) + (-1)^z K_{C_1}^2(zT_s) \quad (\text{Eq 6-44})$$

In addition, Appendix J demonstrates the equality given in (Eq 6-45) when K_b is high enough.

$$\left| \sum_{k=k_0}^{k_0+K_b} (-1)^{k+1} [R_{0,k}^2(\hat{t}, \hat{\theta}) - R_{1,k}^2(\hat{t}, \hat{\theta})] \right| = \frac{2E_b}{T_s}(K_b + 1)C_{\theta} \quad (\text{Eq 6-45})$$

Eventually, the normalized phase discriminator implemented in the synchronization module is defined in (Eq 6-46).

$$\bar{D}_{\theta}(\hat{\theta}) = \frac{\sum_{k=k_0}^{k_0+K_b} (-1)^{k+1} [Im\{R_{0,k}^2(\hat{t}, \hat{\theta})\} - Im\{R_{1,k}^2(\hat{t}, \hat{\theta})\}]}{2 \left| \sum_{k=k_0}^{k_0+K_b} (-1)^{k+1} [R_{0,k}^2(\hat{t}, \hat{\theta}) - R_{1,k}^2(\hat{t}, \hat{\theta})] \right|} \quad (\text{Eq 6-46})$$

S-curve

The S-curve is the representation of the discriminator output, \bar{D}_{θ} , as a function of carrier phase estimation error, ε_{θ} . Making the ratio between (Eq 6-44) and (Eq 6-45), the noiseless normalized discriminator is equal to $\frac{1}{2} \sin(2\varepsilon_{\theta})$ when K_b is high enough. Note that in the linearity region, \bar{D}_{θ} is equal to ε_{θ} . Figure 6-4 illustrates the S-curve of the phase discriminator and compares it to the discriminator outputs run on a C2Link signal generated by a Matlab software C2Link generator. The normalized discriminator output (blue curve in Figure 6-4) has been obtained with the following procedure. One GMSK C2Link signal is generated using a Matlab generator. The phase θ and the delay τ of the generated signal are randomly chosen. Then, successive matched filter outputs are computed considering several values of $\hat{\theta}$ and $\hat{t} = \tau$. The normalized discriminator is eventually computed from (Eq 6-46) with $K_b = 500$ successive matched filter outputs and plotted as a function of $\hat{\theta}$.

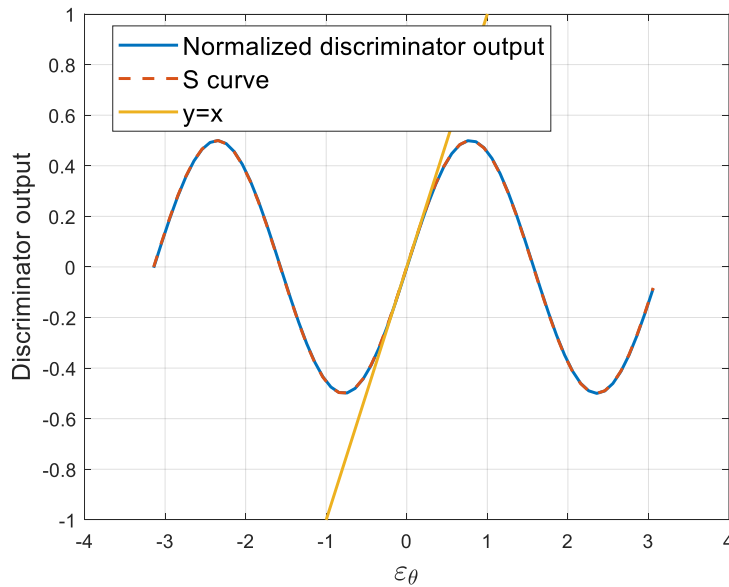


Figure 6-4: Phase discriminator S curve

In the linearity region of the S curve, Figure 6-4 shows that the normalized discriminator output is proportional to ε_{θ} .

6-1.3.4.2 Design of PLL loop filter and NCO

The block scheme of a phase tracking loop is reminded in Figure 6-5.

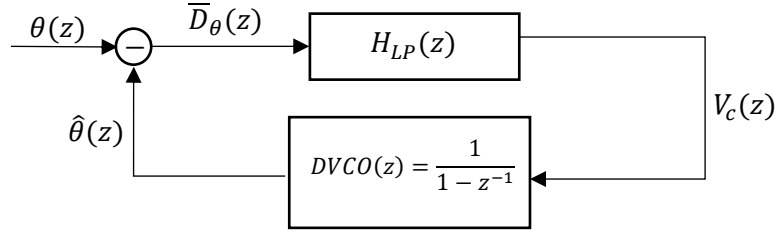


Figure 6-5: C2Link PLL block diagram

The C2Link tracking loop architecture is the same than the GNSS phase tracking loop.

- H_{LP} is a low pass filter which aim is to filter the noise of the discriminator and to control its response time.
- V_c is the output of the low pass filter.
- $DVCO$ is a digital voltage controlled oscillator, which aim is to update the phase estimation $\hat{\theta}$.

The PLL implemented in the software synchronization module of this PhD thesis is a 3rd order PLL. The low-pass loop filter transfer function is given in (Eq 6-47).

$$H_{LP}(z) = \frac{(K_1 + K_2 + K_3) - (2K_1 + K_2)z^{-1} + K_1z^{-2}}{1 - 2z^{-1} + z^{-2}} \quad (\text{Eq 6-47})$$

$$K_1 = \frac{60}{23}B_\theta K_b T_i \quad K_2 = \frac{4}{9}K_1^2 \quad K_3 = \frac{2}{27}K_1^3$$

B_θ is the PLL loop bandwidth.

Since the PLL open loop transfer function is $H_{LP}(z)DVCO(z)$, the phase estimation update depends on past phase estimation as well as on the current and past discriminator outputs. The result is given in (Eq 6-48).

$$\hat{\theta}(k+1) = 3\hat{\theta}(k) - 3\hat{\theta}(k-1) + \hat{\theta}(k-2) + (K_1 + K_2 + K_3)V_d(k) - (2K_1 + K_2)V_d(k-1) + K_1V_d(k-2) \quad (\text{Eq 6-48})$$

To guarantee the stability of the loop, a rule of thumb used by [89] and [90] consists of bounding the loop bandwidth B_θ to the loop update rate $K_b T_s$. This rule of thumb is presented in (Eq 6-49).

$$B_\theta \leq \frac{1}{10K_b T_s} \quad (\text{Eq 6-49})$$

The synchronization module of this PhD thesis has chosen to set B_θ to $\frac{1}{10K_b T_s}$.

6-1.3.5 Design of Delay Lock Loop

The objective of the DLL is to return a delay estimation $\hat{\tau}$ maximizing $\Lambda_L(\hat{\tau}, \hat{\theta})$. The DLL operates in parallel of the PLL. C2Link DLL architecture is identical to the GNSS DLL presented in Chapter 2 section 2-3.3.3.2. Similarly to the PLL, the DLL contains:

- A discriminator D_τ whose objective is to estimate the difference between the delay of the received signal τ and the estimated delay $\hat{\tau}$ used to generate the local replica.
- A low pass loop filter whose objective is to attenuate the influence of noise at the matched filters output.
- A NCO whose objective is to update the delay estimation $\hat{\tau}$.

This section describes the delay lock loop implemented in the PhD thesis software synchronization module. It is split in 3 parts. First, a discriminator is identified from the derivative of the log-likelihood function with respect to \hat{t} . Second, this discriminator is normalized analyzing its noiseless response. Third, the DLL low-pass filter and NCO are presented.

6-1.3.5.1 DLL discriminator

The value of \hat{t} maximizing $\Lambda_L(\hat{t}, \hat{\theta})$ is a zero of $\frac{d\Lambda_L}{d\hat{t}}$. The derivation of Λ_L according to \hat{t} is given in (Eq 6-50).

$$\frac{d\Lambda_L}{d\hat{t}}(\hat{t}, \hat{\theta}) = \frac{4}{N_0^2} \sum_{k_0 \leq 2k < 2k+1 \leq k_0 + K_b} \begin{bmatrix} Re\{R_{1,2k}(\hat{t}, \hat{\theta})\} \frac{dRe\{R_{1,2k}\}}{d\hat{t}}(\hat{t}, \hat{\theta}) \\ + Im\{R_{0,2k}(\hat{t}, \hat{\theta})\} \frac{dIm\{R_{0,2k}\}}{d\hat{t}}(\hat{t}, \hat{\theta}) \\ + Re\{R_{0,2k+1}(\hat{t}, \hat{\theta})\} \frac{dRe\{R_{0,2k+1}\}}{d\hat{t}}(\hat{t}, \hat{\theta}) \\ + Im\{R_{1,2k+1}(\hat{t}, \hat{\theta})\} \frac{dIm\{R_{1,2k+1}\}}{d\hat{t}}(\hat{t}, \hat{\theta}) \end{bmatrix} \quad (\text{Eq 6-50})$$

Approximating $\frac{d}{d\hat{t}}(Re\{R_{i,k}(\hat{\theta}, \hat{t})\})$ by $\frac{Re\{R_{i,k}(\hat{\theta}, \hat{t} + \Delta T)\} - Re\{R_{i,k}(\hat{\theta}, \hat{t} - \Delta T)\}}{2\Delta T}$ and $\frac{d}{d\hat{t}}(Im\{R_{i,k}(\hat{\theta}, \hat{t})\})$ by $\frac{Im\{R_{i,k}(\hat{\theta}, \hat{t} + \Delta T)\} - Im\{R_{i,k}(\hat{\theta}, \hat{t} - \Delta T)\}}{2\Delta T}$, $i \in \{0; 1\}$, (Eq 6-50) is reduced to (Eq 6-51).

$$\begin{aligned} & \frac{d\Lambda_L}{d\hat{t}}(\hat{t}, \hat{\theta}) \\ &= \frac{4}{N_0^2} \sum_{k_0 \leq 2k < 2k+1 \leq k_0 + K_b} \begin{bmatrix} Re\{R_{1,2k}(\hat{t}, \hat{\theta})\} \frac{Re\{R_{1,2k}(\hat{\theta}, \hat{t} + \Delta T)\} - Re\{R_{1,2k}(\hat{\theta}, \hat{t} - \Delta T)\}}{2\Delta T} \\ + Im\{R_{0,2k}(\hat{t}, \hat{\theta})\} \frac{Im\{R_{0,2k}(\hat{\theta}, \hat{t} + \Delta T)\} - Im\{R_{0,2k}(\hat{\theta}, \hat{t} - \Delta T)\}}{2\Delta T} \\ + Re\{R_{0,2k+1}(\hat{t}, \hat{\theta})\} \frac{Re\{R_{0,2k+1}(\hat{\theta}, \hat{t} + \Delta T)\} - Re\{R_{0,2k+1}(\hat{\theta}, \hat{t} - \Delta T)\}}{2\Delta T} \\ + Im\{R_{1,2k+1}(\hat{t}, \hat{\theta})\} \frac{Im\{R_{1,2k+1}(\hat{\theta}, \hat{t} + \Delta T)\} - Im\{R_{1,2k+1}(\hat{\theta}, \hat{t} - \Delta T)\}}{2\Delta T} \end{bmatrix} \end{aligned} \quad (\text{Eq 6-51})$$

As a consequence, a potential discriminator can be defined from 6 matched filters outputs:

- Prompt matched filters: $R_{i,k}^p(\hat{t}, \hat{\theta}) = R_{i,k}(\hat{t}, \hat{\theta})$, $i \in \{0; 1\}$
- Early matched filters: $R_{i,k}^E(\hat{t}, \hat{\theta}) = R_{i,k}(\hat{t} - \Delta T, \hat{\theta})$, $i \in \{0, 1\}$
- Late matched filters: $R_{i,k}^L(\hat{t}, \hat{\theta}) = R_{i,k}(\hat{t} + \Delta T, \hat{\theta})$, $i \in \{0, 1\}$

ΔT is the time spacing between early/late matched filters output and the prompt matched filter output; ΔT should be lower than T_s . The non-normalized discriminator built from prompt, early and late matched filters is given in (Eq 6-52).

$$D_{\tau}(\hat{t}) = \frac{1}{2\Delta T} \sum_{\substack{k=k_0 \\ k \text{ even}}}^{k_0+K_b} \left[\begin{aligned} &Re\{R_{1,k}^P(\hat{t}, \hat{\theta})\} (Re\{R_{1,k}^L(\hat{t}, \hat{\theta})\} - Re\{R_{1,k}^E(\hat{t}, \hat{\theta})\}) \\ &Im\{R_{0,k}^P(\hat{t}, \hat{\theta})\} (Im\{R_{0,k}^L(\hat{t}, \hat{\theta})\} - Im\{R_{0,k}^E(\hat{t}, \hat{\theta})\}) \end{aligned} \right] \\ + \frac{1}{2\Delta T} \sum_{\substack{k=k_0 \\ k \text{ odd}}}^{K_b} \left[\begin{aligned} &Re\{R_{0,k}^P(\hat{t}, \hat{\theta})\} (Re\{R_{0,k}^L(\hat{t}, \hat{\theta})\} - Re\{R_{0,k}^E(\hat{t}, \hat{\theta})\}) \\ &Im\{R_{1,k}^P(\hat{t}, \hat{\theta})\} (Im\{R_{1,k}^L(\hat{t}, \hat{\theta})\} - Im\{R_{1,k}^E(\hat{t}, \hat{\theta})\}) \end{aligned} \right] \quad (\text{Eq 6-52})$$

6-1.3.5.2 DLL discriminator normalization

The development of $D_{\tau}(\hat{t})$ is detailed in Appendix K. Appendix K shows that $D_{\tau}(\hat{t})$ can be approximated by (Eq 6-53).

$$D_{\tau}(\hat{t}) = -\frac{2E_b}{T_s} (K_b + 1) \frac{1}{\Delta T} \left[\begin{aligned} &\cos^2 \varepsilon_{\theta} (C_{\tau, C_0}^{even} + 2C_{\tau, C_1 C_0}^{odd} + C_{\tau, C_1}^{even}) \\ &\sin^2 \varepsilon_{\theta} (C_{\tau, C_0}^{odd} + 2C_{\tau, C_1 C_0}^{even} + C_{\tau, C_1}^{odd}) \end{aligned} \right] \varepsilon_{\tau} \quad (\text{Eq 6-53})$$

Coefficients C_{τ, C_i}^{even} , C_{τ, C_i}^{odd} , $C_{\tau, C_1 C_0}^{odd}$ and $C_{\tau, C_1 C_0}^{even}$ are defined in (Eq 6-54) for $i \in \{0; 1\}$.

$$C_{\tau, C_i}^{even} = \sum_{\substack{z=-5 \\ z \text{ even}}}^5 \left[K_{C_i}(zT_s) \frac{dK_{C_i}}{dx}(zT_s + \Delta T) + K_{C_i}(zT_s + \Delta T) \frac{dK_{C_i}}{dx}(zT_s) \right] \\ C_{\tau, C_i}^{odd} = \sum_{\substack{z=-5 \\ z \text{ odd}}}^5 \left[K_{C_i}(zT_s) \frac{dK_{C_i}}{dx}(zT_s + \Delta T) + K_{C_i}(zT_s + \Delta T) \frac{dK_{C_i}}{dx}(zT_s) \right] \\ C_{\tau, C_1 C_0}^{odd} = \sum_{\substack{z=-5 \\ z \text{ odd}}}^5 \left[K_{C_1 C_0}(zT_s + \Delta T) \frac{dK_{C_1 C_0}}{dx}(zT_s) + K_{C_1 C_0}(zT_s) \frac{dK_{C_1 C_0}}{dx}(zT_s + \Delta T) \right] \\ C_{\tau, C_1 C_0}^{even} = \sum_{\substack{z=-5 \\ z \text{ even}}}^5 \left[K_{C_1 C_0}(zT_s + \Delta T) \frac{dK_{C_1 C_0}}{dx}(zT_s) + K_{C_1 C_0}(zT_s) \frac{dK_{C_1 C_0}}{dx}(zT_s + \Delta T) \right] \quad (\text{Eq 6-54})$$

Functions $\frac{dK_{C_i}}{dx}$, $i \in \{0; 1\}$ and $\frac{dK_{C_1 C_0}}{dx}$ are illustrated in Figure 6-6.

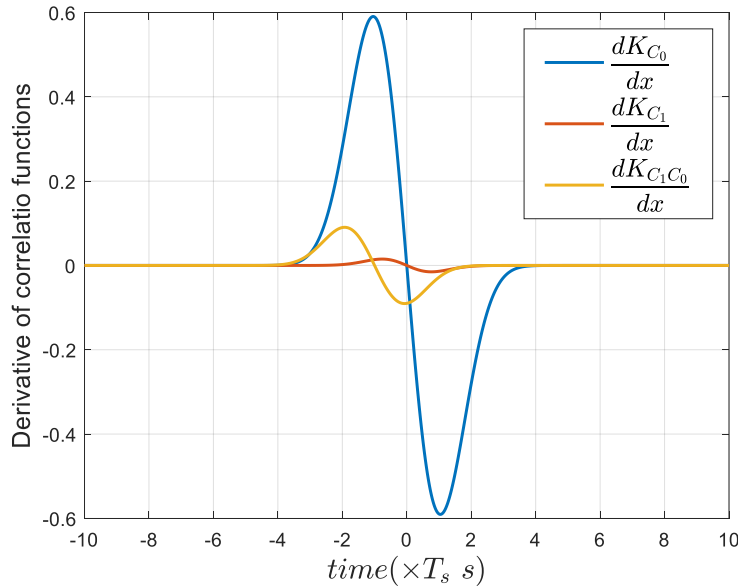


Figure 6-6: Derivative of correlation functions

It is now proposed to normalize D_τ , removing the slope in (Eq 6-53). To achieve this goal, it is proposed to consider the normalization method of (Eq 6-55) introduced in [91].

$$N_2 = \frac{1}{2\Delta T} \sum_{\substack{k=k_0 \\ k \text{ even}}}^{k_0+K_b} \left[\text{Re}\{R_{1,k}^P(\hat{t}, \hat{\theta})\}(\text{Re}\{R_{1,k}^L(\hat{t}, \hat{\theta})\} + \text{Re}\{R_{1,k}^E(\hat{t}, \hat{\theta})\}) \right] \\ + \frac{1}{2\Delta T} \sum_{\substack{k=k_0 \\ k \text{ odd}}}^{K_b} \left[\text{Re}\{R_{0,k}^P(\hat{t}, \hat{\theta})\}(\text{Re}\{R_{0,k}^L(\hat{t}, \hat{\theta})\} + \text{Re}\{R_{0,k}^E(\hat{t}, \hat{\theta})\}) \right] \\ \left[\text{Im}\{R_{0,k}^P(\hat{t}, \hat{\theta})\}(\text{Im}\{R_{0,k}^L(\hat{t}, \hat{\theta})\} + \text{Im}\{R_{0,k}^E(\hat{t}, \hat{\theta})\}) \right] \quad (\text{Eq 6-55})$$

Supposing that tracking error ε_τ is small, and re-using the calculations done earlier, it can be shown that N_2 (see Appendix K) can be approximated by (Eq 6-56).

$$N_2 = \frac{2E_b}{T_s} (K_b + 1) \frac{1}{\Delta T} \left[\cos^2 \varepsilon_\theta (C_{N_2, C_0}^{\text{even}} + 2C_{N_2, C_1 C_0}^{\text{odd}} + C_{N_2, C_1}^{\text{even}}) \right] \\ \left[\sin^2 \varepsilon_\theta (C_{N_2, C_0}^{\text{odd}} + 2C_{N_2, C_1 C_0}^{\text{even}} + C_{N_2, C_1}^{\text{odd}}) \right] \\ C_{N_2, C_i}^{\text{even}} = \sum_{\substack{z=-5 \\ z \text{ even}}}^5 K_{C_i}(zT_s) (K_{C_i}(zT_s + \Delta T) + K_{C_i}(zT_s - \Delta T)) \\ C_{N_2, C_i}^{\text{odd}} = \sum_{\substack{z=-5 \\ z \text{ odd}}}^5 K_{C_i}(zT_s) (K_{C_i}(zT_s + \Delta T) + K_{C_i}(zT_s - \Delta T)) \quad (\text{Eq 6-56}) \\ C_{N_2, C_1 C_0}^{\text{even}} = \sum_{\substack{z=-5 \\ z \text{ even}}}^5 K_{C_1 C_0}(zT_s) (K_{C_1 C_0}(zT_s + \Delta T) + K_{C_1 C_0}(zT_s - \Delta T)) \\ C_{N_2, C_1 C_0}^{\text{odd}} = \sum_{\substack{z=-5 \\ z \text{ odd}}}^5 K_{C_1 C_0}(zT_s) (K_{C_1 C_0}(zT_s + \Delta T) + K_{C_1 C_0}(zT_s - \Delta T))$$

The discriminator D_τ is eventually normalized as in (Eq 6-57).

$$\bar{D}_\tau(\hat{t}) = -\frac{D_\tau(\hat{t})}{N_2} \frac{C_{N_2, C_0}^{\text{even}} + 2C_{N_2, C_1 C_0}^{\text{odd}} + C_{N_2, C_1}^{\text{even}}}{C_{\tau, C_0}^{\text{even}} + 2C_{\tau, C_1 C_0}^{\text{odd}} + C_{\tau, C_1}^{\text{even}}} \quad (\text{Eq 6-57})$$

Providing that tracking errors ε_τ and ε_θ are small, $\bar{D}_\tau(\hat{t})$ is approximated by ε_τ . This normalization technique is only valid if ε_τ and ε_θ are small enough. $\bar{D}_\tau(\hat{t})$ cannot be approximated by ε_τ if it is not the case.

S curve

The S curve is now illustrated, plotting the normalized discriminator \bar{D}_τ as a function of the delay tracking error ε_τ . The S-curve is the representation of the discriminator output, \bar{D}_τ , as a function of carrier phase estimation error, ε_θ . In the linearity region, \bar{D}_τ is expected to be equal to ε_θ . Figure 6-7 illustrates the S-curve of the phase discriminator and compares it to the discriminator outputs run on a C2Link signal generated by a Matlab software C2Link generator. The normalized discriminator output (blue curve in Figure 6-4) has been obtained with the following procedure. One GMSK C2Link signal is generated using a Matlab generator. The phase θ and the delay τ of the generated signal are randomly chosen. Then, successive matched filter outputs are computed considering several values of \hat{t} and $\hat{\theta} = 0$. The normalized discriminator is eventually computed from (Eq 6-57) with $K_b = 500$ successive matched filter outputs and plotted as a function of \hat{t} .

The output of the discriminator as a function of ε_τ is illustrated in Figure 6-7, considering $\varepsilon_\theta = 0$.

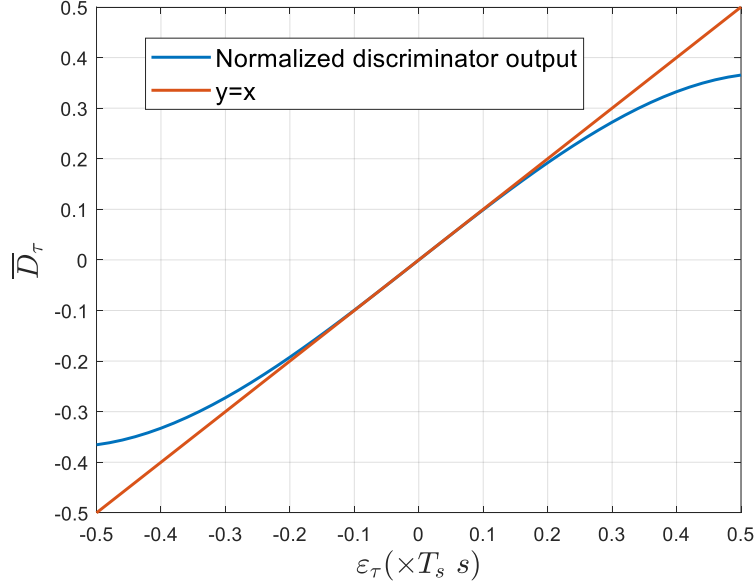


Figure 6-7: Delay discriminator output

As expected, the delay discriminator output \bar{D}_τ is proportional to the delay tracking error ε_τ in its linearity region.

6-1.3.5.3 Design of DLL loop filter and NCO

The DLL block diagram is identical to the PLL block diagram of Figure 6-5. The DLL implemented in the PhD thesis software receiver is a third order DLL. The delay estimation update depends on past time delay estimation as well as current and past discriminator outputs. The result is given in (Eq 6-58).

$$\hat{\tau}(k+1) = 3\hat{\tau}(k) - 3\hat{\tau}(k-1) + \hat{\tau}(k-2) + (K_{1,\tau} + K_{2,\tau} + K_{3,\tau})V_{d,\tau}(k) - (2K_{1,\tau} + K_2)V_{d,\tau}(k-1) + K_1V_{d,\tau}(k-2) \quad (\text{Eq 6-58})$$

$V_{d,\tau} = \bar{D}_\tau(\hat{\tau})$ is the delay discriminator output and $K_{1,\tau}$, $K_{2,\tau}$, $K_{3,\tau}$ are the DLL low-pass filter coefficients. They are provided in (Eq 6-59).

$$K_1 = \frac{60}{23}B_\tau K_b T_s \quad K_2 = \frac{4}{9}K_1^2 \quad K_3 = \frac{2}{27}K_1^3 \quad (\text{Eq 6-59})$$

In this PhD thesis synchronization module, B_τ is set to $\frac{1}{10K_b T_s}$, which is sufficient to guarantee the stability of the tracking loop.

6-1.4 Demodulation module

The objective of the demodulation module is to recover the transmitted bits from the noisy received signal. In this section, a Viterbi algorithm is implemented to recover the most likely transmitted sequence of bits. This demodulation strategy is usually used in the literature to process modulations with memory [88] [92] [93]. Indeed, the Viterbi algorithm is relevant for CPM demodulation process to cope with the inter-symbol interferences. As a reminder, the C2Link channel coding is not implemented in this PhD thesis; if the channel coding was implemented a Soft Output Viterbi Algorithm (SOVA) or a BCJR algorithm should be implemented instead (although the principles presented in this section will remain the same).

Considering a sequence of K_b bits, the most likely sequence $\hat{\mathbf{a}}$ that will be demodulated is the one maximizing the integral term of (Eq 6-20) in the ML function and reminded in (Eq 6-60).

$$\Delta(\hat{\mathbf{a}}) = \text{Re} \left\{ \int_{k_0 T_s}^{(k_0+K_b)T_s} y(t) s_L^*(t, \hat{t}, \hat{\theta}, \hat{\mathbf{a}}) dt \right\}$$

$$= \sum_{k_0 \leq 2k < 2k+1 \leq k_0+K_b} \begin{bmatrix} \tilde{\alpha}_{0,2k+1} \text{Re}\{R_{0,2k+1}(\hat{t}, \hat{\theta})\} \\ -\tilde{\alpha}_{0,2k} \tilde{\alpha}_{0,2k-1} \tilde{\alpha}_{0,2k-2} \text{Re}\{R_{1,2k}(\hat{t}, \hat{\theta})\} \\ \tilde{\alpha}_{0,2k} \text{Im}\{R_{0,2k}(\hat{t}, \hat{\theta})\} \\ -\tilde{\alpha}_{0,2k+1} \tilde{\alpha}_{0,2k} \tilde{\alpha}_{0,2k-1} \text{Im}\{R_{1,2k+1}(\hat{t}, \hat{\theta})\} \end{bmatrix} \quad (\text{Eq 6-60})$$

The real and imaginary parts of the sum term in (Eq 6-60) can be identified and are provided in (Eq 6-61).

$$\text{Re}\{S\} = \sum_{k_0 \leq 2k < 2k+1 \leq k_0+K_b} \begin{bmatrix} \tilde{\alpha}_{0,2k+1} C_0(t - \hat{t} - (2k+1)T_s) \\ -\tilde{\alpha}_{0,2k} \tilde{\alpha}_{0,2k-1} \tilde{\alpha}_{0,2k-2} C_1(t - \hat{t} - 2kT_s) \end{bmatrix}$$

$$\text{Im}\{S\} = \sum_{k_0 \leq 2k < 2k+1 \leq k_0+K_b} \begin{bmatrix} \tilde{\alpha}_{0,2k} C_0(t - \hat{t} - 2kT_s) \\ -\tilde{\alpha}_{0,2k+1} \tilde{\alpha}_{0,2k} \tilde{\alpha}_{0,2k-1} C_1(t - \hat{t} - (2k+1)T_s) \end{bmatrix} \quad (\text{Eq 6-61})$$

$$\text{With } S = \sum_{n=k_0}^{k_0+K_b} \hat{\alpha}_{0,n} C_0(t - \hat{t} - nT_s) + \hat{\alpha}_{1,n} C_1(t - \hat{t} - nT_s)$$

Using development of (Eq 6-61), (Eq 6-60) is reduced to (Eq 6-62).

$$\Delta(\hat{\mathbf{a}}) = \sum_{\substack{k=k_0 \\ k \text{ even}}}^{k_0+K_b} \tilde{\alpha}_{0,k} \text{Im}\{R_{0,k}(\hat{t}, \hat{\theta})\} - \tilde{\alpha}_{0,k} \tilde{\alpha}_{0,k-1} \tilde{\alpha}_{0,k-2} \text{Re}\{R_{1,k}(\hat{t}, \hat{\theta})\}$$

$$+ \sum_{\substack{k=k_0 \\ k \text{ odd}}}^{k_0+K_b} \tilde{\alpha}_{0,k} \text{Re}\{R_{0,k}(\hat{t}, \hat{\theta})\} - \tilde{\alpha}_{0,k} \tilde{\alpha}_{0,k-1} \tilde{\alpha}_{0,k-2} \text{Im}\{R_{1,k}(\hat{t}, \hat{\theta})\}$$

(Eq 6-62)

Knowing that at epoch k $\tilde{\alpha}_{0,k}$ is generated, (Eq 6-62) shows that the C2link GMSK modulated signal can be seen as a modulation with two bits of memory, $(\tilde{\alpha}_{k-1} \tilde{\alpha}_{k-2})$. Therefore, a four states trellis is sufficient to implement the Viterbi algorithm and to determine the sequence $(\tilde{\alpha}_{0,k})_{k \in [k_0, K_b]}$ maximizing the path metric Δ . At iteration k , the 4 states are $(\tilde{\alpha}_{k-1} \tilde{\alpha}_{k-2}) \in \{-1; +1\}^2$. Figure 6-8 represents the trellis of the Viterbi demodulation algorithm.

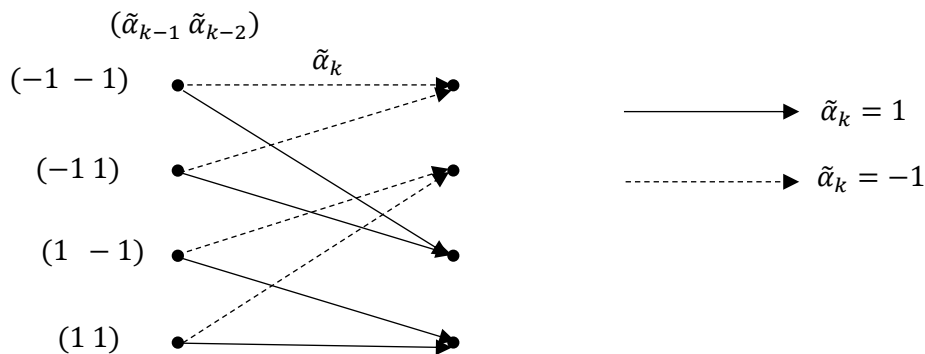


Figure 6-8: 4 states C2Link demodulation Viterbi algorithm

The branch metric of the demodulation Viterbi algorithm is given by (Eq 6-63).

$$\delta_k = \begin{cases} \tilde{\alpha}_{0,k} \text{Im}\{R_{0,k}(\hat{t}, \hat{\theta})\} - \tilde{\alpha}_{0,k} \tilde{\alpha}_{0,k-1} \tilde{\alpha}_{0,k-2} \text{Re}\{R_{1,k}(\hat{t}, \hat{\theta})\} & \text{if } k \text{ is even} \\ \tilde{\alpha}_{0,k} \text{Re}\{R_{0,k}(\hat{t}, \hat{\theta})\} - \tilde{\alpha}_{0,k} \tilde{\alpha}_{0,k-1} \tilde{\alpha}_{0,k-2} \text{Im}\{R_{1,k}(\hat{t}, \hat{\theta})\} & \text{if } k \text{ is odd} \end{cases} \quad (\text{Eq 6-63})$$

The Viterbi algorithm outputs the sequence $(\tilde{\alpha}_{0,k})_{k \in \llbracket k_0; k_0 + K_b \rrbracket}$ maximizing the path metric Δ of (Eq 6-62). Transmitted symbols $(a_k)_{k \in \llbracket k_0; k_0 + K_b \rrbracket}$ are eventually derived from the estimated sequence $(\tilde{\alpha}_k)_{k \in \llbracket k_0; k_0 + K_b \rrbracket}$ according to (Eq 6-64). The demonstration is very similar to the one done in (Eq H-4).

$$a_n = \begin{cases} \tilde{\alpha}_{0,n} \tilde{\alpha}_{0,n-1} & \text{if } n \text{ is even} \\ -\tilde{\alpha}_{0,n} \tilde{\alpha}_{0,n-1} & \text{if } n \text{ is odd} \end{cases} = (-1)^n \tilde{\alpha}_{0,n} \tilde{\alpha}_{0,n-1} \quad (\text{Eq 6-64})$$

6-1.5 Performances of C2Link signal processing modules

This section presents the performances of the signal processing modules. First, it presents the behavior of the discriminator outputs along the time, and it highlights the importance of the loop filters. Second, the performance of demodulation module coupled with the synchronization module presented in section 6-1.3 is compared to the demodulation performance assuming a perfect synchronization.

6-1.5.1 Synchronization performance

The synchronization module is first validated. A C2Link GMSK modulated signal is generated with the PhD thesis software generator and transmitted to the software synchronization module. Figure 6-9 shows the phase and delay tracking errors, considering tracking loop described in sections 6-1.3.4 and 6-1.3.5. In this analysis, K_b is set to 500 symbols. The E_b/N_0 ratio is set to 3.5 dB, which is the minimum value identified by DO-362 [8] so that minimum C2Link requirements are fulfilled.

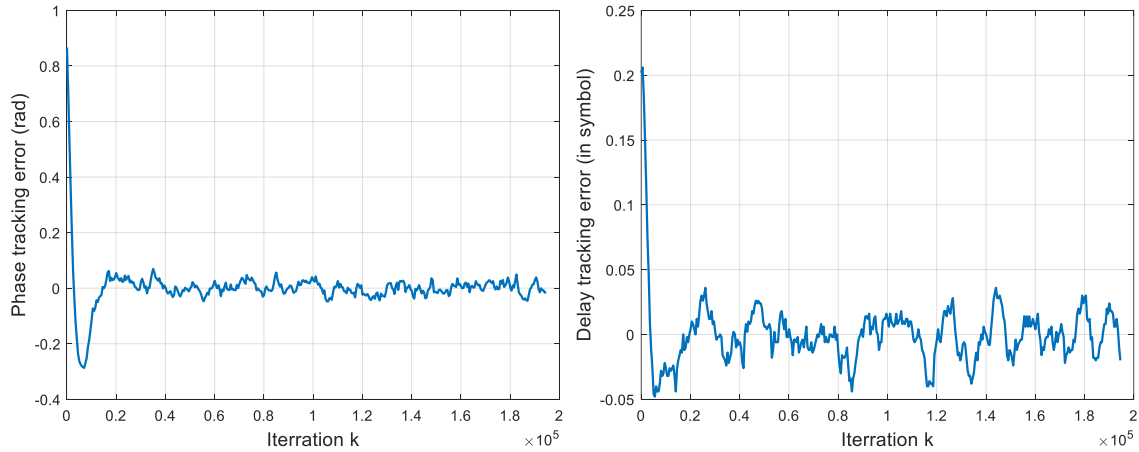


Figure 6-9: Code and delay tracking errors

First, both phase and delay tracking loops converge toward the delay and phase of the received signal. An initial phase and delay estimation errors is initially added at $t = 0$ s and is reflected in Figure 6-9. After convergence, the phase tracking error do not exceed 0.1 rad and the delay tracking error do not exceed 0.05 symbol.

The simulation is run again with the same settings but removing the loop filter. The objective is to highlight the loop filters impact on tracking performances. Figure 6-10 shows the phase and delay tracking errors in absence of tracking loop filters.

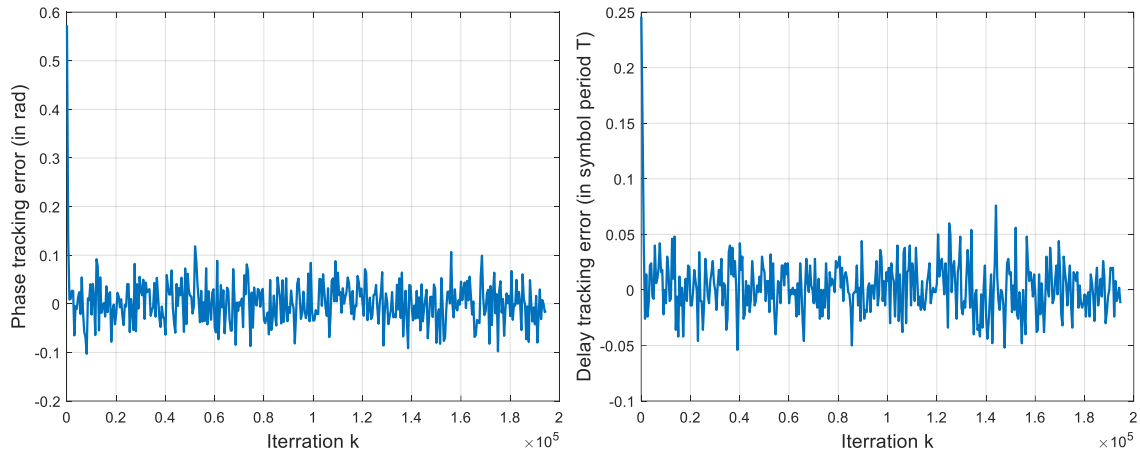


Figure 6-10: Code and delay tracking errors in absence of loop filter

Figure 6-10 shows that even in absence of tracking loop filters, the receiver is able to track the received C2Link GMSK signal as tracking errors converge toward 0. However, a comparison of Figure 6-9 and Figure 6-10 highlights the influence of the tracking loop filter: the standard deviation of the tracking errors is indeed much lower in presence of tracking loop filters. Table 6-2 compares the standard deviation of code and phase tracking errors, in presence and in absence of tracking loop filters. Table 6-2 also indicates the theoretical standard deviation of phase and delay tracking errors in presence of loop filters derived from (Eq 6-65).

$$\sigma_{\varepsilon_{\tau}} = \sqrt{2B_{\tau}K_bT_s\sigma_{D_{\tau}}^2} \quad \sigma_{\varepsilon_{\theta}} = \sqrt{2B_{\theta}K_bT_s\sigma_{D_{\theta}}^2} \quad (\text{Eq 6-65})$$

$\sigma_{D_{\tau}}^2$ and $\sigma_{D_{\theta}}^2$ refer respectively to the normalized delay and phase discriminators variance.

	Standard deviation of delay tracking error ε_{τ} (in symbol)	Standard deviation of phase tracking error ε_{θ} (in rad)
Absence of tracking loop filters	0.0217	0.0390
Presence of tracking loop filters	0.0127	0.0232
Theoretical standard deviation	0.0115	0.0201

Table 6-2: Tracking errors standard deviation with and without tracking loop filters.

Table 6-2 shows that standard deviation of phase tracking error in presence tracking loop filters is two times lower than in absence of tracking loops filter, and standard deviation of delay tracking error in presence tracking loop filters is 1.5 times lower than in absence of tracking loops filter. Also, the observed tracking errors standard deviation are consistent with the theoretical values derived from (Eq 6-65).

6-1.5.2 Demodulation performance

This section analyzes the demodulation performance. As a reminder, C2Link receiver performance is assessed analyzing WER indicator in DO-362 standards. As a consequence, the analysis of the demodulation performance of our receiver has a major significance. Also, BER is the selected indicator in 6-2 to characterize the impact of RFI on C2Link receivers. A C2Link GMSK signal is generated with the PhD thesis generator and transmitted to the signal processing modules (synchronization and demodulation).

Two scenarios are simulated. On one hand, in simulation 1, synchronization stage is assumed ideal, such that matched filter outputs are not affected by delay and phase tracking errors. An AWGN is present at the matched filter output. On the other hand, in simulation 2, non-ideal synchronization

module described in section 6-1.3.4 and 6-1.3.5 is implemented. In simulation 2, matched filter outputs are affected by tracking errors. Figure 6-11 represents the bit error rate (BER) as a function of E_b/N_0 for the two simulations.

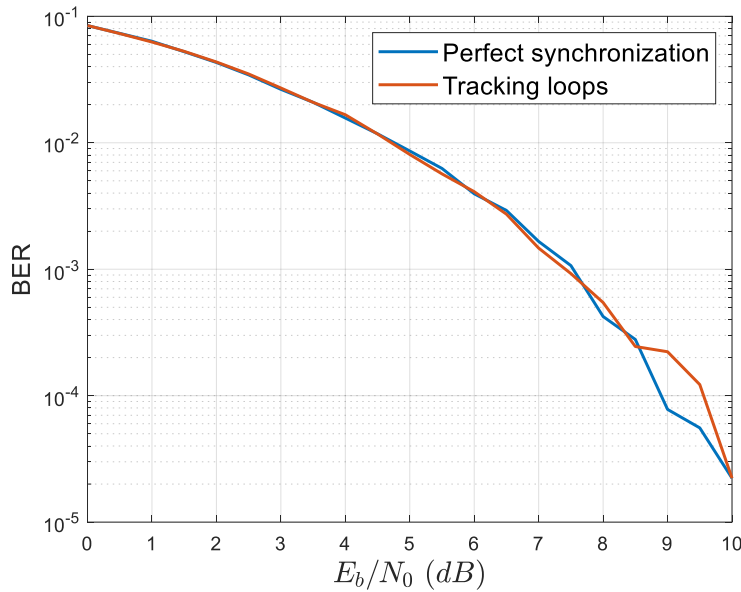


Figure 6-11: Performance of GMSK C2Link demodulation module

The comparison between simulation 1 and simulation 2 results in Figure 6-11 shows that the synchronization module does not impact the performance of the GMSK C2Link receiver in terms of BER. Consequently, BER, or equivalently word error rate (WER), is a relevant indicator to characterize the capacity of the receiver meet DO-362 minimum requirements.

The software receiver BER performance can be compared to the BER performance obtained from theory. [94] and [88] over bound the probability of error by (Eq 6-66).

$$P_b \leq \frac{1}{2} \operatorname{erfc} \left(\frac{d_{min}}{2\sqrt{N_0}} \right) \quad (\text{Eq 6-66})$$

d_{min} is the minimum distance between two different paths in the trellis and can be approximated by (Eq 6-67).

$$d_{min} = \sqrt{E_b} \min_{\mathbf{a}_1 \neq \mathbf{a}_2} \sqrt{T_s \int_0^{K_b T_s} |s_L(t, \hat{t}, \hat{\theta}, \mathbf{a}_1) - s_L(t, \hat{t}, \hat{\theta}, \mathbf{a}_2)|^2 dt} \quad (\text{Eq 6-67})$$

d_{min} is numerically computed generating the different paths in the trellis in this PhD thesis. For GMSK C2Link signal (BT=0.2), (Eq 6-66) upper bound can be reduced to (Eq 6-68) from the brute force analysis conducted in this PhD thesis.

$$P_b \leq \frac{1}{2} \operatorname{erfc} \left(\frac{1.75}{2} \sqrt{\frac{E_b}{N_0}} \right) \quad (\text{Eq 6-68})$$

The theoretical performance is illustrated on Figure 6-12 and compared to the observed BER performances of our software receiver.

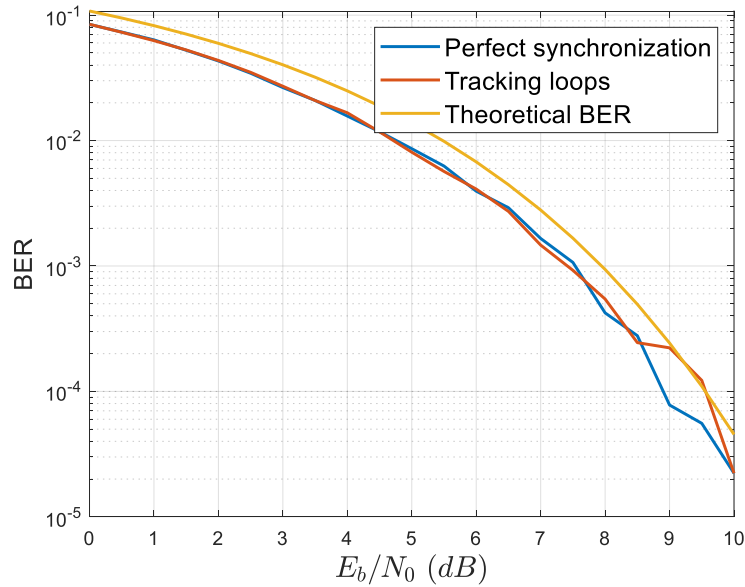


Figure 6-12: Comparison between observed and theoretical BER performance of GMSK C2Link receiver

The demodulation performance of our software receiver is slightly better than the upper bound of (Eq 6-68) by around 0.5 dB for any value of BER. Note that the obtained relationship between d_{min} and E_b of (Eq 6-67) is consistent with [94], and the simulated BER performance is consistent with what is observed in the literature for non-coded GMSK signal [93].

6-2 Impact of continuous wideband RFI on GMSK C2Link receivers

This section analyzes the impact of continuous wideband RFI on GMSK C2Link BER performance degradation. It develops a mathematical model predicting the BER degradation caused by a continuous wideband RFI as a function of its characteristics. This section is at the utmost importance. Indeed, standards highlight that WER (or equivalently BER) is a relevant indicator to assess C2Link receiver performance. Therefore, thanks to degradation prediction model developed in this section, the maximum level of an RFI keeping the WER above the WER threshold (and thus keeping performance objectives fulfilled) can be determined.

It is decomposed in 2 subsections. First, it proposes a mathematical model characterizing the RFI impact as an increase of the noise floor. Second, it validates the proposed theoretical model of the impact of the impact of RFI on BER degradation, observing the GMSK C2Link receiver BER when an RFI is injected.

6-2.1 Theoretical model of RFI impact on BER

This section proposes a mathematical model predicting the BER degradation caused by a continuous wideband RFI. Similarly to the GNSS characterization of continuous wideband RFI as an equivalent noise, the RFI impact is also here characterized as an increase of the noise floor at the matched filter output. The rationale for such a model is the low bandwidth of GMSK C2Link signal, as detailed later.

The equivalent noise is introduced in three steps:

- 1) The RFI power $P_{J,out}$ at the matched filters output is computed.
- 2) The power of an AWGN with constant power spectral density I_0 at the matched filters output is computed.
- 3) I_0 is computed so that the AWGN power at the matched filters output equals $P_{J,out}$.

Step 1:

The equivalent noise of an RFI in a C2Link receiver is defined by the power spectral density of an AWGN generating the same power at the matched filter output as the analyzed RFI does.

Let us characterize a continuous wideband RFI at the receiver antenna port by its spectral footprint as in (Eq 6-69).

$$S_{in}(f) = C_J \bar{S}_{in}(f) \quad (\text{Eq 6-69})$$

C_J is the power of the interference and $\bar{S}_{in}(f)$ is the equivalent baseband unit-power power spectral density of the interference. S_{in} is the equivalent baseband power spectral density of the RFI at the receiver antenna port.

Using Wiener-Lee expression, the RFI power spectral density $S_{out,i}$ at the output of the matched filter of pulse $C_i, i \in \{0; 1\}$ is given by (Eq 6-70).

$$S_{out,i}(f) = |C_i^{mf}(f)|^2 \bar{S}_{in}(f) \quad (\text{Eq 6-70})$$

$C_i^{mf}(f)$ is the transfer function of matched filter of pulse C_i , or equivalently, the Fourier transform of the matched filter impulse response $C_i(T_s - t), i \in \{0; 1\}$, where $(C_i)_{i \in \{0,1\}}$ are the pulses of Laurent decomposition of GMSK signal represented in Figure 6-2. $|C_i^{mf}(f)|$ is represented in Figure 6-13, for $i \in \{0; 1\}$ and for two data rate values (class 1: 34.5 kbits/s and class 4: 138 kbits/s data rates defined in Chapter 3 Table 3-7).

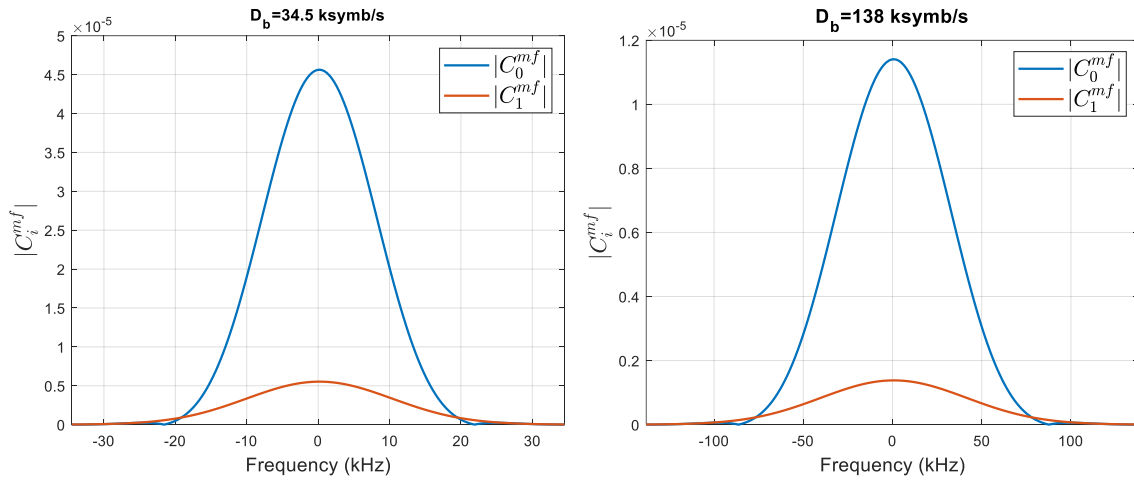


Figure 6-13: GMSK C2Link matched filters transfer functions

As highlighted by Figure 6-13, most of the power is contained in C_0 matched filter output; note that this result confirms the C_i pulses contribution to the GMSK modulated signal power. In addition, the matched filter transfer function bandwidth depends on the transmitted data rate as was expected.

The RFI power at the output of matched filter of pulse C_i is obtained integrating the PSD of the RFI at the matched filter output, (Eq 6-70), and is given in (Eq 6-71).

$$P_i = \int_{-\infty}^{+\infty} S_{out,i}(f) df = C_J \int_{-\infty}^{+\infty} |C_i^{mf}(f)|^2 \bar{S}_{in}(f) df \quad (\text{Eq 6-71})$$

Finally, C2Link signal processing modules (synchronization: DLL and PLL, demodulation) use linear combination of matched filters outputs on pulsed C_0 and C_1 . Therefore, considering that matched

filters outputs on pulse C_0 and C_1 are independent, the total interference power at the matched filter outputs $P_{J,out}$ is given by (Eq 6-72).

$$P_{J,out} = P_0 + P_1 = C_J \int_{-\infty}^{+\infty} \left(|C_0^{mf}(f)|^2 + |C_1^{mf}(f)|^2 \right) \bar{S}_{in}(f) df \quad (\text{Eq 6-72})$$

Step 2:

As the power spectral density I_0 of an AWGN is constant, performing similar operations than in Step 1, the AWGN power at the matched filters output is given by (Eq 6-73) according to the power of each pulse recapped in Table 6-1.

$$P_{AWGN} = I_0 \int_{-\infty}^{+\infty} \left(|C_0^{mf}(f)|^2 + |C_1^{mf}(f)|^2 \right) df = I_0 \int_{-\infty}^{+\infty} C_0(t)^2 + C_1(t)^2 dt \approx I_0 T_s \quad (\text{Eq 6-73})$$

Step 3:

The equivalent noise is defined by I_0 such that $P_{AWGN} = P_{J,out}$. It is deduced from (Eq 6-72) and (Eq 6-73) and can be expressed as in (Eq 6-74).

$$I_0 = \frac{C_J}{T_s} \int_{-\infty}^{+\infty} \left(|C_0^{mf}(f)|^2 + |C_1^{mf}(f)|^2 \right) \bar{S}_{in}(f) df \quad (\text{Eq 6-74})$$

Finally, the impact of the RFI can be characterized by a degradation of the E_b/N_0 ratio, and this degradation is expressed by (Eq 6-75).

$$D_{E_b/N_0} = \frac{N_0 + I_0}{N_0} = 1 + \frac{C_J}{T_s N_0} \int_{-\infty}^{+\infty} \left(|C_0^{mf}(f)|^2 + |C_1^{mf}(f)|^2 \right) \bar{S}_{in}(f) df \quad (\text{Eq 6-75})$$

6-2.2 Validation of the theoretical RFI impact model

Section 6-2.1 models the impact of a continuous wideband RFI on a GMSK C2Link receiver as a E_b/N_0 degradation and thus, as a degradation of the minimum E_b/N_0 required to obtain the targeted BER. The objective of this section is to validate the proposed model, analyzing the BER performance of the developed GMSK C2Link software receiver in presence of continuous wideband RFI.

6-2.2.1 BER degradation for large bandwidth RFI

Figure 6-14 compares the BER performance in presence and in absence of RFI, for two different data rates: $D_b = 34.5 \text{ ksymb/s}$ and $D_b = 138 \text{ ksymb/s}$. The analyzed RFI has a rectangular power spectral density with double-sided bandwidth $BW = 1 \text{ MHz}$ and is centered on the C2Link signal carrier frequency. The RFI power is deduced from (Eq 6-76) and the targeted E_b/N_0 degradation is $D_{E_b/N_0} = 3 \text{ dB}$.

$$\frac{C_J}{N_0} = \frac{T_s (D_{E_b/N_0} - 1)}{\int_{\frac{-BW}{2}}^{\frac{BW}{2}} \left(|C_0^{mf}(f)|^2 + |C_1^{mf}(f)|^2 \right) df} \quad (\text{Eq 6-76})$$

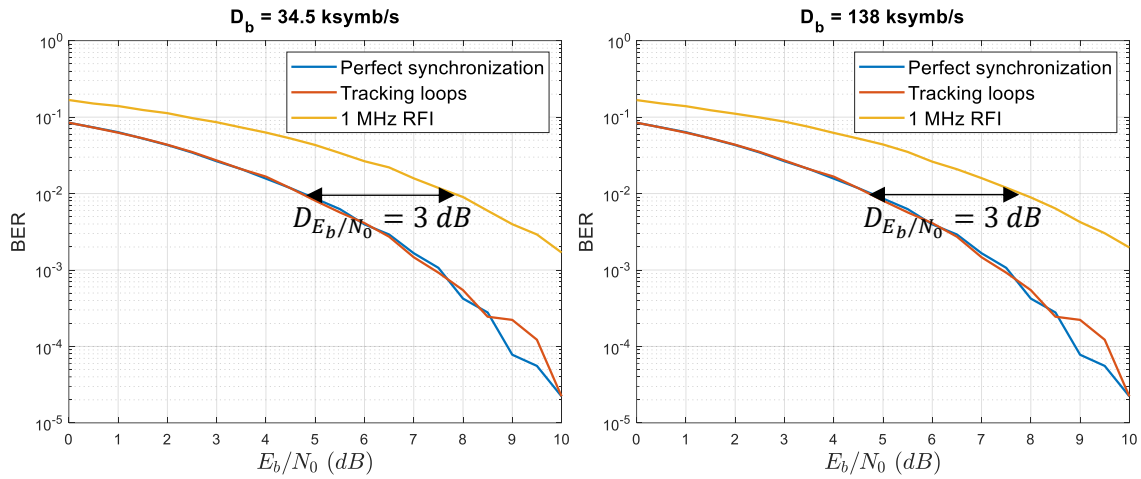


Figure 6-14: BER performance degradation in presence of a 1 MHz RFI, targeting a 3 dB E_b/N_0 degradation

As depicted in Figure 6-14, the BER degradation caused by the RFI is consistent with the targeted E_b/N_0 degradation. In addition, it can be seen that the degradation prediction model is valid for $BW = 1\text{ MHz}$ for the two considered data rate values analyzed in Figure 6-14.

6-2.2.2 BER degradation for narrow bandwidth RFI

Section 6-2.2.1 showed the validity of the prediction model for wideband RFI. However, a counter UAS jamming gun may target a given channel and therefore use a narrower RFI. Nevertheless, it is not expected that the counter UAS jammer signal bandwidth is below the C2Link channel bandwidth. Therefore, the objective of this section is to verify the validity of theoretical model of RFI impact on BER performance in presence of an RFI whose bandwidth is equal to the C2Link signal channel bandwidth. The RFI power is defined from (Eq 6-76) targeting a E_b/N_0 degradation $D_{E_b/N_0} = 3\text{ dB}$. Figure 6-15 illustrates the BER performance of the receiver as a function of E_b/N_0 in presence of narrow RFI, for data class 1 and data class 4 C2Link receivers.

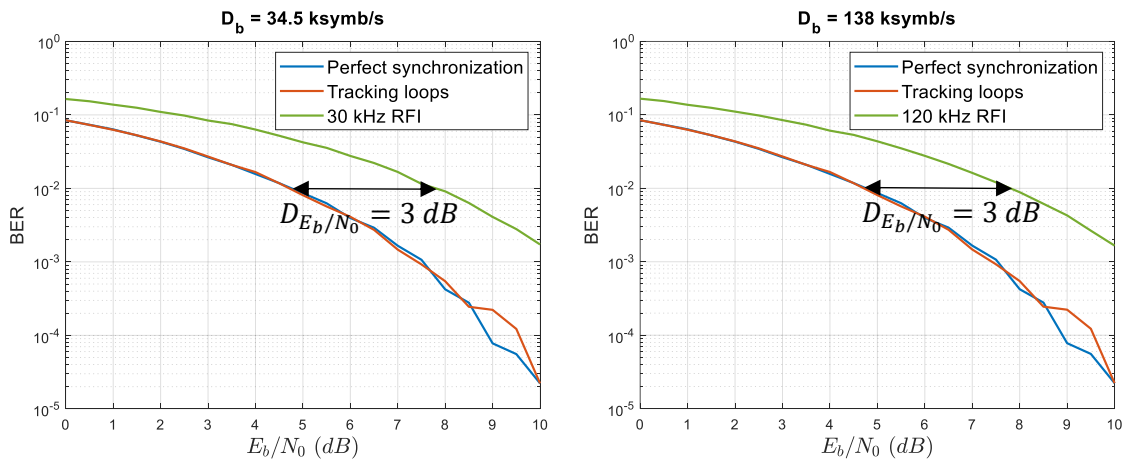


Figure 6-15: BER performance degradation in presence of a narrow RFI, targeting a 3 dB E_b/N_0 degradation

As highlighted by Figure 6-15, the prediction of the RFI impact on BER performance is still valid for RFI which bandwidth is equal to the C2Link channel bandwidth, as the BER curve is shifted by 3 dB as expected. Additional results show that the prediction model is still valid for a data class 1 GMSK C2Link receiver in presence of a 1 kHz RFI. However, this kind of jammer is not expected to be used as part of anti-drone struggle, because it can be easily mitigated by notch filtering.

6-3 Conclusion

This chapter investigates the impact of continuous wideband RFI on C2Link GMSK modulated signal receiver. First, synchronization and demodulation modules are theoretically developed and implemented under the form of a Matlab software receiver. The time delay and carrier phase lock loops are designed from the maximization of the maximum likelihood function. The demodulation module is built using the Viterbi algorithm to mitigate the inter symbol interference induced by the C2Link GMSK modulated signal. The theoretical behavior of the synchronization module as well as the demodulator has been verified from the implementation of the Matlab software receiver. Inspecting the receiver performance in terms of demodulation, it can be seen that the presence of non-perfect synchronization stage or the assumption of ideal synchronization does not affect the BER performance: even with low E_b/N_0 signals, BER is the most constraining operation compared to synchronization. As a result, the BER is a relevant indicator to characterize the GMSK C2Link receiver ability to meet signal processing requirements. Note that the BER performance of the developed Matlab software receiver is consistent with theoretical performance of GMSK modulation with $BT=0.2$ found in literature.

Second, a theoretical model characterizing the impact of continuous wideband RFI on receiver BER performance is proposed. Note that in this chapter, since the impact of RFI on the RFFE block is not investigated, it is assumed that the receiver operates in its linearity region, or in other words, the received RFI power is low enough to not saturate the receiver LNA. The theoretical model key assumption consists in considering the RFI equivalent to a AWGN generating the same power at the matched filters output as the RFI does, denoted as I_0 . Therefore, the receiver BER performance degradation is quantified as a degradation of E_b/N_0 . The theoretical model is validated injecting continuous wideband RFI within the GMSK C2Link software receiver. Injecting a RFI with 1 MHz bandwidth, and setting the RFI power in order to target a 3dB of E_b/N_0 degradation, the BER performance curve as a function of E_b/N_0 behaves as expected: the curve is offset by 3 dB with respect to the nominal curve; the prediction model of RFI impact on receiver BER performance is thus validated. Since the model also needs to be validated for narrower RFI, another simulation is run, injecting a RFI which bandwidth is equal to the C2Link channel bandwidth. Indeed, as part of anti-drone struggle, it can be expected that the jamming signal hits at least the whole targeted channel. For this simulation, the injected RFI power is computed in order to target a 3dB of E_b/N_0 degradation. As expected, receiver BER performance in presence of RFI is consistent with the prediction model.

This chapter does not go further in the prediction of protection area during jamming operations as was done in Chapter 4 because some elements remain unknown. First, the antenna and RFFE block for civil aviation certified C2Link receivers in terms of gain and frequency selectivity are not available, since only C2Link prototypes are currently developed. The C2Link received energy per bit E_b is thus difficult to be precisely estimated. Second, even though UAS traffic prediction already exists, their reliability is not consolidated because of the rapid growing and variability of the UAS traffic. As a consequence, C2Link intra system RFI is difficult to be precisely estimated. These two points must be further investigated as part of anti-drone struggle. Once these two points would be defined, the RFI equivalent model presented in this chapter can be applied in order to determine a protection area during jamming activities.

Chapter 7: Conclusion and future work

This chapter presents the conclusions from the results presented in previous chapters.

7-1 Results from PhD

The overall objective of this PhD is the analysis of civil aviation GNSS and C2Link resiliency facing jamming RFI. This work is part of counter-UAS efforts undertaken by several authorities. Its first goal is to propose a methodology to estimate the portion of an RFI affected area in which civil aviation GNSS and C2Link receivers may not meet their respective minimum requirements (protection area). To reach that goal, several intermediate achievements were necessary, some of them being new results are summarized here. The second goal is to characterize the impact of a common type of interferences referred as chirp. This second objective is part of civil aviation GNSS receiver standardization elaboration. This second objective may also help in determining protection areas during GNSS jamming exercises when the state jammer uses a chirp waveform.

The study conducted to achieve that main goal is presented in chapter 4, which then provides a new methodology to compute protection area during a jamming operation.

That chapter 4 starts by presenting the concept of civil aviation RFI mask, which is the main tool currently used to design jamming protection area. RFI mask provides the maximum authorized power at the GNSS receiver antenna port from non-aeronautical RFI sources. This GNSS interference mask is widely investigated in Appendix B in order to highlight assumptions which may not be relevant when designing a protection area. This mathematical interpretation of the mask, its pedagogical presentation in this thesis, and the identification of the assumptions is an original formulation of this thesis. These assumptions are summarized here. First, the RFI mask is elaborated in 1996 as part of elaboration of RTCA DO-229 standard. It is designed from an analysis of the aeronautical RFI environment of 1996 at the Honolulu Final Approach Fix. Consequently, the aeronautical RFI environment considered by the RFI interference mask is not relevant for protection area design around a jammer for two reasons:

- The aeronautical RFI environment in Honolulu is different from the aeronautical RFI environment in the jammed area.
- The aeronautical RFI components considered to design the GNSS RFI mask are no more up to date, as many GNSS systems have been launched in the last two decades.

Second, the RFI mask is designed for a particular interference waveform, which has a rectangular power spectral density. Therefore, the RFI mask is not applicable if the jammer which is used has a different waveform. In particular, RFI mask may be irrelevant if the jamming gun uses a chirp RFI.

Third, RFI masks are often misinterpreted. Indeed, RFI mask return the *total* authorized non-aeronautical power. However, the victim GNSS receiver is inherently hit by some non-aeronautical sources such as on-board Portable Electronic Devices and terrestrial sources. In some situations, and in particular above areas with a high density of terrestrial emitters, the victim GNSS receiver capacity to meet required performance objectives may be reduced because of these non-aeronautical RFI sources. Therefore, neglecting the contribution of terrestrial emitters and on-board PEDs, as well as other unknown potential non aeronautical sources (and thus considering only the jamming signal in the non-aeronautical sources) may be too optimistic.

To counter these drawbacks of the RFI mask, Chapter 4 follows with the presentation of a new methodology to design protection areas. The key point of this methodology is the precise characterization of the interference environment in the jammed area and during the jamming period. This new methodology is divided in three steps:

- First, a C/N_0 link budget for all signals and all receiver operations (acquisition, tracking, demodulation), $C/N_{0,eff,op,sig}$, is compared to the corresponding receiver operation C/N_0 threshold, $C/N_{0,th,op,sig}$, which is the assumed C/N_0 value such that requirements associated to this operation are fulfilled when $C/N_{0,eff,op,sig} \geq C/N_{0,th,op,sig}$. Note that the C/N_0 link budgets are computed in the vicinity of the jammer, taking into account the local RFI situation. The limiting link budget, if positive, allows the derivation of the maximum non-aeronautical equivalent wideband noise level that could be tolerated by the receiver, keeping all requirements fulfilled.
- Second, the equivalent wideband noise level caused by all non-aeronautical RFI sources $I_{0,non\ aero}$ is derived. The new methodology takes into account terrestrial emitters, on-board PEDs and jamming signal as non-aeronautical sources. One innovation of this PhD is the refinement of the estimation of terrestrial emitters equivalent noise. This new calculation method is based on the exploitation of population density geographical information, assuming that the density of terrestrial emitters is linked with the population density. This approach is indeed compliant with the fundamental idea of the methodology which consists in precisely characterizing the *local* RFI environment.
- Third and last, the protection area is determined identifying all victim receiver positions for which the received non-aeronautical equivalent noise exceeds the assumed level tolerated by the receiver.

Chapter 4 finishes by comparing the protection area designed with the traditional methodology which relies on RFI mask and with the new methodology. The following results are obtained:

- The protection area radius for legacy single frequency GPS L1 C/A receiver is almost divided by two. This is mainly due to a higher elevation angle of GPS SVs during the jamming period than the ICAO 5° elevation mask which is considered in the RFI mask. Therefore, the GNSS receiver power is higher in the new methodology than the one considered in the RFI mask.
- The protection area radius for DFMC receiver is divided by 2.7. In addition to using the new minimum antenna gain towards the upper hemisphere (linked to SV elevation), the new methodology takes advantage of better performances of DFMC receivers in terms of implementation losses and tracking threshold.

The objective of Chapter 5 is to characterize the impact of chirp RFI on civil aviation GNSS receiver. This chapter starts by presenting a mathematical model of chirp RFI and discusses its stationarity at the antenna port. In this mathematical model, the chirp signal at the GNSS receiver antenna port is assumed to be random. The randomness is brought by two parameters.

- A random phase, whose rationale is justified by the impact of transmitter oscillator, antenna and RFFE impact on the received chirp signal.
- A random delay parameter, which is justified by the propagation delay as well as the chirp generation process.

Thanks to these two random parameters, Chapter 5 demonstrates that the chirp signal at the RFFE output is wide sense stationary.

Chapter 5 continues by deriving a theoretical prediction model of C/N_0 degradation caused by the chirp RFI. The fundamental idea of this model is the characterization of the chirp RFI as an equivalent wideband noise. The key parameter to derive the chirp RFI equivalent wideband noise level I_0 is the spectral separation coefficient (SSC), which characterizes the overlap between the chirp power spectral density and the GNSS local replica power spectral density (this is the reason why the wide sense stationarity of the chirp RFI is an important assumption). This theoretical model predicts a strong influence of several parameters on the C/N_0 degradation. The receiver integration time T_i , the chirp sweep period T_{sweep} and the frequency offset Δf between the chirp signal and the GNSS local replica are among the most significant. This C/N_0 degradation prediction model is then compared to simulations run on a matlab receiver and with an IFEN SX3 receiver. C/N_0 is estimated at the output of the matlab and SX3 receivers using several C/N_0 estimators issued from literature: Beaulieu, moment, SNV, NWPR. These simulations allow to identify three conditions of validity of this C/N_0 degradation prediction model in presence of a chirp RFI:

1. Since C/N_0 estimators are based on a particular probabilistic definition of SNIR at the correlator output, the condition of validity of this definition must be fulfilled. In particular, the chirp RFI at the correlator output must be zero-mean and uncorrelated with the GNSS signal.
2. C/N_0 estimators make some assumptions on the distribution of the equivalent noise at the correlator output. Therefore, these assumptions must be fulfilled so that C/N_0 estimators return values consistent with the true effective C/N_0 . For example, Beaulieu and SNV estimators assume an identical distribution of the chirp RFI on the in-phase and quadrature phase correlator outputs. In addition, moment estimator assumes a gaussian distribution of the RFI at the correlator output.
3. Chirp RFI contribution to the correlator outputs must be ergodic such that statistical properties can be recovered from the observation of correlator outputs over a sufficiently long time interval.

If these three conditions are fulfilled, then Chapter 5 shows that the C/N_0 degradation prediction model is accurate.

To cover the cases where these conditions are not met, and in particular when correlator outputs in presence of chirp RFI are not ergodic, so that correlator output noise as well as range noise inflation cannot be predicted from the predicted C/N_0 degradation, chapter 5 also develops an alternative theoretical model focusing on the prediction of successive correlator outputs and code and phase measurements. The correlator outputs are first mathematically derived from the knowledge of the chirp RFI settings. Then, code and phase measurements are successively derived under the form of numerical series, considering typical GNSS tracking loops. These prediction models are validated with simulations run on our Matlab receiver.

The work performed in Chapter 5 is significant for the design and testing of civil aviation GNSS receiver. Indeed, it would help in identifying chirp settings having the worst impact on several GNSS performance indicators (C/N_0 , code and phase measurements). Therefore, this analysis may be of interest for the definition of the testing procedures in presence of chirp RFI.

Finally, chapter 6 is dedicated to the analysis of the C2Link receiver resilience facing RFI. Its objective is to characterize the impact of RFI on C2Link receiver. The definition of the terrestrial C2Link with a GMSK modulation is assumed in this chapter.

Chapter 6 starts by designing synchronization and demodulation modules of a C2Link receiver which is implemented in Matlab. The goal of this first step is to develop a tool which can help in the characterization of the RFI impact on C2Link receiver. Similarly to most of CPFSK receiver, the receiver

which is developed here is based on the Laurent decomposition of GMSK C2Link signal: the GMSK signal can be approximated by a sum of pulse amplitude modulated signals. For C2Link signal definition for which the BT product is 0.2, only two Laurent pulses are non-negligible. Then, the synchronization module is designed based on a non-decision aided approach. In order to define delay and phase discriminators, the log-likelihood function is computed and derived with respect to delay and phase estimation respectively. These discriminators perform algebraic operation on successive matched filter outputs to estimate the delay and phase tracking errors. Then, tracking loop filters are designed based on literature.

In parallel of this synchronization module, the demodulation module is developed. Thanks to the Laurent decomposition, a Viterbi algorithm is suitable to demodulate the transmitted bits. Note that channel coding has not been implemented during this PhD thesis.

The synchronization and demodulation module performance are then characterized in terms of Bit Error Rate. BER (or equivalently subframe error rate) is indeed the performance indicator identified in RTCA DO-362A to assess C2Link receiver capacity to meet RLP. The two following conclusions are issued from the validation process:

- BER performance considering perfect synchronization and synchronization obtained by the developed software are similar. Even for low E_b/N_0 signal, the synchronization module does not add additional BER losses. Therefore, the synchronization is not constraining to respect Required Link Performance. This result highlights the relevance of the BER as selected C2Link performance indicator.
- BER performance of the developed receiver is consistent with the BER theoretically derived.

Eventually, a prediction model of the impact of RFI on C2Link BER performance is developed, computing the E_b/N_0 degradation caused by the RFI. The RFI is here characterized as an equivalent wideband noise. The equivalent wideband noise level is computed from the spectral separation coefficient between the RFI and the GMSK matched filter impulse response. Then, this theoretical BER degradation model is compared to the BER degradation returned by the matlab receiver. The obtained results highlight the relevance of the characterization of the RFI as an equivalent wideband noise.

Chapter 6 does not go further in the derivation of the protection area during C2Link jamming operations. As a matter of fact, some elements remain to be defined. In particular, it is very difficult to estimate intra system RFI since intra system RFI would depend on the UAS traffic. However, the proposed characterization of RFI as wideband noise can be re-used for future determination of C2Link protection area.

7-2 Future work

This work has allowed a better understanding of parameters involved when determining the impact area during a jamming operation. However, some of them would deserve to be refined in order to make the derivation of the GNSS protection area more precise.

In particular, the impact of non-aeronautical terrestrial emitters relies on a NASA analysis performed in 2003. Spurious emission power on current electronic devices is expected much lower than EIRP considered in our analysis, and a new measurement campaign would be useful. On a similar topic, regarding on board non aeronautical emitters, a new measurement campaign for measurement the coupling between PEDs at aircraft window and the new DFMC L1/L5 antenna would also be very useful.

In addition, several assumptions considered in the determination of the GNSS protection area during GNSS jamming seem quite constraining. In particular, our analysis performed in Chapter 4 requests the

GNSS receiver to be able to track all satellites above 5° elevation. To track all signals above 5° elevation is not mandatory to meet ICAO positioning accuracy. Therefore, in order to reduce more the protection area, it can be considered to accept losing the tracking of satellites at low elevation, provided that integrity monitoring requirements remain respected. Making this improvement requires to compute horizontal and vertical protection levels to determine the availability of the GNSS in absence of some of the visible satellites. Performing this analysis, the minimum elevation of the required satellites to meet integrity requirements (also called critical satellites) would be increased, and the protection area would be decreased.

Moreover, the GNSS antenna gain in the lower hemisphere which is considered in this PhD is an upper bound of measurements made on an aircraft model, and sounds quite conservative. A refinement of this antenna gain would be appreciated, as it would lower the assumed jamming RFI power at the victim receiver antenna port, provided that the jammer is below the victim aircraft. This assumption is valid for most of jamming situations. To achieve this objective, a PhD thesis has been launched at ENAC, and one of its goals is to derive the GNSS antenna pattern in the lower hemisphere, characterizing the aircraft shadowing.

Regarding the analysis of the impact of counter UAS or PPDs on GNSS receivers, analysis of real observations of C-UAS antenna patterns, radiating powers, signal waveforms, would also be interesting. In the case of chirp-based jammers in C-UAS or PPDs, additional observations with real emitters and GNSS as well as C2Link receivers would also be interesting. Also, re-using the experimentally backed theoretical results presented in this thesis about the impact of a chirp RFI for the design and the execution of DFMC receivers testing could be very valuable.

Finally, some work also remains to be done about the C2Link analysis. Indeed, the intra-system RFI (C2Link signals different from the signal of interest act as RFI) as well as inter-system RFI have not been considered. The reason explaining why the analysis has not been performed is the lack of visibility in the UAS traffic in the near and medium future as well as the lack of published standard for the C2Link satellite system in the 5030-5091MHz band. Additionally, the isolation between channels, and in particular RFFE pattern, is not characterized yet, and the allocation method of channels to requesting UAS remains under discussion. Therefore, an estimation of C2Link intra system level would have been very unprecise.

The original mathematical interpretation and the assumptions underlying the definition of the civil aviation RFI mask which are presented in the Ph.D. thesis were the basis for the derivation of the nov 2020 ICAO SARPs mask. It is a great expectation to see how the presentation in this Ph.D. thesis may be further debated and re-used in the future in next standardization fora, for update of current documents at RTCA/EUROCAE, ICAO or perhaps even ITU.

Appendix A: GNSS acquisition, tracking and demodulation C/N_0 thresholds

This appendix derives the acquisition, tracking and demodulations thresholds of the different GNSS signal of interest. As a reminder, C/N_0 threshold for a given signal and receiver operation is the assumed minimum C/N_0 of the considered GNSS signal so that minimum requirements for the considered receiver operation are fulfilled. C/N_0 thresholds depend on the strategy chosen by the receiver manufacturer to be compliant with the requirements, as well as signal processing methods implemented in the GNSS receiver. C/N_0 derived in this appendix are used within GNSS receiver standards (DO-235, DO-292A and ED-259). Therefore, strategy and receiver signal processing methods considered in this appendix do not aim to be optimal, but conversely very simple so that GNSS receivers easily meet these thresholds.

This appendix is divided in two sections. First, acquisition C/N_0 thresholds are derived, for legacy and DFMC GNSS receivers. Second, tracking and demodulation thresholds are derived, for legacy and DFMC GNSS receiver as well. For each of the sections, the minimum requirements are presented, and then C/N_0 thresholds are derived considering a very simple signal processing method.

Innovations of this PhD include the derivation of C/N_0 acquisition thresholds for DFMC GNSS receiver in accordance with minimum requirements of ED-259A.

A-1 C/N_0 acquisition thresholds

This section derives C/N_0 acquisition thresholds. It first focuses on DFMC GNSS receiver. Second, it legacy GNSS receiver C/N_0 acquisition thresholds are derived.

A-1.1 DFMC GNSS acquisition thresholds

This section derives C/N_0 acquisition thresholds for DFMC GNSS receivers. It is split in 3 parts. It first presents the acquisition module architecture and mathematically derives the acquisition threshold. Second, it presents initial DFMC acquisition requirements of ED-259 and deduces a strategy compliant with initial acquisition requirements. Inputs for acquisition thresholds calculation are issued from this strategy. Third and last, DFMC acquisition thresholds are computed.

A-1.1.1 C/N_0 acquisition threshold mathematical expression

In this appendix, the acquisition of a GNSS signal is supposed to be performed through a detection test built from correlator outputs. Correlator outputs of GPS L1C/A, Galileo E1, GPS L5 and Galileo E5a have been presented in Chapter 2 section 2-3.3.1.1.

Description of the acquisition process

As described in Chapter 2 section 2-3.3.2, the acquisition of a GNSS signal is performed browsing an acquisition matrix via delay and Doppler settings. For each bin of the acquisition matrix, the detection test is computed from correlator outputs determined with code delay and Doppler frequency estimates of the current bin. The detection test mathematical expression is given by (Eq 2-53) for GPS L1C/A, and (Eq 2-57) for Galileo E1, GPS L5 and Galileo E5a, and reminded in (Eq A-1).

$$T_1 = \sum_{k=1}^{M_{T_1}} I_{L_1}^D(k)^2 + Q_{L_1}^D(k)^2 \quad (\text{Eq A-1})$$

$$T_2 = \sum_{k=1}^{M_{T_2}} \left((I_X^D(k))^2 + (Q_X^D(k))^2 + (I_X^P(k))^2 + (Q_X^P(k))^2 \right)$$

M_{T_1} and M_{T_2} are respectively the number of non-coherent summations. They are limited by the maximum time to acquire each satellite $T_{acq,i}$, the number of correlators N_{corr} and by the number of cells in the acquisition matrix N_{tot} . Also, it depends on the acquisition detector which is used. Indeed, acquisition detector T_2 needs correlator outputs of the pilot and data components whereas acquisition detector T_1 only needs the correlator outputs of the data component. Therefore, the number of correlators can be mathematically expressed by (Eq A-2).

$$M_{T_1} = \left\lfloor \frac{N_{corr} T_{acq,i}}{N_{tot} T_i} \right\rfloor \quad M_{T_2} = \left\lfloor \frac{N_{corr} T_{acq,i}}{2 N_{tot} T_i} \right\rfloor \quad (\text{Eq A-2})$$

Then, this detection test is compared to a detection threshold. If the detection test is higher than the detection threshold, then the searched GNSS signal is declared to be present on the current cell and tracking loops are launched. Conversely, if the detection test is lower than the detection threshold, then the searched GNSS signal is supposed to be absent, and the acquisition process moves to the next bin of the acquisition matrix.

Mathematical expression of C/N_0 acquisition threshold

The C/N_0 acquisition threshold is computed as the minimum C/N_0 value of a GNSS signal such that the probability of successful detection P_D exceeds a targeted value deduced from requirements and assumed acquisition strategy. Of course, the probability of false detection P_{fa} should remain below a reasonable value.

The acquisition method presented in this appendix is based on a Neyman-Pearson detection test, whose null and alternative hypothesis H_0 and H_1 are described hereinafter.

Null hypothesis H_0 :

Under null hypothesis H_0 , the searched GNSS signal is not present. However, another GNSS signal, different from the searched one, is assumed to be present, leading to the presence of a cross-correlation term. $\varepsilon_{\tau,max}$ and $\varepsilon_{f,max}$ refers to code and Doppler estimation errors leading to the highest cross-correlation $\varepsilon_{f,max} = 0$ in the worst-case scenario so that the interfering GNSS signal induces the maximum cross-correlation. Under hypothesis H_0 , the acquisition detector T_1 presented in (Eq 2-53) can be reduced as in (Eq A-3) for GPS L1C/A.

$$T_1 = \sum_{k=1}^{M_{T_1}} \left[\left(\sqrt{\frac{P_j}{2}} d(k) \tilde{R}_{c_D, j, c_D}^{L1}(\varepsilon_{\tau,max}) \cos(\pi \varepsilon_f T_i + \varepsilon_\varphi) + n_{I,L1}^D(k) \right)^2 + \left(\sqrt{\frac{P_j}{2}} d(k) \tilde{R}_{c_D, j, c_D}^{L1}(\varepsilon_{\tau,max}) \sin(\pi \varepsilon_f T_i + \varepsilon_\varphi) + n_{Q,L1}^D(k) \right)^2 \right] \quad (\text{Eq A-3})$$

$\tilde{R}_{c_D, j, c_D}^X$ and $\tilde{R}_{c_P, j, c_D}^X$ are the cross-correlation functions between the data and pilot PRN codes with the data PRN code of signal X . P_j is the total power of the interfering GNSS signal. $n_{I,L1}^D$ and $n_{Q,L1}^D$ are AWGN components with power equal to $\sigma_n^2 = \frac{\beta N_0}{4 T_i}$ according to Chapter 2 section 2-3.3.1.2.

T_1 can be normalized by the noise power σ_n^2 so that the normalized acquisition detector \bar{T}_1 follows a non-central Chi-square distribution with $2M_{T_1}$ degrees of freedom. The non-centrality parameter is given by (Eq A-4) for GPS L1C/A.

$$\lambda_0^{T_1} = \frac{P_J}{2\sigma_n^2} \sum_{k=1}^{M_{T_1}} \tilde{R}_{c_{D,J},c_D}^{L1}(0)^2 = \frac{2T_i}{\beta N_0} P_J M_{T_1} \tilde{R}_{c_{D,J},c_D}^{L1}(\varepsilon_{\tau,max})^2 = 2T_i \frac{C_J}{N_0} M_{T_1} K_J^{T_1} \quad (\text{Eq A-4})$$

$$K_J^{T_1} = \frac{\tilde{R}_{c_{D,J},c_D}^{L1}(\varepsilon_{\tau,max})^2}{\tilde{R}_{c_{D,J},c_D}^{L1}(0)^2} \quad C_J = \frac{P_J \tilde{R}_{c_{D,J},c_D}^{L1}(0)^2}{\beta}$$

Similarly, and assuming that the contribution of navigation bits and secondary codes are random, uncorrelated and with zero-mean, it can be shown that the normalized acquisition detector $\bar{T}_2 = T_2/\sigma_n^2$ follows a non-centered Chi-square distribution with $4M_{T_2}$ degrees of freedom and non-centrality parameter given by (Eq A-5).

$$\lambda_0^{T_2} = 2T_i \frac{C_J}{N_0} M_{T_2} K_J^{T_2}$$

$$K_J^{T_2} = \frac{(\tilde{R}_{c_{D,J},c_D}^X(\varepsilon_{\tau,max})^2 + \tilde{R}_{c_{P,J},c_D}^X(\varepsilon_{\tau,max})^2 + \tilde{R}_{c_{D,J},c_P}^X(\varepsilon_{\tau,max})^2 + \tilde{R}_{c_{P,J},c_P}^X(\varepsilon_{\tau,max})^2)}{\tilde{R}_{c_{D,J},c_D}^X(0)^2 + \tilde{R}_{c_{P,J},c_P}^X(0)^2} \quad (\text{Eq A-5})$$

$$C_J = \frac{P_J (\tilde{R}_{c_{D,J},c_D}^X(0)^2 + \tilde{R}_{c_{P,J},c_P}^X(0)^2)}{2\beta}$$

$K_J^{T_l}$, with $l \in \{1; 2\}$, is the cross-correlation between the interfering signal PRN code and the PRN code of the local replica. The cross-correlation level between two different PRN codes depends mainly on the length of one PRN code. Consistently with the values proposed in DO-235C [6], DO-292 [12] and [29], the values used in this appendix for $K_J^{T_1}$ and $K_J^{T_2}$ are recapped in Table A-1.

	GPS L1C/A	Galileo E1	GPS L5 / Galileo E5a
Cross-correlation $K_J^{T_l}$	-24 dB	-29.5 dB	-34 dB

Table A-1: Cross correlation RFI for acquisition

$\frac{C_J}{N_0}$ is set to 50 dB-Hz for all kinds of signal.

Alternative hypothesis H_1 :

Under alternative hypothesis H_1 , the searched signal is supposed to be present which means the pair of Doppler frequency and code delay of the cell being tested correspond to the Doppler frequency and code delay of the received signal. In this case, thanks to the correlation properties between PRN codes of the same satellite signal, it can be assumed $\tilde{R}_{c_{D,c_P}}^X(\varepsilon_{\tau}) \ll \tilde{R}_{c_{D,c_D}}^X(\varepsilon_{\tau})$ and $\tilde{R}_{c_{P,c_D}}^X(\varepsilon_{\tau}) \ll \tilde{R}_{c_{P,c_P}}^X(\varepsilon_{\tau})$.

Under hypothesis H_1 , the normalized acquisition detector \bar{T}_1 follows a non-centered Chi-square distribution with $2M_{T_1}$ degrees of freedom. In this case, the amplitude of other satellites signals at the correlator output area assumed to be much lower than the amplitude of the targeted signal and thus they are neglected. The non-centrality parameter is given in (Eq A-6).

$$\lambda_1^{T_1} = \sum_{k=1}^{M_{T_1}} \frac{P_{L1}}{2\sigma_n^2} \tilde{R}_{c_{D,c_D}}^{L1}(\varepsilon_{\tau})^2 \text{sinc}^2(\pi\varepsilon_f T_i) \quad (\text{Eq A-6})$$

In addition, ε_{τ} and ε_f can be considered as constant over the dwell time. Therefore, Equation (Eq A-6) can be reduced to (Eq A-7).

$$\lambda_1^{T_1} = 2M_{T_1} T_i \frac{C_{L1}}{N_0} \left(\frac{\tilde{R}_{c_D, c_D}^{L1}(\varepsilon_\tau)}{\tilde{R}_{c_D, c_D}^{L1}(0)} \right)^2 \text{sinc}^2(\pi \varepsilon_f T_i) \quad (\text{Eq A-7})$$

Likewise, the normalized acquisition detector \bar{T}_2 follows a Chi-square distribution with $4M_{T_2}$ degrees of freedom. The non-centrality parameter is given in (Eq A-8).

$$\lambda_1^{T_2} = 2M_{T_2} T_i \frac{C_X}{N_0} \frac{\tilde{R}_{c_D, c_D}^X(\varepsilon_\tau)^2 + \tilde{R}_{c_P, c_P}^X(\varepsilon_\tau)^2}{\tilde{R}_{c_D, c_D}^X(0)^2 + \tilde{R}_{c_P, c_P}^X(0)^2} \text{sinc}^2(\pi \varepsilon_f T_i) \quad (\text{Eq A-8})$$

Probability of detection:

Knowing the distribution of the acquisition detectors under hypothesis H_0 and H_1 , it is possible to compute the probability of detection, P_D , as a function of the GNSS signal C_X/N_0 , where X is the GNSS signal of interest. The probability of detection is calculated in two steps. First, the detection threshold is set to respect the false alarm probability target P_{fa} . Second, the probability of detection, which is the probability that the acquisition detector exceeds the threshold in presence of the GNSS signal, is computed.

- Step 1: The detection threshold $T_h^l, l \in \{1; 2\}$, is defined from the distribution of the acquisition detector T_l and on the probability of false alarm P_{fa} . $T_h^l, l \in \{1; 2\}$ is derived from fundamental equation (Eq A-9).

$$\mathbb{P}(T_l > T_h^l | H_0) = P_{fa} \quad (\text{Eq A-9})$$

It has been seen that under hypothesis H_0 , T_l/σ_n^2 follows a Chi-square distribution with $2lM_{T_l}$ degrees of freedom and non-centrality parameter $\lambda_0^{T_l}$. Therefore, the detection threshold can be mathematically expressed by (Eq A-10).

$$T_h = \sigma_n^2 F_{X_{2lM_{T_l}, \lambda_0^{T_l}}}^{-1} (1 - P_{fa}) \quad (\text{Eq A-10})$$

$F_{X_{K, \lambda}}^2$ is the cumulative density function of a Chi square distribution with K degrees of freedom and non-centrality parameter λ . As an important remark, the detection threshold does not depend on the characteristics of the searched GNSS signal, in particular its C/N_0 .

- Step 2: Under hypothesis H_1 , T_l/σ_n^2 follows a Chi-square distribution with $2lM_{T_l}$ degrees of freedom and non-centrality parameter $\lambda_1^{T_l}$. Note that $\lambda_1^{T_l}$ depends on the C/N_0 of the searched GNSS signal. In addition, $\lambda_1^{T_l}$ also depends on the synchronization errors ε_τ and ε_f . The probability of detection, considering ε_τ and ε_f at fixed values, is given by (Eq A-11).

$$P_d \left(\frac{C}{N_0}, \varepsilon_\tau, \varepsilon_f \right) = \mathbb{P}(T_l \geq T_h | H_1) = 1 - F_{X_{2lM_{T_l}, \lambda_1^{T_l}}} \left(\frac{T_h}{\sigma_n^2} \right) \quad (\text{Eq A-11})$$

Eventually, ε_τ and ε_f can be considered as random variables uniformly distributed over $\left[-\frac{\delta d}{2}; \frac{\delta d}{2}\right]$ and $\left[-\frac{\delta f}{2}; \frac{\delta f}{2}\right]$. The average probability of detection is given by (Eq A-12).

$$P_D \left(\frac{C}{N_0} \right) = \mathbb{E} \left(P_d \left(\frac{C}{N_0}, \varepsilon_\tau, \varepsilon_f \right) \right), \varepsilon_\tau \hookrightarrow \mathbf{u} \left(\left[-\frac{\delta d}{2}; \frac{\delta d}{2}\right] \right), \varepsilon_f \hookrightarrow \mathbf{u} \left(\left[-\frac{\delta f}{2}; \frac{\delta f}{2}\right] \right) \quad (\text{Eq A-12})$$

Acquisition threshold:

The acquisition threshold is the minimum C/N_0 value such that the average probability of detection $P_D\left(\frac{C}{N_0}\right)$ exceeds the probability of successful acquisition of a signal P_{acq} . Acquisition threshold is mathematically expressed by (Eq A-13).

$$Th_{acq} = \min\left(\frac{C}{N_0} \mid P_D\left(\frac{C}{N_0}\right) \geq P_{acq}\right) \quad (\text{Eq A-13})$$

A-1.1.2 Initial DFMC acquisition requirements

The objective of this section is to present and to analyze TTF requirements for DFMC receivers in order to propose some inputs needed to compute acquisition thresholds. DFMC TTF requirements are first introduced and discussed. Second, a DFMC acquisition strategy compliant with the requirements is described in order to propose additional inputs needed to the acquisition threshold derivation.

A-1.1.2.1 Presentation of DFMC TTF requirements

Three different DFMC TTF requirements are analyzed here.

DMS:306:

The equipment shall output a valid position within 5 minutes with a 95% probability of success after power application given the following conditions:

- Latitude and longitude initialized within 60 nautical miles;
- Time and date initialized within 1 minute;
- Valid GPS and GAL almanac data available and unobstructed satellite visibility;
- Under Normal Acquisition Interference Conditions;
- GPS and GAL signals from Minimum Signal Conditions to Maximum Signal Conditions;
- Valid ionospheric data available.

This requirement is very similar to the legacy TTF requirement, for which a valid position shall be output with 95% probability of success using GPS L1C/A signals only. The difference with legacy TTF requirement is the availability of Galileo signals.

DMS:199:

The equipment shall output a valid SBAS L5 augmented position within 15 minutes with a 95% probability of success after power application given the following conditions:

- Latitude and longitude initialized within 60 nautical miles;
- Time and date initialized within 1 minute;
- Valid GPS, GAL, and SBAS almanac data and unobstructed satellite visibility;
- Under Normal Acquisition Interference Conditions;
- GPS and GAL signals from Minimum Signal Conditions to Maximum Signal Conditions;
- At least one SBAS L5 signal (PRN code) at Minimum Signal Conditions, without the associated SBAS L1 signal (same PRN code), broadcasting messages augmenting GPS only.

DMS:210:

The equipment shall output a valid SBAS L5 augmented position within 15 minutes with a 95% probability of success after power application given the following conditions:

- Latitude and longitude initialized within 60 nautical miles;
- Time and date initialized within 1 minute;
- Valid GPS, GAL, and SBAS almanac data and unobstructed satellite visibility;
- Under Normal Acquisition Interference conditions;
- GPS and GAL signals from Minimum Signal Conditions to Maximum Signal conditions;
- At least one SBAS L5 signal (PRN code) at Minimum Signal Conditions, without the associated SBAS L1 signal (same PRN code), broadcasting messages augmenting Galileo only.

DMS:199 and DMS:210 are equivalent and request a DFMC navigation solution. The difference between these two requirements is the constellation augmented by the Satellite Based Augmentation System (SBAS). Indeed, in DMS:199, GPS signals are augmented by the SBAS, whereas Galileo signals are augmented by SBAS in DMS:210.

Conditions associated to the TTFB requirements can be interpreted as follows. First, the position and time are roughly known. This estimation of the time and position helps the positioning algorithm to output a more precise navigation position in a limited time, since it limits the number of Doppler bins in the estimation matrix. Second, almanacs are supposed to be known and an open sky configuration is considered. This condition is important. Indeed, it may help the acquisition process since signals can be acquired in a decreasing elevation order, or from the highest C/N_0 value to the lowest value. Third, normal acquisition interference conditions are defined in ED-259 [13]. As part of GNSS receiver testing, interferences are considered by injecting additional average white gaussian noise (AWGN) into the receiver. Therefore, the interference increases the noise floor term N_0 . The noise power spectral density is part of the acquisition threshold, so this condition does not impact the calculation of the acquisition threshold but rather the definition of the associated certification test. Fourth, GNSS signal are assumed to be from minimum to maximum signal conditions. Signal conditions are defined in ED-259 in term of minimum and maximum GNSS signal power at the antenna port. Similar to the previous condition, the GNSS signal power is part of the acquisition threshold, so this condition does not impact the calculation of noise condition but rather the certification test derivation. Fifth, DMS:306 supposes the knowledge of valid ionospheric data. This assumption is important to perform integrity monitoring with receiver autonomous integrity monitoring (RAIM) in order to ensure that the output position is valid. However, it does not impact the calculation of the acquisition threshold. Sixth and last, DMS:199 and DMS:210 precises the settings for SBAS satellite generation. More precisions are given in ED-259.

A-1.1.2.2 Acquisition strategy compliant with TTFB requirements

An acquisition strategy, compliant with requirements presented in section A-1.1.2.1, is presented here. From the strategy, some inputs to the acquisition threshold derivation are proposed. These inputs are:

- Allocated time to acquire each signal: At least four signals are needed to fulfill DMS:306, whereas at least nine signals are needed to fulfill DMS:199 (four GPS L1C/A signals, four GPS L5 signals, and one SBAS L5 signal) and DMS:210 (four Galileo E1 signals, four Galileo E5a signals, and one SBAS L5signal). The sum of the allocated times for each signal should not exceed the TTFB: 5 min for DMS:306, 15 min for DMS:210 and DMS:199.
- Probability of successful acquisition of each signal: The probability of successful acquisition of a given signal is the probability to detect the signal, knowing it is in view, within the allocated

time. Considering that the successive acquisitions are independent from each other, the probability of TTFF success is the product of the probability of successful acquisition of each targeted individual signal. According to the requirements, the probability of TTFF success must be higher than 0.95.

This section is divided in four paragraphs. First, for each pair of constellation and frequency band, a duration is allocated to compute a navigation solution. Second, calculation of a first fix for a given constellation and frequency is further analyzed in order to propose an allocated time to acquire each individual signal. Third, the probability of successful acquisition for individual GNSS signal is proposed. Fourth, a verification that the time to perform DFMC acquisition does not exceed the TTFF for each requirement is done.

A-1.1.2.2.1 Time allocation for each system

The proposed allocated time to perform a first fix for each pair of constellation and frequency band are summarized in Table A-2. Acquisition, tracking and demodulation of at least four signal of a given system must be performed during the associated allocated time. Note that at least 5 min are required to download the SBAS message. An extra 1 min is added to perform the acquisition of the SBAS signal.

	GPS		Galileo		SBAS acquisition and demodulation
Signal	L1C/A	L5	E1	E5	L5
Allocated time	5 min	5 min	6.5 min	5 min	6 min

Table A-2: Proposed allocated time to perform a first fix for each pair of constellation and frequency band

A-1.1.2.2.2 Time allocation for each signal

The calculation of a first fix for a given core constellation and frequency is performed in three steps.

- **Step 1:** A first GNSS signal is acquired. Once the first space vehicle (SV) is acquired, the receiver clock can be synchronized with the first acquired GNSS signal. Therefore, the receiver clock contribution to Doppler uncertainty is removed for the acquisition of subsequent satellites, leading to a smaller Doppler space search.
- **Step 2:** Subsequent signals are acquired.
- **Step 3:** Additional operations necessary to compute a first fix are performed. These operations include the launching of the tracking loops, the removal of false detection (a false detection consists in detecting a signal even though the searched GNSS signal is not present), demodulation of navigation message, and integrity monitoring to ensure the validity of the output position. This step allows to guarantee the validity of the first fix, thanks to the time allocation for integrity processing and signal demodulation.

For the different pairs of constellation/frequency bands, proposed allocated time for each step is indicated in Table A-3.

		Time allocated to 1 st SV acquisition (s)	Time allocated to each of the 2 nd , 3 rd and 4 th SV acquisition (s)	Time allocated to Step 3: Demodulation, integrity, verification, ... (s)	Total TTFF (min)
GPS	L1C/A	60	30	150*	5
	L5	60	30	150*	5
Galileo	E1	96	48	150*	6.5
	E5a	60	30	150*	5

Table A-3: Sharing of the allocated time between the different first fix computation steps

*150s allocated to demodulation, integrity and verification is set on DO-235C [6] and on DO-292 [12].

Note that in DMS:199 and DMS:210, the second systems computing a first fix may take advantage of the first fix computed by the first system; in other words, GPS may profit from the first fix obtained from Galileo and the other way around. This benefit is not considered in this paper. Instead, acquisition thresholds are computed so that each system can perform a standalone acquisition (under conditions detailed in the requirements).

A-1.1.2.2.3 Probability of successful acquisition of a single satellite signal

Assuming that the acquisition of each individual SV is independent from the other, the probability of succeed the initial acquisition is given by (Eq A-14).

$$P_{success} = \prod_{i=1}^{N_{acq}} P_{acq,i} \quad (\text{Eq A-14})$$

Where $P_{acq,i}$ is the probability of successfully acquiring SV i in the allocated time, and N_{acq} is the total number of SVs to be acquire in order to comply with TTFF requirements.

TTFF requirements impose $P_{success} = 0.95$. In addition, to fulfill DMS:306, $N_{acq} = 4$ SVs are needed, whereas $N_{acq} = 9$ SVs are needed to fulfill DMS:210 and DMS:199. The most constraining requirements in terms of probability of success are clearly DMS:199 and DMS:210. In this paper, it is proposed to set $P_{acq,i}$ to the same value for all satellites. Therefore, the probability to successfully acquire SV i is given by (Eq A-15) (with $N_{acq} = 9$).

$$P_{acq} = P_{acq,i} = (P_{success})^{\frac{1}{N_{acq}}} \quad (\text{Eq A-15})$$

In this article, P_{acq} is rounded up to 0.995.

A-1.1.2.2.4 Compliance with TTFF requirements

In this section, the compliance of the proposed time allocation with the TTFF requirements is investigated.

Compliance with DMS:306

In DMS:306, 5 Galileo and 5 GPS signals, on both the L1/E1 and L5/E5a frequency bands, are supposed to be available. Since 5 min are allocated to compute a first fix with GPS L1C/A signal, and since the probability of successful acquisition is $(P_{acq})^4 = 0.98 > 0.95$, then this requirement is fulfilled.

Compliance with DMS:199

To fulfill requirement DMS:199, the receiver must perform three operations: calculation of a first fix with GPS L1C/A signals, calculation of a first fix with GPS L5 and to acquire and demodulate SBAS signal in order to augment the GPS navigation solution. Clearly, from the time allocation presented in Table A-2, these three operations cannot be performed successively without exceeding the total acquisition time of DMS:199 (15 min).

Therefore, to be compliant with DMS:199, DFMC first fix operations can take place in that order.

- 1) Between t=0 s and t=5 min, the receiver computes a first fix with GPS L1C/A signals.
- 2) Between t=5 min and t=10 min, the receiver computes a first fix with GPS L5 signals.
- 3) In parallel of the previous action, the receiver acquires and demodulates SBAS signal between t=9 min and t=15 min.

Figure A-1 illustrates this dual frequency GPS acquisition process.

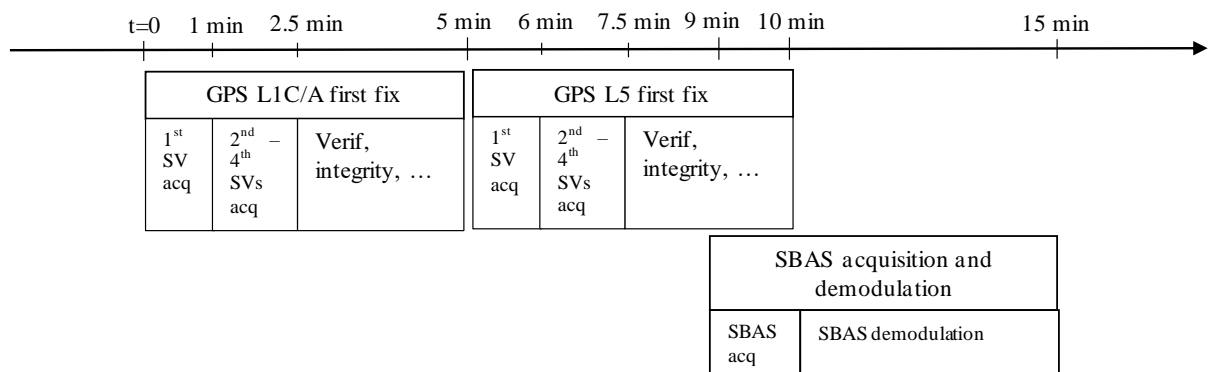


Figure A-1: GPS acquisition strategy compliant with DMS:199

The limiting resource when computing a first fix is the number of correlators. In this appendix, correlator is complex, meaning that one correlator output corresponds to a pair of in-phase and quadrature phase correlator outputs. The availability of a high number of correlators is necessary to perform acquisition of GNSS signals. Conversely, once a GNSS signal is acquired, only a few correlators are required to track the GNSS signal and to perform demodulation, verification, and integrity monitoring. From Figure A-1, even though the SBAS acquisition and demodulation step starts in parallel of GPS L5 first fix step, SBAS signal acquisition is initiated after that GPS L5 signals have been acquired. As a consequence, the acquisition strategy presented here should not be over-demanding in terms of number of correlators.

In addition, the probability to successfully meet TTFF requirement is $(P_{acq})^9 = 0.995^9 > 0.95$. Therefore, this DFMC acquisition strategy is compliant with DMS:199.

Compliance with DMS:210

To fulfill DMS:210, the receiver must perform three operations: calculation of a first fix with Galileo E1 signals, calculation of a first fix with Galileo E5a signal, and acquisition and demodulation of SBAS signal in order to augment Galileo navigation solution.

To be compliant with DMS:210, it is proposed that DFMC acquisition operations take place in that order:

- 1) Between $t=0$ s and $t=6.5$ min, the receiver computes a first fix with Galileo signals.
- 2) Between $t=6.5$ min and $t=11.5$ min, the receiver computes a first fix with Galileo E5a signals.
- 3) In parallel of the previous action, the receiver acquires and demodulates SBAS signal between $t=9$ min and $t=15$ min.

Figure A-2 illustrates this dual frequency Galileo acquisition process.

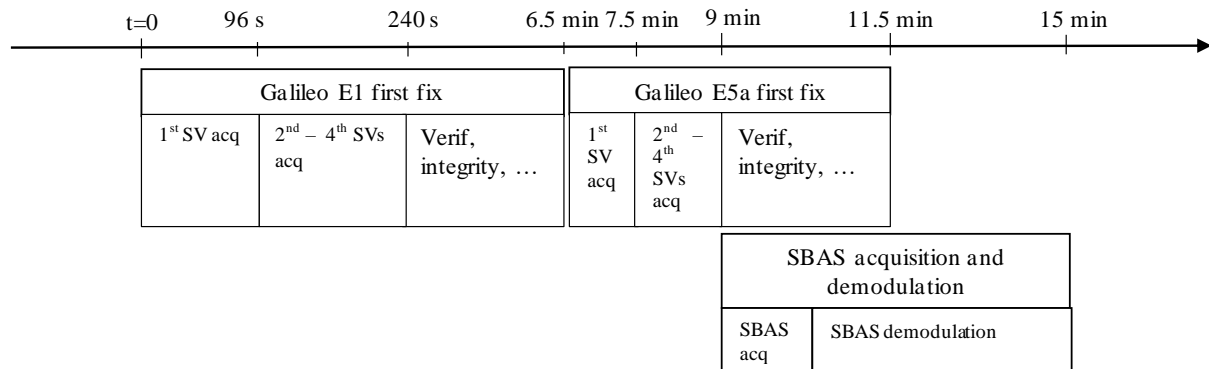


Figure A-2: Galileo acquisition strategy compliant with DMS:210

With this strategy, SBAS signal acquisition begins after Galileo E5a signals acquisition ends. Consequently, this strategy should not be over-demanding in terms of number of correlators as already argued for DMS:199 requirement.

In addition, the probability to successfully meet TFF requirement is $(P_{acq})^9 = 0.995^9 > 95\%$. Therefore, this DFMC acquisition strategy is compliant with DMS:210.

A-1.1.3 Numerical calculation of DFMC C/N_0 acquisition threshold

This sections numerically computes C/N_0 acquisition thresholds in accordance with DFMC initial acquisition requirements. It is divided in two parts. First, inputs needed to derive acquisition thresholds are identified and numerically evaluated. Second, C/N_0 acquisition thresholds are computed.

A-1.1.3.1 Inputs for C/N_0 acquisition thresholds

Settings that are necessary to derive acquisition thresholds value are identified and numerically evaluated below.

- Allocated time to acquire each satellite $T_{acq,i}$
 $T_{acq,i}$ with $i \in \llbracket 1; 4 \rrbracket$, is the allocated time to acquire the i^{th} SV, and is presented in Table A-3.
- Probability of successful acquisition of a signal P_{acq}
 P_{acq} is set to 0.995 for each GNSS signal, according to section A-1.1.2.2.3.
- Uncertainty on the Doppler frequency
 Considering uncertainties due to user dynamics, almanac, date and receiver clock drift, DO-292 [12] estimated the total uncertainty on velocity at 51 m/s for en-route operations and 300 m/s for ground acquisition, when no clock synchronization were assumed. These velocity uncertainties can be translated into frequency uncertainties summarized in Table A-4. Once

the first SV has been acquired, receiver clock can synchronize with the GNSS signal, so the frequency uncertainty significantly drops for the acquisition of subsequent SVs.

		En-route operations	On the ground operations
Doppler uncertainty on L1/E1 frequency band (Hz)	1 st SV acquisition	$F = \pm 268 \text{ Hz}$	$F = \pm 1500 \text{ Hz}$
	2 nd – 4 th SV acquisition	$F = \pm 150 \text{ Hz}$	$F = \pm 150 \text{ Hz}$
Doppler uncertainty on L5/E5a frequency band (Hz)	1 st SV acquisition	$F = \pm 200 \text{ Hz}$	$F = \pm 1200 \text{ Hz}$
	2 nd – 4 th SV acquisition	$F = \pm 120 \text{ Hz}$	$F = \pm 120 \text{ Hz}$

Table A-4: Doppler uncertainty for the different GNSS signals

In this appendix, to consider a worst case, on-ground frequency uncertainty value will be considered.

- Uncertainty on the GNSS signal code delay

The uncertainty on the code delay is linked with the length of the PRN code. GPS L1C/A codes is 1023 chips long, Galileo E1 PRN codes are 4092 chips long and GPS L5 and Galileo E5a codes are 10230 chips long. For GPS L1C/A and Galileo E1, the code delay must be searched browsing the whole PRN code length, for the first and subsequent SVs acquisition. Concerning GPS L5 and Galileo E5a, the whole PRN code must be browsed as well for first SV acquisition. However, after having acquired the first SV, code delay uncertainty may be decreased according to DO-292 [12] to 7570 chips. Table A-5 recaps the code delay uncertainty for the different GNSS signals to acquire.

		Code delay uncertainty
GPS L1C/A	1 st SV acquisition	$D = \pm 1023 \text{ chips}$
	2 nd – 4 th SV acquisition	$D = \pm 1023 \text{ chips}$
Galileo E1	1 st SV acquisition	$D = \pm 4092 \text{ chips}$
	2 nd – 4 th SV acquisition	$D = \pm 4092 \text{ chips}$
GPS L5/Galileo E5a	1 SV acquisition	$D = \pm 10230 \text{ chips}$
	2 nd – 4 th SV acquisition	$D = \pm 7570 \text{ chips}$

Table A-5: Code delay uncertainty for the different GNSS signals to acquire

- Number of cells in the acquisition matrix

The number of cells in the acquisition matrix can be mathematically expressed by (Eq A-16).

$$N_{tot} = L \times H$$

$$L = \left\lceil \frac{D}{\delta d} \right\rceil \quad H = \left\lceil \frac{F}{\delta f} \right\rceil \quad (\text{Eq A-16})$$

δd is the width of one code delay bin, and δf is the width of one frequency bin. $\lceil \cdot \rceil$ is the ceiling operator.

The settings for δd and δf depend on the maximum acceptable loss of GNSS signal power due to imperfect synchronization of the local replica with the GNSS received signal. Indeed, the maximum synchronization errors due code delay and frequency imperfect synchronization are respectively $\delta d/2$ and $\delta f/2$. The associated loss of GNSS signal power, respectively denoted

ΔC_d (loss of power due to imperfect code delay synchronization) and ΔC_f (loss of power due to imperfect frequency synchronization), are given in (Eq A-17).

$$\Delta C_d = \left(\frac{\bar{R}_x^Y\left(\frac{\delta d}{2}\right)}{\bar{R}_x^Y(0)} \right)^2 \quad \Delta C_f = \text{sinc}^2\left(\pi \frac{\delta f}{2} T_i\right) \quad (\text{Eq A-17})$$

Where T_i is the integration time. Acquisition is usually performed by coherent integrating (correlation duration) over one PRN sequence to avoid finding navigation and secondary code bit transition inside the integration. Therefore, in this thesis, $T_i = 1 \text{ ms}$ when acquiring GPS L1C/A, GPS L5 and Galileo E5a signals and $T_i = 4 \text{ ms}$ for Galileo E1 SV acquisition. In the literature [95] [29], δf is often set to $\frac{1}{2T_i}$, resulting in a maximum power loss because of frequency miss-synchronization $\Delta C_f = -0.9 \text{ dB}$. This setting is also adopted in this appendix.

The code delay is linked to the shape of the cross-correlation function. [10] sets the size of a code delay cell width, δ , to half a chip, so that the loss due to code delay miss-synchronization ΔC_d does not exceed -2.6 dB (for an infinite RFFE filter bandwidth).

Concerning Galileo E1 signal, Figure 2-8 shows that the slope of the correlation function is around three time higher than the slope of the GPS correlation function. Therefore, [29] proposes to divide by three the code delay cell width compared to the GPS case. Adopting this setting, $\delta d = \frac{1}{6} T_{chip}$, where T_{chip} is the chip period.

Table A-6 summarizes the number of cells in the acquisition matrix.

		Code delay uncertainty D	Code delay cell width δd	Number of code delay cells L	Frequency uncertainty F	Frequency cell width δf	Number of frequency cells H	Total number of cells N_{tot}
GPS L1C/A	1 st SV acquisition	1023 chips	$\frac{1}{2}$ chip	2046	3000 Hz	500 Hz	6	12276
	2 nd – 4 th SV acquisition	1023 chips	$\frac{1}{2}$ chip	2046	300 Hz	500 Hz	1	2046
Galileo E1	1 st SV acquisition	4092 chips	$\frac{1}{6}$ chip	24552	3000 Hz	125 Hz	24	589248
	2 nd – 4 th SV acquisition	4092 chips	$\frac{1}{6}$ chip	24552	300 Hz	125 Hz	3	73656
GPS L5 Galileo E5a	1 st SV acquisition	10230 chips	$\frac{1}{2}$ chip	20460	2400 Hz	500 Hz	5	102300
	2 nd – 4 th SV acquisition	7570 chips	$\frac{1}{2}$ chip	15140	240 Hz	500 Hz	1	15140

Table A-6: Size of the acquisition matrix for the different GNSS signals to acquire

Note the size of the acquisition matrix for the acquisition of the first Galileo E1 SV is much higher than for the other signals. This is mainly due to the lower frequency and code delay cell widths.

- Probability of false alarm P_{fa}

P_{fa} is the probability to detect a GNSS signal in a given cell when the signal is not there, either because the satellite is not in view or because the cell's Doppler and code delay values of the local replica do not correspond to the Doppler and code delay values of the received GNSS signal. The probability of false alarm is set in order to limit the number of false detections while browsing the whole acquisition matrix.

The probability of false alarm is set in DO-235B [10] to 10^{-3} . The mean value of false detections, browsing the entire acquisition matrix, is then $N_{tot}P_{fa}$. Note that for GPS L1C/A 1st SV acquisition, the average number of false detections is higher than 12. To have few false detections is not a problem since the verification process described in section A-1.1.2.2.2 aims to detect and remove the false detections. This false alarm value for GPS L1C/A is re-used in this appendix as an input for acquisition threshold calculation.

For GPS L5 and Galileo E5a, DO-292 proposes to set P_{fa} to 10^{-4} following a simple reasoning. Indeed, since there are 10 times more code delay cells in GPS L5/Galileo E5a acquisition matrix than in GPS L1C/A acquisition matrix and since the number of frequency cells is lower for GPS L5/Galileo E5a than for GPS L1C/A, to set P_{fa} to 10^{-4} does not increase the average number of false detections. This P_{fa} value is used for GPS L5/Galileo E5a acquisition.

A finer apportionment is done for Galileo E1. Indeed, P_{fa} is set so that the average number of false detections in Galileo E1 acquisition matrix is the same than in GPS L1C/A acquisition matrix. The probability of false detections, for 1st Galileo E1 SV acquisition and subsequent Galileo E1 SVs acquisition, is thus given by (Eq A-18).

$$P_{fa,1}^{E1} = \frac{N_{tot,1}^{L1}}{N_{tot,1}^{E1}} P_{fa}^{L1} \quad (Eq A-18)$$

$$P_{fa,1}^{E1} = \frac{N_{tot,2}^{L1}}{N_{tot,2}^{E1}} P_{fa}^{L1}$$

Where $N_{tot,i}^X$ is the number of cells in the acquisition matrix of the first ($i = 1$) or subsequent ($i = 2$) SV of system X . Values for $N_{tot,i}^X$ can be extracted from Table A-6: Size of the acquisition matrix for the different GNSS signals to acquire. P_{fa}^{L1} is the probability of false detection for GPS L1C/A acquisition. Probabilities of false detection are summarized in Table A-7.

		Probability of false detection P_{fa}
GPS L1C/A	1 st SV acquisition	10^{-3}
	2 nd – 4 th SV acquisition	10^{-3}
Galileo E1	1 st SV acquisition	$2.08 \cdot 10^{-5}$
	2 nd – 4 th SV acquisition	$2.78 \cdot 10^{-5}$
GPS L5/Galileo E5a	1 st SV acquisition	10^{-4}
	2 nd – 4 th SV acquisition	10^{-4}

Table A-7: Probabilities of false detection for the different signals to acquire

Because of the higher number of cells in Galileo E1 acquisition matrix compared to GPS L1C/A, P_{fa} must be lower for Galileo E1 to maintain the same average number of false detections when the whole acquisition matrix is browsed.

- Number of complex correlators N_{corr}

The number of correlators is a key parameter in the calculation of the acquisition thresholds. In this thesis, correlators are considered as complex, thus one correlator output refers to a pair of one in-phase and one quadrature phase correlator outputs. However, there is no requirement on that point. Thus, receiver manufacturers can decide the number of implemented correlators allocated to acquisition. Instead of speculating on the number of correlators used by the receiver, this appendix provides the acquisition threshold as a function of the number of correlators allocated to the acquisition process.

A-1.1.3.2 Numerical evaluation of C/N_0 acquisition thresholds

Figure A-3 , Figure A-4 and Figure A-5 represent the evolution of $P_D \left(\frac{C}{N_0} \right)$ as a function of C/N_0 for the different SVs to respectively acquire GPS L1C/A, Galileo E1 and GPS L5 / Galileo E5a signals, considering the inputs values presented in section A-1.1.3.1. Several numbers of correlators are considered. The RFFE bandwidth is set to 2 MHz for GPS L1C/A, to 12 MHz for Galileo E1, and to 20 MHz for GPS L5 and Galileo E5a.

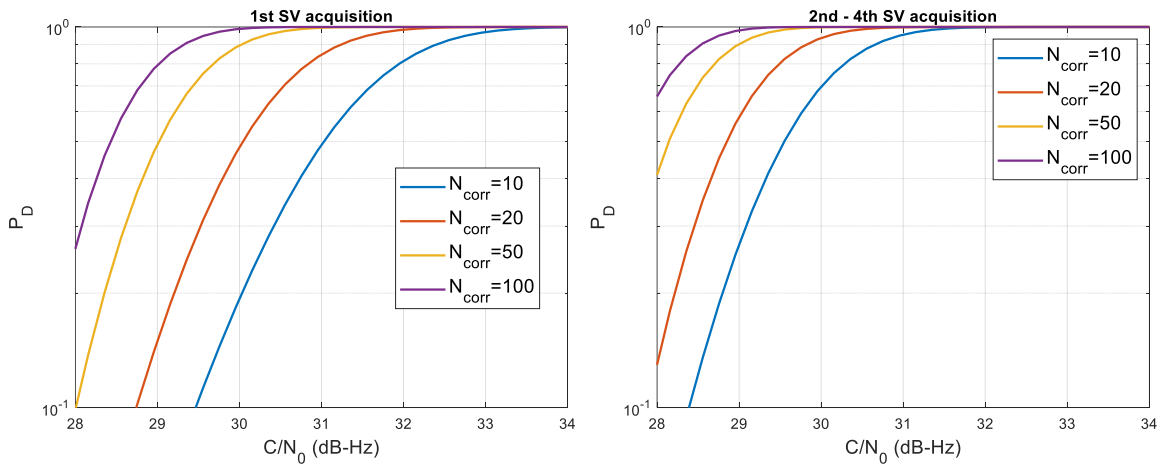


Figure A-3: Probability of detection for GPS L1C/A SVs

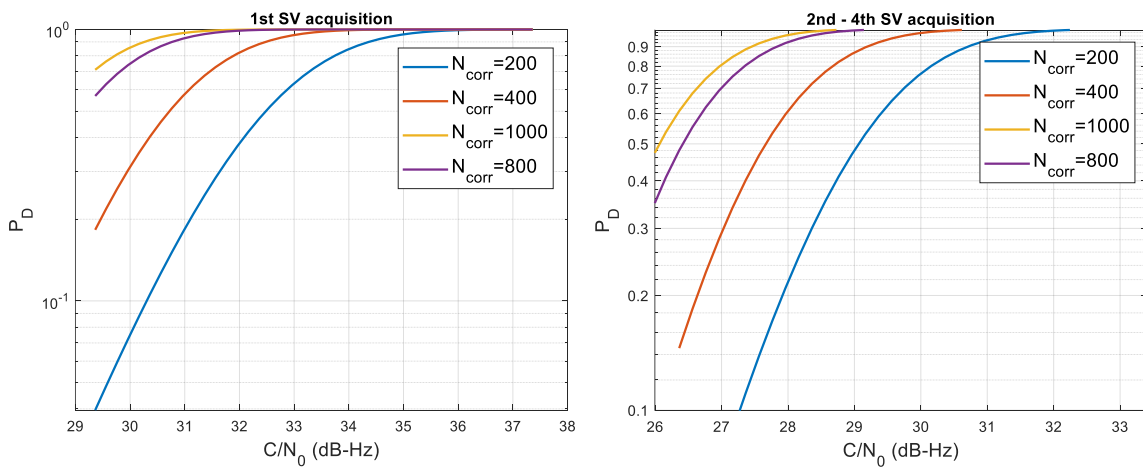


Figure A-4: Probability of detection for Galileo E1 SVs

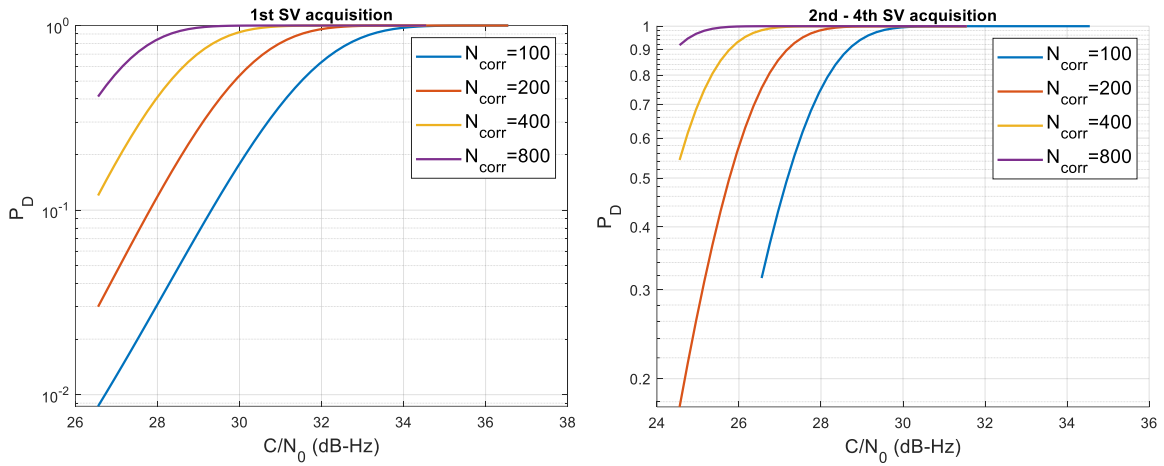


Figure A-5: Probability of detection for GPS L5 and Galileo E5a SVs

Eventually, Figure A-6 represents the acquisition thresholds for the different signals to be acquired as part of the first fix determination, as a function of the number of correlators allocated to the acquisition N_{corr} .

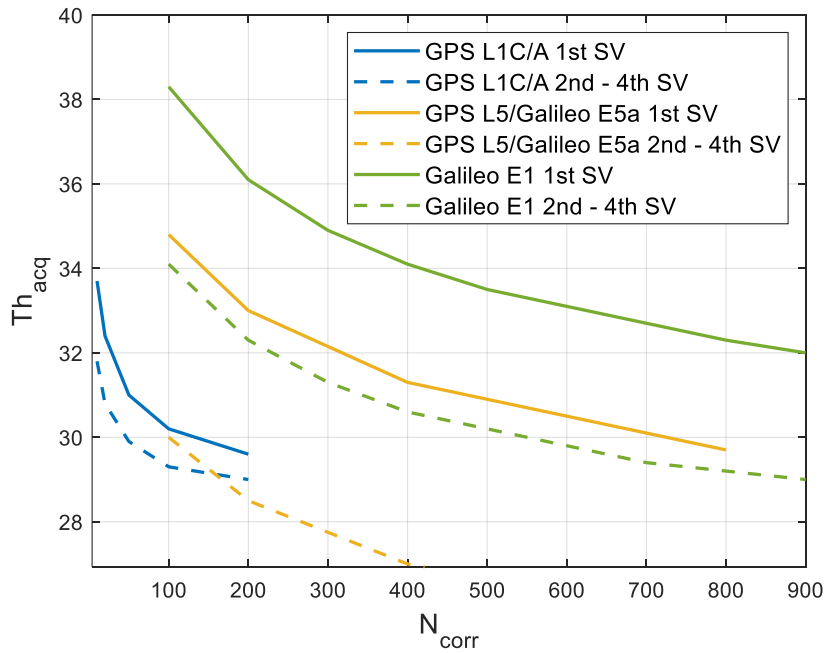


Figure A-6: Acquisition thresholds as a function of the number of correlators

The highest acquisition thresholds, for both the first SV acquisition and subsequent SVs acquisition, concerns Galileo E1 signal. This observation is mainly due to the high number of cells in the Galileo E1 acquisition matrix (see Table A-6).

Acquisition thresholds identified in certification documents DO-235C and DO-292 to assess the acquisition performance of GPS L1C/A, Galileo E1, GPS L5 and Galileo E5a are summarized in Table A-8.

	GPS L1C/A		Galileo E1		GPS L5/Galileo E5a	
	1 st SV acquisition	2 nd – 4 th SV acquisition	1 st SV acquisition	2 nd – 4 th SV acquisition	1 st SV acquisition	2 nd – 4 th SV acquisition
Number of correlators N_{corr}	20	10	400	400	200	200
Acquisition threshold Th_{acq}	32.4	31.7	34.1	30.6	33	28.5

Table A-8: Acquisition thresholds identified by standardization for DFMC equipment

The number of correlators is low for GPS L1C/A, as the analysis of GPS L1C/A acquisition thresholds has first been conducted for GPS L1C/A legacy receiver in late 90's. The capacity of these receiver in terms on correlator number was lower than the current receivers. In addition, as GPS L1C/A acquisition thresholds are quite favorable, there is no need to review this assumption on the number of correlators. Because of acquisition thresholds for Galileo E1, Galileo E5a and GPS L5 are much higher, there is a need to consider a higher number of correlators in standardization document in order to limit the acquisition threshold. However, the number of complex correlators is easily achievable by current GNSS receivers.

A-1.2 Legacy C/N_0 acquisition threshold

DO-229E [11] requests the legacy receiver to be able to output a first valid position in less than 5 min under the following assumptions:

- Latitude and longitude initialized within 60 nautical miles;
- Time and date within 1 minute;
- Valid almanac data and unobstructed satellite visibility

This requirement is very similar to DO-306 DFMC requirement, except that only the GPS L1C/A of are interest in this requirement. As a consequence, assuming the same time allocation than the one presented in Table A-3 to perform the three steps of GPS L1C/A first fix described in A-1.1.2.2.2, the legacy C/N_0 acquisition thresholds are identic than the ones computed for GPS L1C/A in Table A-8:

- $Th_{acq} = 32.4$ dBHz for first GPS L1C/A SV acquisition.
- $Th_{acq} = 31.7$ dBHz for subsequent GPS L1C/A SVs acquisition.

A-2 C/N_0 tracking and demodulation thresholds

This section provides C/N_0 tracking and demodulation thresholds for Galileo E1, GPS L1C/A and SBAS L1 signals.

DO-235C identified 4 tracking performance indicators which must be analyzed to compute the tracking and demodulation C/N_0 threshold:

- Pseudorange accuracy: The pseudo-range accuracy is characterized through the code delay estimation standard deviation. Note that code delay is assumed to be smoothed with carrier phase measurement. ICAO SARPs required a maximum pseudorange standard deviation of 70 cm for GPS L1C/A legacy measurement. It is reduced to 15 m for DFMC measurements.
- Phase lock loop tracking jitter: Phase measurement standard deviation must be limited to guarantee the lock of the PLL, and therefore the continuity of the GNSS service. A 15° maximum tracking jitter is assumed as a performance target for GPS L1C/A and SBAS L1, as this value approximately corresponds to the Costas loop lock threshold. Since Galileo E1

tracking is applied on the pilot component only, an objective of 30° is assumed for Galileo PLL standard deviation target.

- Demodulation word error rate: For each signal, the maximum word error rate is requested to be lower than 10^{-3} .
- Probability of cycle slip: Although not directly a requirement, the probability of cycle slip indicator must be investigated. Indeed, a too high probability of cycle slip would cause continuity problems. DO-235C considers a maximum probability of cycle slip of 10^{-5} as a performance target.

Table A-9 summarizes the different tracking and demodulation performance indicators, and the associated targeted value for the GPS L1C/A, SBAS L1 and Galileo E1 signals.

	Pseudorange standard deviation	PLL standard deviation	WER	Probability of cycle slip
GPS L1C/A (legacy)	70 cm	15°	10^{-3}	10^{-5}
GPS L1C/A (DFMC)	15 cm	15°	10^{-3}	10^{-5}
SBAS L1	-	15°	10^{-3}	10^{-5}
Galileo E1	15 cm	30°	10^{-3}	10^{-5}

Table A-9: Tracking and demodulation performance indicators, and associated targeted performance

The analysis of the different tracking and demodulation performance indicators identified in Table A-9 is detailed in DO-235C Appendix D. It is proposed to re-use thresholds of DO-235C Appendix D for the different indicators in this appendix. They are presented in Table A-10.

	Pseudorange standard deviation	PLL standard deviation	WER	Probability of cycle slip	Selected Tracking/Demodulation threshold
GPS L1C/A (legacy)	29.93	23.7	28	27.7	29.93
GPS L1C/A (DFMC)	29	23.7	28	27.7	29
SBAS L1	-	25.8	29.7	29	30
Galileo E1	29	19.9	28.5	25.5	29

Table A-10: Thresholds for the different tracking performance indicators, and selected tracking/demodulation C/N_0 thresholds (dB-Hz)

Appendix B: ICAO GNSS RFI mask

As presented in Chapter 4, GNSS RFI masks specify the maximum power from non-aeronautical RFI that can be tolerated by GNSS civil aviation receiver keeping minimum performance objectives (defined as 1-sigma range accuracy values in ICAO SARPs derived from tracking accuracy, but also assumed for acquisition and data demodulation in spectrum compatibility regulations) fulfilled. The objective of this appendix is to provide a mathematical justification to RFI masks. The interest of providing such a mathematical estimation of maximum tolerated power from non-aeronautical RFI sources by GNSS civil aviation receivers is to help in the interpretation of RFI mask, and to understand its limitation when it is used for deriving protection area during GNSS jamming exercises.

This appendix is divided in three sections. First, the general methodology to compute the maximum tolerable power from non-aeronautical sources by GNSS civil aviation receiver is presented. Second, this methodology is illustrated for the legacy civil aviation single frequency L1 C/A receiver RFI mask. Third, the methodology is applied for civil aviation DFMC receiver, in order to demonstrate that maximum tolerated power from non-aeronautical RFI sources by Galileo E1 receiver is higher than the DFMC RFI mask.

B-1 Maximum tolerated power from non-aeronautical sources

This section provides a general methodology to compute the maximum tolerated power from non-aeronautical RFI sources. This section is divided in two parts. First, the fundamental idea of the methodology is explained. Second, the methodology is fully detailed.

B-1.1 Fundamental idea of GNSS RFI mask

As defined in the introduction, RFI masks, strictly called interference thresholds in ICAO SARPs, provide the maximum power, C_{max} , that a non-aeronautical interference can have without preventing the aeronautical GNSS receiver from complying with performance objectives when inherently affected by aeronautical RFI. The nominal performance of an aeronautical GNSS receiver, and its capacity to meet minimum requirements, are here assumed to be characterized through an effective C/N_0 threshold: if a GNSS signal effective C/N_0 is above the C/N_0 threshold for a given receiver signal processing operation (acquisition, tracking, demodulation), then minimum requirements are assumed to be met. In this appendix, a RFI is thus characterized as an equivalent wideband noise as presented in Chapter 2 section 2-4.3. In other words, the presence of RFI makes the effective C/N_0 decrease, the capacity of the GNSS receiver to meet requirements is therefore degraded and the minimum requirements may not be fulfilled if the effective C/N_0 in presence of RFI is below the C/N_0 threshold.

The fundamental idea when computing the maximum non-aeronautical tolerable power consists in computing the minimum recovered effective C/N_0 in presence of aeronautical RFI and to compare it with the C/N_0 threshold for the different receiver operations (acquisition, tracking, demodulation). This C/N_0 link budget analysis should be performed at each point on Earth, since the RFI mask must be applicable worldwide. From the link budget analysis, the maximum equivalent noise level from non-aeronautical RFI sources that can be tolerated by the receiver is determined for each receiver signal processing operation op by finding the maximum equivalent noise level $I_{0,non\ aero,max}(op)$ dB W/Hz that can be added to the effective noise level in presence of aeronautical RFI $N_{0,eff,aero}$ such that recovered $C/N_{0,eff}$ remains above the considered receiver operation op C/N_0 threshold, where $N_{0,eff}$ is the effective noise in presence of both aeronautical and non-aeronautical RFI sources. Eventually, the non-aeronautical equivalent noise $I_{0,non\ aero,max}(op)$ level in dB W/Hz can be

translated into a power in dBW for any RFI from the knowledge of RFI central frequency and power spectral density. ICAO SARPs and RTCA SC159 GNSS RFI mask assumes that the non-aeronautical RFI power spectral density is rectangular.

B-1.2 Detail of the calculation of the maximum tolerable non-aeronautical RFI power

This section details the fundamental idea behind GNSS RFI mask presented in section B-1.1. The maximum tolerable non-aeronautical RFI power is deduced in two successive steps:

- Step 1: C/N_0 link budget analysis in presence of aeronautical RFI
- Step 2: Deduction of the maximum tolerable non-aeronautical RFI power

These two steps are detailed in this section.

B-1.3 Step 1: C/N_0 link budget analysis in presence of aeronautical RFI

The objective of this first step is to compute, for each pair of GNSS signal sig and GNSS receiver signal processing operations op , the maximum equivalent wideband noise $I_{0,non\ aero,max}(sig, op)$ level that can be allocated to non-aeronautical RFI such that the effective $C/N_{0,eff}$ remains above the C/N_0 threshold $Th(sig, op)$ for the considered receiver operation op . This objective is achieved computing a C/N_0 link budget for the different signals and receiver operations at the world position where the C/N_0 link budget margin above the threshold is the lowest. The different pairs of signal and receiver operations that are investigated in this appendix include:

- GPS L1C/A acquisition and tracking,
- Galileo E1 acquisition and tracking,
- SBAS L1 demodulation.

Presentation of C/N_0 link budget

The C/N_0 link budget table is very similar to the one presented in Chapter 4 section 4-2.1.1. The C/N_0 link budget table is reminded in Table B-1.

Line	Parameter	Value
1	Minimum received power of the total signal from the SV	dBW
2	Minimum antenna gain G_{min}	dB
3	Implementation losses	dB
4	Recovered satellite power C	(1)+(2)-(3)
5	Thermal noise PSD N_0	dBW/Hz
6	Total wideband equivalent continuous aeronautical RFI PSD level $I_{0,aero,WB}$	dBW/Hz
7	Effect of the receiver saturation: N_{Lim}, PDC_{Lim}	dB
8	Efficient noise PSD level $N_{0,eff,aero}$	dBW/Hz
9	Receive carrier to noise density ratio $C/N_{0,eff,aero}$	(4)-(18)
10	C/N_0 operation threshold of the total signal	
11	Margin	(9)-(10)
	Remaining I0tolerable $I_{0,non\ aero,max}(sig, op)$	dBW/Hz

Table B-1: C/N_0 link budget table for GNSS RFI mask elaboration

The difference between the C/N_0 link budget table used for RFI mask elaboration and the one used to compute protection areas is the way to compute G_{min} and $I_{0,aero,WB}$. Indeed, RFI mask should be applicable at any time and worldwide, so the C/N_0 link budgets inputs shall be time independent and associated with the world location for which the resulting $I_{0,non\ aero,max}(sig, op)$ is the lowest.

However, mathematical expressions of the different terms of Table B-1 are identical to the ones presented in Chapter 4 section 4-2.1.

Minimum receiver antenna gain G_{min}

In Chapter 4 section 4-2.1.2, the minimum antenna gain offered by the on-board GNSS receiver antenna in the direction of arrival of the useful GNSS satellite signal considered to compute protection area depends on the time. However, since RFI mask are not time dependent, the minimum antenna gain value used in Table B-1 must be a lower bound of the time varying $G_{min}(t)$.

ICAO SARPs request GNSS receivers to be able to track SVs whose elevation is 5° in nominal RFI environment with aeronautical interference and maximum tolerable non aeronautical interference. It is therefore proposed to re-use this assumption in tracking and demodulation link budgets. Minimum antenna gain value in tracking and demodulation C/N_0 link budgets would be derived from this 5° elevation angle, and would depend on the considered antenna (legacy or DFMC).

Regarding acquisition C/N_0 link budgets, minimum elevations of satellites to be acquired are slightly relaxed compared to the 5° elevation mask for the following reasons:

- Only 4 satellites are necessary for success of the initial acquisition process (DO-229 initial acquisition requirement).
- Since approximate position, time, and almanacs are known when performing initial acquisition according to initial acquisition requirements presented in Appendix A section A-1.1, the GNSS receiver would be able to try and acquire SVs with highest known elevation (and therefore highest antenna gain) first.

Therefore, minimum antenna gains for C/N_0 acquisition link budgets are computed as follows:

1. GPS and Galileo 24 SVs core constellations are run over one ground track period, and at each instant and each position in the worldwide grid, the elevation of highest SVs $E_i(lat, lon, t)$ is recovered (i is the rank of the SV).
2. For each position of the worldwide grid, the minimum elevation of highest SVs among all instants is recovered as in (Eq B-1).

$$E_i^{min}(lat, lon) = \min_t E_i(lat, lon, t) \quad (\text{Eq B-1})$$

3. To take into account Earth orbit drift from one orbit period to the following one, for each position in the world, the minimum elevation of highest SVs at the considered latitude and along all user longitudes is kept.

$$E_i^{mask}(lat) = \min_{lon} E_i^{min}(lat, lon) \quad (\text{Eq B-2})$$

4. Eventually, the minimum antenna gain $G_{min}(lat)$ for a position whose latitude is lat is deduced from the elevation $E_i^{mask}(lat)$ and the minimum receiver antenna pattern of Figure 2-18. In order to take into account the probability that one satellite is in unscheduled outage, it is considered that the highest GPS and Galileo SVs are unavailable.

Aeronautical equivalent noise

The second term which is time dependent in link budgets of Chapter 4 section 2.1.1 is the aeronautical equivalent wideband noise level, and more precisely the inter and intra system RFI equivalent noise level. The inter and intra system RFI equivalent noise level at an instant t and at position (lat, lon) is given by Chapter 4 (Eq 10) and is reminded in (Eq 4-11).

$$\begin{aligned}
I_{0,GNSS}(lat, lon, t) &= L_{imp,gnss} \sum_{system} I_{0,system}(lat, lon, t) \\
I_{0,system}(lat, lon, t) &= \sum_{SV \text{ visible}} G_{norm}(lat, lon, SV, t) G_{Rx}(lat, lon, SV, t) \sum_{sig} P(sig) SSC(sig, vict)
\end{aligned} \tag{Eq B-3}$$

As a reminder, $L_{imp,gnss}$ refers to implementation losses applied for incoming intra and inter system interfering signals and is set to 0 dB. G_{norm} is the normalized received power and is given in Figure 4-4 for the different systems. G_{Rx} is the average receiver antenna gain given in Figure 4-5. sig corresponds to the different signals transmitted by the considered GNSS system. $P(sig)$ is the maximum received power of interfering signal sig , and $SSC(sig, vict)$ is the spectral separation coefficient between interfering signal sig and victim receiver $vict$.

For SBAS systems, $I_{0,system}(lat, lon, t)$ does not depend on the time t since SBAS satellites are geostationary. For SBAS systems, $I_{0,system}$ is therefore given by (Eq B-4).

$$\begin{aligned}
I_{0,SBAS}(lat, lon) &= G_{agg}^{SBAS}(lat, lon) \sum_{sig} P(sig) SSC(sig, vict) \\
G_{agg}^{SBAS}(lat, lon) &= \sum_{SBAS \text{ SVs visible}} G_{norm}(lat, lon, SV) G_{Rx}(lat, lon, SV)
\end{aligned} \tag{Eq B-4}$$

Conversely, for MEO constellations, $I_{0,system}(lat, lon, t)$ depends on t and must therefore be upper bounded for GNSS masks elaboration. $I_{0,system}(lat, lon, t)$ for a MEO system MEO is upper bounded as follows:

1. MEO constellations are run over one orbit period. At each instant and for each position in the world grid, the aggregate gain is computed with (Eq B-5).

$$G_{agg,MEO}(lat, lon, t) = \sum_{MEO \text{ SVs visible}} G_{norm}(lat, lon, SV, t) G_{Rx}(lat, lon, SV, t) \tag{Eq B-5}$$

2. Then the maximum aggregate gain along time and across all longitudes to cover Earth orbit drift is deduced with (Eq B-6).

$$G_{agg,MEO}^{max}(lat) = \max_{t,lon} G_{agg,MEO}(lat, lon, t) \tag{Eq B-6}$$

3. The upper bound of $I_{0,system}(lat, lon, t)$ is deduced with (Eq B-7) for MEO systems.

$$I_{0,MEO}(lat) = G_{agg,MEO}^{max}(lat) \sum_{sig} P(sig) SSC(sig, vict) \tag{Eq B-7}$$

Eventually, the upper bound of inter and intra system RFI equivalent noise level which is considered as part of GNSS RFI mask elaboration is given by (Eq B-8).

$$I_{0,GNSS}^{mask}(lat, lon) = L_{imp,gnss} \left(\sum_{SBAS \text{ system}} I_{0,SBAS}(lat, lon) + \sum_{MEO \text{ system}} I_{0,MEO}(lat) \right) \tag{Eq B-8}$$

Since the other aeronautical RFI equivalent noise components (AMSS, case emission) are assumed to be constant, then the total aeronautical equivalent noise to be inserted in Table B-1 for RFI masks elaboration is given by (Eq B-9).

$$I_{0,aero,WB}(lat, lon) = I_{0,case \text{ em}} + I_{0,AMSS} + I_{0,GNSS}^{mask}(lat, lon) \tag{Eq B-9}$$

Summary

This section described C/N_0 link budget considered when elaborating GNSS RFI masks. Some inputs of C/N_0 link budgets vary in time and must therefore be bounded. These inputs are the receiver minimum antenna gain and inter and intra system RFI equivalent noise. Other inputs of the C/N_0 link budgets are identical to the ones presented in Chapter 4 section 4-2.1.

To identify the maximum tolerable non-aeronautical equivalent wideband noise level, the C/N_0 link budgets must be computed at every position in the world, for all the considered pairs of signal and receiver signal processing operation. For a given pair of signal and receiver signal processing operation, $I_{0,non\ aero,max}(sig, op)$ is computed at the position where the link budget margin is the lowest. The minimum value of $I_{0,non\ aero,max}(sig, op)$ among all receiver operations op , denoted $I_{0,non\ aero,max}^{mask}(sig)$, is eventually the main input to derive the maximum power from non-aeronautical RFI sources that can be tolerated by GNSS receiver processing signal sig .

B-1.4 Step 2: Maximum tolerable non-aeronautical RFI power

Step 1 derives the maximum non-aeronautical RFI equivalent noise $I_{0,non\ aero,max}^{mask}(sig)$ that can be tolerated by a receiver processing signal sig . The objective of step 2 is then to convert this equivalent wideband noise level in dBW/Hz into a power level in dBW.

Mathematical derivation of maximum tolerable power from non-aeronautical RFI

The maximum tolerable power $C_{max}(sig, RFI)$ from a non-aeronautical RFI source tolerated by a receiver processing signal sig is given by (Eq B-10).

$$C_{max}(sig, RFI) = \frac{1}{SSC(RFI, sig)} I_{0,non\ aero,max}^{mask}(sig) \quad (\text{Eq B-10})$$

$SSC(RFI, sig)$ is the spectral separation coefficient between the considered non-aeronautical RFI and the victim GNSS receiver local replica processing signal sig .

Thus, $C_{max}(sig, RFI)$ depends on the considered RFI characteristics. The non-aeronautical RFI which is taken into account as part of GNSS RFI mask elaboration has a rectangular power spectral density, with double sided bandwidth denoted BW and central frequency offset with respect to L1 denoted Δf . Under these assumptions, $SSC(RFI, sig)$ can be simplified by (Eq B-11).

$$\begin{aligned} SSC(RFI, sig) &= SSC(BW, \Delta f, sig) \\ &= \frac{1}{BW} \int_{\Delta f - BW/2}^{\Delta f + BW/2} |H_{RF+ant}(f)|^2 (S_{sig}(f) * |H_{ID}(f)|^2) df \\ & \quad |H_{ID}(f)|^2 = T_i \text{sinc}^2(\pi f T_i) \end{aligned} \quad (\text{Eq B-11})$$

S_{sig} is the normalized power spectral density of the local replica used for signal sig processing, and H_{ID} is the integrate and dump filter transfer function. H_{RF+ant} is the equivalent RFFE plus antenna frequency rejection transfer function at baseband. Its bandwidth is denoted B_{RF} . T_i is the integration time.

T_i has a strong impact on the spectral separation coefficient. Indeed, the integrate and dump filter transfer function depends on the integration time. The longer the integration time is, the narrower the integrate and dump filter bandwidth is. Figure B-1 illustrates the impact of the integration time on the locally generated GNSS signal replica power spectral density at the correlator output, plotting $S_{sig}(f) * |H_{ID}(f)|^2$ for two different integration times: 1 ms and 20 ms. The victim signal which is processed is GPS L1C/A PRN 1.

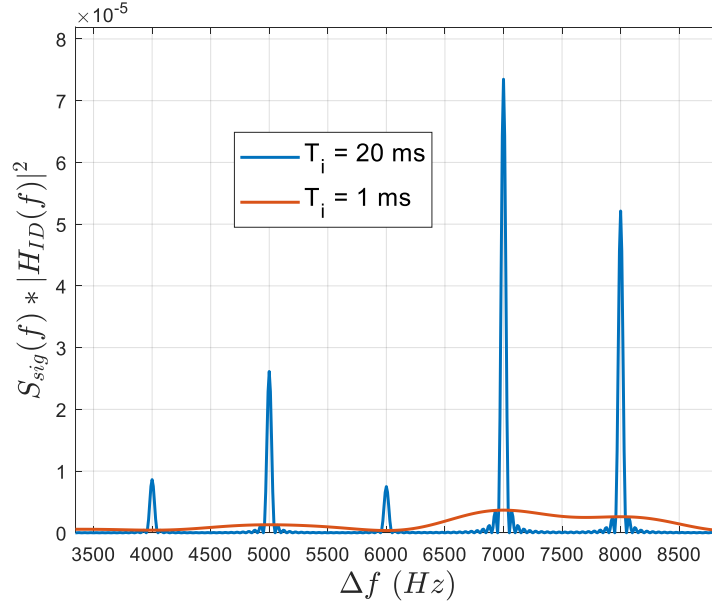


Figure B-1: Power spectral density of the victim GPS L1C/A PRN 1 local replica after filtering by the integrate and dump filter

Since PRN code is periodic, the local GNSS replica power spectral density is discrete. Each line of the local GNSS code is then filtered by the integrate and dump filter, whose transfer function has a sinc shape. The width of the main lobe is inversely proportional to the integration duration T_i . As a result, the spectrum of the local GNSS replica is more spread when the integration time is short. Therefore, a narrow bandwidth interference is expected to impact more basic signal processing operations which implement longer integration time such as tracking.

Link between $C_{max}(sig, RFI)$ and RFI masks

RFI masks is a tool mostly used for GNSS spectrum compatibility. It should provide a lower bound of $C_{max}(sig)$ for the different signals to be processed by the GNSS receiver.

In band RFI mask provides the maximum allowable power from a non-aeronautical RFI whose central frequency is within the L1 frequency band (1559-1610 MHz ARNS band) as a function of the RFI bandwidth BW . The in-band maximum tolerable power from non-aeronautical RFI $C_{max}^{in\ band}(BW)$ is defined by (Eq B-12).

$$C_{max}^{in\ band}(BW) = \min_{sig, L1+\Delta f \in [1559;1610]MHz} C_{max}(sig, RFI(BW, \Delta f)) \quad (\text{Eq B-12})$$

sig refers to the different PRN signals of interest. The in-band RFI mask should therefore be a lower-bound of $C_{max}^{in\ band}(BW)$.

Out-of-band RFI mask provides the maximum allowable power to a non-aeronautical CW RFI whose bandwidth is 700 Hz as a function of the RFI central frequency. The maximum power of a non-aeronautical RFI whose bandwidth is 700 Hz that can be tolerated by the receiver is defined by (Eq B-13).

$$C_{max}^{out\ of\ band}(\Delta f) = \min_{sig} C_{max}(sig, RFI(BW = 700\ Hz, \Delta f)) \quad (\text{Eq B-13})$$

sig refers to the different PRN signals of interest. The out-of-band RFI mask should therefore be a lower-bound of $C_{max}^{out\ of\ band}(\Delta f)$.

RFI masks are illustrated in Figure 4-1.

B-2 Legacy RFI mask

This section illustrates the elaboration of RFI mask for legacy civil aviation single frequency GPS L1 C/A receiver. It first provides C/N_0 link budget analysis computed in 1996 at locations leading to low C/N_0 link budget margins. Second, it derives the maximum tolerable power from non-aeronautical RFI $C_{max}(sig, RFI)$ as a function of the RFI bandwidth BW and compares it with the legacy in-band RFI mask. Third, it derives the maximum tolerable power from non-aeronautical RFI $C_{max}(sig, RFI)$ as a function of the RFI central frequency and compares it with the legacy out-of-band RFI mask.

B-2.1 Legacy C/N_0 link budgets

The RFI mask was originally elaborated in 1996 to protect GPS legacy receiver, since other GNSS were not operational yet. Thus, when the legacy RFI mask has been derived, only a few GNSS systems were considered. In particular, Beidou contribution to $I_{0,GNSS}$ was not considered. Thus, based on critical satellite analysis, DO-235B provides inter-intra system interference level on a GPS legacy receiver at different critical positions which are summarized in Table B-2. Table B-2 also summarized other aeronautical RFI equivalent noise components which have been considered when elaborating legacy RFI mask. Even though the inter/intra system RFI equivalent noise are not up to date in Table B-2 since other inter and intra system RFI components should be considered currently, these values have been originally used for the derivation of the L1 legacy RFI mask of DO-229 and ICAO SARPs. For comparison purpose, the same aeronautical RFI equivalent noise values are considered in this section.

	GPS			SBAS
	1 st SV acquisition	Subsequent SVs acquisition	Tracking	Demodulation
Location	5°S, 150°E	5°S, 150°E	Honolulu (HNL)	Barrow, Alaska (BRW)
$I_{0,GPS}$	-205.68	-205.68	-204.64	-205.62
$I_{0,Galileo}$	-213.3	-213.3	-213.3	-213.3
$I_{0,SBAS}$	-214.54	-214.54	-211.57	-214.93
$I_{0,QZSS}$	-209.19	-209.19	-210.91	-
Total $I_{0,GNSS}^{mask}$	-203.25	-203.25	-202.67	-204.52
$I_{0,AMSS}$	-215.94	-215.94	-	-
$I_{0,case\ em}$	-209.77	-209.77	-209.77	-209.77
Total $I_{0,aero,WB}$	-202.19	-202.19	-201.89	-203.39

Table B-2: Aeronautical RFI equivalent noise components for legacy link budgets

Some remarks can be done on the values used in Table B-2:

- DO-235B indicates that Galileo equivalent noise used in all link budgets is the global maximum value. However, $I_{0,Galileo}$ seems to be very low compared to the Galileo equivalent noise computed with current constellation.
- In DO-235B, AMSS is supposed to be turned off during approach flight phases. Since DO-235B establishes GPS tracking and SBAS demodulation during approach phases, no contribution of AMSS is considered for that link budgets.
- In DO-235B, $I_{0,case\ em}$ is computed considering 10 cockpit screen devices, but this has been updated for DO23C to include 2 additional devices.

C/N_0 link budgets are presented in Table B-3, with the aeronautical components' inputs from Table B-2.

Parameter (Units)	GPS			SBAS
	1st SV acquisition	4th SV acquisition	Tracking	Demodulation
Min. SV Earth Surface Power (dBW)	-158,50	-158,50	-158,50	-158,50
Receive Antenna Gain (dBic)	-0,72	-1,30	-5,50	-4,45
Implementation Loss (dB)	2,50	2,50	2,50	2,50
RFI-free Post-Corr Carrier Pwr (dBW)	-161,72	-162,30	-166,50	-165,45
IOaero (dBW/Hz)	-202,19	-202,19	-201,89	-203,39
Nlim	1,00	1,00	1,00	1,00
PDC	0,01	0,01	0,01	0,01
$N_{0,EFF}$ dBW/Hz	-198,75	-198,75	-198,62	-199,26
Effective C/N0eff (dB-Hz)	37,03	36,45	32,12	33,81
C/N0 threshold (dB-Hz)	32,40	31,70	29,93	30,00
Link Margin (dB)	4,63	4,75	2,19	3,81
Remaining I0tolerable (dBW/Hz)	-195,99	-195,81	-200,50	-197,83

Table B-3: C/N₀ link budgets at critical locations for legacy RFI mask elaboration

Receiver antenna gain used in acquisition link budgets of Table B-3 are taken from DO-235B and correspond to the minimum observed elevations of highest and fourth highest GPS satellites at the position 5°S, 150°E where IGNSS is the largest. Implementation losses for legacy receivers has been computed in Table 4-4.

The limiting C/N₀ link budget is the tracking one. The maximum equivalent noise from a non-aeronautical source which can be tolerated by a legacy receiver is $I_{0,non\ aero,max}^{mask}(sig) = -200.5\ dBW/Hz$. This value is the main input when deriving $C_{max}(sig, RFI)$.

B-2.2 Legacy in-band RFI mask

This section derives $C_{max}^{in\ band}$ as a function of the non-aeronautical RFI bandwidth BW and compares it with the in-band legacy RFI mask. Since the limiting link budget for legacy receiver corresponds to the tracking operation, $C_{max}^{in\ band}(BW)$ is computed considering a 20 ms integration time. Figure B-2 illustrates $C_{max}^{in\ band}(BW)$ for legacy receivers as well as the in-band RFI mask. Note that since the RFI central frequency is within the GNSS frequency band, the RFFE filter does not impact the RFI power spectral density.

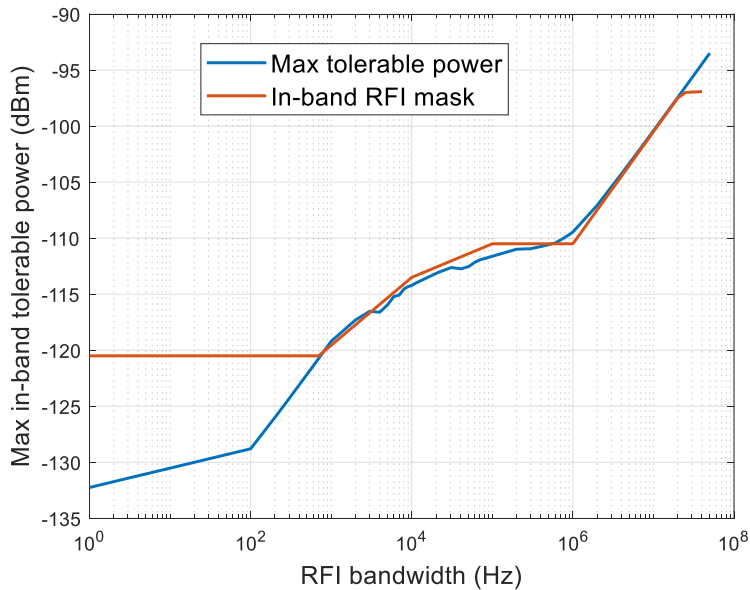


Figure B-2: Maximum in-band non-aeronautical RFI tolerable power $C_{max}^{in\ band}$ for legacy receiver and in-band legacy RFI mask

As developed in section B-1.4, since the limiting case for GPS L1C/A signal is a tracking scenario (20 ms integration time), narrowband interferences have a strong impact on the signal processing. However, it is very unlikely that a narrowband interference stays frequency synchronized with the GNSS local signal for a long time period. This is the reason explaining that the mask is clipped at value for RFI of 700 Hz and not lowered for RFI value lower than 700 Hz.

The maximum non aeronautical interference power for GPS L1C/A receivers (legacy and DFMC) is also below the mask for interference bandwidth in the [30 kHz; 500 kHz] interval. That means that the RFI mask does not prevent from a potential loss of continuity in GPS L1C/A signal processing. That can be explained by the fact that RFI mask has originally been built for legacy receiver certification testing procedures. However, the in-band testing procedures for legacy are conducted considering a single PRN code (GPS L1C/A PRN 6) according to DO-229, whose central frequency offset with respect to L1 is set to 3 kHz. As a consequence, in-band RFI mask may be inappropriate to resolve spectrum compatibility matters.

B-2.3 Legacy out-of-band RFI mask

This section derives $C_{max}^{out\ of\ band}(\Delta f)$ from (Eq B-13) and compares it to the out-of-band legacy RFI mask. Since the limiting link budget for legacy receiver corresponds to the tracking operation, $C_{max}^{out\ of\ band}(\Delta f)$ is computed considering a 20 ms integration time. In addition, the RFFE plus antenna frequency rejection equivalent filter impacts any RFI which is out-of-band. The legacy antenna minimum frequency rejection is defined in DO-301 and illustrated in Figure 2-18. However, there is no requirement on the minimum RF/IF RFFE rejection of GPS L1C/A legacy receiver. Thus, it is proposed to estimate the minimum front-end RF/IF frequency rejection so that the maximum non-aeronautical tolerated power for the legacy GPS L1C/A receiver $C_{max}^{out\ of\ band}(BW)$ fits as well as possible with the legacy out-of-band interference mask. Figure B-3 shows the minimum front-end filter which is estimated. This filter serves as a reference in this appendix.

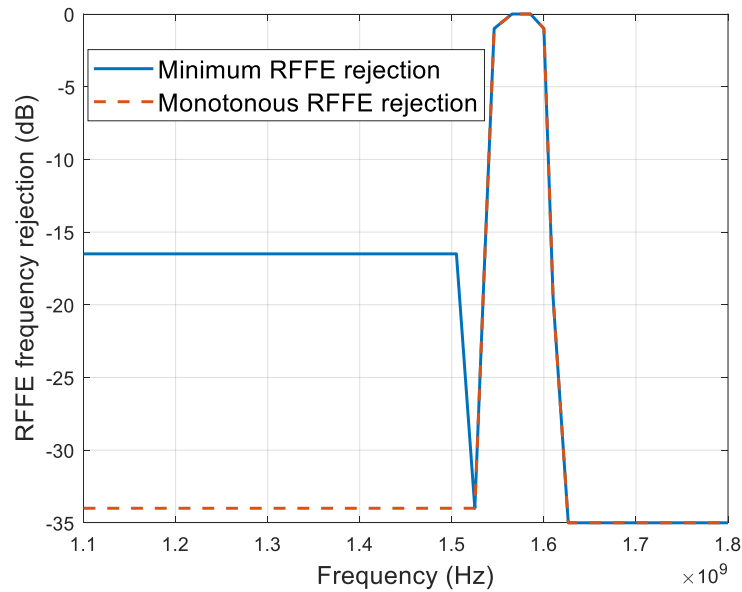


Figure B-3: Minimum and monotonous RFFE rejection for GPS L1C/A legacy receivers

The blue curve in Figure B-3 represents the minimum RF/IF frequency rejection that must be brought by the RFFE stage so that $C_{max}^{out\ of\ band}(\Delta f)$ remains above the out-of-band legacy RFI mask. The corresponding filter is referred to as minimum RF/IF filter in this appendix. Note that the transfer function of the minimum RF/IF RFFE filter is not monotonous on the left hand side. As a result, it is proposed to clip the rejection of the front-end module to 34 dB for frequency below 1525 MHz (orange dash curve) so that the filter is more realistic. On the right-hand side, the rejection reaches 35 dB at 1626.5MHz. This filter is called reference filter in this thesis. For both the minimum and reference filters, the rejection does not decrease more than 1.95 dB/MHz. This slope seems easily achievable.

Eventually, the maximum power of a 700 Hz CW RFI $C_{max}^{out\ of\ band}$ tolerated by a GPS L1C/A legacy receiver is shown in Figure B-4 as a function of the RFI central frequency, considering the minimum and reference RFFE filter frequency rejection. A 20 ms integration time is used since the limiting function of the GPS L1C/A legacy receiver is tracking.

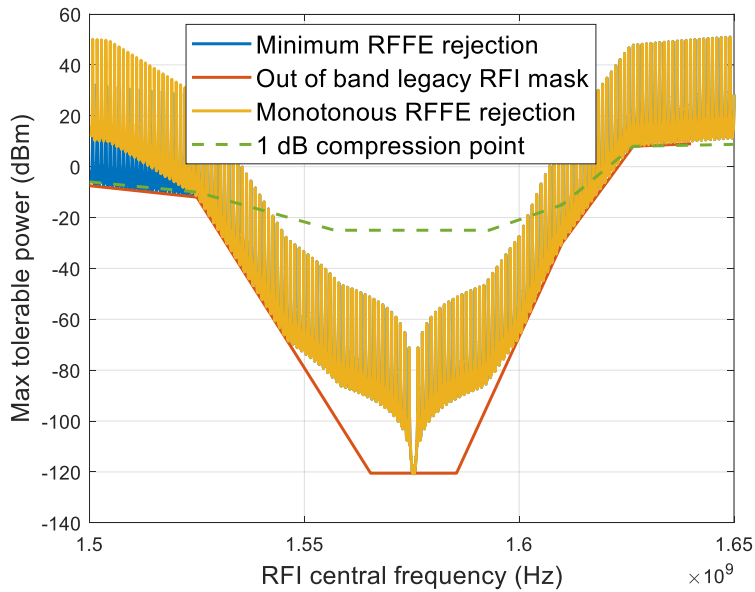


Figure B-4: Maximum out-of-band non-aeronautical RFI tolerable power $C_{max}^{out\ of\ band}(\Delta f)$ for legacy receiver and out-of-band RFI mask

The maximum tolerable power presents some peaks, regularly spaced every 1 MHz. These peaks correspond to frequencies for which the local code power spectral density is low (remember that the local replica power spectral density has a sinc square shape, with zeros every multiple of the chipping rate). The maximum tolerable interference power computed with the minimum RF/IF front-end filter is just above the legacy interference mask. The reference RF/IF front-end filter brings additional rejection if the interference central frequency is below 1525 MHz, thus the maximum tolerable power is increased below 1525 MHz. In the upper frequency band, the interference mask is limited by the 1 dB compression point of the antenna, whereas for other frequencies, the GNSS signal processing is more constraining than the saturation of the analog to digital converter.

B-3 DFMC RFI masks

This section derives the maximum in band and out-of-band RFI power $C_{max}^{in\ band}$ and $C_{max}^{out\ of\ band}$ that can be tolerated by DFMC receivers processing GPS L1C/A, SBAS L1 and Galileo E1. The consideration of GPS L5, Galileo E5a and SBAS L5 signals is out of the scope of this thesis. This section is split in three parts. First, inputs of the C/N_0 link budget which are different from the ones considered in Chapter 4 section 4-2.1 are detailed and $I_{0,non\ aero,max}(sig, op)$ is computed at each position in the world for the different considered pairs of signal and receiver signal processing operations. Then for each signal sig , $I_{0,non\ aero,max}^{mask}(sig)$ is derived. Second, maximum in-band RFI power $C_{max}^{in\ band}(BW)$ which can be tolerated by DFMC receiver is computed and compared to the in-band DFMC RFI mask. Third, maximum out-of-band RFI power $C_{max}^{out\ of\ band}(\Delta f)$ which can be tolerated by DFMC receiver is computed and compared to the out-of-band DFMC RFI mask.

B-3.1 DFMC C/N_0 link budgets

This section derives C/N_0 link budgets which are used when elaborating DFMC RFI masks. In this section, C/N_0 link budget inputs which are different than those considered in Chapter 4 section 4-2.1 are detailed. These inputs which are different include:

- The minimum receiver antenna gain.
- The inter and intra system RFI equivalent noise.

C/N_0 link budgets are then computed at any point in the world in order to determine the maximum tolerable non-aeronautical RFI equivalent noise $I_{0,non\ aero,max}^{mask}(sig)$ level that can be tolerated by DFMC GNSS receiver module processing signal sig .

Inter and intra system RFI equivalent noise

This section describes maximum inter and intra system RFI equivalent noise level faced by DFMC receiver as a function of its location. It is derived according to the methodology presented in section B-1.3. Conversely to legacy receiver analysis of section B-2.1, all current GNSS systems contributions to $I_{0,GNSS}^{mask}$ are here taken into account.

Figure B-5 illustrates the inter and intra system RFI equivalent noise computed with (Eq B-8) and the method described in section B-1.3, when the victim receiver local replica is either BPSK modulated (for GPS L1C/A and SBAS L1 DFMC receiver module) or BOC(1,1) modulated (for Galileo E1 DFMC GNSS receiver module). A 12 MHz double-sided DFMC GNSS receiver is considered.

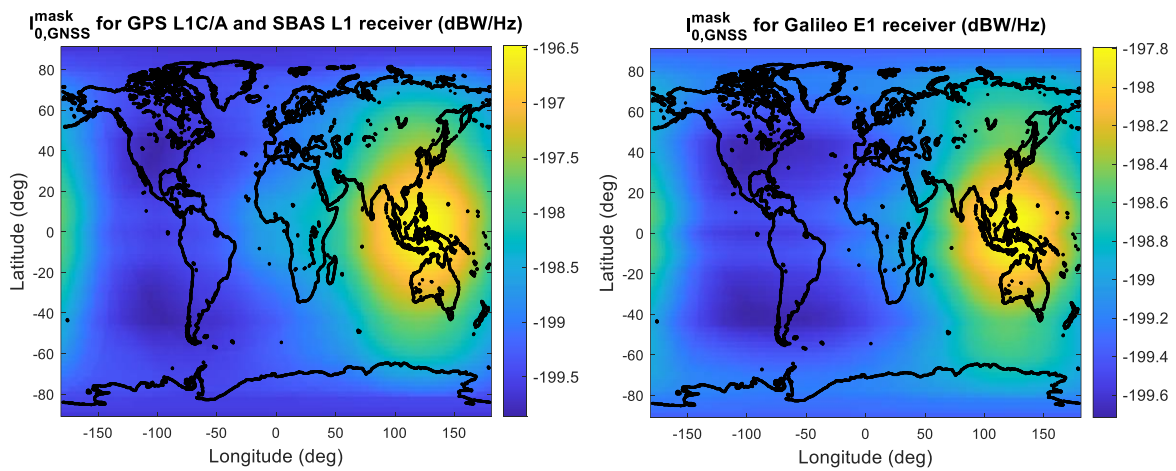


Figure B-5: $I_{0,GNSS}^{mask}(sig)$ for DFMC GNSS receivers

The inter/intra system interference hot spot is located in the South-East of Asia. Indeed, many SBAS geosynchronous satellites and regional constellations are transmitting in this region (QZSS, Beidou GEO). The $I_{0,GNSS}^{mask}$ hot spot is located at position 5°N, 122.5°E for GPS L1C/A and SBAS L1 signals, and at position 7.5°N, 122.5°E for Galileo E1 signals. Note that the inter and intra system equivalent noise values computed here for DFMC receivers are much stronger than the $I_{0,GNSS}^{mask}$ values used for legacy single frequency GPS L1 C/A receiver analysis and reported in Table B-2, because of the consideration of additional systems.

Minimum DFMC receiver antenna gain G_{min}

For acquisition analysis, G_{min} is computed according to the procedure described in section B-1.3 as a function of the latitude. The minimum elevation of highest GPS and Galileo satellites, and the corresponding minimum antenna gain G_{min} , are plotted in Figure B-6 and Figure B-7 as a function of the latitude.

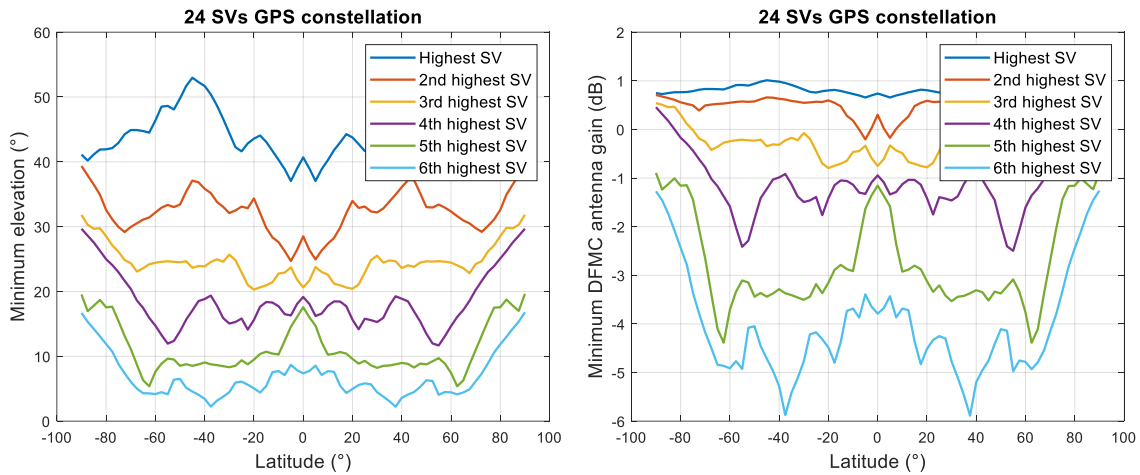


Figure B-6: Minimum elevation and minimum DFMC antenna gain of highest GPS SVs (24 SVs constellation) as a function of latitude

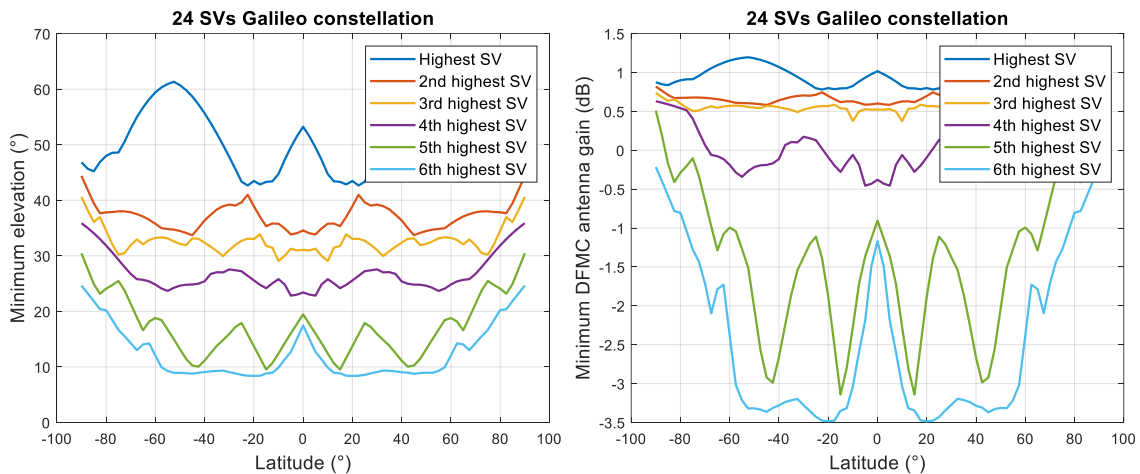


Figure B-7: Minimum elevation and minimum DFMC antenna gain of highest Galileo SVs (24 SVs constellation) as a function of latitude

It can be noticed that at least 6 Galileo SVs are always visible at any location on Earth, whereas only 5 GPS SVs are sometimes visible at some positions. As an important remark, the highest Galileo SVs are supposed to be in unscheduled outage when establishing C/N_0 acquisition link budgets as part of GNSS RFI masks elaboration. This hypothesis is not considered for GPS, since current GPS constellation holds 31 or 32 SVs, and Apr 2020 GPS SPS Specs also considers a 30SV constellation, so a conservative assumption is already taken into account by considering a 24 GPS SVs constellation.

DFMC C/N_0 link budgets

C/N_0 link budgets can now be derived. For each pair of signal and GNSS receiver signal processing operation, the maximum tolerable non-aeronautical equivalent noise $I_{0,non\ aero,max}(sig,op)$ level is represented in Figure B-8 for acquisition and tracking receiver operations.

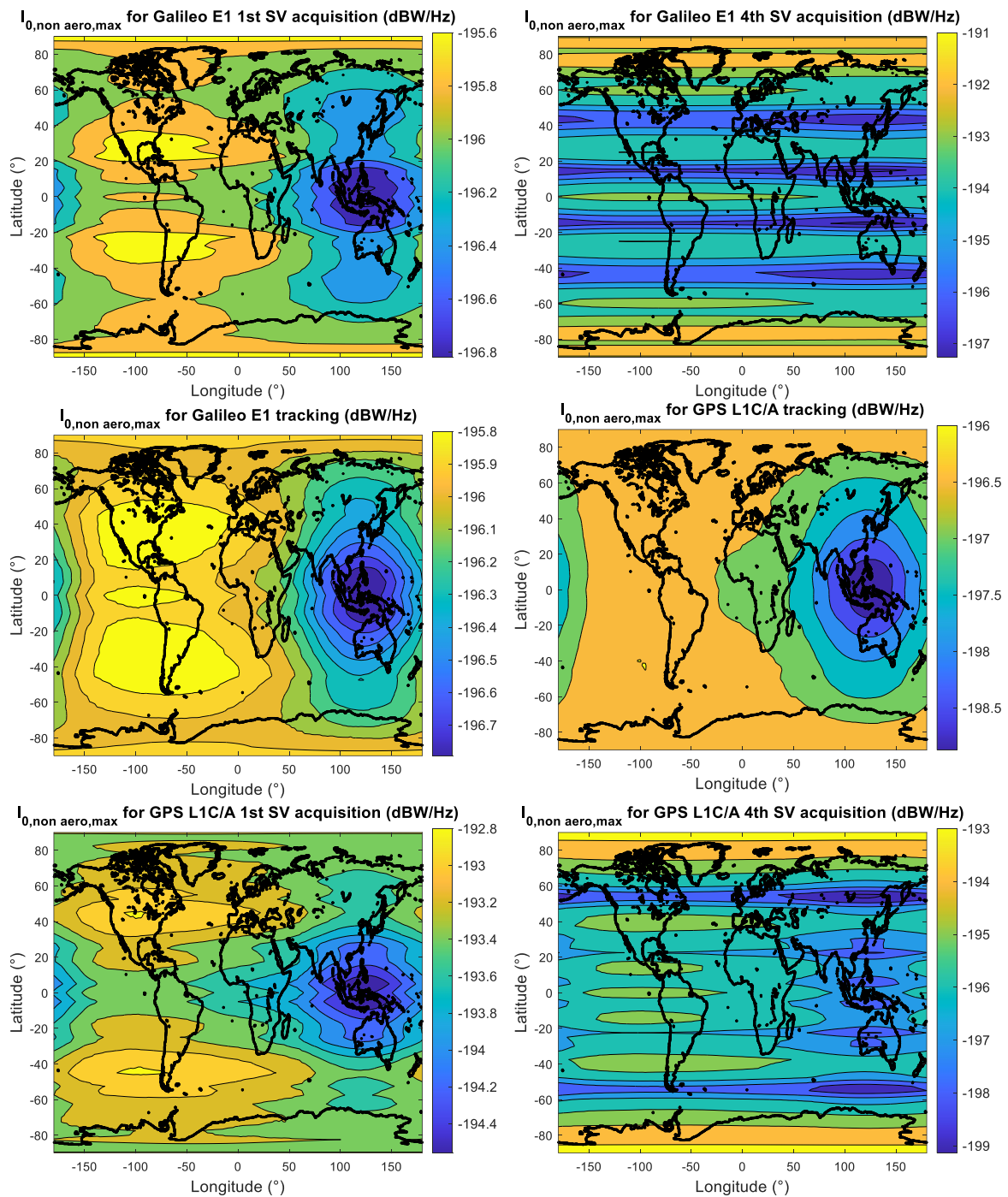


Figure B-8: $I_{0,non\ aero,max}(sig, op)$ for GPS L1C/A and Galileo E1 signals, for acquisition and tracking receiver operations

Worst worldwide DFMC C/N_0 link budgets are detailed in Table B-4. The SBAS L1 demodulation link budget is established at two locations: Mehamn (North of Norway) and Barrow (Alaska). Indeed, because of the high latitude of those locations, the GNSS receiver antenna gain offered towards SBAS geostationary SVs is expected to be very low and therefore, the link budgets at those locations are expected to be among the worst in the EGNOS and WAAS coverage area.

	GPS			WAAS	EGNOS	Galileo		
Parameter (Units)	1st SV acquisition	4th SV acquisition	Tracking	Demodulation	Demodulation	1st SV acquisition	4th SV acquisition	Tracking

Location	5°S 122.5°E	55°N 115°E	5°N 122.5°E	71.28°N 156.8°W	71°N 21.82°E	5°N 122.5°E	15°N 122.5°E	7.5°N 122.5°E
Min. SV Earth Surface Power (dBW)	-158,50	-158,50	-158,50	-158,50	-158,50	-157,90	-157,90	-157,90
Receive Antenna Gain (dBic)	0,66	-2,50	-4,50	-4,32	-3,34	0,59	-3,14	-4,50
Implementation Loss (dB)	1,50	1,50	1,50	1,50	1,50	1,90	1,90	1,90
RFI-free Post-Corr Carrier Pwr (dBW)	-159,34	-162,50	-164,50	-164,32	-163,34	-159,21	-162,94	-164,30
I _{0aero} (dBW/Hz)	-196,20	-197,40	-196,19	-198,66	-198,60	-197,42	-197,50	-197,41
N _{lim}	1,50	1,50	1,50	1,50	1,50	1,50	1,50	1,50
PDC	0,01	0,01	0,01	0,01	0,01	0,01	0,01	0,01
N _{0,EFF} dBW/Hz	-195,01	-195,90	-195,01	-196,77	-196,73	-195,92	-195,97	-195,91
Effective C/N _{0eff} (dB-Hz)	35,67	33,40	30,51	32,45	33,39	36,70	33,03	31,61
C/N ₀ threshold (dB-Hz)	32,40	31,70	29,00	30,00	30,00	34,10	30,60	29,00
Link Margin (dB)	3,27	1,70	1,51	2,45	3,39	2,60	2,43	2,61
Remaining I ₀ tolerable (dBW/Hz)	-194,55	-199,13	-198,87	-198,02	-196,04	-196,82	-197,26	-196,79

Table B-4: DFMC link budgets at worst worldwide locations

From Table B-4 and Figure B-8, it appears that the limiting receiver operations are:

- Tracking/Demodulation for GPS L1C/A and SBAS L1, and $I_{0,non\ aero,max}^{mask}(sig) = -199.13\ dBW/Hz$ for GPS L1C/A and SBAS L1 BPSK modulated signals.
- Acquisition of the 4th highest SV for Galileo E1 signals, and $I_{0,non\ aero,max}^{mask}(sig) = -197.26\ dBW/Hz$ for Galileo E1 signals.

These inputs are used to derive the maximum tolerable power for GPS L1C/A and Galileo E1 receivers.

B-3.2 DFMC in-band RFI mask

This section derives $C_{max}^{in\ band}$ for the L1 processing channel of DFMC receivers as a function of the non-aeronautical RFI bandwidth BW and compares it with the in-band DFMC RFI mask. Note that L1 DFMC and legacy single frequency GPS L1 C/A in-band RFI masks are identical. Figure B-9 shows:

- The minimum value of $C_{max}(sig, RFI(BW, L1 + \Delta f \in [1559; 1610]MHz))$ among all Galileo E1 signals for DFMC Galileo receiver, which corresponds to the maximum power from a non-aeronautical RFI that can be tolerated by Galileo E1 signal processing module of the receiver. The limiting C/N_0 link budget is obtained for acquisition operation, so an integration time of 4 ms is considered.
- The minimum value of $C_{max}(sig, RFI(BW, L1 + \Delta f \in [1559; 1610]MHz))$ among all GPS L1C/A and SBAS L1 signals for DFMC GPS and SBAS receiver, which corresponds to the maximum power from a non-aeronautical RFI that can be tolerated by GPS L1C/A signal processing module of the receiver. The limiting C/N_0 link budget is obtained for tracking operation, so an integration time of 20 ms is considered.
- The in-band RFI mask.

Since the RFI central frequency is within the GNSS frequency band, the RFFE filter does not impact the RFI power spectral density.

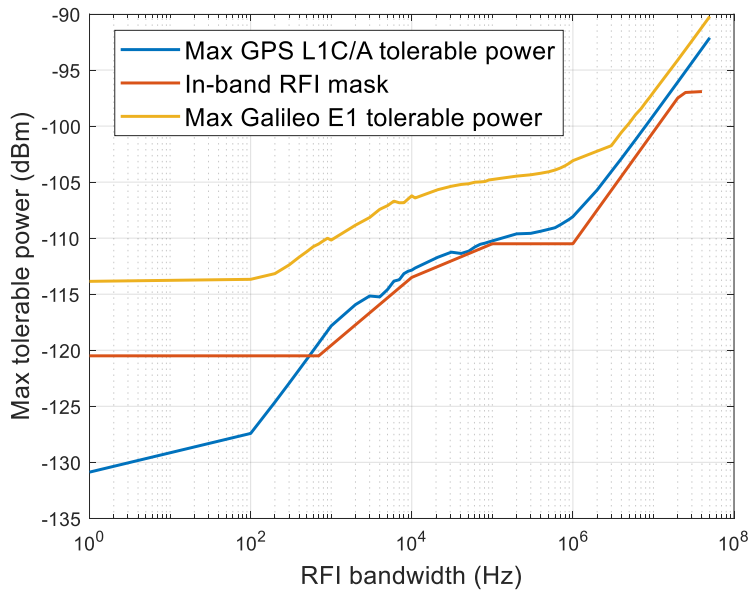


Figure B-9: Maximum tolerable power and in-band RFI mask for DFMC receivers

Some conclusions can be deduced from the interpretation of Figure B-9:

- The maximum tolerable power from non-aeronautical sources for a Galileo receiver (in yellow) is much higher than the maximum non-aeronautical power tolerated by a GPS L1/CA receiver (in blue). The main reason is that the tolerated non-aeronautical equivalent noise level is 1.87 dB higher for a Galileo E1 receiver than for a GPS L1C/A receiver.
- As developed above, since the limiting case for GPS L1C/A signal is a tracking scenario (20 ms integration time), narrowband interferences have a strong impact on the signal processing. However, it is very unlikely that a narrowband interference stays frequency synchronized with the GNSS local signal for a long time period. This is the reason explaining that the mask is clipped to the value for RFI of 700 Hz and not lowered for interference value lower than 700 Hz.
- Conversely to the legacy analysis, the maximum non aeronautical interference power for DFMC GPS L1C/A receivers is above the in-band RFI mask for interference bandwidth in the [30 kHz; 500 kHz] interval. Even though aeronautical RFI equivalent noise is higher in the DFMC evaluation compared to the analysis used for legacy evaluation, DFMC receivers also brings additional RFI robustness mean: the maximum antenna gain and implementation losses are indeed lower for DFMC receiver than for legacy receiver, and the GPS L1C/A tracking threshold has been decreased for DFMC receivers. These improvements allow to compensate the rise of $I_{0,aero,WB}$.

B-3.3 DFMC out-of-band RFI mask

This section derives $C_{max}^{out\ of\ band}(\Delta f)$ for GPS L1C/A and Galileo E1 DFMC modules and compares it to the out-of-band RFI mask. In this section, the reference RF/IF filter introduced in section B-2.3 is considered to derive $C_{max}^{out\ of\ band}(\Delta f)$. Also, the antenna brings some frequency rejection. The frequency rejection brought by DFMC antenna is illustrated in Figure 2-18.

Figure G-1 represents:

- The minimum value of $C_{max}(sig, RFI(BW = 700\ Hz, \Delta f))$ among all Galileo E1 signals for DFMC Galileo receiver, which corresponds to the maximum power from a non-aeronautical

RFI that can be tolerated by Galileo E1 signal processing module of the receiver as a function of the frequency offset Δf between the RFI central frequency and L1. The limiting C/N_0 link budget is obtained for acquisition operation, so an integration time of 4 ms is considered.

- The minimum value of $C_{max}(sig, RFI(BW = 700 \text{ Hz}, \Delta f))$ among all GPS L1C/A and SBAS L1 signals for DFMC GPS and SBAS receiver, which corresponds to the maximum power from a non-aeronautical RFI that can be tolerated by GPS L1C/A signal processing module of the receiver as a function of the frequency offset Δf between the RFI central frequency and L1. The limiting C/N_0 link budget is obtained for tracking operation, so an integration time of 20 ms is considered.
- The L1 portion of the out-of-band DFMC RFI mask published in Nov 2020 ICAO SARPs.
- The L1 portion of the out-of-band DFMC RFI mask version of DO-235C.

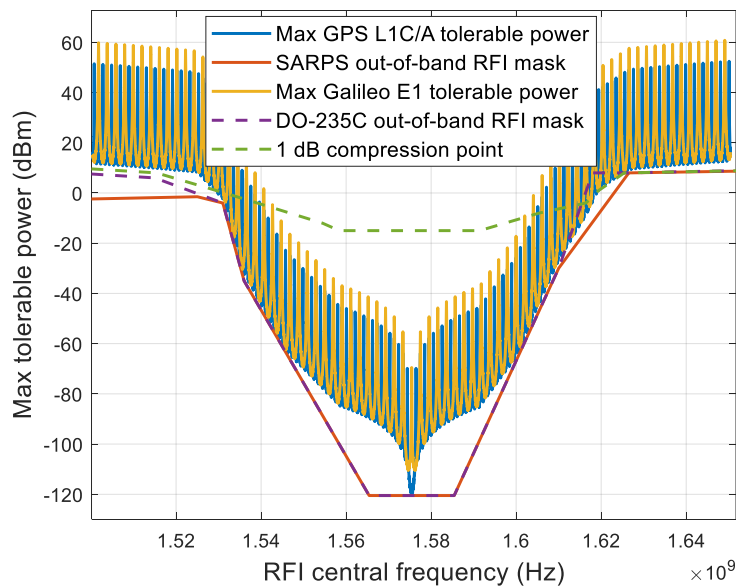


Figure B-10: Maximum tolerable power and out-of-band RFI mask for DFMC receivers

The maximum tolerable power for both Galileo and GPS modules is above the DFMC out-of-band RFI mask of ICAO SARPs. In the upper frequency region (above 1626.5 MHz), the DFMC RFI mask is constrained by the 1 dB compression point of the DFMC antenna (see Figure 2-17). In the lower interference area (below 1531 MHz), the ICAO SARPs RFI mask is well below the 1 dB compression point as well as the maximum interference power tolerated by GPS L1C/A and Galileo E1 receiver modules. Indeed, it appears that the L5 receiver module tolerates less interference power in this frequency area [96].

DO-235C DFMC out-of-band RFI mask has been raised in comparison to the ICAO DFMC out-of-band mask in the frequency range [1610;1626] for spectrum compatibility with AMSS, and in particular with Iridium Certus system. This raise of the RFI mask, as well as the raise of the DFMC antenna 1 dB compression point requirement, was allowed by agreement of GNSS receiver and GNSS antenna manufacturers who mentioned they should be able to bring additional frequency rejection in comparison to the minimum RF/IF RFFE filter. Also, for frequency below 1531 MHz, the DFMC out-of-band RFI mask has been raised in DO-235C for similar reasons.

B-4 Conclusion

This appendix derives the maximum power from non-aeronautical RFI that can be tolerated by legacy and DFMC GNSS receivers to fulfill their minimum requirements. The objective of such a calculation is to highlight the hypotheses which are assumed when using GNSS RFI mask for spectrum compatibility purpose.

The calculation of the maximum power from a non-aeronautical RFI that can be tolerated by the receiver is performed in two steps:

- First, C/N_0 link budgets are computed under worst GNSS signal and aeronautical RFI conditions for the different receiver signal processing operations. These link budgets allow to determine the non-aeronautical RFI equivalent noise which can be tolerated by the receiver.
- Second, the maximum non-aeronautical RFI equivalent noise that can be tolerated by the receiver is converted into a power depending on the characteristics of the considered non-aeronautical RFI. When it comes to RFI mask, the non-aeronautical RFI is considered to have a rectangular power spectral density, so its main characteristics are its bandwidth and its central frequency.

Then, in-band and out-of-band maximum power from non-aeronautical RFI tolerable by legacy and DFMC receiver is computed. Main conclusions of the comparison of this maximum tolerable power with official RFI masks are:

- In band maximum tolerable power for legacy receiver is computed with the not up-to-date aeronautical RFI environment which has been considered to derive legacy in-band RFI mask. Even with this environment, the maximum tolerable power is sometimes below the in-band legacy RFI mask. Thus, the in-band RFI mask should be reviewed with an updated aeronautical RFI environment.
- A minimum RFFE frequency rejection is derived so that legacy out-of-band maximum tolerable power is above the out-of-band legacy RFI mask. This minimum frequency rejection seems to be easily achievable by receiver manufacturer.
- Thanks to better capability in terms of minimum and maximum antenna gain, implementation losses and tracking threshold, in-band and out-of-band maximum power from a non-aeronautical RFI and tolerated by a DFMC receiver is above the DFMC RFI masks.

The highlighted hypotheses behind RFI masks are re-used in Chapter 4.

Appendix C: Autocorrelation of chirp signal

The objective of this appendix is to derive the autocorrelation function of the chirp signal at the RFFE output given in (Eq 5-19) and reminded in (Eq C-1).

$$s_{PPD,RFout}(t) = \sqrt{2C_J} \cos(2\pi(f_{IF} + \Delta f_j^c + f_{J,dopp})t + \varphi_0 - \varphi_\delta) \sum_{k=-\infty}^{+\infty} c_w(t - \delta - kT_{sweep}) - \sqrt{2C_J} \sin(2\pi(f_{IF} + \Delta f_j^c + f_{J,dopp})t + \varphi_0 - \varphi_\delta) \sum_{k=-\infty}^{+\infty} s_w(t - \delta - kT_{sweep}) \quad (\text{Eq C-1})$$

Where

$$c_w(t) = \begin{cases} \cos\left(2\pi \int_0^t f_{i_0,in}(u) du\right) & \text{if } t \in [0; T_{sweep}] \\ 0 & \text{elsewhere} \end{cases}$$

and

$$s_w(t) = \begin{cases} \sin\left(2\pi \int_0^t f_{i_0,in}(u) du\right) & \text{if } t \in [0; T_{sweep}] \\ 0 & \text{elsewhere} \end{cases}$$

We remind that:

- $\delta = \frac{\delta_{ini}}{1-\alpha}$. δ follows a uniform distribution over $[0, T_{sweep}]$
- φ_0 is a random phase UD over $[0, 2\pi]$
- $\varphi_\delta = 2\pi(f_0 + \Delta f_j^c)\delta_{ini}$ is also assumed to be a random phase UD over $[0, 2\pi]$

Starting from the chirp signal expression given in Chapter 5 (Eq 19) and reminded above, the autocorrelation of the chirp signal can be expressed by (Eq C-2).

$$\begin{aligned}
R_{s_{PPD,RFout}}(\tau) &= \mathbb{E}[s_{PPD,RFout}(t)s_{PPD,RFout}(t-\tau)] \\
&= 2C_J \mathbb{E} \left[\begin{aligned} &\cos(2\pi(f_{IF} + \Delta f_j^c + f_{J,dopp})t + \varphi_0 - \varphi_\delta) \cos(2\pi(f_{IF} + \Delta f_j^c + f_{J,dopp})(t-\tau) + \varphi_0 - \varphi_\delta) \\ &\sum_{k=-\infty}^{+\infty} \sum_{m=-\infty}^{+\infty} c_w(t-\delta - kT_{sweep})c_w(t-\tau-\delta - mT_{sweep}) \end{aligned} \right] \\
&- 2C_J \mathbb{E} \left[\begin{aligned} &\cos(2\pi(f_{IF} + \Delta f_j^c + f_{J,dopp})t + \varphi_0 - \varphi_\delta) \sin(2\pi(f_{IF} + \Delta f_j^c + f_{J,dopp})(t-\tau) + \varphi_0 - \varphi_\delta) \\ &\sum_{k=-\infty}^{+\infty} \sum_{m=-\infty}^{+\infty} c_w(t-\delta - kT_{sweep})s_w(t-\tau-\delta - mT_{sweep}) \end{aligned} \right] \\
&- 2C_J \mathbb{E} \left[\begin{aligned} &\cos(2\pi(f_{IF} + \Delta f_j^c + f_{J,dopp})(t-\tau) + \varphi_0 - \varphi_\delta) \sin(2\pi(f_{IF} + \Delta f_j^c + f_{J,dopp})t + \varphi_0 - \varphi_\delta) \\ &\sum_{k=-\infty}^{+\infty} \sum_{m=-\infty}^{+\infty} c_w(t-\tau-\delta - kT_{sweep})s_w(t-\delta - mT_{sweep}) \end{aligned} \right] \\
&+ 2C_J \mathbb{E} \left[\begin{aligned} &\sin(2\pi(f_{IF} + \Delta f_j^c + f_{J,dopp})t + \varphi_0 - \varphi_\delta) \sin(2\pi(f_{IF} + \Delta f_j^c + f_{J,dopp})(t-\tau) + \varphi_0 - \varphi_\delta) \\ &\sum_{k=-\infty}^{+\infty} \sum_{m=-\infty}^{+\infty} s_w(t-\delta - kT_{sweep})s_w(t-\tau-\delta - mT_{sweep}) \end{aligned} \right] \tag{Eq C-2}
\end{aligned}$$

(Eq C-2) can be simplified. Indeed, the first mathematical expectation term is developed in (Eq C-3).

$$\begin{aligned}
&\mathbb{E} \left[\begin{aligned} &\cos(2\pi(f_{IF} + \Delta f_j^c + f_{J,dopp})t + \varphi_0 - \varphi_\delta) \cos(2\pi(f_{IF} + \Delta f_j^c + f_{J,dopp})(t-\tau) + \varphi_0 - \varphi_\delta) \\ &\sum_{k=-\infty}^{+\infty} \sum_{m=-\infty}^{+\infty} c_w(t-\delta - kT_{sweep})c_w(t-\tau-\delta - mT_{sweep}) \end{aligned} \right] \\
&= \mathbb{E} \left[\mathbb{E} \left[\begin{aligned} &\cos(2\pi(f_{IF} + \Delta f_j^c + f_{J,dopp})t + \varphi_0 - \varphi_\delta) \cos(2\pi(f_{IF} + \Delta f_j^c + f_{J,dopp})(t-\tau) + \varphi_0 - \varphi_\delta) \\ &\sum_{k=-\infty}^{+\infty} \sum_{m=-\infty}^{+\infty} c_w(t-\delta - kT_{sweep})c_w(t-\tau-\delta - mT_{sweep}) \end{aligned} \middle| \delta \right] \right] \\
&= \mathbb{E} \left[\begin{aligned} &\sum_{k=-\infty}^{+\infty} \sum_{m=-\infty}^{+\infty} c_w(t-\delta - kT_{sweep})c_w(t-\tau-\delta - mT_{sweep}) \\ &\mathbb{E} \left[\frac{\cos(2\pi(f_{IF} + \Delta f_j^c + f_{J,dopp})\tau) + \cos(2\pi(f_{IF} + \Delta f_j^c + f_{J,dopp})(2t-\tau) + 2\varphi_0 - 2\varphi_\delta)}{2} \middle| \delta \right] \end{aligned} \right] \\
&= \cos(2\pi(f_{IF} + \Delta f_j^c + f_{J,dopp})\tau) \mathbb{E} \left[\frac{1}{2} \sum_{k=-\infty}^{+\infty} \sum_{m=-\infty}^{+\infty} c_w(t-\delta - kT_{sweep})c_w(t-\tau-\delta - mT_{sweep}) \right] \\
&= \frac{1}{2} \cos(2\pi(f_{IF} + \Delta f_j^c + f_{J,dopp})\tau) \sum_{k=-\infty}^{+\infty} \sum_{m=-\infty}^{+\infty} \mathbb{E}[c_w(t-\delta - kT_{sweep})c_w(t-\tau-\delta - mT_{sweep})] \\
&= \frac{1}{2} \cos(2\pi(f_{IF} + \Delta f_j^c + f_{J,dopp})\tau) \sum_{m=-\infty}^{+\infty} \sum_{k=-\infty}^{+\infty} \frac{1}{T_{sweep}} \int_0^{T_{sweep}} c_w(t-\delta - kT_{sweep})c_w(t-\tau-\delta - mT_{sweep})d\delta \\
&= \frac{1}{2} \cos(2\pi(f_{IF} + \Delta f_j^c + f_{J,dopp})\tau) \sum_{m=-\infty}^{+\infty} \sum_{k=-\infty}^{+\infty} \frac{1}{T_{sweep}} \int_{t-(k+1)T_{sweep}}^{t-kT_{sweep}} c_w(u)c_w(u-\tau-(m-k)T_{sweep})du \\
&= \frac{1}{2} \cos(2\pi(f_{IF} + \Delta f_j^c + f_{J,dopp})\tau) \sum_{m'=-\infty}^{+\infty} \sum_{k=-\infty}^{+\infty} \frac{1}{T_{sweep}} \int_{t-(k+1)T_{sweep}}^{t-kT_{sweep}} c_w(u)c_w(u-\tau-m'T_{sweep})du \\
&= \frac{1}{2} \cos(2\pi(f_{IF} + \Delta f_j^c + f_{J,dopp})\tau) \sum_{m'=-\infty}^{+\infty} \frac{1}{T_{sweep}} \int_{-\infty}^{+\infty} c_w(u)c_w(u-\tau-m'T_{sweep})du \\
&= \frac{1}{2} \cos(2\pi(f_{IF} + \Delta f_j^c + f_{J,dopp})\tau) \frac{1}{T_{sweep}} \sum_{m'=-\infty}^{+\infty} R_{c_w}(\tau + m'T_{sweep})
\end{aligned} \tag{Eq C-3}$$

R_{c_w} is the autocorrelation of the deterministic signal c_w , defined in (Eq 5-18).

$$R_{c_w}(\tau) = \int_{-\infty}^{+\infty} c_w(t)c_w(t-\tau)dt$$

$$R_{s_w}(\tau) = \int_{-\infty}^{+\infty} s_w(t)s_w(t-\tau)dt$$

Similarly, the other mathematical expectation terms of (Eq C-2) are developed in (Eq C-4).

$$\begin{aligned} & \mathbb{E} \left[\cos(2\pi(f_{IF} + \Delta f_J^c + f_{J,dopp})t + \varphi_0 - \varphi_\delta) \sin(2\pi(f_{IF} + \Delta f_J^c + f_{J,dopp})(t-\tau) + \varphi_0 - \varphi_\delta) \right. \\ & \quad \left. \sum_{k=-\infty}^{+\infty} \sum_{m=-\infty}^{+\infty} c_w(t-\delta-kT_{sweep})s_w(t-\tau-\delta-mT_{sweep}) \right] \\ & = -\frac{1}{2} \sin(2\pi(f_{IF} + \Delta f_J^c + f_{J,dopp})\tau) \frac{1}{T_{sweep}} \sum_{m'=-\infty}^{+\infty} R_{c_w,s_w}(\tau + m'T_{sweep}) \\ & \mathbb{E} \left[\cos(2\pi(f_{IF} + \Delta f_J^c + f_{J,dopp})(t-\tau) + \varphi_0 - \varphi_\delta) \sin(2\pi(f_{IF} + \Delta f_J^c + f_{J,dopp})t + \varphi_0 - \varphi_\delta) \right] \\ & \quad \sum_{k=-\infty}^{+\infty} \sum_{m=-\infty}^{+\infty} c_w(t-\tau-\delta-kT_{sweep})s_w(t-\delta'-mT_{sweep}) \\ & = \frac{1}{2} \sin(2\pi(f_{IF} + \Delta f_J^c + f_{J,dopp})\tau) \frac{1}{T_{sweep}} \sum_{m'=-\infty}^{+\infty} R_{c_w,s_w}(\tau + m'T_{sweep}) \\ & \mathbb{E} \left[\sin(2\pi(f_{IF} + \Delta f_J^c + f_{J,dopp})t + \varphi_0 - \varphi_\delta) \sin(2\pi(f_{IF} + \Delta f_J^c + f_{J,dopp})(t-\tau) + \varphi_0 - \varphi_\delta) \right] \\ & \quad \sum_{k=-\infty}^{+\infty} \sum_{m=-\infty}^{+\infty} s_w(t-\delta-kT_{sweep})s_w(t-\tau-\delta-mT_{sweep}) \\ & = \frac{1}{2} \cos(2\pi(f_{IF} + \Delta f_J^c + f_{J,dopp})\tau) \frac{1}{T_{sweep}} \sum_{m'=-\infty}^{+\infty} R_{s_w}(\tau + m'T_{sweep}) \end{aligned} \quad (\text{Eq C-4})$$

R_{s_w} is the autocorrelation of the deterministic signal s_w , defined in (Eq 5-18). R_{c_w,s_w} is the cross-correlation of signals c_w and s_w .

Injecting (Eq C-3) and (Eq C-4) into (Eq C-2), it comes that the autocorrelation function of the chirp signal can be expressed by (Eq C-5).

$$R_{s_{PPD,RFOut}}(\tau) = C_J \cos(2\pi(f_{IF} + \Delta f_J^c + f_{J,dopp})\tau) \frac{1}{T_{sweep}} \left[\begin{aligned} & \sum_{m'=-\infty}^{+\infty} R_{c_w}(\tau + m'T_{sweep}) \\ & + \sum_{m'=-\infty}^{+\infty} R_{s_w}(\tau + m'T_{sweep}) \end{aligned} \right] \quad (\text{Eq C-5})$$

Appendix D: Power spectral density of chirp signal

The objective of this appendix is to derive the functions $C_w(f)$ and $S_w(f)$, which are the Fourier transforms of the deterministic chirp signal components $c_w(t)$ and $s_w(t)$ involved in the autocorrelation functions $R_{c_w}(\tau)$ and $R_{s_w}(\tau)$ of $c_w(t)$ and $s_w(t)$ at the RFFE output in order to deduce the chirp signal power spectral density.

We remind that the signal model is given in (Eq D-1), assuming $\Delta f_j^c + f_{j,dopp} = 0$.

$$S_{PPD,RFout}(t) = \sqrt{2C_J} \cos(2\pi f_{IF}t + \varphi_0 - \varphi_\delta) \sum_{k=-\infty}^{+\infty} c_w(t - \delta - kT_{sweep}) - \sqrt{2C_J} \sin(2\pi f_{IF}t + \varphi_0 - \varphi_\delta) \sum_{k=-\infty}^{+\infty} s_w(t - \delta - kT_{sweep}) \quad (\text{Eq D-1})$$

Where

$$c_w(t) = \begin{cases} \cos\left(2\pi \int_0^t f_{i_0,in}(u) du\right) & \text{if } t \in [0; T_{sweep}] \\ 0 & \text{elsewhere} \end{cases}$$

and

$$s_w(t) = \begin{cases} \sin\left(2\pi \int_0^t f_{i_0,in}(u) du\right) & \text{if } t \in [0; T_{sweep}] \\ 0 & \text{elsewhere} \end{cases}$$

We remind that the autocorrelation function of this random stationary signal is as obtained in (Eq C-5):

$$R_{SPPD,RFout}(\tau) = C_J \cos(2\pi f_{IF}\tau) \frac{1}{T_{sweep}} \left[\sum_{m=-\infty}^{+\infty} R_{c_w}(\tau + m'T_{sweep}) + \sum_{m=-\infty}^{+\infty} R_{s_w}(\tau + m'T_{sweep}) \right]$$

Where we have defined $R_{c_w}(\tau)$ and $R_{s_w}(\tau)$ as the autocorrelations of the finite energy deterministic signals $c_w(t)$ and $s_w(t)$:

$$R_{c_w}(\tau) = \int_{-\infty}^{+\infty} c_w(t)c_w(t - \tau)dt$$

$$R_{s_w}(\tau) = \int_{-\infty}^{+\infty} s_w(t)s_w(t - \tau)dt$$

The power spectrum density $S_{PPD,RFout}(f)$ is the Fourier Transform of the autocorrelation function $R_{SPPD,RFout}(\tau)$.

(Eq D-1) can be re-written by (Eq D-2).

$$R_{S_{PPD},RF_{out}}(\tau) = C_J \cos(2\pi f_{IF} \tau) \frac{1}{T_{sweep}} \left[(R_{C_w}(\tau) + R_{S_w}(\tau)) * \sum_{m=-\infty}^{+\infty} \delta(\tau + mT_{sweep}) \right] \quad (\text{Eq D-2})$$

That Fourier Transform will involve the Fourier Transform of $R_{C_w}(\tau)$ and $R_{S_w}(\tau)$, and we know that these Fourier Transforms are $|C_w(f)|^2$ and $|S_w(f)|^2$, where $C_w(f)$ and $S_w(f)$ are the individual Fourier transforms of the deterministic chirp signal components $c_w(t)$ and $s_w(t)$.

(Eq 5-22) provides an expression for the power spectral density of the chirp signal at the RFFE block output. The Fourier transform of (Eq D-2) is given in (Eq 5-21).

$$S_{PPD,RF_{out}}(f) = \frac{C_J}{T_{sweep}} \left(|C_w(f)|^2 + |S_w(f)|^2 \right) \frac{1}{T_{sweep}} \sum_{m=-\infty}^{+\infty} \delta\left(f - \frac{m}{T_{sweep}}\right) * \frac{\delta(f - f_{IF}) + \delta(f + f_{IF})}{2} \quad (\text{Eq D-3})$$

Therefore, (Eq 5-21) can be re-written by (Eq 5-22).

$$S_{PPD,RF_{out}}(f) = C_J \left[\sum_{m=-\infty}^{+\infty} c_m \delta\left(f - \frac{m}{T_{sweep}}\right) \right] * \frac{\delta(f - f_{IF}) + \delta(f + f_{IF})}{2} \quad (\text{Eq D-4})$$

$$\text{With } c_m = \frac{1}{T_{sweep}^2} \left(\left| C_w\left(\frac{m}{T_{sweep}}\right) \right|^2 + \left| S_w\left(\frac{m}{T_{sweep}}\right) \right|^2 \right).$$

As we can see, this PSD is expressed as a function of coefficients $c_m = \frac{1}{T_{sweep}^2} \left(\left| C_w\left(\frac{m}{T_{sweep}}\right) \right|^2 + \left| S_w\left(\frac{m}{T_{sweep}}\right) \right|^2 \right)$.

This appendix develops and simplifies this expression.

The calculation of C_w is detailed in (Eq D-5).

$$\begin{aligned} C_w(f) &= \int_{-\infty}^{+\infty} c_w(t) e^{-i2\pi f t} dt = \int_0^{T_{sweep}} \cos\left(\frac{\pi B}{T_{sweep}} t^2 - \pi B t\right) e^{-i2\pi f t} dt \\ &= \frac{I_1(f) + I_2(f)}{2} \\ I_1(f) &= \int_0^{T_{sweep}} e^{i\left(\frac{\pi B}{T_{sweep}} t^2 - \pi B t\right)} e^{-i2\pi f t} dt \\ I_2(f) &= \int_0^{T_{sweep}} e^{-i\left(\frac{\pi B}{T_{sweep}} t^2 - \pi B t\right)} e^{-i2\pi f t} dt \end{aligned} \quad (\text{Eq D-5})$$

I_1 is further developed in (Eq D-6).

$$\begin{aligned}
I_1(f) &= \int_0^{T_{\text{sweep}}} e^{i\left[\frac{\pi B}{T_{\text{sweep}}}t^2 - (2\pi f + \pi B)t\right]} dt \\
&= e^{-i\frac{\pi T_{\text{sweep}}}{4B}(2f+B)^2} \int_0^{T_{\text{sweep}}} e^{i\frac{\pi}{2}\left(\sqrt{\frac{2B}{T_{\text{sweep}}}}t - \sqrt{\frac{T_{\text{sweep}}}{2B}}(2f+B)\right)^2} dt
\end{aligned} \tag{Eq D-6}$$

Making a variable change in (Eq D-6), I_1 can be developed in (Eq D-7).

$$I_1(f) = \sqrt{\frac{T_{\text{sweep}}}{2B}} e^{-i\frac{\pi T_{\text{sweep}}}{4B}(2f+B)^2} \int_{-\sqrt{\frac{2T_{\text{sweep}}}{B}}f - \sqrt{\frac{BT_{\text{sweep}}}{2}}}^{\sqrt{\frac{BT_{\text{sweep}}}{2}} - \sqrt{\frac{2T_{\text{sweep}}}{B}}f} e^{i\frac{\pi}{2}u^2} du \tag{Eq D-7}$$

(Eq D-7) can be expressed using the Fresnel cosine and sine integral functions, respectively denoted C and S , and defined in (Eq D-8).

$$C(x) = \int_0^x \cos\left(\frac{\pi}{2}u^2\right) du \quad S(x) = \int_0^x \sin\left(\frac{\pi}{2}u^2\right) du \tag{Eq D-8}$$

I_1 can thus be re-written as in (Eq D-9).

$$I_1(f) = \sqrt{\frac{T_{\text{sweep}}}{2B}} e^{-i\frac{\pi T_{\text{sweep}}}{4B}(2f+B)^2} \left[\begin{aligned} &C\left(\sqrt{\frac{BT_{\text{sweep}}}{2}} + \sqrt{\frac{2T_{\text{sweep}}}{B}}f\right) + C\left(\sqrt{\frac{BT_{\text{sweep}}}{2}} - \sqrt{\frac{2T_{\text{sweep}}}{B}}f\right) \\ &+ iS\left(\sqrt{\frac{BT_{\text{sweep}}}{2}} + \sqrt{\frac{2T_{\text{sweep}}}{B}}f\right) + iS\left(\sqrt{\frac{BT_{\text{sweep}}}{2}} - \sqrt{\frac{2T_{\text{sweep}}}{B}}f\right) \end{aligned} \right] \tag{Eq D-9}$$

Similarly, integral I_2 is expressed in (Eq D-10).

$$I_2(f) = \sqrt{\frac{T_{\text{sweep}}}{2B}} e^{i\frac{\pi T_{\text{sweep}}}{4B}(2f-B)^2} \left[\begin{aligned} &C\left(\sqrt{\frac{BT_{\text{sweep}}}{2}} + \sqrt{\frac{2T_{\text{sweep}}}{B}}f\right) + C\left(\sqrt{\frac{BT_{\text{sweep}}}{2}} - \sqrt{\frac{2T_{\text{sweep}}}{B}}f\right) \\ &- iS\left(\sqrt{\frac{BT_{\text{sweep}}}{2}} + \sqrt{\frac{2T_{\text{sweep}}}{B}}f\right) - iS\left(\sqrt{\frac{BT_{\text{sweep}}}{2}} - \sqrt{\frac{2T_{\text{sweep}}}{B}}f\right) \end{aligned} \right] \tag{Eq D-10}$$

Eventually, C_w is deduced injecting (Eq D-9) and (Eq D-10) in (Eq D-5). Likewise, the Fourier transform S_w of the windowed signal s_w is expressed in (Eq D-11).

$$S_w(f) = \frac{1}{2i} I_1(f) - \frac{1}{2i} I_2(f) \tag{Eq D-11}$$

It can be remarked that the sum of square modulus of C_w and S_w can be simplified according to (Eq D-12).

$$\begin{aligned}
|C_w(f)|^2 + |S_w(f)|^2 &= \frac{1}{2}|I_1(f)|^2 + \frac{1}{2}|I_2(f)|^2 = |I_1(f)|^2 \\
&= \frac{T_{\text{sweep}}}{2B} \left| \begin{array}{l} C \left(\sqrt{\frac{BT_{\text{sweep}}}{2}} + \sqrt{\frac{2T_{\text{sweep}}}{B}} f \right) + C \left(\sqrt{\frac{BT_{\text{sweep}}}{2}} - \sqrt{\frac{2T_{\text{sweep}}}{B}} f \right) \\ + iS \left(\sqrt{\frac{BT_{\text{sweep}}}{2}} + \sqrt{\frac{2T_{\text{sweep}}}{B}} f \right) + iS \left(\sqrt{\frac{BT_{\text{sweep}}}{2}} - \sqrt{\frac{2T_{\text{sweep}}}{B}} f \right) \end{array} \right|^2
\end{aligned} \tag{Eq D-12}$$

c_m can therefore be reduced to (Eq D-13).

$$\begin{aligned}
c_m &= \frac{1}{T_{\text{sweep}}^2} \left(\left| C_w \left(\frac{m}{T_{\text{sweep}}} \right) \right|^2 + \left| S_w \left(\frac{m}{T_{\text{sweep}}} \right) \right|^2 \right) \\
&= \frac{1}{2BT_{\text{sweep}}} \left| \begin{array}{l} C \left(\sqrt{\frac{BT_{\text{sweep}}}{2}} + \sqrt{\frac{2}{BT_{\text{sweep}}}} m \right) + C \left(\sqrt{\frac{BT_{\text{sweep}}}{2}} - \sqrt{\frac{2}{BT_{\text{sweep}}}} m \right) \\ + iS \left(\sqrt{\frac{BT_{\text{sweep}}}{2}} + \sqrt{\frac{2}{BT_{\text{sweep}}}} m \right) + iS \left(\sqrt{\frac{BT_{\text{sweep}}}{2}} - \sqrt{\frac{2}{BT_{\text{sweep}}}} m \right) \end{array} \right|^2
\end{aligned} \tag{Eq D-13}$$

Eventually, the power spectral density of the chirp jammer can be simplified by (Eq D-14).

$$S_{PPD,RFout}(f) = C_J \left[\sum_{m=-\infty}^{+\infty} c_m \delta \left(f - \frac{m}{T_{\text{sweep}}} \right) \right] * \frac{\delta(f - f_{IF}) + \delta(f + f_{IF})}{2} \tag{Eq D-14}$$

Appendix E: Asymptotic behavior of C/N_0 estimators in presence of RFI

The objective of this appendix is to analyze the asymptotic behavior of C/N_0 estimators in presence of RFI. In this appendix, the following assumptions on the RFI are considered:

- The GPS signal power is much higher than the RFI and noise power at the correlator outputs,
- The mean value of the RFI at the correlator output is null,
- The RFI at the correlator output is independent from the GPS signal.

The in-phase and quadrature phase correlator outputs, in presence of RFI and neglecting useful signal component code and phase tracking errors, can be expressed as in (Eq E-1):

$$\begin{aligned} I_P(k) &= \sqrt{\frac{C}{2}} + I_{PPD}(k) + n_I(k) \\ Q_P(k) &= Q_{PPD}(k) + n_Q(k) \end{aligned} \quad (\text{Eq E-1})$$

I_{PPD} and Q_{PPD} are respectively the contribution of the chirp RFI to in-phase and quadrature phase correlator outputs. Assuming the RFI is a random stationary signal, as the result of LTI filtering, these correlator output components are also modelled as random stationary signals. The variances of I_J and Q_J , independent of k because the RFI is assumed random stationary are respectively denoted P_I and P_Q . According to Condition 4, the RFI is centered at the correlator output. In other words,

$$\lim_{K \rightarrow +\infty} \frac{1}{K} \sum_{k=1}^K I_{PPD}(k) = \lim_{K \rightarrow +\infty} \frac{1}{K} \sum_{k=1}^K Q_{PPD}(k) = 0 \quad (\text{Eq E-2})$$

$(n_I(k))_{k \in \mathbb{N}}$ and $(n_Q(k))_{k \in \mathbb{N}}$ are noise samples on the in-phase and quadrature phase correlator outputs. They are assumed to be independent and identically distributed centered gaussian random variables with variance $\frac{N_0}{4T_i}$. In addition, the $(n_I(k))_{k \in \mathbb{N}}$ and $(n_Q(k))_{k \in \mathbb{N}}$ samples are assumed independent from $(I_{PPD}(k))_{k \in \mathbb{N}}$ and $(Q_{PPD}(k))_{k \in \mathbb{N}}$.

The behavior of SNV, Beaulieu and Moment estimators are analyzed here. According to condition 1, ergodicity is assumed.

Analysis of SNV estimator in presence of RFI

The SNV estimator is defined by (Eq E-3).

$$\widehat{C/N_{0,SNV}} = \frac{1}{T_i} \cdot \frac{\left(\frac{1}{N_s} \cdot \sum_{k=1}^{N_s} I_P(k) \right)^2}{\frac{1}{N_s} \cdot \sum_{k=1}^{N_s} (I_P(k)^2 + Q_P(k)^2) - \left(\frac{1}{N_s} \cdot \sum_{k=1}^{N_s} I_P(k) \right)^2} \quad (\text{Eq E-3})$$

Because the interference and the noise are centered,

$$\lim_{N_s \rightarrow +\infty} \left(\frac{1}{N_s} \cdot \sum_{k=1}^{N_s} I_P(k) \right)^2 = \frac{C}{2} \quad (\text{Eq E-4})$$

In addition,

$$\lim_{N_s \rightarrow +\infty} \left[\frac{1}{N_s} \cdot \sum_{k=1}^{N_s} (I_P(k)^2 + Q_P(k)^2) - \left(\frac{1}{N_s} \cdot \sum_{k=1}^{N_s} I_P(k) \right)^2 \right] = \mathbb{V}(I_P) + \mathbb{E}(Q_P^2) \quad (\text{Eq E-5})$$

Because the interference is independent from the noise,

$$\mathbb{V}(I_P) = \mathbb{V}(I_{PPD}) + \mathbb{V}(n_I) = P_I + \frac{N_0}{4T_i} \quad (\text{Eq E-6})$$

Likewise, since Q_{PPD} and n_Q are centered,

$$\mathbb{E}(Q_P^2) = \mathbb{V}(Q_P) = \mathbb{V}(Q_{PPD} + n_Q) = \mathbb{V}(Q_{PPD}) + \mathbb{V}(n_Q) = P_Q + \frac{N_0}{4T_i} \quad (\text{Eq E-7})$$

Therefore,

$$\lim_{N_s \rightarrow +\infty} C/\widehat{N_{0,SNV}} = \frac{1}{T_i} \frac{C/2}{\frac{2N_0}{4T_i} + P_I + P_Q} = \frac{C}{N_0 + 2T_i(P_I + P_Q)} \quad (\text{Eq E-8})$$

Assuming that chirp correlator outputs have the same distribution on the in-phase and quadrature phase channel, P_I and P_Q are equal to $\frac{I_0}{4T_i}$. Under this assumption, (Eq E-8) can be reduced to (Eq E-9).

$$\lim_{N_s \rightarrow +\infty} C/\widehat{N_{0,SNV}} = \frac{C}{N_0 + I_0} = C/N_{0,eff} \quad (\text{Eq E-9})$$

Analysis of Beaulieu estimator in presence of RFI

The Beaulieu estimator is defined by (Eq E-10).

$$C/\widehat{N_{0,B}} = \frac{1}{T_i} \cdot \left(\frac{1}{N_s} \cdot \sum_{k=1}^{N_s} \frac{(|I_P(k)| - |I_P(k-1)|)^2}{\frac{1}{2}(I_P(k)^2 + I_P(k-1)^2)} \right)^{-1} \quad (\text{Eq E-10})$$

The denominator of each individual term of the sum can be developed in (Eq E-11).

$$\begin{aligned} I_P(k)^2 + I_P(k-1)^2 &= \left(\sqrt{\frac{C}{2}} + I_{PPD}(k) + n_I(k) \right)^2 + \left(\sqrt{\frac{C}{2}} + I_{PPD}(k-1) + n_I(k-1) \right)^2 \\ &= C + \sqrt{2C}(I_{PPD}(k) + I_{PPD}(k-1)) + \sqrt{2C}(n_I(k) + n_I(k-1)) \\ &\quad + I_{PPD}(k)^2 + I_{PPD}(k-1)^2 + n_I(k)^2 + n_I(k-1)^2 + 2I_{PPD}(k)n_I(k) \\ &\quad + 2I_{PPD}(k-1)n_I(k-1) \end{aligned} \quad (\text{Eq E-11})$$

As the RFI and the noise are assumed centered, all of the cross-products will tend to have zero mean. In addition, assuming that the GNSS signal power is much higher than RFI and noise power at the I_P correlator output, the denominator can be approximated by $I(k)^2 + I(k-1)^2 \approx C$.

The numerator of each individual term of the sum can also be developed in (Eq E-12).

Assuming again that the GNSS signal power is much higher than RFI and noise power at the I_P correlator output, there is a high probability that $I_P > 0$. Negative values of I_P can also occur, but these cases are assumed to be rare and are not expanded in this appendix.

In the case of positive I_P , we therefore assume:

$$(|I_P(k)| - |I_P(k-1)|)^2 = (I_P(k) - I_P(k-1))^2$$

$$\begin{aligned}
(I_P(k) - I_P(k-1))^2 &= (I_{PPD}(k) - I_{PPD}(k-1) + n_I(k) - n_I(k-1))^2 \\
&= I_{PPD}(k)^2 + I_{PPD}(k-1)^2 + n_I(k)^2 + n_I(k-1)^2 \\
&\quad - 2I_{PPD}(k)I_{PPD}(k-1) + 2I_{PPD}(k)n_I(k) - 2I_{PPD}(k)n_I(k-1) \\
&\quad - 2I_{PPD}(k-1)n_I(k) + 2I_{PPD}(k-1)n_I(k-1) - 2n_I(k)n_I(k-1)
\end{aligned} \tag{Eq E-12}$$

Eventually, as we assume that the GNSS signal power is much higher than RFI and noise power at the I_P correlator output, so that the sum of ratios is converted into a simple sum because the denominator is constant and equal to $\frac{C}{2}$, and also because all $I_I n_I$ cross-products tend to have a zero mean, the limit of Beaulieu estimator is given in (Eq E-13).

$$\begin{aligned}
\lim_{N_s \rightarrow +\infty} \widehat{C/N_{0,B}} &= \frac{1}{T_i} \left(\frac{2}{C} (2\mathbb{V}(I_{PPD}) + 2\mathbb{V}(n_I) - 2\mathbb{E}(I_{PPD}(k)I_{PPD}(k-1))) \right)^{-1} \\
&= \frac{1}{T_i} \frac{C}{2 \frac{2N_0}{4T_i} + 2P_I - 2\mathbb{E}(I_{PPD}(k)I_{PPD}(k-1))} \\
&= \frac{C}{N_0 + 4T_i P_I - 4T_i \mathbb{E}(I_{PPD}(k)I_{PPD}(k-1))}
\end{aligned} \tag{Eq E-13}$$

Assuming that successive chirp correlator outputs are independent, $\mathbb{E}(I_{PPD}(k)I_{PPD}(k-1)) = 0$ since chirp correlator output are assumed to be centered. Under this assumption, (Eq E-13) can be reduced to (Eq E-14).

$$\lim_{N_s \rightarrow +\infty} \widehat{C/N_{0,B}} = \frac{C}{N_0 + I_0} = C/N_{0,eff} \tag{Eq E-14}$$

Analysis of moment estimator in presence of RFI

The moment estimator is defined by (Eq E-15).

$$\begin{aligned}
\widehat{M}_2 &= \frac{1}{N_s} \cdot \sum_{k=1}^N I_P(k)^2 + Q_P(k)^2 & \widehat{M}_4 &= \frac{1}{N_s} \cdot \sum_{k=1}^{N_s} (I_P(k)^2 + Q_P(k)^2)^2 \\
\widehat{C/N_{0,MM}} &= \frac{1}{T_i} \frac{\sqrt{2\widehat{M}_2^2 - \widehat{M}_4}}{\widehat{M}_2 - \sqrt{2\widehat{M}_2^2 - \widehat{M}_4}}
\end{aligned} \tag{Eq E-15}$$

The order 2 and 4 moments are developed in (Eq E-16) and (Eq E-17).

$$\begin{aligned}
\lim_{N_s \rightarrow +\infty} \widehat{M}_2 &= \mathbb{E}(I_P^2) + \mathbb{E}(Q_P^2) = \mathbb{V}(I_P^2) + \mathbb{E}(I_P)^2 + \mathbb{V}(Q_P)^2 \\
&= P_I + \frac{N_0}{4T_i} + \frac{C}{2} + P_Q + \frac{N_0}{4T_i} = \frac{C}{2} + 2\frac{N_0}{4T_i} + P_I + P_Q
\end{aligned} \tag{Eq E-16}$$

$$\lim_{N_s \rightarrow +\infty} \widehat{M}_4 = \mathbb{E}(I_P^4) + 2\mathbb{E}(I_P^2 Q_P^2) + \mathbb{E}(Q_P^4) \tag{Eq E-17}$$

Each component of (Eq E-17) is then computed in (Eq E-18), (Eq E-19) and (Eq E-20).

$$\mathbb{E}(I_P^4) = \left(\begin{aligned} & \frac{C^2}{4} + \mathbb{E}(I_{PPD}^4) + \mathbb{E}(n_I^4) \\ & + 4\mathbb{E} \left(\left(\frac{C}{2} \right)^{\frac{3}{2}} I_{PPD} + \left(\frac{C}{2} \right)^{\frac{3}{2}} n_I + \sqrt{\frac{C}{2}} I_{PPD}^3 + I_{PPD}^3 n_I + \sqrt{\frac{C}{2}} n_I^3 + I_{PPD} n_I^3 \right) \\ & + 6\mathbb{E} \left(\frac{C}{2} I_{PPD}^2 + \frac{C}{2} n_I^2 + I_{PPD}^2 n_I^2 \right) \\ & + 12\mathbb{E} \left(\frac{C}{2} I_{PPD} n_I + \sqrt{\frac{C}{2}} I_{PPD}^2 n_I + \sqrt{\frac{C}{2}} I_{PPD} n_I^2 \right) \end{aligned} \right) \quad (\text{Eq E-18})$$

$$= \frac{C^2}{4} + M_I^4 + 3 \left(\frac{N_0}{4T_i} \right)^2 + 3CP_I + 3C \frac{N_0}{4T_i} + 6P_I \frac{N_0}{4T_i}$$

$$\mathbb{E}(Q_P^4) = M_Q^4 + 3 \left(\frac{N_0}{4T_i} \right)^2 + 6P_Q \frac{N_0}{4T_i} \quad (\text{Eq E-19})$$

$$\begin{aligned} & \mathbb{E}(I_P^2 Q_P^2) \\ & = \mathbb{E} \left(\left(\frac{C}{2} + I_{PPD}^2 + n_I^2 + \sqrt{2C} I_{PPD} + \sqrt{2C} n_I + 2I_{PPD} n_I \right) (Q_{PPD}^2 + n_Q^2 + 2Q_{PPD} n_Q) \right) \\ & = \mathbb{E} \left(\begin{aligned} & \frac{C}{2} Q_{PPD}^2 + \frac{C}{2} n_Q^2 + C Q_{PPD} n_Q + I_{PPD}^2 Q_{PPD}^2 + I_{PPD}^2 n_Q^2 + 2I_{PPD}^2 Q_{PPD} n_Q + n_I^2 Q_{PPD}^2 \\ & + n_I^2 n_Q^2 + 2n_I^2 Q_{PPD} n_Q + \sqrt{(2C)} I_{PPD} Q_{PPD}^2 + \sqrt{2C} I_{PPD} n_Q^2 + 2\sqrt{2C} I_{PPD} Q_{PPD} n_Q \\ & + \sqrt{2C} n_I Q_{PPD}^2 \\ & + \sqrt{2C} n_I n_Q^2 + 2\sqrt{2C} n_I Q_{PPD} n_Q + 2I_{PPD} n_I Q_{PPD}^2 + 2I_{PPD} n_I n_Q^2 + 4I_{PPD} n_I Q_{PPD} n_Q \end{aligned} \right) \quad (\text{Eq E-20}) \\ & = \frac{C}{2} P_Q + \frac{C}{2} \frac{N_0}{4T_i} + P_I P_Q + P_I \frac{N_0}{4T_i} + P_Q \frac{N_0}{4T_i} + \left(\frac{N_0}{4T_i} \right)^2 \end{aligned}$$

Eventually, (Eq E-17) can be reduced to the result given by (Eq E-21).

$$\lim_{N_s \rightarrow +\infty} \widehat{M}_4 = \left(\begin{aligned} & \frac{C^2}{4} + M_I^4 + M_Q^4 + 8P_I \frac{N_0}{4T_i} + 8P_Q \frac{N_0}{4T_i} + \\ & 4C \frac{N_0}{4T_i} + 3CP_I + CP_Q + 2P_I P_Q + 8 \left(\frac{N_0}{4T_i} \right)^2 \end{aligned} \right) \quad (\text{Eq E-21})$$

The numerator of the moment estimator tends toward (Eq E-22).

$$\lim_{N_s \rightarrow +\infty} 2 \cdot \widehat{M}_2^2 - \widehat{M}_4 = \frac{C^2}{4} + 2P_I^2 + 2P_Q^2 - M_I^4 - M_Q^4 - CP_I + CP_Q + 2P_I P_Q \quad (\text{Eq E-22})$$

If the signal power at the correlator output is much higher than the noise and interference power at the correlator output, then the numerator can be simplified by (Eq E-23).

$$\lim_{N_s \rightarrow +\infty} \sqrt{2 \cdot \widehat{M}_2^2 - \widehat{M}_4} \approx \frac{C}{2} \quad (\text{Eq E-23})$$

In addition, the denominator can be reduced in (Eq E-24) using order 1 Taylor expansion.

$$\begin{aligned}
\lim_{N_s \rightarrow +\infty} \widehat{M}_2 - \sqrt{2\widehat{M}_2^2 - \widehat{M}_4} &= \frac{C}{2} + 2\frac{N_0}{4T_i} + P_I + P_Q \\
&- \frac{C}{2} \left(1 + 4\frac{P_I^2 + P_Q^2}{C^2} - 2\frac{M_I^4 + M_Q^4}{C^2} + 2\frac{P_Q - P_I}{C} + 4\frac{P_I P_Q}{C^2} \right) \\
&= 2\frac{N_0}{4T_i} + 2P_I - 2\frac{P_I P_Q}{C} - 2\frac{P_I^2 + P_Q^2}{C} + \frac{M_I^4 + M_Q^4}{C}
\end{aligned} \tag{Eq E-24}$$

Eventually, the moment estimator tends toward the result of (Eq E-25).

$$\lim_{N_s \rightarrow +\infty} C/\widehat{N}_{0,MM} = \frac{C}{N_0 + 4T_i P_I - 4T_i \frac{P_I P_Q}{C} - 4T_i \frac{P_I^2 + P_Q^2}{C} + 2T_i \frac{M_I^4 + M_Q^4}{C}} \tag{Eq E-25}$$

Assuming that:

- Chirp correlator outputs' distribution on the in-phase channel and quadrature phase channel are identic: $P_I = P_Q = \frac{I_0}{4T_i}$, and $M_I^4 = M_Q^4$,
- Chirp correlator output's distribution on the in-phase channel and quadrature phase channel are Gaussian: $M_I^4 = M_Q^4 = 3P_I^4 = 3\left(\frac{I_0}{4T_i}\right)^2$,

(Eq E-25) can be reduced to (Eq E-26).

$$\begin{aligned}
\lim_{N_s \rightarrow +\infty} C/\widehat{N}_{0,MM} &= \frac{C}{N_0 + I_0 - \frac{4T_i}{C} \left(\frac{I_0}{4T_i}\right)^2 - \frac{4T_i}{C} \left(\frac{I_0}{4T_i}\right)^2 - \frac{4T_i}{C} \left(\frac{I_0}{4T_i}\right)^2 + \frac{4T_i}{C} 3 \left(\frac{I_0}{4T_i}\right)^2} \\
&= \frac{C}{N_0 + I_0} = C/N_{0,eff}
\end{aligned} \tag{Eq E-26}$$

Appendix F: Fourier transform of chirp signal

The objective of this appendix is to derive the Fourier transform of function f_n expressed in (Eq 5-34).

By definition, the Fourier transform of signal f_n is given by (Eq F-1).

$$\begin{aligned}
 F_n(f) &= \int_{-\infty}^{+\infty} f_n(t) e^{-i2\pi f t} dt = \int_0^{T_{sweep}} \cos(\alpha t^2 + \beta t + \gamma_n) e^{-i2\pi f t} dt \\
 &= \frac{1}{2} \int_0^{T_{sweep}} e^{i(\alpha t^2 + (\beta - 2\pi f)t + \gamma_n)} dt + \frac{1}{2} \int_0^{T_{sweep}} e^{-i(\alpha t^2 + (\beta + 2\pi f)t + \gamma_n)} dt \\
 &= \frac{1}{2} Int_1 + \frac{1}{2} Int_2
 \end{aligned} \tag{Eq F-1}$$

$$Int_1 = \int_0^{T_{sweep}} e^{i(\alpha t^2 + (\beta - 2\pi f)t + \gamma_n)} dt \quad Int_2 = \int_0^{T_{sweep}} e^{-i(\alpha t^2 + (\beta + 2\pi f)t + \gamma_n)} dt$$

Analytical expression of Int_1 is developed below.

$$\begin{aligned}
 Int_1 &= \int_0^{T_{sweep}} e^{i(\alpha t^2 + (\beta - 2\pi f)t + \gamma_n)} dt = e^{i\gamma_n} \int_0^{T_{sweep}} e^{i\left(\sqrt{\alpha}t + \frac{\beta - 2\pi f}{2\sqrt{\alpha}}\right)^2 - \frac{i(\beta - 2\pi f)^2}{4\alpha}} dt \\
 &= e^{i\gamma_n - \frac{i(\beta - 2\pi f)^2}{4\alpha}} \int_0^{T_{sweep}} e^{i\left(\sqrt{\alpha}t + \frac{\beta - 2\pi f}{2\sqrt{\alpha}}\right)^2} dt
 \end{aligned} \tag{Eq F-2}$$

Making the change of variable $u = \sqrt{\frac{2}{\pi}}\left(\sqrt{\alpha}t + \frac{\beta - 2\pi f}{2\sqrt{\alpha}}\right)$ in (Eq F-2), Int_1 can be further developed in (Eq F-3).

$$Int_1 = \sqrt{\frac{\pi}{2\alpha}} e^{i\gamma_n - \frac{i(\beta - 2\pi f)^2}{4\alpha}} \int_{\frac{\beta - 2\pi f}{\sqrt{2\pi\alpha}}}^{\sqrt{\frac{2\alpha}{\pi}}T_{sweep} + \frac{\beta - 2\pi f}{\sqrt{2\pi\alpha}}} e^{i\frac{\pi}{2}u^2} du \tag{Eq F-3}$$

α and β are defined in (Eq 5-32) and their definition is reminded in (Eq F-4).

$$\alpha = \frac{\pi B}{T_{sweep}} \tag{Eq F-4}$$

$$\beta = 2\pi(\Delta f_J^c + f_{J,dopp} - \hat{f}_{D,k}) - \pi B = 2\pi(\Delta f_J + \varepsilon_f) - \pi B$$

Replacing α and β by their mathematical expressions of (Eq 5-32), (Eq F-3) can be re-expressed as in (Eq F-5).

$$Int_1 = \sqrt{\frac{T_{sweep}}{2B}} e^{i\gamma_n - \frac{iT_{sweep}(2\pi(\Delta f_J + \varepsilon_f) - \pi B)^2}{4\pi B}} \int_{\sqrt{\frac{2T_{sweep}}{B}}(\Delta f_J + \varepsilon_f - f) - \sqrt{\frac{BT_{sweep}}{2}}}^{\sqrt{\frac{2T_{sweep}}{B}}(\Delta f_J + \varepsilon_f - f) + \sqrt{\frac{BT_{sweep}}{2}}} e^{i\frac{\pi}{2}u^2} du \tag{Eq F-5}$$

$$= \sqrt{\frac{T_{sweep}}{2B}} e^{i\gamma_n - \frac{iT_{sweep}(2\pi(\Delta f_J + \varepsilon_f - f) - \pi B)^2}{4\pi B}} \begin{pmatrix} C\left(\sqrt{\frac{BT_{sweep}}{2}} + \sqrt{\frac{2T_{sweep}}{B}}(\Delta f_J + \varepsilon_f - f)\right) \\ +iS\left(\sqrt{\frac{BT_{sweep}}{2}} + \sqrt{\frac{2T_{sweep}}{B}}(\Delta f_J + \varepsilon_f - f)\right) \\ C\left(\sqrt{\frac{BT_{sweep}}{2}} - \sqrt{\frac{2T_{sweep}}{B}}(\Delta f_J + \varepsilon_f - f)\right) \\ +iS\left(\sqrt{\frac{BT_{sweep}}{2}} - \sqrt{\frac{2T_{sweep}}{B}}(\Delta f_J + \varepsilon_f - f)\right) \end{pmatrix}$$

C and S refer to Fresnel integral. They are defined in (Eq F-6).

$$C(t) = \int_0^t \cos\left(\frac{\pi}{2}u^2\right) du \quad S(t) = \int_0^t \sin\left(\frac{\pi}{2}u^2\right) du \quad (\text{Eq F-6})$$

The analytical expression of Int_2 can be computed following the same methodology, and the result is provided in (Eq F-7).

$$Int_2 = \sqrt{\frac{T_{sweep}}{2B}} e^{-i\gamma_n + \frac{iT_{sweep}(2\pi(\Delta f + \varepsilon_f + f) - \pi B)^2}{4\pi B}} \begin{pmatrix} C\left(\sqrt{\frac{BT_{sweep}}{2}} + \sqrt{\frac{2T_{sweep}}{B}}(\Delta f + \varepsilon_f + f)\right) \\ -iS\left(\sqrt{\frac{BT_{sweep}}{2}} + \sqrt{\frac{2T_{sweep}}{B}}(\Delta f + \varepsilon_f + f)\right) \\ C\left(\sqrt{\frac{BT_{sweep}}{2}} - \sqrt{\frac{2T_{sweep}}{B}}(\Delta f + \varepsilon_f + f)\right) \\ -iS\left(\sqrt{\frac{BT_{sweep}}{2}} - \sqrt{\frac{2T_{sweep}}{B}}(\Delta f + \varepsilon_f + f)\right) \end{pmatrix} \quad (\text{Eq F-7})$$

Eventually, the Fourier transform of f_n is deduced injecting (Eq F-5) and (Eq F-7) in (Eq F-1).

Appendix G: Laurent decomposition of GMSK signal

The objective of this appendix is to present the linear decomposition of continuous phase frequency shift keying (CPFSK) modulated signals. Laurent decomposition was introduced and demonstrated in [85].

From (Eq 3-6) and (Eq 3-8), the equivalent baseband unit power GMSK modulated C2Link signal can be expressed by (Eq G-1).

$$s_{BB}(t) = e^{i2\pi m_f \sum_{n=-\infty}^{+\infty} a_n \varphi(t-nT_s)} \quad (\text{Eq G-1})$$

The Laurent decomposition is based on (Eq G-2) result, since $a_n \in \{-1; 1\}$.

$$\begin{aligned} e^{i2\pi m_f a_n \varphi(t-nT_s)} &= \cos(2\pi m_f \varphi(t-nT_s)) + j a_n \sin(2\pi m_f \varphi(t-nT_s)) \\ &= \sin\left(\frac{\pi}{2} - 2\pi m_f \varphi(t-nT_s)\right) + j a_n \sin(2\pi m_f \varphi(t-nT_s)) \end{aligned} \quad (\text{Eq G-2})$$

Let us introduce the function ψ defined by (Eq G-3).

$$\psi(t) = \begin{cases} 2\pi m_f \varphi(t) & \text{if } t \leq L_{BT} T_s \\ \frac{\pi}{2} - 2\pi m_f \varphi(t - L_{BT} T_s) & \text{if } t \geq L_{BT} T_s \end{cases} \quad (\text{Eq G-3})$$

$L_{BT} = 5$ is the length of the support of the function q defined by $q(t) = \frac{1}{2T_s} \text{rect}_{T_s} * h(t)$, where h is the gaussian filter impulse response. For $BT=0.2$ as specified for C2Link signals, $L_{BT} = 5$. Function ψ is plotted in Figure G-1.

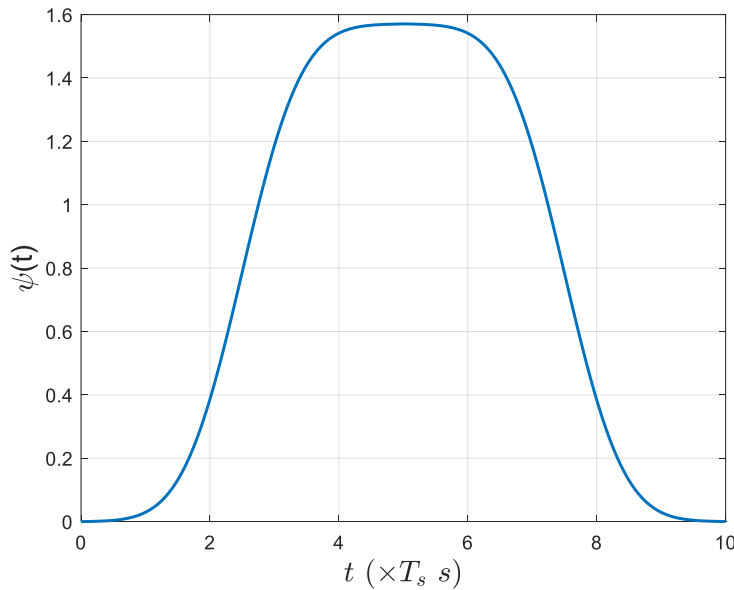


Figure G-1: Illustration of function ψ

Since $m_f = 1/2$ for GMSK signals, $\psi(t)$ is maximum at $t = L_{BT} T_s$ and is equal to $\pi/2$ since $\varphi(t) = 1/2$ for $t \geq L_{BT} T_s$. In addition, the support of ψ is $[0; 2L_{BT} T_s]$.

Then, let us introduce the family of functions $(S_n)_{n \in \mathbb{Z}}$ defined by (Eq G-4).

$$S_n(t) = \sin(\psi(t + nT_s)) = S_0(t + nT_s) \quad (\text{Eq G-4})$$

$e^{i2\pi m_f \varphi(t - nT_s)}$ can be expressed as a function of S_n . Indeed, (Eq G-2) and (Eq G-3) can be simplified considering results of (Eq G-5) and (Eq G-6). (Eq G-5) and (Eq G-6) have been obtained thanks to properties of ψ and φ .

- If $t - nT_s \leq L_{BT}T_s$, remarking that $\psi(t - nT_s) = \frac{\pi}{2} - \psi(L_{BT}T_s + t - nT_s)$.

$$\begin{aligned} \frac{\pi}{2} - 2\pi m_f \varphi(t - nT_s) &= \frac{\pi}{2} - \psi(t - nT_s) = \psi(L_{BT}T_s + t - nT_s) \\ \sin\left(\frac{\pi}{2} - 2\pi m_f \varphi(t - nT_s)\right) &= S_{L_{BT}-n}(t) \quad \sin\left(2\pi m_f \varphi(t - nT_s)\right) = S_{-n}(t) \end{aligned} \quad (\text{Eq G-5})$$

- If $L_{BT}T_s \leq t - nT_s$:

$$\begin{aligned} \frac{\pi}{2} - 2\pi m_f \varphi(t - nT_s) &= \frac{\pi}{2} - 2\pi m_f \varphi(t - (n - L_{BT})T_s - L_{BT}T_s) \\ &= \psi(t - (n - L_{BT})T_s) \\ \sin\left(\frac{\pi}{2} - 2\pi m_f \varphi(t - nT_s)\right) &= S_{L_{BT}-n}(t) \quad \sin\left(2\pi m_f \varphi(t - nT_s)\right) = S_{-n}(t) \end{aligned} \quad (\text{Eq G-6})$$

Injecting (Eq G-5) and (Eq G-6) in (Eq G-2) and (Eq G-3), $e^{i2\pi m_f \varphi(t - nT_s)}$ can be expressed as in (Eq G-7).

$$e^{i2\pi m_f a_n \varphi(t - nT_s)} = S_{L_{BT}-n}(t) + j^{a_n} S_{-n}(t) \quad (\text{Eq G-7})$$

Supposing that $t \in [NT_s, (N + 1)T_s]$, $2\pi m_f a_n \varphi(t - nT_s) = a_n \frac{\pi}{2}$ for $n \leq N - L_{BT}$. Replacing $e^{i2\pi m_f a_n \varphi(t - nT_s)}$ by its expression of (Eq G-7) in (Eq G-1), the equivalent baseband GMSK modulated signal can be expressed by (Eq G-8).

$$\begin{aligned} s_{BB}(t) &= e^{i\frac{\pi}{2} \sum_{n=-\infty}^{N-L} a_n} \prod_{n=N-L_{BT}+1}^{N-L} e^{i2\pi m_f a_n \varphi(t - nT_s)} \\ &= e^{i\frac{\pi}{2} \sum_{n=-\infty}^{N-L} a_n} \prod_{n=N-L_{BT}+1}^N \left(S_{L_{BT}-n}(t) + j^{a_n} S_{-n}(t) \right) \end{aligned} \quad (\text{Eq G-8})$$

Making the change of variable $n' = N - n$, (Eq G-8) can be rewritten as in (Eq G-9).

$$\begin{aligned} s_{BB}(t) &= e^{i\frac{\pi}{2} \sum_{n=-\infty}^{N-L} a_n} \prod_{n=0}^{L_{BT}-1} \left(S_{n-(N-L_{BT})}(t) + j^{a_{N-n}} S_{n-N}(t) \right) \\ &= e^{i\frac{\pi}{2} \sum_{n=-\infty}^{N-L} a_n} \prod_{n=0}^{L_{BT}-1} \left(S_0(t + (n + L_{BT} - N)T_s) \right. \\ &\quad \left. + j^{a_{N-n}} S_0(t + (n - N)T_s) \right) \end{aligned} \quad (\text{Eq G-9})$$

Remember that $L_{BT} = 5$ for a BT product of 0.2. (Eq G-9) can therefore be re-expressed as in (Eq G-10).

$$s_{BB}(t) = e^{i\frac{\pi}{2}\sum_{n=-L}^{N-L} a_n} \begin{bmatrix} (S_0(t - (N - 5)T_s) + j^{a_N}S_0(t - NT_s)) \\ (S_0(t - (N - 6)T_s) + j^{a_{N-1}}S_0(t - (N - 1)T_s)) \\ (S_0(t - (N - 7)T_s) + j^{a_{N-2}}S_0(t - (N - 2)T_s)) \\ (S_0(t - (N - 8)T_s) + j^{a_{N-3}}S_0(t - (N - 3)T_s)) \\ (S_0(t - (N - 9)T_s) + j^{a_{N-4}}S_0(t - (N - 4)T_s)) \end{bmatrix} \quad (\text{Eq G-10})$$

Developing the product term in (Eq G-10), it appears that s_{BB} is a function of pulse function C_i defined in (Eq G-11) and their shifted versions $C_i(t - NT_s)$.

$$\begin{aligned} C_0(t) &= S_0(t)S_0(t + T_s)S_0(t + 2T_s)S_0(t + 3T_s)S_0(t + 4T_s) \\ C_1(t) &= S_0(t)S_0(t + 2T_s)S_0(t + 3T_s)S_0(t + 4T_s)S_0(t + 6T_s) \\ C_2(t) &= S_0(t)S_0(t + T_s)S_0(t + 3T_s)S_0(t + 4T_s)S_0(t + 7T_s) \\ C_3(t) &= S_0(t)S_0(t + 3T_s)S_0(t + 4T_s)S_0(t + 6T_s)S_0(t + 7T_s) \end{aligned} \quad (\text{Eq G-11})$$

...

Pulses C_i are represented in Figure 6-2.

For simplicity, only pulses C_0, C_1, C_2 and C_3 are considered in the rest of the derivation, even though s_{BB} is in reality a function of $2^{L_{BT}-1} = 16$ pulses. The rationale for this assumption is that the amplitude of pulses $(C_i)_{i \in \llbracket 4; 15 \rrbracket}$ is very low compared to the amplitude of C_0 . Considering that the support of S_0 is $[0; 2L_{BT}T_s]$, the supports of C_0, C_1, C_2 and C_3 are respectively $[0; (L_{BT} + 1)T_s]$, $[0; (L_{BT} - 1)T_s]$, $[0, (L_{BT} - 2)T_s]$ and $[0, (L_{BT} - 2)T_s]$. Neglecting the contribution of $(C_i)_{i \in \llbracket 4; 15 \rrbracket}$ and developing all terms, the GMSK signal at baseband can be approximated by (Eq G-12).

$$\begin{aligned} s_{BB}(t) &= \sum_{n=-\infty}^{+\infty} \alpha_{0,n}C_0(t - nT_s) + \alpha_{1,n}C_1(t - nT_s) + \alpha_{2,n}C_2(t - nT_s) + \alpha_{3,n}C_3(t - nT_s) \\ \alpha_{0,n} &= e^{i\frac{\pi}{2}\sum_{k=-\infty}^n a_k} & \alpha_{1,n} &= e^{i\frac{\pi}{2}(\sum_{k=-\infty}^n a_k - a_{n-1})} \\ \alpha_{2,n} &= e^{i\frac{\pi}{2}(\sum_{k=-\infty}^n a_k - a_{n-2})} & \alpha_{3,n} &= e^{i\frac{\pi}{2}(\sum_{k=-\infty}^n a_k - a_{n-1} - a_{n-2})} \end{aligned} \quad (\text{Eq G-12})$$

Appendix H: GMSK local replica derivation

The objective of this Appendix is to write the GMSK local replica introduced in (Eq 6-18) under the form of (Eq 6-21).

Considering only two Laurent pulses, the local replica is given by (Eq H-1).

$$s_L(\hat{t}, \hat{\theta}, \hat{\mathbf{a}}) = e^{i\hat{\theta}} \sum_{n=k_0}^{k_0+K_b} \hat{\alpha}_{0,n} C_0(t - \hat{t} - nT_s) + \hat{\alpha}_{1,n} C_1(t - \hat{t} - nT_s) \quad (\text{Eq H-1})$$

$$\hat{\alpha}_{0,n} = e^{i\frac{\pi}{2} \sum_{k=-\infty}^n \hat{a}_k} \quad \hat{\alpha}_{1,n} = e^{i\frac{\pi}{2} (\sum_{k=-\infty}^n \hat{a}_k - \hat{a}_{n-1})}$$

$\hat{\alpha}_{1,n}$ can be written as a function of $\hat{\alpha}_{0,n}$, $\hat{\alpha}_{0,n-1}$ and $\hat{\alpha}_{0,n-2}$. Indeed,

$$\hat{\alpha}_{1,n} = e^{-i\frac{\pi}{2} \hat{a}_{n-1}} \hat{\alpha}_{0,n} = -j \hat{\alpha}_{n-1} \hat{\alpha}_{0,n} \quad (\text{Eq H-2})$$

In addition, $\hat{\alpha}_{n-1}$ can be expressed as a function of $\hat{\alpha}_{0,n-1}$ and $\hat{\alpha}_{0,n-2}$ as demonstrated in (Eq H-3).

$$\hat{\alpha}_{0,n-1} \hat{\alpha}_{0,n-2} = e^{i\frac{\pi}{2} \sum_{k=-\infty}^{n-1} \hat{a}_k} e^{i\frac{\pi}{2} \sum_{k=-\infty}^{n-2} \hat{a}_k} = \prod_{k=-\infty}^{n-1} (j \hat{a}_k) \prod_{k=-\infty}^{n-2} (j \hat{a}_k) \quad (\text{Eq H-3})$$

$$= j \hat{\alpha}_{n-1} \prod_{k=-\infty}^{n-2} (j \hat{a}_k)^2$$

For simplicity, let us assume that $\prod_{k=-\infty}^1 (j \hat{a}_k)^2 = 1$, or equivalently $\sum_{k=-\infty}^1 \hat{a}_k \in 4\mathbb{Z}$. Under this assumption, (Eq H-3) can be re-expressed as in (Eq H-4).

$$\hat{\alpha}_{0,n-1} \hat{\alpha}_{0,n-2} = j \hat{\alpha}_{n-1} j^{2(n-2)} = (-1)^n j \hat{\alpha}_{n-1} = \begin{cases} -j \hat{\alpha}_{n-1} & \text{if } n \text{ is even} \\ j \hat{\alpha}_{n-1} & \text{if } n \text{ is odd} \end{cases} \quad (\text{Eq H-4})$$

Injecting (Eq H-4) into (Eq H-2), $\hat{\alpha}_{1,n}$ is eventually expressed as a function of $\hat{\alpha}_{0,n}$, $\hat{\alpha}_{0,n-1}$ and $\hat{\alpha}_{0,n-2}$ in (Eq H-5).

$$\hat{\alpha}_{1,n} = \begin{cases} \hat{\alpha}_{0,n} \hat{\alpha}_{0,n-1} \hat{\alpha}_{0,n-2} & \text{if } n \text{ is even} \\ -\hat{\alpha}_{0,n} \hat{\alpha}_{0,n-1} \hat{\alpha}_{0,n-2} & \text{if } n \text{ is odd} \end{cases} \quad (\text{Eq H-5})$$

Thus, the GMSK local replica expression of (Eq H-1) can be developed in (Eq H-6).

$$s_L(t, \hat{t}, \hat{\theta}, \hat{\mathbf{a}}) = e^{i\hat{\theta}} \sum_{k_0 \leq 2k < 2k+1 \leq k_0+K_b} \left[\hat{\alpha}_{0,2k+1} C_0(t - (2k+1)T_s) + \hat{\alpha}_{0,2k} \hat{\alpha}_{0,2k-1} \hat{\alpha}_{0,2k-2} C_1(t - 2kT_s) \right] + \hat{\alpha}_{0,2k} C_0(t - 2kT_s) - \hat{\alpha}_{0,2k+1} \hat{\alpha}_{0,2k} \hat{\alpha}_{0,2k-1} C_1(t - (2k+1)T_s) \quad (\text{Eq H-6})$$

The result of (Eq H-6) is then used in Chapter 6 to further develop the likelihood function.

Appendix I: Derivative of GMSK log-likelihood function with respect to $\hat{\theta}$

The objective of this appendix is to compute the derivative of the GMSK log likelihood function given in (Eq 6-33) with respect to $\hat{\theta}$. Under low SNR assumption, the log likelihood is given by (Eq I-1).

$$\Lambda_L(\hat{\tau}, \hat{\theta}) = \sum_{\substack{k_0 \leq 2k < 2k+1 \leq k_0+K_b \\ (k_0+K_b)T_s}} \left[\begin{aligned} &Re\{R_{0,2k+1}(\hat{\tau}, \hat{\theta})\}^2 + Re\{R_{1,2k}(\hat{\tau}, \hat{\theta})\}^2 \\ &+ Im\{R_{0,2k}(\hat{\tau}, \hat{\theta})\}^2 + Im\{R_{1,2k+1}(\hat{\tau}, \hat{\theta})\}^2 \end{aligned} \right]$$

$$R_{0,x}(\hat{\tau}, \hat{\theta}) = \int_{\substack{k_0 T_s \\ (k_0+K_b)T_s}}^{k_0 T_s} y(t) e^{-i\hat{\theta}} C_0(t - \hat{\tau} - xT_s) dt \quad (\text{Eq I-1})$$

$$R_{1,x}(\hat{\tau}, \hat{\theta}) = \int_{k_0 T_s} y(t) e^{-i\hat{\theta}} C_1(t - \hat{\tau} - xT_s) dt$$

In addition, in absence of noise, the received equivalent baseband signal $y(t)$ can be expressed as in (Eq I-2).

$$y(t) = \sqrt{2C_{Rx}} e^{i\theta} s_{GMSK}(t - \tau) \quad (\text{Eq I-2})$$

C_{Rx} is the power of the real GMSK signal at receiver RFFE output, θ is the phase introduced by the propagation channel, τ is the delay introduced by the propagation channel and s_{GMSK} is the equivalent baseband unit power transmitted GMSK signal.

The log-likelihood function of (Eq I-1) therefore be re-written as in (Eq I-3).

$$\Lambda_L(\hat{\tau}, \hat{\theta}) = 2C_{Rx} \sum_{\substack{k_0 \leq 2k < 2k+1 \leq k_0+K_b \\ (k_0+K_b)T_s}} \left[\begin{aligned} &Re\{e^{i(\theta-\hat{\theta})} R_{0,2k+1}^T(\hat{\tau})\}^2 + Re\{e^{i(\theta-\hat{\theta})} R_{1,2k}^T(\hat{\tau})\}^2 \\ &+ Im\{e^{i(\theta-\hat{\theta})} R_{0,2k}^T(\hat{\tau})\}^2 + Im\{e^{i(\theta-\hat{\theta})} R_{1,2k+1}^T(\hat{\tau})\}^2 \end{aligned} \right]$$

$$R_{0,x}^T(\hat{\tau}) = \int_{\substack{k_0 T_s \\ (k_0+K_b)T_s}}^{k_0 T_s} s_{GMSK}(t - \tau) e^{-i\hat{\theta}} C_0(t - \hat{\tau} - xT_s) dt \quad (\text{Eq I-3})$$

$$R_{1,x}^T(\hat{\tau}) = \int_{k_0 T_s} s_{GMSK}(t - \tau) e^{-i\hat{\theta}} C_1(t - \hat{\tau} - xT_s) dt$$

The derivative of $Re\{e^{i(\theta-\hat{\theta})} R_{0,k}^T(\hat{\tau})\}^2$ with respect to $\hat{\theta}$ is computed in (Eq I-4), remarking that $R_{0,k}^T(\hat{\tau})$ does not depend on $\hat{\theta}$ and that $R_{0,k}^T(\hat{\tau})$ and $R_{1,k}^T(\hat{\tau})$ are complex.

$$\begin{aligned}
\frac{d}{d\hat{\theta}} \operatorname{Re}\{e^{i(\theta-\hat{\theta})} R_{0,k}^T(\hat{t})\}^2 &= 2\operatorname{Re}\{e^{i(\theta-\hat{\theta})} R_{0,k}^T(\hat{t})\} \frac{d}{d\hat{\theta}} \left(\operatorname{Re}\{e^{i(\theta-\hat{\theta})} R_{0,k}^T(\hat{t})\} \right) \\
&= 2\operatorname{Re}\{e^{i(\theta-\hat{\theta})} R_{0,k}^T(\hat{t})\} \frac{d}{d\hat{\theta}} \left(\frac{e^{i(\theta-\hat{\theta})} R_{0,k}^T(\hat{t}) + e^{-i(\theta-\hat{\theta})} R_{0,k}^{T*}(\hat{t})}{2} \right) \\
&= 2\operatorname{Re}\{e^{i(\theta-\hat{\theta})} R_{0,k}^T(\hat{t})\} \frac{-ie^{i(\theta-\hat{\theta})} R_{0,k}^T(\hat{t}) + ie^{-i(\theta-\hat{\theta})} R_{0,k}^{T*}(\hat{t})}{2} \\
&= 2\operatorname{Re}\{e^{i(\theta-\hat{\theta})} R_{0,k}^T(\hat{t})\} \frac{e^{i(\theta-\hat{\theta})} R_{0,k}^T(\hat{t}) - e^{-i(\theta-\hat{\theta})} R_{0,k}^{T*}(\hat{t})}{2i} \\
&= 2\operatorname{Re}\{e^{i(\theta-\hat{\theta})} R_{0,k}^T(\hat{t})\} \operatorname{Im}\{e^{i(\theta-\hat{\theta})} R_{0,k}^T(\hat{t})\}
\end{aligned} \tag{Eq I-4}$$

Similarly, the derivation of $\operatorname{Im}\{e^{i(\theta-\hat{\theta})} R_{0,k}^T(\hat{t})\}^2$ is presented in (Eq I-5).

$$\begin{aligned}
\frac{d}{d\hat{\theta}} \operatorname{Im}\{e^{i(\theta-\hat{\theta})} R_{0,k}^T(\hat{t})\}^2 &= 2\operatorname{Im}\{e^{i(\theta-\hat{\theta})} R_{0,k}^T(\hat{t})\} \frac{d}{d\hat{\theta}} \left(\operatorname{Im}\{e^{i(\theta-\hat{\theta})} R_{0,k}^T(\hat{t})\} \right) \\
&= 2\operatorname{Im}\{e^{i(\theta-\hat{\theta})} R_{0,k}^T(\hat{t})\} \frac{d}{d\hat{\theta}} \left(\frac{e^{i(\theta-\hat{\theta})} R_{0,k}^T(\hat{t}) - e^{-i(\theta-\hat{\theta})} R_{0,k}^{T*}(\hat{t})}{2i} \right) \\
&= 2\operatorname{Im}\{e^{i(\theta-\hat{\theta})} R_{0,k}^T(\hat{t})\} \frac{-ie^{i(\theta-\hat{\theta})} R_{0,k}^T(\hat{t}) - ie^{-i(\theta-\hat{\theta})} R_{0,k}^{T*}(\hat{t})}{2i} \\
&= -2\operatorname{Im}\{e^{i(\theta-\hat{\theta})} R_{0,k}^T(\hat{t})\} \frac{e^{i(\theta-\hat{\theta})} R_{0,k}^T(\hat{t}) + e^{-i(\theta-\hat{\theta})} R_{0,k}^{T*}(\hat{t})}{2} \\
&= -2\operatorname{Re}\{e^{i(\theta-\hat{\theta})} R_{0,k}^T(\hat{t})\} \operatorname{Im}\{e^{i(\theta-\hat{\theta})} R_{0,k}^T(\hat{t})\}
\end{aligned} \tag{Eq I-5}$$

The derivation of $\operatorname{Re}\{e^{i(\theta-\hat{\theta})} R_{1,k}^T(\hat{t})\}^2$ and $\operatorname{Im}\{e^{i(\theta-\hat{\theta})} R_{1,k}^T(\hat{t})\}^2$ are computed in a similar way.

Eventually, the derivative of the log-likelihood with respect to $\hat{\theta}$ is given by (Eq I-6).

$$\begin{aligned}
\frac{d\Lambda(\hat{t}, \hat{\theta})}{d\hat{\theta}} &= 4C_{Rx} \sum_{k_0 \leq 2k < 2k+1 \leq k_0 + K_b} \left[\begin{aligned} &\operatorname{Re}\{e^{i(\theta-\hat{\theta})} R_{0,2k+1}^T(\hat{t})\} \operatorname{Im}\{e^{i(\theta-\hat{\theta})} R_{0,2k+1}^T(\hat{t})\} + \\ &\operatorname{Re}\{e^{i(\theta-\hat{\theta})} R_{1,2k}^T(\hat{t})\} \operatorname{Im}\{e^{i(\theta-\hat{\theta})} R_{1,2k}^T(\hat{t})\} - \\ &\operatorname{Re}\{e^{i(\theta-\hat{\theta})} R_{0,2k}^T(\hat{t})\} \operatorname{Im}\{e^{i(\theta-\hat{\theta})} R_{0,2k}^T(\hat{t})\} - \\ &\operatorname{Re}\{e^{i(\theta-\hat{\theta})} R_{1,2k+1}^T(\hat{t})\} \operatorname{Im}\{e^{i(\theta-\hat{\theta})} R_{1,2k+1}^T(\hat{t})\} \end{aligned} \right] \\
&= 2 \sum_{k_0 \leq 2k < 2k+1 \leq k_0 + K_b} \left[\begin{aligned} &\operatorname{Re}\{R_{0,2k+1}(\hat{t}, \hat{\theta})\} \operatorname{Im}\{R_{0,2k+1}(\hat{t}, \hat{\theta})\} + \\ &\operatorname{Re}\{R_{1,2k}(\hat{t}, \hat{\theta})\} \operatorname{Im}\{R_{1,2k}(\hat{t}, \hat{\theta})\} - \\ &\operatorname{Re}\{R_{0,2k}(\hat{t}, \hat{\theta})\} \operatorname{Im}\{R_{0,2k}(\hat{t}, \hat{\theta})\} - \\ &\operatorname{Re}\{R_{1,2k+1}(\hat{t}, \hat{\theta})\} \operatorname{Im}\{R_{1,2k+1}(\hat{t}, \hat{\theta})\} \end{aligned} \right]
\end{aligned} \tag{Eq I-6}$$

Appendix J: GMSK receiver phase discriminator

The objective of this appendix is to propose a normalization of the GMSK C2Link phase discriminator presented in (Eq 6-38). This appendix consists in two parts. First, it analyzes the noise free response of the non-normalized phase discriminator as a function of ε_θ , under the assumptions that K_b is sufficiently high, and that transmitted symbols a_k , and thus Laurent symbols $\alpha_{0,k}$ and $\alpha_{1,k}$, are independent, uncorrelated, and identically distributed. Second, it develops the normalization factor of (Eq 6-45) in order to prove that the normalized discriminator of (Eq 6-46) is equal to ε_θ in the linearity region.

J-1 Development of noise free non-normalized discriminator

The noise free discriminator is reminded in (Eq J-1).

$$\begin{aligned}
 D_\theta(\hat{\theta}) &= \sum_{k=k_0}^{k_0+K_b} (-1)^{k+1} [Im\{R_{0,k}^2(\hat{t}, \hat{\theta})\} - Im\{R_{1,k}^2(\hat{t}, \hat{\theta})\}] \\
 R_{0,k}(\hat{\theta}) &= \sqrt{\frac{2E_b}{T_s}} e^{i\varepsilon_\theta} \sum_{n=k-5}^{k+5} \alpha_{0,n} K_{C_0}((k-n)T_s - \varepsilon_\tau) + \alpha_{1,n} K_{C_1 C_0}((k-n)T_s - \varepsilon_\tau) \\
 R_{1,k}(\hat{\theta}) &= \sqrt{\frac{2E_b}{T_s}} e^{i\varepsilon_\theta} \sum_{n=k-5}^{k+5} \alpha_{0,n} K_{C_1 C_0}((n-k)T_s + \varepsilon_\tau) + \alpha_{1,n} K_{C_1}((k-n)T_s - \varepsilon_\tau)
 \end{aligned} \tag{Eq J-1}$$

The development of $R_{0,k}(\hat{\theta})^2$ is done in (Eq J-2), supposing a negligible delay tracking error $\varepsilon_\tau = 0$.

$$\begin{aligned}
 R_{0,k}^2(\hat{\theta}) &= \frac{2E_b}{T_s} e^{2i\varepsilon_\theta} \left[\sum_{n=k-5}^{k+5} \alpha_{0,n} K_{C_0}((k-n)T_s) + \alpha_{1,n} K_{C_1 C_0}((k-n)T_s) \right]^2 \\
 &= \frac{2E_b}{T_s} e^{2i\varepsilon_\theta} \left[\begin{aligned}
 &\sum_{n=k-5}^{k+5} \alpha_{0,n}^2 K_{C_0}^2((k-n)T_s) + \alpha_{1,n}^2 K_{C_1 C_0}^2((k-n)T_s) + \\
 &\sum_{n=k-5}^{k+5} \sum_{\substack{n'=k-5 \\ n' \neq n}}^{k+5} \alpha_{0,n} \alpha_{0,n'} K_{C_0}((k-n)T_s) K_{C_0}((k-n')T_s) + \\
 &\sum_{n=k-5}^{k+5} \sum_{\substack{n'=k-5 \\ n' \neq n}}^{k+5} \alpha_{1,n} \alpha_{1,n'} K_{C_1 C_0}((k-n)T_s) K_{C_1 C_0}((k-n')T_s) + \\
 &2 \sum_{n=k-5}^{k+5} \sum_{n'=k-5}^{k+5} \alpha_{0,n} \alpha_{1,n'} K_{C_0}((k-n)T_s) K_{C_1 C_0}((k-n')T_s)
 \end{aligned} \right]
 \end{aligned} \tag{Eq J-2}$$

Since $\alpha_{0,n}, \alpha_{1,n} \in \{\pm 1; \pm j\}$, then $\alpha_{0,n}^2, \alpha_{1,n}^2 \in \mathbb{R}$. The contribution of the green term of (Eq J-2) in the total discriminator (Eq J-1) is developed in (Eq J-3), knowing that K_{C_0} is even.

$$\begin{aligned}
& \sum_{k=k_0}^{k_0+K_b} (-1)^{k+1} \sum_{n=k-5}^{k+5} \sum_{\substack{n'=k-5 \\ n' \neq n}}^{k+5} \alpha_{0,n} \alpha_{0,n'} K_{C_0}((k-n)T_s) K_{C_0}((k-n')T_s) \\
&= \sum_{k=k_0}^{k_0+K_b} (-1)^{k+1} \sum_{z=-5}^5 \sum_{\substack{z'=5 \\ z' \neq n}}^5 \alpha_{0,k-z} \alpha_{0,k-z'} K_{C_0}(|z|T_s) K_{C_0}(|z'|T_s) = \\
& \begin{cases} k = k_0 \\ k = k_0 + 1 \end{cases} \left[\begin{aligned} & 2(-1)^{k_0+1} \alpha_{0,k_0-5} K_{C_0}(5T_s) [\alpha_{0,k_0-4} K_{C_0}(4T_s) + \dots + \alpha_{0,k_0+5} K_{C_0}(5T_s)] + \\ & 2(-1)^{k_0+1} \alpha_{0,k_0-4} K_{C_0}(4T_s) [\alpha_{0,k_0-5} K_{C_0}(5T_s) + \dots + \alpha_{0,k_0+5} K_{C_0}(5T_s)] + \\ & \dots + \\ & 2(-1)^{k_0+2} \alpha_{0,k_0+1-5} K_{C_0}(5T_s) [\alpha_{0,k_0+1-4} K_{C_0}(4T_s) + \dots + \alpha_{0,k_0+1+5} K_{C_0}(5T_s)] + \\ & 2(-1)^{k_0+2} \alpha_{0,k_0+1-5} K_{C_0}(4T_s) [\alpha_{0,k_0+1-5} K_{C_0}(5T_s) + \dots + \alpha_{0,k_0+1+5} K_{C_0}(5T_s)] + \\ & \dots \end{aligned} \right] \\
& \quad k > k_0 + 1 \left[+ \dots \right]
\end{aligned} \tag{Eq J-3}$$

Now, let us focus on the multiplication term between $K_{C_0}(5T_s)$ and $K_{C_0}(4T_s)$ (in violet), called $P_{4,5}$. Supposing K_b high enough, and considering that $(\alpha_{0,n})$ are uncorrelated, $P_{4,5}$ is simplified in (Eq J-4).

$$P_{4,5} = 2K_{C_0}(5T_s)K_{C_0}(4T_s) \sum_{k=k_0}^{k_0+K_b} (-1)^{k+1} \alpha_{0,k-5} (\alpha_{0,k-4} + \alpha_{0,k+4}) \underset{K_b \text{ high}}{\ll} K_b \tag{Eq J-4}$$

A similar reasoning can be done for other terms of (Eq J-3), therefore, the contribution of the green term of (Eq J-2) to the discriminator is null. Likewise, other double sums of (Eq J-2) are negligible in the noiseless non-normalized discriminator output, provided that K_b is high enough.

A similar development of $R_{1,k}^2(\hat{\theta})$ can be done. Eventually, (Eq J-1) can be approximated by (Eq J-5).

$$D_{\theta}(\hat{\theta}) = \frac{2E_b}{T_s} \sum_{k=k_0}^{k_0+K_b} (-1)^{k+1} \text{Im} \left\{ e^{2i\varepsilon\theta} \sum_{z=-5}^5 \left[\alpha_{0,k-z}^2 K_{C_0}^2(zT_s) + \alpha_{1,k-z}^2 K_{C_1 C_0}^2(zT_s) \right] \right\} \tag{Eq J-5}$$

In addition, let us now develop coefficients $\alpha_{0,k-z}^2$ and $\alpha_{1,k-z}^2$ which are real because $\alpha_{0,n}, \alpha_{1,n} \in \{\pm 1; \pm j\}$. The calculation is performed in (Eq J-6), considering that symbols $(a_i) \in \{\pm 1\}$, and the initial condition of Appendix H ($\sum_{k=-\infty}^{-1} a_k \in 4\mathbb{Z}$).

$$\begin{aligned}
\alpha_{0,k-z}^2 &= \left(\prod_{i=-\infty}^{k-z} ja_i \right)^2 = \left(\prod_{i=0}^{k-z} ja_i \right)^2 = j^{2(k-z+1)} \left(\prod_{i=0}^{k-z} a_i \right)^2 = (-1)^{k-z+1} \\
\alpha_{1,k-z}^2 &= (ja_{k-z})^2 \left(\prod_{i=-\infty}^{k-z-2} ja_i \right)^2 = -\alpha_{0,k-z-2}^2 = (-1)^{k-z}
\end{aligned} \tag{Eq J-6}$$

Injecting (Eq J-6) in (Eq J-5), $D_{\theta}(\hat{\theta})$ can be simplified by (Eq J-7). Indeed, the sum term in the $\text{Im}\{\}$ operator in (Eq J-5) is real and $(-1)^{k+1} \alpha_{0,k-z}^2 = (-1)^z$ and $(-1)^{k+1} \alpha_{1,k-z}^2 = (-1)^{z+1}$.

$$D_{\theta}(\hat{\theta}) = \frac{2E_b}{T_s} \sin(2\varepsilon\theta) \sum_{k=k_0}^{k_0+K_b} \sum_{z=-5}^5 (-1)^z K_{C_0}^2(zT_s) + 2(-1)^{z+1} K_{C_1 C_0}^2(zT_s) + (-1)^z K_{C_1}^2(zT_s) \tag{Eq J-7}$$

Denoting $C_{\theta} = \sum_{k=k_0}^{k_0+K_b} \sum_{z=-5}^5 (-1)^z K_{C_0}^2(zT_s) + (-1)^{z+1} K_{C_1 C_0}^2(zT_s) + (-1)^z K_{C_1}^2(zT_s)$, (Eq J-7) can eventually be simplified by (Eq J-8).

$$D_{\theta}(\hat{\theta}) = \frac{2E_b}{T_s} (K_b + 1) C_{\theta} \sin(2\varepsilon_{\theta}) \quad (\text{Eq J-8})$$

J-2 Normalization of the phase discriminator

The equality of (Eq J-9) can be deduced from (Eq J-5):

$$\left| \sum_{k=k_0}^{k_0+K_b} (-1)^{k+1} [R_{0,k}^2(\hat{t}, \hat{\theta}) - R_{1,k}^2(\hat{t}, \hat{\theta})] \right|^2 = \frac{2E_b}{T_s} C_{\theta} (K_b + 1) \quad (\text{Eq J-9})$$

Therefore, a potential normalized phase discriminator is given by (Eq J-10).

$$\bar{D}_{\theta}(\hat{\theta}) = \frac{D_{\theta}(\hat{\theta})}{2 \left| \sum_{k=k_0}^{k_0+K_b} (-1)^{k+1} [R_{0,k}^2(\hat{t}, \hat{\theta}) - R_{1,k}^2(\hat{t}, \hat{\theta})] \right|^2} = \frac{\sin(2\varepsilon_{\theta})}{2} \xrightarrow[\text{region}]{\text{linearity}} \varepsilon_{\theta} \quad (\text{Eq J-10})$$

Appendix K: GMSK delay discriminator

The objective of this appendix is to propose a normalization of the GMSK C2Link delay discriminator presented in (Eq 6-52). This appendix is made of two parts. First, it analyzes the noiseless response of the non-normalized phase discriminator as a function of ε_τ , under the assumptions that K_b is sufficiently high, and that transmitted symbols are independent, uncorrelated, and identically distributed. Second, it develops the normalization factor of (Eq 6-55) in order to prove that the normalized discriminator of (Eq 6-57) is equal to ε_τ in the linearity region.

K-1 Noise free delay discriminator

Delay discriminator definition

The noise free delay discriminator is reminded in (Eq K-1).

$$D_\tau(\hat{t}) = \frac{1}{2\Delta T} \sum_{\substack{k=k_0 \\ k \text{ even}}}^{K_b} \left[\text{Re}\{R_{1,k}^P(\hat{t}, \hat{\theta})\}(\text{Re}\{R_{1,k}^L(\hat{t}, \hat{\theta})\} - \text{Re}\{R_{1,k}^E(\hat{t}, \hat{\theta})\}) \right. \\ \left. + \text{Im}\{R_{0,k}^P(\hat{t}, \hat{\theta})\}(\text{Im}\{R_{0,k}^L(\hat{t}, \hat{\theta})\} - \text{Im}\{R_{0,k}^E(\hat{t}, \hat{\theta})\}) \right] \\ + \frac{1}{2\Delta T} \sum_{\substack{k=k_0 \\ k \text{ odd}}}^{K_b} \left[\text{Re}\{R_{0,k}^P(\hat{t}, \hat{\theta})\}(\text{Re}\{R_{0,k}^L(\hat{t}, \hat{\theta})\} - \text{Re}\{R_{0,k}^E(\hat{t}, \hat{\theta})\}) \right. \\ \left. + \text{Im}\{R_{1,k}^P(\hat{t}, \hat{\theta})\}(\text{Im}\{R_{1,k}^L(\hat{t}, \hat{\theta})\} - \text{Im}\{R_{1,k}^E(\hat{t}, \hat{\theta})\}) \right] \\ R_{0,k}^X(\hat{t}, \hat{\theta}) = \sqrt{\frac{2E_b}{T_s}} e^{i\varepsilon_\theta} \tilde{R}_{0,k}^X(\hat{t}) \quad R_{1,k}^X(\hat{t}, \hat{\theta}) = \sqrt{\frac{2E_b}{T_s}} e^{i\varepsilon_\theta} \tilde{R}_{1,k}^X(\hat{t}) \quad (\text{Eq K-1})$$

$$\tilde{R}_{0,k}^X(\hat{t}) = \sum_{z=-5}^5 \alpha_{0,k-z} K_{C_0}(zT_s - \varepsilon_\tau + \beta_X \Delta T) + \alpha_{1,k-z} K_{C_1 C_0}(zT_s - \varepsilon_\tau + \beta_X \Delta T) \\ \tilde{R}_{1,k}^X(\hat{t}) = \sum_{z=-5}^5 \alpha_{0,k-z} K_{C_1 C_0}(-zT_s + \varepsilon_\tau - \beta_X \Delta T) + \alpha_{1,k-z} K_{C_1}(zT_s - \varepsilon_\tau + \beta_X \Delta T)$$

$X \in \{P, E, L\}$. $\beta_X = -1$ if $X = E$; $\beta_X = 0$ if $X = P$ and $\beta_X = 1$ if $X = L$.

Matched filter output real and imaginary parts

Real part and imaginary part of $R_{0,k}^X(\hat{t}, \hat{\theta})$ and $R_{1,k}^X(\hat{t}, \hat{\theta})$, $X \in \{P, L, E\}$, are given by (Eq 6-52) to (Eq 6-57).

The discriminator defined in (Eq K-1) is developed.

The real parts and imaginary parts of $R_{0,k}^X(\hat{t}, \hat{\theta})$ and $R_{1,k}^X(\hat{t}, \hat{\theta})$ which intervene in (Eq K-1) can be expressed as in (Eq K-2) and (Eq K-3).

If k is even (first term of (Eq K-1)):

$$\text{Re}\{R_{1,k}^X(\hat{t}, \hat{\theta})\} = \sqrt{\frac{2E_b}{T_s}} [\cos(\varepsilon_\theta) \text{Re}\{\tilde{R}_{1,k}^X(\hat{t})\} - \sin(\varepsilon_\theta) \text{Im}\{\tilde{R}_{1,k}^X(\hat{t})\}] \\ \text{Im}\{R_{0,k}^X(\hat{t}, \hat{\theta})\} = \sqrt{\frac{2E_b}{T_s}} [\cos(\varepsilon_\theta) \text{Im}\{\tilde{R}_{0,k}^X(\hat{t})\} + \sin(\varepsilon_\theta) \text{Re}\{\tilde{R}_{0,k}^X(\hat{t})\}] \quad (\text{Eq K-2})$$

If k is odd (second term of (Eq K-1)):

$$Re\{R_{0,k}^X(\hat{t}, \hat{\theta})\} = \sqrt{\frac{2E_b}{T_s}} [\cos(\varepsilon_\theta) Re\{\tilde{R}_{0,k}^X(\hat{t})\} - \sin(\varepsilon_\theta) Im\{\tilde{R}_{0,k}^X(\hat{t})\}] \quad (\text{Eq K-3})$$

$$Im\{R_{1,k}^X(\hat{t}, \hat{\theta})\} = \sqrt{\frac{2E_b}{T_s}} [\cos(\varepsilon_\theta) Im\{\tilde{R}_{1,k}^X(\hat{t})\} + \sin(\varepsilon_\theta) Re\{\tilde{R}_{1,k}^X(\hat{t})\}]$$

In addition, keeping in mind that $\alpha_{0,k-z} \in \mathbb{R}$ if $k-z$ is odd and $\alpha_{0,k-z} \in i\mathbb{R}$ if $k-z$ is even, and $\alpha_{1,k-z} \in i\mathbb{R}$ if $k-z$ is odd and $\alpha_{1,k-z} \in \mathbb{R}$ if $k-z$ is even, real part and imaginary parts of $\tilde{R}_{0,k}^X(\hat{t})$ and $\tilde{R}_{1,k}^X(\hat{t})$ can be expressed as in (Eq K-4) and (Eq K-5).

If k is even:

$$\begin{aligned} Re\{\tilde{R}_{0,k}^X(\hat{t})\} &= \sum_{\substack{z=-5 \\ z \text{ odd} \\ 5}}^5 \tilde{\alpha}_{0,k-z} K_{C_0}(zT_s - \varepsilon_\tau + \beta_X \Delta T) + \sum_{\substack{z=-5 \\ z \text{ even} \\ 5}}^5 \tilde{\alpha}_{1,k-z} K_{C_1 C_0}(zT_s - \varepsilon_\tau + \beta_X \Delta T) \\ Im\{\tilde{R}_{0,k}^X(\hat{t})\} &= \sum_{\substack{z=-5 \\ z \text{ even} \\ 5}}^5 \tilde{\alpha}_{0,k-z} K_{C_0}(zT_s - \varepsilon_\tau + \beta_X \Delta T) + \sum_{\substack{z=-5 \\ z \text{ odd} \\ 5}}^5 \tilde{\alpha}_{1,k-z} K_{C_1 C_0}(zT_s - \varepsilon_\tau + \beta_X \Delta T) \\ Re\{\tilde{R}_{1,k}^X(\hat{t})\} &= \sum_{\substack{z=-5 \\ z \text{ odd} \\ 5}}^5 \tilde{\alpha}_{0,k-z} K_{C_1 C_0}(-zT_s + \varepsilon_\tau - \beta_X \Delta T) + \sum_{\substack{z=-5 \\ z \text{ even} \\ 5}}^5 \tilde{\alpha}_{1,k-z} K_{C_1}(zT_s - \varepsilon_\tau + \beta_X \Delta T) \\ Im\{\tilde{R}_{1,k}^X(\hat{t})\} &= \sum_{\substack{z=-5 \\ z \text{ even} \\ 5}}^5 \tilde{\alpha}_{0,k-z} K_{C_1 C_0}(-zT_s + \varepsilon_\tau - \beta_X \Delta T) + \sum_{\substack{z=-5 \\ z \text{ odd} \\ 5}}^5 \tilde{\alpha}_{1,k-z} K_{C_1}(zT_s - \varepsilon_\tau + \beta_X \Delta T) \end{aligned} \quad (\text{Eq K-4})$$

If k is odd:

$$\begin{aligned} Re\{\tilde{R}_{0,k}^X(\hat{t})\} &= \sum_{\substack{z=-5 \\ z \text{ even} \\ 5}}^5 \tilde{\alpha}_{0,k-z} K_{C_0}(zT_s - \varepsilon_\tau + \beta_X \Delta T) + \sum_{\substack{z=-5 \\ z \text{ odd} \\ 5}}^5 \tilde{\alpha}_{1,k-z} K_{C_1 C_0}(zT_s - \varepsilon_\tau + \beta_X \Delta T) \\ Im\{\tilde{R}_{0,k}^X(\hat{t})\} &= \sum_{\substack{z=-5 \\ z \text{ odd} \\ 5}}^5 \tilde{\alpha}_{0,k-z} K_{C_0}(zT_s - \varepsilon_\tau + \beta_X \Delta T) + \sum_{\substack{z=-5 \\ z \text{ even} \\ 5}}^5 \tilde{\alpha}_{1,k-z} K_{C_1 C_0}(zT_s - \varepsilon_\tau + \beta_X \Delta T) \\ Re\{\tilde{R}_{1,k}^X(\hat{t})\} &= \sum_{\substack{z=-5 \\ z \text{ even} \\ 5}}^5 \tilde{\alpha}_{0,k-z} K_{C_1 C_0}(-zT_s + \varepsilon_\tau - \beta_X \Delta T) + \sum_{\substack{z=-5 \\ z \text{ odd} \\ 5}}^5 \tilde{\alpha}_{1,k-z} K_{C_1}(zT_s - \varepsilon_\tau + \beta_X \Delta T) \\ Im\{\tilde{R}_{1,k}^X(\hat{t})\} &= \sum_{\substack{z=-5 \\ z \text{ odd} \\ 5}}^5 \tilde{\alpha}_{0,k-z} K_{C_1 C_0}(-zT_s + \varepsilon_\tau - \beta_X \Delta T) + \sum_{\substack{z=-5 \\ z \text{ even} \\ 5}}^5 \tilde{\alpha}_{1,k-z} K_{C_1}(zT_s - \varepsilon_\tau + \beta_X \Delta T) \end{aligned} \quad (\text{Eq K-5})$$

Development of noise free delay discriminator

Let us now develop $Re\{R_{0,k}^P(\hat{t}, \hat{\theta})\}(Re\{R_{0,k}^L(\hat{t}, \hat{\theta})\} - Re\{R_{0,k}^E(\hat{t}, \hat{\theta})\})$ in (Eq K-1) when k is odd. The development is done in (Eq 7-1), denoting $\Delta\tilde{R}_{0,k}(\hat{t}) = \tilde{R}_{0,k}^L(\hat{t}, \hat{\theta}) - \tilde{R}_{0,k}^E(\hat{t}, \hat{\theta})$ and using results of (Eq K-2) to (Eq K-5).

$$\begin{aligned} &Re\{R_{0,k}^P(\hat{t}, \hat{\theta})\}(Re\{R_{0,k}^L(\hat{t}, \hat{\theta})\} - Re\{R_{0,k}^E(\hat{t}, \hat{\theta})\}) \\ &= \frac{2E_b}{T_s} \left[\begin{array}{l} \cos^2(\varepsilon_\theta) Re\{\tilde{R}_{0,k}^P(\hat{t}, \hat{\theta})\} Re\{\Delta\tilde{R}_{0,k}(\hat{t}, \hat{\theta})\} \\ + \sin^2(\varepsilon_\theta) Im\{\tilde{R}_{0,k}^P(\hat{t}, \hat{\theta})\} Im\{\Delta\tilde{R}_{0,k}(\hat{t}, \hat{\theta})\} \\ - \cos(\varepsilon_\theta) \sin(\varepsilon_\theta) Re\{\tilde{R}_{0,k}^P(\hat{t}, \hat{\theta})\} Im\{\Delta\tilde{R}_{0,k}(\hat{t}, \hat{\theta})\} \\ - \cos(\varepsilon_\theta) \sin(\varepsilon_\theta) Im\{\tilde{R}_{0,k}^P(\hat{t}, \hat{\theta})\} Re\{\Delta\tilde{R}_{0,k}(\hat{t}, \hat{\theta})\} \end{array} \right] \quad (\text{Eq 7-1}) \end{aligned}$$

Next, the first term $Re\{\tilde{R}_{0,k}^P(\hat{t}, \hat{\theta})\}Re\{\Delta\tilde{R}_{0,k}(\hat{t}, \hat{\theta})\}$ of (Eq 7-1) is developed in (Eq K-6).

$$\begin{aligned}
& Re\{\tilde{R}_{0,k}^p(\hat{t}, \hat{\theta})\} Re\{\Delta\tilde{R}_{0,k}(\hat{t}, \hat{\theta})\} \\
&= \left[\sum_{\substack{z=-5 \\ z \text{ even}}}^5 \tilde{\alpha}_{0,k-z} K_{C_0}(zT_s - \varepsilon_\tau) + \sum_{\substack{z=-5 \\ z \text{ odd}}}^5 \tilde{\alpha}_{1,k-z} K_{C_1 C_0}(zT_s - \varepsilon_\tau) \right] \\
&\times \left[\sum_{\substack{z=-5 \\ z \text{ even}}}^5 \tilde{\alpha}_{0,k-z} \Delta K_{C_0}(zT_s - \varepsilon_\tau) + \sum_{\substack{z=-5 \\ z \text{ odd}}}^5 \tilde{\alpha}_{1,k-z} \Delta K_{C_1 C_0}(zT_s - \varepsilon_\tau) \right] \\
&= \left[\sum_{\substack{z=-5 \\ z \text{ even}}}^5 \tilde{\alpha}_{0,k-z}^2 K_{C_0}(zT_s - \varepsilon_\tau) \Delta K_{C_0}(zT_s - \varepsilon_\tau) \right. \\
&\quad \left. + \sum_{\substack{z=-5 \\ z \text{ odd}}}^5 \tilde{\alpha}_{1,k-z}^2 K_{C_1 C_0}(zT_s - \varepsilon_\tau) \Delta K_{C_1 C_0}(zT_s - \varepsilon_\tau) \right] \\
&\quad + S_{other}
\end{aligned} \tag{Eq K-6}$$

S_{other} gather all double sums of (Eq K-6). From a similar demonstration than the one done in Appendix J, its contribution to the noise free discriminator response can be neglected. In addition, note that $\tilde{\alpha}_{0,k-z}^2$ and $\tilde{\alpha}_{1,k-z}^2$ are equal to 1.

The contribution of all other terms contributing in $D_\tau(\hat{t})$ can be computed in a similar way. Eventually, $D_\tau(\hat{t})$ can be simplified as in (Eq K-7).

$$\begin{aligned}
D_\tau(\hat{t}) &= \frac{2E_b}{T_s} \frac{1}{2\Delta T} (K_b + 1) \left(\cos^2(\varepsilon_\theta) \left(S_{\tau, C_0}^{even}(\varepsilon_\tau) + 2S_{\tau, C_1 C_0}^{odd}(\varepsilon_\tau) + S_{\tau, C_1}^{even}(\varepsilon_\tau) \right) \right. \\
&\quad \left. + \sin^2(\varepsilon_\theta) \left(S_{\tau, C_0}^{odd}(\varepsilon_\tau) + 2S_{\tau, C_1 C_0}^{even}(\varepsilon_\tau) + S_{\tau, C_1}^{odd}(\varepsilon_\tau) \right) \right) \\
S_{\tau, C}^{even}(\varepsilon_\tau) &= \sum_{\substack{z=-5 \\ z \text{ even}}}^5 K_C(zT_s - \varepsilon_\tau) \Delta K_C(zT_s - \varepsilon_\tau) \\
S_{\tau, C}^{odd}(\varepsilon_\tau) &= \sum_{\substack{z=-5 \\ z \text{ odd}}}^5 K_C(zT_s - \varepsilon_\tau) \Delta K_C(zT_s - \varepsilon_\tau)
\end{aligned} \tag{Eq K-7}$$

With $C \in \{C_0, C_1, C_1 C_0\}$.

Coefficients $S_{\tau, C}^{even}(\varepsilon_\tau)$ and $S_{\tau, C}^{odd}(\varepsilon_\tau)$ can be developed using first order Taylor expansion formula supposing that ε_τ is small enough (linearity region). The development is done in (Eq K-8).

$$\begin{aligned}
S_{\tau, C}^{even}(\varepsilon_\tau) &= \sum_{\substack{z=-5 \\ z \text{ even}}}^5 K_C(zT_s - \varepsilon_\tau) \Delta K_C(zT_s - \varepsilon_\tau) \\
&= \sum_{\substack{z=-5 \\ z \text{ even}}}^5 \left[\left(K_C(zT_s) - \varepsilon_\tau \frac{dK_C}{dx}(zT_s) \right) \left(K_C(zT_s + \Delta T) - \varepsilon_\tau \frac{dK_C}{dx}(zT_s + \Delta T) \right) \right. \\
&\quad \left. - \left(K_C(zT_s) + \varepsilon_\tau \frac{dK_C}{dx}(zT_s) \right) \left(-K_C(zT_s - \Delta T) + \varepsilon_\tau \frac{dK_C}{dx}(zT_s - \Delta T) \right) \right]
\end{aligned} \tag{Eq K-8}$$

$$= \left(\begin{array}{l} \sum_{\substack{z=-5 \\ z \text{ even}}}^5 K_C(zT_s)K_C(zT_s + \Delta T) - \sum_{\substack{z=-5 \\ z \text{ even}}}^5 K_C(zT_s)K_C(zT_s - \Delta T) \\ -\varepsilon_\tau \left(\sum_{\substack{z=-5 \\ z \text{ even}}}^5 K_C(zT_s) \frac{dK_C}{dx}(zT_s + \Delta T) - \sum_{\substack{z=-5 \\ z \text{ even}}}^5 K_C(zT_s) \frac{dK_C}{dx}(zT_s - \Delta T) \right) \\ -\varepsilon_\tau \left(\sum_{\substack{z=-5 \\ z \text{ even}}}^5 \frac{dK_C}{dx}(zT_s)K_C(zT_s + \Delta T) - \sum_{\substack{z=-5 \\ z \text{ even}}}^5 \frac{dK_C}{dx}(zT_s)K_C(zT_s - \Delta T) \right) + o(\varepsilon_\tau) \end{array} \right)$$

Making the variable change $z' = -z$ in the green terms of (Eq K-8), and keeping in mind that K_C is even and $\frac{dK_C}{dx}$ is odd, simplification of (Eq K-9) can be applied.

$$\begin{aligned} \sum_{\substack{z=-5 \\ z \text{ even}}}^5 K_C(zT_s)K_C(zT_s - \Delta T) &= \sum_{\substack{z=-5 \\ z \text{ even}}}^5 K_C(zT_s)K_C(zT_s + \Delta T) \\ \sum_{\substack{z=-5 \\ z \text{ even}}}^5 K_C(zT_s) \frac{dK_C}{dx}(zT_s - \Delta T) &= - \sum_{\substack{z=-5 \\ z \text{ even}}}^5 K_C(zT_s) \frac{dK_C}{dx}(zT_s + \Delta T) \\ \sum_{\substack{z=-5 \\ z \text{ even}}}^5 \frac{dK_C}{dx}(zT_s)K_C(zT_s - \Delta T) &= - \sum_{\substack{z=-5 \\ z \text{ even}}}^5 \frac{dK_C}{dx}(zT_s)K_C(zT_s + \Delta T) \end{aligned} \quad (\text{Eq K-9})$$

Eventually, $S_{\tau,C}^{even}(\varepsilon_\tau)$ can be simplified in the linearity region by (Eq K-10), for $C \in \{C_0, C_1, C_1 C_0\}$.

$$\begin{aligned} S_{\tau,C}^{even}(\varepsilon_\tau) &= -2\varepsilon_\tau C_{\tau,C}^{even} \\ C_{\tau,C}^{even} &= \sum_{\substack{z=-5 \\ z \text{ even}}}^5 \left[K_C(zT_s) \frac{dK_C}{dx}(zT_s + \Delta T) + \frac{dK_C}{dx}(zT_s)K_C(zT_s + \Delta T) \right] \end{aligned} \quad (\text{Eq K-10})$$

The same development can be done for $S_{\tau,C}^{odd}(\varepsilon_\tau)$. Finally, under its linearity region, the non-normalized noise free delay discriminator can be simplified by (Eq K-11).

$$D_\tau(\hat{t}) = -\frac{2E_b}{T_s} \frac{1}{\Delta T} (K_b + 1) \varepsilon_\tau \left(\cos^2(\varepsilon_\theta) (C_{\tau,C_0}^{even} + 2C_{\tau,C_1 C_0}^{odd} + C_{\tau,C_1}^{even}) + \sin^2(\varepsilon_\theta) (C_{\tau,C_0}^{odd} + 2C_{\tau,C_1 C_0}^{even} + C_{\tau,C_1}^{odd}) \right) \quad (\text{Eq K-11})$$

K-2 Normalization of the delay discriminator

It is proposed to use the normalization factor introduced in (Eq 6-55) and reminded in (Eq K-12) to normalize $D_\tau(\hat{t})$.

$$\begin{aligned} N_2 &= \frac{1}{2\Delta T} \sum_{\substack{k=k_0 \\ k \text{ even}}}^{k_0+K_b} \left[\text{Re}\{R_{1,k}^P(\hat{t}, \hat{\theta})\}(\text{Re}\{R_{1,k}^L(\hat{t}, \hat{\theta})\} + \text{Re}\{R_{1,k}^E(\hat{t}, \hat{\theta})\}) \right. \\ &\quad \left. + \text{Im}\{R_{0,k}^P(\hat{t}, \hat{\theta})\}(\text{Im}\{R_{0,k}^L(\hat{t}, \hat{\theta})\} + \text{Im}\{R_{0,k}^E(\hat{t}, \hat{\theta})\}) \right] \\ &\quad + \frac{1}{2\Delta T} \sum_{\substack{k=k_0 \\ k \text{ odd}}}^{K_b} \left[\text{Re}\{R_{0,k}^P(\hat{t}, \hat{\theta})\}(\text{Re}\{R_{0,k}^L(\hat{t}, \hat{\theta})\} + \text{Re}\{R_{0,k}^E(\hat{t}, \hat{\theta})\}) \right. \\ &\quad \left. + \text{Im}\{R_{1,k}^P(\hat{t}, \hat{\theta})\}(\text{Im}\{R_{1,k}^L(\hat{t}, \hat{\theta})\} + \text{Im}\{R_{1,k}^E(\hat{t}, \hat{\theta})\}) \right] \end{aligned} \quad (\text{Eq K-12})$$

The difference between (Eq 1) and (Eq 6-55) is that early and late matched filter outputs are summed in (Eq 6-55). The normalization factor N_2 is expected to not depend on ε_τ in the linearity region.

Re-using the same development from (Eq K-1) to (Eq K-8), it can be shown that the normalization factor N_2 can be expressed as in (Eq K-13).

$$N_2 = \frac{2E_b}{T_s} (K_b + 1) \frac{1}{\Delta T} \left(\cos^2 \varepsilon_\theta \left(S_{N_2, C_0}^{even}(\varepsilon_\tau) + 2S_{N_2, C_1 C_0}^{odd}(\varepsilon_\tau) + S_{N_2, C_1}^{even}(\varepsilon_\tau) \right) \right. \\ \left. \sin^2 \varepsilon_\theta \left(S_{N_2, C_0}^{odd}(\varepsilon_\tau) + 2S_{N_2, C_1 C_0}^{even}(\varepsilon_\tau) + S_{N_2, C_1}^{odd}(\varepsilon_\tau) \right) \right) \\ S_{N_2, C}^{even}(\varepsilon_\tau) = \sum_{\substack{z=-5 \\ z \text{ even} \\ 5}}^5 K_C(zT_s - \varepsilon_\tau) (K_C(zT_s - \varepsilon_\tau + \Delta T) + K_C(zT_s - \varepsilon_\tau - \Delta T)) \\ S_{N_2, C}^{odd}(\varepsilon_\tau) = \sum_{\substack{z=-5 \\ z \text{ odd} \\ 5}}^5 K_C(zT_s - \varepsilon_\tau) (K_C(zT_s - \varepsilon_\tau + \Delta T) + K_C(zT_s - \varepsilon_\tau - \Delta T)) \quad (\text{Eq K-13})$$

From (Eq K-13), $S_{N_2, C}^{even}$ and $S_{N_2, C}^{odd}$ are further developed in order to prove that N_2 does not depend on ε_τ in the linearity region.

First order Taylor development of $S_{N_2, C}^{even}(\varepsilon_\tau)$ and $S_{N_2, C}^{odd}(\varepsilon_\tau)$ is detailed in (Eq K-14).

$$S_{N_2, C}^{odd}(\varepsilon_\tau) = 2 \sum_{\substack{z=-5 \\ z \text{ even} \\ 5}}^5 K_C(zT_s) K_C(zT_s + \Delta T) + o(\varepsilon_\tau) \\ S_{N_2, C}^{even}(\varepsilon_\tau) = 2 \sum_{\substack{z=-5 \\ z \text{ odd} \\ 5}}^5 K_C(zT_s) K_C(zT_s + \Delta T) + o(\varepsilon_\tau) \quad (\text{Eq K-14})$$

As a consequence, N_2 can be simplified by (Eq K-15).

$$N_2 = \frac{2E_b}{T_s} (K_b + 1) \frac{1}{\Delta T} \left(\cos^2(\varepsilon_\theta) (C_{N_2, C_0}^{even} + 2C_{N_2, C_1 C_0}^{odd} + C_{N_2, C_1}^{even}) \right. \\ \left. + \sin^2(\varepsilon_\theta) (C_{N_2, C_0}^{odd} + 2C_{N_2, C_1 C_0}^{even} + C_{N_2, C_1}^{odd}) \right) \\ C_{N_2, C}^{even} = \sum_{\substack{z=-5 \\ z \text{ even} \\ 5}}^5 K_C(zT_s) K_C(zT_s + \Delta T) \\ C_{N_2, C}^{odd} = \sum_{\substack{z=-5 \\ z \text{ odd} \\ 5}}^5 K_C(zT_s) K_C(zT_s + \Delta T) \quad (\text{Eq K-15})$$

It is therefore proposed to introduce the normalized delay discriminator \bar{D}_τ defined by (Eq K-16).

$$\bar{D}_\tau(\hat{t}) = \frac{D_\tau(\hat{t})}{N_2} \frac{C_{N_2, C_0}^{even} + 2C_{N_2, C_1 C_0}^{odd} + C_{N_2, C_1}^{even}}{C_{\tau, C_0}^{even} + 2C_{\tau, C_1 C_0}^{odd} + C_{\tau, C_1}^{even}} \quad (\text{Eq K-16})$$

Providing that ε_τ and ε_θ are small enough, and that K_b is sufficiently high, $\bar{D}_\tau(\hat{t})$ can be approximated by ε_τ . Note that if ε_θ is too high, the proposed normalization may be not efficient.

References

- [1] SESAR Joint Undertaking, "European Drones Outlook Study - Unlocking the value for Europe," 2016.
- [2] J. Antunes, "UAVs and Airplanes Flying in a Single European Sky," *Commercial UAV news*, 2016.
- [3] EASA, "Drone Incident Management at Aerodromes - Part 1: The challenge of unauthorised drones in the surroundings of aerodromes," 2021.
- [4] T. Essary, "These Drone-Hunting Eagles Aren't Messing Around," *Time*, 2017.
- [5] C. Vallance, "Anti-drone laser weapon hub to be created in Scotland," *BBC*, 2022.
- [6] RTCA, "DO 235C - Assessment of Radio Frequency Interference Relevant to the GNSS L1 Frequency Band," 2022.
- [7] RTCA, "DO 292A - Assessment of Radio Frequency Interference Relevant to the GNSS L5/E5A Frequency Band," 2022.
- [8] RTCA, "DO-362 - Command and Control (C2) Data Link Minimum Operational Performance Standards (MOPS) (Terrestrial)." 2016.
- [9] RTCA, "DO-377 - Minimum Aviation System Performance Standards for C2 Link Systems Supporting Operations of Unmanned Aircraft Systems in U.S. Airspace." 2019.
- [10] RTCA, "DO 235B - Assessment of Radio Frequency Interference Relevant to the GNSS L1 Frequency Band," Mar. 2008.
- [11] RTCA, "DO 229E - Minimum Operational Performance Standards (MOPS) for GPS/WAAS Airborne Equipment," Dec. 2016.
- [12] RTCA, "DO 292 - Assessment of Radio Frequency Interference Relevant to the GNSS L5/E5A Frequency Band," Jul. 2004.
- [13] Eurocae, "ED259 - Minimum Operational Performance Standard for Galileo/Global Positioning System/Satellite Based Augmentation System Airborne Equipment," 2023.
- [14] International Telecommunication Union, "Radio Regulations - Articles," vol. 1, p. 442, 2020.
- [15] International Civil Aviation Organization (ICAO), "International standards and recommended practices for aeronautical telecommunications," *Annex 10 to the convention of international civil aviation*, 2020.
- [16] GMV, "SBAS systems," 2011. https://gssc.esa.int/navipedia/index.php/SBAS_Systems
- [17] Google, "GBAS ground station." <https://www.google.com/maps/d/viewer?mid=14gN6lowjgVlIkjwgKKIUyJz6OXQ&ll=2.874751533561095%2C0.630702798107805&z=2>
- [18] ICAO, "Global Navigation Satellite System (GNSS) Manual - Doc 9849 AN/457." 2005.
- [19] A. Martineau, "Performance of Receiver Autonomous Integrity Monitoring (RAIM) for Vertically Guided Approaches," 2008.
- [20] SAIC (GPS SE&I), "NAVSTAR GPS Space Segment/Navigation User Interfaces - IS GPS 200M," p. 245, 2021.
- [21] GSA, "European GNSS (Galileo) Open Service - Signal in space Interface Control Documents," 2021.
- [22] J.-A. Avila-Rodriguez *et al.*, "CBOC: an implementation of MBOC," in *CNES-ESA, 1st Workshop on GALILEO Signals and Signal Processing*, Toulouse, France, 2006, p. 11.
- [23] SAIC (GPS SE&I), "NAVSTAR GPS Space Segment/User Segment L5 Interfaces - IS GPS 705H," p. 125, 2021.
- [24] N. Cs and A. Dempster, "The Galileo E5 AltBOC: Understanding the Signal Structure," Jan. 2009.
- [25] A. J. Van Dierendonck, "GPS Receivers," in *Global Positioning System: Theory and Applications*, American Institute of Aeronautics and Astronautics, Inc., vol. 163, 1996.
- [26] J. Holmes, *Spread Spectrum Systems for GNSS and Wireless Communications*, Artech House. 2007.
- [27] M. Foucras *et al.*, "Study on the cross-correlation of GNSS signals and typical approximations," *GPS Solut*, vol. 21, no. 2, pp. 293–306, Apr. 2017, doi: 10.1007/s10291-016-0556-7.

- [28] C. Macabiau, L. Ries, F. Bastide, and J.-L. Issler, "GPS L5 receiver implementation issues," in *ION GPS/GNSS 2003, 16th International Technical Meeting of the Satellite Division of The Institute of Navigation*, Portland, United States, Sep. 2003, p. pp 153-164. [Online]. Available: <https://hal-enac.archives-ouvertes.fr/hal-01021723>
- [29] O. Julien, J.-L. Issler, and L. Ries, "Investigation of Galileo E1 OS/SoL acquisition, tracking and data demodulation thresholds for civil aviation," Portland, OR, Sep. 2011, pp. 1264–1276.
- [30] D. Borio, L. Lo Presti, and P. Mulassano, "Spectral separation coefficients for digital GNSS receivers," Florence, Italy, 2006.
- [31] J. Betz, "Effect of Partial-Band Interference on Receiver Estimation of C/N0: Theory," *Proceedings of the 2001 National Technical Meeting of The Institute of Navigation*, Long Beach, California, pp. 817–828, Jan. 2001.
- [32] J. L. Madrid-Cobos, A. Bodero-Alonso, E. Chatre, A. Konovaltsev, C. J. Hegarty, and I. Fernandez-Hernandez, "Keeping interference at bay for critical infrastructure," *GPS World*, 2020.
- [33] C. J. Hegarty, "Analytical Model for GNSS Receiver Implementation Losses," *Navigation: Journal of the Institute of Navigation*, pp. 29–44, Mar. 2011.
- [34] ICD Galileo, "European GNSS (Galileo) Open Service Signal-in-Space Interface Control Document," 2021.
- [35] M. Petovello, E. Falletti, M. Pini, and L. Lo Presti, "Are C/N0 estimators equivalent in all situations?," *Inside GNSS*, pp. 20–27, 2010.
- [36] M. Pini, E. Falletti, and M. Fantino, "Performance Evaluation of C/N0 Estimators Using a Real Time GNSS Software Receiver," in *2008 IEEE 10th International Symposium on Spread Spectrum Techniques and Applications*, Bologna, Italy, 2008, pp. 32–36. doi: 10.1109/ISSSTA.2008.12.
- [37] A. Bourkane, "Estimation du rapport signal à bruit d'un signal GPS par filtrage non linéaire," Université du Littoral Côte d'Opale, 2015.
- [38] N. Beaulieu, A. Toms, and D. Pauluzzi, "Comparison of four SNR estimators for QPSK modulations," *IEEE Communications Letters*, vol. 4, no. 2, pp. 43–45, 2000, doi: 10.1109/4234.824751.
- [39] M. Bakkali, A. Stephenne, and S. Affes, "Generalized Moment-Based Method for SNR Estimation," in *2007 IEEE Wireless Communications and Networking Conference*, Kowloon, China, 2007, p. pp 2226-2230. doi: 10.1109/WCNC.2007.416.
- [40] A. Garcia-Pena, C. Macabiau, O. Julien, M. Mabilieu, and P. Durel, "Impact of DME/TACAN on GNSS L5/E5a Receiver," in *2020 International Technical Meeting of The Institute of Navigation*, San Diego, California, Feb. 2020, pp. 207–221. doi: 10.33012/2020.17207.
- [41] RTCA, "DO-160G - Environmental Conditions and Test Procedures for Airborne Equipment," 2010.
- [42] A. Garcia-Pena, C. Macabiau, J. Ashley, D. Baraban, P. Durel, and M. Mabilieu, "Model and observation of the impact of JTIDS/MIDS on GNSS C/N_0 degradation," in *2020 IEEE/ION Position, Location and Navigation Symposium (PLANS)*, Portland, OR, USA, Apr. 2020, pp. 584–595. doi: 10.1109/PLANS46316.2020.9110159.
- [43] J. J. Ely, T. X. Nguyen, S. V. Koppen, and J. H. Beggs, "Wireless Phone Threat Assessment and New Wireless Technology Concerns for Aircraft Navigation Radios."
- [44] T. X. Nguyen, S. V. Koppen, J. J. Ely, R. A. Williams, L. J. Smith, and M. T. P. Salud, "Portable wireless device threat assessment for aircraft navigation radios," in *2004 International Symposium on Electromagnetic Compatibility (IEEE Cat. No.04CH37559)*, Silicon Valley, CA, USA, 2004, pp. 809–814. doi: 10.1109/ISEMC.2004.1349926.
- [45] K. M. Peterson and R. J. Erlandson, "Analytic Statistical Model for Aggregate Radio Frequency Interference to Airborne GPS Receivers from Ground-Based Emitters: Analytic Statistical Model for Aggregate Radio Frequency Interference," *Navigation*, vol. 59, no. 1, pp. 25–35, Mar. 2012, doi: 10.1002/navi.4.
- [46] ITU, "RECOMMENDATION ITU-R P.528-5 - A propagation prediction method for aeronautical mobile and radionavigation services using the VHF, UHF and SHF bands," p. 29, 2021.

- [47] O. Towlson, D. Payne, P. Eliardsson, V. Manikundalam, M. Pattinson, and M. Dumville, "GNSS Strike 3 project: Threat database analysis report," GSA, 2019.
- [48] S. Pullen, G. Gao, C. Tedeschi, and J. Warburton, "The Impact of Uninformed RF Interference on GBAS and Potential Mitigations," *Proceedings of the 2012 International Technical Meeting of The Institute of Navigation*, pp. 780–789, 2012.
- [49] Inside GNSS, "FCC Fines Operator of GPS Jammer That Affected Newark Airport GBAS," *Inside GNSS*, 2013.
- [50] T. Kraus, R. Bauernfeind, and B. Eissfeller, "Survey of In-Car Jammers - Analysis and Modeling of the RF signals and IF samples (suitable for active signal cancellation)," in *24th International Technical Meeting of The Satellite Division of the Institute of Navigation*, Portland, Oregon, Sep. 2011, pp. 430–435.
- [51] RTCA, "DO-301 - Minimum Operational Performance Standards (MOPS) for GNSS Airborne Active Antenna Equipment for the L1 Frequency Band," Dec. 2006.
- [52] Eurocae, "ED 259A - Minimum operational performance standard for Galileo/Global Positioning System/satellite-based augmentation system airborne equipment," ED-259A, 2019.
- [53] RTCA, "DO-373 - MOPS for GNSS Airborne Active Antenna Equipment for the L1/E1 and L5/E5a Frequency Bands," 2018.
- [54] M. Johnson and R. Erlandson, "GNSS Receiver Interference: Susceptibility and Civil Aviation Impact," in *Proceedings of the 8th International Technical Meeting of the Satellite Division of The Institute of Navigation (ION GPS 1995)*, Palm Springs, 1995, pp. 781–791.
- [55] ICAO, *ICAO Cir 328: Unmanned aircraft systems (UAS)*. Montréal: International Civil Aviation Organization, 2011.
- [56] ITU, "ITU-R M.2171 - Characteristics of Unmanned Aircraft Systems and Spectrum Requirements to Support their Safe Operation in Non-Segregated Airspace." 2009.
- [57] ICAO, "ICAO Unmanned Aviation Bulletin 2020/1," p. 2, 2020.
- [58] Canso, "ICAO GREPECAS/18 - WP/20: Project Loon - Floating Cell Phone Towers in the Sky," Punta Cana, Dominican Republic, 2018.
- [59] ICAO, "Remotely Piloted Aircraft system (RPAS) Concept of Operations (CONOPS) for International IFR operations," p. 30, 2017.
- [60] ICAO, "ICAO Model UAS Regulations - Part 101 and Part 102." 2020.
- [61] ICAO, "ICAO model UAS Regulations- Part 149," p. 11, 2020.
- [62] European Commission, *Commission Delegated Regulation (EU) 2019/945*. 2019.
- [63] European Commission, *Commission Delegated Regulation (EU) 2019/947*. 2019.
- [64] DSAC, "Usages de Loisir et Professionnels Simplifiés des Aéronefs sans Equipages à Bord - Catégorie Ouverte." 2022.
- [65] DSAC, "Usages de Loisir et Professionnels Simplifiés des Aéronefs sans Equipages à Bord - Catégorie Spécifique." 2022.
- [66] Eurocae, "WG-105 Strategy Terms of Reference." 2016.
- [67] JARUS, "RPAS 'Required C2 Performance' (RLP) Concept." 2016.
- [68] ITU, "Radio Regulations." 2020.
- [69] J. G. Proakis, *Digital Communications*, McGraw-Hill International Edition. 2001.
- [70] A. Garcia Peña, C. Macabiau, G. Novella, O. Julien, M. Mabileau, and P. Durel, "RFI GNSS L5/E5a Mask Derivation," in *Proceedings of the 33rd International Technical Meeting of the Satellite Division of The Institute of Navigation (ION GNSS+ 2020)*, 2020, pp. 188–205. doi: <https://doi.org/10.33012/2020.17540>.
- [71] Eurocontrol, "EUROCONTROL Guidelines on a Process for Civil-Military GNSS Interference Testing," 2021.
- [72] C. J. Hegarty, "Analytical Model for GNSS Receiver Implementation Losses," *Navigation*, vol. 58, no. 1, pp. 29–44, Mar. 2011, doi: 10.1002/j.2161-4296.2011.tb01790.x.
- [73] Code of Federal Regulations, "Title 47 Part 15 - Radio Frequency Devices." 1989.

- [74] T. X. Nguyen, S. V. Koppen, J. J. Ely, R. A. Williams, and L. J. Smith, "Portable Wireless LAN Device and Two-Way Radio Threat Assessment for Aircraft Navigation Radios," *NASA/TP-2003-212438*, p. 227, 2003.
- [75] G. Novella *et al.*, "Impact of terrestrial emitters on civil aviation GNSS receivers," in *Proceedings of the 35rd International Technical Meeting of the Satellite Division of The Institute of Navigation (ION GNSS+ 2022)*, Denver, 2022.
- [76] ITU, "RECOMMENDATION ITU-R P.676-12 - Attenuation by atmospheric gases and related effects," p. 33, 2019.
- [77] F. J. Gallego, "A population density grid of the European Union," *Population and Environment*, vol. 31, no. 6, pp. 460–473, Jul. 2010, doi: 10.1007/s11111-010-0108-y.
- [78] T. Louail *et al.*, "From mobile phone data to the spatial structure of cities," *Sci Rep*, vol. 4, no. 1, p. 5276, May 2015, doi: 10.1038/srep05276.
- [79] GSA, "European GNSS Service Center." <https://www.gsc-europa.eu/gsc-products/almanac>
- [80] N. G. Ferrara, M. Z. H. Bhuiyan, S. Söderholm, L. Ruotsalainen, and H. Kuusniemi, "A new implementation of narrowband interference detection, characterization, and mitigation technique for a software-defined multi-GNSS receiver," *GPS Solut*, vol. 22, no. 4, p. 106, Oct. 2018, doi: 10.1007/s10291-018-0769-z.
- [81] D. Borio and P. Closas, "A Fresh Look at GNSS Anti-Jamming," *Inside GNSS*, pp. 54–61, 2017.
- [82] C. H. Kang, S. Y. Kim, and C. G. Park, "A GNSS interference identification using an adaptive cascading IIR notch filter," *GPS Solut*, vol. 18, no. 4, pp. 605–613, Oct. 2014, doi: 10.1007/s10291-013-0358-0.
- [83] D. Borio, J. Fortuny-Guasch, and C. O'Driscoll, "Spectral and Spatial Characterization of GNSS Jammers," in *7th GNSS Vulnerabilities and Solutions Conference*, Baška, Krk island, Croatia, 2013, pp. 26–44.
- [84] J. E. Chin and C. E. Cook, "The Mathematics of Pulse Compression: A Problem in System Analysis," *Sperry Engineering Review*, vol. 12, pp. 11–16, 1959.
- [85] P. Laurent, "Exact and Approximate Construction of Digital Phase Modulations by Superposition of Amplitude Modulated Pulses (AMP)," *IEEE Trans. Commun.*, vol. 34, no. 2, pp. 150–160, Feb. 1986, doi: 10.1109/TCOM.1986.1096504.
- [86] E. Vassallo and M. Visintin, "Carrier phase synchronization for GMSK signals," *Int. J. Satell. Commun.*, vol. 20, no. 6, pp. 391–415, Nov. 2002, doi: 10.1002/sat.729.
- [87] M. K. Simon, "MAP-motivated carrier synchronization of GMSK based on the laurent AMP representation," 1998, p. 6.
- [88] G. K. Kaleh, "Simple coherent receivers for partial response continuous phase modulation," *IEEE Journal on Selected Areas in Communications*, vol. 7, no. 9, pp. 1427–1436, 1989, doi: 10.1109/49.44586.
- [89] C. S. Vaucher, "Appendix A: PLL Stability Limits Due to the Discrete-Time PFD/CP Operation," in *Architectures for RF frequency synthesizers*, vol. 693, 2002.
- [90] D. Collins, "A Fully Differential Phase-Locked Loop With Reduced Loop Bandwidth Variation," Masters by research, National University of Ireland, Maynooth, 2011.
- [91] O. Julien, "Design of Galileo L1F Receiver Tracking Loops," University of Calgary, Calgary, Alberta, 2005.
- [92] M. A. Mendlovitz, "Improved Hard and Soft Decision Coherent Trellis Demodulators for Partial Response Binary Continuous Phase Modulation," Unpublished, 2001. Accessed: Sep. 02, 2022. [Online]. Available: <http://rgdoi.net/10.13140/2.1.1876.1608>
- [93] G. L. Lui and K. Tsai, "VITERBI AND SERIAL DEMODULATORS FOR PRE-CODED BINARY GMSK," *International Telemetry Conference Proceedings*, p. 10, 2021.
- [94] K. Murota and K. Hirade, "GMSK Modulation for Digital Mobile Radio Telephony," *IEEE Transactions on Communications*, vol. 29, no. 7, pp. 1044–1050, 1981, doi: 10.1109/TCOM.1981.1095089.
- [95] F. Bastide, O. Julien, C. Macabiau, and B. Roturier, "Analysis of L5/E5 acquisition, tracking and data demodulation thresholds," in *Proceedings of the 15th International Technical Meeting of*

the Satellite Division of The Institute of Navigation (ION GPS 2002), Portland, OR, Sep. 2002, pp. 2196–2207.

- [96] A. J. Garcia Peña, C. Macabiau, G. Novella, O. Julien, M. Mabillean, and P. Durel, “In-band RFI GNSS L5/E5a Mask Definition,” in *ION GNSS+ 2020, 33rd International Technical Meeting of the Satellite Division of the Institute of Navigation*, Virtual event, United States, Sep. 2020, p. pp 188-205. doi: 10.33012/2020.17540.